



**D 6.1**

**DELIVERABLE**

**PROJECT INFORMATION**

Project Title: **Harmonized approach to stress tests for critical infrastructures against natural hazards**

Acronym: **STREST**

Project N°: 603389

Call N°: FP7-ENV-2013-two-stage

Project start: 01 October 2013

Duration: 36 months

**DELIVERABLE INFORMATION**

Deliverable Title: **Integrated report detailing analyses, results and proposed hierarchical set of stress tests for the six CIs covered in STREST**

Date of issue: 31 May 2016

Work Package: WP6 – Exploratory applications of new stress test concepts to critical infrastructures

Editor/Author: Kyriazis Pitilakis  
(Aristotle University of Thessaloniki)

Reviewers: Matjaž Dolšek, Anže Babič (UL)  
Simona Esposito (ETH)

REVISION: Final



Project Coordinator: Prof. Domenico Giardini  
Institution: ETH Zürich  
e-mail: [gardini@sed.ethz.ch](mailto:gardini@sed.ethz.ch)  
fax: + 41 446331065  
telephone: + 41 446332610



---

# Abstract

The exploratory application of ST@STREST multi-level framework to six key representative Critical Infrastructures (CIs) in Europe is presented, namely: a petrochemical plant in Milazzo (IT), large dams of the Valais region (CH), hydrocarbon pipelines (TK), the Gasunie national gas storage and distribution network (NL), the port infrastructure of Thessaloniki (GR) and an industrial district in the region of Tuscany (IT). The application to the selected CIs is presented following the workflow of ST@STREST, comprised by four phases: Pre-Assessment phase; Assessment phase; Decision phase; and Report phase.

*Keywords: Critical Infrastructures, Non-nuclear stress test, Extreme events, Earthquake, Tsunami, Industrial installation, Petrochemical plant, Large dams, Pipelines, Gas network, Ports, Industrial buildings*





---

## **Acknowledgments**

The research leading to these results has received funding from the European Community's Seventh Framework Programme [FP7/2007-2013] under grant agreement n° 603389.



---

## Deliverable Contributors

AUTH	Kyriazis Pitilakis Sotiris Argyroudis Stavroula Fotopoulou Stella Karafagka Anastasios Anastasiadis Dimitris Pitilakis Dimitris Raptakis Evi Riga Aggelos Tsinaris Katerina Mara
INGV	Jacopo Selva Sarfraz Iqbal Manuela Volpe Roberto Tonini Fabrizio Romano Beatriz Brizuela Alessio Piatanesi Roberto Basili Stefano Lorito
AMRA	Ernesto Salzano Anna Basco
EPFL	Anton J. Schleiss José P. Matos
KOERI	Sinan Akkar Yin Cheng Eren Uckan Mustafa Erdik
TNO	Wim Courage Johan Reinders
EUCENTRE	Helen Crowley Daniela Rodrigues



---

# Table of Contents

<b>Abstract</b> .....	<b>i</b>
<b>Acknowledgments</b> .....	<b>iii</b>
<b>Deliverable Contributors</b> .....	<b>v</b>
<b>Table of Contents</b> .....	<b>vii</b>
<b>List of Figures</b> .....	<b>xi</b>
<b>List of Tables</b> .....	<b>xxiii</b>
<b>1 Introduction</b> .....	<b>1</b>
<b>2 CI-A1 ENI/Kuwait oil refinery and petrochemical plant, Milazzo, Italy</b> .....	<b>3</b>
2.1 INTRODUCTION .....	3
2.2 PHASE 1: PRE-ASSESSMENT PHASE .....	3
2.2.1 Data collection .....	3
2.2.2 Earthquake hazard .....	6
2.2.3 Tsunami hazard .....	13
2.2.4 Risk Measures and Objectives .....	17
2.2.5 Set-up of the Stress Test.....	20
2.3 PHASE 2: ASSESSMENT PHASE .....	20
2.3.1 Component Level Assessment (ST-L1a).....	20
2.3.2 System Level Assessment for Single Hazard (ST-L2b / L2d) .....	23
2.4 PHASE 3: DECISION PHASE .....	27
2.4.1 Risk objectives check .....	27
2.4.2 Disaggregation/Sensitivity Analysis.....	30
2.4.3 Guidelines and critical events .....	31
2.5 PHASE 4: REPORT PHASE .....	34
<b>3 CI-A2 Large dams in the Valais region of Switzerland</b> .....	<b>35</b>
3.1 INTRODUCTION .....	35
3.1.1 General description of the CI .....	35
3.1.2 Summary of the proposed stress test .....	37
3.2 PHASE 1: PRE-ASSESSMENT PHASE .....	42
3.2.1 Data collection .....	42
3.2.2 Risk Measures and Objectives .....	56
3.2.3 Set-up of the Stress Test.....	57

---

3.3	PHASE 2: ASSESSMENT PHASE .....	58
3.3.1	Component Level Assessment (ST-L1a).....	58
3.3.2	System Level Assessment for Single Hazard (ST-L2b /L2d) .....	59
3.3.3	System Level Assessment for Multiple Hazards (ST-L3c / L3d) .....	60
3.4	PHASE 3: DECISION PHASE .....	74
3.4.1	Risk objectives check .....	74
3.4.2	Disaggregation/Sensitivity Analysis .....	75
3.4.3	Guidelines and critical events .....	78
3.5	PHASE 4: REPORT PHASE .....	79
<b>4</b>	<b>CI-B1 Major hydrocarbon pipelines, Turkey .....</b>	<b>81</b>
4.1	INTRODUCTION .....	81
4.2	PHASE 1: PRE-ASSESSMENT PHASE .....	82
4.2.1	Data collection .....	82
4.2.2	Risk Measures and Objectives .....	87
4.2.3	Set-up of the Stress Test.....	88
4.3	PHASE 2: ASSESSMENT PHASE .....	89
4.3.1	Component Level Assessment (ST-L1a).....	89
4.4	PHASE 3: DECISION PHASE .....	99
4.4.1	Risk objectives check and Risk mitigation strategies .....	99
4.4.2	Disaggregation/Sensitivity Analysis .....	100
4.4.3	Guidelines and critical events .....	100
<b>5</b>	<b>CI-B2 Gasunie national gas storage and distribution network, Holland</b>	<b>102</b>
5.1	INTRODUCTION .....	102
5.2	PHASE 1: PRE-ASSESSMENT PHASE .....	102
5.2.1	Data collection .....	102
5.2.2	Risk Measures and Objectives .....	108
5.2.3	Set-up of the Stress Test.....	111
5.3	PHASE 2: ASSESSMENT PHASE .....	112
5.3.1	Component Level Assessment (ST-L1a).....	112
5.3.2	System Level Assessment for Single Hazard (ST-L2a) .....	113
5.4	PHASE 3: DECISION PHASE .....	120
5.4.1	Risk objectives check .....	120
5.4.2	Disaggregation/Sensitivity Analysis .....	122
5.4.3	Guidelines and critical events .....	128

---

5.5	PHASE 4: REPORT PHASE .....	129
<b>6</b>	<b>CI-B3 Port infrastructures of Thessaloniki, Greece .....</b>	<b>130</b>
6.1	INTRODUCTION .....	130
6.2	PHASE 1: PRE-ASSESSMENT PHASE .....	131
6.2.1	Data collection .....	131
6.2.2	Risk Measures and Objectives .....	140
6.2.3	Set-up of the Stress Test.....	141
6.3	PHASE 2: ASSESSMENT PHASE .....	141
6.3.1	Component Level Assessment (ST-L1a).....	141
6.3.2	System Level Assessment for Single Hazard (ST-L2b / L2d / L3d) .....	146
6.4	PHASE 3: DECISION PHASE .....	178
6.4.1	Risk objectives check .....	178
6.4.2	Disaggregation/Sensitivity Analysis .....	178
6.4.3	Guidelines and critical events .....	180
6.5	PHASE 4: REPORT PHASE .....	181
6.6	CLASSICAL EXPERT ELICITATION IN IMPLEMENTATION OF STRESS TEST .	183
6.6.1	Introduction .....	183
6.6.2	Overview of the expert elicitation tasks .....	184
6.6.3	Elicitation experiments.....	186
6.6.4	Elicitation results.....	193
<b>7</b>	<b>CI-C1 Industrial district, Italy .....</b>	<b>211</b>
7.1	INTRODUCTION .....	211
7.2	PHASE 1: PRE-ASSESSMENT PHASE .....	211
7.2.1	Data collection .....	211
7.2.2	Risk Measures and Objectives .....	218
7.2.3	Set-up of the Stress Test.....	220
7.3	PHASE 2: ASSESSMENT PHASE .....	221
7.3.1	Component Level Assessment (ST-L1a).....	221
7.3.2	System Level Assessment for Single Hazard (ST-L2b) .....	224
7.3.3	System Level Assessment for Multiple Hazards .....	230
7.4	PHASE 3: DECISION PHASE .....	230
7.4.1	Risk objectives check .....	230
7.4.2	Disaggregation/Sensitivity Analysis .....	230
7.4.3	Guidelines and critical events .....	233

---

7.5 PHASE 4: REPORT PHASE .....	233
<b>8 Conclusions-Discussion .....</b>	<b>237</b>
<b>References .....</b>	<b>240</b>
<b>A Appendix.....</b>	<b>253</b>
<b>B Appendix.....</b>	<b>257</b>



---

## List of Figures

Fig. 2.1	Population distribution- in $-/km^2$ .....	4
Fig. 2.2	Overview of population areas considered.....	5
Fig. 2.3	Overview of population density as used in QRA.....	6
Fig. 2.4	Grid of potential epicenters around Milazzo considered in the PSHA analysis. Grid points within a 50 km radius from Milazzo are displayed as red dots .....	7
Fig. 2.5	Geometrical parameters defining the orientation of a rupture plane (taken from Aki & Richards, 1980) and schematic representation of the principal focal mechanisms, which are defined by the rake angle .....	7
Fig. 2.6	Definition of geometrical variables for the representation of dip-slip ruptures on a known fault geometry, (a) vertical longitudinal section and (b) cross-section (Chioccarelli & Iervolino, 2013) .....	8
Fig. 2.7	Probability distribution of hypocenter location along the rupture plane. Down-dip and along-strike positioning are assumed independent random variables with marginal densities shown in alignment with the relevant fault plane dimensions .....	11
Fig. 2.8	Linear regression of (log-) aspect ratio $Q=L/W$ of the rupture plane against log-rupture area.....	11
Fig. 2.9	Seismicity in terms of cumulative frequency of events surpassing given values of magnitude for each grid point in the discretization of the area around the port of Milazzo .....	12
Fig. 2.10	Hazard curve for Milazzo in terms of MAF of exceedance of PGA, calculated according to the methodology presented .....	12
Fig. 2.11	A) Map of the whole simulation domain used for the application at the target site Milazzo (Sicily, Italy). The red star is the location of a crustal event for which we provide the map of the maximum wave height ( $H_{max}$ ), as an example; The zoom highlights the points along the 50 m isobath used to produce the $H_{max}$ profiles for the input of the Cluster Analysis. B) Close-up view of the simulation domain showing the telescopic nested grids for tsunami simulation with gradually increasing resolution (0.1, 0.025, 0.00625 arc-min). C) Bathymetric image of the finest grid (resolution=0.00625 arc-min), where the locations of the 95 receiver points are shown (red points) .....	15
Fig. 2.12	A) Maximum wave height distribution originated from the crustal event indicated with the red star in Fig. 2.11 ( $M=8.0$ ); B) Time history of the corresponding wave height for one randomly selected receiver .....	16
Fig. 2.13	A) Ensemble hazard curves for one randomly selected point in the target area, for two intensity measures: Maximum Flow Depth (left) and Maximum Moment (right); in both cases, the bold red line is the mean of the Ensemble, while the dotted lines report the confidence interval in terms of 16 <sup>th</sup> and 84 <sup>th</sup> percentiles. B) Mean hazard map for flow depth considering an annual probability threshold	

---

of $10^{-4}$ . C) Mean annual probability map for a maximum moment threshold of $5 \text{ m}^3\text{s}^{-2}$ .....	17
Fig. 2.14 Steps in a QRA and most important parameters .....	18
Fig. 2.15 Main steps in a QRA and the standard methods .....	18
Fig. 2.16 Locational risk – Single causes only. Larger figures are included in Appendix I ...	28
Fig. 2.17 Location of LPG Spheres (red squares) .....	29
Fig. 2.18 Locational risk – Cumulated risks .....	30
Fig. 2.19 Location of the cross-section of the locational risk (red line) .....	31
Fig. 2.20 Locational risk transect .....	31
Fig. 2.21 Societal risk without accounting for natural hazards- with and without LPG tanks	32
Fig. 2.22 Societal risk- industrial, earthquake or tsunami induced .....	33
Fig. 2.23 Societal risk- cumulated risks .....	33
Fig. 3.1 Simulation of the propagation of a dam-break flood wave through an urban area. The time lapse between illustrations is of 20 minutes .....	36
Fig. 3.2 Implementation of two large Alpine dams in Switzerland: Les Toules and Mauvoisin. Both are placed in tributaries of the Rhone River and, in the event of a failure, the main urban areas where losses could be expected are relatively far downstream. Neither of these dams is analyzed in this document .....	38
Fig. 3.3 Overall scheme of the analysis framework, with a clear separation between upstream and downstream areas. From Salzano et al. (2015) .....	39
Fig. 3.4 Scheme of hazards, elements, system states, and interactions considered in the application of the GenMR framework to large dams. Adapted from Mignan et al. (2015) and presented in Matos et al. (2015) .....	41
Fig. 3.5 Example simulation of the dam-reservoir system affected by a 10 000 year flood and a 5 000 year return period earthquake. On top: reservoir volume evolution. In the middle: outflow evolution. In the bottom: element state evolution. Adapted from Matos et al. (2015) .....	42
Fig. 3.6 Peak ground accelerations (PGA) admitted for the area under study with uncertainty bounds.....	43
Fig. 3.7 Peak flood inflows to the reservoir.....	44
Fig. 3.8 Probability density of a flood's duration .....	44
Fig. 3.9 Probability of floods throughout the year .....	45
Fig. 3.10 Adimensionalized hydrograph of the flood events .....	45
Fig. 3.11 Probability of floods throughout the year .....	46
Fig. 3.12 Probability of bottom outlet malfunctions .....	47
Fig. 3.13 Probability of hydropower system malfunctions.....	47
Fig. 3.14 Target reservoir volumes .....	48
Fig. 3.15 Base inflows to the reservoir.....	48

---

---

Fig. 3.16	Fragility curves of damage states of the dam as a function of PGA .....	49
Fig. 3.17	Maximum outflows of the reservoir as a function of the normalized volume of the reservoir .....	50
Fig. 3.18	Fragility curves of damage states of the spillway as a function of PGA .....	50
Fig. 3.19	Fragility curves of damage states of the bottom outlet as a function of PGA .....	51
Fig. 3.20	Fragility curves of damage states of the hydropower system as a function of PGA .....	51
Fig. 3.21	Depiction of the downstream area under study and the adopted computational grid. Reproduced from Salzano et al. (2015) .....	53
Fig. 3.22	Fragility curves derived for 1 story reinforced concrete buildings. Adapted from Suppasri et al. (2013).....	54
Fig. 3.23	Fragility curves derived for 2 stories reinforced concrete buildings. Adapted from Suppasri et al. (2013).....	54
Fig. 3.24	Fragility curves derived for 3 or more stories reinforced concrete buildings. Adapted from Suppasri et al. (2013) .....	54
Fig. 3.25	Results of the ST-L2 scenario based assessment. A 10 000 year earthquake occurs when the reservoir is full.....	59
Fig. 3.26	Results of a ST-L3 scenario based assessment. A 10 000 year earthquake occurs when the reservoir is full and is followed by a 500 year flood .....	60
Fig. 3.27	Results of a ST-L3 scenario based assessment. A 20 000 year earthquake occurs when the reservoir is full and is followed by a 2 500 year flood .....	61
Fig. 3.28	Inundation resulting from an overtopping of the dam using expected breach progression parameters according to Froehlich (2008).....	62
Fig. 3.29	Illustration of the distribution of breach parameters obtainable for one single dam failure.....	64
Fig. 3.30	Sampled parameters used to characterize the domain of possible breaches .....	65
Fig. 3.31	Catalogue of 5 000 hydrographs that characterize the domain of possible outflows from the dam .....	66
Fig. 3.32	Accuracy of the SVR models in predicting hydrograph features .....	66
Fig. 3.33	Catalogue of outflow hydrographs whose downstream flood was fully simulated. Adapted from Salzano et al. (2015).....	67
Fig. 3.34	Depiction of the hexagonal tiles that cover the map .....	67
Fig. 3.35	Inundation calculated for a low peak discharge, low volume breach hydrograph..	68
Fig. 3.36	Inundation calculated for a high peak discharge, high volume breach hydrograph .....	69
Fig. 3.37	Examples of inundation depths estimated through the regression models fitted for several tiles. Points were numerically simulated. Lines correspond to interpolated values. Adapted from Salzano et al. (2015) .....	70
Fig. 3.38	Return period of 1 story reinforced concrete buildings being washed away.....	71

---

Fig. 3.39	Most likely damage to 3 or more stories reinforced concrete buildings in the event of a dam failure upstream.....	72
Fig. 3.40	Return period of buildings collapsing or being washed away as a consequence of dam failures.....	73
Fig. 3.41	F-N curve based on collapsed or washed away built volume following a dam failure upstream.....	74
Fig. 3.42	Example of a coincidence of events leading to failure.....	75
Fig. 3.43	Disaggregation of failures caused by earthquakes.....	76
Fig. 3.44	Disaggregation of failures caused by internal erosion.....	76
Fig. 3.45	Distribution of failures in time.....	77
Fig. 3.46	Distribution of earthquakes in time.....	77
Fig. 3.47	Distribution of internal erosion in time.....	77
Fig. 3.48	Distribution of floods in time.....	77
Fig. 3.49	Histogram of reservoir levels when breaches start to develop.....	78
Fig. 4.1	Overview of BTC pipeline.....	83
Fig. 4.2	Details of pipe-fault crossings #1 and # 2.....	84
Fig. 4.3	Details of pipe-fault crossings # 3.....	84
Fig. 4.4	Details of pipe-fault crossings # 4.....	85
Fig. 4.5	Details of pipe-fault crossings # 5.....	85
Fig. 4.6	Typical trench for fault crossing, Erzurum fault zone.....	87
Fig. 4.7	Grading system for the global outcome of Stress Test (Esposito et al., 2016; 2017).....	88
Fig. 4.8	Modeled and actual fault layout for Petersen et al. (2011) PFDHA approach for strike-slip earthquakes. The accuracy of observation represents the combined effects of fault mapping accuracy and rupture complexity on the modeled and actual rupture conditions (From Cheng and Akkar, 2016).....	89
Fig. 4.9	Proposed MC-based permanent fault displacement hazard assessment procedure.....	91
Fig. 4.10	Seismic hazard curves of fault displacement at the pipe-fault crossings.....	94
Fig. 4.11	Maximum tensile (a) and compressive (b) pipe strains for the pipes at pipe-fault crossings with respect to different intersection angles.....	97
Fig. 4.12	Pipeline fragility for (a) tension failure and (b) compression failure.....	98
Fig. 5.1	Selected sub system of the gas distribution network (right) located above main natural gas field (top left).....	103
Fig. 5.2	Presentation of diameters (mm) present in the modeled sub network (black lines on background indicate the earthquake zones).....	104
Fig. 5.3	Presentation of pipe wall thickness (mm) present in the modeled sub network (black lines on background indicate the earthquake zones).....	104

---

---

Fig. 5.4	Presentation of pipe yield stresses (MPa) present in the modeled sub network (black lines on background indicate the earthquake zones) .....	105
Fig. 5.5	Presentation of pipe operational pressures (bar) present in the modeled sub network (black lines on background indicate the earthquake zones).....	105
Fig. 5.6	Locations of stations in the modeled sub network: source stations (green) demand stations (red) and M&R stations (blue). Pipeline colors and color bar refer to the pressures in the pipe sections.....	106
Fig. 5.7	Division of Groningen area in seismic zones (Dost et al., 2013) .....	107
Fig. 5.8	Example of societal risk curve and guidance value. ....	109
Fig. 5.9	Indicative grading boundaries with respect to annual probabilities of exceedance for network connectivity loss $CL$ .....	110
Fig. 5.10	Schematic representation of Stress test method (Esposito et al., 2016; 2017) ...	111
Fig. 5.11	Annual failure probabilities (per km) for the pipe sections .....	112
Fig. 5.12	Annual failure probabilities for the stations .....	113
Fig. 5.13	Soil liquefaction fragilities of two soil profiles in the Groningen area (Miraglia et al., 2015) .....	114
Fig. 5.14	Distribution of reliability indices for failure due to soil liquefaction for different pipe sections .....	116
Fig. 5.15	Calculated pipe fragilities with respect to transient seismic load effects. Different solid lines correspond to different pipe properties. The red dotted line is taken from (Lanzano et al., 2013) .....	117
Fig. 5.16	Locations of the pipe sections with different fragility curves (from Fig. 5.15). Shown are PGV values that lead to a 50% probability of failure .....	117
Fig. 5.17	Annual probabilities of exceedance for network connectivity loss $CL$ (top) and serviceability ratio $SR$ (bottom) .....	119
Fig. 5.18	Convergence check in terms of coefficient of variation for ( $SR$ ) and ( $1-CL$ ).....	119
Fig. 5.19	Obtained grading for the individual pipelines ( $M_{max} = 6$ ; annual rate =30) .....	121
Fig. 5.20	Obtained grading for the individual stations ( $M_{max} = 6$ ; annual rate =30) .....	121
Fig. 5.21	Exceedance frequencies for connectivity loss relative to (indicative) grading boundaries.....	122
Fig. 5.22	Disaggregation of seismic events contributing to three levels of $CL$ (top) and $SR$ (bottom).....	123
Fig. 5.23	Disaggregation of seismic zones contributing to three levels of $CL$ (top) and $SR$ (bottom).....	124
Fig. 5.24	Disaggregation of pipe failures contributing to $CL \leq 0.1$ .....	125
Fig. 5.25	Disaggregation of pipe failures contributing to $CL \leq 0.5$ .....	126
Fig. 5.26	Sensitivity of $CL$ (top) and $SR$ (bottom) with respect to the maximum value of magnitude.....	127

---

Fig. 5.27	Sensitivity of <i>CL</i> (top) and <i>SR</i> (bottom) with respect to the annual rate of earthquake events with $M \geq 1.5$ .	128
Fig. 6.1	Flowchart of the ST@STREST framework for the stress test application in the port of Thessaloniki	130
Fig. 6.2	Geographical representation of Thessaloniki's port infrastructures considered in the study	132
Fig. 6.3	Location of the sampling boreholes, down-hole and cross-hole tests, microtremor measurements and 1D cross-sections of the broader Thessaloniki port area. The location of the new field microtremor measurements (M-1, M-2, M-3, M-4) are also shown.	133
Fig. 6.4	Final phase velocity dispersion curves determined at the four investigated sites together with those obtained by Apostolidis et al. (2004) for the sites A-1 and A-2 (see Fig. 6.3).	135
Fig. 6.5	$V_s$ profiles for sites A (left), B (middle) and C (right) together with a general geotechnical characterization according to USCS classification	136
Fig. 6.6	Digital elevation map of Thessaloniki's port area (initial model)	137
Fig. 6.7	Fragility curves for the quay wall (left) and the crane (right) for ground shaking	139
Fig. 6.8	Tsunami fragility curves for the warehouse (left) and the crane (right)	139
Fig. 6.9	Site specific hazard curves for ground shaking and tsunami	142
Fig. 6.10	Example of shake map in terms of PGA on rock for one event ( $M = 5.8$ , $R = 20$ km NNE of Port).	147
Fig. 6.11	Mean annual frequency (MAF) of exceedance values for the normalized performance loss of the container terminal (TCoH, right) and the bulk cargo terminal (TCaH, left) for the seismic hazard case. The green, blue and red continuous lines correspond to the boundaries between risk grades AA (negligible), A (ALARP), B (possibly unjustifiable risk), and C (intolerable).	148
Fig. 6.12	A) Map of the whole simulation domain used for the application at the target site Thessaloniki (Central Macedonia, Greece). The red star is the location of a crustal event for which we provide the map of the maximum wave height ( $H_{max}$ ), as an example; The zoom highlights the points along the 50 m isobath used to produce the $H_{max}$ profiles for the input of the Cluster Analysis. B) Close-up view of the simulation domain showing the telescopic nested grids for tsunami simulation with gradually increasing resolution (0.1, 0.025, 0.00625 arc-min). C) Bathymetric image of the finest grid (resolution=0.00625 arc-min), where the locations of the 70 receiver points are shown (red points).	151
Fig. 6.13	A) Maximum wave height distribution originated from the crustal event indicated with the red star in Figure 1 ( $M=8.0$ ). B) Time history of the corresponding wave height for one randomly selected receiver.	152
Fig. 6.14	A) Ensemble hazard curves for one randomly selected point in the target area, for two intensity measures: Maximum Flow Depth (left) and Maximum Momentum Flux (right); in both cases, the bold red line is the mean of the Ensemble, while the dotted lines report the confidence interval in terms of 16th and 84th percentiles. B) Mean hazard map for maximum momentum flux considering an	

---

---

	annual probability threshold of $10^{-5}$ . C) Mean annual probability map for a maximum flow depth of 1 m. ....	153
Fig. 6.15	Mean annual frequency (MAF) of exceedance values for the normalized performance loss of the bulk cargo terminal (TCaH, left) and for the buildings in complete damage state (right) for the tsunami hazard case. The green, blue and red continuous lines correspond to the boundaries between risk grades AA (negligible), A (ALARP), B (possibly unjustifiable risk), and C (intolerable). ....	154
Fig. 6.16	Mean annual frequency (MAF) of exceedance values for the normalized performance loss of the bulk cargo terminal (TCaH, left) and for the buildings in complete damage state (right) considering alternative models for the tsunami hazard. ....	155
Fig. 6.17	Comparison of the 5% damped median acceleration spectra of Akkar and Bommer (2010), Akkar et al. (2014a), Cauzzi et al. (2015) and Danciu and Tselentis (2007) for the 475 (left) and the 4975 (right) years scenarios .....	156
Fig. 6.18	Comparison of the 5% damped median and the median plus 0.5 standard deviation acceleration spectra of Akkar and Bommer (2010) with SHARE uniform hazard spectrum for Thessaloniki port area, the EC8 elastic response spectrum and Pitilakis et al. (2013) spectrum for the 475 years scenario.....	157
Fig. 6.19	Comparison of the 5% damped median and the median plus 1 standard deviation acceleration spectra of Akkar and Bommer (2010) with SHARE uniform hazard spectrum for Thessaloniki port, the EC8 elastic response spectrum and Pitilakis et al. (2013) spectrum for the 4975 years scenario.....	158
Fig. 6.20	Average elastic response spectrum of the input motions in comparison with the corresponding median plus 0.5 standard deviations Akkar and Bommer (2010) spectrum for the 475 years scenario .....	160
Fig. 6.21	Target median plus one standard deviation Akkar and Bommer (2010) spectrum for the 4975 years scenario and matched spectra for the considered records	161
Fig. 6.22	3D spectral element model to simulate deterministically the extreme scenario. ..	162
Fig. 6.23	5% damped pseudo-acceleration response spectra of the two horizontal components (EW and NS) and the geometric mean of horizontal components (GM) in comparison with the median Akkar and Bommer (2010) spectrum for the three Thessaloniki port sites (piers 3, 6 and 1). ....	164
Fig. 6.24	Comparison of the computed elastic response spectra derived from the EQL approach for soil profiles A (left) and C (right) with the corresponding spectra provided by EC8, Pitilakis et al. (2012, 2013) and SHARE for the selected seismic scenarios .....	167
Fig. 6.25	Median $\pm$ standard deviation elastic 5% response spectra at the ground surface for soil profile A using the EQL (left) and NL (right) approaches for the 475 years scenario (top) and the 4975 years scenario I (bottom).....	170
Fig. 6.26	Variation of effective confinement (left) and settlement with depth (right) for soil profile A for the 475 years scenario (top) and the 4975 years scenario (bottom). ....	171

---

Fig. 6.27	Spatial distribution of the losses of Thessaloniki's buildings for the 475 years scenario - EQL approach .....	173
Fig. 6.28	Spatial distribution of the losses of Thessaloniki's buildings for the 475 years scenario - NL approach .....	173
Fig. 6.29	Spatial distribution of the losses of Thessaloniki's buildings for the 4975 years scenario I- EQL approach .....	174
Fig. 6.30	Spatial distribution of the losses of Thessaloniki's buildings for the 4975 years scenario I- NL approach .....	174
Fig. 6.31	Spatial distribution of the components functionality for the 475 years scenario - EQL approach .....	176
Fig. 6.32	Spatial distribution of the components functionality for the 475 years scenario - NL approach .....	176
Fig. 6.33	Spatial distribution of the components functionality for the 4975 years scenario I- EQL approach .....	177
Fig. 6.34	Spatial distribution of the components functionality for the 4975 years scenario I- NL approach .....	177
Fig. 6.35	ST-L2b – Ground Shaking: Correlation of damaged cranes to port performance (TCaH and TCoH) .....	179
Fig. 6.36	ST-L2b – Ground Shaking: Correlation of non-functional EPN distribution substations to port performance (TCaH and TCoH).....	180
Fig. 6.37	Assessment of experts' judgments for screening the all identified single and selective multiple natural hazards relevant to PoTh.....	196
Fig. 6.38	Assessment of experts' judgments for screening the all identified port infrastructure relevant to PoTh. The asterisk (*) sign shows that those port infrastructures are connected to the external networks of the port .....	198
Fig. 6.39	Three categories are identified: non relevant (blue), partially relevant (light green), and relevant (red). The category is assigned based on the equal weights only as votes smaller or equal to 1, between 2 and 6, and larger or equal to 7, respectively .....	199
Fig. 6.40	Comparisons of assessed risks of screened hazards under EW, AW and PW for p1 and p2 .....	200
Fig. 6.41	Comparisons of conditional assessed risks of screened port infrastructures under EW, AW and PW for p1 and p2.....	203
Fig. 6.42	Pie chart representation of scores on models in LEVEL 1a under three weighting schemes .....	206
Fig. 6.43	Pie chart representation of scores on models in LEVEL 1a under three weighting schemes .....	206
Fig. 6.44	Pie chart representation of scores on models in LEVEL 2a under three weighting schemes .....	208
Fig. 6.45	Pie chart representation of scores on models in LEVEL 2b under three weighting schemes .....	208

---



---

Fig. 6.46 Pie chart representation of scores on models in BS-Branch under three weighting schemes .....	209
Fig. 6.47 Pie chart representation of scores on models in IS-Branch under three weighting schemes .....	210
Fig. 7.1 Definition of the industrial precast buildings considered for Tuscany .....	212
Fig. 7.2 Structural configuration and assumed position of openings in a) Type 1 and b) Type 2 industrial building (Casotto et al., 2015) .....	212
Fig. 7.3 Location of the 425 industrial facilities in the <i>Regione Toscana</i> database .....	213
Fig. 7.4 SHARE logic tree (Woessner et al., 2015) .....	215
Fig. 7.5 Mean hazard map for Tuscany based on SHARE logic tree with $V_{S30} = 800\text{m/s}$ (in terms of PGA with 10% probability of exceedance in 50 years).....	216
Fig. 7.6 Estimates of site conditions in Tuscany from topographic slope ( <a href="http://earthquake.usgs.gov/hazards/apps/vs30/predefined.php">http://earthquake.usgs.gov/hazards/apps/vs30/predefined.php</a> ) .....	217
Fig. 7.7 Mean hazard map for Tuscany based on SHARE logic tree with local site conditions based on $V_{S30}$ proxy (in terms of PGA with 10% probability of exceedance in 50 years) .....	217
Fig. 7.8 Mean hazard map for Tuscany based on <i>reduced</i> SHARE logic tree with local site conditions based on $V_{S30}$ proxy (in terms of PGA with 10% probability of exceedance in 50 years) .....	218
Fig. 7.9 Grading system for global outcome of stress test.....	219
Fig. 7.10 Location of the 300 industrial facilities in the province of Arezzo .....	220
Fig. 7.11 Annual probability of collapse of the low-code Type 2 buildings in Arezzo .....	222
Fig. 7.12 Annual probability of collapse of the pre-code Type 1 buildings in Arezzo.....	223
Fig. 7.13 Annual probability of collapse of the pre-code Type 2 buildings in Arezzo.....	223
Fig. 7.14 Annual probability of collapse of all industrial buildings in Arezzo.....	223
Fig. 7.15 Mean vulnerability model for structural components .....	224
Fig. 7.16 Mean vulnerability model for non-structural components .....	224
Fig. 7.17 Mean vulnerability model for contents .....	225
Fig. 7.18 Mean vulnerability model for business interruption (the y axis in this case also represents the mean number of days of disruption).....	225
Fig. 7.19 Workflow for developing loss exceedance curves (Silva et al., 2014b) .....	226
Fig. 7.20 Loss exceedance curves for all structural components in Arezzo (the loss exceedance curve for each of the branches of the logic tree is shown with a thin line and the mean across all branches is shown with a thick line) .....	227
Fig. 7.21 Loss exceedance curves for all non-structural components in Arezzo (the loss exceedance curve for each of the branches of the logic tree is shown with a thin line and the mean across all branches is shown with a thick line) .....	227

---

Fig. 7.22	Loss exceedance curves for all contents of industrial facilities in Arezzo (the loss exceedance curve for each of the branches of the logic tree is shown with a thin line and the mean across all branches is shown with a thick line) .....	228
Fig. 7.23	Loss exceedance curves for all business interruption in Arezzo (the loss exceedance curve for each of the branches of the logic tree is shown with a thin line and the mean across all branches is shown with a thick line) .....	228
Fig. 7.24	Total loss exceedance curves for all industrial facilities in Arezzo (the loss exceedance curve for each of the branches of the logic tree is shown with a thin line and the mean across all branches is shown with a thick line) .....	229
Fig. 7.25	Disaggregation of average annual loss according to building sub-class for each component of loss .....	230
Fig. 7.26	Disaggregation of hazard events contributing to business interruption loss with mean annual rate of $10^{-3}$ and $10^{-4}$ .....	231
Fig. B.1	Variation of median PGA and median PGA $\pm 1$ standard deviation with depth for the 475 years scenario .....	257
Fig. B.2	Variation of median PGA and median PGA $\pm 1$ standard deviation with depth for the 4975 years scenario I .....	258
Fig. B.3	Variation of median PGA and median PGA $\pm 1$ standard deviation with depth for the 4975 years scenario II .....	259
Fig. B.4	Elastic 5% damped median and median $\pm 1$ standard deviation acceleration response spectra at the ground surface for the three soil profiles derived from the EQL and NL approach for the 475 years seismic scenario .....	260
Fig. B.5	Elastic 5% damped median and median $\pm 1$ standard deviation acceleration response spectra at the ground surface for the three soil profiles derived from the EQL and NL approach for the 4975 years seismic scenario I .....	261
Fig. B.6	Elastic 5% damped median and median $\pm 1$ standard deviation acceleration response spectra at the ground surface for the three soil profiles derived from the EQL and NL approach for the 4975 years seismic scenario II .....	262
Fig. B.7	Median and median $\pm 1$ standard deviation spectral ratios for the three soil profiles derived from the EQL and NL approach for the 475 years seismic scenario ...	263
Fig. B.8	Median and median $\pm 1$ standard deviation spectral ratios for the three soil profiles derived from the EQL and NL approach for the 4975 years seismic scenario I .....	264
Fig. B.9	Median and median $\pm 1$ standard deviation spectral ratios for the three soil profiles derived from the EQL and NL approach for the 4975 years seismic scenario II .....	265
Fig. B.10	Variation of excess pore pressure profiles with depth for the three soil profiles for the 475 years (left) and 4975 years (right) scenarios.....	266
Fig. B.11	Variation of effective confinement with depth for the three soil profiles for the 475 years (left) and 4975 years (right) scenarios.....	267
Fig. B.12	Variation of maximum shear strain profiles with depth for the three soil profiles for the 475 years (left) and 4975 years (right) scenarios.....	268

---

---

Fig. B.13 Variation of maximum residual horizontal ground displacement profiles with depth for the three soil profiles for the 475 years (left) and 4975 years (right) scenarios .....269

Fig. B.14 Variation of maximum vertical ground displacement profiles with depth for the three soil profiles for the 475 years (left) and 4975 years (right) scenarios .....270



---

## List of Tables

Table 2.1 Legend for the population density.....	5
Table 2.2 Technology hazard matrix .....	21
Table 2.3 List of chemicals, expressed by the hazard classification of CLP (EC 1272/2008) and the corresponding amount as given in the Seveso Directive (2002).....	22
Table 2.4 Standard scenarios and frequencies stationary vessels.....	23
Table 2.5 Standard scenarios and frequencies above ground pipelines (VROM, 2005a)....	23
Table 2.6 Pool surfaces .....	24
Table 2.7 Scenarios and frequencies stationary vessels due to natural hazards.....	24
Table 2.8 Ignition probabilities .....	26
Table 2.9 Definition flammability classes.....	26
Table 2.10 Representative substances .....	27
Table 2.11 BLEVE probability.....	27
Table 3.1 Parameters of bottom outlet and hydropower system malfunctions defined by their meta-distributions .....	46
Table 3.2 Fragility of the dam to marginal overtopping events. The probability is defined as the probability of a damage state to be met or exceeded .....	49
Table 3.3 Parameters of the distribution of recovery rates for the outlet elements .....	51
Table 4.1 Information of faults crossing the investigated major hydrocarbon pipeline, and their fault-pipe intersections .....	86
Table 4.2 The properties of the pipe and soil at the fault-pipe intersections .....	86
Table 4.3 API5L-X65 steel properties considered in the numerical analyses.....	86
Table 4.4 Probabilities defined for the STREST grade.....	88
Table 4.5 Seismic features of the fault segments crossing BTC pipeline.....	93
Table 4.6 Checkout of the design level of hazard.....	95
Table 4.7 Checkout of the design-based assessment.....	95
Table 4.8 Soil spring properties calculated from.....	96
Table 4.9 Logarithmic means and standard deviations of pipeline fragilities against tension and compression failures .....	98
Table 4.10 Checkout of risk-based assessment with annual exceedance probability.....	99
Table 4.11 Aggregated probability of BTC pipeline failure due to fault displacements at pipe-fault crossings .....	100
Table 4.12 Aggregated probability of BTC pipeline failure due to fault displacements at pipe-fault crossings after the risk mitigation strategies.....	101

---

Table 5.1 Gutenberg-Richter parameters (Dost et al., 2013) .....	108
Table 5.2 Stress test results for Gasunie-GTS sub-network .....	129
Table 6.1 Boreholes at the broader Thessaloniki Port area (Anastasiadis et al., 2001).....	133
Table 6.2 Microtremor array measurements at port area (Apostolidis et al., 2004).....	134
Table 6.3 Geophysical data close to Thessaloniki port (*1: Raptakis and Makra, 2010; *2: ITSAK's Equipment and Instrumentation Upgrade project, 2002-2006) .....	134
Table 6.4 New microtremor array measurements in Thessaloniki port .....	135
Table 6.5 Fragility functions used in the risk analyses .....	140
Table 6.6 Earthquake hazard component check .....	143
Table 6.7 Tsunami hazard component check.....	144
Table 6.8 List of records used for the dynamic analyses for the 475 years scenario .....	160
Table 6.9 List of records used to derive the synthetic motions for the 4975 years scenario .....	161
Table 6.10 Kinematic source parameters for the 3D extreme scenario.....	163
Table 6.11 Comparison of the computed median PGA at the ground surface derived from the EQL approach for soil profiles A, B and C with the corresponding PGA provided by EC8, Pitilakis et al. (2012, 2013) and SHARE for the selected seismic scenarios .....	166
Table 6.12 Estimated median normalized performance loss of the port system for TCaH and TCoH and comparison with risk objectives for the scenario based assessment. .....	175
Table 6.13 Summary report of the Stress Test outcomes .....	181
Table 6.14 Identified potential hazards.....	188
Table 6.15 Taxonomy of Port of Thessaloniki (PoTh) .....	190
Table 6.16 Screening criteria for Single Hazards (SHs) .....	193
Table 6.17 Screening criteria for Multiple Hazards (MHs) .....	194
Table 6.18 Screening criteria for Single Port Infrastructures (SPIs).....	194
Table 6.19 Screening criteria for Interaction/Interdependent Port Infrastructures (IPIs) ....	195
Table 6.20 Screened hazards considered to be most relevant to PoTh.....	197
Table 6.21 Experts' judgments for the port infrastructures for the relevancy to PoTh.....	198
Table 6.22 Most relevant interdependencies for the Port of Thessaloniki (PoTh) .....	199
Table 6.23 Prioritization of the screened hazards to PoTh under three weighting schemes for p1 .....	201
Table 6.24 Prioritization of the screened hazards to PoTh under three weighting schemes for p2 .....	201
Table 6.25 Prioritization of the screened port infrastructures under three weighting schemes for p1 .....	204

---

Table 6.26	Prioritization of the screened port infrastructures under three weighting schemes for p2 .....	204
Table 6.27	Estimated scores on alternative models for LEVEL 1a.....	205
Table 6.28	Estimated scores on alternative models for LEVEL 1b.....	206
Table 6.29	Estimated scores on alternative models for LEVEL 2a.....	207
Table 6.30	Estimated scores on alternative models for LEVEL 2b.....	207
Table 6.31	Estimated scores on alternative models for BS-Branch .....	209
Table 6.32	Estimated scores on alternative models for IS-Branch.....	210
Table 7.1	Number of buildings in <i>Regione Toscana</i> database according to subclass .....	213
Table 7.2	Number of buildings in Arezzo according to subclass .....	221
Table 7.3	Number of buildings in Arezzo according to customer base.....	221
Table 7.4	Parameters (median $\theta$ and logarithmic standard deviation $\beta$ ) of lognormal fragility functions for structural components (STREST D4.3) .....	221
Table 7.5	Average annual losses for Arezzo portfolio .....	229
Table 7.6	Contribution of each building subclass to each component and total average annual loss .....	231
Table 7.7.	Percentage of each customer base AAL to the total business interruption AAL	233
Table 7.8.	Summary report of the Stress Test outcomes .....	235
Table 8.1.	Grading range for the six case studies of STREST .....	239
Table A.1	Geotechnical characteristics of soil profile A .....	253
Table A.2	Geotechnical characteristics of soil profile B.....	254
Table A.3	Geotechnical characteristics of soil profile C.....	255





# 1 Introduction

Critical Infrastructures (CIs) provide the essential services to the society and represent the backbone of economy, security and health. An infrastructure is constituted by an interconnection of assets, therefore the characterization of the system and adequate simulation of its behaviour in the case of extreme natural events is a challenging issue. The safety and resiliency of society is a top priority today and is strongly dependent on the resiliency of CIs. In this respect, advanced and standardized tools for hazard and risk assessment of CIs are required, including low-probability high-consequences (LP-HC) events (so-called extreme events) and the systematic application of these new tools to whole classes of critical infrastructures. In the framework of STREST, a new engineering risk based multi-level framework for stress tests named ST@STREST for non-nuclear CIs of different classes is proposed (STREST D5.1 Esposito et al., 2016). The aims of ST@STREST are to verify the safety and the risk of individual components as well as of whole CI system with respect to extreme events and to compare the response of the CI to acceptable values. The methodology is based on a common CI taxonomy and rigorous models for the hazard, vulnerability, performance and resilience assessment under different natural hazards. A multi-level framework is proposed, based on the complexity of the analysis (e.g. quantification of epistemic uncertainty, expert elicitation), the risk assessment approaches (single or multi-hazard, probabilistic or scenario based) as well as the available resources for conducting the stress tests. A formalized multiple expert integration process has been also developed dealing with the management of epistemic uncertainty called EU@STREST (Epistemic Uncertainty at STREST) (Selva et al., 2015) and integrated into the stress test Workflow (STREST D5.1 Esposito et al., 2016).

ST@STREST is demonstrated by means of an examples of six critical infrastructures in Europe, namely: the ENI/Kuwait oil refinery and petrochemical plant in Milazzo, Italy, by taking into account an impact of earthquakes and tsunamis (Chapter 2); the large dams in the Valais region of Switzerland under multi-hazard effects, considering earthquakes, floods, internal erosion, bottom outlet malfunctions, and hydropower system malfunction (Chapter 3); the major hydrocarbon pipelines in Turkey, focusing to seismic threats at pipe-fault crossing locations (Chapter 4); the Gasunie national gas storage and distribution network in Holland, exposed to earthquake and liquefaction effects (Chapter 5); the port infrastructures of Thessaloniki in Greece, subjected to earthquake, tsunami and liquefaction hazards (Chapter 6); and the industrial district in the region of Tuscany, Italy, exposed to seismic hazard (Chapter 7). To show the practical implementation of EU@STREST procedure, an exemplificative experiment to simulate the procedure to be followed during a future stress test for non- nuclear critical infrastructures has been carried in Chapter 6.

The selected case studies are representative of the CIs categories identified in STREST: i) individual, single-site infrastructures with high risk and potential for high local impact and regional or global consequences; ii) distributed and/or geographically-extended infrastructures with potentially high economic and environmental impact, iii) distributed, multiple-site infrastructures with low individual impact but large collective impact or dependencies.

The application of ST@STREST is presented following the workflow of ST@STREST, comprised by four phases: Pre-Assessment phase; Assessment phase; Decision phase; and Report phase. In the Pre-Assessment phase all the data available on the CI and on the hazard of interest is collected. The goal, the time frame and the most appropriate Stress Test Level to apply to test the CI are then defined. In the Assessment phase, the stress test is performed at Component and System Level. In the Decision phase, the stress test outcomes are checked i.e. the results of risk assessment are compared with the objectives defined in Pre-Assessment phase. Then critical events, i.e. events that most likely cause a given level of loss value are identified and risk mitigation strategies and guidelines are formulated based on the identified critical events and presented in the Report phase.

## **2 CI-A1 ENI/Kuwait oil refinery and petrochemical plant, Milazzo, Italy**

### **2.1 INTRODUCTION**

This report describes the main results of Task 6.1 and reports the results of the Quantitative Risk Analysis performed for the single-site critical infrastructure, CI-A1: ENI/Kuwait oil refinery (petrochemical plant), located in Milazzo (Italy), when subjected to the impact of earthquakes and tsunamis.

The entire work produced for the industrial site under interest has been based on non-lucrative aims, either directly or indirectly, but scientific and technology advancement.

All the information, data and analysis for the industrial installation have been retrieved from public data, civil protection information, regional databases and relevant risk (Seveso) reports. However, results of this report are strictly confidential, and should be only considered as an example of a general methodology developed within STREST project.

All the definitions, methodology and concepts described in the following sections are detailed in the deliverables of this project and will not be reported here for the sake of brevity.

The procedure follows the standard procedure for CPQRA (Chemical Process Quantitative Risk Analysis) but includes the vulnerability of the industrial system to natural events, the definition and evaluation of relevant accidental scenarios derived from the interaction of natural events with industrial equipment, and the final overall industrial risks related to either anthropogenic (industrial) causes or to the system failure related to natural disasters (NaTech risks).

The Quantitative Risk Assessment (QRA) reported in the following is devoted to specific case study of a refinery located in Milazzo (IT) but the procedure can be applied to any similar industrial installation.

TNO (NL), partner of the STREST project, owns the software named RiskCurves® (TNO, 2015) which have been used for this case study. These algorithms, together with the adopted methodology, are worldwide considered among of the most advanced tools for the analysis of industrial risks. For the aims of this project, they have been implemented with new procedures related to natural events, as described in STREST D4.1 (Salzano et al., 2015).

### **2.2 PHASE 1: PRE-ASSESSMENT PHASE**

#### **2.2.1 Data collection**

The refinery of Milazzo (Raffineria di Milazzo) is located in the north part of the island of Sicily, in Italy. It is an industrial complex which transforms crude oil into a series of oil products currently available on the market (lpg, gasoline, jet fuel, diesel and fuel oil) and

comprises a number of auxiliary services. Total production currently stands at circa 9.3 million tons.

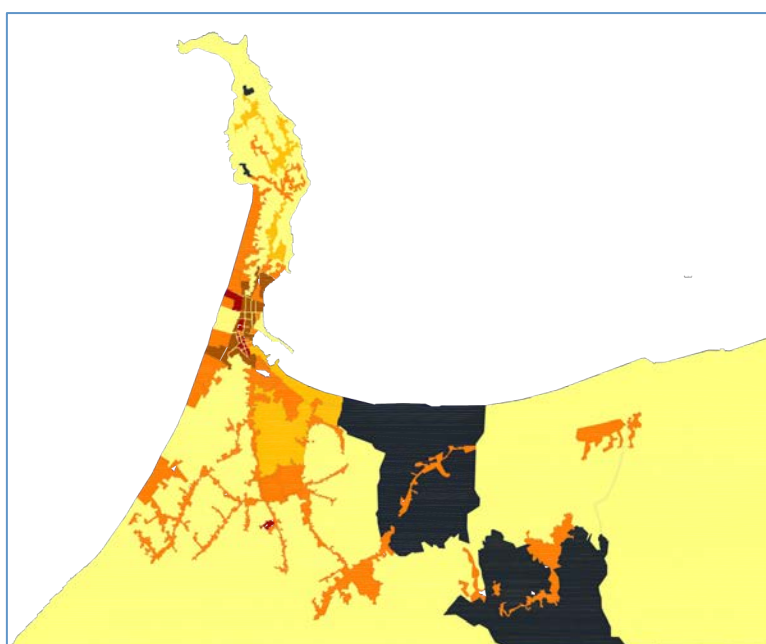
The refinery has many storage tanks containing a large variety of hydrocarbons, such as LPG, gasoline, gasoil, crude oil and atmospheric and vacuum residues.

The capacities of the tanks vary from 100 m<sup>3</sup> (fuel oil, gasoil, gasoline, kerosene) to 160 000 m<sup>3</sup> (crude oil). All tanks are located in catch basins (bunds) with concrete surfaces. Solely the LPG is stored in pressurized spheres, all other substances in single containment tanks. A filling degree of 80 % is assumed. Details of the equipment, process and operations are reported in the following sections. Further insights can be read on the public report issued by the company within the obligation of Seveso Directive.

In a QRA the societal risk, i.e. the risk to the community from identified risk sources, usually expressed as F-N curves, is determined. In order to do so, the (actual) presence of persons in the surroundings needs to be taken into account, since the numbers of persons present influences the societal risk. Only persons within the impact area of the site need to be taken into account. Persons on-site are not considered for the external risk.







Distinction is made in a QRA between the number of persons present during the day and during the night. This is of importance, because depending on the function of a building, people are present during day and/ or night and some risks only occur during day-time or night time. For example, no/ few persons are present in office buildings and schools during night-time but many persons are present during day time. This is different for houses, where during night-time more persons are present compared to day time. Also the location of persons (indoors or outdoors) is important: persons residing indoors are protected (up to a certain level) against toxic clouds or heat radiation. An activity that might only occur during day time could be (un)loading.

Fig. 2.1 presents the population distribution as supplied to TNO. The legend for the colors is given in Table 2.1.



**Fig. 2.1 Population distribution- in /km<sup>2</sup>**

**Table 2.1 Legend for the population density**

Legend	Population density range (-/km <sup>2</sup> )	Representative population density (-/km <sup>2</sup> )
	0	0
	0-250	125
	250-1 000	625
	1 000-5 000	3 000
	5 000-10 000	7 500
	10 000-113 318	62 000

The supplied information does not contain information on the day and night distribution of the people present or the type of activities (housing, offices, industry, etc.). For the present QRA no distinction is made between the day and night population presence: it is assumed that the population distribution applies to both day and night time. Fig. 2.2 shows the population areas that have been accounted for in the QRA. The numbers marked in yellow are the numbers of the population areas and have no specific meaning.

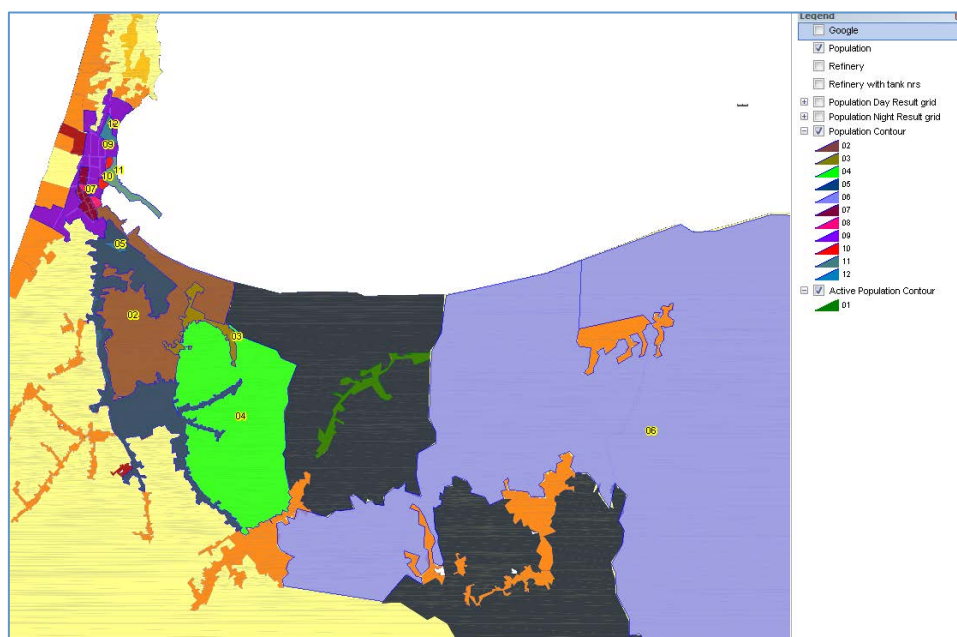


**Fig. 2.2 Overview of population areas considered**

The next figure (Fig. 2.3) shows the resulting population density.

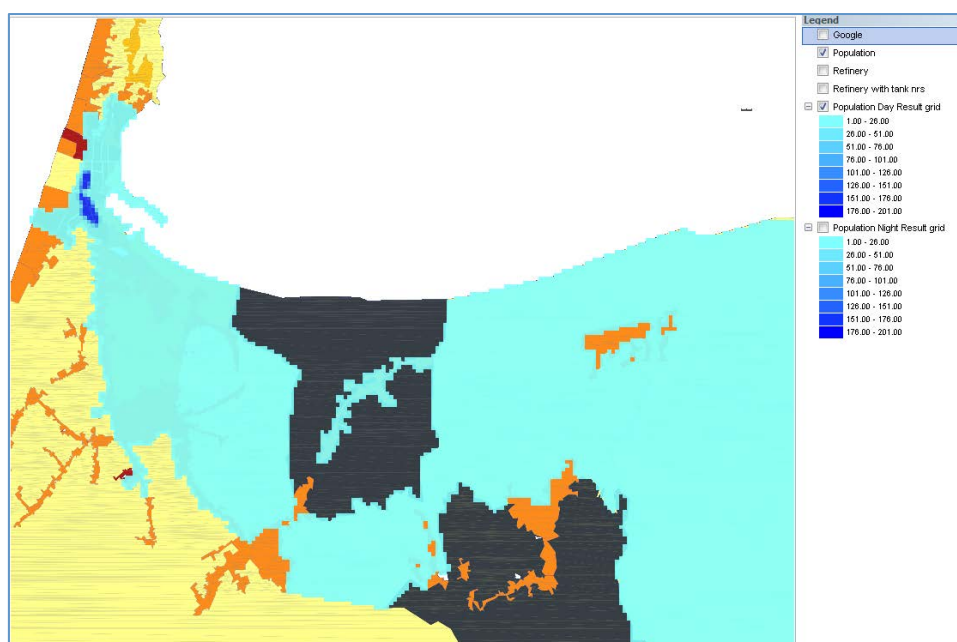


**Fig. 2.3 Overview of population density as used in QRA**

For releases of dangerous substances, the evaporation and dispersion of these substances to the atmosphere are of importance. Evaporation and dispersion depend on the wind speed and on atmospheric stability amongst others. The distribution of the wind direction determines in which direction the dispersion will occur and which areas will be affected by a toxic or explosive cloud. Wind speed and wind direction also influence the size, the tilt and the direction of a torch fire or pool fire.

For the purpose of this QRA no specific wind rose has been used. Regarding the meteorological conditions, the following assumptions have been formulated:

- Two weather classes (as reported in the Yellow Book (VROM, 2005a)) have been considered:
  - D5: neutral atmosphere with 5 m/s wind speed, occurs during both day time and night time
  - F1.5: very stable atmosphere with 1.5 m/s, occurs only during the night time
- The probability of a specific wind direction is random, that is to say: the wind rose is circular.

### **2.2.2 Earthquake hazard**

The probabilistic seismic hazard analysis (PSHA) presented in this section concerns the Italian port of Milazzo, situated in northern Sicily. For the purposes of this study, the area around Milazzo was discretized into a grid of forty-eight points (potential seismic event epicenters) with a grid spacing of approximately 25 km, as shown in the following Fig. 2.4.

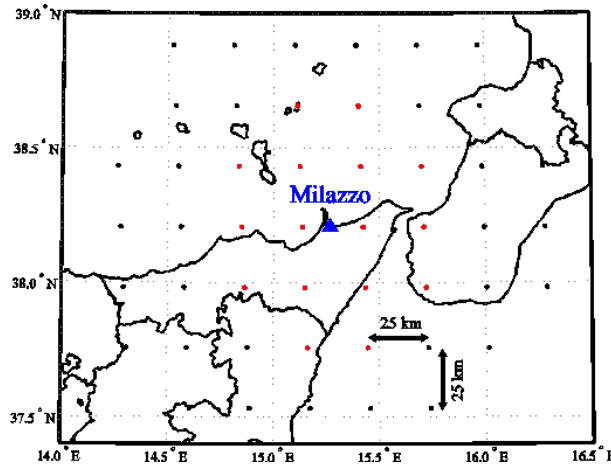


**Fig. 2.4 Grid of potential epicenters around Milazzo considered in the PSHA analysis. Grid points within a 50 km radius from Milazzo are displayed as red dots**

For each single point on this grid, the Italian National Institute of Geophysics and Volcanology (Istituto Nazionale di Geofisica e Vulcanologia - INGV) provided the joint probability mass of strike, dip and rake, for a total of around three-thousand four-hundred “rupture scenarios” of non-trivial probability. This information forms the basis of the following elaboration, as it allows the probabilistic assignment of finite-fault geometries to all scenarios that enter the PSHA calculations.

Note that in what follows, the joint probability of strike, dip and rake of each rupture scenario (which also define focal mechanism) will be denoted as  $P[\text{rup}]$  for the sake of brevity. ZtoR (depth to top of rupture) was not included as a covariate in the joint probability mass of these rupture scenarios; it was assumed stochastically dependent on magnitude and taken as five kilometers for all events of magnitude less than six-point-five and one kilometer for events of greater magnitude, following the practice of USGS hazard calculations for the US.

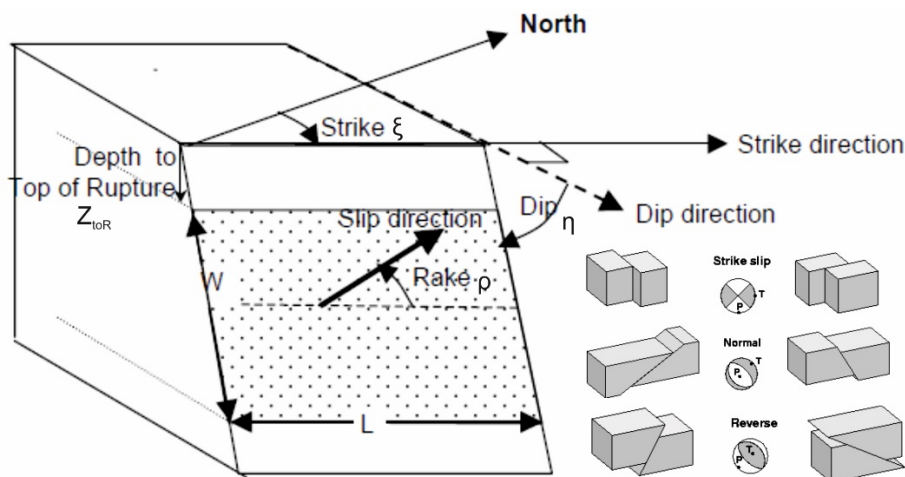


**Fig. 2.5 Geometrical parameters defining the orientation of a rupture plane (taken from Aki & Richards, 1980) and schematic representation of the principal focal mechanisms, which are defined by the rake angle**

Seismic hazard is typically expressed in terms of the mean annual frequency (MAF) of exceeding specific level of seismic intensity (or intensity measure - IM). For one case, where it was necessary to take finite-fault into account for hazard computation (Chioccarelli & Iervolino, 2013), MAF was calculated as per Eq. (2.1):

$$\lambda_{S_a > s_a} = v \cdot \int_m \int_l \int_p \int_h \int_{x_r} P[S_a > s_a | m, l, p, x_r] \times f_{P,H|L}(p, h | l) \cdot f_{X_r|L}(x_r | l) \cdot f_{L|M}(l | m) \cdot f_M(m) \cdot dm \cdot dl \cdot dp \cdot dh \cdot dx_r \quad (2.1)$$

In the equation, the random variables L, P, H and X<sub>r</sub>, whose physical meaning can be deduced from the next figure (Fig. 2.6), define dip-slip (DS) rupture geometry under the simplifying assumption that the rupture plane will always maintain the known-a-priori aspect ratio of the fault dimensions.

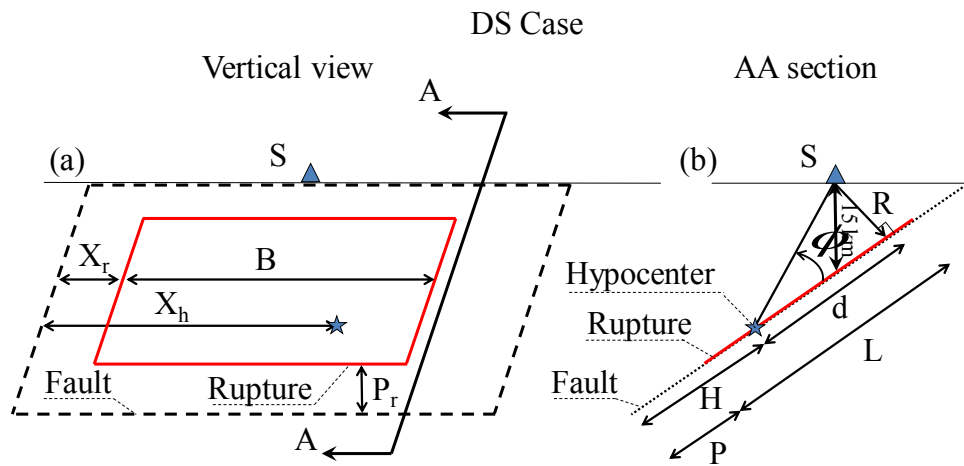


**Fig. 2.6** Definition of geometrical variables for the representation of dip-slip ruptures on a known fault geometry, (a) vertical longitudinal section and (b) cross-section (Chioccarelli & Iervolino, 2013)

The term:

$$P[S_a > s_a | m, l, p, x_r]$$

represents the conditional probability of exceeding a fixed spectral acceleration level, given magnitude and rupture-to-site distance.

Regarding probability densities, it should be remarked that the conditional density of rupture width given magnitude:

$$f_{L|M}(l | m)$$

can be derived from regression models of rupture area against magnitude by invoking the aforementioned assumption of constant aspect ratio, while:

$$f_{P,H|L}(p, h | l)$$

and



$$f_{X_r|L}(x_r|l)$$

are the result of an assumed uniform distribution of hypocenters upon the fault plane, truncated to account for the geometrical constraints imposed by the limits of the fault dimensions. Further details can be found in Chioccarelli & Iervolino (2013).

In order to adapt the same framework to the case at hand, where no fixed (known) fault configuration is assumed and instead a multitude of rupture scenarios must be stochastically accounted for, the MAF of exceeding a spectral acceleration threshold is given by Eq. (2.2):

$$\begin{aligned} \lambda_{IM>im} = & \sum_{i,j} v_i \cdot P[\text{rup}_j|e_i] \cdot \int_m \int_z \int_a \int_v \int_x \int_y P[IM > im|m, a, q, x, y, z, \text{rup}_j, e_i] \\ & \cdot f_{X,Y}(x, y) \cdot f_{Q|A}(q|a) \cdot f_{A|M}(a|m) \cdot f_{Z_{\text{toR}}|M}(z|m) \cdot f_{M_i}(m) \cdot dx \cdot dy \cdot dq \cdot da \cdot dz \cdot dm \end{aligned} \quad (2.2)$$

The term:

$$P[\text{rup}_j|e_i]$$

represents the joint probability mass of strike  $\xi$ , dip  $\eta$  and rake  $\rho$  associated with the  $j$ -th rupture scenario conditional on event realization at the  $i$ -th epicenter-grid point (conditional probability of rupture scenario given epicenter). This is symbolically expressed by the next equation:

$$P[\text{rup}_j|e_i] = P[\xi, \eta, \rho|e_i] \quad (2.3)$$

The conditional probability of exceeding a given level of spectral acceleration given magnitude, rupture area ( $A$ ), fault plane aspect ratio ( $Q$ ), hypocenter position on the plane (two-element random vector  $\{X, Y\}$ ), depth to top of rupture ( $Z_{\text{toR}}$ ) and rupture scenario, and the term:

$$P[IM > im|m, a, q, x, y, z, \text{rup}_j, e_i]$$

can be calculated by applying a ground motion prediction equation (GMPE). In the present application, the GMPE proposed by Boore and Atkinson (2008) was employed. The joint density of the two components defining the hypocenter's position upon the rupture plane:

$$f_{X,Y}(x, y)$$

is calculated according to the work of Mai et al. (2005). This is a refinement with respect to previous equation, where hypocenters were assumed uniformly distributed upon the rupture plane. The marginal density along the strike ( $X$ ) is taken as having a truncated Gaussian distribution while the one along-dip ( $Y$ ) as having a truncated Weibull distribution. The joint density is taken as the product of the marginal, assuming stochastic independence between  $X$  and  $Y$ .

In the absence of the simplifying assumption of a constant aspect ratio for all possible ruptures, fixed at the aspect ratio of the constraining fault dimensions, a more elaborate, probabilistic approach had to be adopted in this case. The conditional probability density of aspect ratio given rupture area:

$$f_{Q|A}(q|a)$$

is assumed to follow a log-normal distribution, whose parameters are estimated on the basis of an ordinary least squares regression analysis (Fig. 2.7 and Fig. 2.8).

$$\begin{aligned} \log_{10} Q &= 0.2326 \cdot \log_{10} A - 0.2922 \\ \hat{\sigma}_{\log_{10} Q} &= 0.1565 \end{aligned} \quad (2.4)$$

The notation  $\hat{\sigma}$  appearing in the above equation refers to the estimator of the standard deviation (assumed constant) derived from the regression residuals. This regression model was derived using fifty-one European events with magnitudes between 4.50 and 7.20 and various focal mechanisms (Konstantinou, 2014). Purely strike-slip events such as the M7.6 Kocaeli earthquake (Turkey, 1999) were not included in this regression. In the literature, one can find empirical predictive equations for length, width and rupture area, all regressed separately against magnitude (Wells & Coppersmith, 1994). Also, regression models for the aspect ratio of the rupture plane dimensions given magnitude can be found (Dorwick & Rhoades, 2004). However, such models can provide the marginal distribution of each variable (given magnitude), while the variables themselves are not necessarily independent. In fact, for the purposes of the present computation, the joint distribution of width and length given magnitude would be ideally required (or equivalently the joint distribution of rupture area and aspect ratio given magnitude). In order to overcome this problem, it was assumed that by conditioning aspect ratio to rupture area (which depends on magnitude), renders its distribution stochastically independent of magnitude. This assumption is implicit in Eq. (2.4). The conditional density of rupture area given magnitude:

$$f_{A|M}(a|m)$$

was taken from Wells and Coppersmith (1994). As for the conditional density of depth to top of rupture given magnitude:

$$f_{z_{toR}|M}(z|m)$$

it bears only reminding that this is derived by the simple, almost-deterministic consideration described earlier ( $z=5$  km when  $m<6.5$  and  $z=1$  km for  $m\geq 6.5$ ). Finally, the probability density of magnitude at the  $i$ -th grid point:

$$f_{M_i}(m)$$

was extracted from the seismicity curves (cumulative frequency of events surpassing a certain magnitude) provided for the present discretization of potential epicenters (curves for all grid points show in Fig. 2.8). The hazard curve for Milazzo in terms of peak ground acceleration (PGA), obtained by implementing the methodology presented above, can be found in Fig. 2.9 and Fig. 2.10.

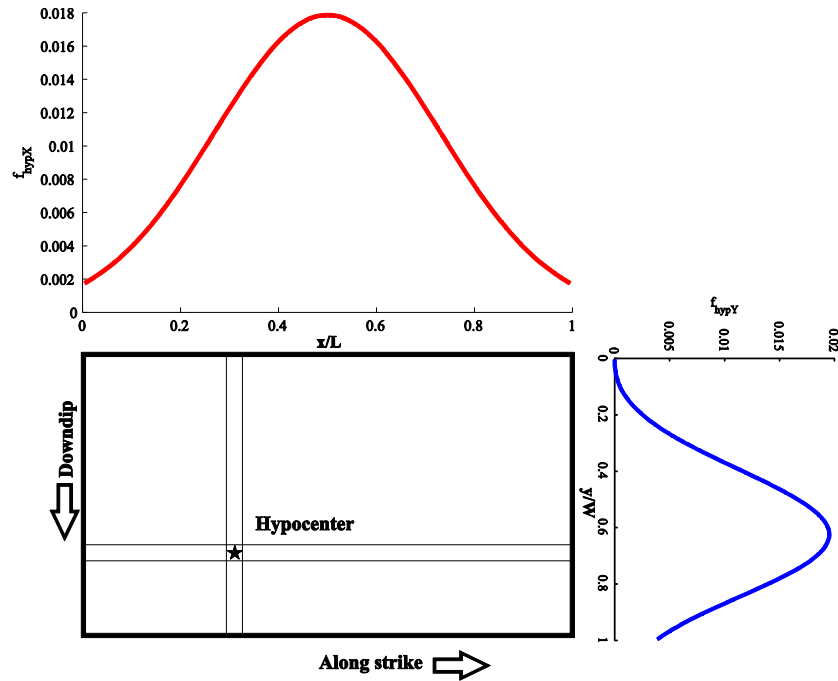


**Fig. 2.7** Probability distribution of hypocenter location along the rupture plane. Downdip and along-strike positioning are assumed independent random variables with marginal densities shown in alignment with the relevant fault plane dimensions

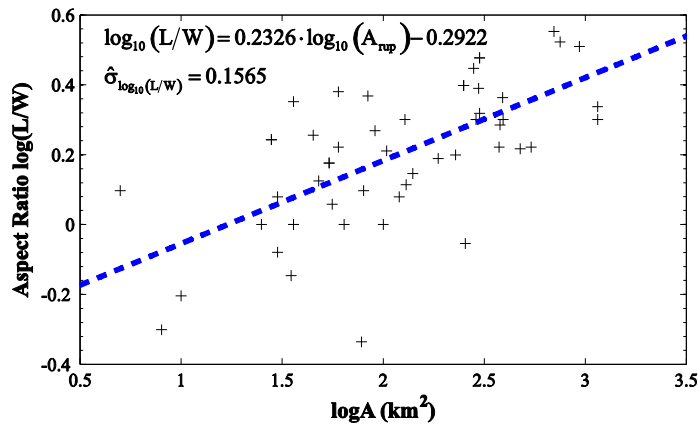


**Fig. 2.8** Linear regression of (log-) aspect ratio  $Q=L/W$  of the rupture plane against log-rupture area

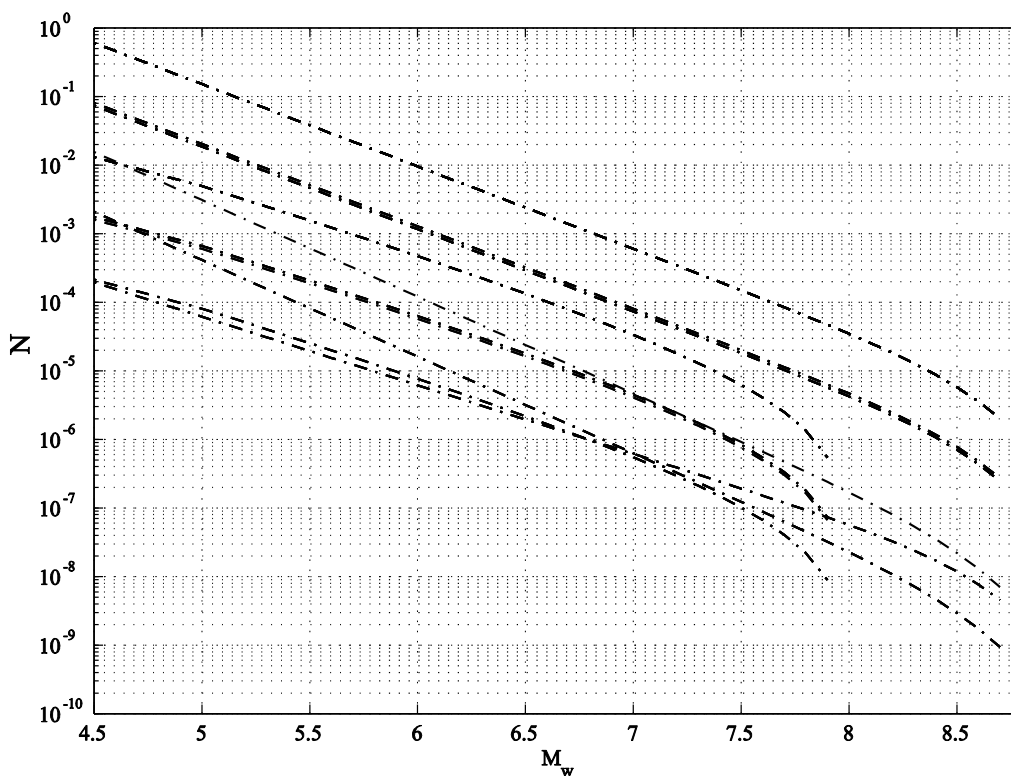


**Fig. 2.9** Seismicity in terms of cumulative frequency of events surpassing given values of magnitude for each grid point in the discretization of the area around the port of Milazzo

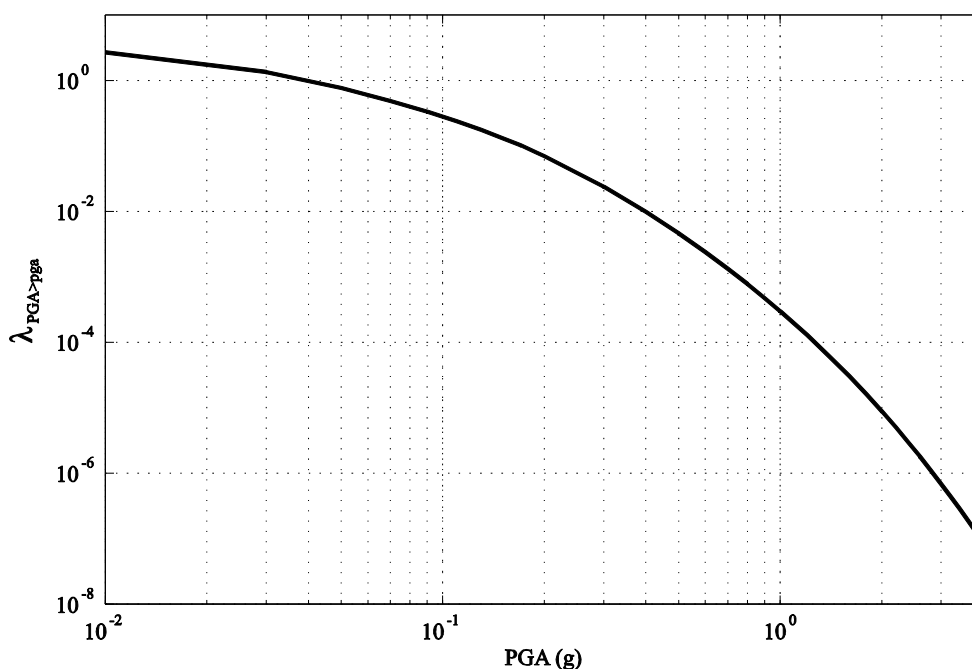


**Fig. 2.10** Hazard curve for Milazzo in terms of MAF of exceedance of PGA, calculated according to the methodology presented

### 2.2.3 Tsunami hazard

Probabilistic Tsunami Hazard Analysis (PTHA) is a methodology to assess the exceedance probability of different thresholds of hazard intensity, at a specific site or region in a given time period, due to whatever source. Different potential tsunamigenic sources should be considered, such as earthquakes, landslides, meteorite impacts or atmospheric phenomena. Here, we focus only on tsunamis of seismic origin, which is the dominant component of PTHA in most of the areas of the world, both in terms of occurrence and in terms of effects (Parsons & Geist, 2009). Following the definition proposed in Lorito et al. (2015), we deal with Seismic PTHA (SPTHA), that is, tsunamis generated by co-seismic sea floor displacements due to earthquakes.

A very large number of numerical simulations of tsunami generation, propagation and inundation on high resolution topo-bathymetric models are in principle required, in order to give a robust evaluation of SPTHA at a local site, honoring the full aleatory variability of the seismic sources (the aleatory uncertainty). Consequently, the computational effort can be extremely demanding and in practice unfeasible and the issue is traditionally solved by limiting the variability of the sources (Gonzalez et al., 2009) and/or reducing the computational effort of numerical models by not modeling the near-coast and inland propagation of the tsunamis (Sørensen et al., 2012). These approaches make the calculation of SPTHA a computationally affordable task, but could lack in accuracy in uncertainty estimation and/or in definition of the hazard in-land.

To reduce the computational cost, while keeping results stable and consistent with respect to explore the full variability of the sources, we developed a method to approach the uncertainty in SPTHA (Selva et al., 2016a), based on 4 steps: 1) a full exploration of the aleatory uncertainty through an Event Tree (ET, Lorito et al., 2015; Selva et al., 2016a) that account for all available sources of information (e.g. Basili et al., 2013); 2) the propagation of all potential sources till off-shore; 3) a 2 stage filtering procedure based on Cluster Analysis on the results off-shore in order to define a sub-set of “representative” events which approximate the hazard in the target area, in order to enable the inundation modeling (Lorito et al., 2015); 4) the quantification of the epistemic uncertainty through Ensemble modeling based on alternative implementations of steps 1 to 3 (Marzocchi et al., 2015; Selva et al., 2016a).

STEP 1 is based on the development of the Event Tree for different seismic regions, which are assumed independent. Within the Event Tree, all the relevant source parameters (aleatory variability) are explored through a controlled hierarchical discretization, and conditional probability distributions set based on all the available information about the potential seismic sources (seismic catalogues, focal mechanism catalogues, known fault databases, scaling laws, 3D geometries of major faults, etc.). The seismicity related to the main and better-known fault interfaces (e.g. Interface Seismicity, IS) is treated separately from the rest of the seismicity (Background Seismicity, BS), in order to optimize the use of the available information and not to lose potential for the other sources. Alternative implementations of the Event Tree are then proposed, in order to explore the epistemic uncertainty.

In STEP 2, the complete set of source scenarios defined from the ET is implemented to obtain a regional SPTHA, in terms of maximum offshore tsunami wave height ( $H_{max}$ ) at discrete points (along the 50 m iso-bath). It is worth noting that, as the number of sources may be very high ( $>10^6$ ), such scenarios are not explicitly simulated but are computed as the

linear combination of pre-calculated waveforms resulting from elementary Gaussian-shaped initial sea level elevation, according to a Green's function approach (Molinari et al., 2016).

In STEP 3, the offshore  $H_{max}$  is analyzed applying a two-step filtering procedure, in order to reduce the number of numerical simulations required to retrieve the site specific SPTHA based on the inundation maps: firstly, sources which produce a negligible contribution to  $H_{max}$  on a set of control points located on the 50 m isobath offshore of the target site are excluded, assuming that they would lead to negligible inundation at the nearby coast; secondly, a cluster analysis is carried out on the filtered sources, based on the resulting tsunami propagation patterns, not on the similarity or the proximity of the sources. Basically, sources which produce similar offshore  $H_{max}$  profiles along the set of control points in front of the target coast are assumed to produce as much similar inundation patterns and, consequently, one representative simulation for each cluster (not for each source) must be executed. The probability of occurrence of the entire cluster is attributed to the selected representative source. This strategy allows for a 75-80% reduction of the number of required simulations, while satisfactorily preserving the accuracy of the obtained inundation maps (Lorito et al., 2015). From the cluster analysis performed on the set of possible scenarios defined by the ET, a subset of representative causative earthquakes is inferred, which is used as initial condition for the tsunami generation, propagation and inundation simulations. For BS, the initial sea level elevation is obtained by modeling the fault dislocation with Okada (Okada, 1985) and applying the Kajiura filter to take into account the effect of the water depth on the tsunami generation process (Kajiura, 1963). The subduction scenarios are simulated by modeling the slab as a 2D triangular mesh honoring the interface profile, associating to each element of the mesh (i.e. each triangle) a unitary Okada source and suitably combining such sub-faults in order to reproduce the slip along the slab.

In STEP 4, the epistemic uncertainty, that is, the uncertainty due to the adopted model parameters and the modeling assumptions, is treated by means of an ensemble modeling approach (Marzocchi et al., 2015), with the implementation of alternative models (e.g. alternative formulations for the probability distributions of the ET). Each model is weighted according to the confidence and the possible correlations between the models (Selva et al., 2016a).

Within the project STREST, we considered two target sites, Milazzo (Sicily, Italy) in the Southern Tyrrhenian sea, and Thessaloniki (Central Macedonia, Greece) in Northern Aegean sea (Selva et al., 2016b). A common regional assessment (STEPS 1 and 2, above) has been set up, by considering all the potential seismic sources in the Mediterranean Sea. IS class included the seismicity occurring on subduction interfaces of the Calabrian and the Hellenic arcs (hereinafter those will be referred to as CA and HA, respectively). BG class, mainly associated to crustal seismicity, has been modeled on a grid with areas of constant size approximately 25 km x 25 km covering the whole Mediterranean Sea. The total number of scenarios considered was approximately  $2 \times 10^7$ . More than  $1 \times 10^4$  alternative implementations have been considered to quantify the epistemic uncertainty. All the details of the adopted Event Tree can be found in Selva et al., 2016a).

The common regional results provided the input for the site specific analysis. This task has been carried out separately for Milazzo and Thessaloniki. For each site, a reference profile off-shore at the isobath of 50 m has been selected. We here describe the application for Milazzo, whereas the Thessaloniki application is reported in section 6.

We considered seven points off-shore the Milazzo target area, as reported in Fig. 2.11. The  $H_{max}$  values of each scenario defined in steps 1 and 2 represented the input for the filtering

procedure. Scenarios with  $H_{\max} < 0.2$  m have been filtered out. Then, a *k*-Means Cluster Analysis has been performed, separately for groups of scenarios with similar maximum  $H_{\max}$  along the profile. The number of clusters in each group has been set as the minimum number leading to a within-cluster average distance smaller than 20% of the maximum  $H_{\max}$  of the group. The scenario closer to the centroid of each cluster has been finally selected as the “reference scenario” for the cluster (adopting a distance based on a cost function, see Lorito et al., 2015). We obtained 153 clusters (34 for CA, 17 for HA, 102 for BS), for which an explicit numerical simulation of inundation has been performed.

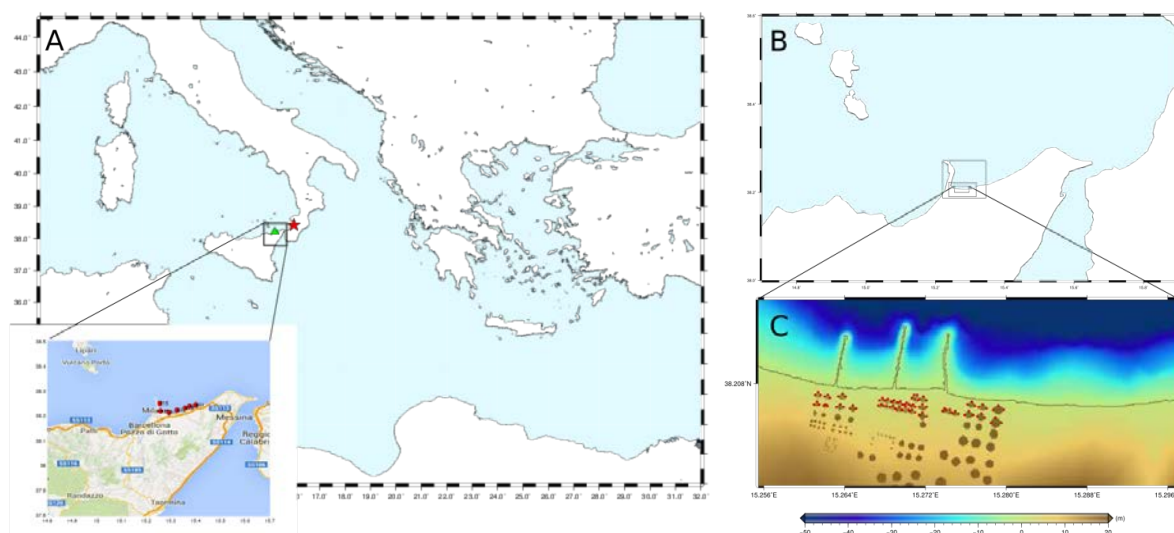


**Fig. 2.11 A) Map of the whole simulation domain used for the application at the target site Milazzo (Sicily, Italy). The red star is the location of a crustal event for which we provide the map of the maximum wave height ( $H_{\max}$ ), as an example; The zoom highlights the points along the 50 m isobath used to produce the  $H_{\max}$  profiles for the input of the Cluster Analysis. B) Close-up view of the simulation domain showing the telescopic nested grids for tsunami simulation with gradually increasing resolution (0.1, 0.025, 0.00625 arc-min). C) Bathymetric image of the finest grid (resolution=0.00625 arc-min), where the locations of the 95 receiver points are shown (red points)**

The numerical simulations were performed using a non-linear shallow-water multi-GPU code developed at the University of Malaga, Spain (HySEA) (Gonzalez Vida et al., 2015). The code is based on a mixed finite difference/finite volume method. Grid nesting allows to gradually increasing simulation resolution as tsunami wavelength decreases while approaching the target site, to preserve accuracy on progressively smaller areas while saving computational time. For this specific application, we used 4-level nested bathymetric grids with refinement ratio equal to 4 and increasing resolution from 0.4 arc-min (~740 m) to 0.1 arc-min (~185 m) to 0.025 arc-min (~46 m) to 0.00625 arc-min (~11 m), as reported in Fig. 2.11-B. The largest grid was obtained by resampling the SRTM15+ bathymetric model. The finest 3 grids have been produced by interpolation from TINITALY (for the emerged part) and EMODNET (for the sea part), working on grids of 0.00625 arc-min that have been resampled at 0.1 arc-min and 0.025 arc-min.

The results of each simulation have been stored as maximum flow depth (FlowDepth, m) and maximum momentum flux (MomMax,  $\text{m}^3\text{s}^{-2}$ ), in each point of the inner grid, and as time history for both quantities at the 95 receiver points, with a sampling step 30 sec for an overall duration of 8 hours. The receiver points are strategically located at the edges of some storage tanks belonging to an oil refinery, representing an important target for the hazard assessment (red dots in Fig. 2.11-C). In Fig. 2.12, we report one example of simulation results for the grid and for the time history in one randomly selected target point.

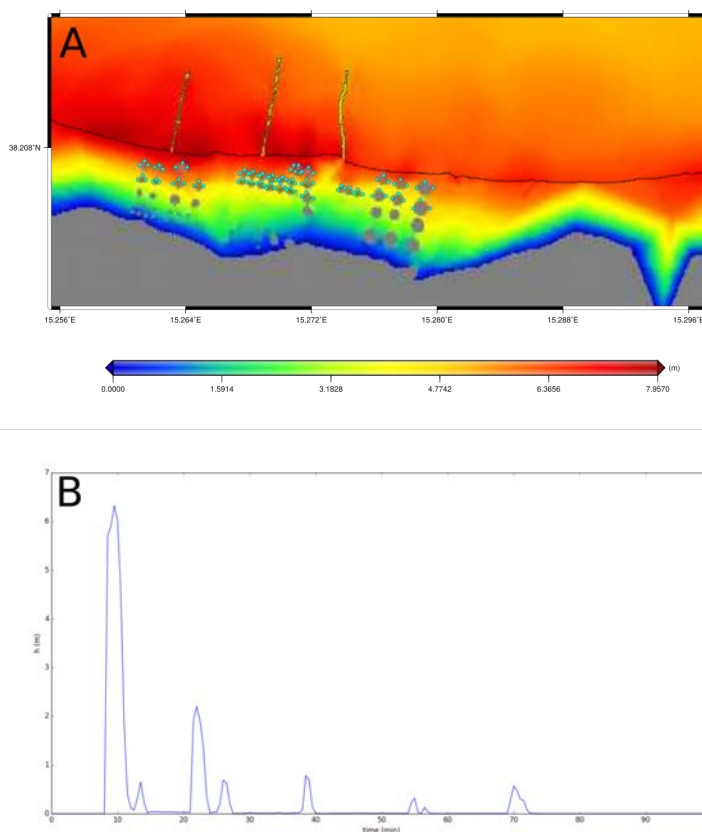


**Fig. 2.12 A) Maximum wave height distribution originated from the crustal event indicated with the red star in Fig. 2.11 ( $M=8.0$ ); B) Time history of the corresponding wave height for one randomly selected receiver**

To each one of the “representative scenarios” is finally assigned the probability of all the scenarios owing to its cluster, then the results are aggregated to obtain the final SPTHA results (Lorito et al., 2015; Selva et al., 2016a). All the alternative probability assessments set up for the Event Tree are adopted separately, obtaining a family of hazard curves in each target point. These curves, along with the credibility weight assigned to each of these alternative models, are given as input to the Ensemble model, in order to produce the quantification of hazard curves and relative epistemic uncertainty (for more details see Selva et al., 2016a; Volpe et al., in prep). The results consist of a set of ensemble hazard curves for each point of the inner grid domain. One example of such curves is reported in Fig. 2.13-A, for two intensity measures (maximum flow depth and maximum moment). The hazard curves are then post-processed to obtain hazard maps and probability maps. For sake of example, we report in Fig. 2.13-B the hazard map for flow depth considering an annual probability threshold of  $10^{-4}$ , and in Fig. 2.13-C the annual probability map for a maximum



moment threshold of  $5 \text{ m}^3\text{s}^{-2}$ . In both cases, the mean of the ensemble models is considered. Similar maps can be obtained at any statistics of the epistemic uncertainty.

The kind and format of the results are suitable and they have been provided for subsequent risk analysis at this site within the framework of the STREST project.

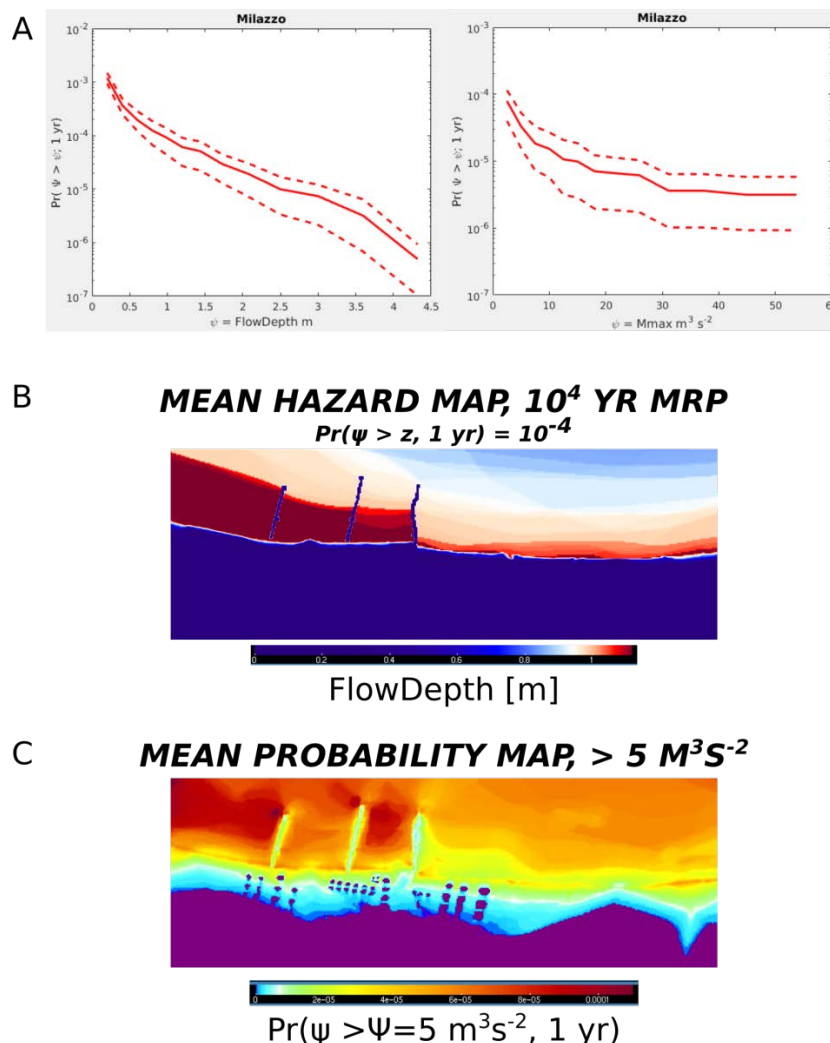


**Fig. 2.13** A) Ensemble hazard curves for one randomly selected point in the target area, for two intensity measures: Maximum Flow Depth (left) and Maximum Moment (right); in both cases, the bold red line is the mean of the Ensemble, while the dotted lines report the confidence interval in terms of 16<sup>th</sup> and 84<sup>th</sup> percentiles. B) Mean hazard map for flow depth considering an annual probability threshold of  $10^{-4}$ . C) Mean annual probability map for a maximum moment threshold of  $5 \text{ m}^3\text{s}^{-2}$

## 2.2.4 Risk Measures and Objectives

In a QRA the likelihood of accidents during industrial activities and transport of hazardous materials and the consequences of the accidents are analyzed and expressed in a risk figure. For the determination of the risk of the activities, several aspects have to be quantified, as depicted in Fig. 2.14.

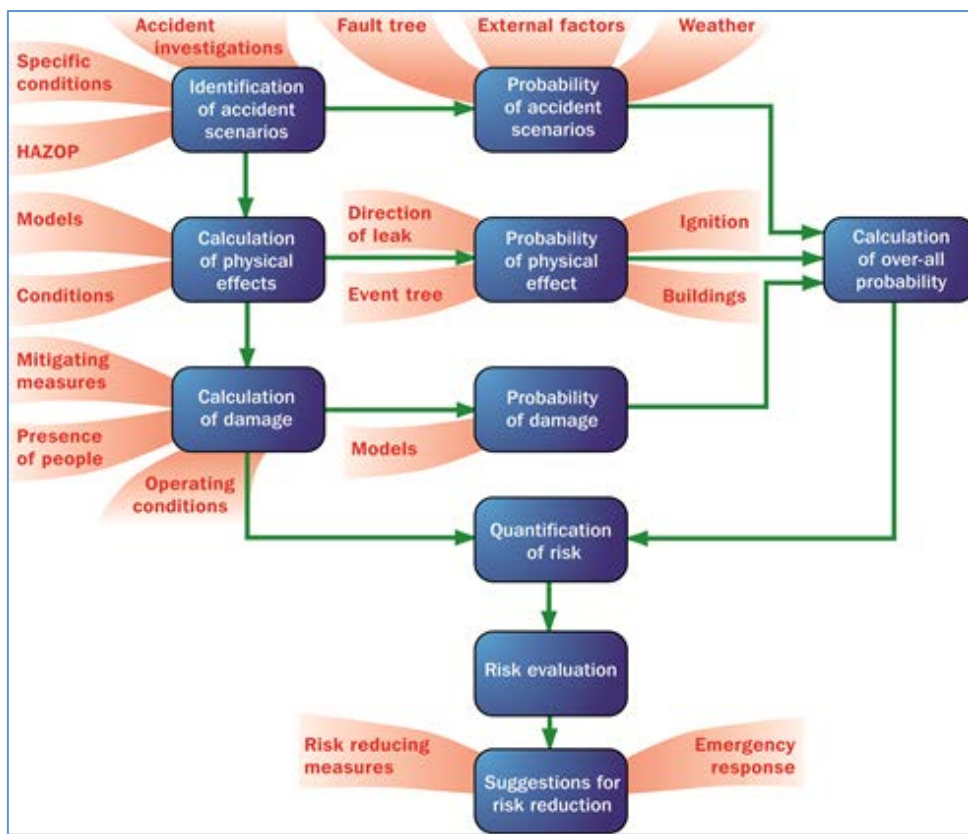


Fig. 2.14 Steps in a QRA and most important parameters

As it can be observed, many factors influence the over-all risk. For the sake of comparability of studies, standard methods have been then developed in the Netherlands, to a large extent by TNO (VROM, 2005a-d). These so-called colored books are used worldwide and have been used for the STREST project.

Fig. 2.15 shows the relation between the different steps in a QRA and the standard methods.

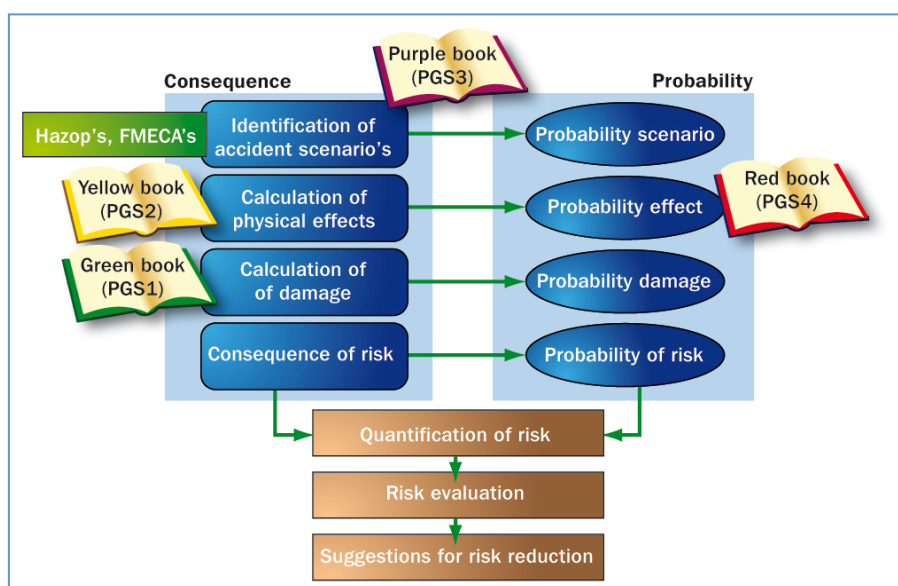


Fig. 2.15 Main steps in a QRA and the standard methods

A QRA starts with the description of the area (e.g. industrial site; transport route) and the activities present. The conditions (temperature, pressure, substances, composition, etc.), inventories, dimensions and location of the different activities with hazardous materials are collected. The next step is to select the activities that can pose an (off-site) risk to the public or to the site personnel. The first selection is based on the use of hazardous chemicals (toxic, flammable or explosive substances) in an industrial site or during transport. For large industrial sites (e.g. refinery, large chemical plant), with many activities with hazardous chemicals, further selection (so-called sub-selection method) is possible in order to limit the number of scenarios taken into account in the QRA, based upon the risk of the substance, the process conditions and the quantity. This method aims at limiting the QRA to those activities that can potentially create accidents resulting in fatalities off-site.

Once the hazardous activities are identified, the accident scenarios need to be identified. This means that system ruptures and leaks are identified, which are considered to be credible, for all selected activities. The credibility is based on engineering judgment and on study of incidents from the past. Scenario selection can be based on Hazops (HAZard and OPerability study) or FMECA (Failure Mode, Effects and Criticality Analysis) or guidelines such as the Purple Book (VROM, 2005c) can be used.

For the defined accident scenarios the physical effects and consequences need to be assessed. These are influenced by the release rate, the weather conditions and calculation models/ methods etc. Physical effects evaluated are toxic concentrations, heat radiation (pool fire, flash fire, torch fire, fire ball) and overpressure. The Yellow Book (VROM, 2005a) contains models for the calculation of physical effects and has been implemented in the EFFECTS and RiskCurves software (TNO, 2015).

Exposure to heat radiation, explosion peak over-pressure and toxic clouds can cause injuries and fatalities. Vulnerability models relating heat radiation, over-pressure and toxic concentrations to lethal consequences are given in the Green Book (VROM, 2005b) and have been implemented in the TNO software.

The probability of scenarios, physical effects and damage is influenced by many parameters and is of great influence on the risk.

The probability can be assessed using fault trees or case study or the Red or Purple Book.

In an event tree, the development of the accident in time is presented, including:

- Frequency of the initial events (e.g. failure or leakage of a storage vessel);
- Probability of failure of an emergency system intervention or a human intervention;
- Probability of ignition in the case of a flammable substance. Distinction is made between direct ignition and delayed ignition. Direct ignition means that the flammable material is immediately ignited after release, resulting in a pool fire, a flare, vapour cloud fire (possibly with overpressure effects) or fire ball. Delayed ignition means that the released material is ignited after dispersion in the atmosphere resulting in possibly much larger consequence areas.

The probability assessment of the consequences also includes the annual frequency distribution of the weather conditions (wind direction, wind speed and Pasquill stability class). The stability class and the wind velocity determine the dispersion of flammable or toxic clouds in the surroundings. Weather data can often be obtained via weather stations as present on (local) airports.

Risk is determined by two attributes; the adverse effects (consequences) of an accident and the frequency that these consequences occur. Risk is a function of both attributes. In this QRA study two types of risk are considered, based on Dutch legislation (Min I&E, 2010). The following definitions for risks are used: locational risk and societal risk.

#### **2.2.4.1 Locational risk**

The locational risk is the frequency per year that a hypothetical person will be lethally affected by the consequences of possible accidents during an activity with hazardous materials, e.g. a chemical plant or transport activities.

This risk indicator is a function of the distance between the exposed person and the activity, regardless whether actually people are living in the area, or at the specified location. Locational risk (LR) is presented in contours on maps of the surroundings; the contours connect locations of equal LR. The locational risk is also referred to as the individual risk.

#### **2.2.4.2 Societal risk**

The societal risk is the cumulative frequency that a minimum number of people will simultaneously be killed due to possible accidents during an activity with hazardous materials.

Here, the actual presence of people in the surroundings is taken into account. The societal risk for transport activities is calculated per single kilometer. Societal risk is also called 'group risk'.

#### **2.2.5 Set-up of the Stress Test**

The STREST Level 1a (ST-L1) is first performed in this chapter for the analysis of technological (industrial) risks related to the oil refinery. The Level 2a (ST-L2a) is then conducted based on Level-1a. No epistemic uncertainty is considered in STREST Level 2a.

### **2.3 PHASE 2: ASSESSMENT PHASE**

Natural events may dramatically interact with industrial equipment thus producing relevant accidents which may produce further struggle to population, which is already under emergency for the occurrence of the natural event, economical damage and lacks of strategic goods (Krausman et al., 2011; Salzano et al., 2013). In order to assess Natech risk, the intensity and the hazard of the natural event, and the corresponding equipment vulnerability must be assessed.

#### **2.3.1 Component Level Assessment (ST-L1a)**

Within the chemical process industry, different equipment exists, each characterised by different structural characteristics and functions. In addition, any chemical process is intended to convert raw materials or intermediate products to final products. Hence, the hazard of the substance, during processing or storage, has to be evaluated, too.

The primary sources that have the propensity to cause accidents can be determined either using the safety report of the plant or through existing risk assessment documentation. However, the selection of relevant hazardous equipment is an important step of the risk analysis procedure, because it allows the reduction of the costs and time needed for the application of the method.

For the aims of this project, equipment have been then categorized in three classes with respect to the design standard: i) Atmospheric equipment (storage tank and process); ii) Pressurised equipment (cylindrical buried; cylindrical over-ground; spheres); and iii) Pipeline system. For each component, vulnerability functions have been assessed and reported in the STREST D4.1 (Salzano et al., 2015).

Quite clearly, the technological hazard cannot neglect the hazards associated with the intrinsic chemical and physical hazards related to the processed or stored substances. Equipment items processing or storing flammable/toxic, highly flammable/toxic or extremely flammable/toxic substances according to the Classification, Labelling and Packaging Regulation (CLP-Regulation (EC) No 1272/2008), have surely to be considered as relevant sources of accidental events. Interestingly, studies have shown that earthquake-triggered structural damage involving water tanks is very similar to tanks containing hazardous materials and their behaviour can be described by a very similar methodology.

Besides, the physical state (gas, liquid, solid) and the operating conditions, which depend on the specific analysed process, are of also extreme importance. Eventually, a hazard matrix has been first developed and may be adopted for risk assessment (Table 2.2).

**Table 2.2 Technology hazard matrix**

<b>1: low 4: high</b>	<b>Liquefied gas</b>	<b>Overheated Liquid</b>	<b>Gas</b>	<b>Cryogenic liquid</b>	<b>Liquid</b>
Pressurised	4	3	3	2	1
Atmospheric	4	3	2	2	1
Pipeline	3	2	2	2	1

This result may be used for prioritizing the case study and the consequence assessment, but must be crossed with the chemical hazard.

To this aim, the REACH Regulation (the Regulation on Registration, Evaluation, Authorisation and Restriction of Chemicals of the European Union, adopted to improve the protection of human health and the environment from the risks that can be posed by chemicals) is useful, if added to the information given by the Seveso Directives (e.g. Dir 2012/18/EU of the European Parliament and of the Council of 4 July 2012 on the control of major-accident hazards involving dangerous substances, amending and subsequently repealing council directive 96/82/EC) and with CLP (Guidance to Regulation (EC) No 1272/2008 on classification, labelling and packaging (CLP) of substances and mixtures, Version 4.1, June 2015, ECHA-15-G-05-EN). Indeed, the CLP informs on the hazard characteristic for any substance, and the Seveso Directives includes a list of chemicals and related threshold amount to consider the same chemicals as dangerous for workers, population and environment. The list reported in Table 2.3 has been synthesized for the sake of brevity. Further details can be found in the cited Directives and regulations. Eventually, the substances to be considered will be only those that are stored or manipulated in sufficient amount to produce damage, i.e. the amount reported in Table 2.3.

**Table 2.3 List of chemicals, expressed by the hazard classification of CLP (EC 1272/2008) and the corresponding amount as given in the Seveso Directive (2002)**

Hazard categories	Amount (tons)
Section 'H' – HEALTH HAZARDS	
H1 ACUTE TOXIC Category 1, all exposure routes	5
H2 ACUTE TOXIC Category 2, all exposure routes; Category 3, inhalation exposure route	50
H3 STOT SPECIFIC TARGET ORGAN TOXICITY – SINGLE EXPOSURE STOT SE Category 1	50
Section 'P' – PHYSICAL HAZARDS	
P1a EXPLOSIVES, Unstable explosives or Explosives, Division 1.1, 1.2, 1.3, 1.5 or 1.6, or Substances or mixtures having explosive properties according to method A.14 of Regulation (EC) No 440/2008 and do not belong to the hazard classes Organic peroxides or Self- reactive substances and mixtures	10
P1b EXPLOSIVES, Explosives, Division 1.4	50
P2 FLAMMABLE GASES Flammable gases, Category 1 or 2	10
P3a FLAMMABLE AEROSOLS, Flammable aerosols Category 1 or 2, containing flammable gases Category 1 or 2 or flammable liquids Category 1	150
P3b FLAMMABLE AEROSOLS, 'Flammable' aerosols Category 1 or 2, not containing flammable gases, Category 1 or 2 nor flammable liquids category 1)	5 000
P4 OXIDISING GASES Oxidising gases, Category 1	50
P5a FLAMMABLE LIQUIDS, Flammable liquids, Category 1, or Flammable liquids Category 2 or 3 maintained at a temperature above their boiling point, or Other liquids with a flash point ≤ 60 °C, maintained at a temperature above their boiling point	10
P5b FLAMMABLE LIQUIDS, Flammable liquids Category 2 or 3 where particular processing conditions, such as high pressure or high temperature, may create major-accident hazards, or Other liquids with a flash point ≤ 60 °C where particular processing conditions, such as high pressure or high temperature, may create major-accident hazards	50
P5c FLAMMABLE LIQUIDS, Flammable liquids, Categories 2 or 3 not covered by P5a and P5b	5 000
P6a SELF-REACTIVE SUBSTANCES AND MIXTURES and ORGANIC PEROXIDES, Self-reactive substances and mixtures, Type A or B or organic peroxides, Type A or B	10
P6b SELF-REACTIVE SUBSTANCES AND MIXTURES and ORGANIC PEROXIDES, Self-reactive substances and mixtures, Type C, D, E or F or organic peroxides, Type C, D, E, or F	50
P7 PYROPHORIC LIQUIDS AND SOLIDS Pyrophoric liquids, Category 1 Pyrophoric solids, Category 1	50
P8 OXIDISING LIQUIDS AND SOLIDS Oxidising Liquids, Category 1, 2 or 3, or Oxidising Solids, Category 1, 2 or 3	50
Section 'E' – ENVIRONMENTAL HAZARDS	
E1 Hazardous to the Aquatic Environment in Category Acute 1 or Chronic 1	100
E2 Hazardous to the Aquatic Environment in Category Chronic 2	200
Section 'O' – OTHER HAZARDS	
O1 Substances or mixtures with hazard statement EUH014	100
O2 Substances and mixtures which in contact with water emit flammable gases, Category 1	100
O3 Substances or mixtures with hazard statement EUH029	50

### 2.3.2 System Level Assessment for Single Hazard (ST-L2b / L2d)

#### 2.3.2.1 Probabilistic Risk Assessment

The standard scenarios and frequencies are taken from the Purple Book (VROM, 2005c). Table 2.4 gives the standard frequencies for atmospheric single containment tanks and pressurized vessels.

**Table 2.4 Standard scenarios and frequencies stationary vessels**

Scenario	Frequency (-/yr)	
	Atmospheric vessels- single containment	Pressurized vessels
Instantaneous release of the complete inventory	5.00E-06	5.00E-07
Continuous release of the complete inventory in 10 min at a constant rate of release	5.00E-06	5.00E-07
Continuous release from a hole with an effective diameter of 10 mm	1.00E-04	1.00E-05

Normally two pipeline failure modes are considered for QRA's: a full bore rupture and a small leak. Depending on the configuration of the pipeline a full bore rupture could result in a two sided outflow: outflow determined by the upstream equipment/ conditions and back flow from the downstream equipment. In order to consider pipeline failure correctly, detailed information on the pipeline layout, conditions and safety measures are necessary. This detailed information is not available and pipeline scenarios as defined in the Purple Book have not been taken into account. As pipelines might be more vulnerable to natural hazards than storage vessels, completely ignoring the pipelines would result in an underestimation of the impact of natural hazards on the risk. For that reason an additional scenario (failure mode) has been defined: the full bore rupture of the pipeline connected to the storage vessel, resulting in the loss of containment of the storage vessel. Backflow from downstream equipment is not considered. The failure frequency of the pipeline connection is based on the PB and a 1 m pipeline length, see Table 2.5.

**Table 2.5 Standard scenarios and frequencies above ground pipelines (VROM, 2005a)**

Scenario	Frequency (-/yr)		
	Diameter < 75 mm	75 mm =< Diameter =< 150 mm	Diameter > 150 mm
Full bore rupture	1.00E-06	3.00E-07	1.00E-07

Most tanks are located in large catch basins that encompass several tanks. Each tank is located in a dedicated sub-basin: small leakages remain contained in the sub-basin where the leakage occurs without spreading to the other tanks, and for larger leakages the liquid can spread to the neighboring sub-basin, but remains contained within the main-basin. For the large leak scenarios (instantaneous and 10 minute release), it has been assumed that the liquid will spread beyond the sub-basin. These scenarios have been located at the center of the main-basin. For the instantaneous scenario it has been assumed that due to overtopping a surface of 1.5 times the main-basin area is covered by liquid (see Table 2.6).

**Table 2.6 Pool surfaces**

Scenario	Pool surface considered
Instantaneous release tank	1.5 · main-basin
10 minute release tank	main-basin
10 mm leak tank	sub-basin

Failing of the bund (basin) walls is not considered. The impact of natural hazards on the accident or release scenarios and frequencies is discussed. The release frequencies are given in Table 2.7. These frequencies have been calculated by taking into account the methodology described in STREST D4.1 (Salzano et al., 2015), where equipment vulnerability with respect to the intensity of the natural events has been assessed by taking into account the construction characteristics of equipment and, more important, the new limit states based on the release of content.

**Table 2.7 Scenarios and frequencies stationary vessels due to natural hazards**

Scenario	Frequency (-/yr)		
	<i>Atmospheric vessels- single containment</i>	<i>Pressurized vessels</i>	<i>Pipelines</i>
<b>Earthquake</b>			
Instantaneous release of the complete inventory	$3.70 \cdot 10^{-3}$	$1.16 \cdot 10^{-9}$	
Continuous release of the complete inventory in 10 min at a constant rate of release	$3.70 \cdot 10^{-3}$	$1.16 \cdot 10^{-9}$	
Continuous release from a hole with an effective diameter of 10 mm	$7.33 \cdot 10^{-2}$	0	
Full bore rupture			$5.56 \cdot 10^{-2}$
<b>Tsunami</b>			
Instantaneous release of the complete inventory	$1.85 \cdot 10^{-5}$ - $3.47 \cdot 10^{-4}$	0	
Continuous release of the complete inventory in 10 min at a constant rate of release	$1.85 \cdot 10^{-5}$ - $3.47 \cdot 10^{-4}$	0	
Continuous release from a hole with an effective diameter of 10 mm	0	0	
Full bore rupture			0
<b>Earthquake + Tsunami</b>			
Instantaneous release of the complete inventory	$3.7 \cdot 10^{-3}$ - $4.05 \cdot 10^{-3}$	$1.16 \cdot 10^{-9}$	
Continuous release of the complete inventory in 10 min at a constant rate of release	$3.7 \cdot 10^{-3}$ - $4.05 \cdot 10^{-3}$	$1.16 \cdot 10^{-9}$	
Continuous release from a hole with an effective diameter of 10 mm	$7.33 \cdot 10^{-2}$	0	
Full bore rupture			$5.56 \cdot 10^{-2}$



For earthquake induced releases, the release frequencies are location independent: all atmospheric vessels have the same release frequency, as well as the pressurized vessels and pipelines. No small releases are observed for pressurized vessels. The frequencies refer to the probability of failure of one or more tanks as a result of the earthquake or tsunami. It is assumed that one catch basin is large enough to hold the volume of the failing tanks and that the catch basin remains intact during and after an earthquake or tsunami. Hence the pool size is not affected by the number of tanks collapsing. Similar as for the industrial risks, for the instantaneous scenario it has been assumed that due to overtopping a surface of 1.5 times the main-basin area is covered by liquid. The effect calculations are based on the released volume of one tank.

For tsunami induced releases the location of the vessel determines the release frequency. Only vessels within approximately 250 m from the shore line will suffer damage due to the tsunami and release their contents. The release frequency is not the same for all vessels. That is the reason why in the table a frequency range is given. All pressurized vessels are located further from the shore. No pipeline ruptures or small leakages are caused by the tsunami, no matter where the vessels or pipelines are located. For more information on the release frequency, please refer to WP4.

### **2.3.2.2 Scenario based Assessment**

Flammable substances can be ignited upon release. Direct ignition will lead to a pool fire (liquids) or jet fire (gases). If a liquid is not ignited immediately, it will start to evaporate and a flammable atmosphere could be formed, which will disperse with the wind. If a gas is not ignited immediately, the gas will also disperse.

Ignition of that flammable cloud will result in a flash fire, with possibly an explosion (causing overpressure effects), if the cloud is obstructed. It has been assumed that the consequences of a delayed ignition are minor compared to the consequences of a pool fire for the flammable liquids: only pool fires have been considered. A special phenomenon occurs upon the instantaneous release of a liquefied gas. An instantaneous release is followed by an instantaneous evaporation and a physical explosion, called Boiling Liquid Expanding Vapour Explosion (BLEVE). Often the gas cloud is ignited resulting in a fireball. There are two causes for the occurrence of a BLEVE:

- As a result of mechanical impact or a material defect the tank tears open instantaneously at saturated pressure at ambient temperature. This is called a "cold" BLEVE;
- A BLEVE arising from a fire near the tank. The fire may arise by the release of flammable liquid from a nearby tank. The heat radiation of the fire heats up the contents of the (liquefied) gas tank and the pressure in the gas tank rises. When the wall temperature at the top (gas side) reaches above 500°C, the steel tank wall will weaken and collapse. This is called a "warm" BLEVE. Due to the higher pressure of the gas in the tank when it collapses, the consequences of a warm BLEVE are larger than of a cold BLEVE.

Only a cold BLEVE has been taken into account. For a warm BLEVE a (pool) fire heating the LPG tanks is required. It is assumed that the flammable liquid pool formed as a result of the collapse of the atmospheric storage tanks (see previous paragraph) does not reach the area with the LPG tanks and that a pool fire under the LPG spheres is not possible.

The probability of ignition depends on the flammability of a substance and the quantity released. Table 2.8 presents the ignition probabilities according to the Purple Book.

**Table 2.8 Ignition probabilities**

Source		Direct ignition probability (-)				
		Substance				
Continuous	Instantaneous	K3,4	K2	K1 liquid	K0, Gas, low reactive	K0, Gas, average/ high reactive
< 10 kg/s	< 1000 kg	0	0.01	0.065	0.02	0.2
10-100 kg/s	1000- 10 000 kg	0	0.01	0.065	0.04	0.5
> 100 kg/s	> 10 000 kg	0	0.01	0.065	0.09	0.7

Table 2.9 gives the definition of the substance classification. Not all substances present on site are considered individually and representative substances have been determined.

**Table 2.9 Definition flammability classes**

Category	WMS category	Definition
K0	Extremely flammable	Liquid with flash point < 0°C and boiling point =< 35°C Gases that may ignite at normal temperature and pressure when exposed to air
K1	Highly flammable	Liquid with flash point < 21°C but which are not extremely flammable
K2	Flammable	Liquid with flash point >= 21°C and =<55°C
K3		Liquid with flash point >55°C and =< 100°C
K4		Liquid with flash point > 100°C

Table 2.10 shows which representative substance is used for each product. Atmospheric residue, heavy vacuum gas oil and vacuum residue have not been considered in the QRA. For all flammable liquids considered, the ignition probability of K1-liquids is assumed- this is a conservative approach. The probability of a BLEVE is given in Table 2.11.

**Table 2.10 Representative substances**

Product	Representative substance
Atm residue	NA
Crude	Pentane
Fuel oil	Nonane
Gasoil	Nonane
Gasoline	Pentane
HVGO	NA
Jet/ kerosine	Nonane
LPG	Propane
Naphtha	Pentane
Others	Pentane
VAC residue	NA

**Table 2.11 BLEVE probability**

	Probability BLEVE
Stationary installations	0.7

## 2.4 PHASE 3: DECISION PHASE

### 2.4.1 Risk objectives check

No (limited) vulnerable objects or installations are allowed in areas where the locational risk is higher than  $10^{-6}$ /yr. Vulnerable objects are dwellings, medical centers, hospitals, schools etc. Limited vulnerable objects are offices, shopping malls, commercial activities etc.

A maximum allowed societal risk standard does not exist; only a guidance value has been defined. This guidance value means that the authorities will allow the proposed activity if the societal risk is below the guidance value. The authorities are allowed to accept activities with higher societal risks than the guidance value or activities causing an increase in the risk in certain circumstances. In such a case the authorities have to balance the pros and cons of the proposed activity.

After the risks of the activities have been calculated, the risks are compared with risk acceptance standards. If needed, risk-reducing measures can be identified. Distinction can be made between preventive and repressive measures and between measures acting on the consequences and on the probability.

The risks of each separate event are first compared: solely industrial, earthquake or tsunami induced risks. Fig. 2.16 presents the locational risk contours. The black crosses indicate the location of the scenarios.

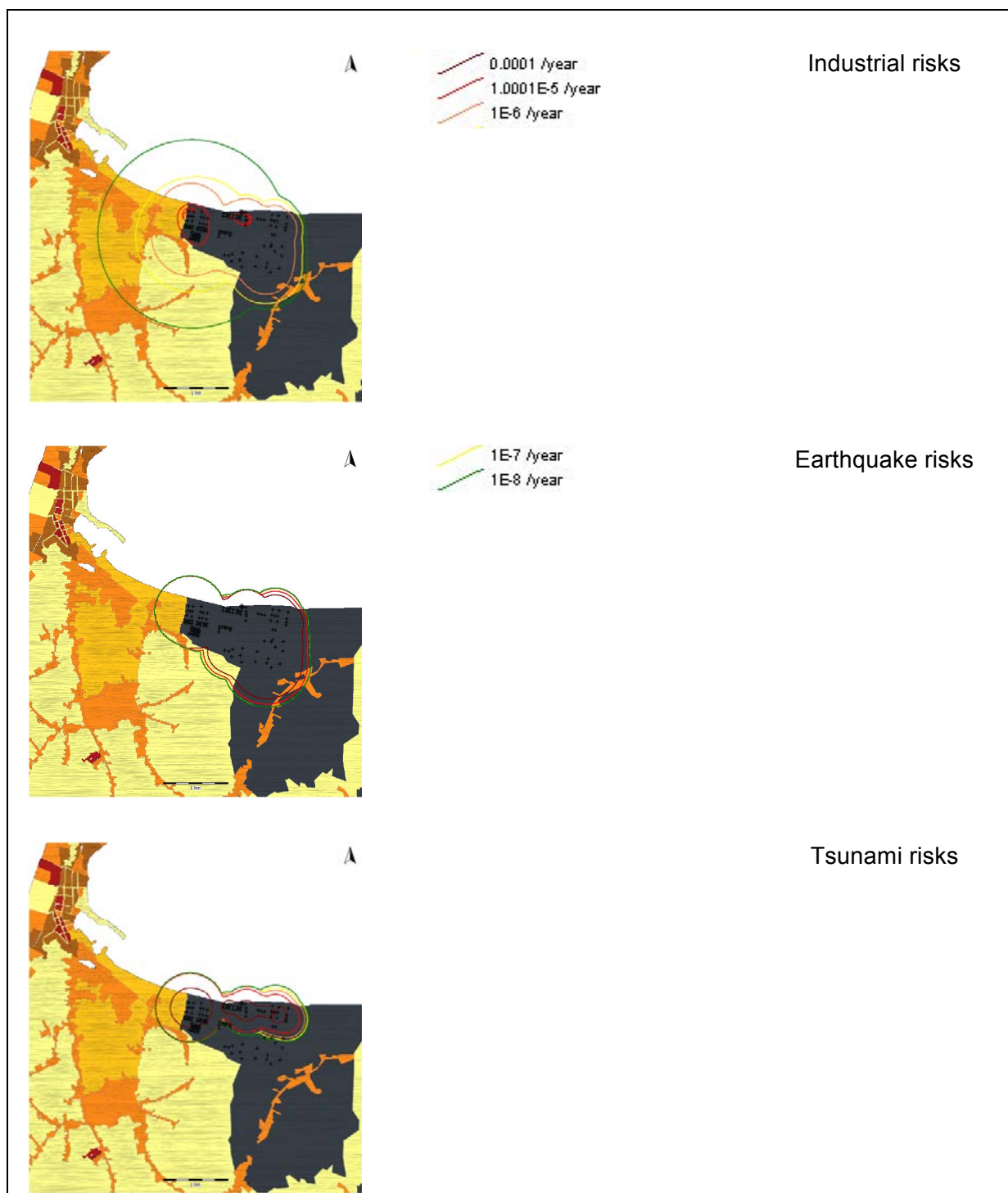


**Fig. 2.16 Locational risk – Single causes only. Larger figures are included in Appendix I**

The industrial risks result in large contours, especially for the lower risk levels ( $10^{-7}$ ,  $10^{-8}$ /yr). These contours are dominated by the risks related to the LPG storage vessels. The location of the LPG tanks is given in Fig. 2.17 by the red squares.

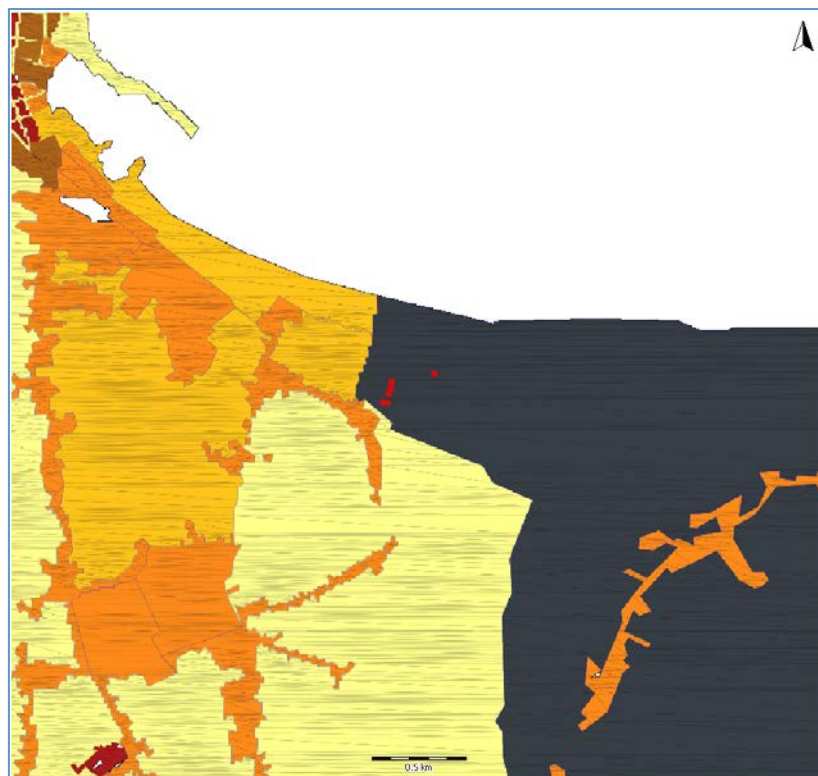


**Fig. 2.17 Location of LPG Spheres (red squares)**

When only considering earthquake induced risks the  $10^{-7}$  and  $10^{-8}$ /yr risk contours are smaller. This is due to the lower release frequency for the LPG vessels. The higher risk levels ( $> 10^{-6}$ /yr) are dominated by the atmospheric vessels. These have a higher release frequency compared to the industrial risks, resulting in larger  $10^{-5}$  and  $10^{-4}$ /yr contours.

The industrial risks on the right side of the site are mainly caused by the atmospheric tanks. When comparing the industrial risks with the earthquake induced risks, one can observe that the risks on the right side of the site have increased by a factor of approx. 1000: for the earthquake induced risks the,  $10^{-4}$ /yr contour is located at almost the same location as the  $10^{-7}$ /yr contour of the industrial risks. This is due to the failure frequency of the atmospheric tanks: failure due to earthquake is a factor 1000 higher than failure due to industrial activities.

The risks associated with tsunami-induced releases are the smallest of the three release causes. Only atmospheric vessels close to the shore will result in releases. Vessels located further away do not pose risks.

### 2.4.2 Disaggregation/Sensitivity Analysis

Fig. 3.18 shows the location risk when considering Industrial risks + earthquake induced risks, Industrial risks + tsunami induced risks and Industrial risks + earthquake and tsunami induced risks. The three events have been considered as independent.

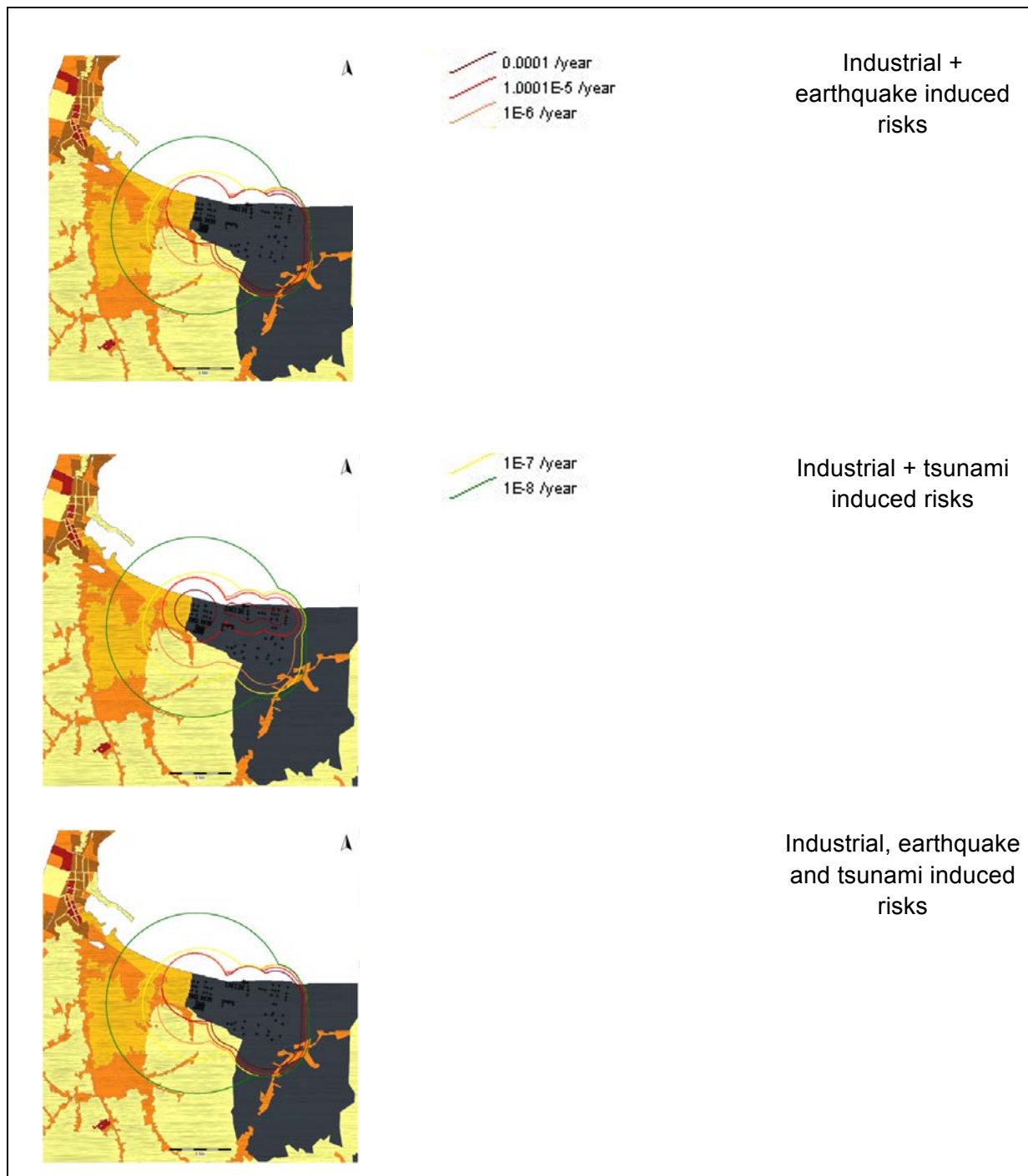


**Fig. 2.18 Locational risk – Cumulated risks**

The most dominant risks are the industrial and earthquake induced risks.

### 2.4.3 Guidelines and critical events

For a better comparison of the locational risk, a horizontal cross-section of the locational risk is made. This line is given in Fig. 2.19.

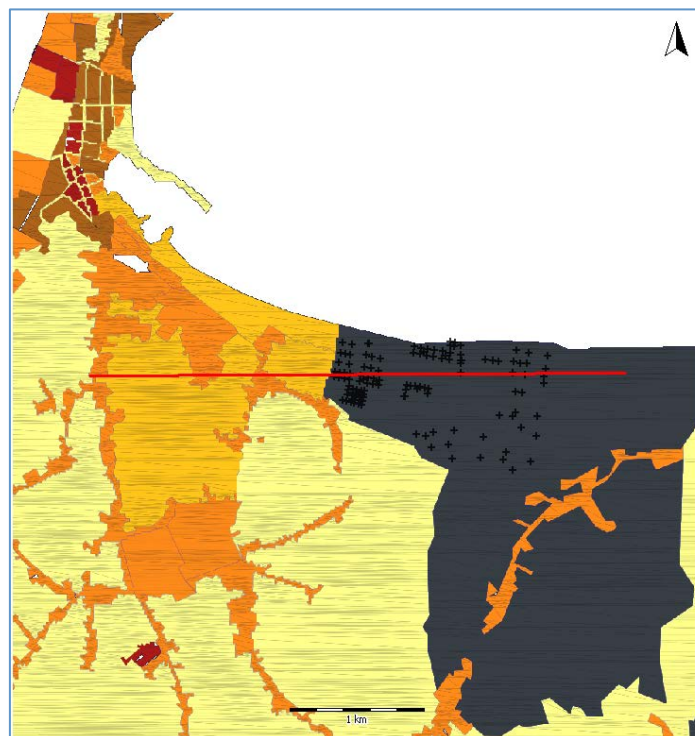


Fig. 2.19 Location of the cross-section of the locational risk (red line)

The locational risk along the red line is given in the next figure. The distance 0 m corresponds to the left end of the red line in Fig. 2.20.

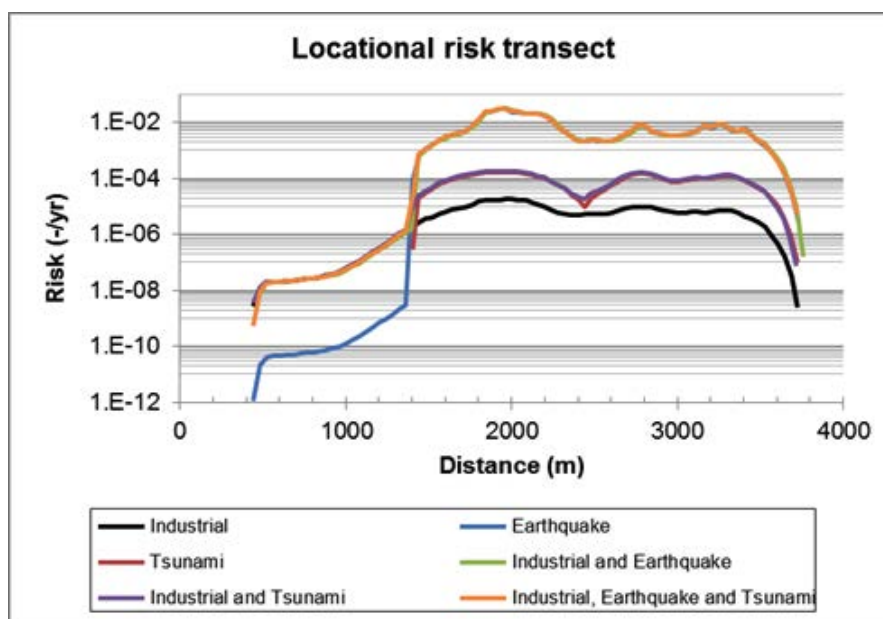


Fig. 2.20 Locational risk transect



The black line (industrial risks) is overlapped by the purple (industrial + tsunami), orange (industrial + earthquake + tsunami) and green (industrial + earthquake) lines between 0 and 1400 m. The red line (tsunami) starts at 1400 m and is overlapped by the purple line (industrial + tsunami). Beyond 1400 m the orange (industrial + earthquake + tsunami) line, blue line (earthquake) and green line (industrial + earthquake) overlap.

This figure shows that for this pilot case low risks ( $< 10^{-6}$  /yr) are dominated by the industrial risks as these risks are caused by failure of the LPG vessels. Earthquake and tsunami do not damage these vessels. Tsunami results in approximately 10 times higher risk along the transect line and earthquakes in approximately 1000 times higher risk.

Naturally induced hazards cause an increase in the total risks. As a tsunami only damages a limited number of the vessels along the shore line, the risk increase is limited.

Similar results, for earthquakes only and simplified analysis for the earthquake hazard, have been found in other works (Salzano et al., 2003; Campedel et al., 2005; Fabbrocino et al., 2008; Salzano et al., 2009).

The societal risk for the base situation (without accounting for natural hazards) is presented in Fig. 2.21.

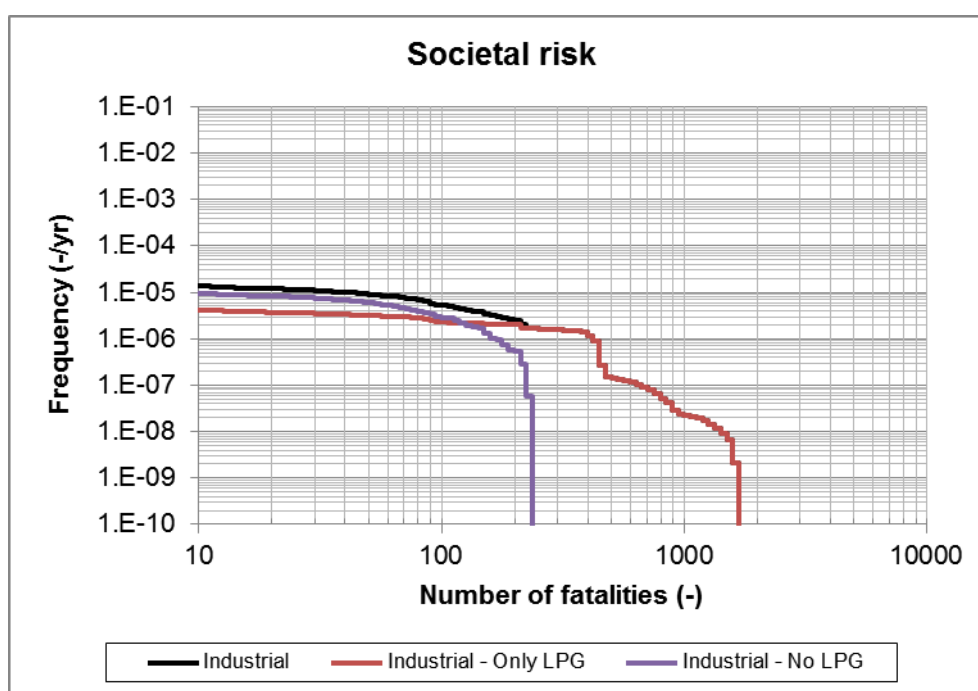


**Fig. 2.21 Societal risk without accounting for natural hazards- with and without LPG tanks**

The societal risk is mainly caused by the LPG tanks, as can be seen by comparing the black and red line. By not accounting for the LPG tanks (purple line), the maximum number of fatalities is reduced from 1650 to 220.

Fig. 2.22 shows the societal risk per cause. Up to approx. 200 fatalities the naturally induced hazards have a higher frequency of occurring, due to the higher failure frequency of the atmospheric vessels. Larger numbers of fatalities are only caused by industrial risks or by earthquakes - this is due to the failure of the LPG vessels.



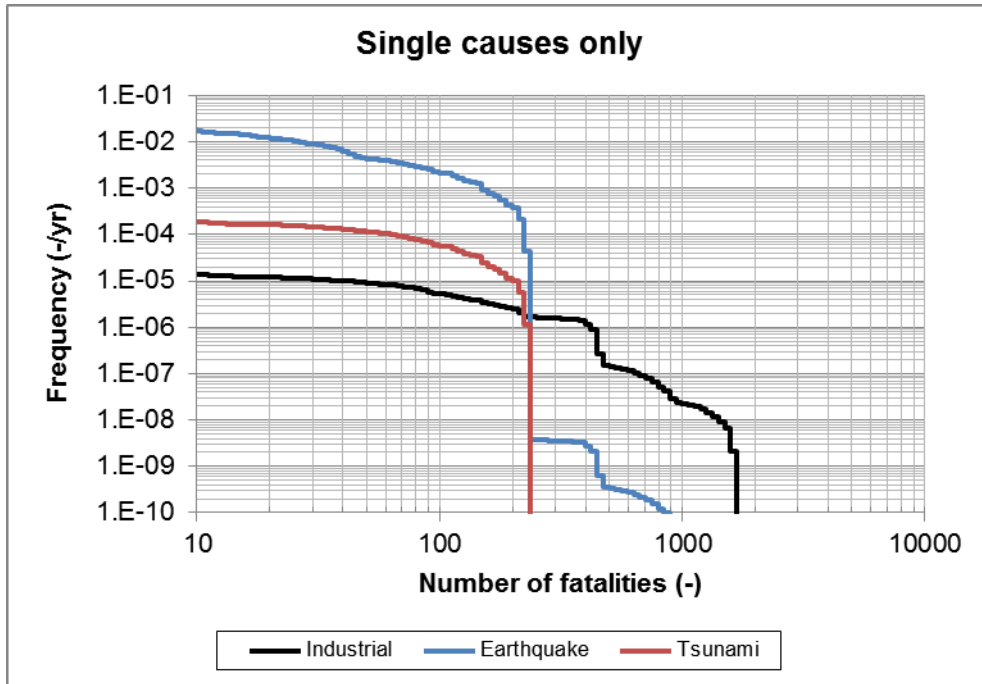


**Fig. 2.22 Societal risk- industrial, earthquake or tsunami induced**

The cumulated risks are given in Fig. 2.23 (the orange and green line overlap).

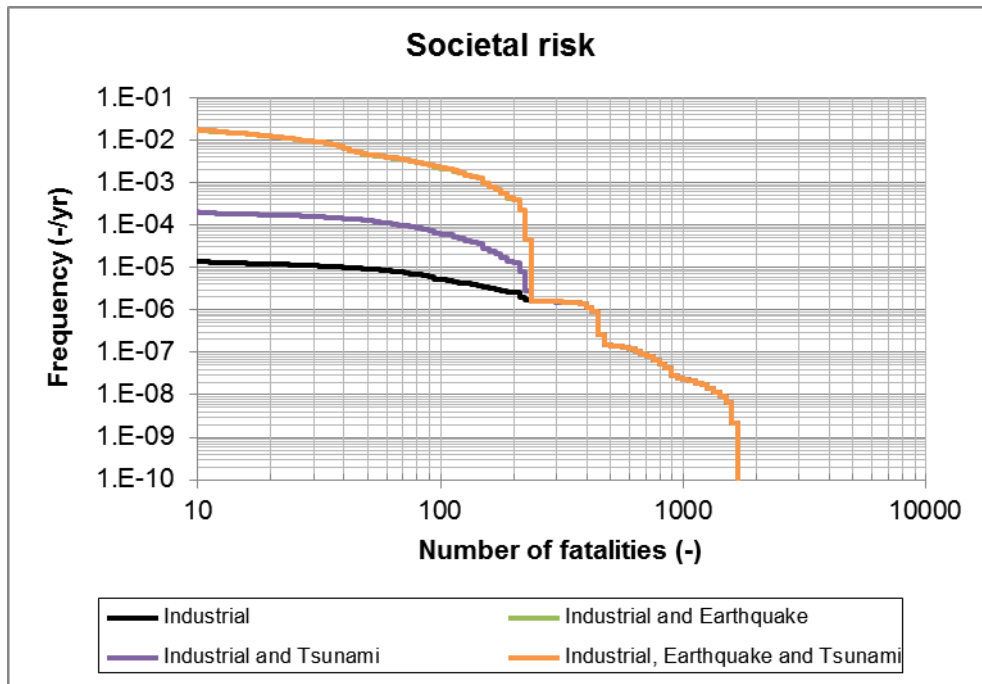


**Fig. 2.23 Societal risk- cumulated risks**

Fatalities up to approx. 200 are dominated by earthquakes; more than 200 fatalities are dominated by the industrial causes.

## 2.5 PHASE 4: REPORT PHASE

Naturally induced hazards can play an important role in the total risk associated with the presence of installations with dangerous goods. In this study the effect of an increased frequency (caused by earthquakes or tsunamis) of a number of release scenarios on locational and societal risk was assessed.

The impact of natural induced hazards depends on many (location specific) factors. For the specific site analyzed in this work, a tsunami only damages a limited number of the atmospheric storage vessels along the shore line. Hence the increase on the total risk is limited. Nonetheless, the overloading of emergency response should be considered, at least for the tanks along the coastline.

Of more importance is the effect of an earthquake, which significantly increases the failure frequency of atmospheric storage tanks. Neither an earthquake nor a tsunami significantly increases the failure frequency of, and hence risk imposed by, pressurized vessels (like LPG spheres). As for the considered site the risk is largely dominated by the LPG tanks (which fail due to industrial-related causes) the impact of the natural hazards is limited.

All in all though, naturally induced hazards should be considered when determining the overall risk and the risks associated with natural disaster.

This pilot case has been performed to show the impact of naturally induced hazards on the outcome of a quantitative risk assessment (QRA) of an industrial site holding dangerous substances. The aim was not to perform a detailed QRA of the pilot site (for such exercise much more detailed information would have been required) but merely to show how (the more common) scenarios are affected by an increased release frequency caused by earthquakes and tsunamis.

Other scenarios that may be relevant in cases of earthquakes or tsunamis have not been evaluated. For instance failure of multiple tanks has not been taken into account. This may result in released volumes exceeding the catch basins capacity, and hence lead to larger pool sizes, especially in case of failure of catch basins.

Also domino effects have not been considered. For instance, if a pool of flammable material extends to an area with LPG spheres, BLEVEs may occur. Neither has the effect of debris (or large objects like ships) carried land inward with a tsunami, been taken into account. Such phenomena will result in larger effect areas, and may hence increase the number of casualties. However, it should be realized that the natural hazards we are considering here (earthquakes and tsunamis) have a large areal impact. This means many of the fatalities calculated in the QRA, would have occurred also had such an installation not been present, because of the collapse of houses and other buildings. In other words, the additional number of casualties caused by the damaged industrial installations may very well be much smaller.

## **3 CI-A2 Large dams in the Valais region of Switzerland**

### **3.1 INTRODUCTION**

#### **3.1.1 General description of the CI**

Although the definition of what comprises a large dam can be discussed, accepting a dam height criteria of more than 15 m there are about 60 000 of large dams in the World registered by the International Commission on Large Dams (ICOLD). Of course, dams can go well beyond this threshold, with the highest dam ever built – the Chinese Jinping-I Dam, completed in 2013 – rising to some staggering 305 m.

In Switzerland alone, there are 184 major dams that fall under the supervision of the Swiss Federal Office of Energy (SFOE), being 25 over 100 m tall and 4 topping the 200 m mark.

Dams can hold a substantial amount of energy in the form of water stored in the reservoirs. When this water is abruptly released, downstream activities are severely affected and people's lives endangered.

Although design, maintenance, and surveillance practices depend on national legislations, the international guidelines (e.g. ICOLD) that many national codes reflect aim to avoid dam failures altogether, this being true even in the face of extreme natural events (such as floods or earthquakes). Worldwide this objective has been, at least so far, very well met. Fortunately, in the last decades relatively few large dams have failed due to natural causes in countries that enforce the internationally accepted best practices in terms of dam safety.

In terms of design, two main types of large dams can be highlighted: embankment and concrete dams. While numerous subclasses exist, embankment dams can be summarily divided into earthfill and rockfill structures, depending on the materials used, while most concrete dams can be broadly identified as arch, gravity, or buttress, depending on the load distribution within the structure and the interaction with the foundation and the abutments.

Regardless of their specific characteristics, dams operate by storing substantial volumes of water in the upstream reservoir, the release of this water to downstream areas being controlled according to operational guidelines and targets. In view of that, in order to correctly frame risk and vulnerability assessments for dams, one should consider, beyond the dam body, the foundation, the reservoir, the appurtenant structures (e.g. spillways, bottom outlets, or hydropower systems) and, most importantly, the downstream areas potentially affected by floods.

Following a dam failure or breach, typically characterized by an uncontrolled release of the reservoir, a large amount of water travels downstream in the form of a dam-break wave. Such waves move extremely fast and have enormous eroding power, as well as transport capacity. They affect downstream areas more seriously than natural floods due to their velocity, magnitude, and the large amount of debris usually carried. While the dam-reservoir system is vulnerable to several hazards and monetary losses associated with it in the event

of a failure amount to very large figures, the larger share of the losses associated with a dam failure are likely to occur downstream (Fig. 3.1).

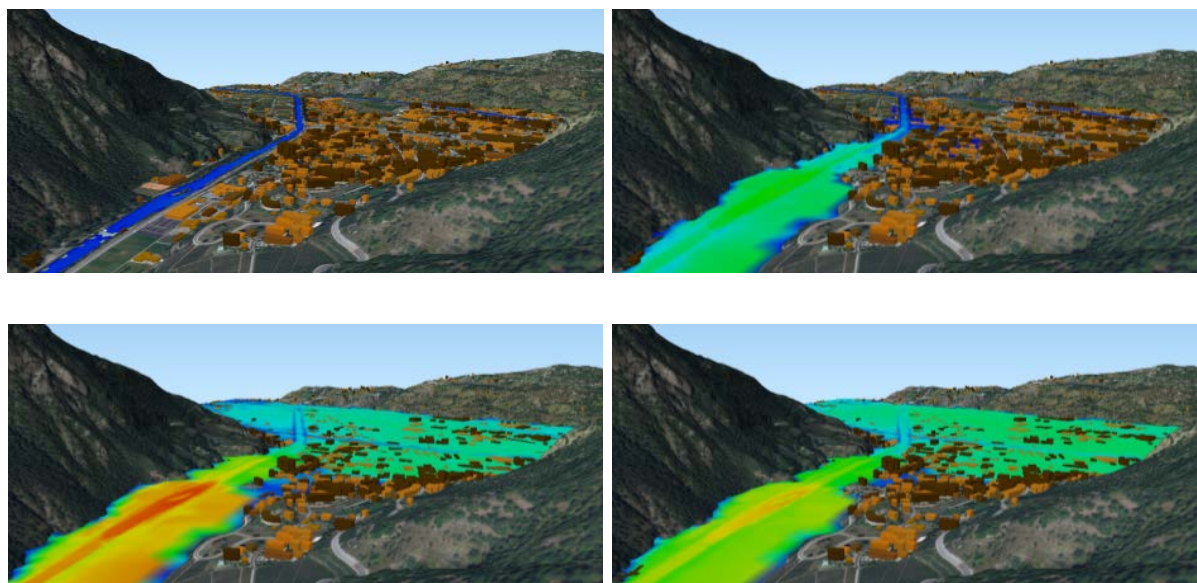


**Fig. 3.1 Simulation of the propagation of a dam-break flood wave through an urban area. The time lapse between illustrations is of 20 minutes**

Dam engineering progressed remarkably in the course of the 20<sup>th</sup> century. On par with this progress, dam safety standards have been evolving as a response to historical disasters and new knowledge being gathered. Following each of the major dam failures that did occur during the 20<sup>th</sup> century, the dam engineering community has improved its effectiveness at preventing disasters and, today, remarkable tools are available to predict the response of dams to a broad range of hazards.

Large dams are designed (and retrofitted if needed) to withstand rare events (e.g. 10 000 return period or maximum credible earthquakes, 10 000 return period or probable maximum flood). The ways in which to cope with individual actions are well known for a whole range of potentially dangerous hazards and, to some extent, even combinations of different events are contemplated in guidelines (two examples are that following a major earthquake dams should be able to route a flood, and that extreme floods must not lead to unsafe reservoir levels even in the face of limited mechanical equipment malfunctions).

Dam safety is most commonly tested using deterministic frameworks where the system's response is simulated and analyzed for a given number of limit cases. This kind of testing relies on the assumption that the limit cases being evaluated adequately represent all other combinations and that could potentially lead to a failure. Although the deterministic approach has proven very successful, the aforementioned assumption leaves countless possibly disastrous combinations of events unchecked.

An additional limitation of the deterministic approach is that the probability of occurrence of the limit cases under test is not necessarily known and, therefore, even if the risk associated with the infrastructure can qualitatively be considered small, it remains unknown in quantitative terms.

Probabilistic approaches to dam safety assessment do exist (applied for example in Canada or Australia), but they pose problems of their own. From a political and societal standpoint, the legal acceptance that a large dam can fail – even if with an extremely reduced probability – may lead to complex issues. From a technical perspective, large dams' features change widely in order to adapt to each project's specificities and their behavior is not easily – nor should it be – predicted without the laborious undertaking of customized numerical simulations (e.g. Gunn et al., 2016; Zenz and Goldgruber, 2013). Due to these simulations' demands, including them in a broader probabilistic framework can be very difficult.

Safety assessments for large dams have been routinely carried out for decades. These often include geological surveys, numerical modeling of the dam structures, hydrological studies focusing on flood hazards, and hydraulic evaluations of outlet structures. The engineering supporting these endeavors is well developed, but presents as a possible weakness the fact that emphasis is placed on extreme hazards and the combinations of less unlikely events are not necessarily focused.

As more and more knowledge is amassed about dams' responses to specific hazards, and engineering practices evolve, the main sources of risk may be argued to be shifting from very rare natural hazards to chains or combinations of less unlikely events. These may be the unfortunate coincidence of several hazards or “mishaps” related to human errors or equipment malfunctions (e.g. Hartford and Baecher, 2004). Dealing with such chains of events is a complex task by virtue of possible inter- and intra-hazard interactions. Tackling it within a deterministic framework is nothing short of cumbersome.

This chapter aims to address the aforementioned historical bias towards a focus on extreme events. In doing so, attention is given to a probabilistic framework that allows to adequately model hazard intra- and inter-actions, as well as epistemic uncertainty. The computational tool adopted to perform the task is the Generic Multi-Risk (GenMR) framework. GenMR is based on a sequential Monte Carlo method and its principles are well described in Mignan (2014). Obviously, reliable outcomes are very much dependent on realistic inputs.

The work described below is a follow-up to STREST's D4.1 (Salzano et al., 2015) where the basis of the methodology is laid out. For further details the reader can refer to that document, as in order to avoid repetitions, the nuts and bolts of the developed model will not be dealt with here.

In the following subsections, the methodology is described based on a conceptual case study of a large alpine earthfill dam. The infrastructure is approximately 100 m high, with a reservoir capable of holding over 100 000 000 m<sup>3</sup> of water. It is equipped with a spillway in order to cope with excessive water levels, a bottom outlet that allows for the control of the volume of water stored, and a hydropower system through which the main purpose of the dam is fulfilled: producing energy. As previously mentioned, the dam interacts substantially with the reservoir and, accordingly, both are explicitly modeled. The modeled system includes also the valley below the dam down to a distance of roughly 30 km, where a sizable urban agglomeration is assumed to exist.

### **3.1.2 Summary of the proposed stress test**

The proposed stress test does not aim to substitute the large dam safety evaluations based on deterministic frameworks that are in practice today, but rather complement them. In fact, that kind of detailed study should be on par with the scenario based assessments of ST-L3 and its requirements may well exceed the resources made available to the completion of this



chapter. Also, they require expertise on a whole range of topics including structural engineering, geotechnical engineering, hydrology, hydraulics, mechanical engineering, and electrical engineering, among others.

As mentioned previously, when dam failures do occur, the bulk of the losses take place in downstream areas as the result of the passing dam-break flood wave. As such, in order to qualify the risks associated with a large dam it is advisable to look not only into the dam-reservoir system itself, but also into the propagation of the flood wave and its effects on downstream areas (Fig. 3.2).



**Fig. 3.2 Implementation of two large Alpine dams in Switzerland: Les Toules and Mauvoisin. Both are placed in tributaries of the Rhone River and, in the event of a failure, the main urban areas where losses could be expected are relatively far downstream. Neither of these dams is analyzed in this document**

Albeit important to estimate losses and risk, downstream areas do not affect the dam-reservoir system. Exploiting this, the proposed stress test effectively divides the domain of interest into upstream and downstream subsystems, being the former responsible for evaluating what combinations of hazards may lead to failures and with what probability, and the latter used as a means to compute losses Fig. 3.3.

Although comprising all key steps of a recommended stress test, the work presented herein, deals with a conceptual system and makes assumptions about the frequency and actions of main hazards and the responses of the key components of the system. These are defined

on the pre-assessment phase (PHASE 1) and have direct impacts on ST-L1a, the component level assessment of the assessment phase (PHASE 2).

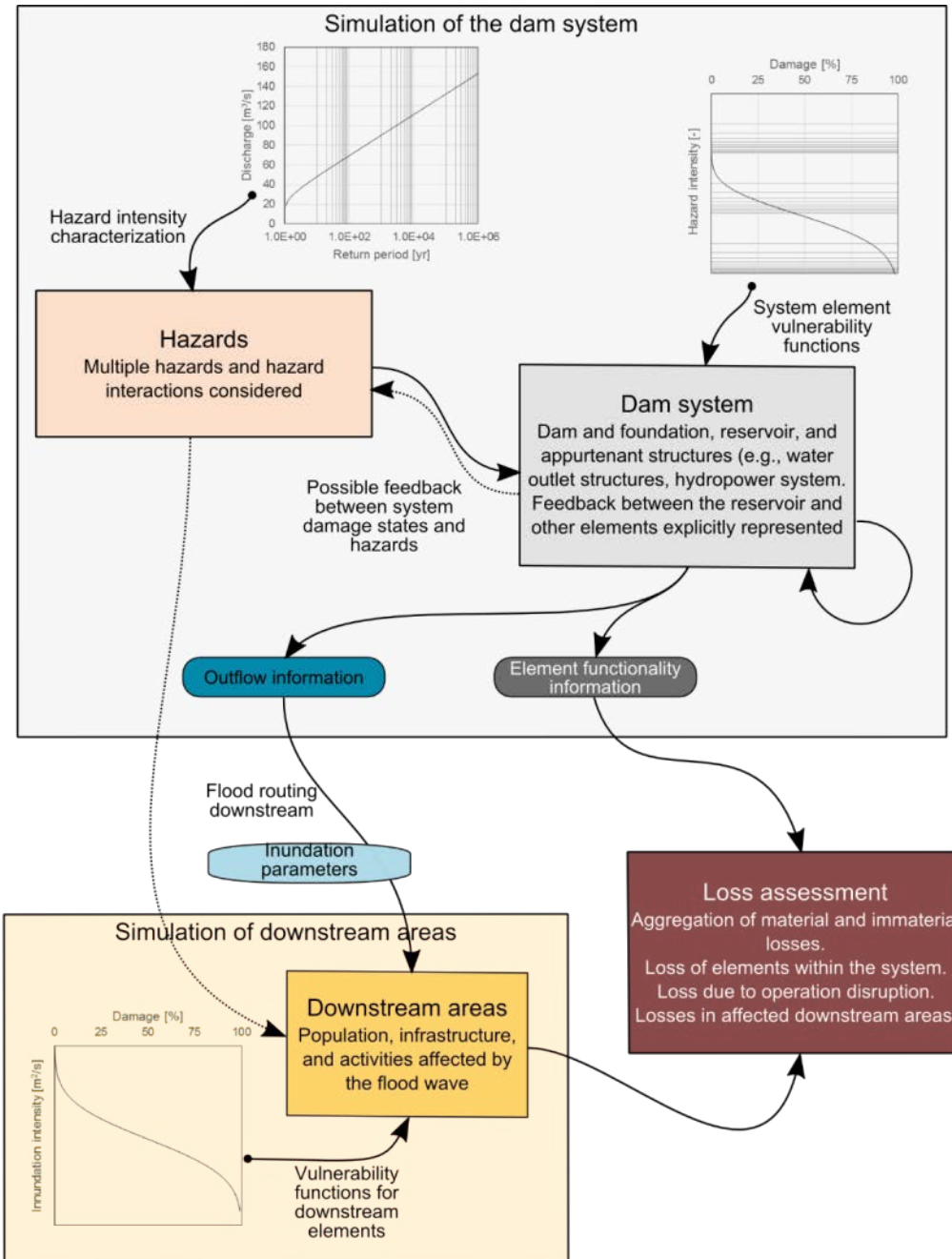


**Fig. 3.3 Overall scheme of the analysis framework, with a clear separation between upstream and downstream areas. From Salzano et al. (2015)**

Still in PHASE 2, the system is evaluated when exposed to single (ST-L2) and multiple hazards (ST-L3). For both levels probabilistic and scenario based assessments are made. Earthquakes and floods, arguably the most relevant hazards affecting large dams, were independently modeled under the scope ST-L2. The effects of multiple hazards, evaluated in ST-L3, consider the five main hazards: earthquakes, floods, internal erosion, bottom outlet

malfunctions, and hydropower system malfunctions. The probabilistic assessment that is made explores direct and indirect coincidences, intra, and interactions of these hazards, damage states, and reservoir levels. Some telling examples of intra and interactions relevant to large dams may be:

- Extreme earthquake and rare flood → spillway structure damaged → uncontrolled rise of the reservoir level → overtopping of the dam → dam failure.
- Rare earthquake → damaged embankment → increased probability of internal erosion → extreme internal erosion → dam failure.
- Extreme flood and bottom outlet malfunction → abnormally high reservoir level → increased probability of internal erosion → extreme internal erosion → dam failure.

As described in STREST D4.1 (Salzano et al., 2015), a custom GenMR framework is used to simulate the main types of interactions that may be present in a dam-reservoir system. The relationships between hazards, elements and system states that were considered are schematized in Fig. 3.4.

It is normal that the levels of alpine reservoirs oscillate substantially during the year as a consequence of highly variable inflows. This variability is promoted by the accumulation of snow during the autumn and winter and its melting during the spring and summer. When addressing scenarios this feature is not particularly relevant, but when computing probabilities and, particularly, accounting for multiple hazards, it is very important. In reality, reservoir levels affect the way in which the dam responds to actions or the chances of internal erosion events taking place. Also, even for floods with well-established return periods the fact that they tend to concentrate in spring and summer should affect significantly the odds of two or more events occurring in close succession.

To conveniently capture these effects the dam-reservoir system is fully simulated for periods of one year starting in March, when the reservoir levels are normally low. Insight into these simulations is provided by Fig. 3.5, where the effects of a rare combination of events on the system can be inspected (stored volume in the reservoir, outflows, and element integrity).

In relation to earlier work (Mignan et al., 2015, 2014; Salzano et al., 2015), the GenMR framework was further customized in order to account for epistemic uncertainty. This was accomplished by overhauling the code to work based on functional programming and, therefore, accommodate randomly generated model parameters. The functional approach can be used to enforce epistemic uncertainty on general inputs (such as inflows), the definition of hazards (for example on their intensity), element features (recovery functions and vulnerability and/or fragility), or even intra and interactions.



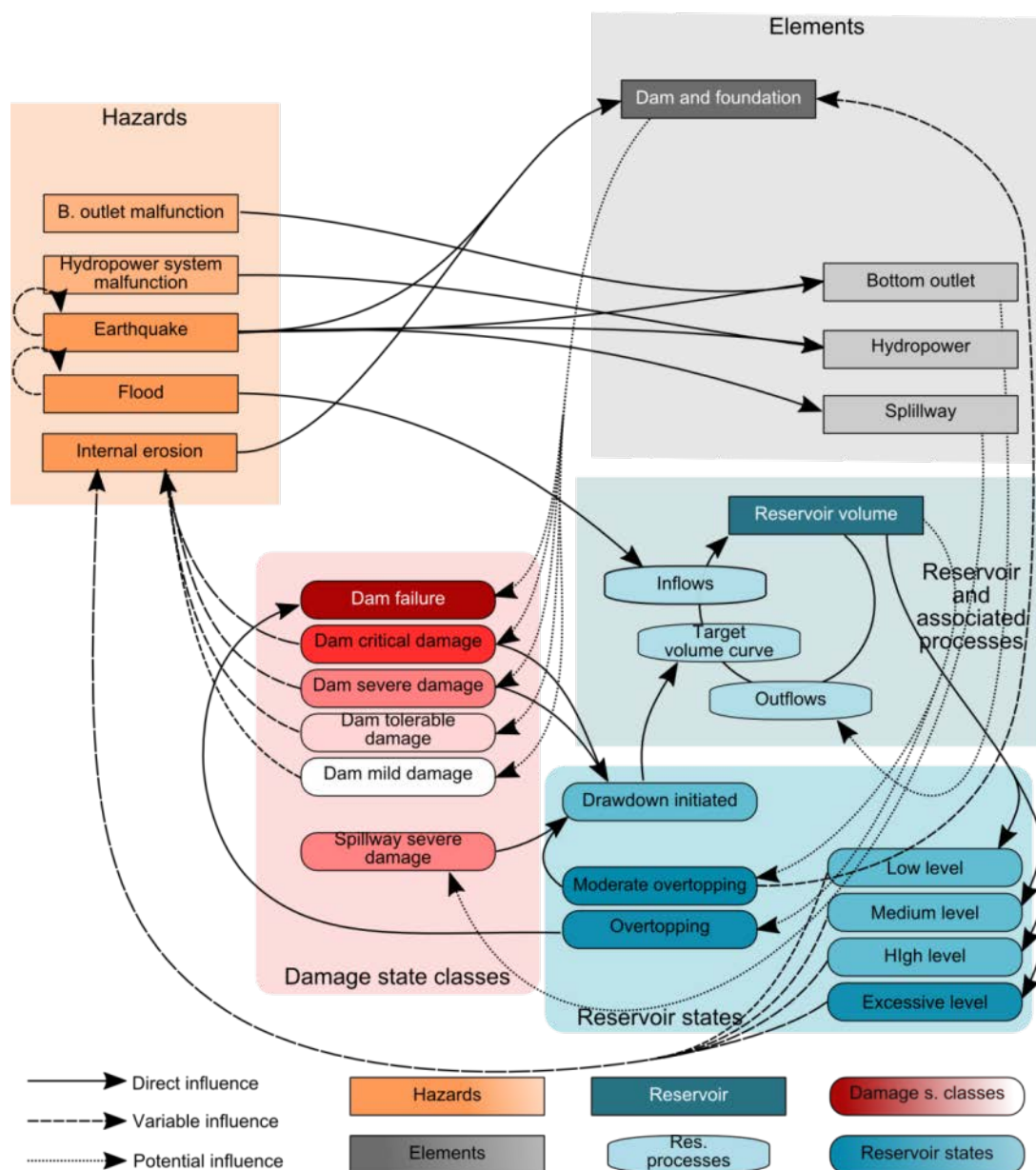


**Fig. 3.4** Scheme of hazards, elements, system states, and interactions considered in the application of the GenMR framework to large dams. Adapted from Mignan et al. (2015) and presented in Matos et al. (2015)

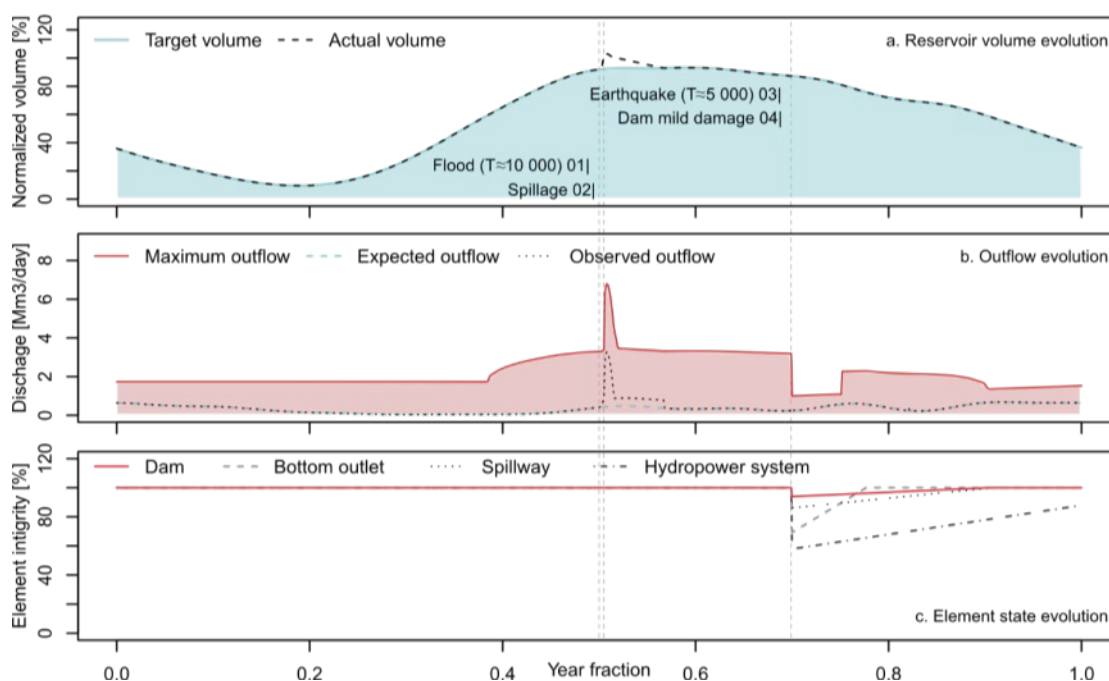


**Fig. 3.5** Example simulation of the dam-reservoir system affected by a 10 000 year flood and a 5 000 year return period earthquake. On top: reservoir volume evolution. In the middle: outflow evolution. In the bottom: element state evolution. Adapted from Matos et al. (2015)

## 3.2 PHASE 1: PRE-ASSESSMENT PHASE

### 3.2.1 Data collection

#### 3.2.1.1 Hazards

In agreement with STREST's stated goals, the present work focuses on natural hazards. Among these, dams are notably affected by earthquakes, floods, and mass slides. In addition, embankment dams are critically vulnerable to episodes of internal erosion and seepage, floating wooden debris can lead to the blockage of spillways, and Alpine dams are potentially vulnerable to icing. A significantly more extensive list could be made and, naturally, it is not possible to account for all possible hazards in parallel.

References on the characterization of earthquakes and flood hazards are numerous and, in every large dam design or safety assessment, they are accounted for in detail. Convenient summaries of the vast body of knowledge amassed on both subjects and its application to dams can be found in the bulletins of ICOLD (2014, 2012, 2003, 2001, 1992). Mass slides, including landslides, rockslides, debris flows, or avalanches, have also been addressed by ICOLD (2000). In relation to earthquakes and floods, they are more site-specific and arguably harder to quantify. Also, their effects on the dam-reservoir system are heavily dependent on reservoir geometry (Sarrasin, 2015).

Icing can have an impact on the forces acting on a dam's structure, however, it affects mostly mechanical equipment such as spillway gates and, as stated before, our conceptual spillway was assumed to be uncontrolled. As such, icing was not accounted for.

Another hazard that was not accounted for is linked to wooden debris. These can follow a large flood event, where the associated storm can prompt the fall of an unusual number of trees. Floating downstream, these trees can accumulate in reservoirs in great numbers and either block outlet structures such as surface spillways or jam mechanical equipment such as gates.

GenMR accounts for discrete intervals of hazard intensity. In the case of primary hazards, these intervals were divided from a return period of  $10^{2.7}$  (roughly equivalent to 500 years), to a return period of  $10^8$  (roughly equivalent to 80 000 000 years), with exponent variations of 0.1. In all, 27 bins were analyzed.

### 3.2.1.1.1 Earthquake

The Swiss dam safety regulations (OSOA, Ordonnance sur la Sécurité des Ouvrages d'Accumulation) (Federal Office for Water and Geology, 2002) were used to compute the expected seismic hazard. In order to do so, Medvedev-Sponheuer-Karnik (MSK) intensities of ground shaking for return periods of 1 000, 5 000, 10 000 years were quantified and used to fit a law in the form of Eq. (3.1) here  $I_{MSK}$  represents the ground shaking intensity,  $T$  stands for the return period, and  $a$  and  $b$  are constants:

$$I_{MSK} = \left(\frac{\ln T}{b}\right)^a \quad (3.1)$$

From those values the Peak Ground Acceleration (PGA) could be derived using Eq. (3.2).

$$PGA = 10^{[0.26 \cdot I_{MSK} - 1.81]} \quad (3.2)$$

In relation to earlier work epistemic uncertainty on the seismic intensity was added. This was done by assuming that, instead of fixed, the  $a$  and  $b$  parameters of Eq. (3.1) vary according normal distributions, respectively  $a \sim N(0.3887, 0.0005)$  and  $b \sim N(0.0289, 0.002)$ . It should be emphasized that these uncertainties are not physically based. That does not, however, reduce the value of these exploratory results.

The resulting laws are illustrated in Fig. 3.6 as a function of the return period of the earthquake.

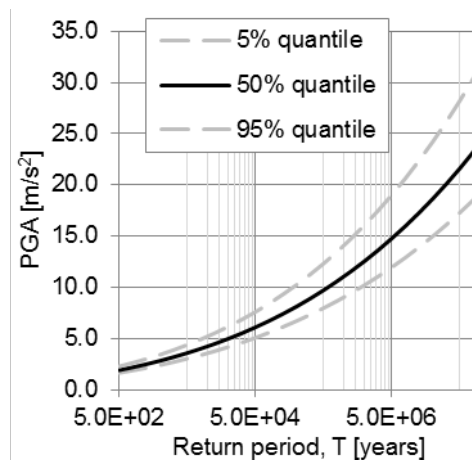


**Fig. 3.6 Peak ground accelerations (PGA) admitted for the area under study with uncertainty bounds**

### 3.2.1.1.2 Flood

The probability of the peak discharge was modeled using the Generalized Extreme Value (GEV) distribution, one of the common options to probabilistically represent peak discharges and one particularly interesting as it is theoretical extreme value distribution:

$$F(x|\mu, \sigma, \xi) = e^{\left(-\left[1+\xi\left(\frac{x-\mu}{\sigma}\right)\right]^{-1/\xi}\right)} \quad (3.3)$$

As for the earthquake hazard, epistemic uncertainty was added to the model. The parameters of the distribution –  $\mu$  (location),  $\sigma$  (scale), and  $\xi$  (shape) – were made to vary according to normal laws:  $\mu \sim N(27.68, 0.1)$ ,  $\sigma \sim N(9.08, 0.3)$ , and  $\xi \sim N(0, 0.05)$ . The admitted extreme discharge distribution, framed by its 5 and 95% uncertainty bounds, is presented in Fig. 3.7.

Not only peak discharge, but also duration and time of occurrence must be associated with a certain flood event. Although possibly modeled by joint distributions (e.g. Favre et al., 2004; Grimaldi and Serinaldi, 2006), peak discharges and flood durations can also display very low correlations. Following some exploratory work the assumption that no correlation exists between both was made. As such, flood durations were modeled independently from peak discharges. This was accomplished resorting to a log-normal distribution whose log-mean and log-standard deviation were made to vary normally according to  $N(1.5, 0.3)$  and  $N(0.2, 0.01)$  respectively. The distribution and its uncertainty are illustrated in Fig. 3.8.

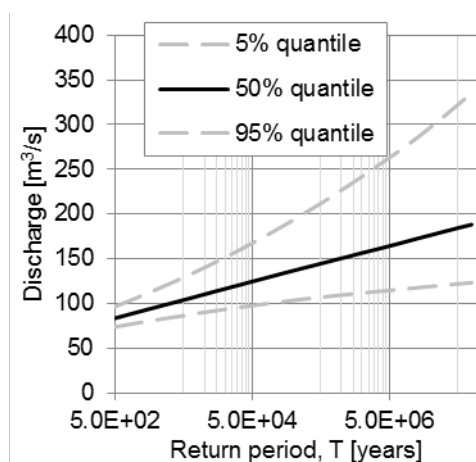


**Fig. 3.7 Peak flood inflows to the reservoir**

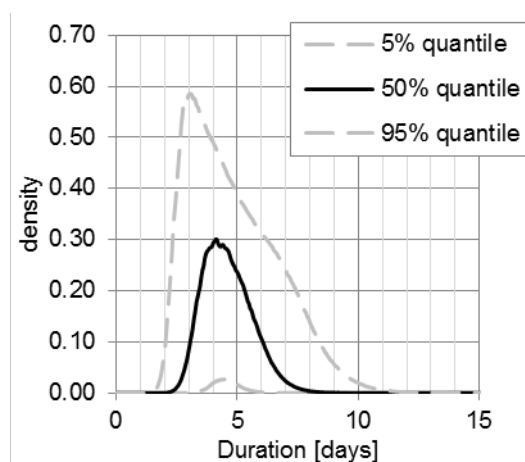


**Fig. 3.8 Probability density of a flood's duration**

Conforming to the typical hydrologic cycle of the Alps it was supposed that the probability of a flood event taking place is not constant throughout the year. In a simplified manner, it was assumed that the distribution of flood events follows roughly the distribution of discharges inflowing to the dam. Inter-annual uncertainty was also added to this aspect of the floods. The resulting distribution is shown in Fig. 3.9.

Being the magnitude, duration, and time of occurrence of the floods fully described, one last aspect of the hazard remains undefined. Like the previous variables, the shape of the flood was loosely inspired in hydrological observations in the region; it is depicted in Fig. 3.10. Uncertainty was not added to the shape of the hydrograph for the purpose of this work.

Including it would not be difficult, however, by using the functional programming GenMR that was prepared.

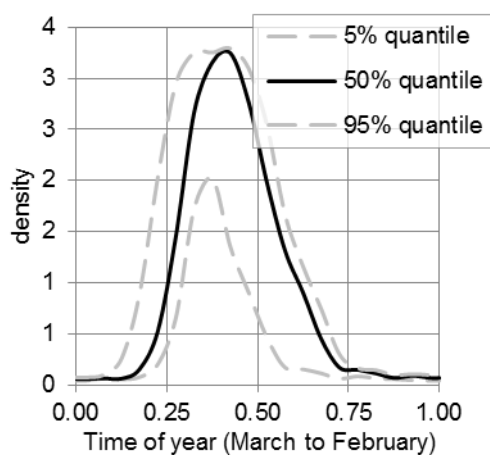


**Fig. 3.9 Probability of floods throughout the year**

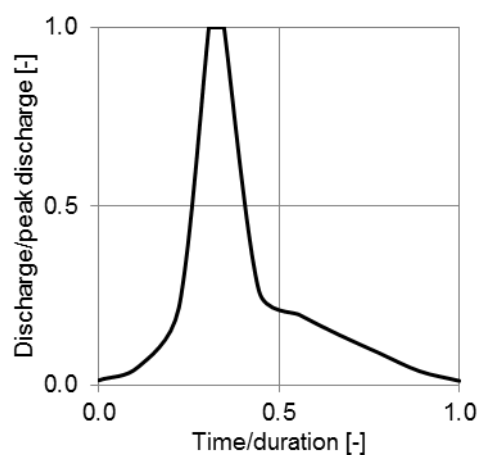


**Fig. 3.10 Adimensionalized hydrograph of the flood events**

In a final note on floods, it should be stated that uncertainty was characterized in simple terms for demonstrative purposes and parameters were not the result of a detailed analysis. The tools to do so are however well-known to the hydrological community.

### 3.2.1.1.3 Internal erosion

Internal erosion, while not present in concrete dams, is one of the hazards that poses more risk to embankment dams. The analysis and mechanics of the internal erosion processes are however complex due to the multiple factors that affect its occurrence (e.g. foundation material, dam composition and design, quality of the construction, reservoir levels, or maintenance standards) and the relatively small historical record of internal erosion episodes in large dams (conditioning the employment of statistical approaches). Frameworks for its inclusion in probabilistic risk assessments have been developed (e.g. Altarejos-Garcia et al., 2014) and more recently approaches compared in the 13<sup>th</sup> ICOLD International Benchmark Workshop on Numerical Analysis of Dams (Gunn et al., 2016). Despite this a significant amount of uncertainty shrouds the probability of internal erosion events taking place.

Avoiding complex physical considerations, in the scope of this work expert judgment was used to quantify the phenomenon for the studied conceptual dam resorting to a cumulative log-normal distribution function. Although the phenomenon is assumed to be rare, on average starting to affect the structure significantly beyond a 10 000 year return period, it is marked by acknowledgeable epistemic uncertainty. The log-mean values were drawn from a  $N(-12, 1)$  distribution, while the log-standard deviation was sampled from a  $N(1, 0.2)$ . The resulting internal erosion intensities are shown in Fig. 3.11.

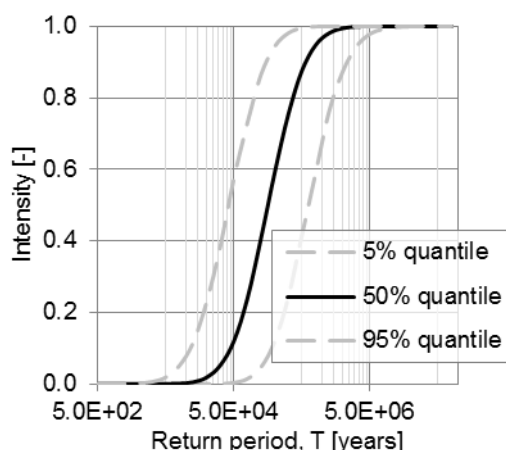


**Fig. 3.11 Probability of floods throughout the year**

The intensity of internal erosion phenomena could be characterized in several ways related to the outflow of water and/or sediments that would have to be translated into damages through vulnerability or fragility functions. Given the lack of data that was already mentioned, it was deemed unnecessary to perform those intermediate steps. As such, the intensity of this hazard directly represents the damage to the dam.

#### **3.2.1.1.4 Bottom outlet and hydropower system malfunctions**

The bottom outlet and the hydropower system are necessarily comprised of mechanical equipment and can, therefore, malfunction. The probability of these malfunctions has been studied in the past (e.g. Pohl, 2000) but remains hard to quantify for a particular infrastructure as they may vary widely according to the material and technology they employ and the surveillance and maintenance practices adopted by the dam operator.

As was done for internal erosion, the intensity of both these hazards was modeled directly as the damage to the component following log-normal cumulative distribution functions. The functions are illustrated in Fig. 3.12 and Fig. 3.13. Parameters are stated in Table 3.1.

**Table 3.1 Parameters of bottom outlet and hydropower system malfunctions defined by their meta-distributions**

Hazard	Function	Parameters	
		Log-mean	Log-standard deviation
Bottom outlet malfunction	cumulative log-normal	$\sim N(-12.0, 1.0)$	$\sim N(4.0, 0.2)$
Hydropower system malfunction	cumulative log-normal	$\sim N(-11.0, 1.0)$	$\sim N(3.8, 0.2)$

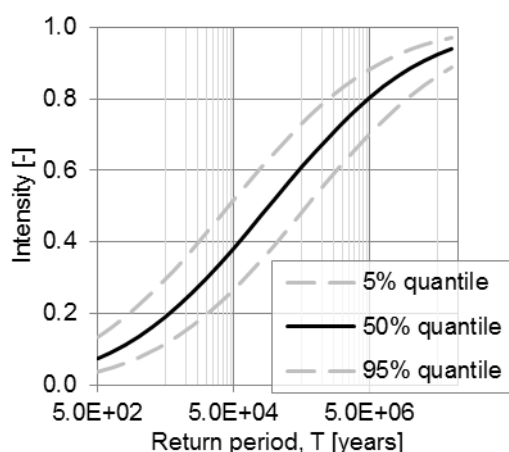


**Fig. 3.12 Probability of bottom outlet malfunctions**

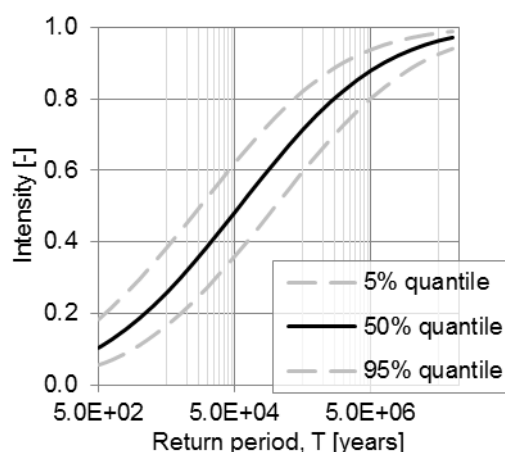


**Fig. 3.13 Probability of hydropower system malfunctions**

### 3.2.1.1.5 Overtopping

Overtopping takes place when the water level in the reservoir rises above a dam's crest. This hazard is particularly relevant for embankment dams as along with it comes the risk of material along the embankment slope being progressively washed away downstream leading to the failure of the dam.

Approximately, the crest should be overtopped by more than 0.5 m in order for a breach to materialize. As such a surrogate "marginal hazard" hazard, corresponding to overtopping heights up to 0.5 m, was created.

For reduced overtopping highs there might even be no damage at all to the dam. As a means to model such behavior, marginal overtopping is "triggered" for a water level above the crest uniformly sampled between 0.1 and 0.5 m.

### 3.2.1.2 Elements

#### 3.2.1.2.1 Reservoir

The reservoir is not structural, but it is nonetheless a key element to take into account under the scope of a stress test. It is mainly through the evolution of the water level on the reservoir that the different components considered in the analysis interact. Within the proposed framework it is mainly defined by its height-volume curve, inflows (excluding flood events), and target outflows.

In the conceptual case studied here, the level of full supply of the reservoir holds 100 000 000 m<sup>3</sup> of water and raises up to 84 m. By virtue of uneven inflows throughout the year, due to rainfall annual distribution and the building-up of a snow pack during winter, neither inflows nor expected reservoir levels are constant. Their mean annual distribution is presented in Fig. 3.14 and Fig. 3.15, respectively.

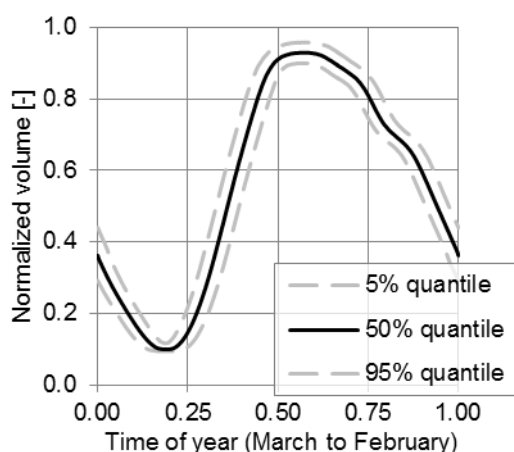


Fig. 3.14 Target reservoir volumes

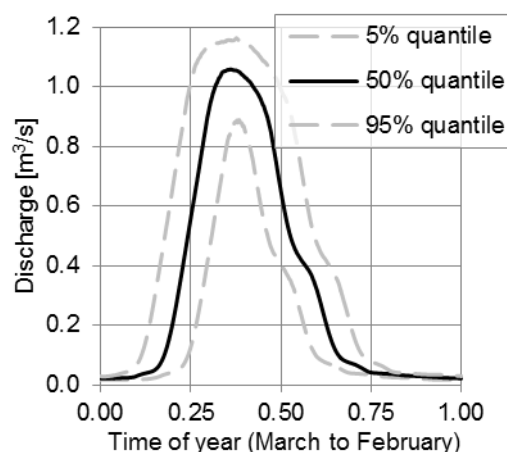


Fig. 3.15 Base inflows to the reservoir

### 3.2.1.2.2 Dam and foundation

The dam is essentially what prevents the uncontrolled release of the reservoir. The foundation's role depends substantially on the type of dam under consideration, namely whether the structure is an arch dam with substantial transfer of forces to lateral abutments or a gravity based alternative by which the mobilized forces are mostly transferred to the foundation. Beyond this simple introduction, the interaction between foundation and dam can be framed in much more complex terms, for example once issues such as percolation and the development of faults are taken into account.

Being the conceptual case under study based on an embankment dam, whose behavior very loosely blends with that of a typical foundation, both elements were bundled together in the interest of parsimony.

The dam was considered directly vulnerable to three main hazards: earthquakes, internal erosion, and overtopping, the latter branching into a further subcategory of marginal overtopping.

Aligning with the idea of exploring several possibilities with the GenMR framework, the responses of the dam to these main hazards are modeled differently. Fragility functions of the log-normal type were adopted to characterize the damages potentially caused by earthquakes, while vulnerability functions were chosen to model internal erosion, bottom outlet loss of functionality, and hydropower system malfunctions. Finally, overtopping consequences have been defined according to constant fragility functions.

The admitted fragility of the dam to earthquakes is illustrated in Fig. 3.16. Again, the use of fragility functions is a simplification and, in many dam safety studies, detailed finite-element models are used to characterize the dams' responses to a certain actions. The fragility curves were adopted mainly because:

- They are a practical and efficient way of characterizing the structure behavior under the proposed GenMR framework without loss of generality.
- The development of detailed numerical models is time-consuming and is not guaranteed to represent uncertainty well.



- The time needed to eventually run detailed numerical models is hardly compatible with the number of simulations that one should perform in order to have a faithful distribution of dam failures under GenMR:
- And, finally, fragility functions can certainly be derived through the application of detailed numerical models if the desired degree of precision of the safety assessment justifies it.

For this conceptual case the fragility functions' values were obtained resorting to expert judgment. By assuming that the considered Alpine dam conforms to Swiss safety regulations (which is likely to be the case as there is a close monitoring of the large structures and dam safety evaluations are often carried out in the country, leading to rehabilitation and retrofitting works when needed) and that dam designers did a good job in minimizing unnecessary costs, one can loosely infer that the dam will incur limited damage for earthquakes below a 10 000 return period. Also, the uncertainty augments as earthquake intensities increase. Evidently, deriving fragility curves in this fashion would not be appropriate for a real implementation of the methodology, namely as it directly influences the outcomes of the component level assessment in Phase 2 of the stress test.

While a fully developed overtopping event entails the breach and failure of the dam, effects of marginal overtopping are uncertain. Here they have been drawn from the constant fragility functions appearing in Table 3.2.

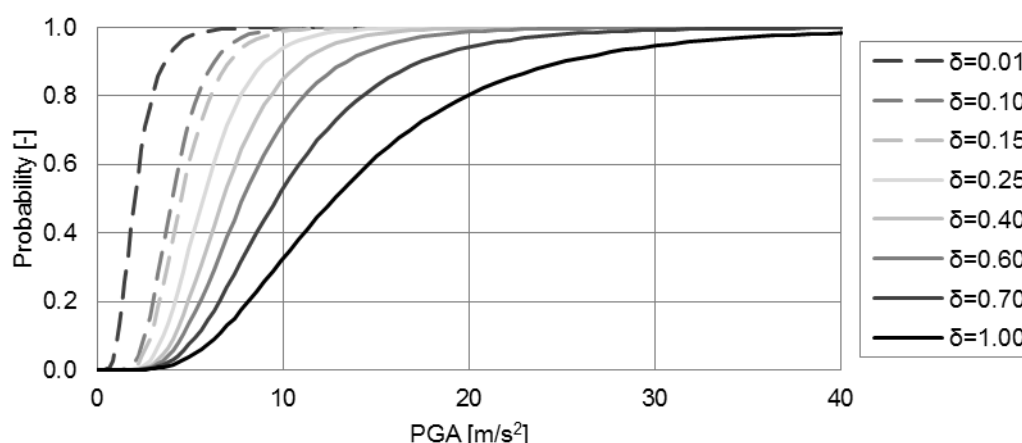


**Fig. 3.16 Fragility curves of damage states of the dam as a function of PGA**

**Table 3.2 Fragility of the dam to marginal overtopping events. The probability is defined as the probability of a damage state to be met or exceeded**

Damage state	Probability
$\delta=0.20$	1.00
$\delta=0.40$	0.30
$\delta=0.60$	0.10
$\delta=0.80$	0.01
$\delta=1.00$	0.00

After being damaged, the dam should undergo reparations. These were also modeled, albeit in a quite simplified fashion, through a linear function whose sole parameter is the recovery slope (fraction of total possible damage recovered per year). Representing epistemic uncertainty, the slope itself was made to vary following a log-normal distribution with log-mean of -1.2 and log-standard deviation of 0.3.

**3.2.1.2.3 Outlet structures (spillway, bottom outlet, and hydropower system)**

As mentioned before, the reservoir level is controlled by a set of outlet structures. In this case a spillway, a bottom outlet and the hydropower system have been considered.

Determining how each structure affects the level of the reservoir is therefore important. Through hydraulic considerations, the maximum outflows from each of these elements and the dam crest (that acts as a weir in the case of overtopping) have been calculated and are depicted in Fig. 3.17.

The derivation of fragility curves for the three components as functions of PGA followed a process alike to the one adopted for the dam. They are presented in Fig. 3.18, Fig. 3.19, and Fig. 3.20.

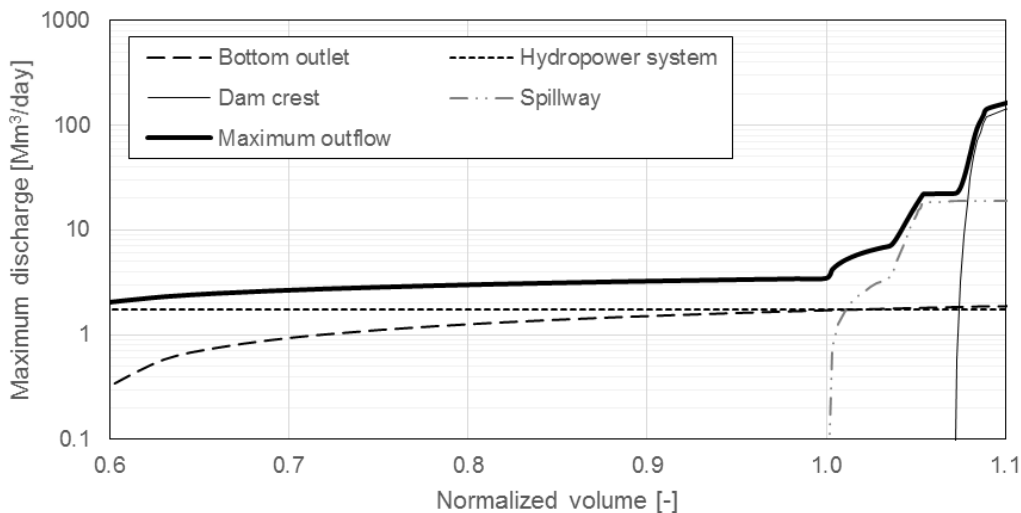


**Fig. 3.17 Maximum outflows of the reservoir as a function of the normalized volume of the reservoir**

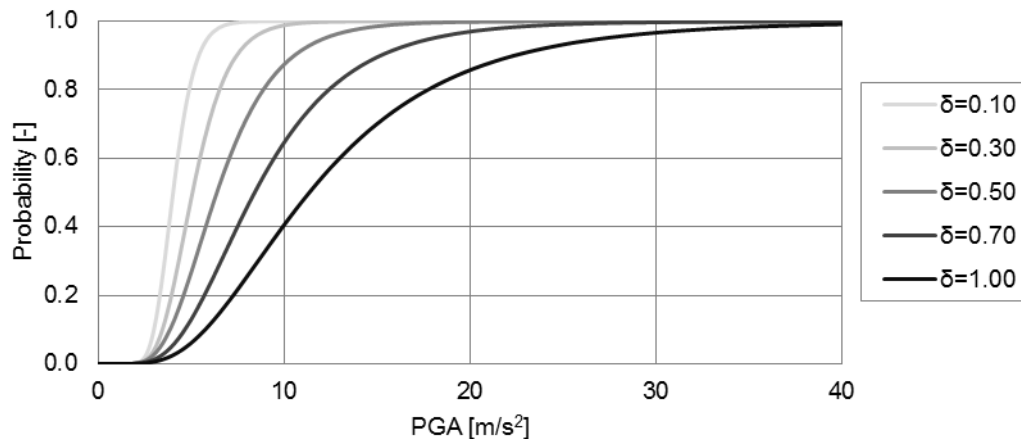


**Fig. 3.18 Fragility curves of damage states of the spillway as a function of PGA**

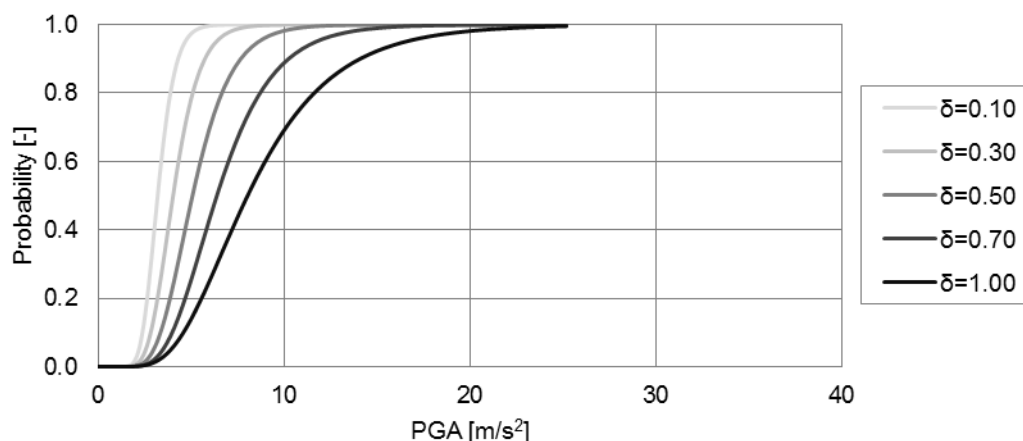


**Fig. 3.19** Fragility curves of damage states of the bottom outlet as a function of PGA

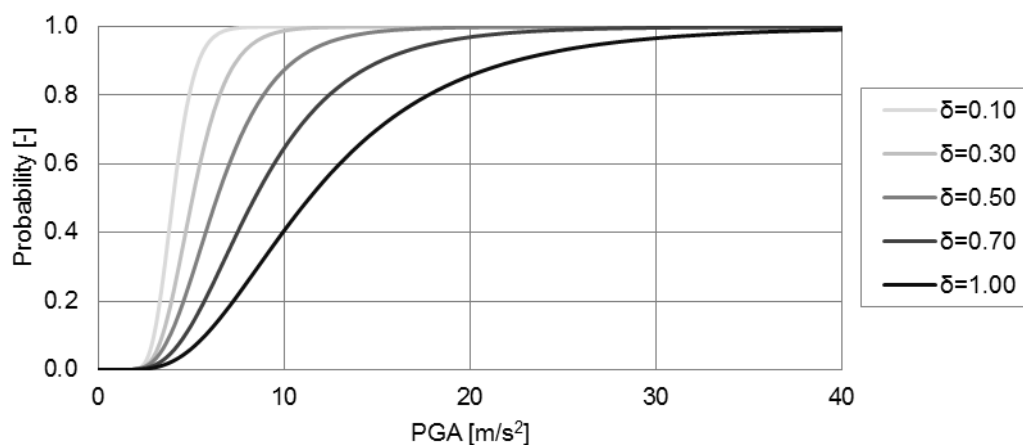


**Fig. 3.20** Fragility curves of damage states of the hydropower system as a function of PGA

Similarly to what was done for the dam, the outlet elements' recoveries are also modeled. The parameters of the log-normal distribution from which the recovery rates are sampled are given in Table 3.3.

**Table 3.3** Parameters of the distribution of recovery rates for the outlet elements

Element	log-mean	log-standard deviation
Spillway	-0.4	0.25
Bottom outlet	1.4	0.2
Hydropower system	-0.1	0.15

### 3.2.1.3 Downstream area

Once a breach does occur, the most relevant consequences are often seen downstream. The dam-break waves that are generated – particularly so in the case of large dams holding

significant reservoir volumes – have the potential to severely damage or even destroy most types of infrastructures in their path. Also, they present a real life threat to populations.

The time of arrival of the flood, the maximum water height, or the velocity of the water are some parameters that may be used to estimate potential losses. These inundation parameters change according several factors, namely:

- The hydrograph of outflows at the breached dam's site.
- The topography and bathymetry of the downstream area.
- The resistance to the flow of the downstream area.
- And inflows from streams affluent to the system.

Beyond these basic factors, the problem can be looked into in a higher level of detail. Examples would be to consider the sediments displaced by the dam-break wave and the changes in terms of macro-roughness that result from trees being torn from the ground or buildings collapsed or washed away.

For the purpose of this study an area stretching down to roughly 30 km from the dam site was modeled using a 1D/2D coupled BASEMENT model (Vetsch et al., 2005). The topography and computation grid of the model are depicted in Fig. 3.21. The topography and bathymetry data were found in the swissALTI3D Digital Elevation Map, made available by the Swiss Federal Office of Topography. It is a raster with a pixel size of 2x2 m, with reported average error of  $\pm 0.5$ m below 2000 m.a.s.l. and between  $\pm 1$  and  $\pm 3$  m above that mark. Infrastructure, structures, and land use information was retrieved from the VECTOR25 dataset, also made available by the Swiss Federal Office of Topography and have been used as a basis to, among other things, estimate terrain roughness'.

Unsurprisingly, there is a significant amount of uncertainty in computations that endeavor to model the losses caused by a dam break flood. Some of those are:

- The shape of the hydrograph outflowing from the breach.
- The simplifications or errors in topographic and bathymetric data.
- The resistance to the flow of the downstream area.
- The errors induced by the numerical modeling of the flood.
- And the errors that stem from an inaccurate or non-existent consideration of sediment displacement and changes in macro-roughness.

When inundation parameters are derived, the last step of estimating how people, buildings, and infrastructures are affected must be dealt with. Because, fortunately, the statistical data about their response is scarce and the problem is hard to address computationally, studies must necessarily include significant approximations and assumptions. Here it was chosen to model damage to buildings as a function of maximum water levels. To do so, fragility curves derived in the aftermath of the Tōhoku disaster were adopted (Suppasri et al., 2013).

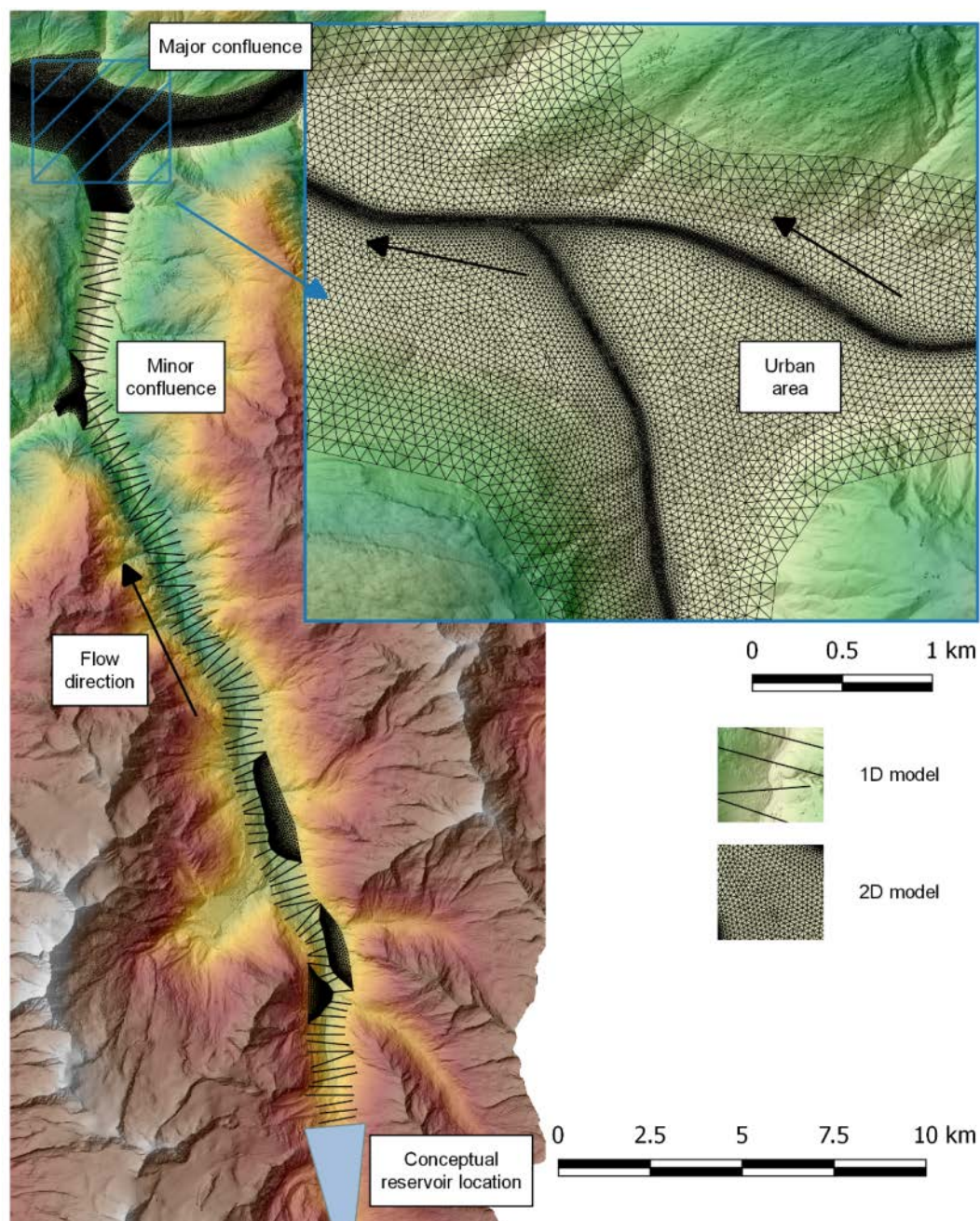


**Fig. 3.21 Depiction of the downstream area under study and the adopted computational grid. Reproduced from Salzano et al. (2015)**

The fragility curves employed in this work are depicted in Fig. 3.22, Fig. 3.23, and Fig. 3.24. They are applicable to 1, 2, and 3 or more stories high reinforced concrete buildings.

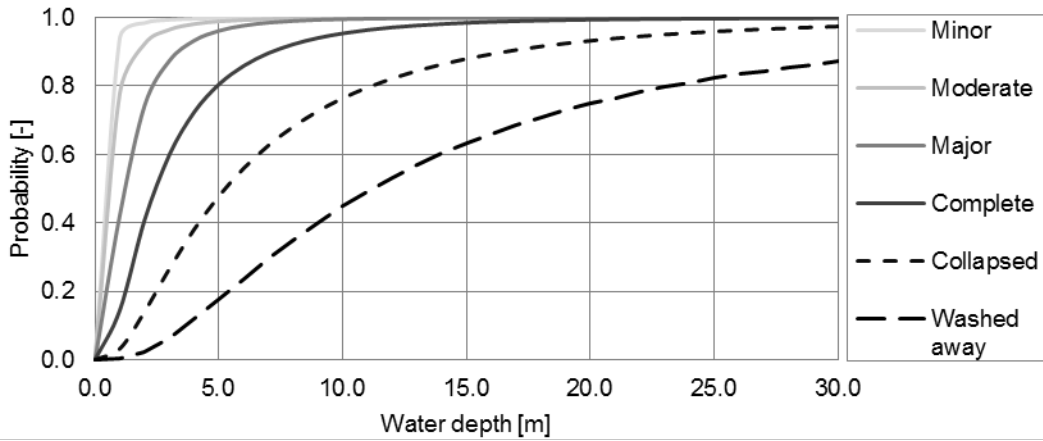


**Fig. 3.22** Fragility curves derived for 1 story reinforced concrete buildings. Adapted from Suppasri et al. (2013)

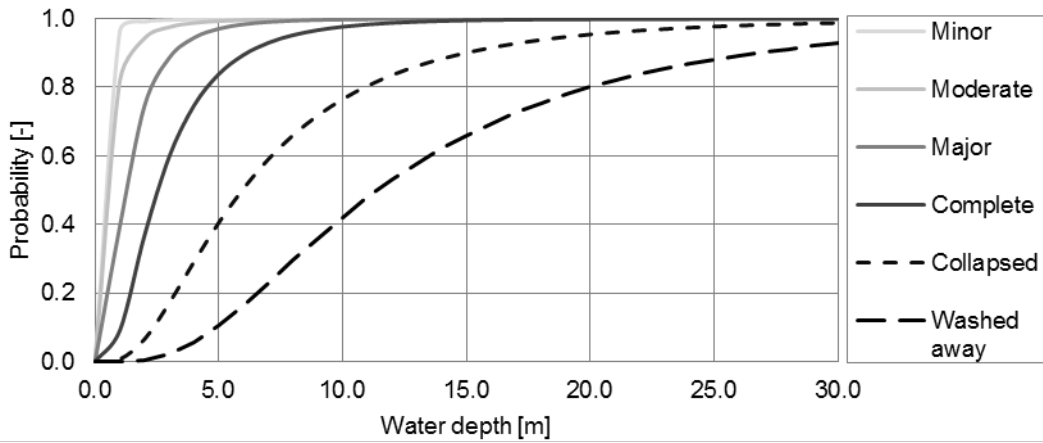


**Fig. 3.23** Fragility curves derived for 2 stories reinforced concrete buildings. Adapted from Suppasri et al. (2013)

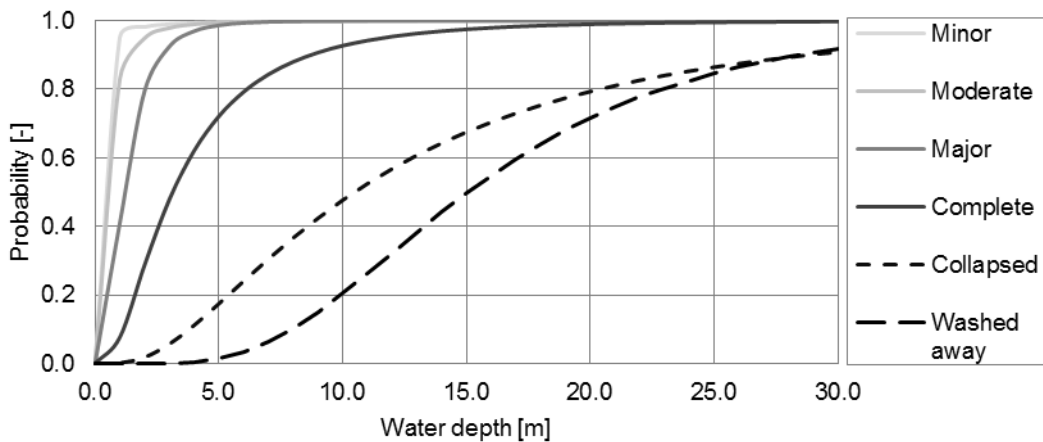


**Fig. 3.24** Fragility curves derived for 3 or more stories reinforced concrete buildings. Adapted from Suppasri et al. (2013)

### **3.2.1.4 System states**

#### **3.2.1.4.1 Damage states and operability**

Acting in practice as secondary hazards, damage states cannot occur without a previous trigger. Each state has, however, the capacity to affect the behaviors of elements or other hazards through the functional programming approach.

Five damage states were used to further characterize the dam and spillway. Assuming that, at 50% integrity, the dam is no longer capable of holding the reservoir, damage states were quantified as follows:

- Dam not damaged: integrity between 95 and 100%,
- Dam mildly damaged: integrity between 90 and 95%,
- Dam tolerably damaged: integrity between 80 and 90%,
- Dam severely damaged: integrity between 70 and 80%, and
- Dam critically damaged: integrity between 50 and 70%.

The spillway was associated with a single damage state – spillway severely damaged – which corresponds to an integrity under 85%. Below that level, the spillway was considered inoperable. Not damage states per se, but relevant nonetheless, are the integrity thresholds below which the remaining outflow structures are assumed not to function. These amount to 90% for the bottom outlet, and 50% for the hydropower system.

#### **3.2.1.4.2 Reservoir states**

Much in the same way as damage states, reservoir levels can exert some influence on the frequency of some hazards and how system components respond to them. Four states were admitted:

- Low level: reservoir storage below 35% capacity,
- Medium level: reservoir storage between 35 and 70% capacity,
- High level: reservoir storage between 70 and 100% capacity, and
- Excessive level: reservoir storage above the full supply level (100% capacity).

In addition to these four states, a special state is possible where a drawdown, in the sequence of which a complete lowering of the reservoir is carried out by any means available, is attempted. The drawdown attempt is assumed to start if either the dam or the spillway become severely damaged or worse.

#### **3.2.1.5 Hazard intra- and inter-actions**

Intra- and inter-actions are present in most dams and may significantly affect the overall risk. They are, nonetheless, seldom taken into account on a systematic basis by the dam engineering community.

Two basic types of interactions were considered: circumstantial and permanent. While the former affect the system while a certain state endures, the latter will take place at a certain point in time and remain in effect until the end of the simulated year.

In the scope of this stress test the following intra and interactions were considered:

- Rare earthquakes on more common internal erosion events (permanent),
- Rare floods on more common ones (permanent),
- Rare internal erosion events on more common ones (permanent),
- Rare earthquakes on more common ones (permanent),
- Reservoir levels' effect on internal erosion (circumstantial), and
- Damage states' effect on internal erosion (circumstantial).

Regarding the first three, following an earthquake, flood, or internal erosion event, only events whose return period is at least 100 times lower will be affected. The magnitude of the effect depends on the ratio of occurrence rate of trigger and affected events: for example, following a massive 100 000 year earthquake, the return period of 1 000 and 100 year internal erosion events would be reduced 10- and 100-fold, respectively. In order to keep the system stable, a minimum threshold of 0.1 years was enforced for all return periods.

The intra-actions among earthquakes are somewhat different, allowing randomly either the increase or decrease of return periods.

Reservoir levels, and even their variations, are known to affect internal erosion occurrence rates through changes in the pore pressures in the dam body and its foundation. In the scope of this work it was assumed that: a low reservoir level would reduce by 1000 the frequency of internal erosion events; a medium level would not affect "base" frequencies; a high level would increase probabilities two-fold; and an extreme level would prompt them to rise by 100-fold. It should be stressed that these changes cancel each other on a one year cycle, thus not affecting overall return periods.

Damage states follow an analogous pattern with tolerable damages increasing the odds of internal erosion taking place by 10, severe damages by 100, and critical damages by 1000.

### **3.2.2 Risk Measures and Objectives**

As highlighted before, when considering dam failures the downstream area can be at least as important as the dam site. The definition of risk measures and objectives should incorporate that.

Setting objectives and establishing risk measures can be difficult and is a very politically charged topic. In many cases the objectives are bound to the upstream system and the occurrence of a breach, being the downstream system studied not in order to assess risk formally, but rather to prepare evacuation plans and design an appropriate alarm system. In this case upstream and downstream-bound objectives have been defined in order to allow the exploration of GenMR's potential.

#### **3.2.2.1 Dam failure probability**

The first objective is that the dam should not fail with a frequency higher than  $10^{-4}$ . In other words, failures should have a return period of more than 10 000 years. Naturally, the risk measure in this case is the failure frequency.



### 3.2.2.2 *Probability of damages in the downstream area*

The second objective is bound to the downstream system. Natural objectives to be set would be related to the expected annual number of lives lost and/or the expected annual monetary losses. In the scope of this work, however, no data was used on the value of property. By the same token, no loss-of-life estimates were performed.

Both issues are worthy topics of research in their own right. Monetary losses because the valuation of property is hard to accomplish; as are the estimation of secondary costs to society and impacts on regional economy. Loss-of-life due to extremely difficult validation of mathematical models that predict it and the enormous uncertainty that underpins human behavior.

Here, focus was placed on the effects of hazard intra- and inter-actions and the consideration of epistemic uncertainty. Estimating monetary and/or life losses would add a significant amount of complexity to the study, but would arguably fail to add significantly to the main novel ideas put forward in the report. As such – although emphasizing that in a real stress test these should probably be considered as objectives – here the objective is bound to the damage sustained by buildings in the downstream area. The metric is the expected annual volume of downstream buildings which collapse or are washed away. The objective is that this volume does not exceed  $7.5 \text{ m}^3/\text{year}$ , what roughly equates to a  $150 \text{ m}^2$ , 5 m high flat or house being lost with a return period of 100 years as a result of dam failure.

Additionally, a third objective based on the characteristic point of risk approach proposed by Esposito et al. (2017) is defined in regard to the previous metric (volume of collapsed or washed away buildings). Following that approach, a F-N curve is prepared from the results of the simulations and its most critical point evaluated in relation to risk. Namely, four risk zones are considered: AA – negligible risk; A – risk as low as reasonably practicable (ALARP); B – possibly unjustifiable risk; and C – intolerable risk. Risk thresholds separate each pair of zones. They were quantified for illustrative purposes as thus:

AA-A:  $7.5 \text{ m}^3/\text{yr}$ ;

A-B:  $75 \text{ m}^3/\text{yr}$ ;

B-C:  $750 \text{ m}^3/\text{yr}$ .

It should be noted that the second objective – the expected annual volume of downstream buildings which collapse or are washed away – and the third objective – based on the characteristic point of risk approach – are not directly comparable as risk objectives. For a comparison to be made, all the points in the F-N curve of the system must be integrated.

### 3.2.3 **Set-up of the Stress Test**

Among the stress test levels proposed within STREST, dams are typically subject to level ST-L2, where a single hazard is evaluated to a great level of technical accuracy. Usually, in this type of single hazard evaluation a limited degree of combination with coincident hazards is included, somewhat extending to the ST-L3 realm.

For example, following recommended practices a dam may be designed to withstand 10 000 year or maximum credible earthquakes without significant water releases, being the structure evaluated resorting to finite element numerical models and checked against a

range of possible failure modes. Checks can also include that after such an earthquake an uncommon flood (such as a 200 year flood) affects the system.

Not only earthquakes, but also other hazards are verified. Floods, being a very relevant source of damage to dams on their own right, are customarily evaluated for 10 000 return periods, probable maximum flood, or roughly equivalent specifications. Within a safety test for floods it is also normal to account for other hazards – for example jamming of mechanical equipment or the inoperability of the hydropower system.

Naturally, ST-L1a component level assessments of the key system elements are also carried out.

Under most national legislations, the backbone of dam safety evaluations is comprised of deterministic scenario based assessments. As was already mentioned, the detailed numerical models under use are hardly compatible with the number of simulations needed to account for probability distributions of several hazards, their intra- and inter-actions, and epistemic uncertainty. Probabilistic approaches are also resorted to, particularly so for dams of limited size which, for one reason or another, do not justify full deterministic assessments. While the application of probabilistic approaches to dam safety is generally regarded as an important development for the future, the methodologies to employ are still the subject of heated discussion and very far from agreed upon.

The stress test carried out here aimed to explore the application of probabilistic methodologies to large dams to a deep level of procedural complexity and was designed as such. Given the limited resources available to complete it, however, this was accomplished at the expense of technical accuracy.

In this light, because the detailed numerical models used to study structural stability are well known to the dam engineering community, their application was by-passed altogether, being the response of system elements to specific hazards based on the assumption that they are up to regulation standards. This affects mainly the ST-L1a assessment, which is considered to be implicitly met.

Stemming from the same choice regarding the scope of the stress test, results from the ST-L2 level do not add significant information to the data collected during the pre-assessment. For illustrative purposes, the earthquake hazard's consequences in terms of dam failures were studied.

Where the real benefits of the methodology are reaped, and where most of the effort was made, is the system level assessment for multiple hazards (ST-L3). There the importance of considering intra- and inter-hazards is analyzed, as is the impact of epistemic uncertainty. It is also under the scope of ST-L3 that the downstream effects of dam-break floods are analyzed.

### **3.3 PHASE 2: ASSESSMENT PHASE**

#### **3.3.1 Component Level Assessment (ST-L1a)**

As put forward previously, the component level assessment, although a stepping stone of the whole stress test procedure, was assumed to be met for the purposes of this conceptual case. The resistance of the components to hazards was represented in a simplified fashion by the use of fragility and vulnerability functions, which are presented in section 3.2.1.

### 3.3.2 System Level Assessment for Single Hazard (ST-L2b /L2d)

#### 3.3.2.1 Scenario based Assessment (ST-L2d)

In this level of the assessment, no uncertainty is taken into account. To accomplish this, the fragility curves described earlier were collapsed into a vulnerability function that retains the expected damages caused to each component. Also, the epistemic uncertainty associated with the intensity of the earthquake hazard was neglected.

In this very simple scenario based assessment, a 10 000 year earthquake shakes the system when the reservoir is at its maximum storage. Results of the simulation can be seen below, in Fig. 3.25. Unsurprisingly, the dam endures tolerable damages, as do the outlet structures, and there is no failure. The outlet capacity is, however, considerably affected due to an inoperable bottom outlet.

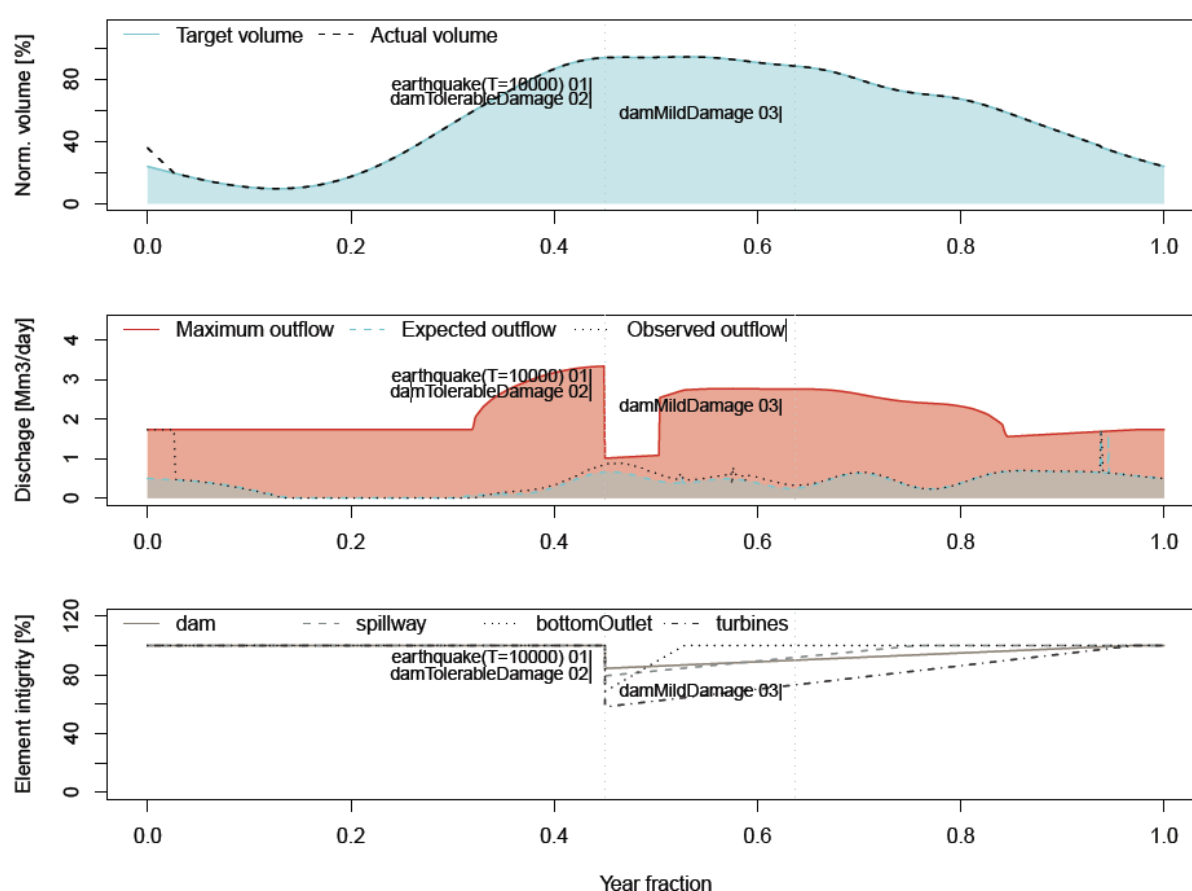


**Fig. 3.25 Results of the ST-L2 scenario based assessment. A 10 000 year earthquake occurs when the reservoir is full.**

#### 3.3.2.2 Probabilistic Risk Assessment (ST-L2b)

On a probabilistic approach, earthquakes with return periods greater than 500 years were sampled in a total of 5 million simulations. Such an analysis is interesting in order to model risk as, on the one hand, earthquakes rarer than 10 000 are sampled and, on the other hand, they are randomly distributed throughout the year. Naturally, events occurring when

the reservoir is low tend to lead to fewer losses. Without integrating the losses downstream – as will be done in the level ST-L3 assessment – little information is gained.

Overall, the return period of failure events due to earthquakes amounted to 130 000 years.

### 3.3.3 System Level Assessment for Multiple Hazards (ST-L3c / L3d)

#### 3.3.3.1 Scenario based Assessment (ST-L3d)

In the scenario based assessment for ST-L3 combinations of earthquake and flood hazards have been evaluated.

The first includes an earthquake (T=10 000) and a flood (T=500) occurring with the reservoir near its highest level. Being at least the earthquake and the flood independent events, one can infer that this combination is extremely unlikely.

The evolution of the system is illustrated in Fig. 3.26. There it can be seen that the dam endures a tolerable damage, as do the outlet structures. The damage sustained by the outlet structures causes a step decrease in the maximum outflow capacity of the dam, so that when the flood arrives the target volume is exceeded by a small margin.

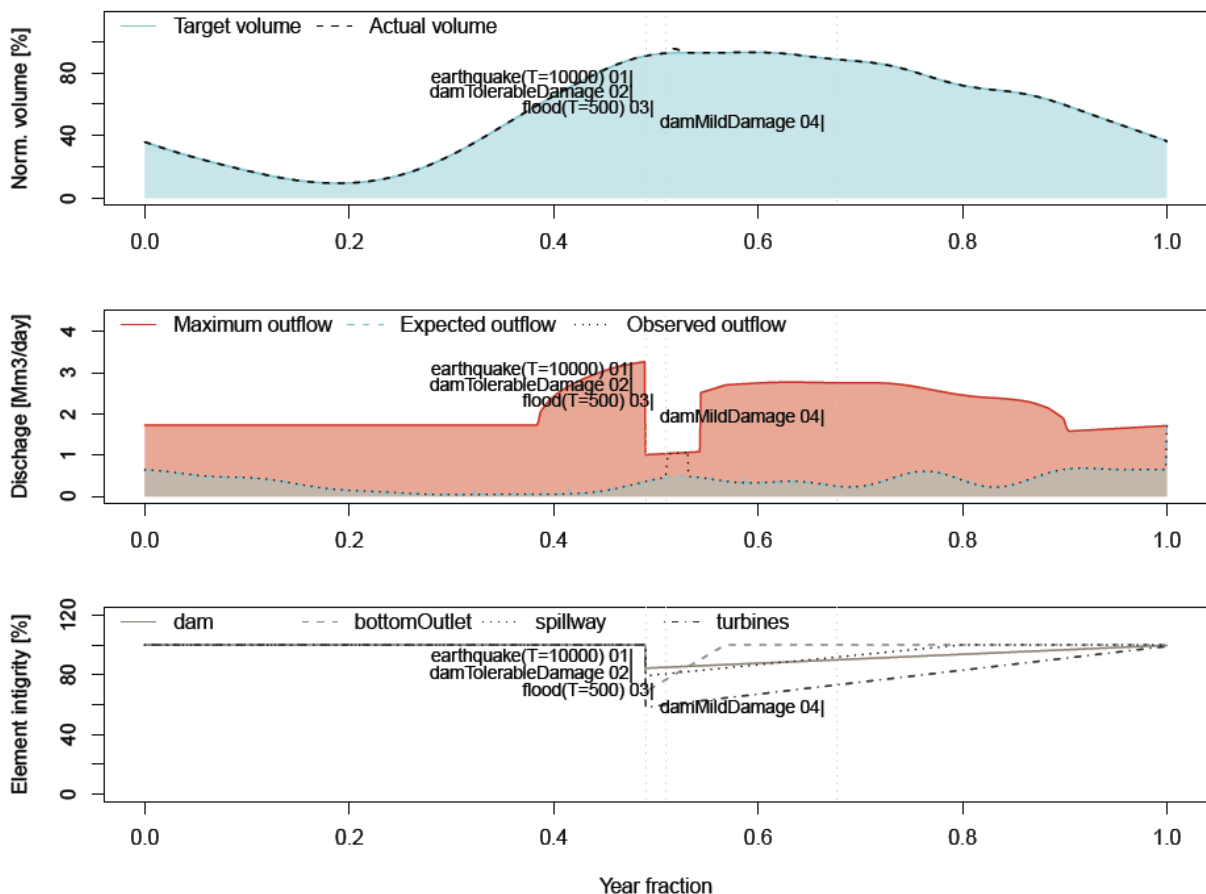


**Fig. 3.26 Results of a ST-L3 scenario based assessment. A 10 000 year earthquake occurs when the reservoir is full and is followed by a 500 year flood**

An even more unlikely scenario, including a 20 000 year earthquake and a 2 500 year flood, was also evaluated. The evolution of the system in this case is presented in Fig. 3.27. Owing to the higher intensity of the earthquake, the dam was severely damaged, which prompted a drawdown attempt. Although the magnitude of the flood was also quite high, the system was able to cope with it.

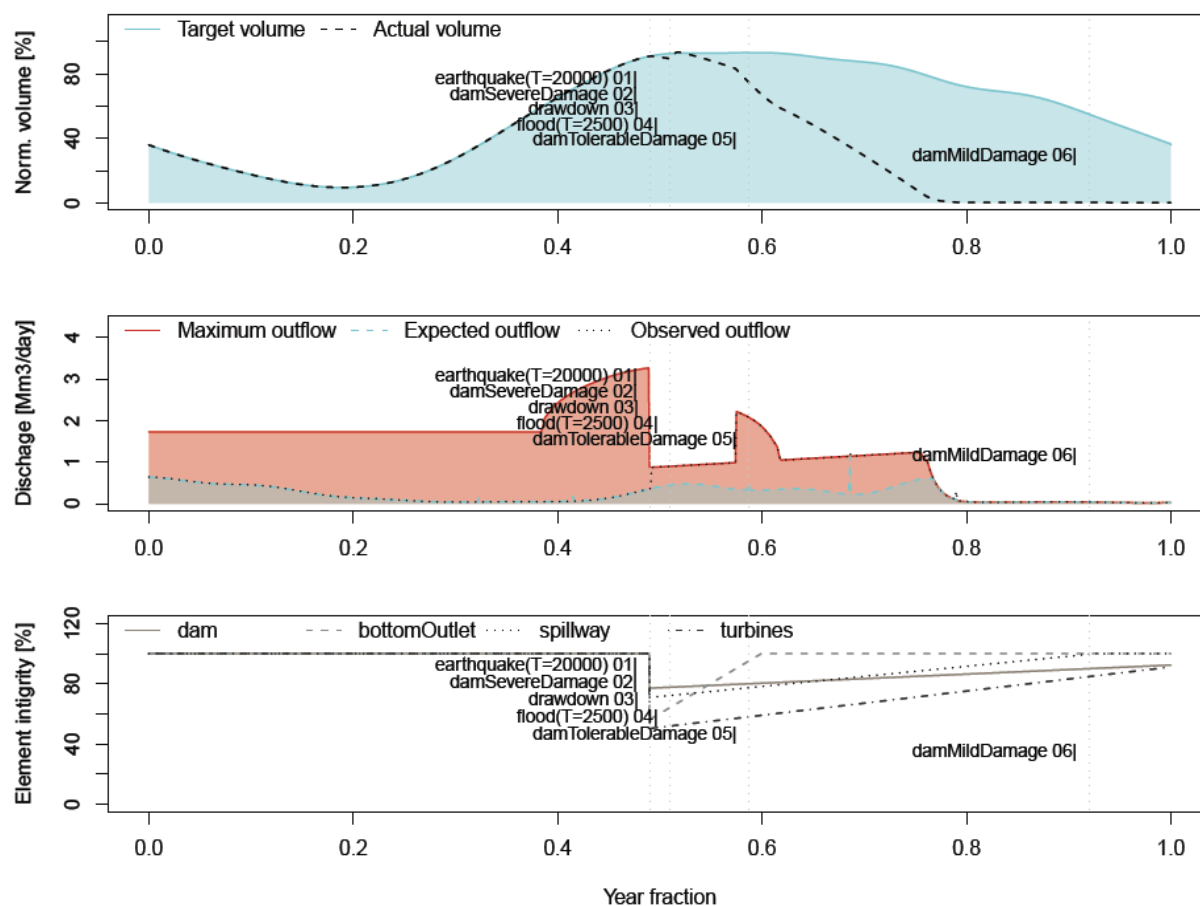


**Fig. 3.27 Results of a ST-L3 scenario based assessment. A 20 000 year earthquake occurs when the reservoir is full and is followed by a 2 500 year flood**

Neither of the tested scenarios is expected to lead to the failure of the system. Despite this, in many scenario based assessments for large dams an eventual breach is usually modeled, mostly as a means to prepare evacuation plans and alarm systems.

This evaluation has been carried out here as well using the BASEMENT (Vetsch et al., 2005) model. The methodology applied for routing the dam-break wave was described in STREST D4.1 (Salzano et al., 2015) and will not be repeated here.

The results are presented in Fig. 3.28. They are illustrative of the high destructive power of such a wave, with some inhabited areas being overrun by up to 30 m of water with very little warning time.

It should be stated that at this level uncertainty sources, introduced in section 3.2.1.3, are not being incorporated into the analysis and, consequently, the results presented above only allow a qualitative estimate of the risks associated with a dam breach.



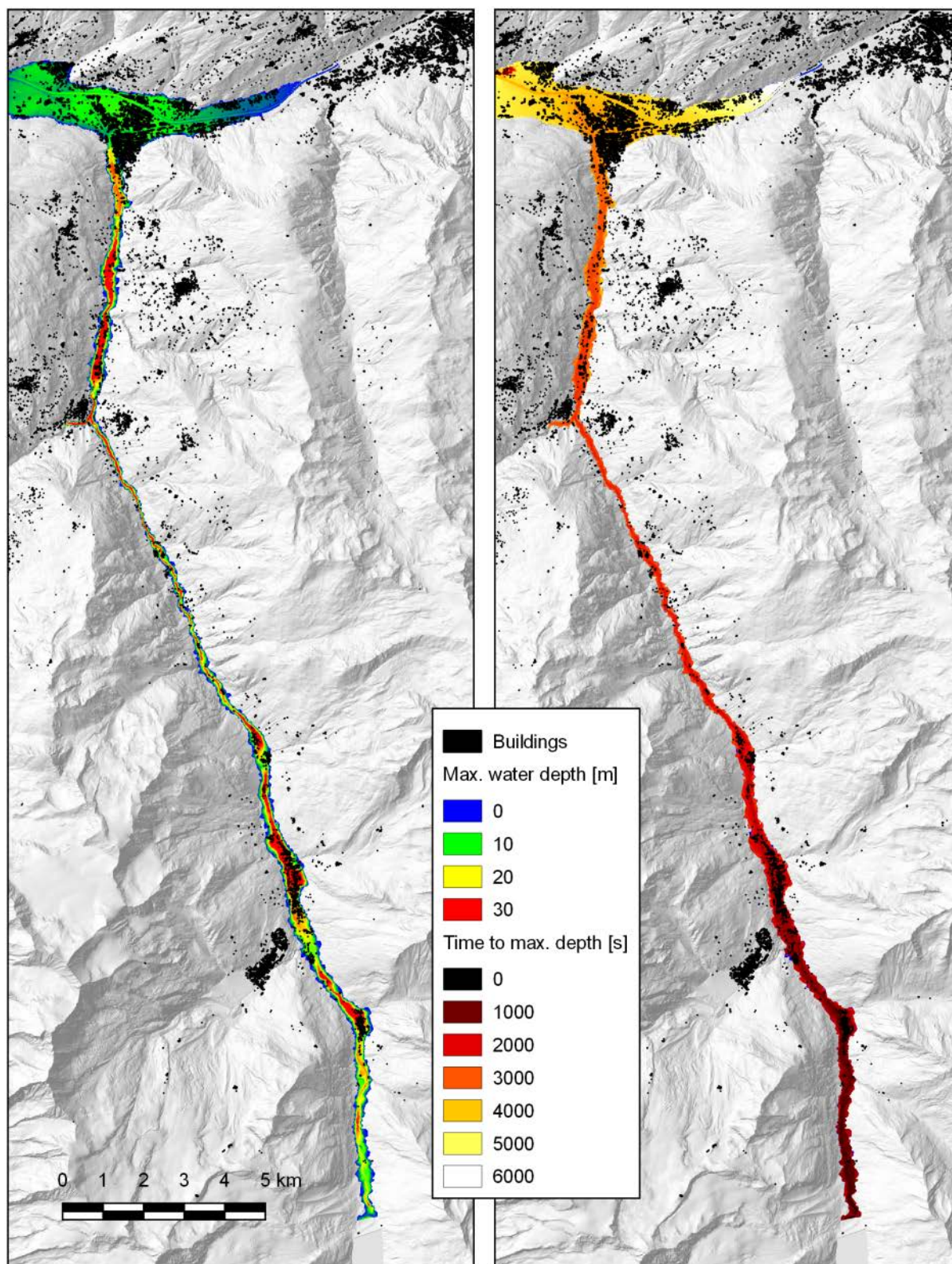


Fig. 3.28 Inundation resulting from an overtopping of the dam using expected breach progression parameters according to Froehlich (2008)

### **3.3.3.2 Probabilistic Risk Assessment (ST-L3c)**

#### **3.3.3.2.1 Upstream system**

Up until now, relatively little information has been extracted from the use of the GenMR framework. This is the case because the hazards and components of the system have been assumed to be fully characterized, being all the interesting and laborious engineering models and considerations that lead to that characterization omitted.

Here a complete uncertainty analysis, from the upstream system to the downstream area is carried out. Not only are hazard intra- and inter-actions explored, but epistemic uncertainty is also put into focus. In order to do so the full potential of the GenMR framework was harnessed.

Focusing first on the upstream system, 20 million simulations were performed including all system elements, all hazards, and all sources of uncertainty (refer to section 3.2.1 for their characterization).

As reported in STREST D4.1 (Salzano et al., 2015), accounting for hazard intra- and inter-actions – something not usually done on a systematic basis among the dam engineering community – a failure was expected approximately every 90 000 years. Here, considering a broad range of sources of uncertainty, breaches were predicted to occur with a considerably lower return period close to 25 000 years. This result is not to be interpreted in absolute terms owing to the uncertainty that characterizes the input data but, in relative terms, the strong decrease in the return period was surprising and illustrative of the importance of accounting for different sources of uncertainty.

In order to infer what explained this increase in failure occurrence rates, epistemic uncertainty on hazard intensities and element recovery rates was first added to the reference return model that indicated a return period of 90 000 years. As a consequence of this, some additional 20 million simulations pointed to a decrease of the failure return period to 50 000 years.

In conclusion, a nearly 4-fold increase in risk was identified through the consideration of uncertainty, approximately 50% attributable to epistemic uncertainty related to hazards, and 50% linked to uncertainty at the level of the component's responses.

Quite relevantly, it should be emphasized that the addition of uncertainty did not affect the expected values of hazard intensities or the damages endured by any element. Because the system is highly non-linear and the failure events constitute a threshold however, the less severe events that cause unlikely high damages and lead to a failure are not compensated by the more severe events that cause unlikely small damages.

#### **3.3.3.2.2 Modeling of the downstream area**

Truly assessing risk in the downstream area is a task laden with computational difficulties. The most obvious and constraining one is that the time any 2D hydraulic model takes to run renders any Monte Carlo approach unfeasible. In the scope of this work machine learning techniques are used in order to overcome that.

The first step in the assessment of damages in the downstream area is to compute the progression of breach. There are several methodologies to do so (see Zenz and Goldgruber, 2013), all with strengths and weaknesses that is beyond the scope of this work to discuss.

The Froehlich (2008) approach was chosen due to its simplicity, wide acceptance among the dam engineering community, and probabilistic framing.

According to the Froehlich (2008) approach, the breach develops as a function of the failure mode (overtopping or internal erosion), the volume of water in the reservoir, the height of the dam, and the final height of the breach. Outputs are the time of formation of the breach, its final width, and its side slopes. In addition, Froehlich (2008) provides statistical distributions for each of these variables. As an illustration, a sample of 100 breach parameters possible for one single failure condition are shown in Fig. 3.29.

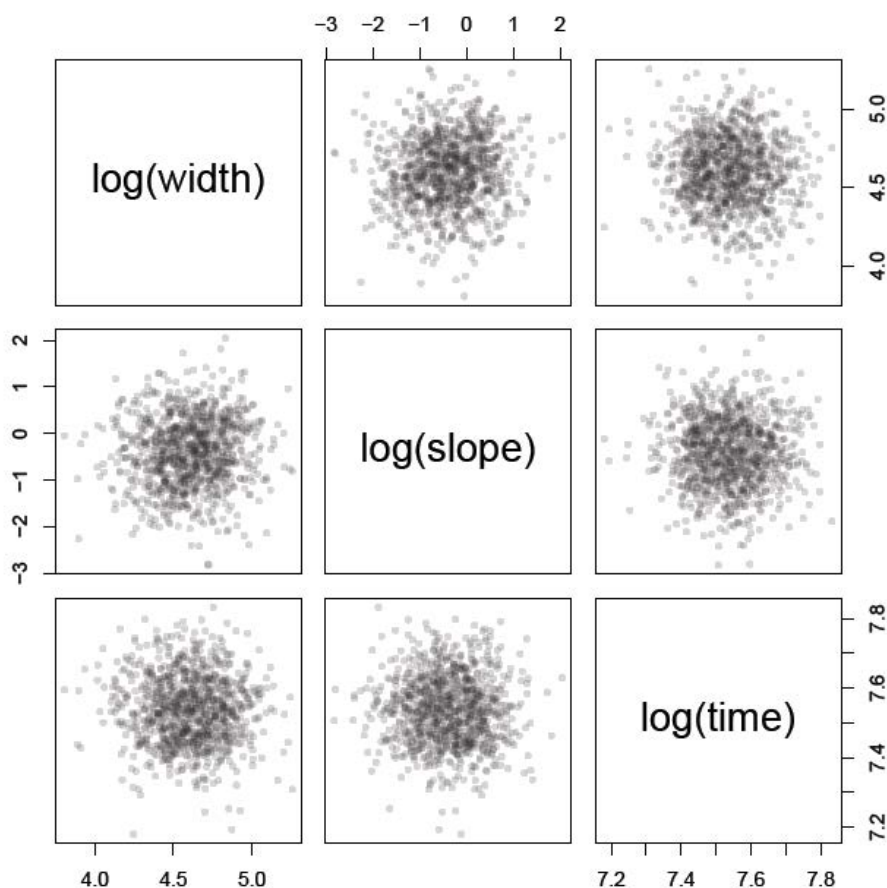


**Fig. 3.29 Illustration of the distribution of breach parameters obtainable for one single dam failure**

Once the possible breach geometries and time of formation are defined, the next step is to use that information to generate the hydrograph of outflows from the reservoir. The software HEC-RAS 5 from the U.S. Army Corps of Engineers' Hydrologic Engineering Center was used to accomplish this.

All that needed to characterize the hydrograph is a 1D model that runs quite fast. Even so, in order to model the uncertainty of the breach's development, for every failure being generated out of GenMR it is desirable to produce several sets of breach parameters. As a means to circumvent the need to run a HEC-RAS model for every one of these cases, a machine learning model was employed. Non-linear Support Vector Regression (SVR) (Drucker et al., 1996) with Gaussian kernels were used to emulate the information contained in the hydrographs produced by HEC-RAS.



To train the SVR models 5 000 sets of breach parameters were randomly sampled in an attempt to cover the domain of all possible breaches (Fig. 3.30). As can be seen from the figure, Monte Carlo sampling is important as due to physical constraints the distributions, particularly that of time of formation, depart from the initially assumed log-normal.

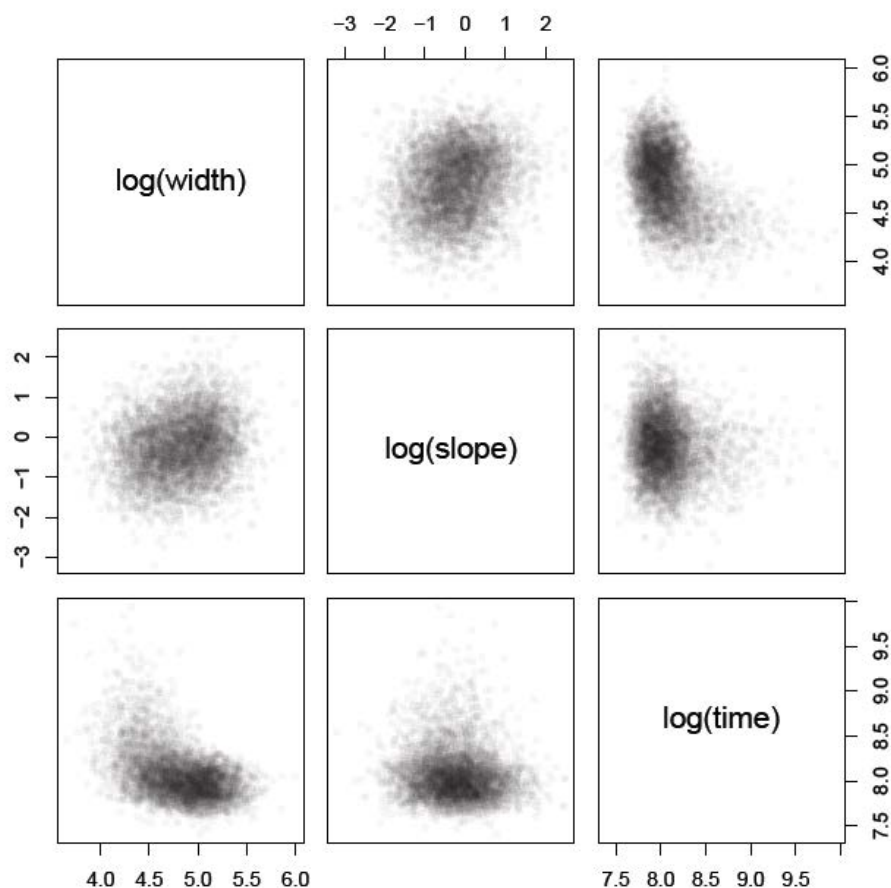


**Fig. 3.30** Sampled parameters used to characterize the domain of possible breaches

HEC-RAS was then ran in order to obtain 5 000 corresponding hydrographs. Results are presented in Fig. 3.31. It is interesting to note that outflows from the same dam can vary widely not only in terms of volume, but particularly of peak discharge. Also, it is curious to note how the mode (overtopping or piping) can on rare occasions contribute to offset the formation of the breach in time.

In a simplification necessary to a posterior step, each of the hydrographs was characterized according to three features: peak flow, ascending slope of the hydrograph, and descending slope of the hydrograph. The SVR models were thus trained to approximate the latter based on the outputs of the Froehlich approach, effectively substituting the HEC-RAS software and performing computations orders of magnitude faster.

The quality of the SVR models is depicted in Fig. 3.32, where “observed” values that result from the application of HEC-RAS are plotted against SVR predictions. While the great majority of the predictions are very good, falling on the diagonal of the regression plots, some cases, particularly of peak discharges, tend to be overestimated. Although a hypothesis to be further analyzed, it is believed that the majority of those points coincide with cases of numerical instability of the HEC-RAS simulations, which occasionally produce

unrealistic results. In that light the use of SVR might have the additional benefit of “filtering” outliers.

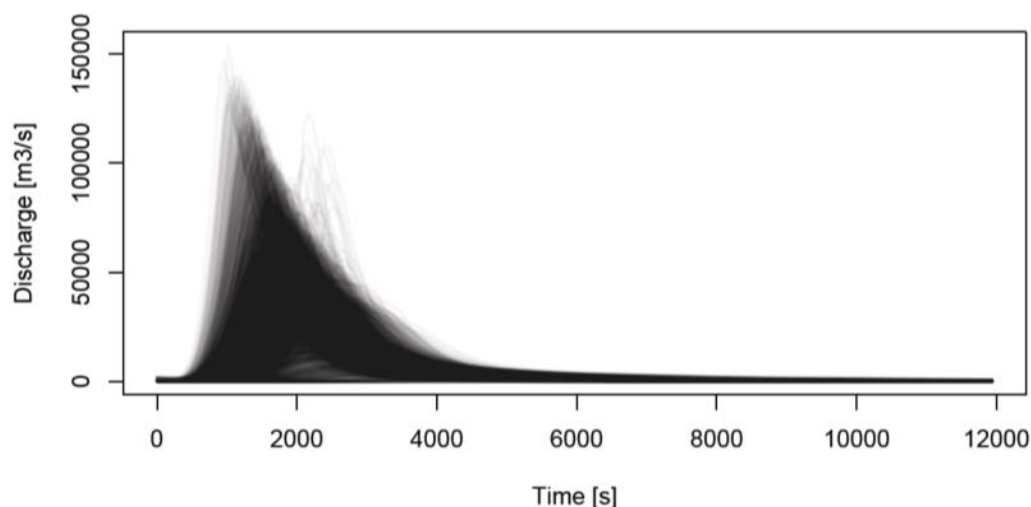


**Fig. 3.31 Catalogue of 5 000 hydrographs that characterize the domain of possible outflows from the dam**

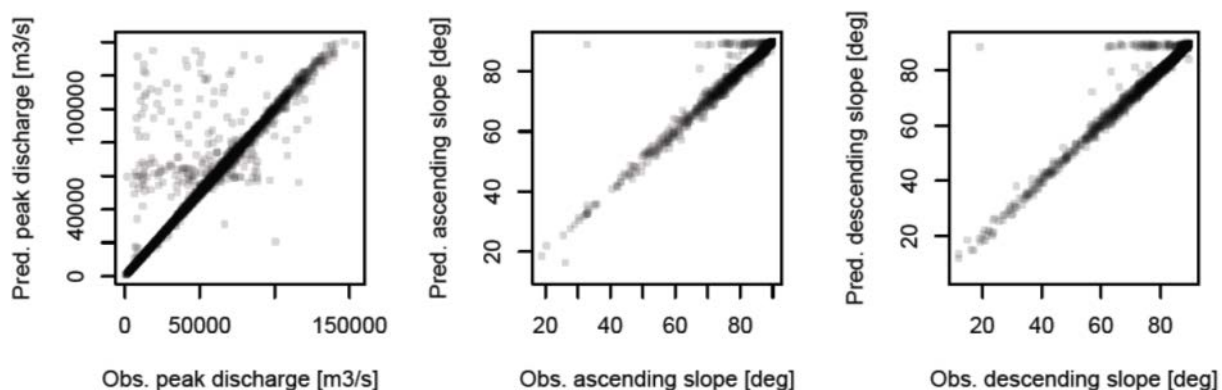


**Fig. 3.32 Accuracy of the SVR models in predicting hydrograph features**

Having a procedure and the computationally performing models necessary to sample hydrograph features from dam failure cases, the next challenge is to derive the inundation parameters (for example maximal water depth, time of arrival of the flood, or peak flow velocities) that correspond to each hydrograph in different places of the downstream area.

Following the procedure described in detail in STREST’s D4.1 (Salzano et al., 2015), a catalogue of 21 breach hydrographs (Fig. 3.33) was fully simulated using the BASEMENT software, resulting in 21 corresponding inundation maps that cover the whole of the downstream area. The maps of maximum inundation depths at the extremes of the catalogue are displayed in Fig. 3.35 and Fig. 3.36. The number of hydraulic simulations was limited to 21 as each run of the model can take several hours.

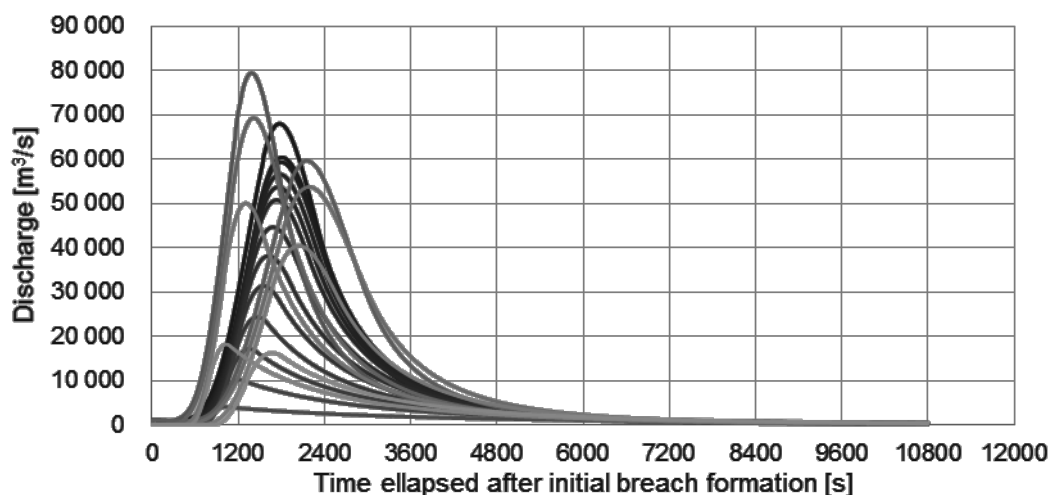


**Fig. 3.33** Catalogue of outflow hydrographs whose downstream flood was fully simulated. Adapted from Salzano et al. (2015)

Machine learning was used again to dramatically reduce computation times. SVRs were now driven at predicting inundation parameters, namely maximal inundation depth, at locations throughout the potentially flooded area. With this in mind the map was divided into small hexagonal tiles, being a SVR model trained for each one of them (Fig. 3.34). The SVR models are capable of predicting well inundation depths from the outflow hydrograph features that have been introduced above, as shown in Fig. 3.37.

With the aid of the proposed methodology it is possible to implement a Monte Carlo approach and get a quantitative estimate of the probability of certain inundation parameters being observed at specific locations downstream of the dam. A process that would otherwise take weeks or even months of computation can be completed in a matter of a few hours.

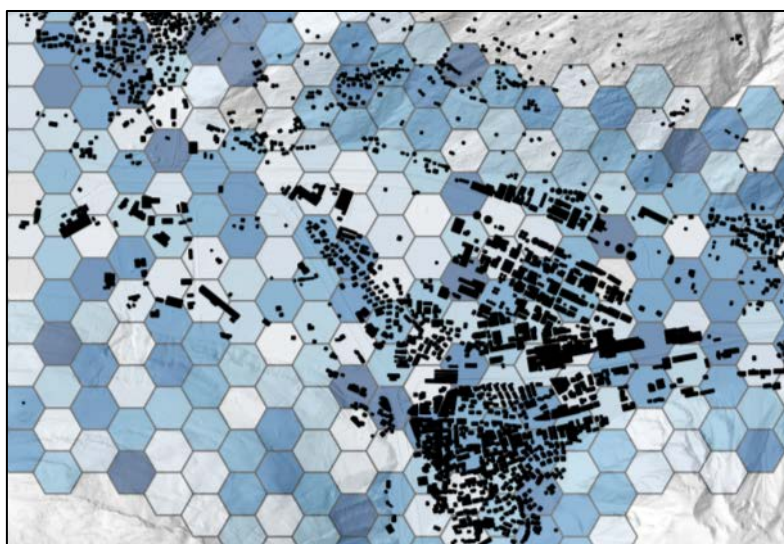


**Fig. 3.34** Depiction of the hexagonal tiles that cover the map



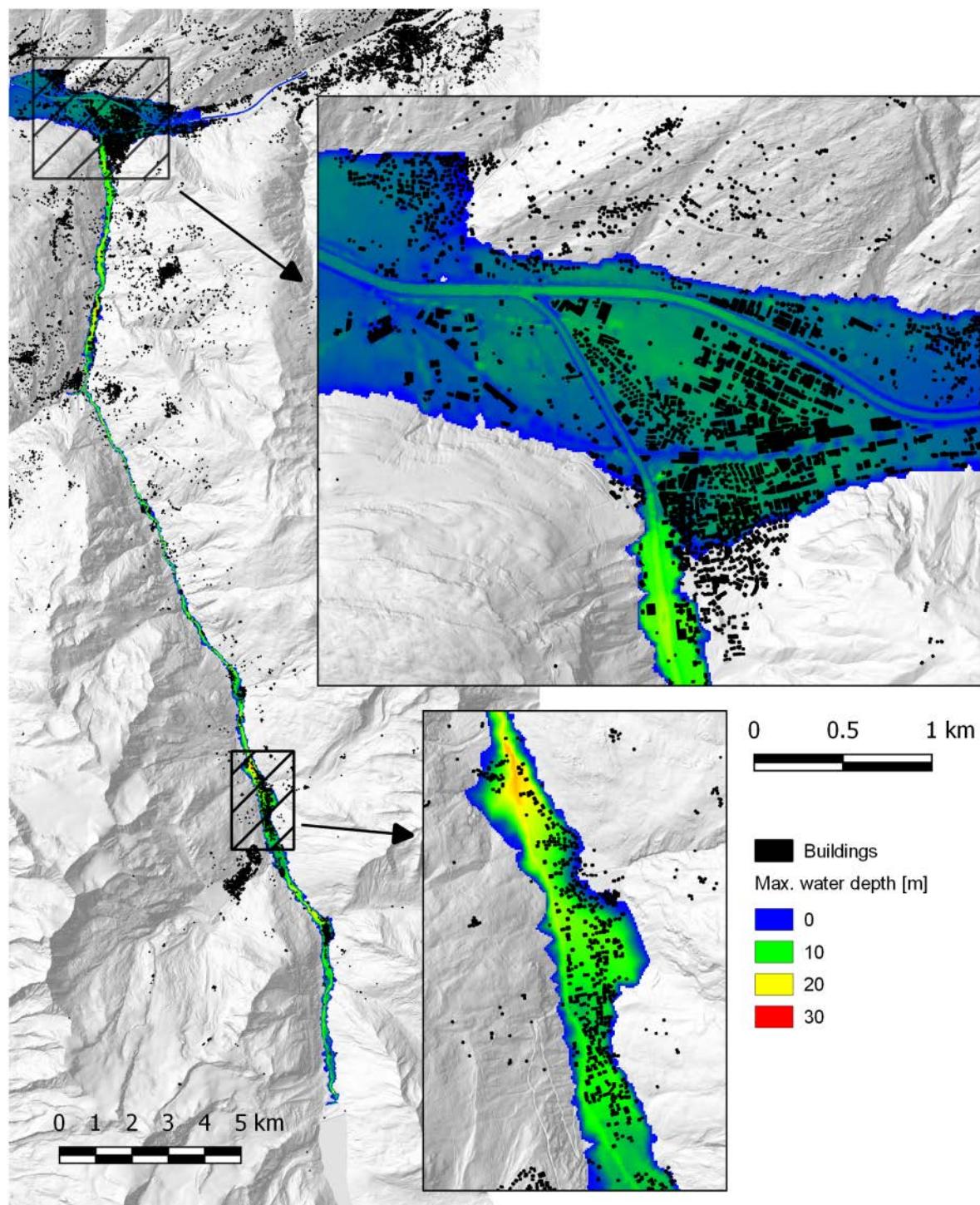
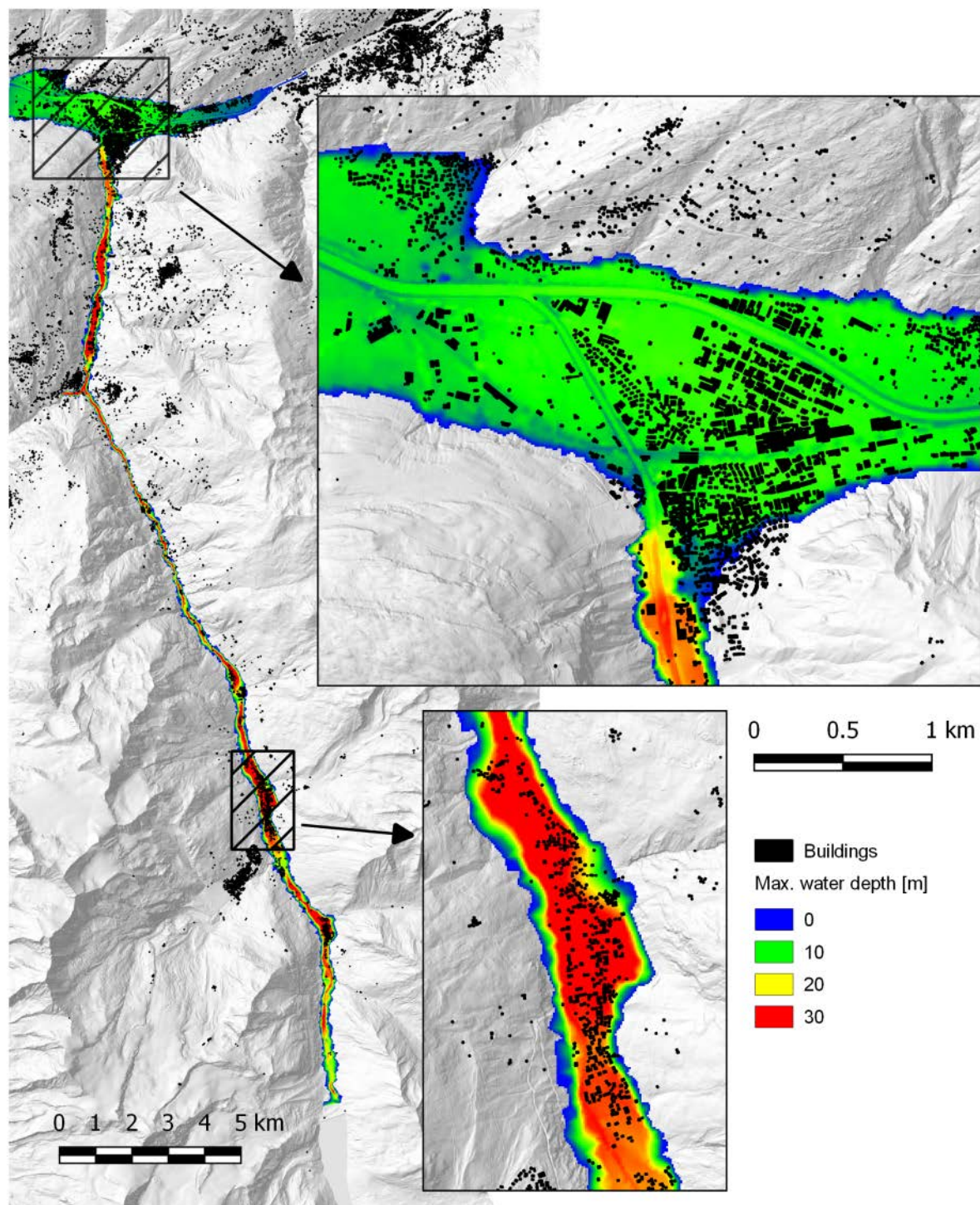
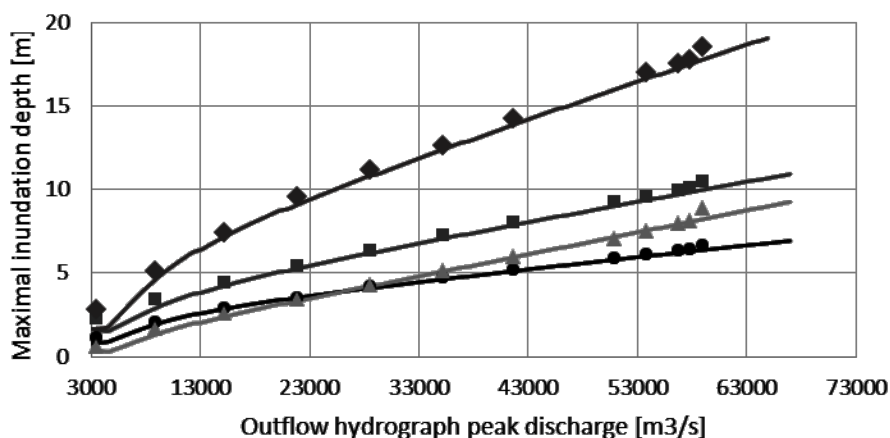


Fig. 3.35 Inundation calculated for a low peak discharge, low volume breach hydrograph



**Fig. 3.36** Inundation calculated for a high peak discharge, high volume breach hydrograph





**Fig. 3.37 Examples of inundation depths estimated through the regression models fitted for several tiles. Points were numerically simulated. Lines correspond to interpolated values. Adapted from Salzano et al. (2015)**

### 3.3.3.2.3 Assessing damages on the downstream area

From the 20 million simulations that were performed, 802 resulted in a dam breach. From these, 8020 sets of breach parameters were sampled and an equivalent number of inundation parameters predicted over the downstream area.

Using the fragility curves for 1, 2, and 3 or more stories-high reinforced concrete buildings presented in section 3.2.1.3, states for buildings of each type within each hexagonal tile were then computed. As a result, one can obtain a probability distribution for each type of building and location.

As an example, Fig. 3.38 contains information about the likelihood of reinforced concrete 1 story buildings being washed away as a consequence of the dam's breach.

Another type of information that can be retrieved is conditional on a failure taking place. In Fig. 3.39 the most likely states of a reinforced concrete building with 3 or more stories after the passage of the dam-break wave can be seen.

Naturally, once the computations are complete it is trivial to match specific buildings to the appropriate fragility curves and obtain individualized return periods for any desired damage states. In Fig. 3.40 the return period of the building in the potentially affected area collapsing or being washed away is presented.

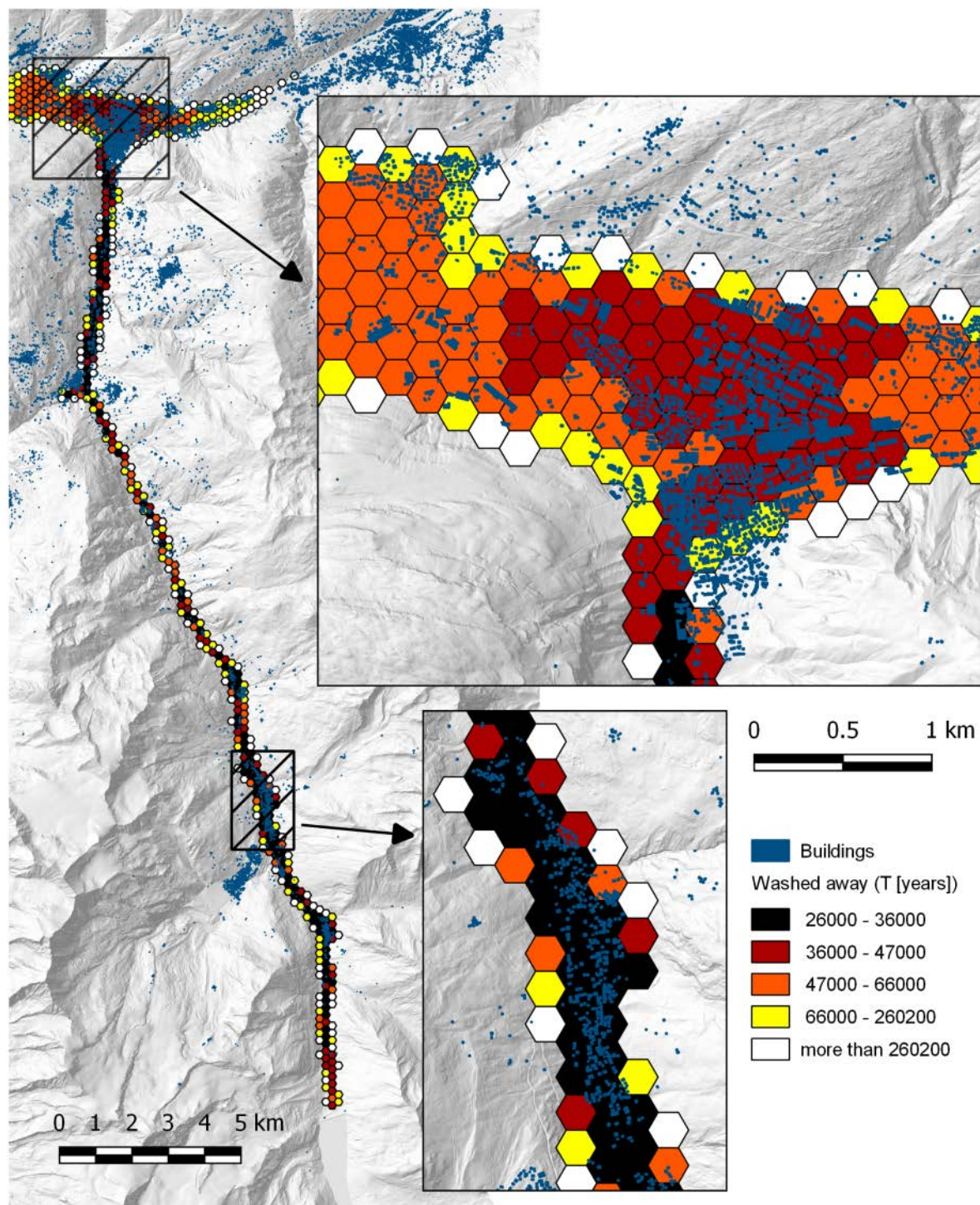
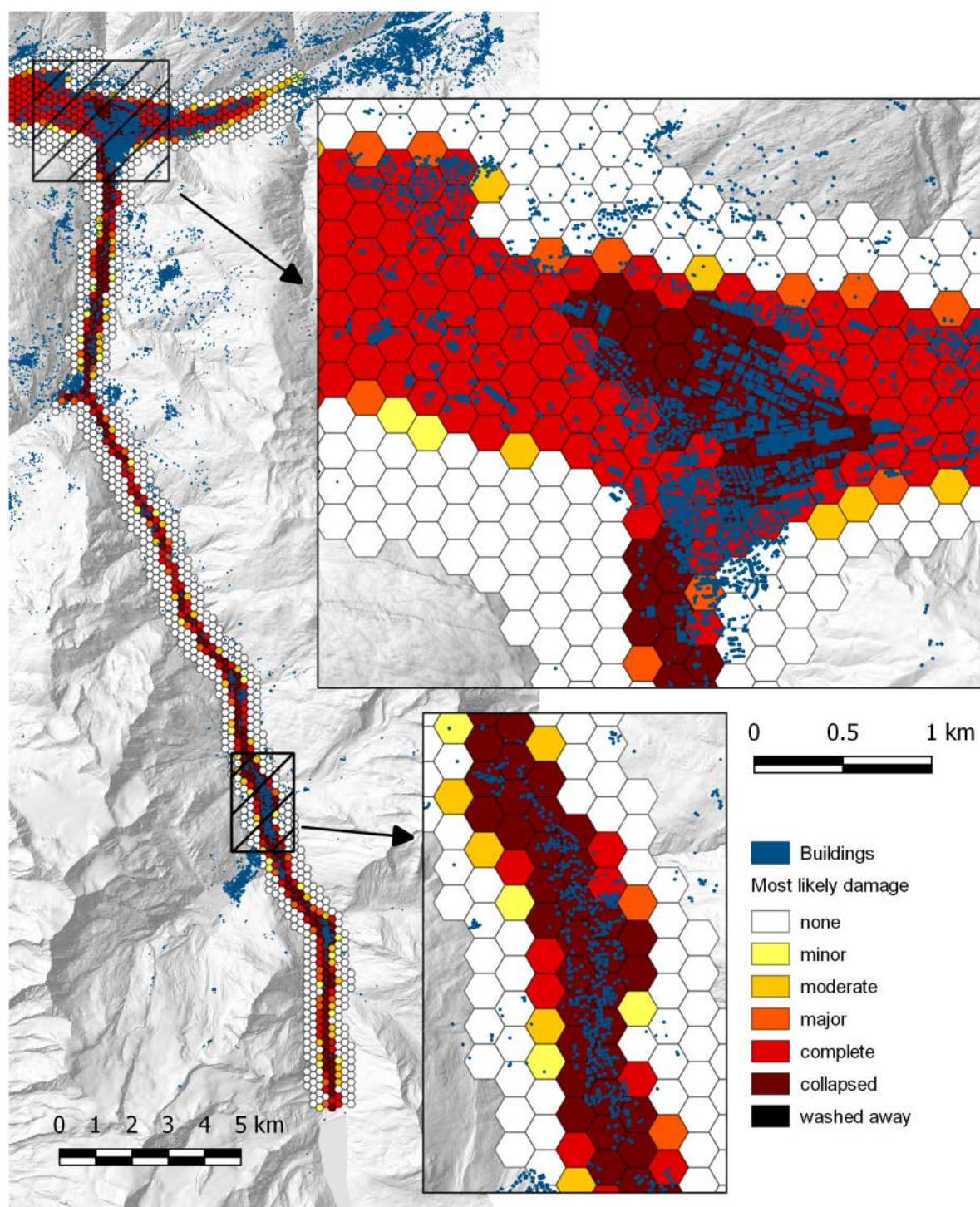


Fig. 3.38 Return period of 1 story reinforced concrete buildings being washed away





**Fig. 3.39** Most likely damage to 3 or more stories reinforced concrete buildings in the event of a dam failure upstream



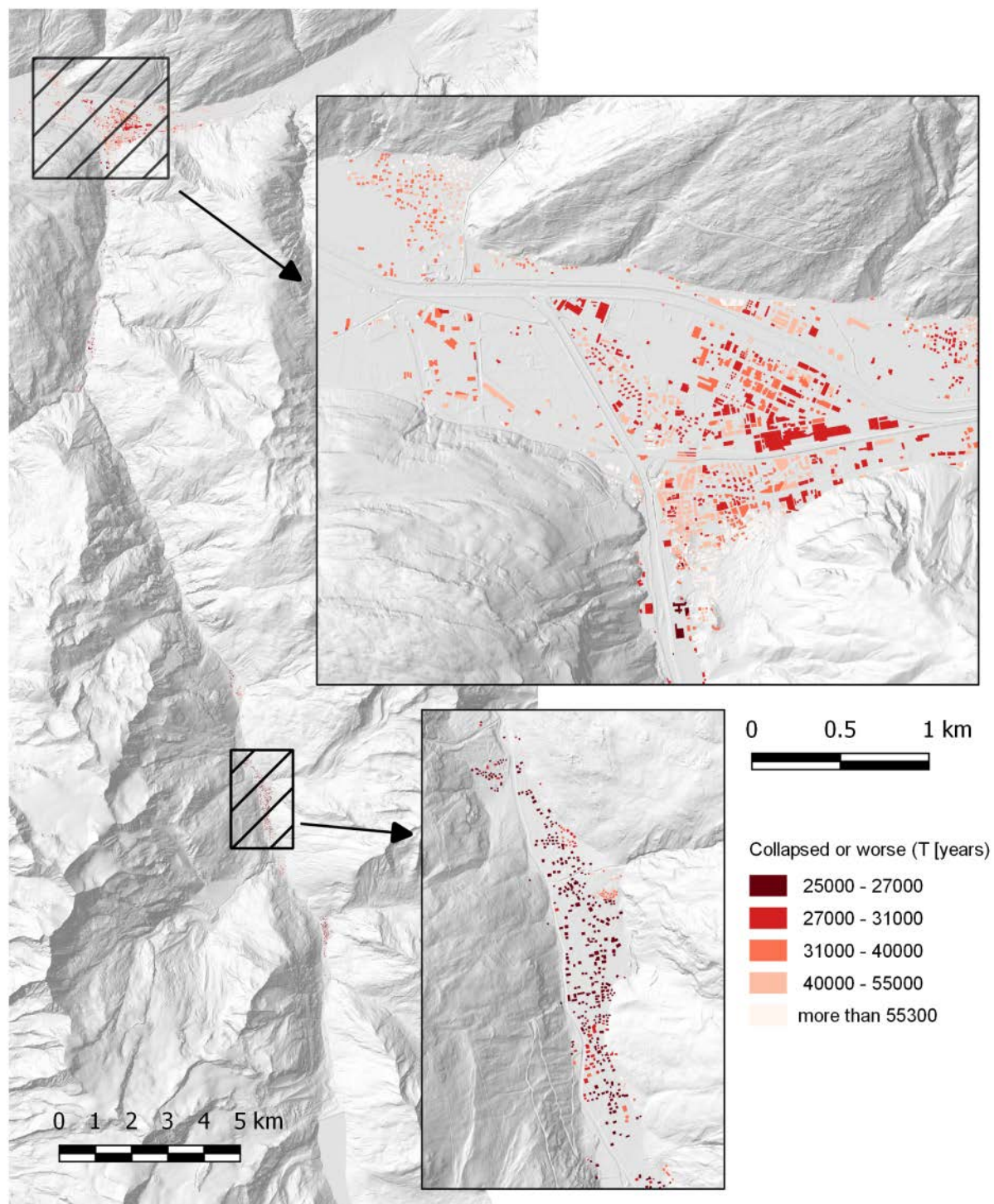


**Fig. 3.40 Return period of buildings collapsing or being washed away as a consequence of dam failures**

### 3.4 PHASE 3: DECISION PHASE

#### 3.4.1 Risk objectives check

Even considering for a wide range of uncertainties and hazards, with a return period of 25 000 years for failures, the dam meets the desired objective of having, on average, one breach per 10 000 years. It should be noted that the absolute value is very much affected by assumptions of the structure's fragility to earthquakes and the probabilities of internal erosion, both grossly estimated.

In what concerns damages in the downstream area, the goal was to limit expected damages to the loss of one habitation per 100 years. In concrete terms, this was assumed to be equivalent to an average loss  $7.5 \text{ m}^3$  per year due to dam failures. After integrating expected losses in the downstream area, however, a substantially higher value of  $200 \text{ m}^3$  of built volume lost per year was estimated. As a consequence, the second risk objective was not met.

Following the characteristic point of risk approach proposed by Esposito et al. (2017), one can inspect results further using an F-N curve. In this case the curve was prepared in respect to the cumulative frequency of built volume being collapsed or washed away as a consequence of a dam break upstream.

In Fig. 3.41 the F-N curve for the studied conceptual case is presented. Along with it four zones of acceptability are depicted. In agreement with Esposito et al. (2017), AA indicates negligible risk, A risk as low as reasonably practicable (ALARP), B a possibly unjustifiable risk, and C an intolerable risk. The threshold AA-A corresponds to a risk of  $7.5 \text{ m}^3/\text{yr}$ , A-B to  $75 \text{ m}^3/\text{yr}$ , and finally B-C to  $750 \text{ m}^3/\text{yr}$  (roughly equivalent to a habitation per year)<sup>1</sup>. It must be highlighted that these thresholds were set in order to maintain coherence with initially set goals and serve an exclusively illustrative purpose.

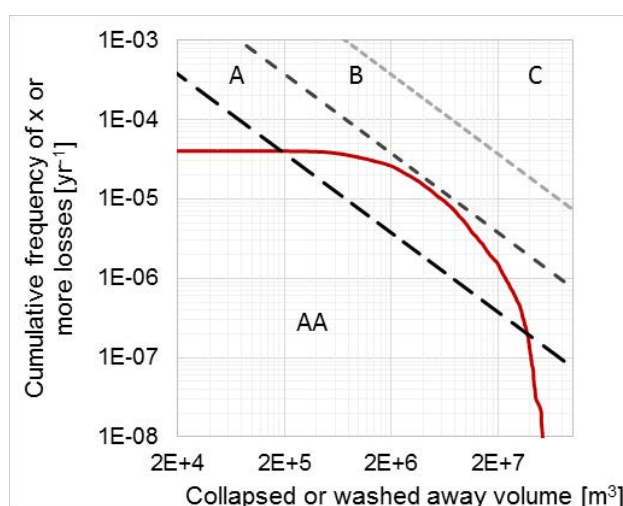


**Fig. 3.41 F-N curve based on collapsed or washed away built volume following a dam failure upstream.**

<sup>1</sup> It should be noted that these risk thresholds (AA-A, A-B, and B-C) are intrinsically different from the expected loss from the system, which integrates all the values along the F-N curve.

Inspecting the figure, we can see that A-B boundary is never crossed, as thus the risk associated with the conceptual dam following the characteristic point of risk approach is acceptable.

### 3.4.2 Disaggregation/Sensitivity Analysis

With some sensitivity analysis having been undertaken as results for the ST-L3 assessments were presented, the focus of this section will be on disaggregation. On this topic, perhaps the first thing that should be noted is that, notwithstanding there having been simulations including relatively intricate combinations of events (e.g. Fig. 3.42), the majority of the failures are prompted by simple occurrences.

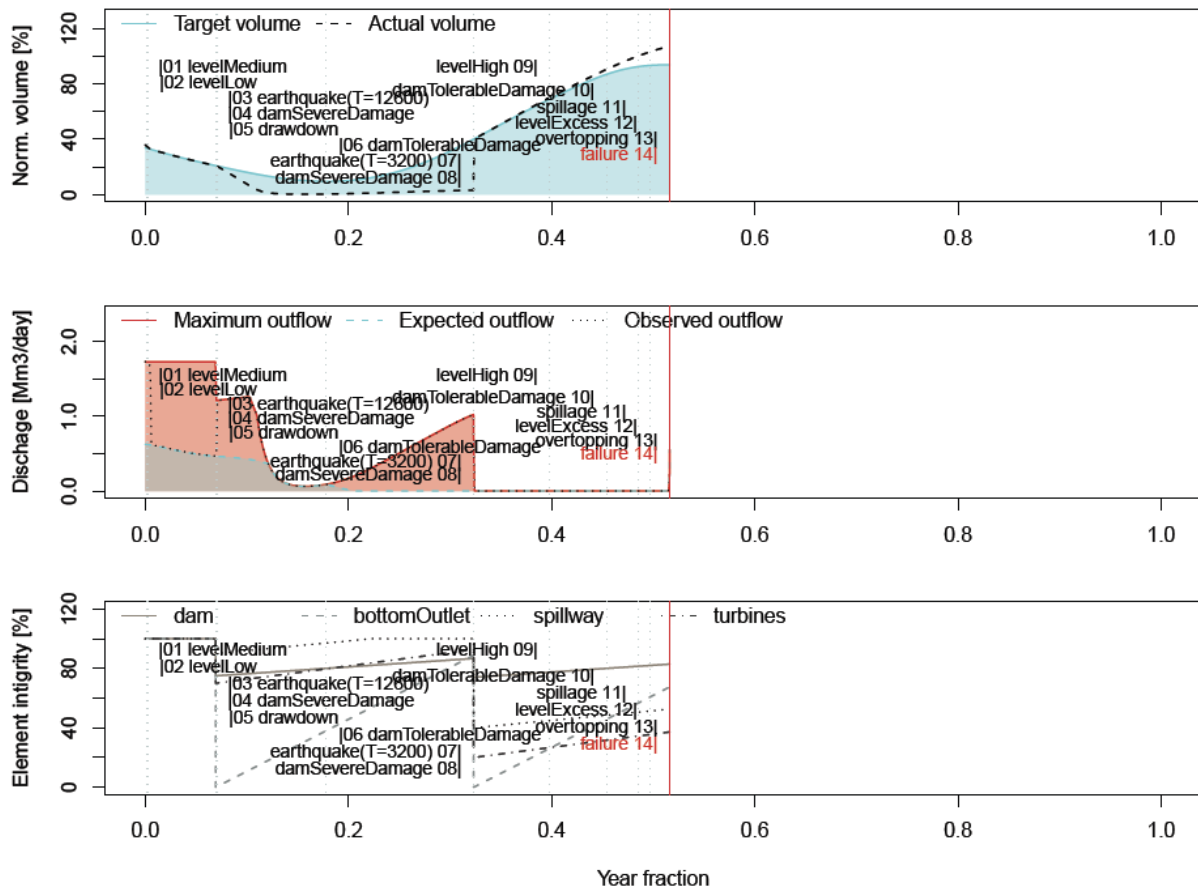


**Fig. 3.42 Example of a coincidence of events leading to failure**

Of the three primary hazards that may affect the dam, earthquakes seem to be by far the most dangerous, intervening in over 75% of the breaches. In second comes internal erosion, responsible for over 20%, and finally flooding, with virtually no critical impacts on the system.

Because excess water is not problematic, the bottom outlet and hydropower system's failures are mostly innocuous.

In addition to the primary events, also marginal overtopping and overtopping have led to failures. It should be said, however, that invariably they have been triggered by an earlier earthquake.

Overall, drawdowns were attempted with a return period of 10 000 years and have been quite effective at preventing a later failure. After the start of a drawdown the dam was breached only in 0.5% of the cases. Approximately, 90% of these events were triggered by an earlier earthquake, while 10% were prompted by internal erosion.

Looking at what return periods are more critical to the system, it can be seen through Fig. 3.43 that there is a wide range of earthquakes that threaten the system, but the risk peaks approximately at the 10 000 year events. Fig. 3.44 provides similar information for internal erosion. In the latter case the peak stands at the 200 000 year mark.

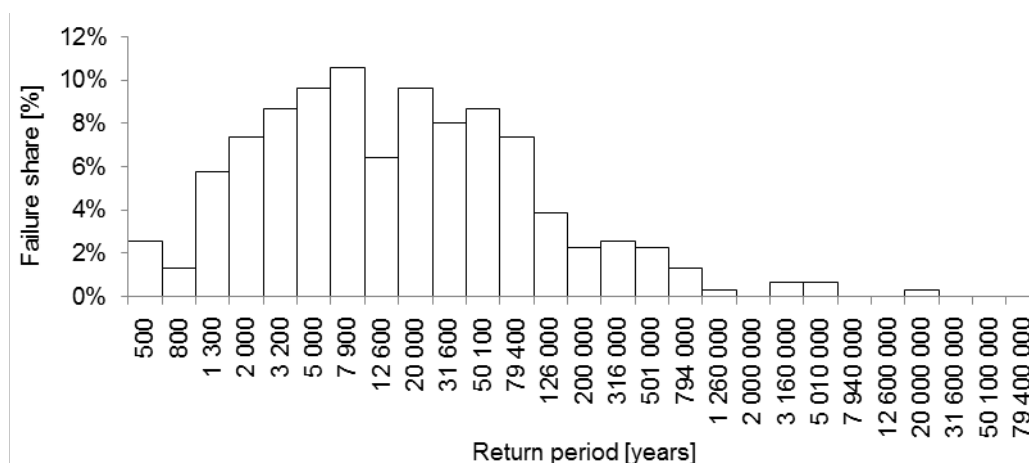


**Fig. 3.43 Disaggregation of failures caused by earthquakes**

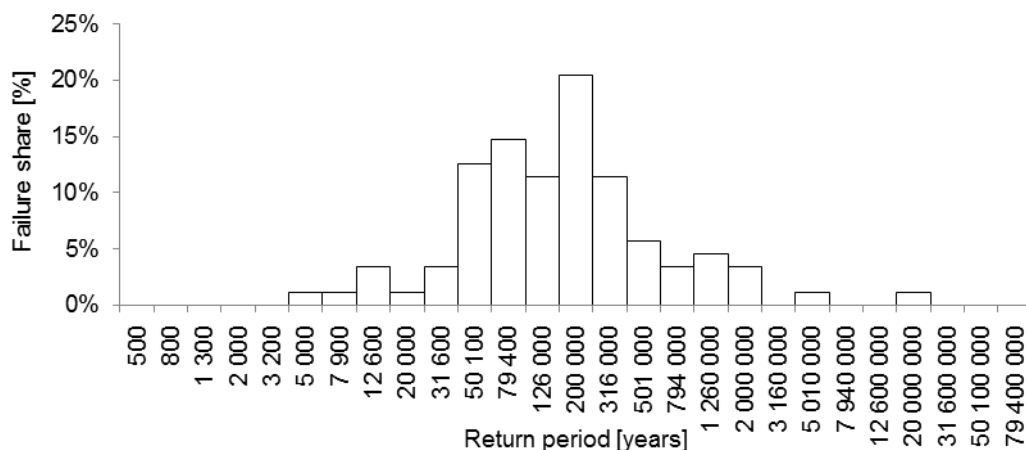


**Fig. 3.44 Disaggregation of failures caused by internal erosion**

Still focusing on Fig. 3.43, one can remark that a fair amount of low intensity earthquakes have been present just before a breach is formed. The result is counter-intuitive, as the dam is prepared to withstand 10 000 year earthquakes. It stems, however, from the consideration of probabilistic responses of the various elements using fragility curves. As an example, for an 800 year return period earthquake there is a probability lower than 0.04 of the dam failing. Such a coincidence equates to a return period of 20 000 years which, however rare, is not at all out of the scope of the analysis.

Inspecting how events are distributed in time is also easily achievable. Results are presented from Fig. 3.45 to Fig. 3.48. Failures appear to have a slight tendency to occur

during the summer and autumn seasons, when the reservoir is at its highest levels. It is most likely that this is due to a simple superposition of the earthquake's uniform distribution with the uneven distribution of internal erosion – affected by the levels of the reservoir. Floods tend to arrive – as expected – during spring and summer.

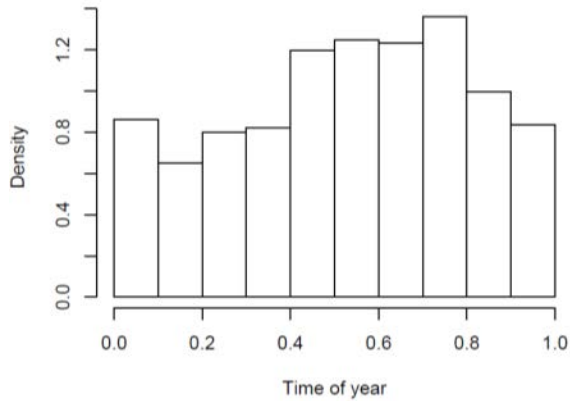


Fig. 3.45 Distribution of failures in time

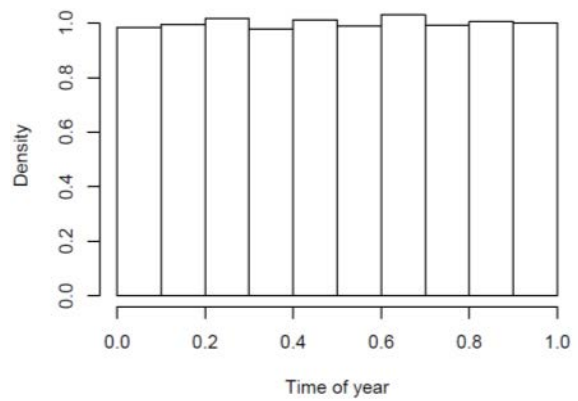


Fig. 3.46 Distribution of earthquakes in time

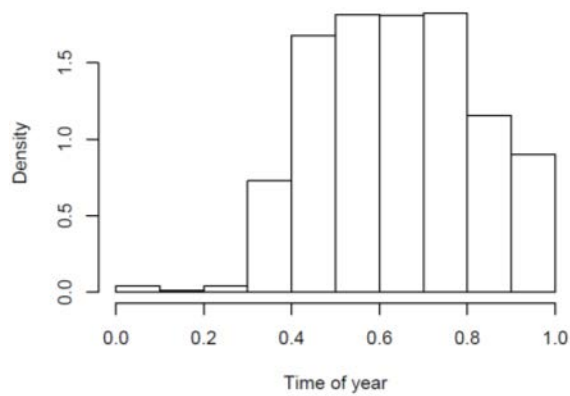


Fig. 3.47 Distribution of internal erosion in time

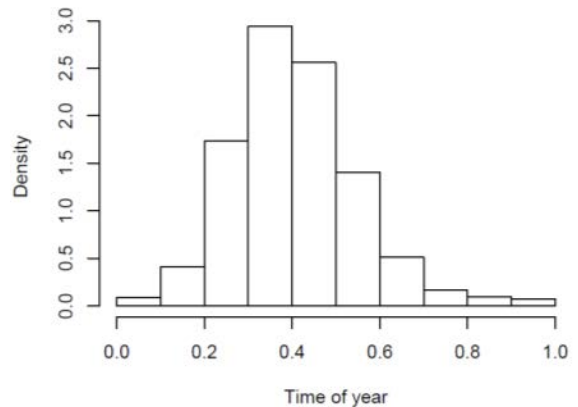
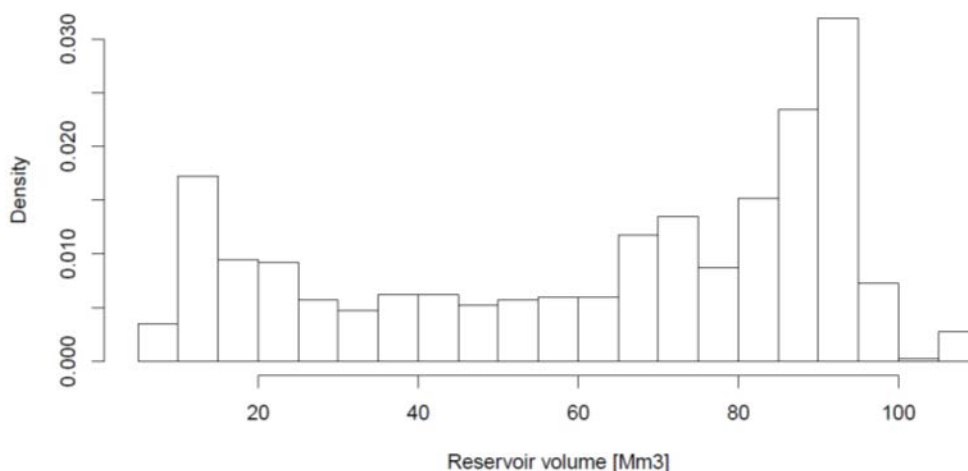


Fig. 3.48 Distribution of floods in time

In what concerns effects downstream, one can analyze the volumes of the reservoir when breaches start to develop (Fig. 3.49). As clearly shown, these volumes span the total possible range of the reservoir and, although there is a bias towards higher volumes, by the independent action of earthquakes failures can occur quite uniformly throughout the year. This, of course, has implications in the estimation of losses in the downstream area.



**Fig. 3.49 Histogram of reservoir levels when breaches start to develop**

Finally, in what damages to downstream buildings are concerned, the main drivers of distinction among the risks associated with individual buildings are, by action of the fragility curves, the building type and size.

### 3.4.3 Guidelines and critical events

Overall it is clear that, for the studied conceptual system, earthquakes pose the most relevant threat. This goes against what has been observed over the past decades worldwide, during which floods and internal erosion lead to the majority of the failures. Evidently, the observation holds true exclusively in relation to this conceptual case.

Partly, the large resilience to floods that the system appears to display may be linked with an unusually large freeboard. Beyond that, it might be an artifact caused by the assumption of independence between peak discharges and flood inflow volumes. This should be taken into account when interpreting this report and illustrates well the impact of base assumptions on final results.

For the conceptual system under study, including epistemic uncertainties nearly halved the estimation of the return period of a failure. The addition of uncertainty in the elements' responses to hazards, in the form of fragility curves, affected the system in a comparable fashion. In total, the sources of uncertainty added to the "base" model contributed to a four-fold increase in the estimated failure rate. Albeit the data used in this work lacks physical base and further scrutiny, it seems safe to affirm those sources of uncertainty should be not be neglected in other applications.

Virtually all overtopping events were prompted by an earthquake that damaged the outlet structures to a point from which the system could not be recovered. A way of addressing and greatly reducing the chances of failure by overtopping would be to upgrade the resilience of the bottom outlet and/ or guarantee its fast recovery.

In what concerns the downstream area, the main message is that, today, it is entirely possible to run stochastic simulations, even when the required numerical models are computationally expensive, even if subterfuges to by-pass the lengthier calculations must be adopted – as was the case here.



A total of 8020 inundations were evaluated, covering a large swath of the range of conceivable outflows from the dam. A possible use of the maps that were produced is to reinforce, provide with shelters, or relocate the buildings which are understood as being too at risk.

### **3.5 PHASE 4: REPORT PHASE**

The stress test described in this chapter is admittedly far from a traditional stress test for a large dam. In many ways it is greatly simplified in relation to the state-of-the-art. This shows particularly in what concerns the characterization of the dam elements' responses to specific hazards. This is particularly true for earthquakes – where detailed numerical models could have been applied – or for internal erosion – extremely challenging to quantify.

This was a deliberate choice. Safety assessments of large dams have been carried out for decades. There is a great amount of accumulated experience in that area and making real and worthy contributions at the component modeling level is very difficult.

Despite that, safety assessments aimed at dams are traditionally deterministic or, if probabilistic, following constraining assumptions and simplifications. In practice this means that dam engineers can make remarkable predictions of the behavior of dams when a few, mostly independent, hazards are considered, but they seldom produce an inclusive and accurate (or at least formally correct) estimate of probabilities and, therefore, of risks.

The flexibility of the GenMR framework, particularly when combined with machine learning methods that allow extraordinary gains in computational performance, makes this inclusive and formally correct estimate of risk attainable. Obviously, this is a highly desirable feature when performing a stress test.

Putting aside all the advantages of GenMR, it is in order to highlight again that, in order to obtain reliable results for the stress test it is crucial that realistic inputs are used. The simplifications that were made regarding the characterization of hazards and their action on elements are not something that is necessary for the application of GenMR. Well on the contrary, GenMR has the latitude to incorporate results from the numerical models that comprise the state-of-the-art in the field. In that light, in real implementations of the proposed stress test, detailed numerical modeling of the system components' response to hazards should not be neglected in any way.

In the present stress test aleatoric and epistemic uncertainties are accounted for to a large extent. Effects that contribute to the increase or reduction of the estimated failure rate and risk, such as hazard interactions or the yearly storage cycle of the reservoirs, are taken into account.

Despite all the limitations of the current approach, it demonstrates that a sound framework exists to tackle the issues related to the probabilistic risk assessment of large dams, particularly so if extended with additional hazards, elements, system states and, of course, reliable base data.

From the three objectives established in this stress test, one, concerning the dam-reservoir system and the probability of failures taking place, was met with a failure return period of 25 000 years, safely above the 10 000 years mark. The second, focusing on the expected losses downstream, was not. Quantitatively the chosen risk metric was more than 25 times

over the objective of 7.5 m<sup>3</sup>/year of built infrastructure collapsed or washed away. The third objective, defined on the basis on an F-N curve, classified the risk as ALARP.

Because once a breach is formed there is little that can be done to protect the physical assets in the wake of the dam-break wave, in order to lower the risk to the objective levels one tends to look at the dam itself: to make it safer. In the present case this would mean, however, that from one failure every 25 000 years on average, the system would need to improve to less than one failure per 750 000 years. Even if that could be accomplished, the area analyzed was limited to roughly 30 km downstream of the dam, but impacts from a failure can be felt much farther away. As a consequence, even a 750 000 year return period would not suffice to meet the second objective of 7.5 m<sup>3</sup>/year of built infrastructure collapsed or washed away.

This taps perhaps on the reasons why the adoption of probabilistic models is such a heated debate among the engineering community. Also, it may be one of the main reasons why large dams are often designed, maintained, and surveyed not to fail even under events such as the maximum credible earthquake or the probable maximum flood.

Putting aside considerations about the nature of the risk objectives that have been chosen, in this conceptual case earthquakes appear to be responsible for the lion's share of the expected losses. They have a direct impact on the dam, but can also lead to the catastrophic elevation of the reservoir through damages to the outlet structures. Investing in a more resilient bottom outlet would virtually prevent overtopping events, being perhaps the most direct and cost-effective way to reduce risk.

The tested system is conceptual and this stress test constitutes mainly a proof of concept. Elements and hazards have been characterized to the best knowledge of the authors, but surely suffer from substantial departures from reality. Particularly floods, a common factor of risk for dams throughout the world, did not assume any significant share of the risk. As a consequence, other hazards such as equipment malfunctions are also mostly innocuous. Without the need for further causes, a more detailed evaluation of the flood hazard should be carried out.



## 4 CI-B1 Major hydrocarbon pipelines, Turkey

### 4.1 INTRODUCTION

Buried pipeline systems are considered as lifelines since they carry materials essential to the support of human life. They are classified as segmented and continuous. Segmented pipes are commonly used in water and sewage networks. Typically, they consist of rigid pipe segments and flexible joints with bell-spigot and rubber gasket type of connections. Damage in segmented pipes happens at joints in the forms of pull-out or joint crushing. On other hand continuous pipes usually consist of steel pipes with welded connections. They are widely used in major hydrocarbon or water transmission lines to transport oil, gas and water from the sources to the end points. In contrast to segmented pipes the joint stiffness in continuous pipes is not much different than the rest of the pipe segment. Typical damage is in the form of local buckling due to beam bending (in normal burial depths) and global (beam) buckling (in shallow burial depths) or in submarine pipelines.

The focus of this chapter is the buried continuous welded steel pipelines (e.g. hydrocarbon pipelines) commonly used as reliable and economic means to transport oil and gas across the world. Such pipelines generally cover long distances and their exposure to the earthquake threats while crossing active faults in earthquake-prone regions cannot be overlooked at the design stage. The continuous steel pipes are not sensitive to transient strains due to ground shaking but they are vulnerable to permanent fault displacements (PFDs) at fault crossings. The 1971 San Fernando, 1994 Northridge, 1999 Kocaeli and 2001 Alaska earthquakes caused serious continuous pipeline damages at fault crossings with human casualties and economic losses. Therefore, reliable seismic hazard and risk assessment of continuous pipelines at fault crossings is important to mobilize the most efficient design and retrofitting techniques for earthquake induced risk mitigation.

When a continuous pipeline is subjected to surface fault rupture, the resulting stresses along the pipeline are complicated because they depend on many factors such as style-of-faulting, pipe material, pipe dimensions (thickness and diameter), pipe alignment with respect to fault strike and soil property surrounding the pipe. There are numerous studies in the literature that investigate the mechanical behavior of a pipeline at fault crossings (e.g. Datta, 1999; Vazouras et al., 2010; Vazouras et al., 2012; Karamitros et al., 2011; Karamitros et al., 2007; Uckan et al., 2015). The results of these studies do not consider the earthquake originated uncertainties that may affect the damage state in the continuous buried pipelines. The probabilistic seismic risk analysis of buried pipelines are focused on segmented pipelines (e.g. McGuire, 1988; Mashaly and Datta, 1989; Pineda-Porras and Ordaz, 2012; Omidvar et al., 2013; Esposito, 2014; Mousavi et al., 2014) by using empirical fragility functions that relate ground shaking (e.g. Katayama et al., 1975; O' Rourke and Jeon, 1999; ALA, 2001, 2005; HAZUS, 2004) or ground strain (e.g. O' Rourke, 2009; O' Rourke et al., 2014) to repair rate. Therefore, probabilistic failure due to fault crossings (i.e., PFDs) critical to continuous steel pipelines is yet to be investigated in sufficient details.

Recent developments in probabilistic PFD hazard (e.g. Stepp et al., 2001; Youngs et al., 2003; Petersen et al., 2011), however, provide good basis to implement probabilistic seismic risk assessment to continuous pipelines. Understanding the probabilistic risk of pipelines at

different earthquake levels would be important to the pipeline operator to take necessary actions for mitigating seismic pipeline vulnerability.

This chapter develops a full probabilistic risk assessment for pipeline failure due to PFD at fault crossings. It uses this tool for running stress tests to assess the seismic performance of such critical infrastructures for low performance-high consequence events. A specific buried steel oil and gas pipeline (Baku-Tbilisi-Ceyhan pipeline; BTC pipeline) is investigated to implement the stress test methodology developed within the context of the STREST project (Esposito et al., 2016; 2017).

Although permanent fault displacement is the only hazard term considered in the stress tests, the hazard due to landslides or liquefaction should not be overlooked for a more realistic performance assessment of continuous pipelines. However, the contribution of multiple hazard components to the overall probabilistic pipeline risk is disregarded at this point. Our probabilistic pipeline PFD risk computations take into account the uncertainties arising from complex fault rupture, geomorphologies resulting in inaccurate mapping, uncertainty in the fault-pipe crossings, pipe buried depths, soil types surrounding the pipe and pipe diameter to pipe thickness ratio. The results presented in this chapter also suggest the re-evaluation of design provisions in the current pipeline design guidelines to reduce the seismic risk of such geographically distributed structural systems.

## **4.2 PHASE 1: PRE-ASSESSMENT PHASE**

### **4.2.1 Data collection**

As the transmission pipeline, the investigated BTC (Baku-Tbilisi-Ceyhan) pipeline, featuring 1758 km long, daily transports about 1% of the world's daily petroleum output, about 1 million barrels, shown in Fig. 4.1. The BTE pipeline has excess capacity today, with 30 billion cubic meters of natural gas a year (<https://de.wikipedia.org/wiki/Baku-Tiflis-Ceyhan-Pipeline>). The diameter of the pipeline is 42 inches throughout most of Azerbaijan and Turkey. In Georgia the pipeline diameter is 46 inches. The pipeline diameter reduces to 34-inches for the last downhill section to the Ceyhan Marine Terminal in Turkey. The BTC pipeline facilities include: 8 pump stations (2 in Azerbaijan, 2 in Georgia, 4 in Turkey), 2 intermediate pigging stations, 1 pressure reduction station and 101 small block valves.

Five main pipe-fault crossing locations are identified along the BTC route. The hazard information at pipe-fault intersections are provided in the Table 4.1. Five pipe-fault crossings are numerated from #1 to #5. Table 4.1 also contains other information, such as location of crossing locations with respect to the fault ( $L$  referred to Fig. 4.8), pipe-fault crossing angles, etc. The geographical details of the pipe-fault intersections from #1 to #5 are described in Fig. 4.2-Fig. 4.5. The pipes crossing these five main seismic faults are featuring with the same pipe diameter of 42 inches (1.0688m) and the same thickness of 20.62mm. The properties of the pipe and soil at the fault-pipe intersections are given in Table 4.2 and Table 4.3, which are useful in the calculation of pipeline strains in the following sections.

The pipeline trench is trapezoidal-shaped and packed with loose to medium granular cohesion-less backfill with minimum soil cover. At the fault crossing point, the pipeline alignment is such that to promote tension in the pipe. The sketch of a typical trench for fault crossing at Erzurum fault zone is shown in Fig. 4.6.



Fig. 4.1 Overview of BTC pipeline

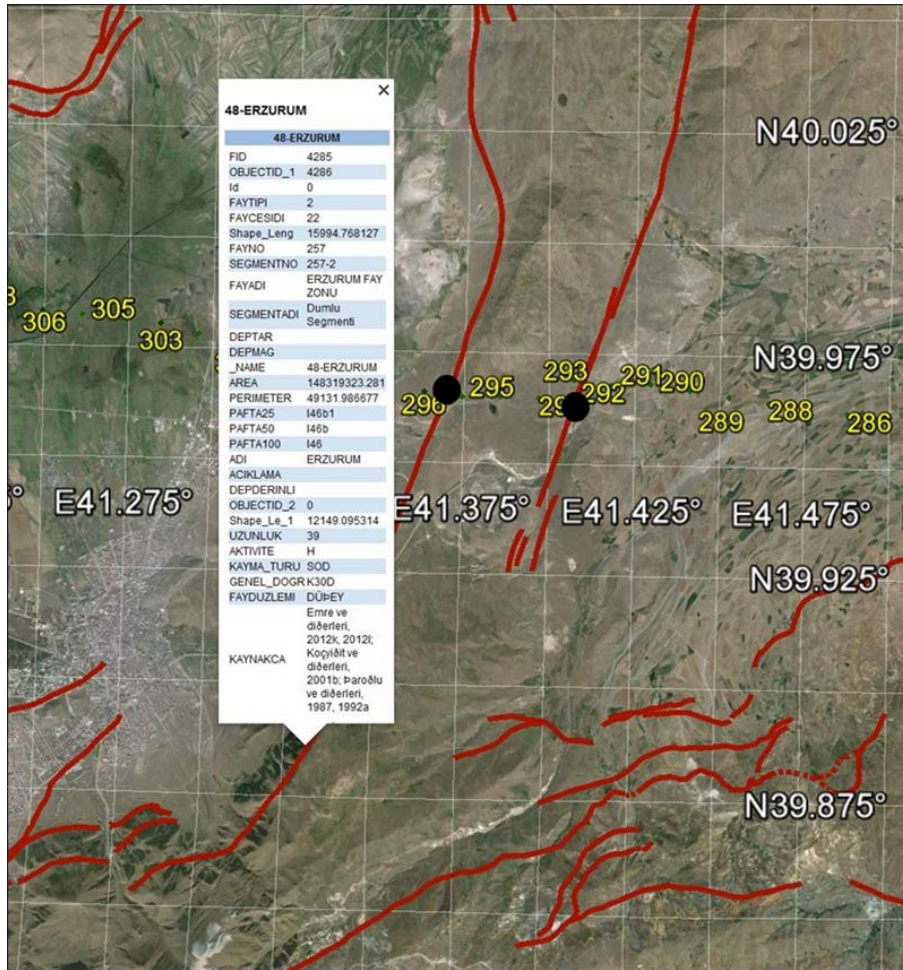


Fig. 4.2 Details of pipe-fault crossings #1 and # 2

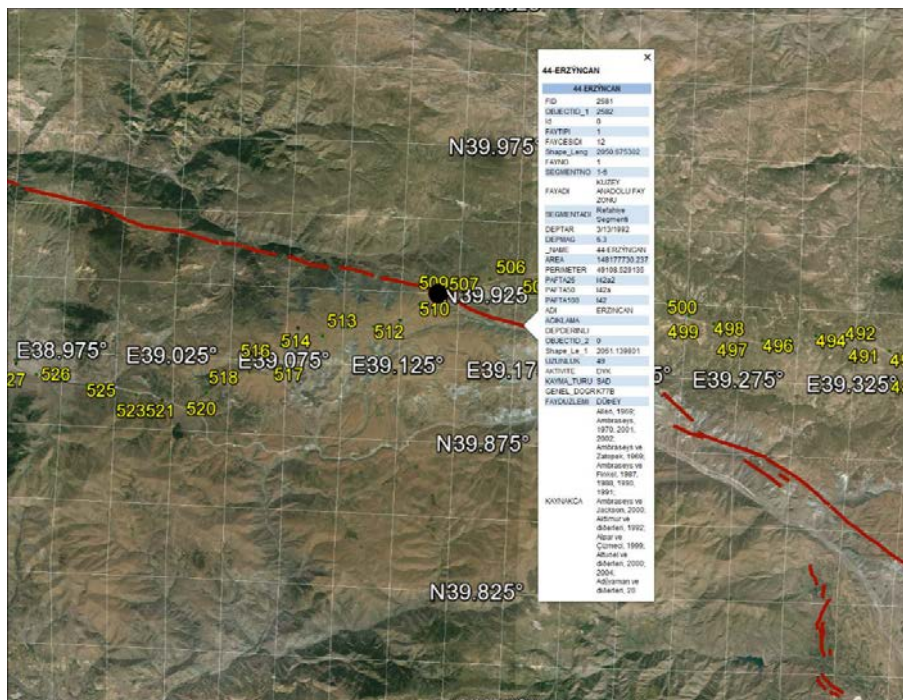


Fig. 4.3 Details of pipe-fault crossings # 3



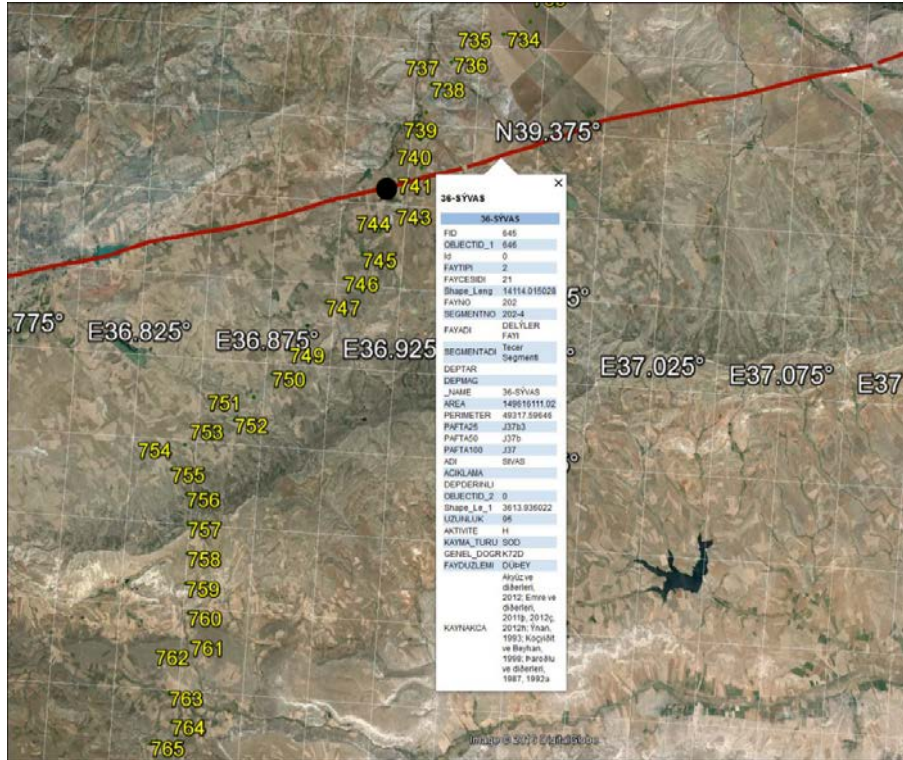


Fig. 4.4 Details of pipe-fault crossings # 4

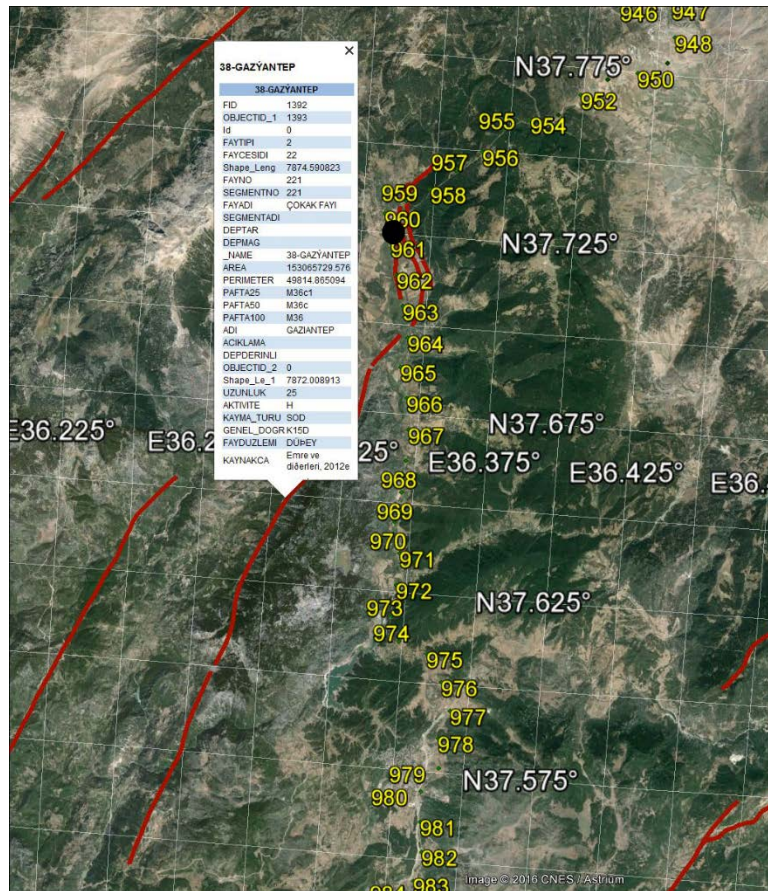


Fig. 4.5 Details of pipe-fault crossings # 5

**Table 4.1 Information of faults crossing the investigated major hydrocarbon pipeline, and their fault-pipe intersections**

Segment	Fault				Pipe-fault intersection			
	Fault Name	Fault length (km)	Fault Type	Fault Name	Fault length (km)	Longitude	Fault Name	Fault length (km)
#1	Erzurum East Fault	42	LL SS	90	~0.1	41.410	39.968	~60
#2	Erzurum West Fault	39	LL SS	90	~0.35	41.371	39.965	~70
#3	North Anatolian Fault	49	RL SS	90	~0.5	39.142	39.925	~30
#4	Deliler Fault Zone	95	LL SS	90	~0.5	36.931	39.360	~45
#5	Çokak Fault Zone	25	LL SS	90	~0.1	36.340	37.734	~90

**Table 4.2 The properties of the pipe and soil at the fault-pipe intersections**

Segment	Name	Buried depth	Pipe D/t	Pipe property	Soil Type
#1	Erzurum East Fault	1.5m	52	API XL Grade X65	Loose-to-Medium sand
#2	Erzurum West Fault	1.5m	52	API 5L Grade X65	Loose-to-Medium sand
#3	North Anatolian Fault	1.5m	52	API 5L Grade X65	Loose-to-Medium sand
#4	Deliler Fault Zone	1.5m	52	API 5L Grade X65	Loose-to-Medium sand
#5	Çokak Fault Zone	1.5m	52	API 5L Grade X65	Loose-to-Medium sand
#1	Erzurum East Fault	1.5m	52	API XL Grade X65	Loose-to-Medium sand

**Table 4.3 API5L-X65 steel properties considered in the numerical analyses**

Yield stress ( $\sigma_1$ )	490MPa
Failure stress ( $\sigma_2$ )	531MPa
Failure strain ( $\epsilon_2$ )	4.0%
Elastic Young's modulus ( $E_1$ )	210 GPa
Yield strain ( $\epsilon_1 = \sigma_1 / E_1$ )	0.233%
Plastic Young's modulus ( $E_1 = (\sigma_2 - \sigma_1) / (\epsilon_2 - \epsilon_1)$ )	1.088 Gpa

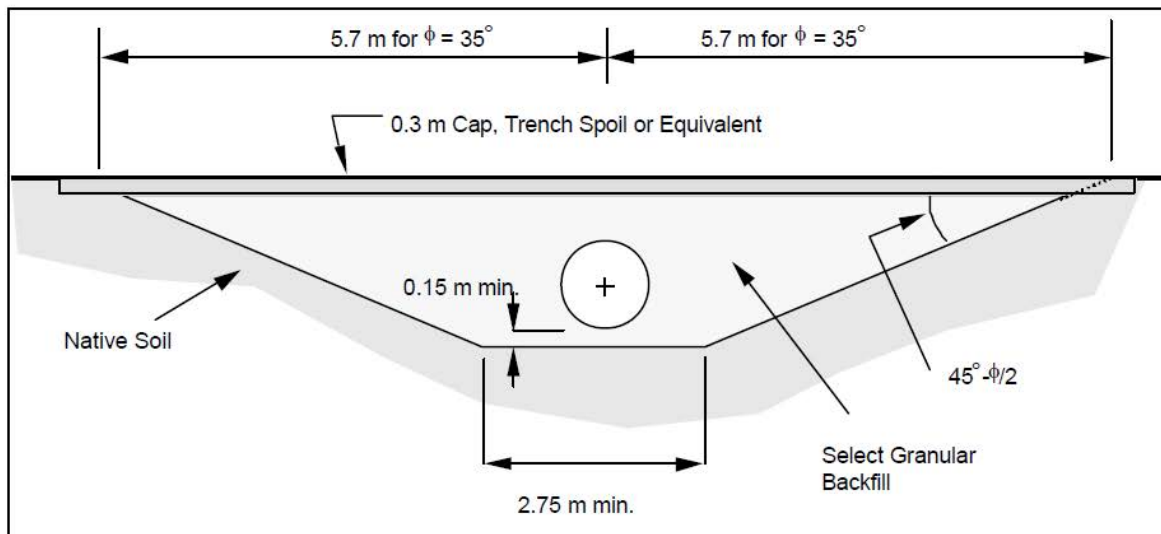


**Fig. 4.6 Typical trench for fault crossing, Erzurum fault zone**

#### 4.2.2 Risk Measures and Objectives

Fault crossing is considered as abrupt lateral PGD hazard in which the displacement field changes immediately within the fault surface and remains constant outside the fault line. As a result of fault offsets axial strains are induced in pipes. The amount of strain depends on the orientation of the pipe with respect to the fault line (crossing angle), slip direction as well as on the soil and pipe properties. Rupture of buried, welded steel pipelines (e.g. used in the BTC pipeline) exposed to large fault displacement is a result of severe compressive buckling of the pipe wall or tensile fracture.

Whether the differential ground movement results in a pipe primarily in tension or compression depends on the relative orientation of the fault and the pipe as well as the direction of faulting. For example, right lateral strike slip faulting with a negative intersection angle (which is measured with the pipe moving clockwise around the pipe-fault intersection point toward faulting direction; the angle is larger than  $-90^\circ$ ) results in axial tension and bending in the pipe. However, left lateral strike slip with a positive crossing angle (which is measured with the pipe moving anticlockwise around the pipe-fault intersection point toward faulting direction; the angle is less than  $90^\circ$ ) results in axial compression and bending. Therefore, the pipeline rupture or loss of pressure integrity (pipeline failure) along BTC pipeline route due to fault offsets is defined as the risk measure.

Eidinger and Avila (1999) propose four performance classes (life safety, key operational, other operational and distribution) in terms of severity of pipe failure at pipe-fault crossings. Under the occurrence of maximum credible earthquake (MCE) these four performance goals are set to four allowable probabilities that are identified as 1% (life safety), 2% (key operational), 10% (other operational) and 50% (distribution). This classification is used and the risk objective for BTC gas and oil pipeline against PFD is described by the probability of the pipeline failure in 2475-year return period (assumed to be the hazard level of MCE although maximum credible earthquake refers to deterministic maximum earthquake that the fault of interest is capable to produce). In reference to the STREST project grading system

(Esposito et al., 2016; 2017) as illustrated in the Fig. 4.7, the probability ranges are defined in Table 4.4 for different grades representing different risk tolerances.

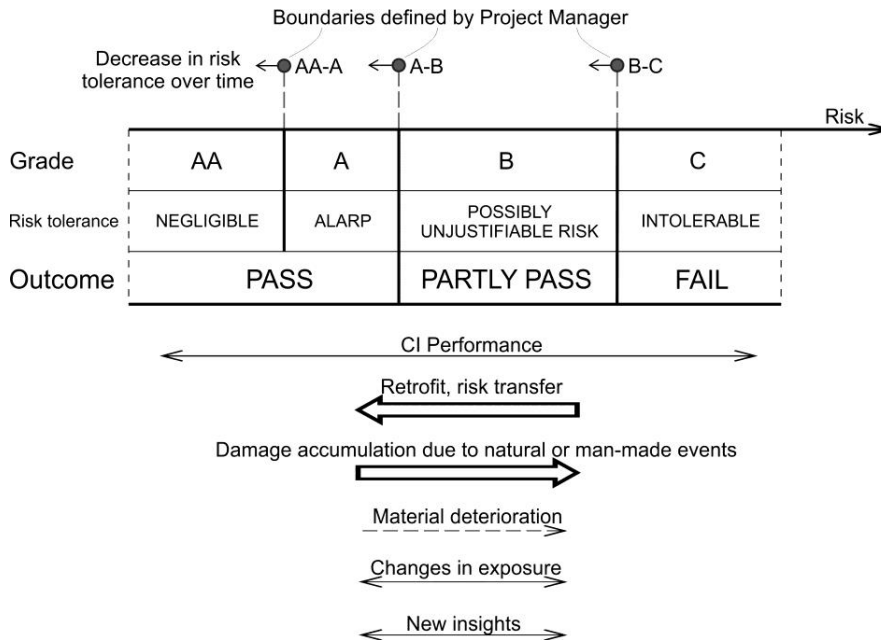


**Fig. 4.7 Grading system for the global outcome of Stress Test (Esposito et al., 2016; 2017)**

**Table 4.4 Probabilities defined for the STREST grade**

Grade	AA	A	B	C
Risk tolerance	NEGLIGIBLE	ALARP	POSSIBLY UNJUSTIFIABLE RISK	INTOLERABLE
Probability range in 2475 years	0%-2%	2%-10%	10%-50%	50%-100%

### 4.2.3 Set-up of the Stress Test

The STREST Level 1a (ST-L1) is first performed for assessing the seismic performance of continuous buried pipelines. Then Level 2a (ST-L2a) is performed based on Level 1a. Three levels of technical accuracy is applied for the test, which are moderate, advanced and high accuracies, corresponding to hazard-based assessment, design-based assessment, and risk-based assessment, respectively. No epistemic uncertainty is introduced in Level 2a because probabilistic PFD hazard and risk consider a level of modeling uncertainty as described in the following sections.



## 4.3 PHASE 2: ASSESSMENT PHASE

### 4.3.1 Component Level Assessment (ST-L1a)

#### 4.3.1.1 Hazard-based assessment

##### 4.3.1.1.1 Theory: Monte-Carlo based probabilistic hazard for PFD

The current state-of-practice (e.g. pipeline designs codes) tends to estimate PFDs deterministically from empirical surface rupture vs. magnitude relationships (e.g. Wells and Coppersmith, 1994). Alternative to this approach, Youngs et al. (2003) developed the probabilistic fault displacement hazard assessment (PFDHA) for the Yucca Mountain Nuclear Waste Repository Project for normal faults to express the annual exceedance rates of fault displacements at different thresholds. The methodology is inspired from conventional probabilistic seismic hazard assessment (PSHA). It is further studied in Petersen et al. (2011) for strike-slip faults by including the mapping accuracy and ruptured fault complexity. Our method uses the Petersen et al. model and it considers the likely occurrence of on-fault ( $D$ ) and off-fault ( $d$ ) displacements. The former displacement occurs on the major ruptured fault and the latter displacement typically represents discontinuous shear-failures at locations far from the principal fault.

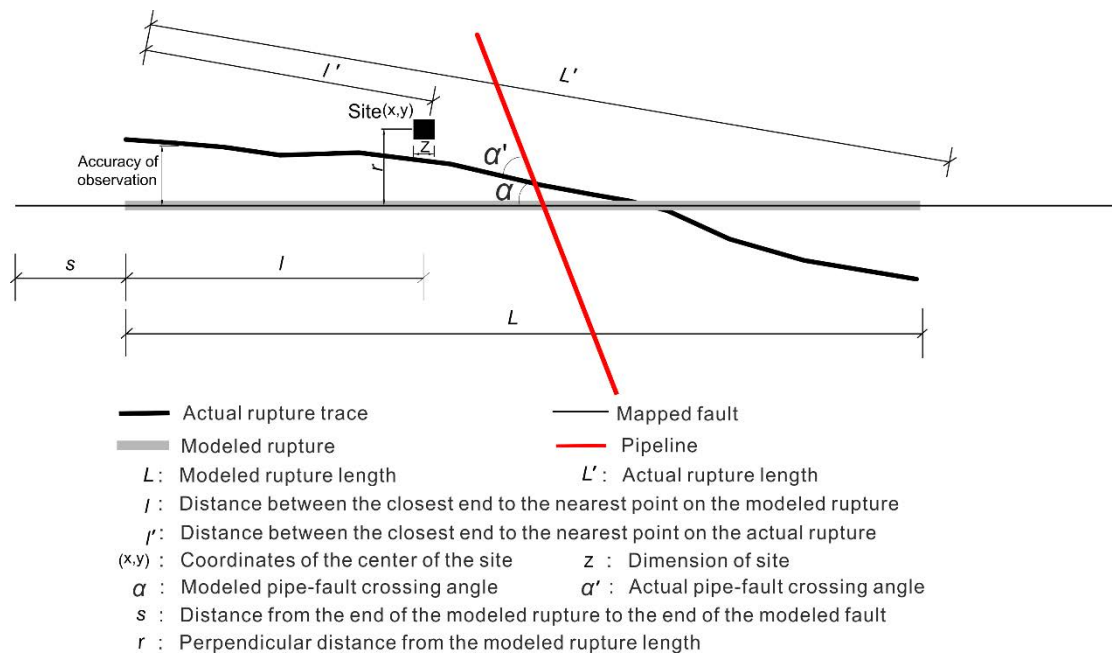


**Fig. 4.8 Modeled and actual fault layout for Petersen et al. (2011) PFDHA approach for strike-slip earthquakes. The accuracy of observation represents the combined effects of fault mapping accuracy and rupture complexity on the modeled and actual rupture conditions (From Cheng and Akkar, 2016)**

Our interpretations of ruptured fault segment and site geometry used in Petersen et al. (2011) are presented in Fig. 4.8. The plot shows the *modeled* and *actual* fault layout. The *modeled* configuration is used in PFDHA by incorporating the uncertainties due to mapping inaccuracy and complexity of fault rupture. The site is represented as a square cell having a

dimension of  $z$  and  $x, y$  denote the coordinates of the center of the site. Fault distance,  $r$ , is the perpendicular distance from the *modeled* rupture length,  $L$ .  $l$  denotes the distance between the closest end to the nearest point on the *modeled* rupture.  $s$  is the distance from the end of the *modeled* rupture to the end of the *modeled* fault. We mimic the potential deviations in the rupture from the mapped (*modeled*) fault trace by introducing offsets normal to the strike of the mapped fault. Petersen et al. (2011) describe these offsets with a set of standard deviations (Tables 2 and 3 in Petersen et al. (2011) at fault crossings) for different categories of mapping accuracy (accurate, approximate, concealed and inferred) and fault complexity (simple or complex).  $L'$  and  $l'$  are the counterparts of  $L$  and  $l$ , respectively. They also address the uncertainty in the relative positions of rupture and site due to intricate variations in fault rupture conditions.

Eq. (4.1) and (4.2) show the annual exceedance rates of on-fault  $\gamma(D \geq D_0)$  and off-fault  $\gamma(d \geq d_0)$  displacements that are given in Petersen et al. (2011).

$$\begin{aligned} \gamma(D \geq D_0) = v_{\min} \int_{m,s} f_{M,S}(m,s) P[sr \neq 0|m] \int_r P[D \neq 0|z, sr \neq 0] \\ \times P[D \geq D_0|l/L, m, D \neq 0] f_{l/L}(l/L) f_R(r) d(l/L) dr dms \end{aligned} \quad (4.1)$$

$$\begin{aligned} \gamma(d \geq d_0) = v_{\min} \int_{m,s} f_{M,S}(m,s) P[sr \neq 0|m] \int_r P[d \neq 0|r, z, sr \neq 0] \\ \times P[d \geq d_0|r, m, d \neq 0] f_R(r) dr dms \end{aligned} \quad (4.2)$$

The probabilistic terms in Eq. (4.1) include (a) the uncertainty in rupture location due to random variation of rupture along the fault as well as the fault complexity and mapping inaccuracy,  $f(r)$ ; (b) the joint probability to characterize the relation between earthquake magnitude ( $m$ ) and rupture location ( $s$ ),  $f_{M,S}(m,s)$ ; (c) the probability of observing surface rupture ( $sr$ ) conditioned on earthquake magnitude,  $P(sr \neq 0|m)$ ; (d) given a nonzero surface rupture the probability of observing a nonzero on-fault displacement at a site of dimension  $z$ ,  $P(D \neq 0|z, sr \neq 0)$  and (e) the probability of on-fault displacement exceeding a threshold  $D_0$  conditioned on rupture geometry and earthquake size. The last conditional probability is lognormal and is developed from an on-fault empirical displacement predictive model (on-fault displacement GMPE). Apart from these probabilistic terms, the minimum rate,  $v_{\min}$ , constrains the frequency of earthquake occurrence in the model. It is a function of magnitude and can be a single rupture rate or can be a function of cumulative earthquakes above a minimum magnitude of engineering significance (Youngs et al., 2003).

The probabilistic terms that describe the annual exceedance rate of off-fault displacements  $\gamma(d \geq d_0)$  show some similarities with Eq. (4.1). In fact, the first three probabilities defined in  $\gamma(D \geq D_0)$  also exist in  $\gamma(d \geq d_0)$ . In the computation of  $\gamma(d \geq d_0)$ , the probability of nonzero off-fault displacement given a nonzero surface rupture  $[P(d \neq 0|r, z, sr \neq 0)]$  not only depends on the size of the site ( $z$ ) but also on the perpendicular distance,  $r$ , between the site and the rupture. This is because the discontinuous off-fault displacements are expected to occur away from the fault due to shears and fractures in the vicinity of principle rupture. The empirical GMPE to describe the probability of off-fault displacement exceeding a threshold  $d_0$   $[P(d \geq d_0|r, m, d \neq 0)]$  is a function of  $r$  and  $m$  for  $\gamma(d \geq d_0)$ . The reader is referred to Petersen et al. (2011) and Youngs et al. (2003) for details of conventional probabilistic fault displacement hazard integral. The next paragraph explains the integration of these probabilities to MC-based PFD hazard.

Our MC-based PFD hazard assessment starts with the generation of synthetic earthquake catalogs to reflect the temporal seismicity of the subject fault. The procedure of generating

synthetic catalogs is already given in Akkar and Cheng (2015). Each synthetic catalog contains a series of events that follows the designated magnitude recurrence model within the predefined catalog period. For each event in the synthetic catalog, Fig. 4.9 shows the proposed procedure to generate probabilistic on-fault and off-fault displacements at the centroids of the cells covered by the region of interest. The grid size is  $z$  and it varies from 25 m to 200 m in Petersen et al. (2011) to account for different levels of accuracy in rupture probability. The mesh gridding is done only within several hundred meters (e.g. 150 m) from each side of the fault because fault displacements decay rapidly with increasing distance from the ruptured fault segment.

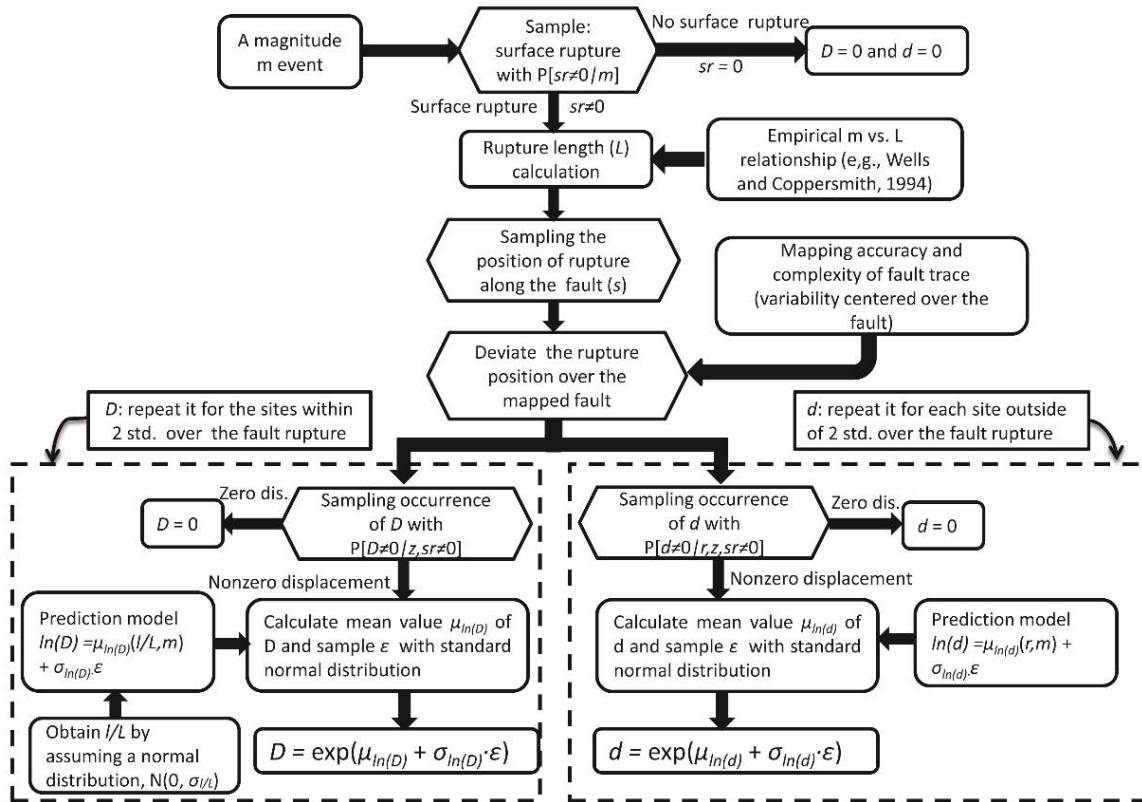


**Fig. 4.9 Proposed MC-based permanent fault displacement hazard assessment procedure**

We first compute the conditional probability of observing surface rupture on the fault,  $P(sr \neq 0 | m)$ , for each scenario event with a designated magnitude  $m$  in the earthquake catalog (Eq. (4.3)).

$$P(sr \neq 0 | m) = \frac{e^{(-12.51 + 2.053m)}}{1 + e^{(-12.51 + 2.053m)}} \quad (4.3)$$

The conditional probability follows Bernoulli distribution that samples the “success” ( $sr \neq 0$ ) or “failure” ( $sr = 0$ ) of a random event under the computed probability given in Eq. (4.3). If Bernoulli distribution samples “failure”, both on- and off-fault displacements are zero for that scenario event. If the earthquake with surface rupture is sampled, an empirical  $m$  vs.  $L$  scaling relationship is used (e.g. Wells and Coppersmith, 1994) to determine the rupture length,  $L$ . The rupture position ( $s$ ) is randomly placed along the entire fault assuming a

uniform distribution. The likely deviation in the rupture location from the mapped fault trace due to mapping uncertainty is determined from a two-sided normal probability distribution proposed by Petersen et al. (2011). (See Table 2 in the referred article). After determining the final location of the ruptured segment, the on- and off-fault displacements are generated as given in the dashed boxes in Fig. 4.9. The random generation of on- and off-fault displacements start with the consideration of probabilities  $P(D \neq 0|_{z, sr \neq 0})$  and  $P(d \neq 0|_{r, z, sr \neq 0})$ . These probabilities are expressed as power functions and are given in a tabular format in Petersen et al. (2011) for different grid sizes. They also follow Bernoulli distribution and if the Bernoulli distribution samples “failure” for any one of these probabilities, the corresponding fault displacement is taken as zero. (In practice,  $P(D \neq 0|_{z, sr \neq 0})$  can be taken as unity and Bernoulli distribution samples “success” whenever a non-zero surface rupture is generated). Otherwise, the on- and off-fault displacements are estimated from the proposed empirical GMPEs by Petersen et al. (2011). The generic forms of these GMPEs are given in Eq. (4.4) and (4.5).

$$\ln(D) = \mu_{\ln(D)}(l/L, m) + \varepsilon\sigma_{\ln(D)} \quad (4.4)$$

$$\ln(d) = \mu_{\ln(d)}(r, m) + \varepsilon\sigma_{\ln(d)} \quad (4.5)$$

$\mu_{\ln(D)}$  and  $\mu_{\ln(d)}$  are the logarithmic mean estimates of on- and off-fault displacements, respectively.  $\sigma_{\ln(D)}$  and  $\sigma_{\ln(d)}$  describe the logarithmic standard deviations associated with the on- and off-fault displacement GMPEs, respectively.  $\varepsilon$  designates the number of standard deviations above or below the logarithmic mean estimates. Consistent with the conventional wisdom in GMPEs,  $D$  and  $d$  are log-normal varieties whereas  $\varepsilon$  is normally distributed in the above expressions. Petersen et al. (2011) propose three alternative prediction equations to estimate on-fault displacements depending on the observed data from the past strike-slip earthquakes. These equations are strictly valid for on-fault sites (cells) after considering the mapping uncertainty and fault complexity while determining the location of ruptured segment on the principal fault. We treat  $l/L$  as a normal variate to consider the uncertainty between the relative positions of rupture and site locations resulting from complexities in rupture process. The off-fault displacement predictive model is used at the sites (cells) encircling the major ruptured fault segment. The off-fault sites are only within few hundred meters from both sides of the ruptured fault segment due to rapid decay of fault displacements with distance.

The algorithm given in Fig. 4.9 is repeated for all the earthquakes in the generated synthetic catalogs to compute the on- and off-fault displacement distributions at the centroid of each cell. The annual exceedance rates of on-fault and off-fault displacements at each cell for predefined threshold levels are determined from the following expressions:

$$\lambda_j(D \geq D_0) = \frac{\text{total number of } D \geq D_0 \text{ at site } j}{\text{total number of simulated earthquake catalogs} \times \text{catalog period}} \quad (4.6)$$

$$\lambda_j(d \geq d_0) = \frac{\text{total number of } d \geq d_0 \text{ at site } j}{\text{total number of simulated earthquake catalogs} \times \text{catalog period}} \quad (4.7)$$

In Eq. (4.6) and (4.7)  $j$  refers to the cell index whereas  $D_0$  and  $d_0$  are the threshold on-fault and off-fault displacements, respectively. The on-fault and off-fault displacement hazard curves at cell  $j$  are obtained from the computation of  $\lambda_j(D \geq D_0)$  and  $\lambda_j(d \geq d_0)$  for a set of  $D_0$  and  $d_0$ , respectively. The total permanent displacement hazard curve at cell  $j$  is the sum of on- and off-fault hazard curves corresponding to cell  $j$ .

#### 4.3.1.1.2 Application in the STREST

The data collection is explained in Section 4.2.1 in the first phase. Table 4.1 provides the basic information of the fault segments crossing the BTC pipelines. The seismic hazard of fault displacements at five pipe-fault crossings defined in Section 4.2.1 is calculated by using the theory described in the section 4.3.1.1.1.

Firstly, characteristic magnitudes for fault segments are calculated from their full rupture lengths (RLD) using Eq. (4.8) from Wells and Coppersmith (1994).

$$M = 4.33 + 1.49 \log_{10}(\text{RLD}) \quad (\sigma = 0.24) \quad (4.8)$$

Pure characteristic model is assumed to be valid for the fault segments and the magnitude range is taken from  $M - \sigma$  to  $M + \sigma$ . The magnitude ranges for the five fault segments are given in Table 4.5. Rupture area (RA) is estimated from the computed magnitudes using Eq. (4.9) from Wells and Coppersmith (1994).

$$\log_{10}(\text{RA}) = -3.42 + 0.9M \quad (4.9)$$

With pure characteristic model, the activity rate is calculated by using the following expression (McGuire, 2004)

$$v_{m_{\min}} = \mu A s \dot{\gamma} \frac{m_{\max} - m_{\min}}{M_{o,\max} - M_{o,\min}} \quad (4.10)$$

$A$  is the ruptured area of fault segment;  $M_{o,\max}$  and  $M_{o,\min}$  are maximum and minimum seismic moments of maximum magnitude ( $m_{\max}$ ) and minimum magnitude ( $m_{\min}$ ), respectively.  $\dot{\gamma}$  is the annual slip rate,  $\gamma = \ln 10$ , where  $c = 1.5$ . The computed activity rates and other seismic information for the investigated fault segments are listed in Table 4.5.

**Table 4.5 Seismic features of the fault segments crossing BTC pipeline**

Pipe-fault crossing Segment	Name	Estimated magnitude $M_w$ (Eq. 8)	Estimated Area ( $\text{km}^2$ ) (Eq. 9)	Characteristic magnitude range	Slip rate (mm/yr)	Activity rate (eqk/year) (Eq. 10)
#1	Erzurum East Fault	6.75	452	6.5-7.0	10	0.0080
#2	Erzurum West Fault	6.7	407	6.5-7.0	10	0.0072
#3	North Anatolian Fault	6.85	556	6.6-7.1	20	0.0140
#4	Deliler Fault Zone	7.27	1327	7.0-7.5	10	0.0042
#5	Cokak Fault Zone	6.4	219	6.15-6.65	10	0.013

The theory described in Section 4.3.1.1.1 is then applied to assess the fault displacement hazard at five different pipe-fault crossings, using the information provided in Table 4.1 and 4.5. The hazard result is shown in Fig. 4.10. The uncertainty of pipe locations on the fault is considered in this project, by assuming the standard deviation of  $l/L$  (described in Fig. 4.7) to

be 0.1. Bilinear fault displacement prediction model in the Petersen et al. (2011) is implemented for the hazard assessment. The hazard results of fault displacements at five pipe-fault crossing locations are given in Fig. 4.10. The permanent fault displacement hazards at the North Anatolian fault and Deliler fault segments are higher than the others because the pipe-fault crossings in these two fault zones are located close to the mid portions of fault segments ( $l/L = \sim 0.5$ ). This fault-pipe crossing location results in higher fault displacements with respect to at the edge of the fault in the bilinear fault displacement prediction model.

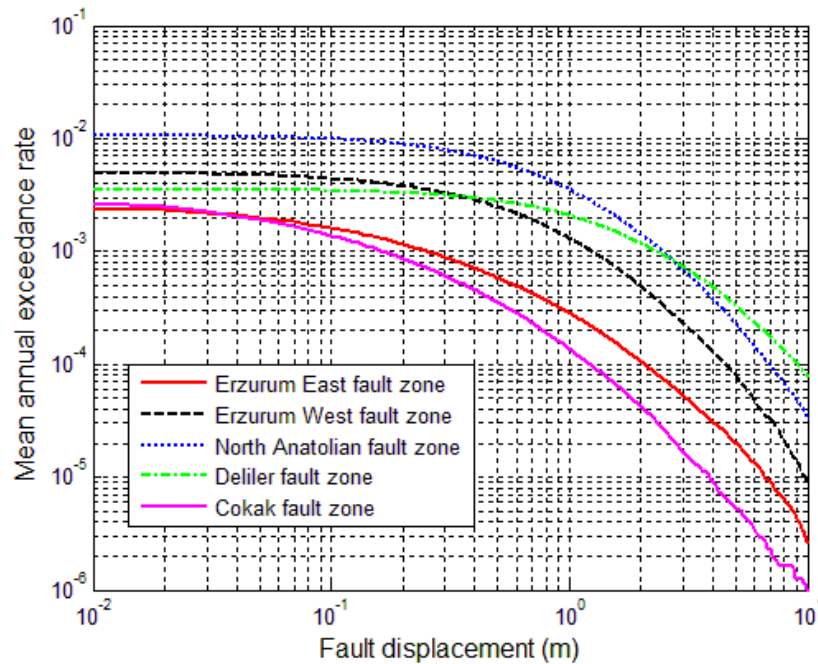


**Fig. 4.10 Seismic hazard curves of fault displacement at the pipe-fault crossings**

According to ALA (2005) guideline, the design level hazard for fault offset is calculated for three classes of pipelines by using the following relationship (Wells and Coppersmith, 1994).

$$\log(AD) = -6.32 + 0.9M \quad (4.11)$$

The transmission continuous gas pipeline of this project is classified as IV for which the design permanent fault displacement is 2.3 times the 475-year AD (average horizontal fault displacement) that is computed from Eq. (4.11). The resulting AD is assumed to represent the hazard level having 2475-year return period (ALA, 2005). The comparisons of design level permanent fault displacements from ALA (2001, 2005) guidelines and those computed from the hazard curves of Fig. 4.10 are listed in Table 4.6. It is observed that the permanent fault displacements of 2475-year return period calculated from this study are larger than the ALA design displacement requirement for pipe-fault crossing # 2, # 3 and # 4 but are less for pipe crossings # 1 and # 5. Therefore the pipes at pipe-fault crossing # 1, # 5 are in compliance with the design hazard level but # 2, # 3 and # 4 do not comply with the design level requirement.

**Table 4.6 Checkout of the design level of hazard**

	Pipe-fault crossings				
	#1	#2	#3	#4	#5
<b>475-year fault displacement in ALA</b>	0.57	<b>0.51</b>	<b>0.70</b>	<b>1.67</b>	0.28
<b>475-year fault displacement in this study</b>	0.04	<b>0.62</b>	<b>1.54</b>	<b>0.98</b>	0.04
<b>2475-year fault displacement (ALA <math>I_{Design}</math>)</b>	1.31	<b>1.18</b>	<b>1.61</b>	<b>3.84</b>	0.63
<b>2475-year fault displacement in this study (<math>I_{Assessment}</math>)</b>	0.73	<b>2.25</b>	<b>3.91</b>	<b>4.49</b>	0.44
<b>Compliance (<math>I_{Design} \geq I_{Assessment}</math>)</b>	Yes	<b>No</b>	<b>No</b>	<b>No</b>	Yes

#### 4.3.1.2 Design-based assessment

The designed-based assessment is performed by comparing the tensile strain under the design fault displacement with the allowable tensile pipeline strain which is determined as 3% according the guidelines. The pipeline strain is estimated from the analytical method of Karamitros et al. (2007), which is also used in the risk-based assessment of pipeline. The calculated pipeline tensile strains at the designated pipe-fault crossings under their design fault displacements as well as their comparisons with the allowable strain are given in Table 4.7. It is observed in Table 4.7 that in the stress test all the pipes crossing faults in compliance with the code.

**Table 4.7 Checkout of the design-based assessment**

Pipe-fault crossing number	Pipe-fault crossing Angle (degree)	Designed fault offset (m)	Tensile strain	Compliance ( $\leq 3\%$ )
#1	60	0.73	0.33%	Yes
#2	70	2.25	0.85%	Yes
#3	30	3.91	2.18%	Yes
#4	45	4.49	2.00%	Yes
#5	90	0.44	0.18%	Yes

#### 4.3.1.3 Risk-based assessment

##### 4.3.1.3.1 Theory: Probabilistic seismic risk assessment of pipelines due to PFD

The pipeline seismic risk against faults rupturing at the surface is represented by the annual exceedance rate of pipeline failure. This is achieved by integrating the probabilistic fault displacement hazard, mechanical response of pipe due to fault displacement and empirical pipe fragility function. The concept is similar to the conventional probabilistic seismic risk assessment (McGuire, 2004). Since both tensile and compressive strains developed along the pipe during an earthquake can cause pipe's failure, the seismic risk of pipe failure should consider the aggregated effects of these two strain components. The formula to calculate the seismic risk are given in Eq. (4.12) and (4.13). Note that the indices  $i$  and  $j$  in the discrete form of Eq. (4.12) stand for discretized fault displacements and pipe-fault crossing angles ( $\alpha$ ) ranging from 1 to  $n$  and 1 to  $m$ , respectively.

$$\begin{aligned}\lambda_{\text{failure}} &= \int_D \int_{\alpha} P(F|\varepsilon_t \& \varepsilon_c(d, \alpha, \theta)) f_D(d) f_A(\alpha) d(d) d(\alpha) \\ &= \sum_{i=1}^n \sum_{j=1}^m P\left(F|\varepsilon_{t_{ij}} \& \varepsilon_{c_{ij}}(d_i, \alpha_j, \theta)\right) \Delta(v_{d_i}) P(\alpha_j)\end{aligned}\quad (4.12)$$

$$\begin{aligned}P(F|\varepsilon_t \& \varepsilon_c(d, \alpha, \theta)) &= 1 - \{1 - P(F_t|\varepsilon_t(d, \alpha, \theta))\} \cdot \{1 - P(F_c|\varepsilon_c(d, \alpha, \theta))\} \\ &= P(F_t|\varepsilon_t(d, \alpha, \theta)) + P(F_c|\varepsilon_c(d, \alpha, \theta)) - P(F_t|\varepsilon_t(d, \alpha, \theta)) \cdot P(F_c|\varepsilon_c(d, \alpha, \theta))\end{aligned}\quad (4.13)$$

In the above equations,  $\lambda_{\text{failure}}$  is total annual rate of pipeline failure at the fault crossing. The term  $P(F|\varepsilon_t \& \varepsilon_c(d, \alpha, \theta))$  represents the probability of pipeline failure due to tensile ( $\varepsilon_t$ ) and compressive ( $\varepsilon_c$ ) strains developed along the pipe at the fault crossing.  $P(F_t|\varepsilon_t(d, \alpha, \theta))$  and  $P(F_c|\varepsilon_c(d, \alpha, \theta))$  are the pipeline failure probabilities due to tensile strain ( $\varepsilon_t$ ) and compressive strain ( $\varepsilon_c$ ), respectively. The probability expressions in the risk integral represent pipe's fragility function for a certain level of pipe strain,  $\varepsilon$ , that varies with the fault displacement,  $d$ , and the fault-pipe crossing angle,  $\alpha$  (Fig. 4.8). The vector  $\theta$  in the fragility function describes the parameters (e.g. pipe buried depth, pipe diameter to thickness ratio and,  $D/t$ , etc.) that can affect pipe's seismic response. The probability distributions of fault displacement and fault-pipe crossing angle are represented by  $f_D(d)$  and  $f_A(\alpha)$ . The probability distribution of  $\alpha$  is characterized by truncated normal distribution. It maps the uncertainties in pipe-fault crossing angle due to fault rupture complexities and deficiencies in fault mapping (variations from  $\alpha$  to  $\alpha'$  as shown in Fig. 4.8). The fault displacement probability is the derivative of PFD hazard curve,  $\lambda_D(d)$  (i.e.,  $d \frac{\lambda(d)}{d(d)}$ ). It represents the mean annual number of events producing fault displacement exactly equal to a given displacement,  $d$ .

#### 4.3.1.3.2 Application in STREST

##### 4.3.1.3.2.1 Pipeline strain states

We use the analytical method in Karamitros et al. (2007) to calculate strains along the pipeline at the fault crossings. The steel type and pipe sizes for strain calculations are already presented in Table 4.2 and Table 4.3. The interaction between pipe and surrounding soil is modeled with bilinear elastoplastic springs following the guidelines of ALA (2001, 2005). The spring properties of the buried soil in this study are presented in Table 4.8. The maximum axial force ( $T_u$ ) surcharged on pipe is independent of depth for soft and stiff clays. However, it increases with depth if the pipeline is surrounded by dense sand. The lateral surcharge ( $Q_u$ ) on pipe increases with depth regardless of soil type. Table 4.8 also shows the assumed yield displacements for axial ( $0.5\Delta_{T_u}$ ) and lateral ( $0.5\Delta_{Q_u}$ ) springs used in pipeline modeling.

**Table 4.8 Soil spring properties calculated from**

Soil type	H (m)	$T_u$ (kN/m)	$0.5\Delta_{T_u}$ (mm)	$Q_u$ (kN/m)	$0.5\Delta_{Q_u}$ (mm)
Loos-to-median sand	1.5m	30	2.5	295	40.6



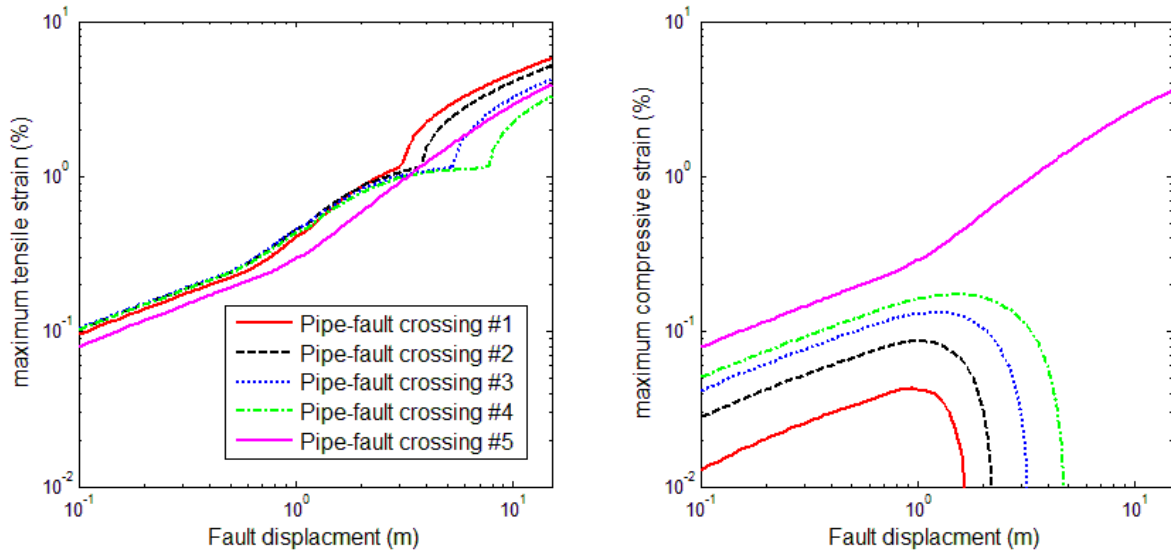


**Fig. 4.11 Maximum tensile (a) and compressive (b) pipe strains for the pipes at pipe-fault crossings with respect to different intersection angles**

Fig. 4.11 shows the change in tensile and compressive strains of pipeline with  $D/t = 52$  at the different fault crossings. The pipe-fault crossing angles  $\alpha$  are  $60^\circ$ ,  $70^\circ$ ,  $30^\circ$ ,  $45^\circ$  and  $90^\circ$  for pipe-fault crossing from #1 to #5, respectively (Table 4.1). Note that compressive strain reduces after it reaches to its maximum in all cases. This is because the strain state in pipe's compression zone changes and tensile strain starts to govern for larger PFDs after maximum compressive strain is reached. The pipeline strains will be integrated with fault displacement hazard and the pipe failure fragility to obtain the annual probability of pipeline failure in the following section.

#### 4.3.1.3.2.2 Pipe failure fragility

The continuous pipeline fragilities developed in this paper relate failure probability to different levels of tensile and compressive strains (i.e.,  $P[\text{failure}|\varepsilon(d, \alpha, \theta)]$ ). Assuming lognormal distribution, the failure fragilities are fitted over the empirical data discussed in the subsequent paragraphs. We adopted minimization of the sum of squared errors method (Baker, 2015) for fitting fragility functions. They are not specific to BTC pipeline as such data lack to develop fragilities specific to the case study of interest.

The tensile strains of 3% and 10% that correspond to 10% and 90% failure probability (Wijewickreme et al., 2005) are used while deriving the fragility for tension failure. These deformation rates and corresponding failure probabilities are meaningful for steel pipelines with good-quality girth welds. The left tail (lower end) of lognormal tension fragility is constrained to yield no-failure at 1% tensile strain. The resulting fragility function is given in Fig. 4.12a.

The development of pipeline fragility for compressive stains is more complicated because failure probability due to compression is a function of  $D/t$  ratio. Wijewickreme et al. (2005) assume that compressive strains corresponding to 10% and 90% failure probability are equal to  $0.4/(D/t)$  and  $2.4/(D/t)$ , respectively. The theoretical commencement of local wrinkling (1.25% compressive strain) is in between  $0.4/(D/t)$  and  $2.4/(D/t)$ . We used an additional constrain that assigns no-failure for compressive strains below  $0.13/(D/t)$  to control

the left tail of compression fragilities. The resulting fragility surface for pipeline failure due to compression is given in Fig. 4.12b for a set of  $D/t$  values. Table 4.9 lists the logarithmic means ( $\theta$ ) and standard deviations ( $B$ ) of fitted lognormal failure fragilities for tension and compression. The ones for compression failure are presented for four  $D/t$  values that are developed in this study. These values will be used to calculate the probabilistic pipeline seismic risk in the following subsection.

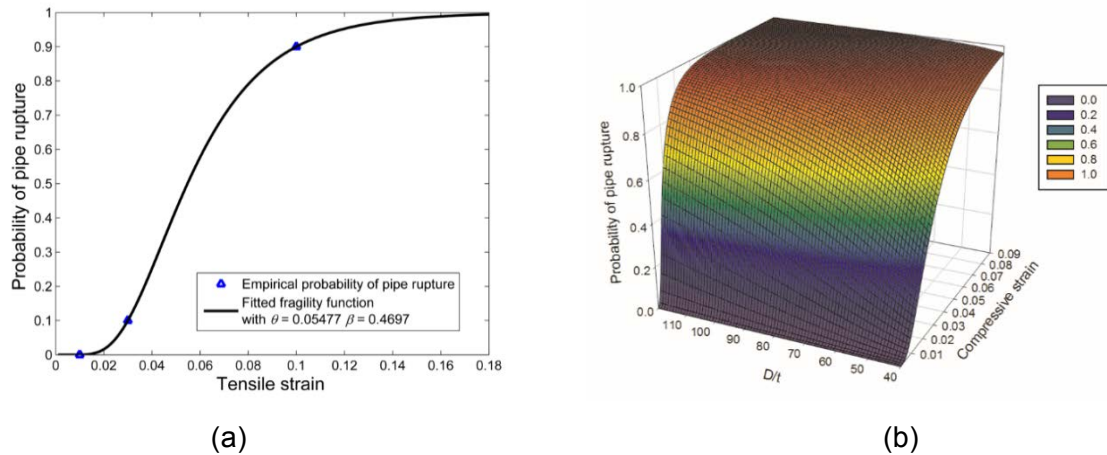


**Fig. 4.12 Pipeline fragility for (a) tension failure and (b) compression failure**

**Table 4.9 Logarithmic means and standard deviations of pipeline fragilities against tension and compression failures**

Failure state	$D/t$	$\theta$	$\beta$
Tension	-	0.05477	0.4697
Compression	52	0.0188	0.6988

#### 4.3.1.3.2.3 Pipe failure risk

The significance of pipe-fault crossing angles on pipeline risk has been discussed in the STREST D4.2 (Kakderi et al., 2015). The annual failure probability ( $P_f$ ) for pipelines at fault crossings is computed for different  $\alpha$  associated with the uncertainty in  $\alpha$  to manifest the inherent complications during the fault rupture process. The inaccuracy in fault-pipe crossing angle is modeled by a truncated normal probability with alternative standard deviations of  $2.5^\circ$  and  $5^\circ$ . The  $D/t$  ratios ( $D/t = 52$ ) are the same for all pipes at fault crossings, shown in Table 4.2. The properties of the pipe cross-sections are provided in Table 4.3. The tensile and compressive strains are calculated from the Karamitros et al. (2007) analysis method. The risk of pipeline at pipe-fault crossings in terms of annual exceedance probability in the risk-based assessment is provided in Table 4.10 for pipelines at different fault crossings with certain and uncertain crossing angles.

There are few papers addressing the performance expectations for the reliability of steel oil and gas pipelines against extreme rare events. Honegger and Wijewickreme (2013) suggest an acceptable rate of pipeline failure from seismic loading not to be greater than  $1/24750$  ( $4.04E-5$ ). Thus, we consider the allowable annual probability of pipeline failure due to fault offset to be  $1/24750$  (i.e.  $4.04E-5$ ).

The comparisons of annual exceedance probabilities from risk-based assessment with the allowable annual probabilities are shown in Table 4.10 for the pipeline cross sections at the designated fault crossings for different levels of certainty in pipe-fault crossing angles. It is observed that the pipes at fault crossings #3 and #4 are not safe against pipeline failure rate. The fact that pipe-fault crossing angles being smaller in these two pipe-fault crossings, result in higher tensile strains that contribute to the higher failure rates.

**Table 4.10 Checkout of risk-based assessment with annual exceedance probability**

Pipe-fault crossing number	$\sigma$			Compliance ( $\leq 4.04 \text{ E-05}$ )
	0	2.5	5	
#1	3.142E-06	3.183E-06	3.304E-06	Yes
#2	1.833E-06	2.256E-06	3.293E-06	Yes
#3	<b>1.967E-04</b>	<b>1.964E-04</b>	<b>1.955E-04</b>	<b>No</b>
#4	<b>5.987E-05</b>	<b>5.981E-05</b>	<b>5.962E-05</b>	<b>No</b>
#5	1.973E-05	--	--	Yes

## 4.4 PHASE 3: DECISION PHASE

### 4.4.1 Risk objectives check and Risk mitigation strategies

As analyzed in the Section 4.3, the component assessment is performed for a series of pipes crossing the designated fault segments. The pipeline failure risk along the whole BTC route due to permanent fault displacement originates from the pipe failure risks at five pipe-fault crossings. Thus the aggregated seismic risk of BTC pipeline due to permanent fault offsets is determined from two alternative boundaries: assuming risks at the fault crossings are perfectly correlated and uncorrelated. The aggregated risk is defined as the annual exceedance probability of the pipeline failure ( $P_f$ ).

To obtain the first boundary (individual pipeline failures are perfectly correlated) probability of survival ( $P_{sc}$ ; unity minus probability of failure) is computed for each pipe-fault crossing. The survival probability computation is given in the below expression where  $k$  is the number of pipe-fault crossing ( $k = 5$  in this project).

$$P_{sc} = \min (P_{sc1}, P_{sc1}, \dots P_{sck})$$

Therefore, the aggregated failure risk probability of BTC route under the perfectly correlated pipeline failures due to permanent fault displacement is estimated as

$$P_{fc} = 1 - P_{sc}$$

To compute the alternative boundary (individual pipeline failures are statistically independent) the probability of survival ( $P_{si}$ ; unity minus probability of failure) is computed from the product of separate survival probabilities of each failure:

$$P_{si} = \prod_{j=1}^k P_{sik}$$

where  $k$  is the number of pipe-fault crossings ( $k = 5$  in this project).

Therefore, the aggregated failure risk probability of BTC route under statistically independent pipe failures due to permanent fault displacements is estimated as:

$$P_{fi} = 1 - P_{si}$$

Using the theory described above, the aggregated probabilities of BTC pipeline failure due to permanent fault displacement for perfectly correlated and statistically independent cases are calculated as given in Table 4.11.  $P_{fi}$  and  $P_{fc}$  are upper and lower bound probabilities, respectively.

**Table 4.11 Aggregated probability of BTC pipeline failure due to fault displacements at pipe-fault crossings**

Return period	$P_{fc}$ (perfectly correlated case)	$P_{fi}$ (statistically independent case)
1 year	1.968E-04	2.882E-04
2475 year	38.56%	51%

Table 4.11 indicates that the probability of BTC pipeline failure due to permanent fault displacements for 2475-year hazard are still very high, which changes from 40% to 50%. Therefore, according to the grading system given in Table 4.4, the pipeline risk in this project is falling in the Grade B: possibly unjustifiable risk. The retrofit is potentially needed for the pipes at pipe-fault intersection locations.

#### 4.4.2 Disaggregation/Sensitivity Analysis

It is observed from Table 4.10 that the probabilities of pipe failure at pipe fault crossings of #3 and #4 are higher than the other pipe-fault crossings. Therefore, the pipe cross sections at fault crossing intersections # 3 and #4 are the critical components to the aggregated risk of the BTC pipeline failure.

#### 4.4.3 Guidelines and critical events

Based on the identification of the critical components of the BTC pipeline failure risk due to permanent fault offsets, the pipes at pipe-fault intersections #3 and #4 are decided to be retrofitted, along with the pipe at the intersection # 5 for the consideration of the uncertainty of pipe-fault crossing angles (the compression of pipe results in higher damage when crossing angle is larger than 90). The effective retrofitting of the pipe cross-sections at these three pipe-fault crossings is to change the pipe-fault intersection angle. Therefore, in the risk mitigation strategies, we change the pipe-fault crossing angles of all these three pipe-fault intersections to  $\sim 80^\circ$ . The resulting aggregated risk probability of BTC pipeline failure due to fault displacement after the proposed risk mitigation strategies are shown in Table 4.12. It is observed that the effectiveness of reducing the failure risk of BTC pipeline are evident with respect to the case before the risk mitigation. Considering the partial correlations of the risk at each fault crossing, the probability of BTC pipeline failure due to fault offset is mostly less than 2% in 2475 years. According to the grading system given in Table 4.4, the BTC pipeline risk is falling in the Grade AA: negligible.

**Table 4.12 Aggregated probability of BTC pipeline failure due to fault displacements at pipe-fault crossings after the risk mitigation strategies**

<b>Return period</b>	<b><math>P_{fc}</math> (perfectly correlated case)</b>	<b><math>P_{fi}</math> (statistically independent case)</b>
1 year	3.142E-06	9.014E-06
2475 year	0.775%	2.206%

## **5 CI-B2 Gasunie national gas storage and distribution network, Holland**

### **5.1 INTRODUCTION**

The Groningen field is a large natural gas field located in the northern Netherlands, contributing to approximately half of the natural gas production in the Netherlands. On- and off-shore natural gas production and distribution is the key component of the national energy supply in the Netherlands. The gas distribution relies on a major gas pipeline infrastructure, with a total length of over 12,000 km of installed pipes in. The production from the Groningen field and other natural gas fields mostly located in the north east part of the country supply the Dutch economy and major export across Europe, via cross-border long distance gas pipelines (European Natural Gas Round-About).

Located in an area of very low tectonic seismicity, gas extraction in the region has led to an increase in seismicity since the early 1990s and in particular after 2003. Initially, this increase, including the 2006 earthquake near Westeremden with a magnitude  $M_L = 3.4$  was considered to be a statistical variation within the uncertainty range of the measurements. A renewed focus on the issue of seismicity induced by gas production in Groningen started in 2012 triggered by the earthquake near Huizinge (16<sup>th</sup> August 2012) with magnitude  $M_L=3.6$ . It was felt as more intense and with a longer duration than previous earthquakes in that area and significantly more building damage was reported as a result of this earthquake. It materialized into the realization that over the past few years seismicity in the Groningen area had increased beyond statistical variation. It was realized that the earthquakes could pose a potential safety risk (WINN\_TA-NAM, 2016).

The current chapter describes the application of the stress test methodology to part of the main gas distribution network of Gasunie Gas Transport Services (Gasunie-GTS). The case consists of a distributed and geographically extended infrastructure with potentially high economic and environmental impact.

### **5.2 PHASE 1: PRE-ASSESSMENT PHASE**

#### **5.2.1 Data collection**

For the use case a sub-network is selected located in the induced earthquake prone area, directly above the main gas field, see Fig. 5.1. The sub-network selected covers an area of approximately 3360 km<sup>2</sup>. It contains 4 MPa (40 bar) to 8 MPa (80 bar) main gas transmission pipes, with a total length in the order of 1000 km. Different pipe diameters are present within this sub-network ranging from 114 millimeters (4 in) to 1219 mm (48 in). Apart from 426 valve stations, it contains compressor stations, measure and regulations stations, reducing stations and a mixing station (11 in total). With respect to the end nodes of the sub-network: 15 feeding stations and 91 receiving stations are accounted for, the latter being sub-divided into approximately 40 industrial, 50 municipal and 1 export.

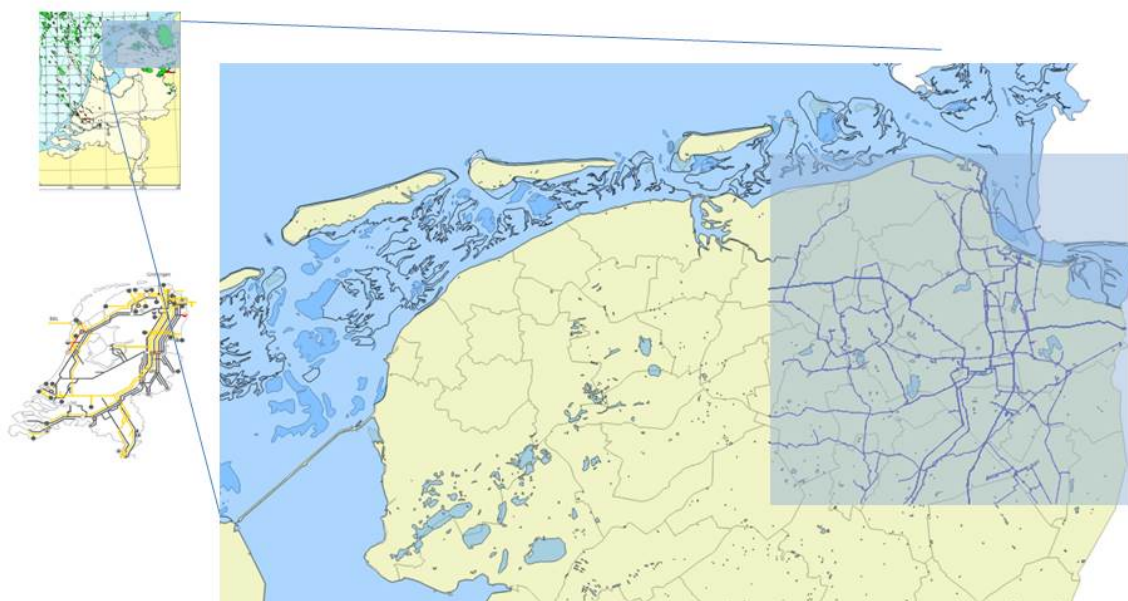


**Fig. 5.1 Selected sub system of the gas distribution network (right) located above main natural gas field (top left)**

GIS databases were obtained from Gasunie-GTS with properties of the pipeline system: coordinates, diameter, wall-thickness, material, yield stress, maximum operational pressure and depth of soil cover.

As the data base originally contained 6378 unique valued combinations of diameter, wall-thickness, yield stress and pressure, these properties were first classified into groups in order to reduce the number of unique sets. This resulted in 136 different pipe configurations composed out of the following values:

- 12 diameter values: from 114 to 1219 mm,
- 39 wall thicknesses: from 4 to 31.5 mm,
- 5 yield strength values: from 241 to 483 MPa, and
- 3 operational pressures: 40, 66 and 80 bar

The corresponding pipe sections in the network to which these properties are assigned are presented graphically in Fig. 5.2 to Fig. 5.5. Due to scaling, a significant number of pipe sections are not visible in these graphs as a number of pipes overlap in the scale used. This primarily concerns the main (high pressure) transport pipes in X and Y direction.

Soil cover depth is assessed as being a stochastic parameter with a mean of 1.5 m and a variation coefficient of 20%. The cover depth will play a role in modelling the maximum uplift displacements in those cases where the soil liquefies as a result of an earthquake.

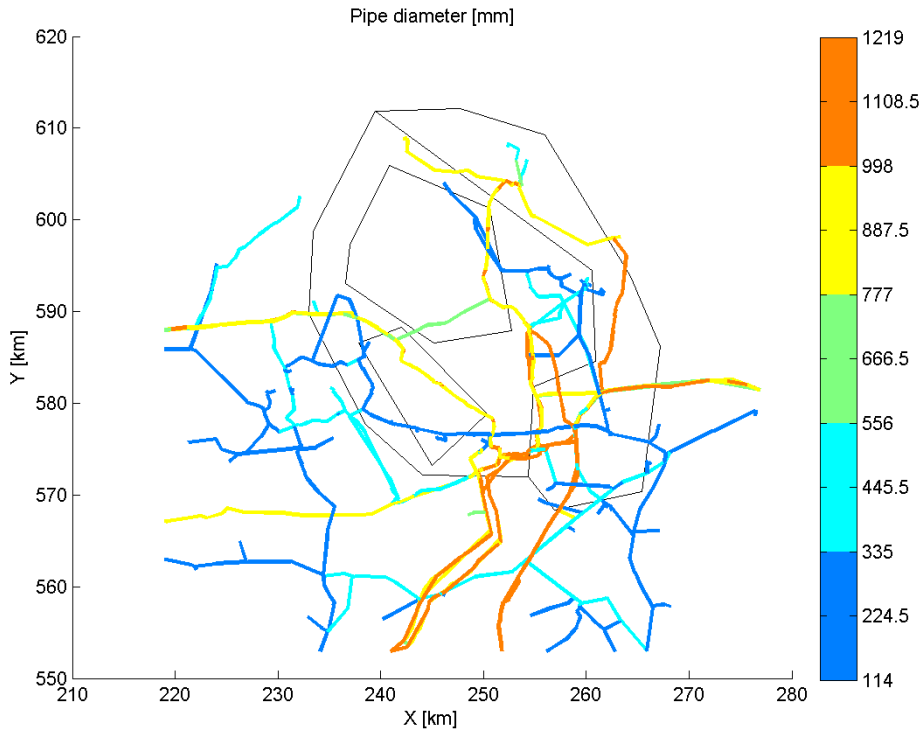


**Fig. 5.2 Presentation of diameters (mm) present in the modeled sub network (black lines on background indicate the earthquake zones)**

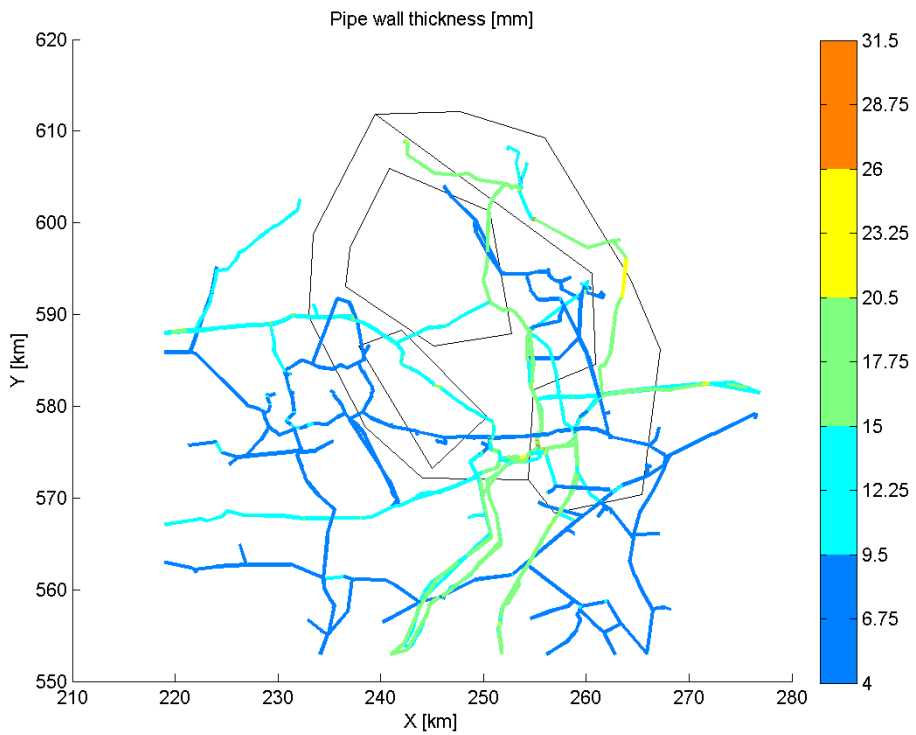


**Fig. 5.3 Presentation of pipe wall thickness (mm) present in the modeled sub network (black lines on background indicate the earthquake zones)**



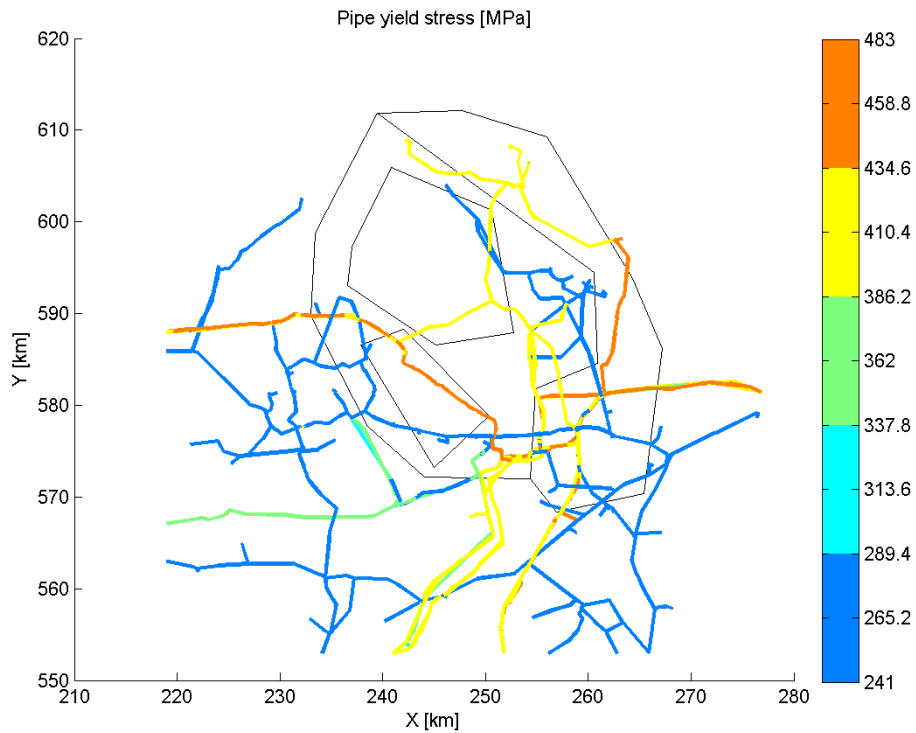


**Fig. 5.4** Presentation of pipe yield stresses (MPa) present in the modeled sub network (black lines on background indicate the earthquake zones)

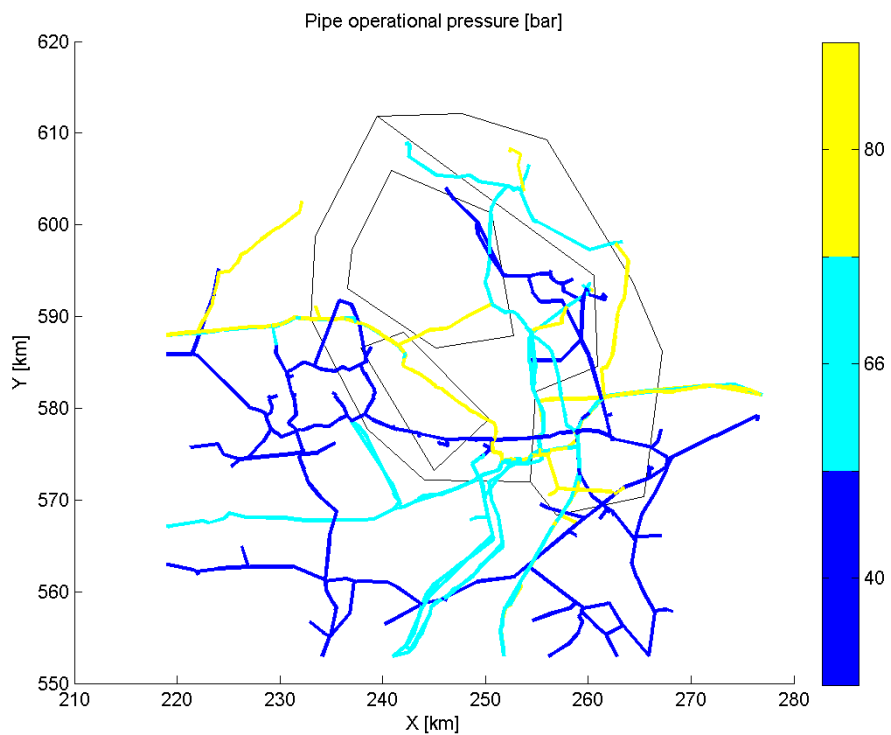


**Fig. 5.5** Presentation of pipe operational pressures (bar) present in the modeled sub network (black lines on background indicate the earthquake zones)

Fig. 5.6 shows the locations and types of stations that are included in the network modeled. Apart from source and demand stations as end nodes, in between nodes are shown and labeled as M&R (measure and regulation stations). Although labeled only as M&R, they in fact stand for either compressor stations, measure and regulations stations, reducing stations or a mixing station. Values next to these stations indicate the number of pipes that are connected to the site of the station.

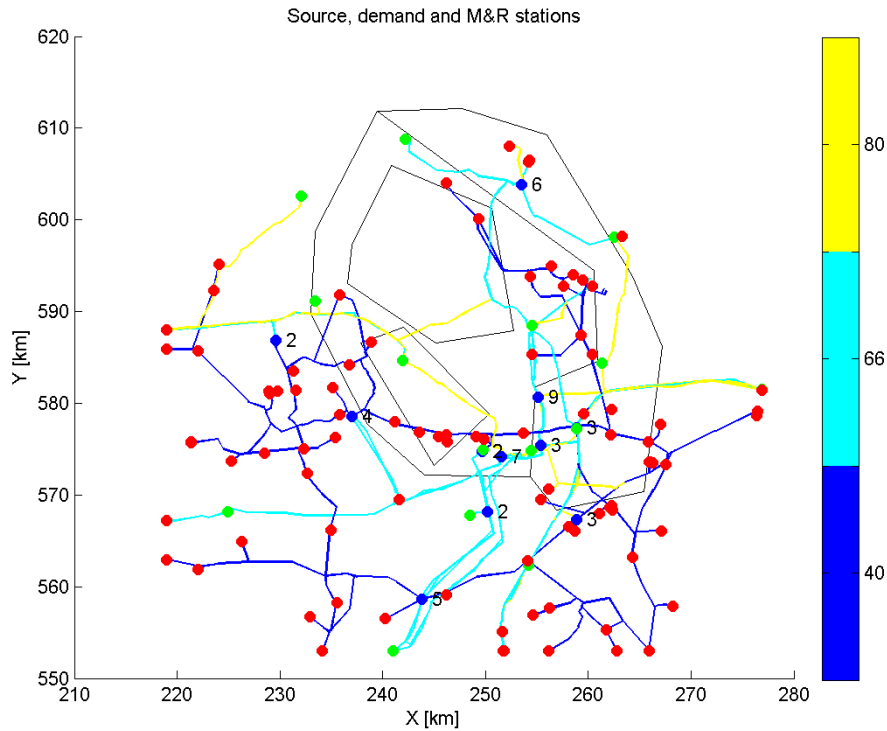


**Fig. 5.6 Locations of stations in the modeled sub network: source stations (green) demand stations (red) and M&R stations (blue). Pipeline colors and color bar refer to the pressures in the pipe sections**

The target hazard is the seismic hazard induced by the gas extraction from the Groningen gas field. Numerous studies have been performed over the past several years and are still ongoing leading to more and more refined models dedicated to the Groningen area (WINN\_TA-NAM, 2016). In the current stress test one of the earlier versions is being adopted. It is easier to model and bound to be conservative compared to the new ones, which in the context of using it in a stress test seems acceptable. The seismic model adopted consists of the following:

Seismic zonation: The seismic area of the Groningen gas field is divided into 4 zones. Within each zone the distributions of the events and their characteristics are assumed to be uniform. The zonation model is the so-called Z1 model from (Dost et al., 2013).

Ground motion prediction equation (GMPE): The (Akkar et al., 2014a) modified modified ground motion prediction equation (GMPE) is adopted, who used data of magnitude  $M > 4$  tectonic earthquakes from Europe and the Middle-East, and modified to include lower magnitude recorded events ( $M_L \leq 3.6$ ) in Groningen (Bommer, 2013).

Magnitude distribution: The Gutenberg-Richter (GR) relation is used to describe the statistical distribution of magnitudes. The relative frequency of stronger events with respect to smaller ones is described by the  $b$ -value, being the slope of the curve relating the logarithm of the cumulative annual frequency of events to magnitude. In addition the activity rate parameter  $a$  can be set.

Maximum magnitude: For Groningen statistical and geo-mechanical studies have been carried out, but this did not yet lead to a satisfactory estimate of  $M_{\max}$ . In most studies  $M_{\max}$  for Groningen is not larger than 5.0 based on literature studies of gas fields around the world (Dost et al., 2013). Bourne et al. (2014) argue that if all strain accumulated over the life cycle of the field was released in one event at the end of production, a physical upper bound for  $M_{\max}$  is obtained of 6.5 for the Groningen area. Arguments based on a finite fault size provide an estimate of  $M_{\max}=5.8$  as a maximum value, although the corresponding fault sizes are expected to be unrealistic for the Groningen area. Nevertheless, in the context of performing a stress test currently a value of  $M_{\max}=6.0$  will be applied in the analysis. Disaggregation of the results will allow for assessing the risk contribution of events with  $M_w \leq 5$ .

Annual event rate: The annual event rate for events with  $M \geq 1.5$  is set to 30 events per year (Dost et al., 2013), although new studies including the effect of reservoir compaction models and the reduced gas production rates tend towards values of 23 events per year (WINN\_TANAM, 2016).

The zonation and corresponding values for the magnitude and frequency distributions are shown in Fig. 5.7 and Table 5.1.

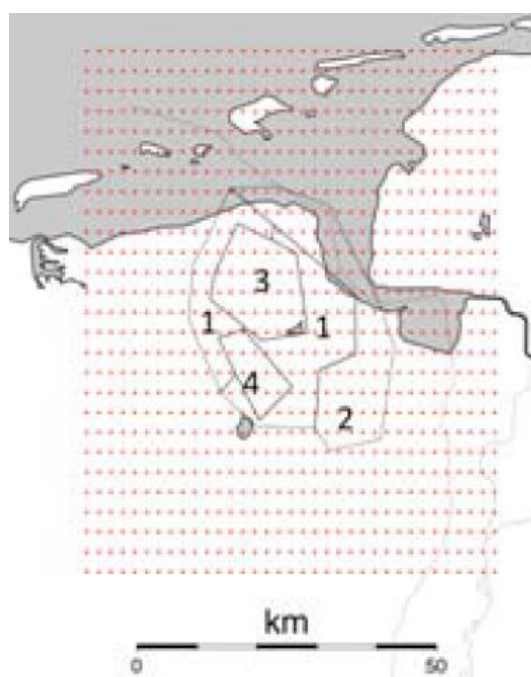


**Fig. 5.7 Division of Groningen area in seismic zones (Dost et al., 2013)**

**Table 5.1 Gutenberg-Richter parameters (Dost et al., 2013)**

Zone Number	Description	a	b	$M_{\min}-M_{\max}$
1	Background	0.364	1	1.5-6
2	Eastern block	0.017	1	1.5-6
3	Central North	0.498	0.8	1.5-6
4	Central South	0.121	1	1.5-6

### 5.2.2 Risk Measures and Objectives

Two risk measures (decision criteria or performance parameters) are used in the Gasunie Case, as described in Esposito (2011) and referenced therein:

- Serviceability Ratio (*SR*)
- Connectivity Loss (*CL*)

The Serviceability Ratio (*SR*) is directly related to the number of demand nodes ( $n$ ) in the utility network, which remain accessible from at least one source node following an earthquake. It is computed according to Eq. 5.1:

$$SR = \frac{\sum_{i=1}^n w_i X_i}{\sum_{i=1}^n w_i} \quad (5.1)$$

In which  $X_i$  represents the functionality of facility (demand node)  $i$ , which is modelled as the outcome of a Bernoulli trial ( $X_i = 1$  if the facility is accessible from at least one supply facility or source node), and  $w_i$  is a weighting factor assigned to the demand node  $i$ .

Connectivity Loss (*CL*) measures the average reduction in the ability of endpoints to receive flow from sources counting the number of the sources connected to the  $i$ -th demand node in the original (undamaged) network ( $N_{source,orig}^i$ ) and then in the possible damaged network ( $N_{source,dam}^i$ ) after an earthquake event. It is expressed by the following equation:

$$CL = 1 - \left\langle \frac{N_{source,dam}^i}{N_{source,orig}^i} \right\rangle \quad (5.2)$$

where  $\langle \rangle$  denotes averaging over all demand nodes.

In the Netherlands a standard for quantified risk assessment (QRA) exists, known as “the colored books”. They were issued by the national “Committee for the Prevention of Disasters” (CPR) and describe the methods to be used for modelling and quantifying the risks associated with dangerous materials (CPR 18E, 1999). Installations, types and frequencies of loss of containment (LOC), calculation methods, risk acceptance criteria and even the computer program to use are prescribed.

Currently the computer program CAROLA (CAROLA, 2010) is used for these calculations in the Netherlands, which is based on PIPESAFE (Acton et al, 2002).

Two types of risk are assessed referring to zoning distances that should be observed for specific activities: Individual risk or Location specific Risk (LR) and Societal Risk (SR). The Locational Risk refers to the annual frequency of a hypothetical person being lethally

affected by the consequences of possible accidents during an activity with hazardous materials, e.g. a chemical plant or transport activities. No (limited) vulnerable objects or installations are allowed in areas where the LR value is more than  $10^{-6}/\text{yr}$ . Societal risk corresponds to the cumulative frequency that a minimum number of people will simultaneously be killed due to possible accidents during an activity with hazardous materials. For pipeline systems, results for SR are presented as a graph per km pipe in which the cumulative frequency (F) is plotted against the number of lethally injured people (N). A maximum allowed societal risk value does not exist; only a guidance value has been defined ( $FN^2=10^{-2}$ ). Fig. 5.8 presents an example of a societal risk (blue) curve and the guidance value (red).

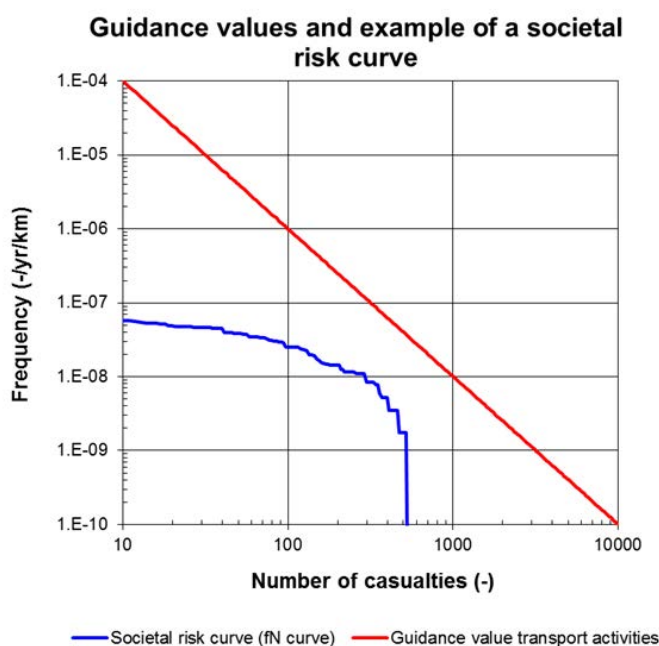


**Fig. 5.8 Example of societal risk curve and guidance value.**

In the current application of the stress test methodology to the Gasunie-GTS case, no full QRA was performed for the 1000 km sub-network. However, in order to define boundary values for the grading system of the ST@STREST methodology (Esposito et al., 2016), values for the annual failure rates are used for pipes and stations such that they relate to values used in standard QRA's.

In the purple book (CPR 18E, 1999) an annual failure frequency per km of  $6 \cdot 10^{-4}$  is prescribed. Taking 25% of these failures as rupture, this leads to an annual rate  $1.5 \cdot 10^{-4}$ . In (Gielisse et al., 2008) the failure rates were reassessed with refined models based on Gasunie data, see also (Laheij et al., 2010). This initially led to an average value of  $6 \cdot 10^{-5}$ . Using observed rupture data as well as an estimated beneficial impact of the statutory one-call system for all digging activities, resulted in a new average failure frequency of  $8 \cdot 10^{-6}$  per km per year. Based on this, the following grading boundaries are proposed for pipe sections:

- AA-A:  $8 \cdot 10^{-6}$  per km per year
- A-B:  $6 \cdot 10^{-5}$  per km per year
- B-C:  $1.4 \cdot 10^{-4}$  per km per year

Below these successive boundaries, grades AA, A and B are respectively assigned as outcome of the stress test. Above boundary B-C a grade C is obtained. The corresponding risk tolerances are: AA – negligible, A – as low as reasonably practicable (ALARP), B – possibly unjustifiable, C – intolerable. The CI passes the stress test if it is classified into grade AA or A. The CI partly passes the stress test if it receives grade B. Finally, the CI fails the stress test if it is given grade C.

For pumps (without additional provisions) the purple book prescribes a value of  $1 \cdot 10^{-4}$  for the annual (catastrophic) failure frequency. Given this value in relation to the purple book value for the pipe sections as well as the corresponding role they play in the QRA calculations an analogy with the pipe grading is proposed for the stations:

AA-A:  $8 \cdot 10^{-6}$  per year

A-B:  $6 \cdot 10^{-5}$  per year

B-C:  $1.4 \cdot 10^{-4}$  per year

Using these boundary values for the grading system enables the asset owner Gasunie-GST to relate the outcome of the stress test to his own QRA's as performed with CAROLA with non-earthquake related failure frequencies.

An as low as reasonable practicable (ALARP) grade of the risk measures is targeted for the existing gas transport network to pass the stress test (Jonkman et al., 2003).

For illustrative purposes only, indicative grading boundaries are attributed to the values of the performance parameter connectivity loss (*CL*). The boundaries used are taken from (Esposito and Stojadinović, 2016). No actual calibrations for these bounds with respect to economic loss or fatalities exist yet for the sub-network at hand and the grading is indicative and provisional. Fig. 5.9 shows the boundaries applied.

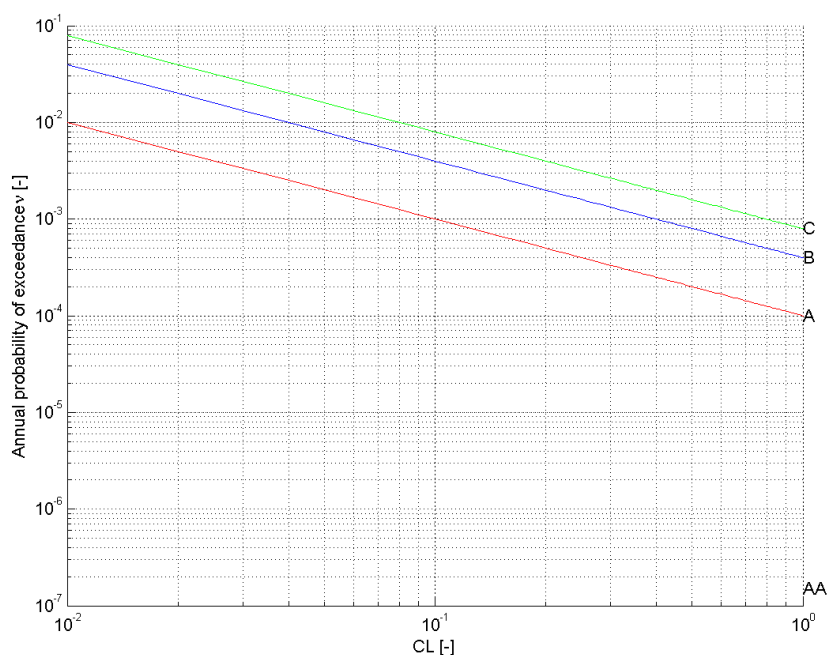


**Fig. 5.9 Indicative grading boundaries with respect to annual probabilities of exceedance for network connectivity loss *CL***

### 5.2.3 Set-up of the Stress Test

The Stress test as proposed in WP 5 (Esposito et al., 2016) is schematically shown in Fig. 5.10. In ST-L1 and ST-L2 only a single hazard is considered. In ST-L3 the effects of multiple hazards are analysed. In the Gasunie case only earthquakes (single hazard) are looked at, so the Stress Test has been performed up till level ST-L2. The actual level is ST-L2a as no epistemic uncertainty is explicitly taken into account.

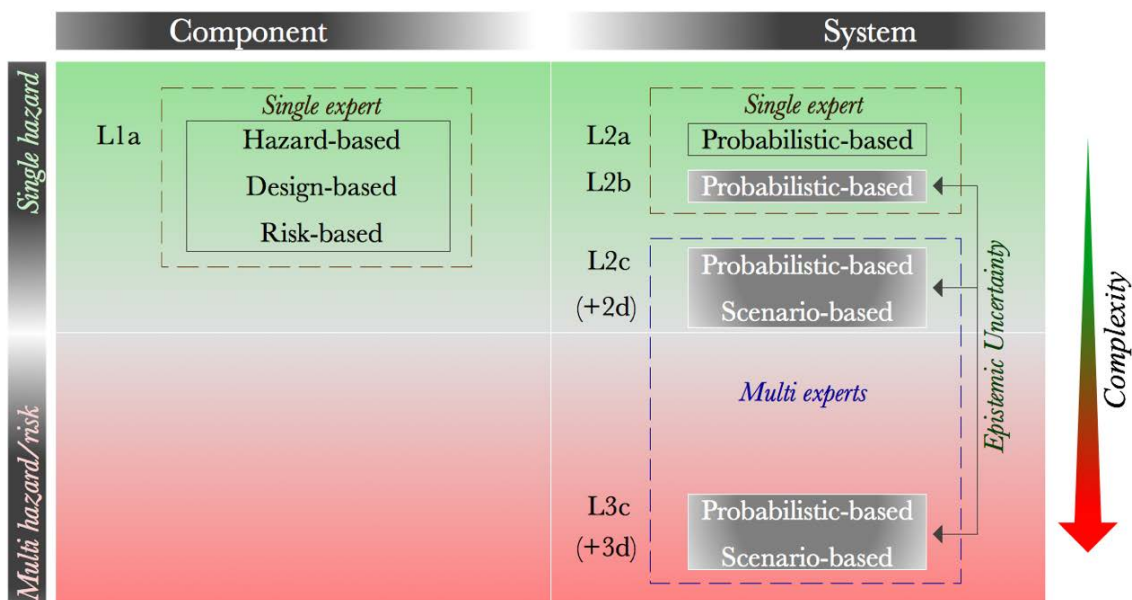


**Fig. 5.10 Schematic representation of Stress test method (Esposito et al., 2016; 2017)**

For Level ST-L2 a full Probabilistic Seismic Risk Analysis using Monte Carlo simulations is to be performed.

ST-L1 considers individual components. For the case at hand, where a probabilistic risk analysis will be performed for the network, the response of individual components will be derived from this network analysis. Hence a risk based approach is applied for individual stations and pipe segments in the network.

No scenario based assessments are performed at network level.

Accuracy levels targeted are classified as Advanced. Detailed information and advanced methods are being used in the stress test. The method adopted for the component level assessment is Risk-based while the System level is performed according to the performance-based earthquake engineering (PBEE) framework (Weatherill et al., 2014). Site specific hazard analyses are being performed and structure specific fragility functions being used.

Although the team performing the Stress test did not actively participate themselves in the on-going research into the man induced seismicity in the Groningen area, use is made of the outcomes of these studies by, among others, the NAM, KNMI, TNO and Deltares as well as by an international community of experts (WINN\_TA-NAM, 2016).

## 5.3 PHASE 2: ASSESSMENT PHASE

### 5.3.1 Component Level Assessment (ST-L1a)

The risk based assessment on component level implies the comparison of the fragility curves and the hazard curves. Fragility curves are specific per component and intensity measure, whereas hazard curves will be location dependent given the geographically extended nature of the network as well as the seismic sources.

Therefore, results from the system level assessment (section 5.3.2) which will be performed through a Monte Carlo simulation are used. Doing so, sampled values of local hazard and fragilities enable the assessment of the failure probabilities on component level.

For pipes, break/rupture is used as failure state. Station failure is selected as moderate damage (malfunctioning). Both failure states lead to network connectivity loss and a reduction of the serviceability ratio.

Fragility curves will be described in section 5.3.2. Seismic hazard was introduced in section 5.2.1 and will also be further commented upon in section 5.3.2.

With the annual event rate of 30 events per year, annual failure probabilities are deduced from the numerical samples..

For the pipe sections the resulting failure probabilities (per km) are presented as a contour plot in Fig. 5.11 whereas corresponding values for the stations are shown in Fig. 5.12.

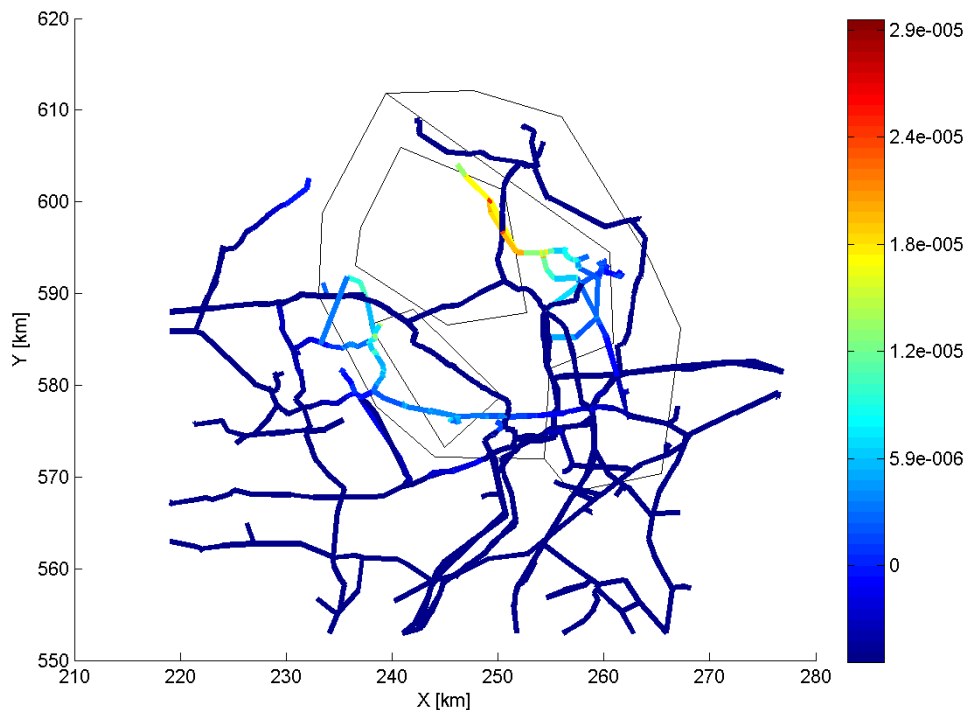


**Fig. 5.11 Annual failure probabilities (per km) for the pipe sections**



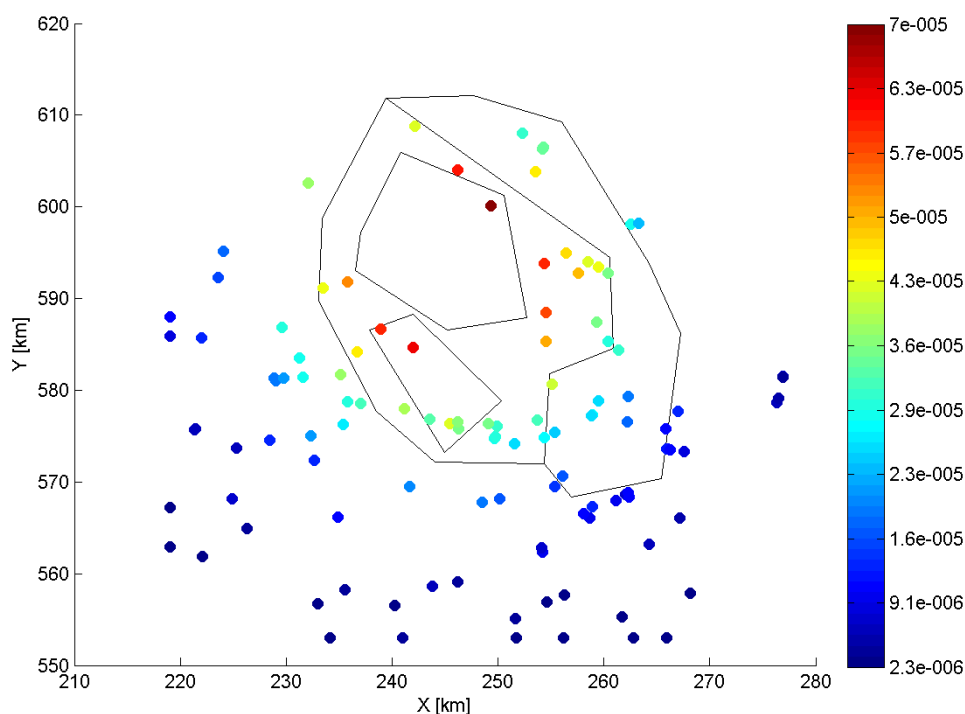


**Fig. 5.12 Annual failure probabilities for the stations**

### 5.3.2 System Level Assessment for Single Hazard (ST-L2a)

The methodology for the evaluation of seismic performance of the network under study consists of five major steps:

- Seismic hazard assessment of the region considering gas depletion as source of the seismic activities.
- Evaluation of the PGA, PGV and permanent deformation (liquefaction) hazard, in order to estimate the seismic demand.
- Seismic demand evaluation at each facility and the distributing elements (pipe segments) within the network to obtain the failure probability through the use of appropriate fragility curves.
- Systemic vulnerability analysis through the use of a connectivity algorithm to integrate the damage of facilities and distributing elements into the damage of the system.
- Probabilistic risk assessment of the case study using Monte Carlo simulation in terms of mean functionality and annual exceedance curve.

The OOFIMS software was used as a basis, kindly provided by the Sapienza - University of Rome, Dept. of Structural & Geotechnical Engineering (Franchin et al, 2011). A specific gas network class was added to the software making use of the available implementation for a water supply network. In addition, a dedicated implementation of the source models and zonings (see 5.2.1) and the GMPE model was added. The modified (Akkar et al., 2014a; 2014b; Bommer, 2013) GMPE describes ground motion values in PGA as well as PGV,

including a site amplification term based on  $V_{s30}$ . Intra and inter event aleatory uncertainties are provided. Between the PGA and PGV a correlation value of 0.8 is used. No spatial correlations are taken into account for the uncertainties.

For pipelines, fragility curves were estimated for the specific pipe sections and for transient as well as permanent deformations (soil liquefaction). For the stations use is made of general fragility curves found in literature. These are discussed first in section 5.3.2.1, after which the Probabilistic Risk Assessment is presented in section 5.3.2.2.

### 5.3.2.1 Fragility Functions

Fragility functions used in the analysis constructed based on:

- the probabilities of soil liquefaction as a function of PGA values
- the probability of pipe failure, given soil liquefaction occurred (permanent seismic load effects),
- the probability of pipe failure as a function of PGV values (transient seismic load effects), and
- the probability of station failure as a function of PGA values

#### The probabilities of soil liquefaction as a function of PGA values

The probability of soil liquefaction was investigated for soil conditions in the Groningen Area. The study is based on the Idriss-Boulanger model (Idriss et al., 2008) and is described in more detail in (Miraglia et al., 2015). Two soil profiles based on CPT tests were analysed by describing the soil properties as stochastic parameters and sampling the liquefaction response of the layers with earthquake events. Without any classification, the two soil profiles are referred to as Soil A and Soil B within this study. The sampling results eventually were summarized as a fragility curve for the soil in state 'liquefied' as a function of PGA values, see Fig. 5.13.

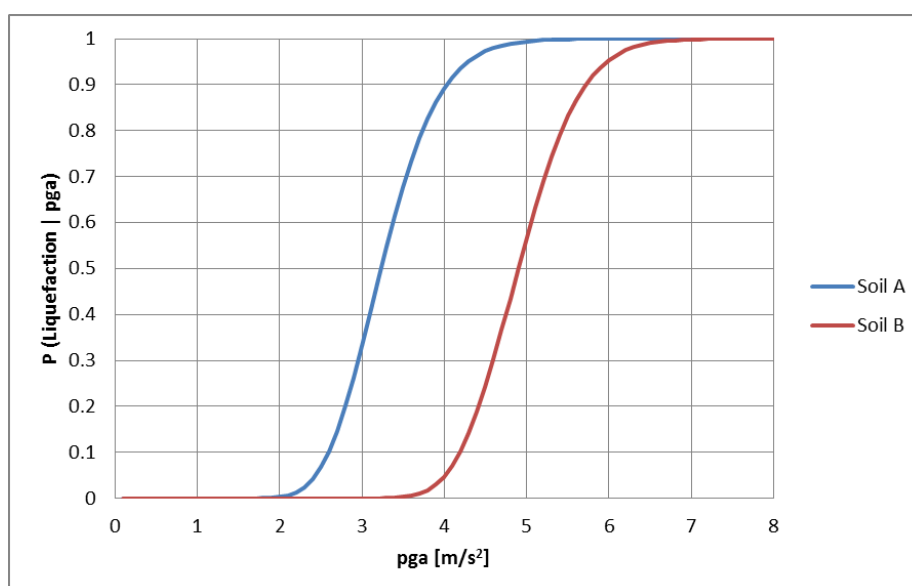


**Fig. 5.13 Soil liquefaction fragilities of two soil profiles in the Groningen area (Miraglia et al., 2015)**

As yet no detailed soil mapping will be used within the current stress test, the likelihood of a component within the network to be combined with either soil A or soil B will be set to 50% per event.

The probability of pipe failure, given soil liquefaction occurred (permanent seismic load effects)

Soil liquefaction can cause permanent displacements, expressing themselves in lateral displacements and or settlements. Besides that, depending on the weight of the pipe segments relative to the volumetric weight of the liquefied soil, pipe segments will start floating or sinking due to gravity. From these three aspects only the latter is considered: substantial lateral spread is not expected in the flat Groningen area, settlements are assumed to be confined to dozens of centimeters, whereas uplift due to buoyancy can reach the value of the soil cover depth. Structural reliability calculations for rupture/break are performed for each of the 136 pipe configurations (distinct sets of values for diameter, wall thickness, yield stress and gas pressure). In these calculations the pipe properties are treated as stochastic variables. The limit state function is formulated as the von Mises stress due to gas pressure as well as bending due to uplift against the yield stress. The bending stress due to uplift was calculated in a mechanical model in which the pipe is embedded in stiff soil at its endings and is allowed to uplift towards ground level. The length of the pipe in liquefied soil is adjusted during the limit state evaluations such that this maximum value (cover depth) is reached. Gas pressure is modelled as a normal distribution with a 10% coefficient of variation. Diameter, wall thickness and yield stress are lognormally distributed with variation coefficients of respectively 3, 3 and 7 %. Finally, also the soil cover depth is modelled stochastically: normal distributed with a mean value of 1.5 m and 20% coefficient of variation. FORM analyses were performed for each situation (pipe configuration) and reliability indices ( $\beta$ ) are calculated as a proxy for the probability of failure given liquefied soil.

The reliability indices obtained range from -4 to +9. A value of -4 leads to failure in case of liquefaction with almost certainty. A reliability index of 0 correlates with a 50% probability of failure, whereas a value 2 corresponds to approximately 2% failure probability. Small diameter pipelines show to be more vulnerable. Fig. 5.14 graphically depicts the distribution of the different values found for the different pipe sections.

Length effects of liquefaction related pipe failure will in the OOFIMS tool be taken into account by assuming a correlation length of 200 m along the pipe.

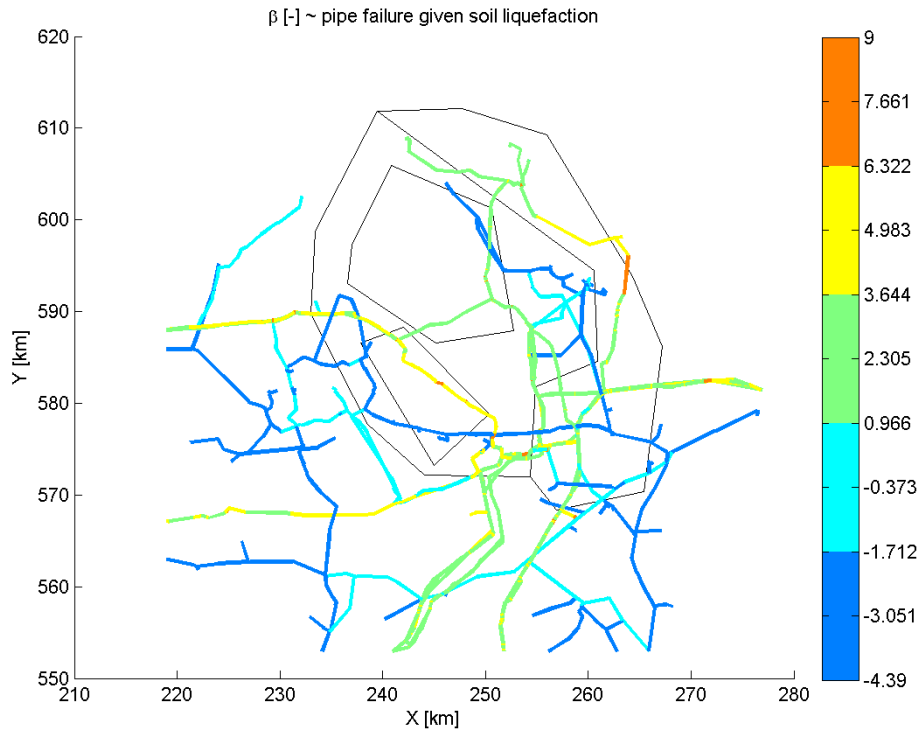


**Fig. 5.14 Distribution of reliability indices for failure due to soil liquefaction for different pipe sections**

The probability of pipe failure as a function of PGV values (transient seismic load effects)

Regarding transient load effects, structural reliability calculations for pipe rupture/break are performed for different pipe geometries with a limit state based on Newmark's shear wave formulae of seismic strain for buried pipelines. In addition stresses due to gas pressure and due to initial curvatures in the pipeline stretches are accounted for. The same stochastic parameters as above are used for diameter, wall thickness, pressure and yield stress are used. The curvature is modelled as a lognormal distribution with mean 2000 m and 100 m standard deviation. In addition the shear wave velocity  $V_{s30}$  is modelled as a lognormal stochastic variable having a mean of 200 m/s and a standard deviation 20 m/s.

Again, FORM analyses were performed for each pipe configuration with different values of seismic load PGV. Thus fragility curves are derived as shown in Fig. 5.15. In this figure also a fragility curve from Lanzano et al. (2013) is presented for reference.

The locations of the pipes with different fragilities are indicated in Fig. 5.16 by showing their PGV values that lead to a 50% probability of failure.

Length effects of transient loading related pipe failure is modelled by using the repair rate ( $RR$  in repairs per km) model according to ALA (2001):

$$RR = K_1 0.002461 pgv \quad (5.3)$$

The corrective factor  $K_1$  is introduced to account for different pipe materials and properties. In our case  $K_1$  values for welded steel are taken with  $K_1 = 0.15$  for pipe diameters larger than 400 mm and  $K_1 = 0.6$  otherwise (small pipes).

For a given section length  $L$ ,  $RR \cdot L$  is interpreted as the expected number of damaged points. This expected value is then used as defining the number of candidate points at which the dedicated fragility curves for pipe rupture are applied. For small pipe sections a minimum value of 1 point is used.

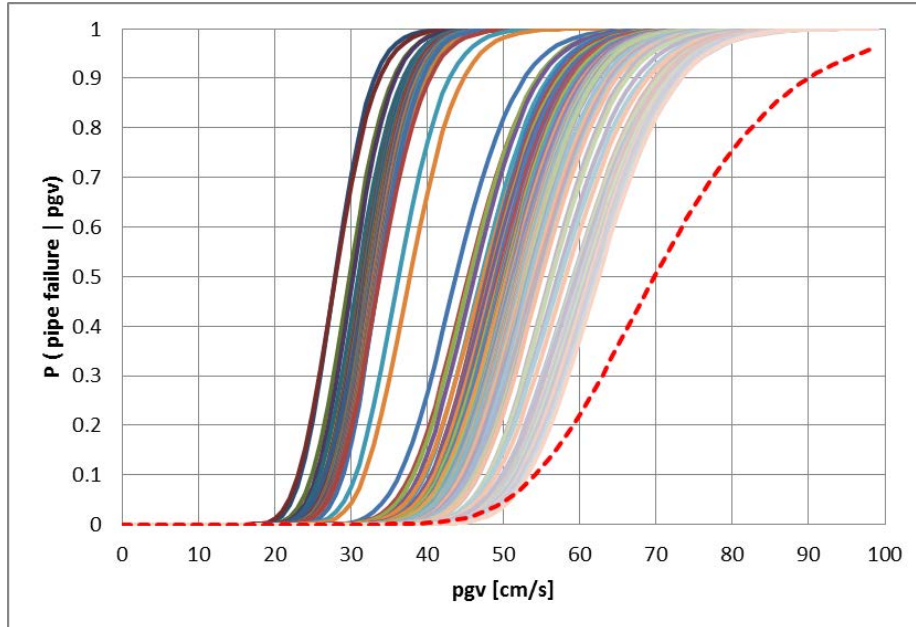


**Fig. 5.15** Calculated pipe fragilities with respect to transient seismic load effects. Different solid lines correspond to different pipe properties. The red dotted line is taken from (Lanzano et al., 2013)

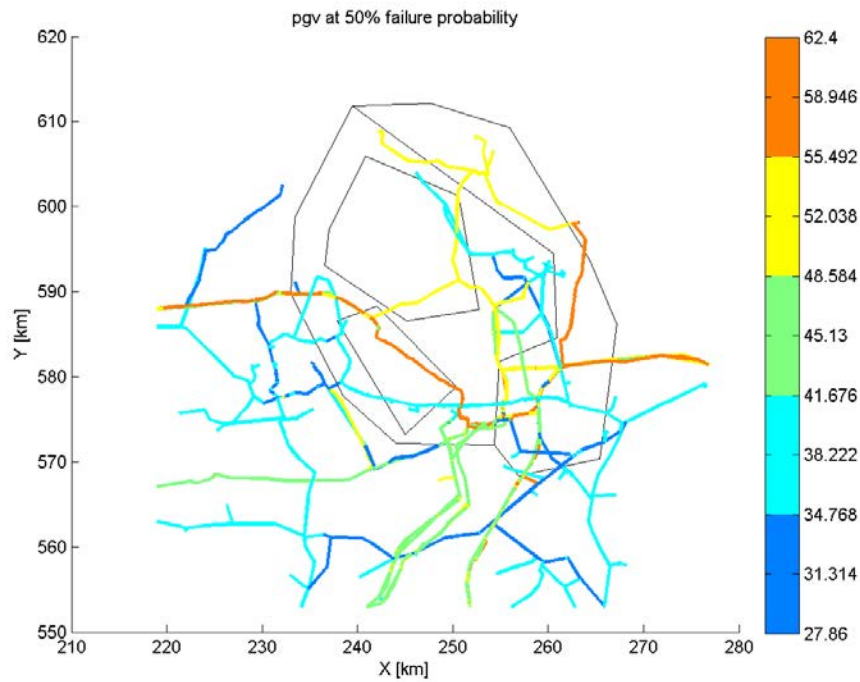


**Fig. 5.16** Locations of the pipe sections with different fragility curves (from Fig. 5.15). Shown are PGV values that lead to a 50% probability of failure

### The probability of station failure as a function of PGA values

For the stations existing fragility curves have been selected (NIBS, 2004). The one selected corresponds to a moderate damage state and is described as a lognormal cumulative distribution with a mean of  $2.4 \text{ m/s}^2$  and a coefficient of variation of 60%. The moderate damage state is selected as it is the first damage state with such malfunctioning that it leads to connectivity loss and a decrease in serviceability ratio. Besides this, the station types vary between compressor stations, measure and regulations stations, reducing stations or a mixing station. All with different mechanical or electrical components, some sheltered in one story masonry buildings and others in open air. Choosing the moderate damage state is partly motivated by selecting a conservative envelope for all types.

#### **5.3.2.2 Probabilistic Risk Assessment (ST-L2a)**

A total of 15.000 samples were realized and results in terms of pipe section failures, station failures, PGA and PGV values, magnitudes, and network performance indicators *CL* and *SR* were saved for post processing and analysis.

Network performance in terms of connectivity loss *CL* and serviceability ratio *SR* were defined as the primary indicators in the stress test.

Fig. 5.17 (top) shows the performance of the network in terms of the annual probability of exceedance for the connectivity loss *CL*. It is calculated as the empirical complementary cumulative distribution function for the *CL* values obtained. A connectivity loss of 1 indicates that no demand node has any connection to a source node anymore. Hence the trend in Fig. 5.17 of the exceedance frequency going to zero for *CL* reaching 1. The rate of this trend and the values for *CL* less than 1 define the quality of the network performance or robustness.

The results show a good performance with respect to this: the annual probability of having a connectivity loss of e.g. 50% or more is  $3.6 \cdot 10^{-5}$ .

The serviceability ratio *SR* is 'complementary' to the connectivity loss: a value of 1 means all demand nodes have at least 1 connection to one of the source nodes, whereas a value of zero means that no demand node can be supplied anymore by a source node.

Annual exceedance frequencies for the serviceability ratio are presented in Fig. 5.17 as well (bottom). Again, the exceedance frequencies are calculated as the empirical complementary cumulative distribution function of the values obtained. The figure shows very high exceedance frequencies for all values of the serviceability ratio, with only a drop at the very end of the horizontal axis near *SR* reaching one. Hence it shows a high robustness of the network, indicating a vast redundancy in possible paths between demand and source nodes.

In order to check the convergence of the calculations, the coefficient of variations for *CL* and *SR* are presented in Fig. 5.18. The figure shows steady values from 10.000 values onwards.

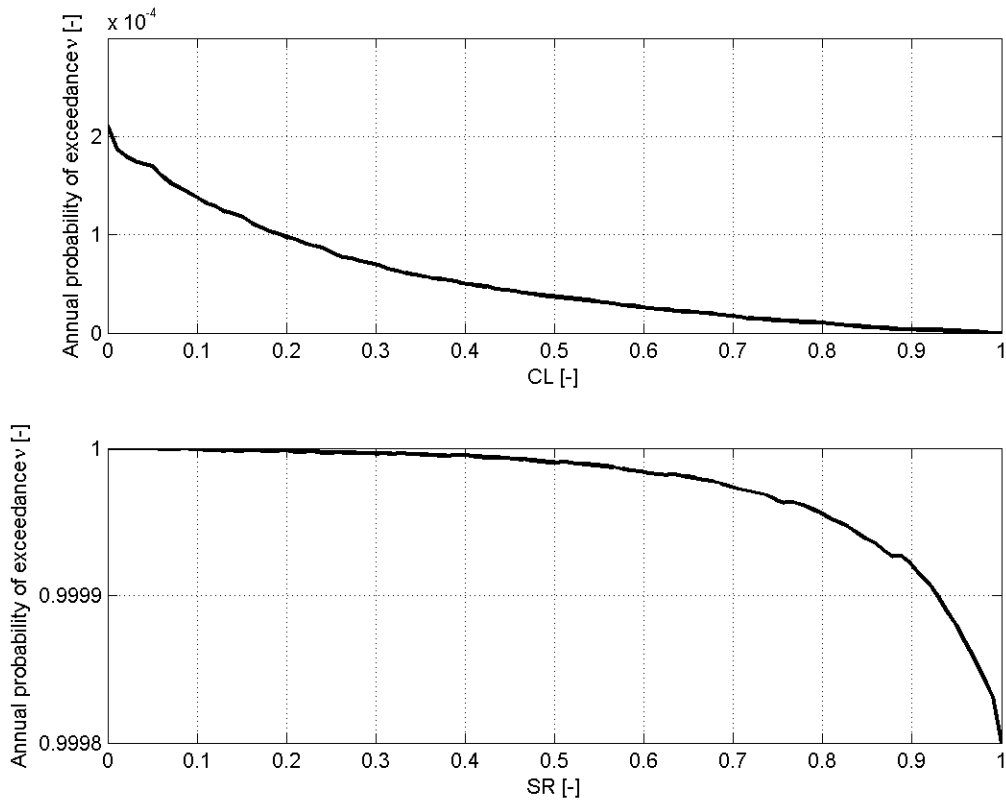


**Fig. 5.17 Annual probabilities of exceedance for network connectivity loss *CL* (top) and serviceability ratio *SR* (bottom)**

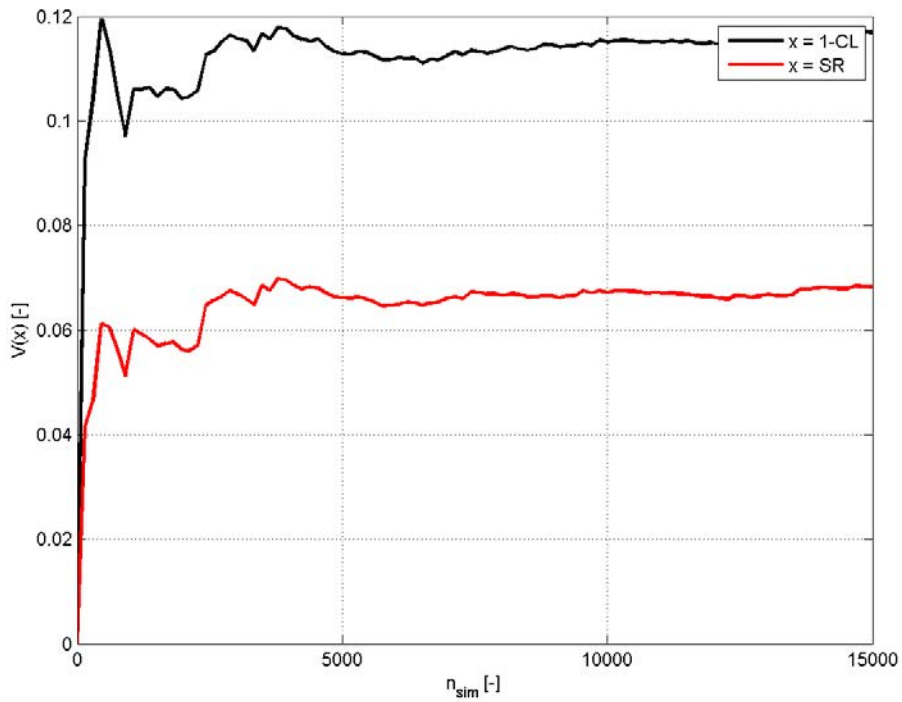


**Fig. 5.18 Convergence check in terms of coefficient of variation for (SR) and (1-CL)**

## **5.4 PHASE 3: DECISION PHASE**

### **5.4.1 Risk objectives check**

An as low as reasonable practicable (ALARP) grade of the risk was targeted for the gas transport network to pass the stress test.

With the component results from section 5.3.1 and the grading boundaries from section 5.2.2 the following results are obtained for the pipe sections and the stations:

- Pipe sections: Most pipe sections obtain grade AA, some obtain grade A. The pipe sections pass the stress test.
- Stations: Most stations are classified with grade AA or A. Some, near or within the seismic zone, obtain grade B. The stations partly pass the stress test.

The grading results are presented in Fig. 5.19 and Fig. 5.20.

Fig. 5.21 presents the values for the connectivity loss relative to the indicative grading boundaries. The network performance complies with grade AA and passes the stress test.

These findings are obtained despite a number of conservative assumptions made with respect to fragilities.

Also the seismic demand was modelled in a conservative way with a maximum magnitude of 6 and a b value of 0.8 for seismic zone 3 in the Gutenberg-Richter model. Design value corresponding to a 475 year return period and with events confined to those less than  $M=5$  leads to a value of  $6 \text{ m/s}^2$  with the current model, whereas (Dost et al., 2013) report a value of  $4.2 \text{ m/s}^2$ .



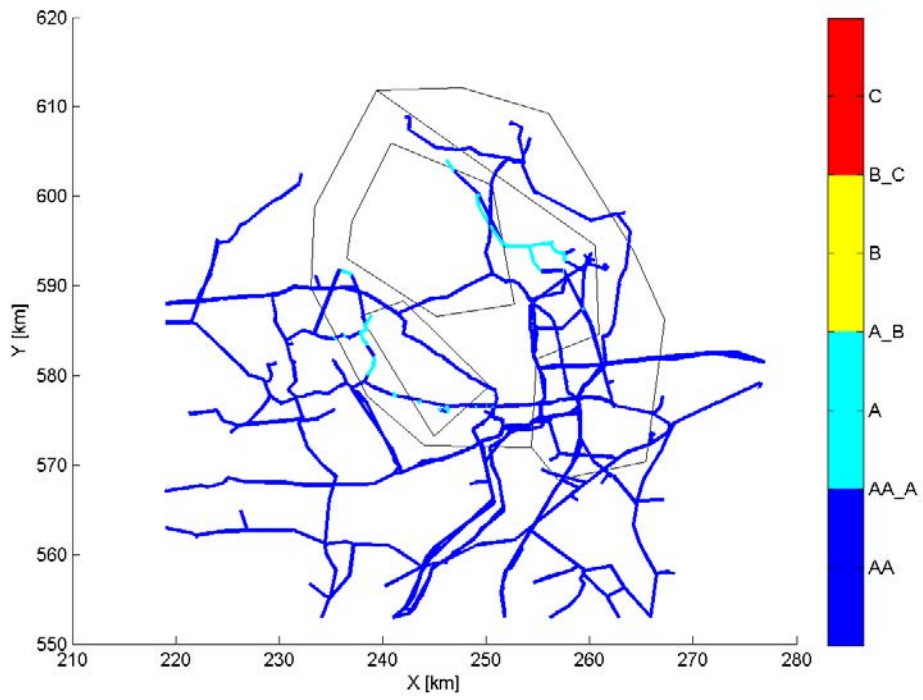


Fig. 5.19 Obtained grading for the individual pipelines (Mmax = 6; annual rate =30)

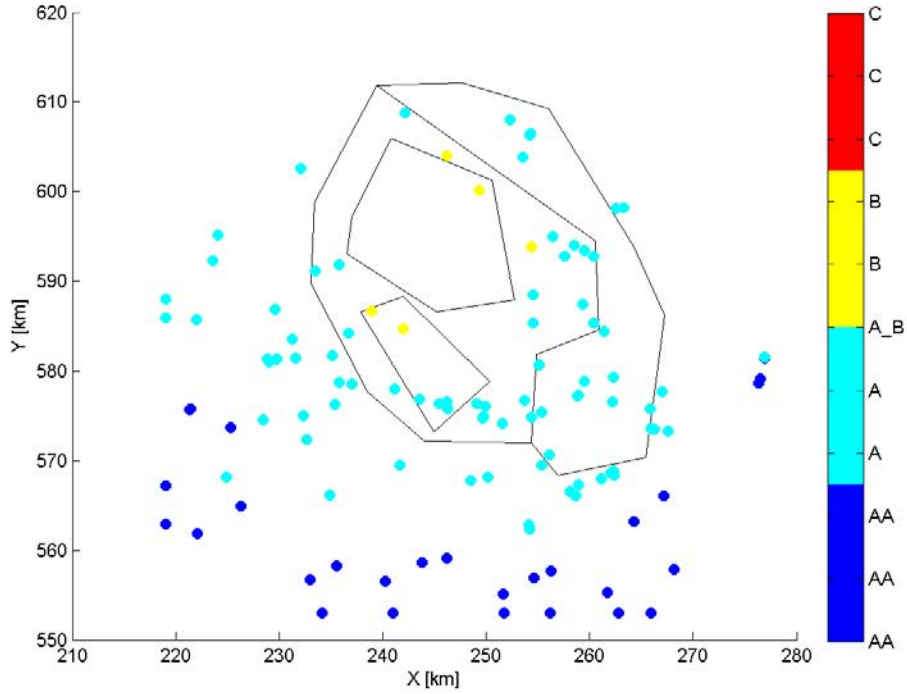
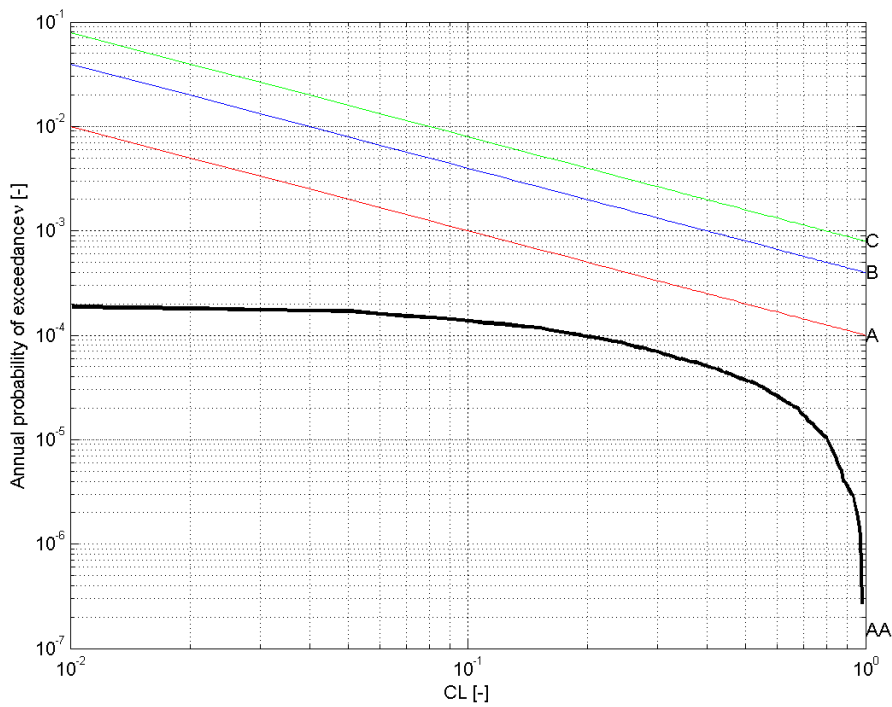


Fig. 5.20 Obtained grading for the individual stations (Mmax = 6; annual rate =30)



**Fig. 5.21 Exceedance frequencies for connectivity loss relative to (indicative) grading boundaries**

## 5.4.2 Disaggregation/Sensitivity Analysis

### 5.4.2.1 Seismic Events

Fig. 5.22 shows the disaggregation of seismic events with respect to magnitude contributing to three levels of CL ( $>0.1$ ,  $>0.5$  and  $>0.9$ ) and SR ( $<0.1$ ,  $<0.5$  and  $<0.9$ ). First network performance losses ( $CL > 0.1$ ) are found from  $M > 3.5$  onwards.

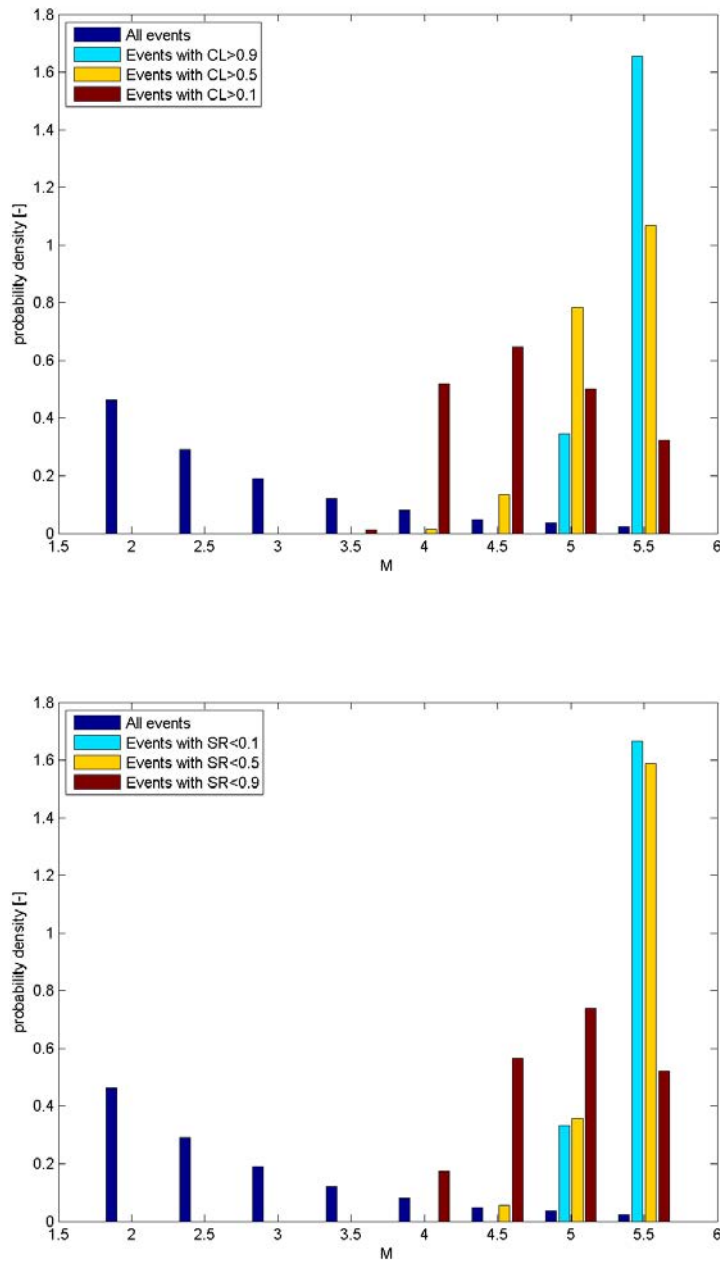
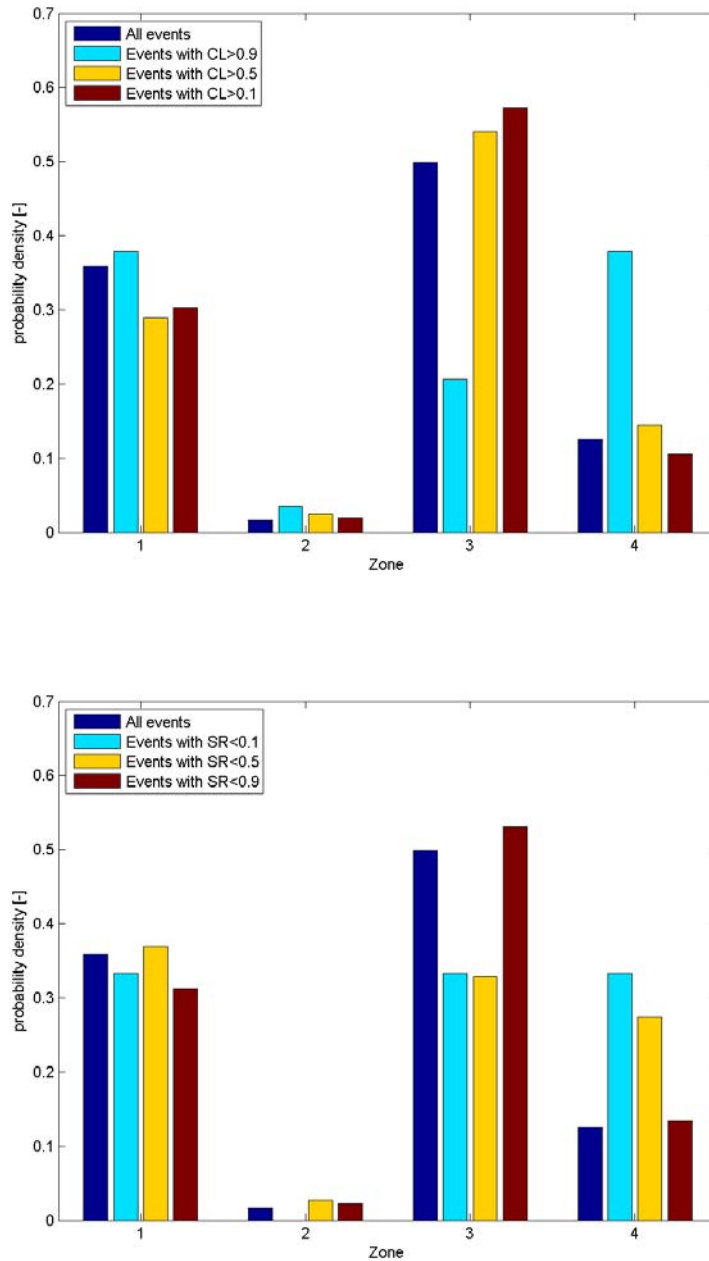


Fig. 5.22 Disaggregation of seismic events contributing to three levels of *CL* (top) and *SR* (bottom)

#### 5.4.2.2 Seismic Zones

Fig. 5.23 shows the disaggregation of seismic zones contributing to three levels of *CL* (>0.1, >0.5 and >0.9) and *SR* (<0.1, <0.5 and <0.9). For all events the values shown for the probabilities reflect the values from

Table 5.1. As such, zone 1 and zone 3 are also seen to contribute most to performance losses. A remarkable observation is that zone 4 will contribute significantly to extreme values of performance loss.



**Fig. 5.23 Disaggregation of seismic zones contributing to three levels of CL (top) and SR (bottom)**

### 5.4.2.3 Pipe components disaggregation

Different pipe geometries, material, pressures, fragility functions and locations lead to different impact on the network performance. In order to identify which pipe sections start first to contribute to performance loss, events with a low performance loss ( $CL \leq 0.1$ ) are selected. For these events the pipe sections are ordered according to the number of failures that occurred. The highest number of failures is then scaled to 1, and the resulting relative frequencies are plotted in Fig. 5.25. Pipe sections to the South-West and North-East of seismic zone 3 show themselves. The pipe section with the maximum number of failures showed 39 failures within the subset of events of approximately 14000. The maximum magnitude within the subset was 4.9.

The same is done for  $CL < 0.5$  as shown Fig. 5.25. The area with failed pipe sections shows to expand to the South and to the East. The maximum number of failures for 1 pipe section now is 1490 within a subset of 14700 samples, containing a maximum event of magnitude 6.

### 5.4.2.4 Station disaggregation

As all stations are modelled with the same fragility functions the only discriminate factor in selecting the most vulnerable ones would be their distance with respect to possible seismic sources and the corresponding attenuation of the seismic load. This information can be obtained from Fig. 5.12. Combined with the number of pipe connections at the corresponding interconnecting stations as shown in Fig. 5.6 their possible contribution to the network performance loss can be identified.

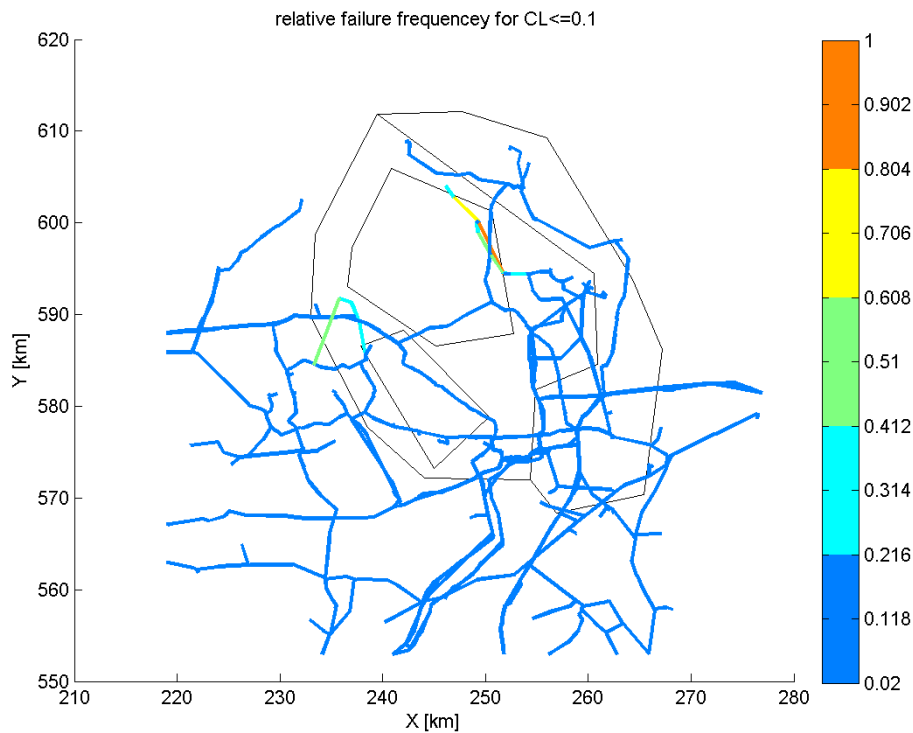
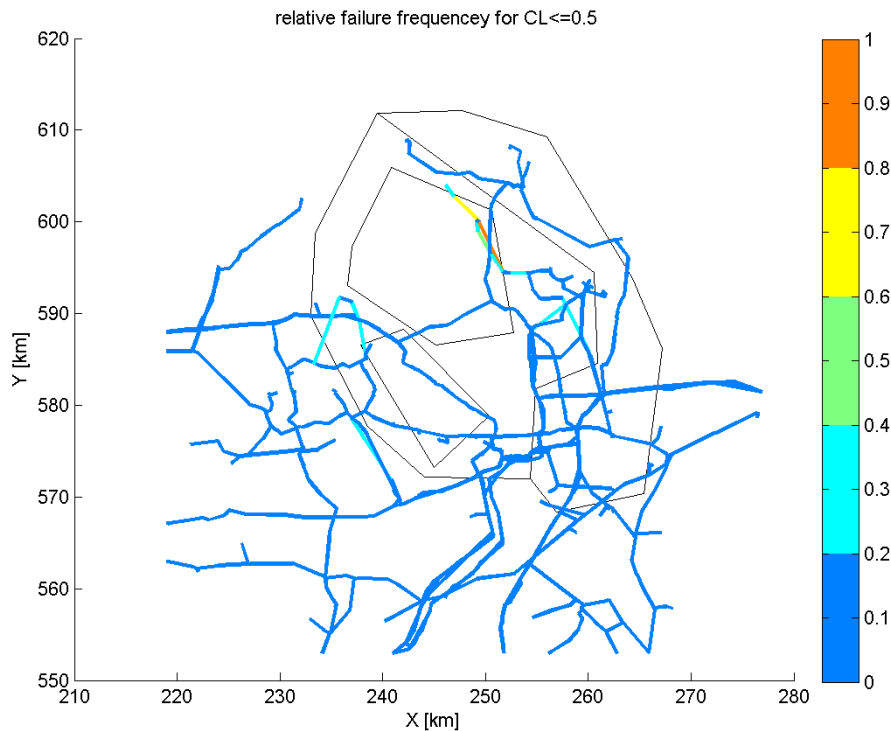


Fig. 5.24 Disaggregation of pipe failures contributing to  $CL \leq 0.1$



**Fig. 5.25 Disaggregation of pipe failures contributing to  $CL \leq 0.5$**

#### **5.4.2.5 Sensitivity of maximum event**

The impact on the performance parameters of allowing events with magnitudes larger than 4 or 5 is shown in Fig. 5.26. Confining the events to a maximum of  $M=5$  as is done in most studies regarding the seismicity in the Groningen area shows a significant improvement of the network performance. For magnitudes less than  $M=4$  hardly any network performance loss is observed.

With respect to the component grading it holds that confining the maximum events to  $M=5$  leads to all stations being in either grade A or AA.

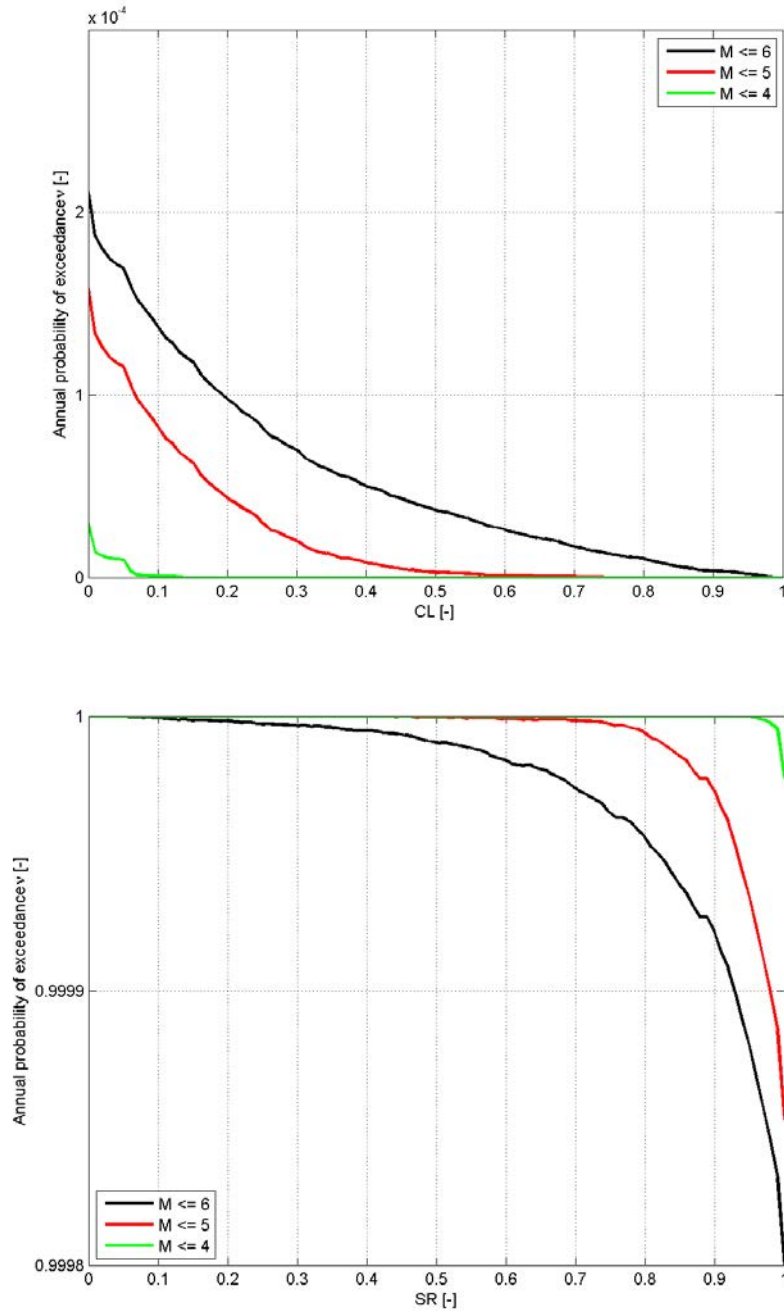


**Fig. 5.26 Sensitivity of CL (top) and SR (bottom) with respect to the maximum value of magnitude**

#### 5.4.2.6 Sensitivity of annual rate of events

In the analyses an annual rate of events with  $M > 1.5$  of 30 is adopted. Recent studies taking into account lower gas production tend to values of 23 events per year with  $M > 1.5$ .

Fig. 5.27 presents the change in performance parameters when the calculations are post processed with two different annual rates.

With respect to the component grading it holds that confining the annual rate to 23 leads to all stations being in either grade A or AA.

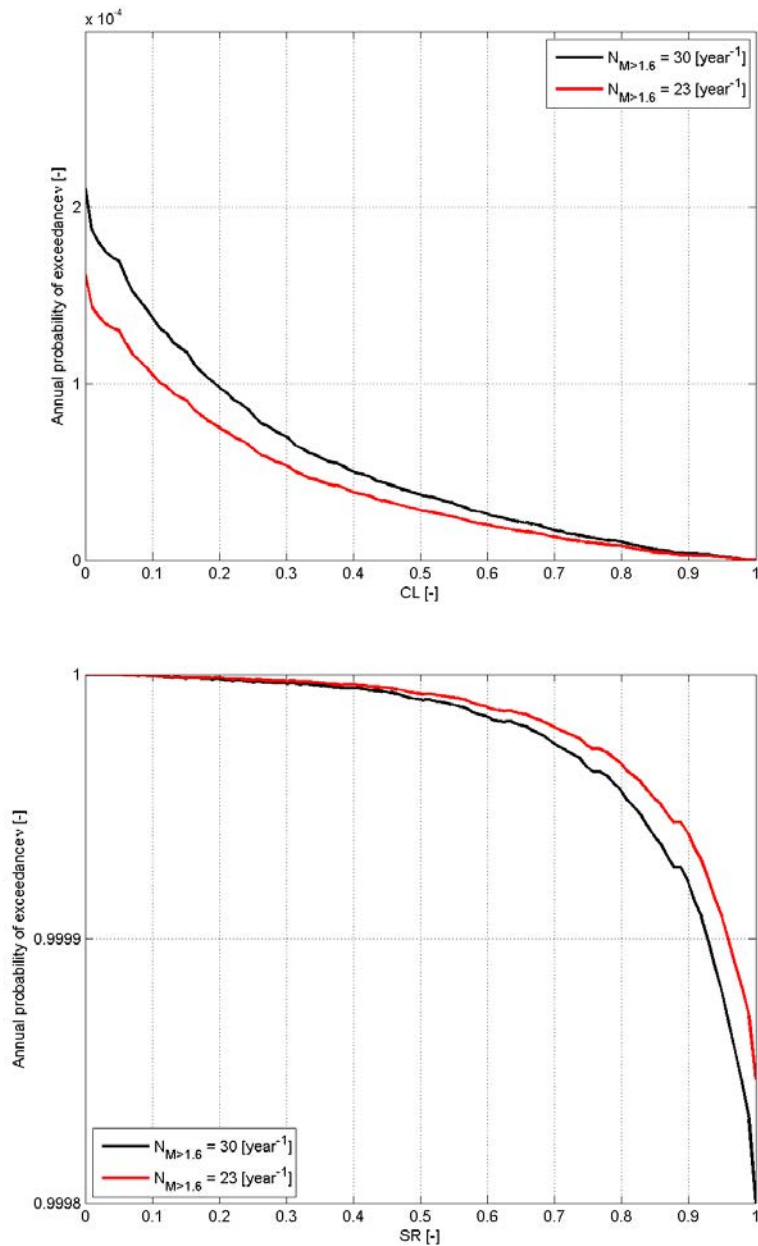


**Fig. 5.27 Sensitivity of CL (top) and SR (bottom) with respect to the annual rate of earthquake events with  $M > 1.5$ .**

### 5.4.3 Guidelines and critical events

With respect to the network as a whole, a strong redundancy in the paths from demand to source nodes is taken into account. This is a strong feature for obtaining the stress test results.

With respect to components, both types (pipe sections and stations) are found to contribute evenly to the network performance indicators as can also be concluded from the component level assessments. From these:



- Specific pipe sections can to some extent be identified as being a weakest link in the network. These sections should be checked on their current actual state assessing the need for upgrading.
- For the stations a rather strong assumption is made with respect to the fragility curve adopted. These should be quantified in more detail and depending to findings retrofitting of stations might be necessary.

In the current analysis soil liquefaction is the dominant failure mechanism. As much uncertainty still exists in the liquefaction fragilities for the Groningen area, further studies into these fragilities and their geographical distribution is recommended.

## 5.5 PHASE 4: REPORT PHASE

The stress test is performed as being initiated by the asset owner, the Gasunie-GTS.

Reporting, in terms of the grade, the critical events, the guidelines for risk mitigation, and the accuracy of the methods adopted in the stress test is accomplished by the current report.

In summary the stress test results are presented in Table 5.2.

**Table 5.2 Stress test results for Gasunie-GTS sub-network**

Item	$M_{max}$	$N_{M>1.6}$	Grading	Result
Pipes sections	6	30	AA, A	Pass
Stations	6	30	AA, A, B	Partly pass
	5	30	AA, A	Pass
	6	23	AA, A	Pass
Network <i>CL</i>	6	30	AA	Pass

In addition to this report, a presentation will be given at the Gasunie-GTS.

Hence, no formal presentation of the outcome of the stress test to (other) CI authorities and/or regulators is foreseen.

## 6 CI-B3 Port infrastructures of Thessaloniki, Greece

### 6.1 INTRODUCTION

The port of Thessaloniki, one of the most important ports in Southeast Europe and the largest transit-trade port in Greece, is one of the case studies, a characteristic example of distributed and/or geographically extended infrastructures with potentially high economic and environmental impact. The port occupies a total space of 1.5 million m<sup>2</sup>, includes 6 piers spreading on a 6200 m long quay and a sea depth down to 12 m, with open and indoors storage areas, suitable for servicing all types of cargo and passenger traffic. The port also has installations for liquid fuel storage, while is located in proximity to the international natural-gas pipeline and is linked to the national and international road and railway network ([www.thpa.gr](http://www.thpa.gr)). In 2015, 1983 ship arrivals have been reported, while the seaborne traffic included 15.248.840 total tonnage of liquid/dry bulk and general cargo, and 351.407 containers (TEUs).

The goal of this case study is to apply the ST@STREST framework to the main port infrastructures in Thessaloniki exposed to different seismic hazards i.e. ground shaking, liquefaction and tsunami. The framework consists of four phases: Pre-Assessment, Assessment, Decision and Report phase, which are performed in sequence. Each phase is subdivided in a number of specific steps as described in Fig. 6.1.

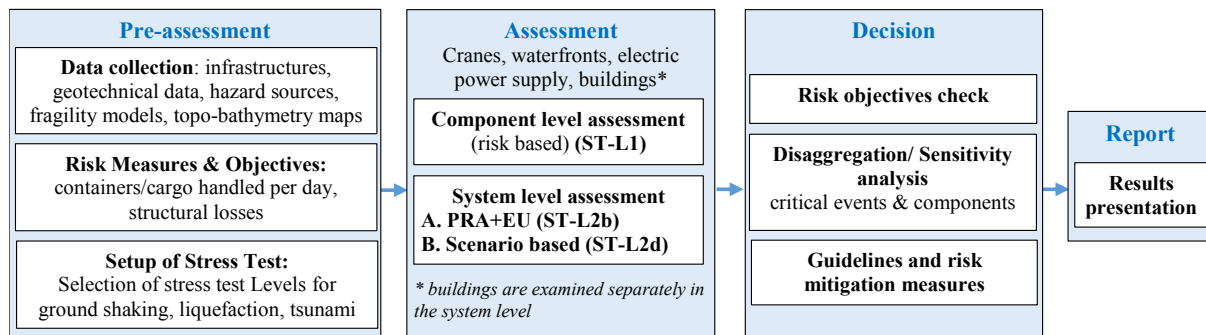


**Fig. 6.1 Flowchart of the ST@STREST framework for the stress test application in the port of Thessaloniki**

*Phase 1 Pre-Assessment:* In the pre-assessment phase all the necessary data is collected and archived in a GIS database. The inventory includes port facilities, various buildings, quay walls, cranes and networks (e.g. electric power supply system). The vulnerability of the infrastructures to the given target hazards (i.e. ground shaking, liquefaction, and tsunami) is assessed using site and case specific or generic fragility functions. Specific risk metrics and objectives are defined related to the functionality of the port system and the structural losses. The stress test levels are selected and the accuracy of the adopted methods in the stress test is defined according to ST@STREST framework.

*Phase 2 Assessment:* The assessment phase comprises two distinctive steps: the component level assessment and the system level assessment (probabilistic and scenario based). In the first one, a risk-based assessment of each component is carried out for earthquake and tsunami hazards to check whether the component passes or fails the minimum requirements for its performance. For that, the target (acceptable) probability of collapse implied by the code, stakeholders and decision-makers needs should be pre-defined for each component. Then in the second step, a probabilistic risk analysis (PRA) is conducted for the whole system separately for earthquake and tsunami hazards considering specific interdependencies between network and components. In addition, at this second step, a scenario-based risk analysis (SBRA) is also performed focusing on site specific response and extreme seismic events.

*Phase 3 Decision:* The estimated response is compared with predefined acceptable risk criteria in order to assess the performance of the CI and decide whether it passes, partly passes or fails the test for all possible events and to define how much the safety of the CI should be improved until the next periodical verification (STREST D5.1 Esposito et al., 2016). The decision phase also includes disaggregation and sensitivity analysis for the identification of the critical components and events, guidelines and strategies to improve the performance and the resilience of the port as a critical facility.

*Phase 4 Report:* This ultimate phase includes presentation of the outcome of the stress test to the port Authority.

## **6.2 PHASE 1: PRE-ASSESSMENT PHASE**

### **6.2.1 Data collection**

#### **6.2.1.1 Port elements**

A GIS database for the port facilities was developed by the Research Unit of Soil Dynamics and Geotechnical Earthquake Engineering (SDGEE, [sdgee.civil.auth.gr](http://sdgee.civil.auth.gr)) at Aristotle University of Thessaloniki in collaboration with the port Authority in the framework of previous national and European projects and it is further updated in STREST project. Waterfront structures, cargo handling equipment, buildings (offices, sheds, warehouses etc.) and the electric power supply system are examined (Fig. 6.2). The STREST D4.4 (Crowley et al., 2016) taxonomy is used to describe the different typologies. Waterfront structures include concrete gravity block type quay walls with simple surface foundation and non-anchored components. Cargo handling equipment has non-anchored components without backup power supply. Four gantry cranes are used for container loading-unloading services located in the western part of the 6<sup>th</sup> pier. The electric power supply to the cranes is assumed to be provided through non-vulnerable lines from the distribution substations that are present inside the port facilities. They are classified as low-voltage substations, with non-anchored components. In total, 85 building and storage facilities are considered in the analyses. The majority is reinforced concrete (RC) buildings comprising principally of low- and mid-rise infilled frame and dual systems with low or no seismic design. The steel buildings are basically warehouses with one or two floors while the unreinforced masonry (URM) buildings are old low-rise and mid-rise structures.

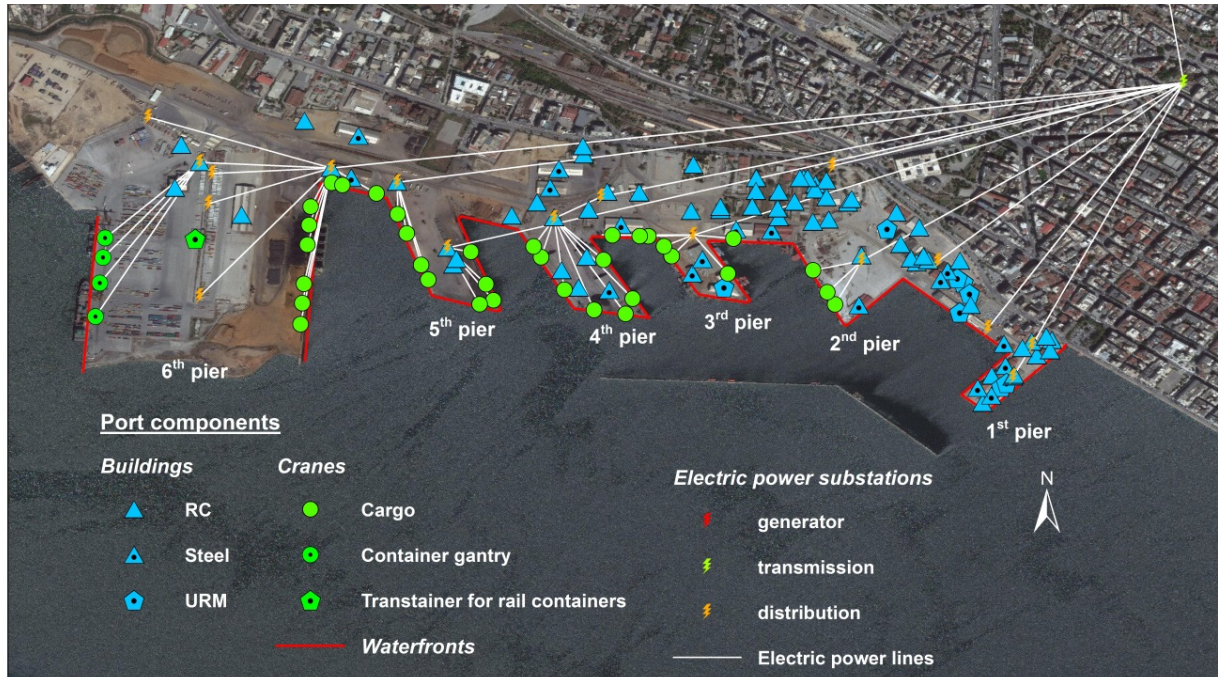


**Fig. 6.2 Geographical representation of Thessaloniki's port infrastructures considered in the study**

### 6.2.1.2 Geotechnical, geological, geophysical data

Soft alluvial deposits, sometimes susceptible to liquefaction, characterize the Port subsoil conditions. The thickness of these deposits close to the sea may reach 150 m to 180 m. A comprehensive set of in-situ geotechnical tests (e.g. drillings, sampling, SPT and CPT tests), detailed laboratory tests and measurements, as well as geophysical surveys (cross-hole, down-hole, array microtremor measurements) at the port broader area (Fig. 6.3) provide all necessary information to perform any kind of site specific ground response analyses (Anastasiadis et al., 2001). Table 6.1 to Table 6.3 present the total number of field geotechnical and geophysical surveys and geotechnical boreholes. A number of representative 1D soil profiles were constructed (Anastasiadis et al., 2001) based on information from detailed 2D cross sections, in-situ and laboratory tests as well as geophysical field surveys (Apostolidis et al., 2004).





**Fig. 6.3** Location of the sampling boreholes, down-hole and cross-hole tests, microtremor measurements and 1D cross-sections of the broader Thessaloniki port area. The location of the new field microtremor measurements (M-1, M-2, M-3, M-4) are also shown.

**Table 6.1** Boreholes at the broader Thessaloniki Port area (Anastasiadis et al., 2001)

Piers	Number of Boreholes	Boreholes Id	Depth (m)	SPT Data	CPT Data	Lab data	USCS Classification	Year
1	4	B-1÷B-2	13.0÷20.0	Yes	No			1996
		B-3	22.0	No	Yes	Yes	Yes	1996
		B-69	26.0	Yes	No			1999
1-2	3	B-68	28.5	Yes	No	Yes	Yes	1999
		B-70÷B71	30.0÷40.0	No	Yes	No	No	
2	4	B-4÷B-7	21.0÷32.0	No	No	No	Yes	1962
4	8	B-8÷B15	17.0÷22.7	No	No	No	Yes	1940
4-5	8	B-22÷B29	30.5÷31.5	Yes	No	Yes	Yes	1962
5	6	B-16÷B-18 B-30÷B-32	19.0÷21.5	Yes	No	Yes	Yes	1962
5-6	3	B-19÷B21	18.0÷20.5	Yes	No	No	Yes	1965
6	35	B-33÷B67	24.0÷36.0	Yes	No	Yes	Yes	1964
								1970
								1972

**Table 6.2 Microtremor array measurements at port area (Apostolidis et al., 2004)**

Map location	Array Id	Depth (m)	Bedrock $V_s$ (m/s)	Circle radius (m)	Analysis Method	Year
Pier 1-2	A-1	180	700	10, 50	SPAC	2001
Over Pier 6 (Customs Office)	A-2	160	600	15	SPAC	2001

**Table 6.3 Geophysical data close to Thessaloniki port (\*1: Raptakis and Makra, 2010; \*2: ITSAK's Equipment and Instrumentation Upgrade project, 2002-2006)**

Map location	Type	Id	Depth (m)	Boreholes	Bottom layer $V_s$ (m/s)	Bottom layer $V_p$ (m/s)	Year
Over Pier 6 (Thermaikos football field)	Cross-hole *1	CH-1	40.0	No	400	-	1993
Pier 3-4 (near the church)	Down-hole *2	DH-1	80.30	Yes	710	2462	2008

New field surveys including array microtremor measurements were conducted at four (4) different sites inside the port (M-1, M-2, M-3 and M-4 in Fig. 6.3 using the SPatial Autocorrelation Coefficient–SPAC method (Aki, 1957) to improve the information for the dynamic properties ( $V_s$  velocities) and the geometry of the main geological formation in the port area. In addition, the ambient noise provides information for the site response characterization of the investigated sites, using the Horizontal to Vertical Spectral Ratio–HVSR method (Nakamura, 1989). The site selection of these new field surveys was based on specific criteria, such as the good spatial distribution of the measurements, the availability in the vicinity of previous specific  $V_s$  data, and geological, geotechnical and borehole information.

Circular arrays of different radii were used in the SPAC measurements. Two to three concentric arrays of different radii were deployed (from 10 to 50m) using four broadband Guralp seismometers CMG-40T (of 30sec natural period) and four high-resolution Reftek recording systems DAS-130 each with its own GPS unit. Three of the stations were installed on the vertices of the equilateral triangle and one on the center of the circle. Ambient ground noise of different wavelengths was recorded for 30 to 35 min for small distances and almost 1 hour for large distances at 200Hz sampling rate. Table 6.4 gives the parameters of the SPAC measurements conducted in the port.

The Spatial Autocorrelation Coefficient method introduced by Aki (1957) was used to process the vertical component of the microtremors. The noise records were baseline corrected and bandpass filtered between 0.1 to 40Hz. For each station pair, average Correlation Coefficients (CC) were computed as the average from many (9 to 18) time windows of 300sec duration each. For each four-station triangle, the results from two different station pairs (between central station and the vertices and between the three vertices of the triangle) provided an azimuthal average for the CC at the corresponding

distance. The average CC determined from each site, were used to determine the experimental phase velocity dispersion curve of Rayleigh waves through an inversion process. The average CC curves are very similar to a Bessel function for the frequency range 1 to 21Hz (the frequency range is different for each distance) and a phase velocity dispersion curve was determined from them.

**Table 6.4 New microtremor array measurements in Thessaloniki port**

Map location	Array ID	Circle radius (m)	Analysis Method	Year
Pier 1-2 (close to passenger station)	M-1	10, 27	SPAC	2015
Pier 2-3 (church)	M-2	10, 20, 50	SPAC	2015
Pier 6	M-3	10, 20	SPAC	2015
Close to pier 6	M-4	10, 20, 50	SPAC	2015

The final phase velocity dispersion curves for the Rayleigh waves for the four investigated sites are shown in Fig. 6.4. The dispersion curves are quite similar to each other and also comparable with those determined by previous microtremor measurements (Apostolidis et al., 2004) performed at sites A-1 and A-2 (see Fig. 6.3). By inverting these dispersion curves the final 1D  $V_s$  profiles were calculated at the four investigated sites. The calculated  $V_s$  profiles for sites M-2, M-1 and M-3 are shown in Fig. 6.5.

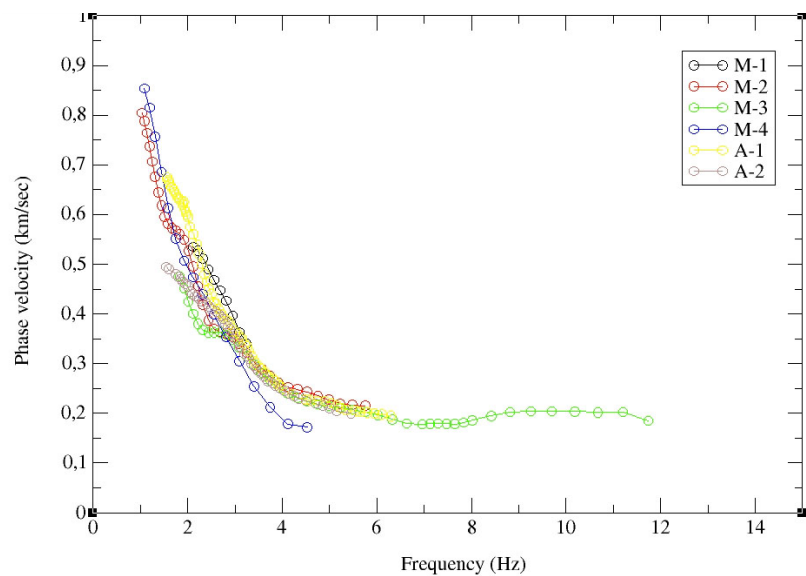


**Fig. 6.4 Final phase velocity dispersion curves determined at the four investigated sites together with those obtained by Apostolidis et al. (2004) for the sites A-1 and A-2 (see Fig. 6.3).**

The site response characteristics, in terms of resonant frequency and amplification factor, of the sites where the microtremor measurements were conducted were determined using the HVSR method (Nakamura, 1989). Regarding HVSR, we used the average spectral ratios computed for 29 windows of 20sec each. Consecutive windows had a 50% overlap. Each

20sec window was cosine-tapered over 10%, and its Fourier amplitude spectrum was smoothed four times with a hanning window before computing the spectral ratio between horizontal and vertical components. The final HVSR are the average for the two horizontal components. The resonant frequency was calculated for all the stations of all the available radii in each site. For all the sites the resonant frequency of the soils is 1.0Hz with amplification above 5, while quite smaller values, around 0.5-0.7Hz, exist for the site M-3.

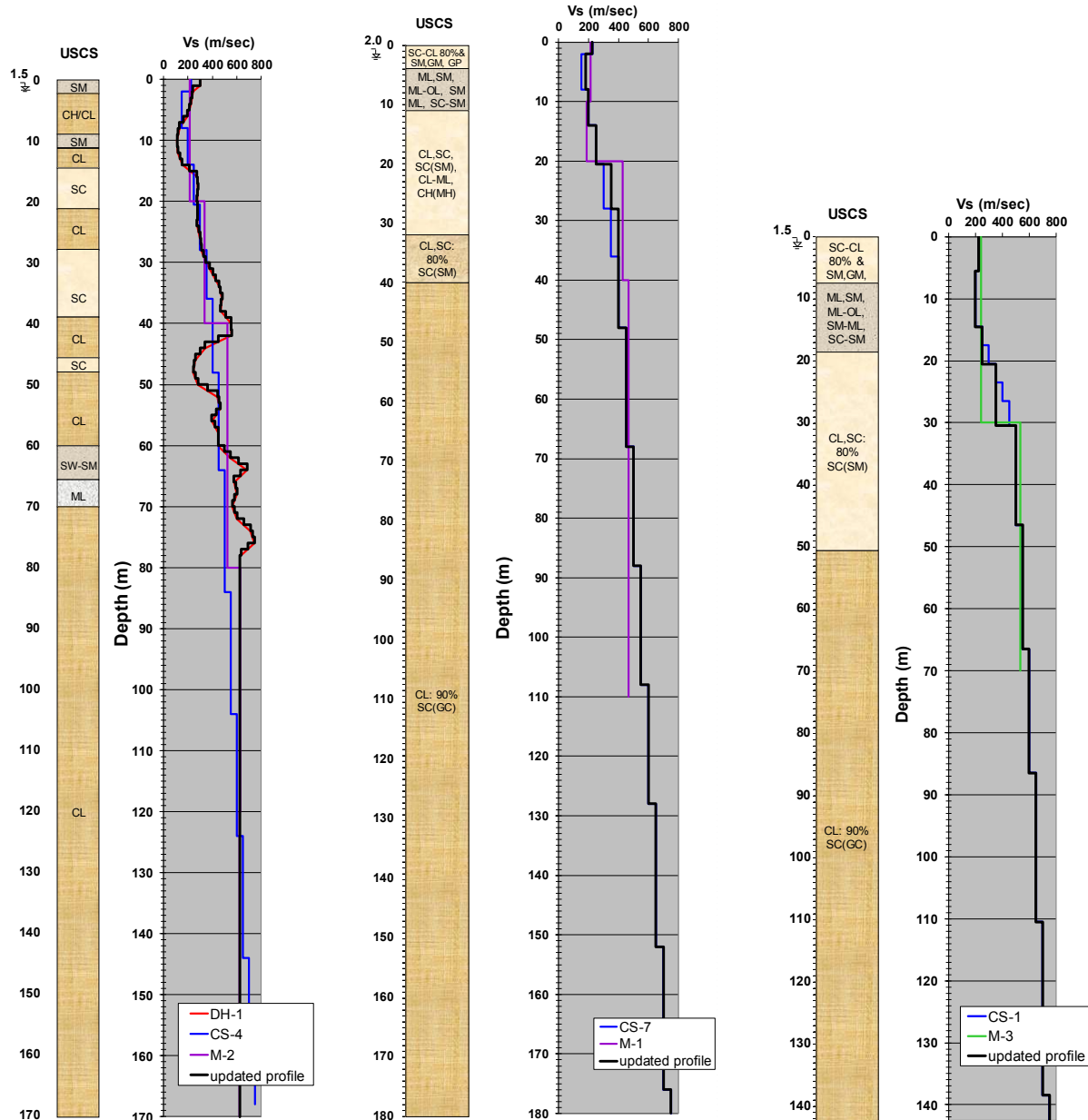


**Fig. 6.5**  $V_s$  profiles for sites A (left), B (middle) and C (right) together with a general geotechnical characterization according to USCS classification

Three representative soil profiles distributed along the area of the port are considered to compute the ground response applying either equivalent linear (EQL) or nonlinear (NL) approaches (see section 6.3.2.2). They are denoted as soil profiles A, B and C and their locations are shown in Fig. 6.3. Profile A is located close to the site of the Down-hole test



(CH-1) (ITSAC Equipment and Instrumentation Upgrade project, 2002-2006) and the existing 1D cross section with code name CS-4, where in situ and laboratory geotechnical surveys were also made available. Profiles B and C are located close to the existing 1D cross sections with code names CS-7 and CS-1 respectively. Profiles A, B and C are also close to the sites where the new array measurements of microtremors with code names M-2, M-1 and M-3 respectively were performed. Fig. 6.5 presents the initial  $V_s$  profiles derived from the past 1D cross sections (for Profiles A, B and C) and the Down-hole test (for Profile A), the  $V_s$  profiles determined from the new array microtremor measurements as well as the finally adopted base-case  $V_s$  profiles for A, B and C soil profiles respectively. The average geophysical and geotechnical characteristics of the finally adopted soil profiles are presented in Appendix A. The fundamental periods  $T_0$  of the selected representative soil profiles were theoretically estimated equal to 1.58sec, 1.60sec and 1.24sec for profiles A, B and C respectively. The G- $\gamma$ -D curves of the soil layers at various depths were determined from extended laboratory tests (Pitilakis and Anastasiadis, 1998). All soil profiles refer to ground type C according to EC8 classification with an average depth varying from 142.0m (Soil Profile C) to 180m (Soil profile B). Knowing, however, that the liquefaction susceptibility in the port area is rather high, they could be also classified as ground type S according to EC8. The evaluation of liquefaction potential and its effects on the buildings and infrastructure performance and vulnerability for the selected soil profiles is presented in section 6.3.2.2 (Scenario based assessment).

### 6.2.1.3 Topobathymetric data

A topobathymetric model was produced for the tsunami simulations, based on nautical and topographic maps and satellite images (Fig. 6.6). The elevation data includes also the buildings and other structures that affect the waves while propagating inland. The resolution of the model is higher in the area of the Port. An initial model was produced by AUTH group, which was further refined by INGV to fulfil the requirements for the tsunami simulations (see section 6.3.2.1).

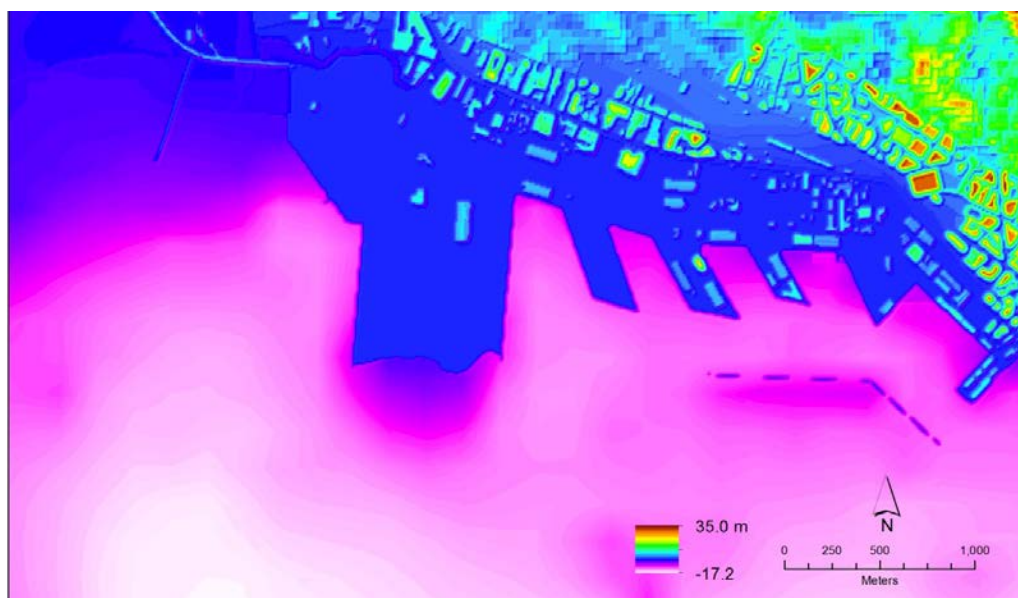


**Fig. 6.6 Digital elevation map of Thessaloniki's port area (initial model)**

#### **6.2.1.4 Target hazards**

The present study focuses on different natural hazards including ground shaking, liquefaction and tsunami. In particular, probabilistic risk analyses are performed separately for the earthquake (including liquefaction) and tsunami hazards. In addition, two different seismic scenarios were defined, which also include the potential for liquefaction, in collaboration with a pool of experts corresponding to return periods of 475 years (i.e. design scenario) and 4975 years (i.e. extreme event scenario). Further details regarding the considered hazards are provided in the assessment phase.

#### **6.2.1.5 Fragility models**

The vulnerability of the Port facilities at component level (i.e. buildings, waterfront structures, cranes etc) is assessed through fragility functions, which describe the probability of exceeding predefined damage states (DS) for given levels of peak ground acceleration (PGA), permanent ground displacement (PGD) and inundation depth for the ground shaking, liquefaction and tsunami hazards respectively (Table 6.5).

The fragility functions used to assess the damages due to liquefaction are generic (NIBS, 2004), while the models used for ground shaking are either case specific (UPGRADE, 2015; SRM-LIFE 2007, present work) or generic (NIBS, 2004; Kappos et al. 2003, 2006).

New seismic fragility curves have been developed for typical quay walls and gantry cranes of the port subjected to ground shaking based on dynamic numerical analyses in collaboration with the National Technical University of Athens (NTUA) in the framework of another research project (UPGRADE, 2015). The model included the quay wall blocks, the surrounding soil and the embankment, as well as concentrated gravity loads on the position of container crane legs and a uniform operational load on the embankment (Kourkoulis et al, 2014). Twelve seismic motions are selected in the analyses to account for seismic scenarios of moderate and high seismicity scaled up to different amplitudes (up to  $\pm 0.3g$ ) and applied at the model base through viscous dampers. Then, for each seismic analysis, the engineering demand parameter (EDP) is estimated. In particular, the ratio of the residual displacement (towards the sea) at the top of the wall ( $u_x$ ) to the height of the quay wall ( $H$ ) is considered as EDP ( $u_x/H$ ) for the quay wall, while the resultant (horizontal and vertical) residual differential displacement of the crane legs ( $du$ ) is taken as EDP for the crane. Finally, lognormal distribution functions are established as a function of the peak ground acceleration (PGA) at free field conditions to represent the fragility curves for predefined damage states (according to PIANC 2001 and NIBS 2004 for the quay wall and the crane respectively). Fig. 6.7 illustrates the fragility curves and its parameters (i.e. median  $m$  and log- standard deviation  $\beta$ ) for the quay wall and the crane.

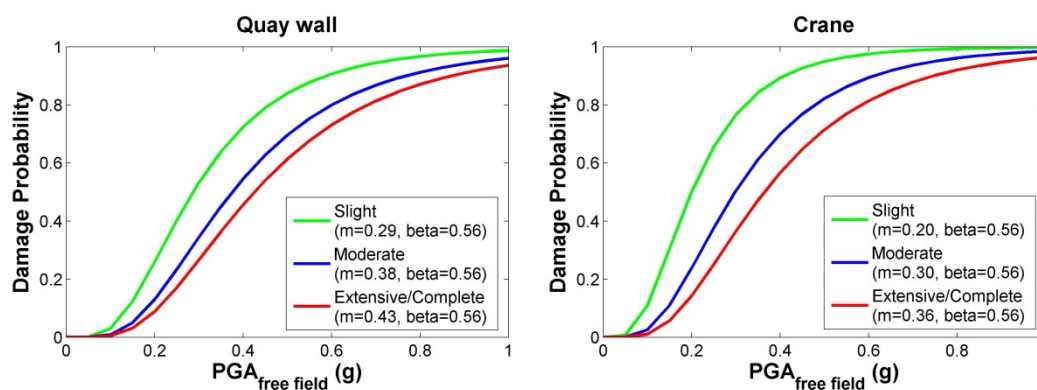


**Fig. 6.7 Fragility curves for the quay wall (left) and the crane (right) for ground shaking**

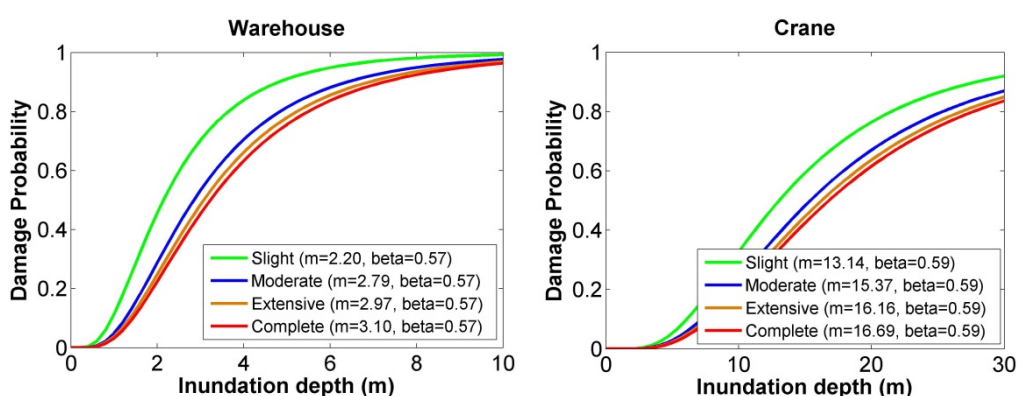


**Fig. 6.8 Tsunami fragility curves for the warehouse (left) and the crane (right)**

Analytical tsunami fragility curves as a function of inundation depth have been developed for representative typologies of the Port RC buildings, warehouses and gantry cranes (Karafagka et al., 2016; Salzano et al., 2015, AUTH contribution) while, for simplicity reasons, the waterfront structures are considered as non-vulnerable to tsunami forces. An extensive numerical parametric investigation has been performed considering different combinations of statically applied tsunami loads based on FEMA (2008) recommendations for gradually increasing tsunami inundation depths. Afterwards, the structure's response in terms of material strain (i.e. the EDP) for the different statically applied tsunami loads is estimated. For the development of fragility curves, a relationship between the numerically calculated material strain (i.e. the EDP) and the gradually increasing inundation depths (i.e. the IM) is established through nonlinear regression analysis. Indicatively, the tsunami fragility curves for warehouses and cranes are presented in Fig. 6.8.

The damage states are correlated with component functionality in order to perform the risk assessments at the system level. The following assumptions are set: (i) the waterfront-pier (berth) is functional if damage is lower than moderate, (ii) the crane is functional if damage is lower than moderate and there is electric power supply (i.e. the physical damages of the substations are lower than moderate) (iii) the berth is functional if the waterfront and at least one crane is functional.

**Table 6.5 Fragility functions used in the risk analyses**

Hazard	Component	Intensity measure	Reference
<b>Ground shaking</b>	RC and URM buildings	PGA	Kappos et al. (2003, 2006)
	Steel buildings		HAZUS (NIBS, 2004)
	Waterfront structures Cranes/cargo handling equipment		UPGRADE (2015) - Fig. 6.7
	Electric power substations (distribution, transmission)		HAZUS (NIBS, 2004), SRM-LIFE (2003-2007)
<b>Liquefaction</b>	Buildings/ Housed electric power substations (all considered typologies)	PGD	HAZUS (NIBS, 2004)
	Waterfront structures		
	Cranes/cargo handling equipment		
<b>Tsunami</b>	RC Buildings/ Electric power substations	Inundation depth	Karafagka et al. (2016)- Fig. 6.8 Salzano et al. (2015)
	Warehouses (Steel and URM buildings)		
	Cranes/cargo handling equipment		

### 6.2.2 Risk Measures and Objectives

In the Pre-Assessment phase, specific risk measures and objectives are defined related to the functionality of the port at system level and the structural losses at component level.

For level 1 assessment (ST-1), the annual probability of structural collapse is taken as the risk measure, and the required objective is sought by reference to European design norms. In particular, the reference target (acceptable) probability of collapse is set equal to  $1.0 \cdot 10^{-5}$  based on the existing practice (e.g. Lazar and Dolšek, 2013; Silva et al., 2014a) corresponding to an acceptable probability equal to 0.05% in 50 years. This value is properly modified based on EC8 prescriptions to account for the importance factor  $\gamma_I$  of the structure.

Since two terminals (container, bulk cargo) are assumed herein, the system performance is measured through the total number of containers handled (loaded and unloaded) per day (TCoH), in Twenty-foot Equivalent Units (TEU), and the total cargo handled (loaded and unloaded) per day (TCaH), in tones. Risk measures related to structural and economic losses of the buildings are also set for the tsunami case and the scenario based assessment. The risk objectives correspond to the boundaries of the grading system proposed in ST@STREST (STREST D5.1 Esposito et al., 2016). The CI passes the stress test if is classified into grade AA (negligible risk) or A (risk being as low as reasonably practicable, ALARP). The CI partly passes the stress test if it receives grade B (possibly unjustifiable risk), while it fails the stress test if it is classified into grade C (intolerable risk).

Since no regulatory boundaries (AA-A, A-B and B-C) exist for the moment for port facilities, to demonstrate the application of the ST@STREST, indicative continuous boundaries, i.e. straight lines on the logarithmic performance curve, were defined for the probabilistic system-wide risk assessment in terms of the annual probability for 100% loss assuming a logarithmic slope equal to 1 (neutral risk), (B-C:  $4.5 \times 10^{-3}$ , A-B:  $2.0 \times 10^{-3}$ , AA-A:  $7.5 \times 10^{-4}$ ). For the scenario based assessment scalar boundaries in terms of the expected performance loss (%) are assigned for the 475 years (B-C: 50, A-B: 30, AA-A: 10) and the 4975 years (B-C: 70, A-B: 50, AA-A: 30) scenarios based on general judgment criteria. It is worth noting that risk objectives related to the structural and economic losses of the buildings for the probabilistic tsunami and the scenario based assessments are not defined since the buildings are considered separately in the systemic analysis and thus their performance is not expected to significantly affect the performance of the port system. The stress test levels are defined and outlined in the following section.

### 6.2.3 Set-up of the Stress Test

Among the stress test levels proposed within STREST, the port infrastructures in Thessaloniki will be basically subjected to ST-1 and ST-2. First, a ST-L1a component level risk based assessment of the key components is carried out. Then, a probabilistic single hazard, ST-2 analysis with epistemic uncertainty (L2b) is undertaken at the system level considering separately seismic and tsunami hazards. Complementary to L2b, a L2d / L3d scenario based system wide risk assessment is conducted to further investigate extreme seismic events (including liquefaction) and site-specific response. Different approaches are considered to account for the scenario based single-risk (L2d) (i.e. due to ground shaking) and multi-risk (L3d) (i.e. due to ground shaking and liquefaction) assessments at the system level. Finally, the formalized multiple expert integration process called EU@STREST (Selva et al., 2015) is implemented as an experiment to simulate the procedure in the port infrastructures. The involvement of multiple experts is critical in the implementation of the stress test at levels 2b/c and 3b/c; however, the results of this experiment are not implemented into the effective risk analysis for the port of Thessaloniki. The elicitation has a purely exemplificative nature at level 3b and 2c and is presented separately in section 6.6.

## 6.3 PHASE 2: ASSESSMENT PHASE

### 6.3.1 Component Level Assessment (ST-L1a)

The aim is to check each component of the port independently for earthquake and tsunami hazards in order to show whether the component passes or fails the pre-defined minimum requirements for its performance implied by the current codes. A risk-based assessment is performed using the hazard function at the location of the component and the fragility function of the component. These two functions are convolved in risk integral in order to obtain probability of exceedance of a designated limit state in a period of time ( $P_f$ ). This probability is estimated on the basis of closed form risk equation (Fajfar and Dolšek, 2012) as follows:

$$P_f = H(\overline{IM}) \exp(0.5 k^2 \beta^2) \quad (6.1)$$

where  $\overline{IM}$  and  $\beta$  are the median and log-standard deviation values respectively of the fragility function,  $H(IM)$  is the hazard function and  $k$  is the logarithmic slope of the hazard function idealized in the following form:

$$H(IM) = k_0 \cdot IM^{-k} \quad (6.2)$$

where  $k_0$  is a constant that depends on the seismicity of the site. Proper  $k$  and  $k_0$  can be obtained by fitting the actual hazard curve provided that the entire hazard function or at least two points from the hazard function are available. For the seismic case (i.e. ground shaking),  $k$  and  $k_0$  were computed from the hazard curve corresponding to return periods equal to 475 and 4975 years for the normal and the extreme event respectively based on the site specific response analyses carried out for three representative soil profiles (scenario-based assessment) (e.g. Fig. 6.9- left). For the tsunami case, at least two points of the mean hazard function estimated from probabilistic tsunami hazard assessment at various locations in the port area were used to estimate these parameters (e.g. Fig. 6.9- right). The target (acceptable) probability of exceedance of a designated limit state for a period of time implied by the code, stakeholders and decision makers ( $P_t$ ) also has to be defined for each component and different limit states. In this application the target probability of exceedance of the collapse damage state is only provided. This probability was initially set to  $1.0 \times 10^{-5}$  based on the existing practice (e.g. Lazar and Dolšek, 2013; Silva et al., 2014a) corresponding to an acceptable probability equal to 0.05% in 50 years and was properly modified based on EC8 prescriptions to account for the importance factor  $\gamma_I$  of the structure based on the following equation:

$$\gamma_I = (P_L / P_{LR})^{(-1/k)} \quad (6.3)$$

where  $P_{LR}$  the reference acceptable probability of collapse (equal to  $10^{-5}$ ) and  $P_L$  the modified acceptable probability of collapse to account for the importance of the structure ( $\gamma_I$ ). In particular, to check whether or not the component is safe against collapse, the finally computed target probability ( $P_t$ ) is compared with the corresponding probability of exceeding the ultimate damage state ( $P_f$ ).

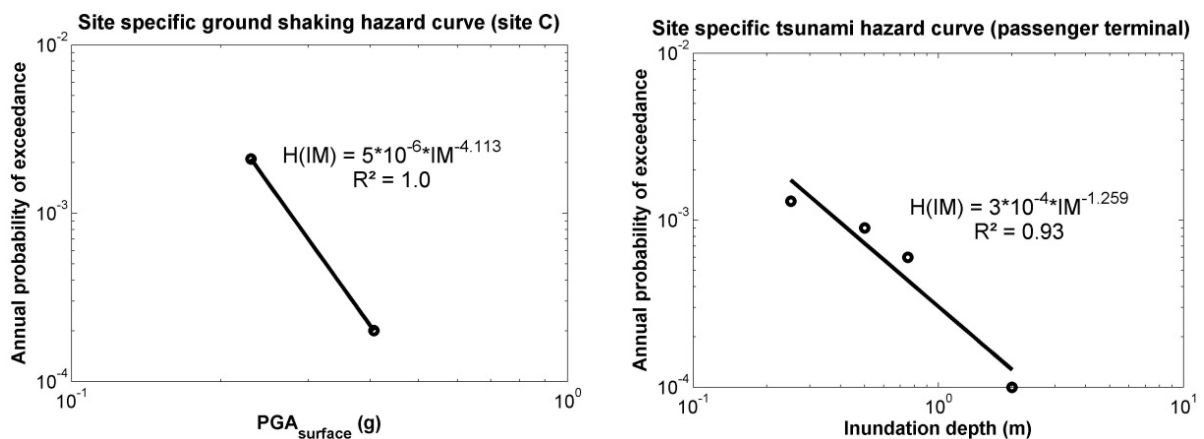


**Fig. 6.9 Site specific hazard curves for ground shaking and tsunami**

As an example the proposed performance assessment approach is applied here to a strategic building of the Port, the passenger terminal, which is a low-rise infilled dual system ( $\gamma_I = 1.2$ ). The probability of exceeding the ultimate damage state ( $P_f$ ), which in this study

corresponds to the collapse damage state, is computed and compared with the target probability of collapse ( $P_t$ ) for both earthquake and tsunami hazards. The hazard function at the location of the structure is estimated as  $10^{-5}$  and  $1.7 \cdot 10^{-4}$  for the seismic (see Fig. 6.9- left and Equation 2) and tsunami (see Fig. 6.9- right and Equation 2) case respectively, while the corresponding probabilities of collapse ( $P_f$ ) are finally computed equal to  $1.4 \cdot 10^{-3}$  and  $2.0 \cdot 10^{-4}$ . These probabilities are higher than the target (acceptable) probability of collapse ( $P_t$ ) estimated equal to  $4.7 \cdot 10^{-6}$  and  $7.9 \cdot 10^{-6}$  for the seismic and tsunami case respectively, indicating that the structure is not safe against exceedance of the collapse limit state due to the considered hazards. Table 6.6 and Table 6.7 present a summary of the component level check for all buildings and infrastructures for the seismic and tsunami case respectively providing a general assessment of the performance and resilience of the Port.

**Table 6.6 Earthquake hazard component check**

Components	Soil profile	Hazard parameters		Fragility parameter		$P_f$	$P_t$	Safety test	
		k	$k_o$	Median PGA (g)					$\beta$
RC buildings	MRF LR LC infilled	A	2.50	$10^{-5}$	0.41	0.73	$4.9 \cdot 10^{-4}$	$6.3 \cdot 10^{-6}$	Not safe
		B	3.94	$5.0 \cdot 10^{-6}$			$1.0 \cdot 10^{-2}$	$4.9 \cdot 10^{-6}$	Not safe
		C	4.11	$5.0 \cdot 10^{-6}$			$1.8 \cdot 10^{-2}$	$4.7 \cdot 10^{-6}$	Not safe
	MRF MR LC infilled	C	4.11	$5.0 \cdot 10^{-6}$	0.26	0.61	$2.8 \cdot 10^{-2}$	$4.7 \cdot 10^{-6}$	Not safe
	MRF HR LC infilled	A	2.50	$10^{-5}$	0.55	0.63	$1.5 \cdot 10^{-4}$	$6.3 \cdot 10^{-6}$	Not safe
	dual LR LC infilled	A	2.50	$10^{-5}$	0.85	0.76	$9.3 \cdot 10^{-5}$	$6.3 \cdot 10^{-6}$	Not safe
		B	3.94	$5.0 \cdot 10^{-6}$			$8.8 \cdot 10^{-4}$	$4.9 \cdot 10^{-6}$	Not safe
		C	4.11	$5.0 \cdot 10^{-6}$			$1.4 \cdot 10^{-3}$	$4.7 \cdot 10^{-6}$	Not safe
	URM buildings	LR	C	4.11	$5.0 \cdot 10^{-6}$	0.51	0.39	$2.9 \cdot 10^{-4}$	$4.7 \cdot 10^{-6}$
MR		A	2.50	$10^{-5}$	0.23	0.60	$1.2 \cdot 10^{-3}$	$6.3 \cdot 10^{-6}$	Not safe
		C	4.11	$5.0 \cdot 10^{-6}$			$4.4 \cdot 10^{-2}$	$4.7 \cdot 10^{-6}$	Not safe
Steel buildings	A	2.50	$10^{-5}$	0.45	0.64	$2.7 \cdot 10^{-4}$	$6.3 \cdot 10^{-6}$	Not safe	

	B	3.94	$5.0 \cdot 10^{-6}$			$2.8 \cdot 10^{-3}$	$4.9 \cdot 10^{-6}$	Not safe
	C	4.11	$5.0 \cdot 10^{-6}$			$4.3 \cdot 10^{-3}$	$4.7 \cdot 10^{-6}$	Not safe
	A	2.50	$10^{-5}$			$2.2 \cdot 10^{-4}$	$6.3 \cdot 10^{-6}$	Not safe
Quay walls	B	3.94	$5.0 \cdot 10^{-6}$	0.29	0.56	$1.6 \cdot 10^{-3}$	$4.9 \cdot 10^{-6}$	Not safe
	C	4.11	$5.0 \cdot 10^{-6}$			$2.3 \cdot 10^{-3}$	$4.7 \cdot 10^{-6}$	Not safe
	A	2.50	$10^{-5}$			$3.4 \cdot 10^{-4}$	$6.3 \cdot 10^{-6}$	Not safe
Cranes	B	3.93	$5.0 \cdot 10^{-6}$	0.36	0.56	$3.2 \cdot 10^{-3}$	$4.9 \cdot 10^{-6}$	Not safe

Table 6.7 Tsunami hazard component check

Components	Map id	Hazard parameters		Fragility parameter		$P_f$	$P_t$	Safety test	
		k	$k_o$	Median h (m)	$\beta$				
RC buildings	MRF LR LC infilled	56	1.26	$3.0 \cdot 10^{-4}$	2.33	0.37	$1.2 \cdot 10^{-4}$	$7.9 \cdot 10^{-6}$	Not safe
		59-60	2.96	$2.4 \cdot 10^{-3}$			$3.6 \cdot 10^{-4}$	$5.8 \cdot 10^{-6}$	Not safe
	MRF MR LC infilled	45,48, 52	0.87	$10^{-4}$	3.74	0.40	$3.4 \cdot 10^{-5}$	$8.5 \cdot 10^{-6}$	Not safe
		49	0.77	$10^{-4}$			$3.8 \cdot 10^{-5}$	$8.7 \cdot 10^{-6}$	Not safe
		50	0.39	$10^{-4}$			$6.1 \cdot 10^{-5}$	$9.3 \cdot 10^{-6}$	Not safe
	MRF HR LC infilled	31-35, 37	1.29	$4.0 \cdot 10^{-4}$	6.19	0.35	$4.3 \cdot 10^{-5}$	$7.9 \cdot 10^{-6}$	Not safe
		36	0.97	$10^{-4}$			$1.8 \cdot 10^{-5}$	$8.4 \cdot 10^{-6}$	Not safe
	dual LR LC infilled	38,43	0.87	$10^{-4}$	1.57	0.44	$7.3 \cdot 10^{-5}$	$8.5 \cdot 10^{-6}$	Not safe
		39	0.43	$10^{-4}$			$8.4 \cdot 10^{-5}$	$9.2 \cdot 10^{-6}$	Not safe
		40	0.61	$10^{-4}$			$7.9 \cdot 10^{-5}$	$8.9 \cdot 10^{-6}$	Not safe
		41	0.76	$10^{-4}$			$7.5 \cdot 10^{-5}$	$8.7 \cdot 10^{-6}$	Not safe





### **6.3.2 System Level Assessment for Single Hazard (ST-L2b / L2d / L3d)**

#### **6.3.2.1 Probabilistic Risk Assessment (ST-L2b)**

The system wide probabilistic risk assessment is made separately for ground shaking, including liquefaction, and tsunami hazard, according to the methodology developed in SYNER-G (Pitilakis et al., 2014) and extended in STREST D4.2 (Kakderi et al., 2015). The objective is to evaluate the probability or mean annual frequency (MAF) of events with the corresponding loss in the performance of the port operations. The analysis is based on an object-oriented paradigm where the system is described through a set of classes, characterized in terms of attributes and methods, interacting with each other. The physical model starts from a pre-defined taxonomy and requires: a) a description of the functioning of the system (intra-dependencies) under undisturbed and disturbed conditions (i.e., in the damaged state following an event); b) a model for the physical and functional damageability of each component (fragility functions); c) identification of all dependencies between systems (inter-dependencies); and d) definition of adequate Performance Indicators (PIs) for components and the system as a whole which represent the previously defined risk metrics. The computational modules include the modeling of: hazard events and intensity parameters (hazard class), physical damages of components and performance of the system (network class), and specific interactions among systems (interdependency models). A Monte Carlo simulation is carried out sampling events and corresponding damages for the given hazard. The exceedance probability of different levels of performance loss is assessed for the system under the effect of any possible event, and the performance curve is produced, which is equivalent of risk curves for non-systemic probabilistic assessments in single (e.g. PEER formula; Cornell and Krawinkler, 2000) and/or multi-risk (e.g. Selva, 2013) analysis.

In the present application the systemic analysis concerns the container and bulk cargo movements affected by the performance of the piers, berths, waterfront and container/cargo handling equipment (cranes) while the interdependency considered here is between the cargo handling equipment and the Electric Power Network (EPN) supplying to cranes. The capacity of berths is related to the capacity of cranes (lifts per hour/tons per hour). The functionality state of each component and the whole port system is assessed based on the computed physical damages, taking also into account system inter- and intra-dependencies. Regarding the analysis of the interdependencies we assume that if a crane node is not fed by the reference EPN node (i.e. electric supply station) with power and the crane does not have a back-up supply, then the crane itself is considered out of service. The functionality of the demand node is based on EPN connectivity analysis (Pitilakis et al., 2014).

#### **Risk assessment for ground shaking**

The seismic hazard model provides the means for: (i) sampling events in terms of location (epicentre), magnitude and faulting type according to the seismicity of the study region and (ii) maps of sampled correlated seismic intensities at the sites of the vulnerable components in the infrastructure ('shakefields' method, Weatherill et al., 2014). When the fragility of components is expressed with different IMs, the model assesses them consistently. Five seismic zones with  $M_{\min}=5.5$  and  $M_{\max}=7.5$  are selected based on the results of SHARE European research project (Giardini et al., 2013, [www.share-eu.org](http://www.share-eu.org)) and the ground motion prediction equation (GMPE) of Akkar and Bommer (2010) to estimate the outcrop ground motion parameters. Seismic events are sampled for the seismic zones affecting the port

area through a Monte Carlo simulation (10,000 runs). The spatial variability is modeled using the correlation models provided by Jayaram and Baker (2009). For each site of a regular grid of points discretizing the study area, the averages of primary IM (PGA) from the specified GMPE were calculated, and the residual was sampled from a random field of spatially correlated Gaussian variables according to the spatial correlation model. The primary IM is then retrieved at vulnerable sites by distance-based interpolation and finally the local IM is sampled conditionally on primary IM. Fig. 6.10 shows an example map with the primary IM (PGA at rock) computed at points of a regular grid, for a sampled event corresponding to a return period of 500 years, modeling the spatial variability of the ground motion. To scale the hazard to the site condition the amplification factors proposed in EC8 (EN 1998-1, 2004) are used in accordance with the site classes that were defined in the study area. HAZUS (NIBS, 2004) and the modeling procedure by Weatherill et al. (2014) are applied to estimate the permanent ground displacements (PGDs) due to liquefaction.

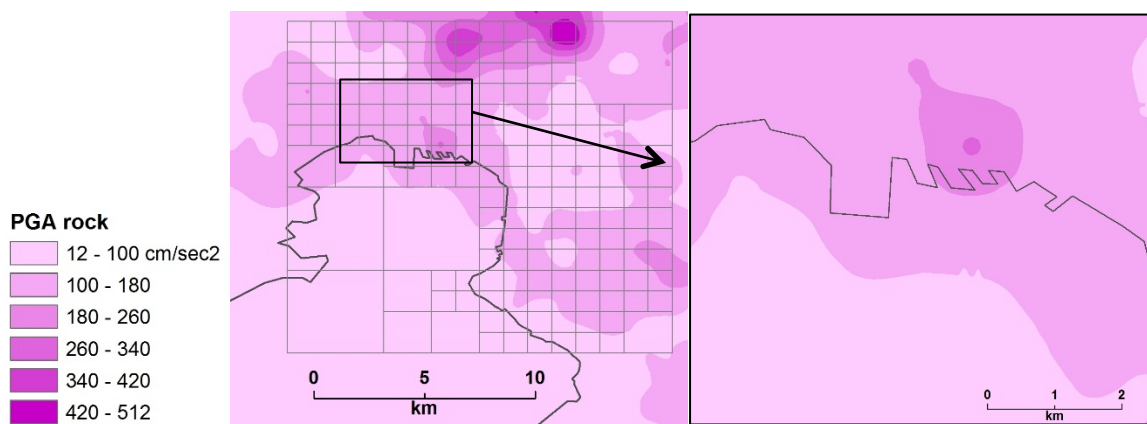


**Fig. 6.10** Example of shake map in terms of PGA on rock for one event ( $M = 5.8$ ,  $R = 20$  km NNE of Port).

The PIs of the port system for both the container and cargo terminal are evaluated for each simulation of the Monte Carlo analysis based on the damages and corresponding functionality states of each component and considering the interdependencies between components. The final computed PIs are normalized to the value referring to normal (non-seismic) conditions assuming that all cranes are working at their full capacity 24 hours per day. Fig. 6.11 shows the MAF of exceedance curves (“performance curve”) for TCoH and TCaH. For performance loss values below 40% TCaH yields higher values of exceedance frequency, while for performance loss over 40% TCoH yields higher values of exceedance frequency.

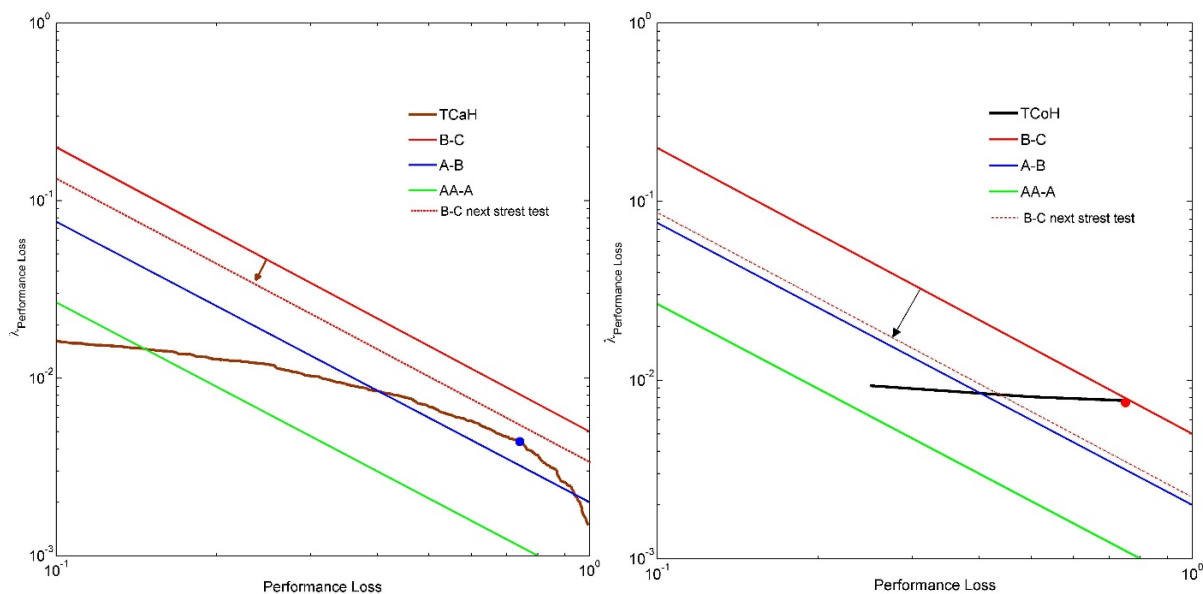


**Fig. 6.11 Mean annual frequency (MAF) of exceedance values for the normalized performance loss of the container terminal (TCoH, right) and the bulk cargo terminal (TCaH, left) for the seismic hazard case. The green, blue and red continuous lines correspond to the boundaries between risk grades AA (negligible), A (ALARP), B (possibly unjustifiable risk), and C (intolerable).**

### Risk assessment for tsunami

Probabilistic Tsunami Hazard Analysis (PTHA) is a methodology to assess the exceedance probability of different thresholds of hazard intensity, at a specific site or region in a given time period, due to whatever source. Different potential tsunamigenic sources should be considered, such as earthquakes, landslides, meteorite impacts or atmospheric phenomena. Here, we focus only on tsunami of seismic origin, which is the dominant component of PTHA in most of the areas of the world, both in terms of occurrence and in terms of effects (Parsons and Geist, 2009). Following the definition proposed in Lorito et al. (2015), we deal with Seismic PTHA (SPTHA), that is, tsunamis generated by co-seismic sea floor displacements due to earthquakes.

A very large number of numerical simulations of tsunami generation, propagation and inundation on high resolution topo-bathymetric models are in principle required, in order to give a robust evaluation of SPTHA at a local site, honoring the full aleatory variability of the seismic sources (the aleatory uncertainty). Consequently, the computational effort can be extremely demanding and in practice unfeasible and the issue is traditionally solved by limiting the variability of the sources (Gonzalez et al., 2009) and/or reducing the computational effort of numerical models by not modeling the near-coast and inland propagation of the tsunamis (Sørensen et al., 2012). These approaches make the calculation of SPTHA a computationally affordable task, but could lack in accuracy in uncertainty estimation and/or in definition of the hazard in-land.

To reduce the computational cost, while keeping results stable and consistent with respect to explore the full variability of the sources, we developed a method to approach the uncertainty in SPTHA (Selva et al., 2016a), based on 4 steps: 1) a full exploration of the aleatory uncertainty through an Event Tree (ET, Lorito et al., 2015; Selva et al., 2016a) that account for all available sources of information (e.g. Basili et al., 2013); 2) the propagation of

all potential sources till off-shore (Molinari et al., submitted); 3) a 2 stage filtering procedure based on Cluster Analysis on the results off-shore in order to define a sub-set of “representative” events which approximate the hazard in the target area, in order to enable the inundation modeling (Lorito et al., 2015); 4) the quantification of the epistemic uncertainty through Ensemble modeling based on alternative implementations of steps 1 to 3 (Marzocchi et al., 2015; Selva et al., 2016a).

Step 1 is based on the development of the Event Tree for different seismic regions, which are assumed independent. Within the Event Tree, all the relevant source parameters (aleatory variability) are explored through a controlled hierarchical discretization, and conditional probability distributions set based on all the available information about the potential seismic sources (seismic catalogs, focal mechanism catalogs, known fault databases, scaling laws, 3D geometries of major faults, etc.). The seismicity related to the main and better known fault interfaces (e.g. Interface Seismicity, IS) is treated separately from the rest of the seismicity (Background Seismicity, BS), in order to optimize the use of the available information for the and not to loose potential other sources. Alternative implementations of the Event Tree are then proposed, in order to explore the epistemic uncertainty.

In Step 2, the complete set of source scenarios defined from the ET is implemented to obtain a regional SPTHA, in terms of maximum offshore tsunami wave height ( $H_{max}$ ) at discrete points (along the 50 m isobath). It is worth noting that, as the number of sources may be very high (>106), such scenarios are not explicitly simulated but are computed as the linear combination of pre-calculated waveforms resulting from elementary Gaussian-shaped initial sea level elevation, according to a Green's function approach (Molinari et al., submitted).

In Step 3, the offshore  $H_{max}$  is analyzed applying a two-step filtering procedure, in order to reduce the number of numerical simulations required to retrieve the site specific SPTHA based on the inundation maps: firstly, sources which produce a negligible contribute to  $H_{max}$  on a set of control points located on the 50 m isobath offshore of the target site are excluded, assuming that they would lead to negligible inundation as well at the nearby coast; secondly, a cluster analysis is carried out on the filtered sources, based on the resulting tsunami propagation patterns, not on the similarity or the proximity of the sources. Basically, sources which produce similar offshore  $H_{max}$  profiles along the set of control points in front of the target coast are assumed to produce as much similar inundation patterns and, consequently, one representative simulation for each cluster (not for each source) must be executed. The probability of occurrence of the entire cluster is attributed to the selected representative source. This strategy allows for a 75-80% reduction of the number of required simulations, while satisfactorily preserving the accuracy of the obtained inundation maps (Lorito et al., 2015). From the cluster analysis performed on the set of possible scenarios defined by the ET, a subset of representative causative earthquakes is inferred, which is used as initial condition for the tsunami generation, propagation and inundation simulations. For BS, the initial sea level elevation is obtained by modeling the fault dislocation with Okada (Okada, 1985) and applying the Kajiura filter to take into account the effect of the water depth on the tsunami generation process (Kajiura, 1963). The subduction scenarios are simulated by modeling the slab as a 2D triangular mesh honoring the interface profile, associating to each element of the mesh (i.e. each triangle) a unitary Okada source and suitably combining such sub-faults in order to reproduce the slip along the slab.

In Step 4, the epistemic uncertainty, that is, the uncertainty due to the adopted model parameters and the modeling assumptions, is treated by means of an ensemble modeling

approach (Marzocchi et al. 2015), with the implementation of alternative models (e.g. alternative formulations for the probability distributions of the ET). Each model is weighted according to the confidence and the possible correlations between the models (Selva et al., 2016a).

Within STREST, we considered 2 target sites, Milazzo (Sicily, Italy) in the Southern Tyrrhenian sea, and Thessaloniki (Central Macedonia, Greece) in Northern Aegean sea (Volpe et al., in prep; Selva et al., 2016b). A common regional assessment (Steps 1 and 2, above) has been set up, by considering all the potential seismic sources in the Mediterranean Sea. IS class included the seismicity occurring on subduction interfaces of the Calabrian and the Hellenic arcs (hereinafter those will be referred to as CA and HA, respectively). BG class, mainly associated to crustal seismicity, has been modeled on a grid with areas of constant size approximately 25 km x 25 km covering the whole Mediterranean Sea. The total number of scenarios considered was approximately  $2 \times 10^7$ . More than  $1 \times 10^4$  alternative implementations have been considered to quantify the epistemic uncertainty. All the details of the adopted Event Tree can be found in Selva et al. (2016a).

The common regional results provided the input for the site specific analysis (Volpe et al.). This task has been carried out separately for Milazzo and Thessaloniki. For each site, a reference profile off-shore at the isobath of 50 m has been selected. We here describe the application for Thessaloniki, whereas the Milazzo application is reported in section 2.

We considered 13 points off-shore the Thessaloniki target area, as reported in Fig. 6.12A. The  $H_{\max}$  values of each scenario defined in steps 1 and 2 represented the input for the filtering procedure. Scenarios with  $H_{\max} < 0.2$  m have been filtered out. Then, a k-Means Cluster Analysis has been performed, separately for groups of scenarios with similar maximum  $H_{\max}$  along the profile. The number of clusters in each group has been set as the minimum number leading to a within-cluster average distance smaller than 20% of the maximum  $H_{\max}$  of the group. The scenario closer to the centroid of each cluster has been finally selected as the “reference scenario” for the cluster (adopting a distance based on a cost function, see Lorito et al., 2015). We obtained 253 clusters (3 for CA, 23 for HA, 227 for BS), for which an explicit numerical simulation of inundation has been performed (Volpe et al., in prep).

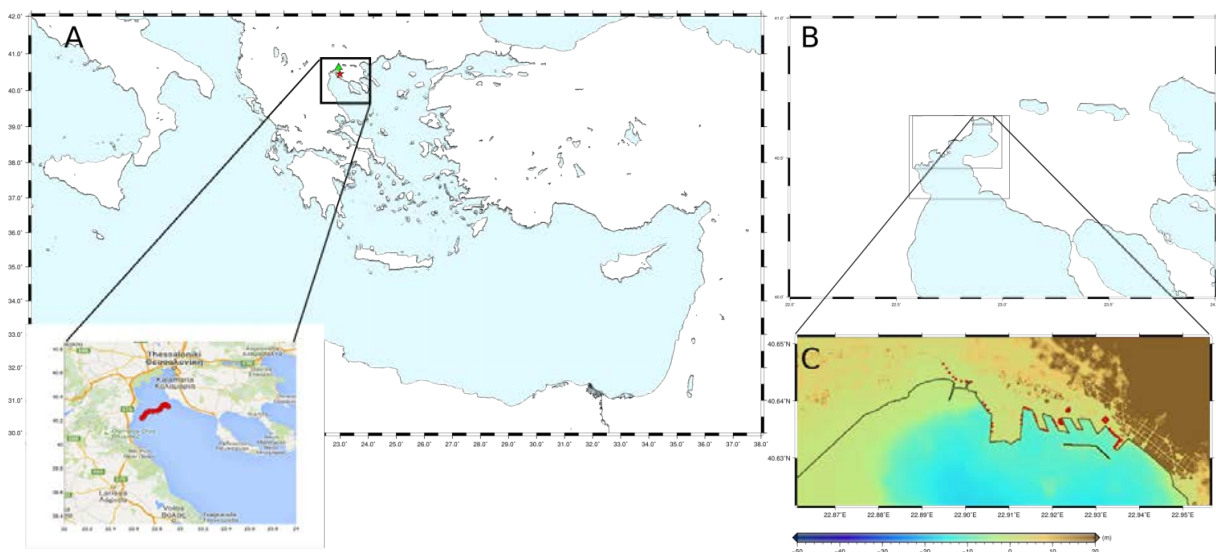


**Fig. 6.12 A) Map of the whole simulation domain used for the application at the target site Thessaloniki (Central Macedonia, Greece). The red star is the location of a crustal event for which we provide the map of the maximum wave height ( $H_{\max}$ ), as an example; The zoom highlights the points along the 50 m isobath used to produce the  $H_{\max}$  profiles for the input of the Cluster Analysis. B) Close-up view of the simulation domain showing the telescopic nested grids for tsunami simulation with gradually increasing resolution (0.1, 0.025, 0.00625 arc-min). C) Bathymetric image of the finest grid (resolution=0.00625 arc-min), where the locations of the 70 receiver points are shown (red points).**

The numerical simulations were performed using a non-linear shallow-water multi-GPU code developed at the University of Malaga, Spain (HySEA, Gonzalez Vida et al., 2015). The code is based on a mixed finite difference/finite volume method. Grid nesting allows to gradually increase simulation resolution as tsunami wavelength decreases while approaching the target site, to preserve accuracy on progressively smaller areas while saving computational time. For this specific application, we used 4-level nested bathymetric grids with refinement ratio equal to 4 and increasing resolution from 0.4 arc-min (~740 m) to 0.1 arc-min (~185 m) to 0.025 arc-min (~46 m) to 0.00625 arc-min (~11 m), as reported in Fig. 6.12B. The largest grid was obtained by resampling the SRTM15+ bathymetric model. The finest 3 grids have been produced by interpolation from the model provided by AUTH (for the emerged part) and EMODNET and navigation charts (for the sea part), working on grids of 0.00625 arc-min that have been resampled at 0.1 arc-min and 0.025 arc-min.

The results of each simulation have been stored as maximum flow depth (Flow Depth, m) and maximum momentum flux ( $Mom_{\max}$ ,  $m^3s^{-2}$ ), in each point of the inner grid, and as time history for both quantities at the 70 receiver points, with a sampling step 30 sec for an overall duration of 8 hours. The receiver points are distributed along the Thessaloniki harbor as well as in correspondence of strategic buildings, tanks, cranes and along a bridge (red dots in Fig. 6.12C). In Fig. 6.13, we report one example of simulation results for the grid and for the time history in one randomly selected target point.

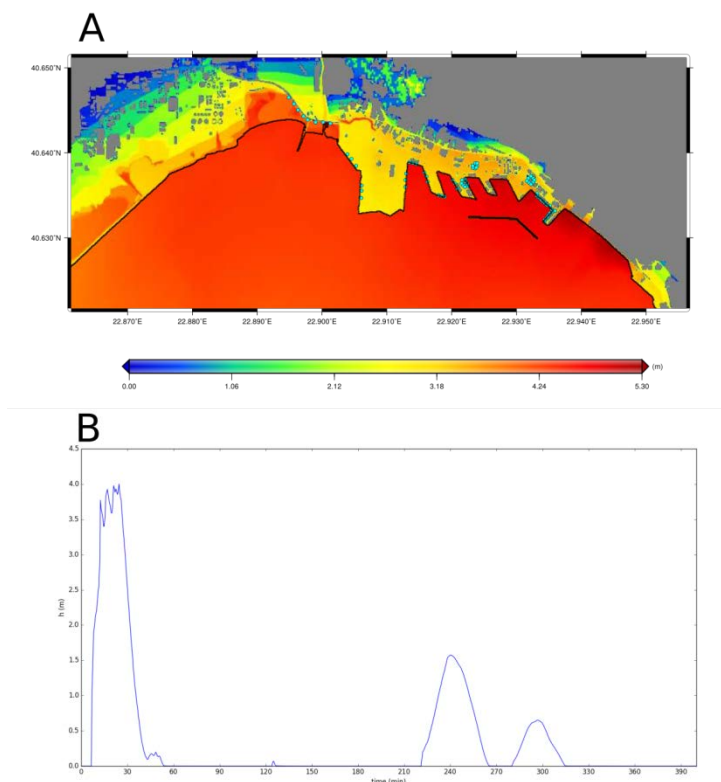
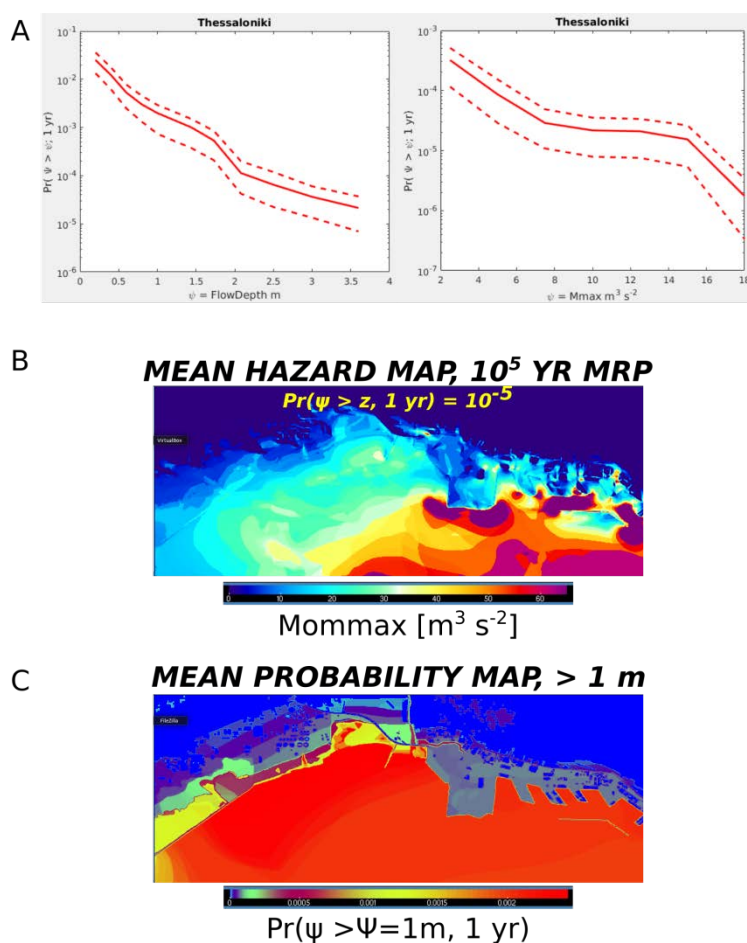


**Fig. 6.13 A) Maximum wave height distribution originated from the crustal event indicated with the red star in Figure 1 ( $M=8.0$ ). B) Time history of the corresponding wave height for one randomly selected receiver.**

To each one of the “representative scenarios” is finally assigned the probability of all the scenarios owing to its cluster, then the results are aggregated to obtain the final SPTHA results (Lorito et al., 2015; Selva et al., 2016a; Volpe et al., in prep). All the alternative probability assessments set up for the Event Tree are adopted separately, obtaining a family of hazard curves in each target point. These curves, along with the credibility weight assigned to each of these alternative models, are given in input to the Ensemble model, in order to produce the quantification of hazard curves and relative epistemic uncertainty (for more details see Selva et al., 2016a; Volpe et al., in prep). The results consist of a set of ensemble hazard curves for each point of the inner grid domain. One example of such curves is reported in Fig. 6.14A, for two intensity measures (maximum flow depth and maximum moment). The hazard curves are then post-processed to obtain hazard maps and probability maps. For sake of example, we report in Fig. 6.14B the hazard map for flow depth considering an annual probability threshold of  $10^{-5}$ , and in Fig. 6.14C the annual probability map for a maximum flow depth of 1 m. In both cases, the mean of the ensemble models is considered. Similar maps can be obtained at any statistics of the epistemic uncertainty.

The kind and format of the results is suitable and it has been provided for subsequent risk analysis at this site within the framework of the STREST project.

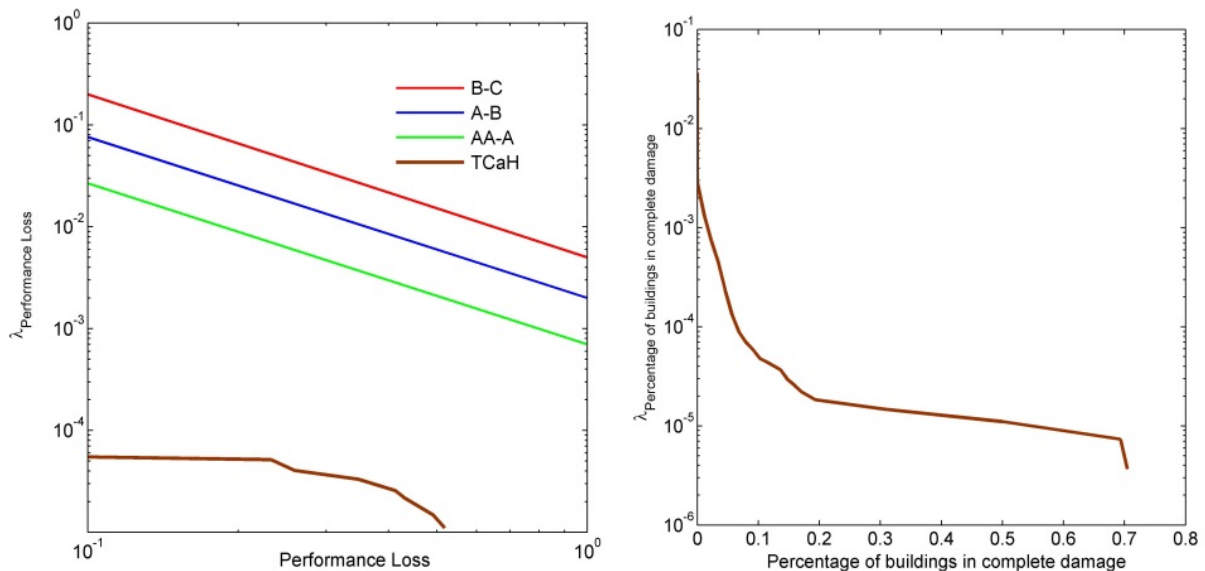




**Fig. 6.14** A) Ensemble hazard curves for one randomly selected point in the target area, for two intensity measures: Maximum Flow Depth (left) and Maximum Momentum Flux (right); in both cases, the bold red line is the mean of the Ensemble, while the dotted lines report the confidence interval in terms of 16th and 84th percentiles. B) Mean hazard map for maximum momentum flux considering an annual probability threshold of  $10^{-5}$ . C) Mean annual probability map for a maximum flow depth of 1 m.

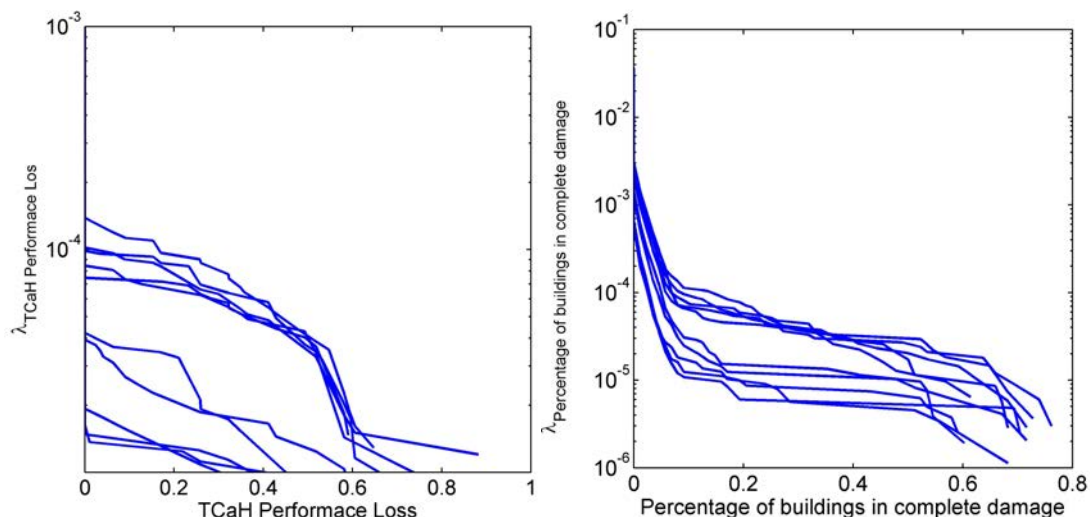
To assess the tsunami risk a hazard module has been developed in order to enable sampling among the 253 representative scenarios, considering the probability of occurrence of the cluster of sources that each scenario represents (Lorito et al., 2015). The inundation simulation results for each sampled scenario are then loaded, in order to retrieve the tsunami intensity for any selected location. Note that, since the SPTHA analysis is based on an explicit simulation of each scenario, spatial correlations of the tsunami intensity are automatically accounted for. Given that the inundation simulation does not integrate potential collapses, tsunami intensity should be retrieved in proximity of each component's perimeter and outside the structure. In order to avoid any unwanted biases (e.g. retrieve the tsunami intensity over the roof of buildings, where the modeled tsunami flow depth is subtracted the height of the building), a characteristic radius has been assigned to each component, and the largest intensity value within the defined circle is obtained. Damages and non-functionalities are then sampled from the respective fragility curves (

Table 6.5) and the retrieved tsunami intensities. The analysis has been implemented for the port infrastructures (cranes, electric power network components and individual buildings) and the PIs for the analyzed system are evaluated. In Fig. 6.15 we show an indicative example for one of the alternative models (i.e. the epistemic uncertainty is not considered here). The container terminal is not expected to experience any loss (TCoH), while the loss in the cargo terminal (TCaH) is negligible. This is due to the non-vulnerable condition of waterfront structures, the high damage thresholds for the cranes (i.e. high inundation values that are not expected in the study area) as described in the fragility curves used in the application and the distance of the electric power substations from the shoreline. Consequently, the annual probabilities for buildings collapses are also low. As an example, in this particular simulation, 10% of the total buildings in the Port (~9 structures) will be completed damaged under tsunami forces with annual probability equal to  $5 \cdot 10^{-5}$ . However, it should be noted that we assumed that it is negligible the probability of damages due to floating ships that may hit the different components of the harbor. This assumption holds if the harbor procedures are correctly connected to tsunami warning systems, enabling the relocalization of eventual ships at the births earlier than the tsunami wave arrival.



**Fig. 6.15 Mean annual frequency (MAF) of exceedance values for the normalized performance loss of the bulk cargo terminal (TCaH, left) and for the buildings in complete damage state (right) for the tsunami hazard case. The green, blue and red continuous lines correspond to the boundaries between risk grades AA (negligible), A (ALARP), B (possibly unjustifiable risk), and C (intolerable).**

The entire procedure is possible for any preselected alternative model of input to the SPTHA ensemble, enabling the propagation of hazard epistemic uncertainty into risk analysis. As an example, in Fig. 6.16 ten alternative models are applied. The differences among the different curves reflect the epistemic uncertainty in the tsunami hazard, showing a considerable dispersion in the loss assessments in terms of TCaH and damaged buildings.



**Fig. 6.16 Mean annual frequency (MAF) of exceedance values for the normalized performance loss of the bulk cargo terminal (TCaH, left) and for the buildings in complete damage state (right) considering alternative models for the tsunami hazard.**

### 6.3.2.2 Scenario based Assessment (ST-L2d / L3d)

A scenario-based system-wide seismic risk analysis is performed complementary to the classical PRA approach described previously, to further investigate extreme events and specific site response.

#### Seismic hazard scenarios

Two different seismic scenarios were defined in collaboration with a pool of experts: the standard seismic design scenario and an extreme scenario corresponding to return periods of  $T_m=475$  years and  $T_m=4975$  years respectively. To perform the site response analyses a target spectrum for seismic bedrock conditions ( $V_s=700-800$  m/s) and a suite of acceleration time histories are needed.

For the 475 years scenario, the target spectrum is defined based on the disaggregation of the probabilistic seismic hazard analysis (SRM-LIFE, 2007; Papaioannou, 2004). This study has shown that the most significant contribution to seismic hazard for Thessaloniki port is associated with the Anthemountas fault system (i.e. a normal fault) regardless of the return period. In particular, for the 475 years scenario, the maximum annual exceedance probability for a certain PGA value with a moment magnitude  $M_w$  of 5.7 and an epicentral distance  $R_{epi}$  of 14.6 km was provided. For the 4975 years scenario, an extreme rupture scenario breaking along the whole Anthemountas fault zone with a characteristic magnitude  $M_w$  of 7.0, close to the maximum magnitude of the seismic source, was assumed. Input data regarding the Anthemountas fault were taken from the Greek Database of Seismogenic Sources GreDaSS (Caputo et al., 2012). The  $R_{jb}$  distance (i.e. the closest distance to the surface projection of the rupture zone) and the rupture distance  $R_{rup}$  (i.e. the closest distance to rupture zone) are estimated as 5 km and 10 km for the 475 years scenario while they are both taken as 5 km for the 4975 years scenario.

Fig. 6.17 shows a comparative plot of the 5% damped median acceleration spectra for the 475 and 4975 years scenarios when using the ground motion prediction equations (GMPEs)

of Akkar and Bommer (2010), Akkar et al. (2014a), Cauzzi et al. (2015) and Danciu and Tselentis (2007). Cauzzi et al. (2015) is a global model, Akkar and Bommer (2010) and Akkar et al. (2014a) are pan-European models while Danciu and Tselentis (2007) is a local model based on existing Greek strong-motion data. A normal rupture mechanism was considered in all models consistently with the seismotectonic setting. A good agreement is observed between the Akkar and Bommer (2010) and Akkar et al. (2014a) spectra although Akkar et al. (2014a) spectrum is more amplified (especially for the extreme scenario) and more constrained in the short-period range. The spectral ordinates of Cauzzi et al. (2015) model are lower with respect the Akkar and Bommer (2010) and Akkar et al. (2014a) models for the 475 years scenario while they are quite close with those of the Akkar et al. (2014a) model for the 4975 years scenario. Danciu and Tselentis (2007) model shows greater variation with respect to the former ones for both hazard scenarios. The differences between the models could be attributed, among other reasons (e.g. the different databases used, the different functional form adopted, the different parameterization of local site conditions), to the different distance metrics used. In particular, in Akkar and Bommer (2010) and Akkar et al. (2014a) models the  $R_{jb}$  distance has been used (although Akkar et al. (2014a) models also allows the use of epicentral and hypocentral distances) while Cauzzi et al (2015) and Danciu and Tselentis (2007) use the  $R_{rup}$  and  $R_{epi}$  distances respectively. The large discrepancies shown by Danciu and Tselentis (2007) model for the 4975 years scenario are also largely associated to the dataset used (335 records from 151 Greek earthquakes) which is based on earthquakes with  $M_w$  that ranges between 4.5 and 6.9. Thus, as noted in Danciu and Tselentis (2007), the extrapolation to earthquake events larger than 6.9 is not recommended.

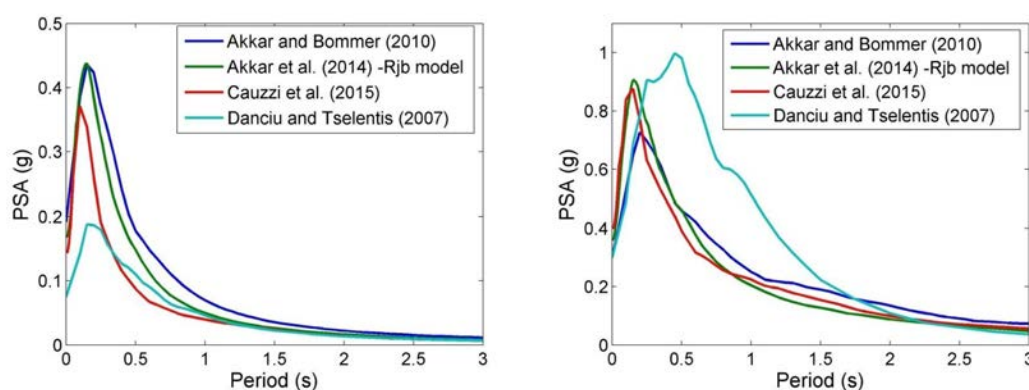


**Fig. 6.17 Comparison of the 5% damped median acceleration spectra of Akkar and Bommer (2010), Akkar et al. (2014a), Cauzzi et al. (2015) and Danciu and Tselentis (2007) for the 475 (left) and the 4975 (right) years scenarios**

In addition to magnitude and distance, both hazard scenarios should include an error term  $\varepsilon$  (which measures the number of standard deviations of logarithmic residuals  $\sigma$  to be accounted for in a GMPE) that will be responsible for an appreciable proportion of spectral ordinates and the contribution from  $\varepsilon$  will grow with the return period (Bommer and Acavedo, 2004). Thus, the median spectral values plus 0.5 and 1 standard deviation were considered for the 475 years and the 4975 years scenarios respectively. This is also in line with the earthquake scenarios selected in Akkar et al. (2014a) to generically represent the moderate seismicity (median + 0.5 $\sigma$  for an  $M_w$  6 event) and high seismicity (median + 1 $\sigma$  for an  $M_w$  7 event) regions in Europe.

Fig. 6.18 shows the spectral ordinates (including the corresponding  $\varepsilon$  term) for the 475 years scenario when using the ground motion prediction equations by Akkar et al. (2014a), Akkar and Bommer (2010), Cauzzi et al. (2015) and Danciu and Tselentis (2007) respectively in comparison with the SHARE uniform hazard spectrum for Thessaloniki port, the EC8 elastic response spectrum for  $PGA=0.16g$  (for the city of Thessaloniki) and soil class A (rock), and the corresponding elastic spectrum provided by Pitilakis et al. (2013).

Similarly, Fig. 6.19 shows the spectral ordinates (including the corresponding  $\varepsilon$  term) for the 4975 years scenario using again the ground motion prediction equations by Akkar et al. (2014a), Akkar and Bommer (2010), Cauzzi et al. (2015) and Danciu and Tselentis (2007) respectively in comparison with the corresponding SHARE uniform hazard spectrum for Thessaloniki port, the EC8 elastic response spectrum for  $PGA=\gamma_i \cdot 0.16g$  (for Thessaloniki city, where  $\gamma_i$ : the importance factor estimated for the extreme scenario equal to 2.19 based on EC8 prescriptions) and soil class A (rock), and the corresponding elastic spectrum provided by Pitilakis et al. (2013).

The median spectra plus the corresponding standard deviations provided by Akkar and Bommer (2010) are selected as the target spectra for the 475 years and the 4975 years respectively since they describe better both hazard scenarios in Thessaloniki port area.

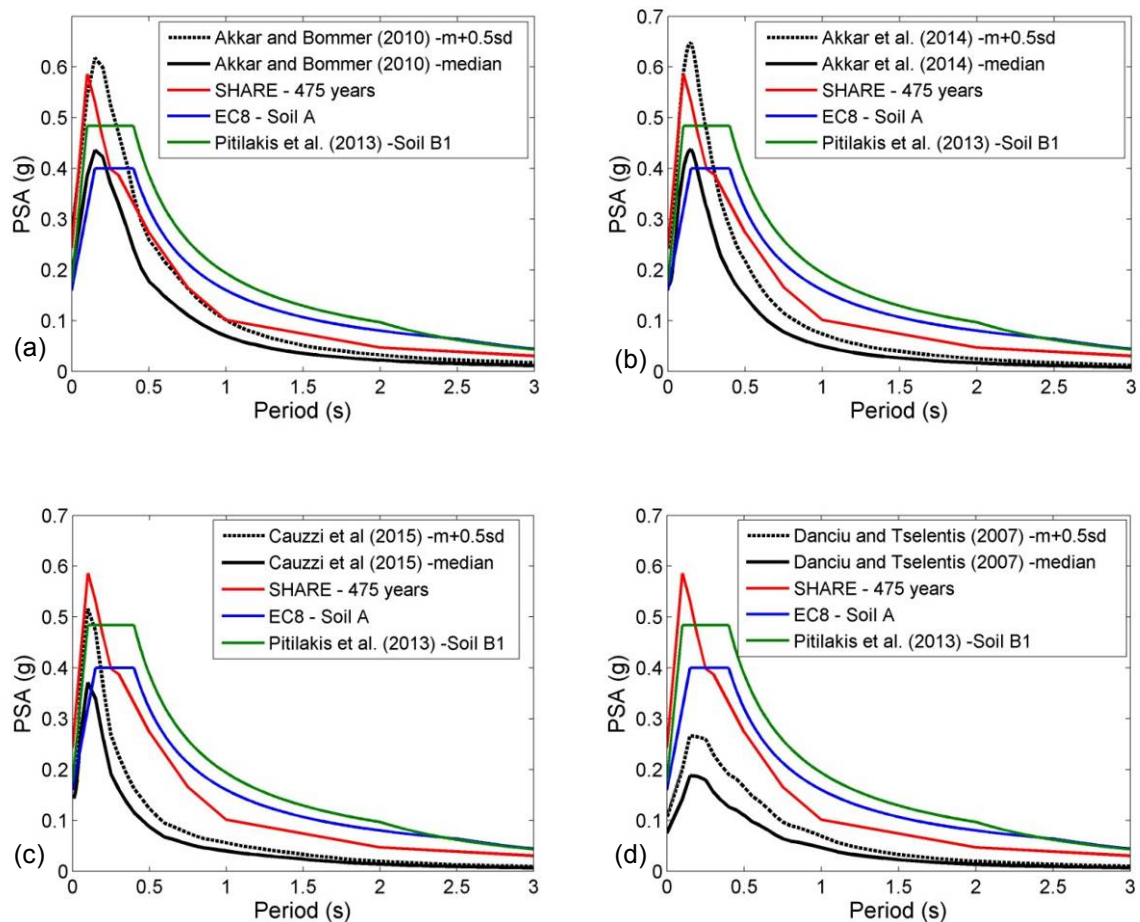


**Fig. 6.18 Comparison of the 5% damped median and the median plus 0.5 standard deviation acceleration spectra of Akkar and Bommer (2010) with SHARE uniform hazard spectrum for Thessaloniki port area, the EC8 elastic response spectrum and Pitilakis et al. (2013) spectrum for the 475 years scenario**



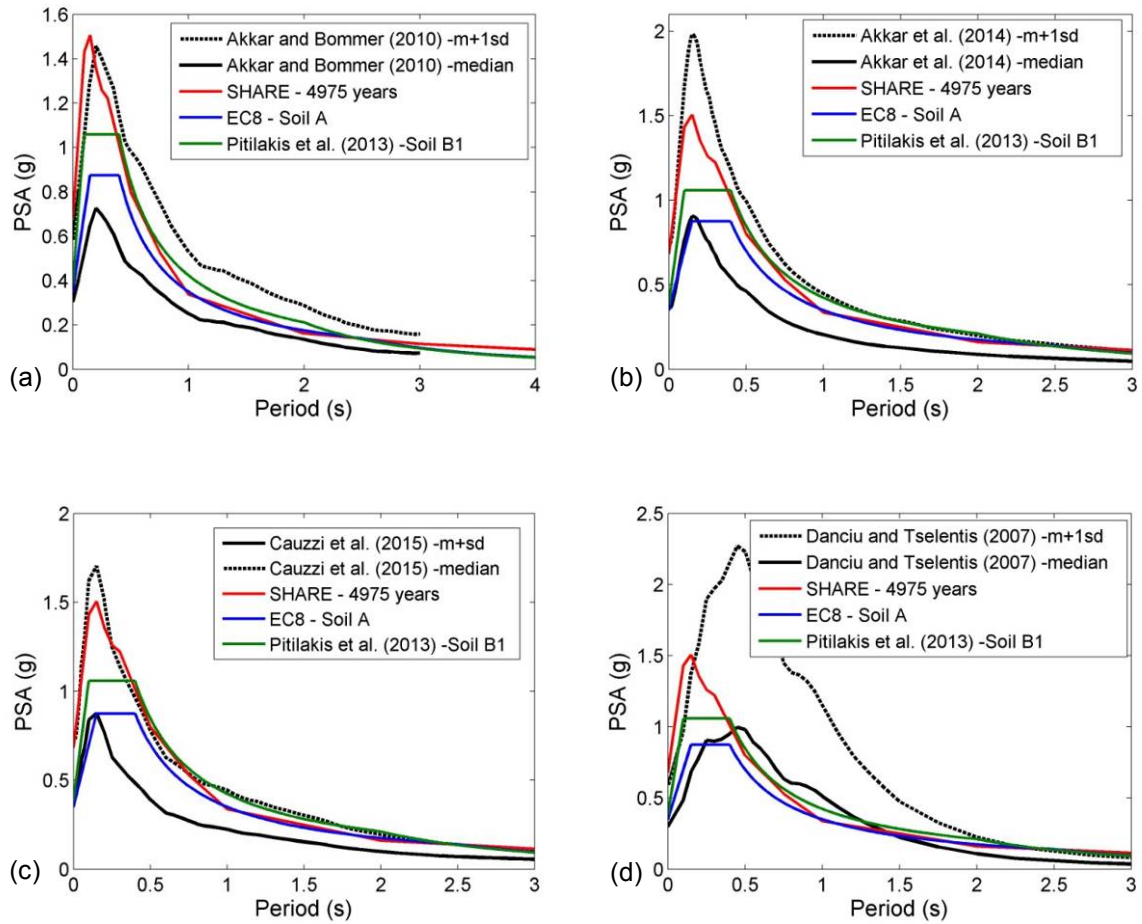


**Fig. 6.19 Comparison of the 5% damped median and the median plus 1 standard deviation acceleration spectra of Akkar and Bommer (2010) with SHARE uniform hazard spectrum for Thessaloniki port, the EC8 elastic response spectrum and Pitilakis et al. (2013) spectrum for the 4975 years scenario**

A set of 15 accelerograms was selected from the European Strong-Motion Database (

Table 6.8) for the 475 years scenario. They are all referring to rock type or stiff soils (ground types A and B according to EC8) with moment magnitude ( $M_w$ ) and epicentral distance  $R$  that range between  $5.5 < M_w < 6.5$  and  $0 < R < 45\text{km}$  respectively. The primary selection criterion is the average acceleration spectra of the set to be of minimal “epsilon” (Baker and Cornell, 2005) at the period range of  $0.00 < T < 2.00\text{sec}$  with respect to the corresponding 5% damped median plus 0.5 standard deviations Akkar and Bommer (2010) spectrum. The optimization procedure is performed using REXEL software (Iervolino et al., 2010) that allows obtaining combinations of accelerograms, which on average are compatible to the reference spectrum. Fig. 6.20 depicts the mean elastic response spectrum of the records in comparison with the corresponding median plus 0.5 standard deviations Akkar and Bommer (2010) spectrum for the 475 years scenario. As shown in the figure, a good match between the two spectra is achieved.

**Table 6.8 List of records used for the dynamic analyses for the 475 years scenario**

Earthquake	Name	Date	Mw	Fault Mechanism	Epicentral Distance [km]	PGA [m/s <sup>2</sup> ]	EC8 Site class	Waveform ID
Umbria Marche (aftershock)		10/6/1997	5.5	normal	5	1.838	A	651
	Valnerina	9/19/1979	5.8	normal	5	1.510	A	242
	SE of Tirana	1/9/1988	5.9	thrust	7	4.037	A	3802
Lazio Abruzzo (aftershock)		5/11/1984	5.5	normal	15	1.411	A	990
	Valnerina	9/19/1979	5.8	normal	5	2.012	A	242
	Kozani	5/13/1995	6.5	normal	17	2.039	A	6115
	Friuli (aftershock)	9/15/1976	6	thrust	12	1.339	A	149
	Umbria Marche 1	9/26/1997	5.7	normal	23	1.645	A	763
	Friuli (aftershock)	9/15/1976	6	thrust	14	2.586	B	134
	Patras	7/14/1993	5.6	strike slip	9	3.337	B	1932
	Kalamata	9/13/1986	5.9	normal	11	2.670	B	414
	Umbria Marche 2	9/26/1997	6	normal	11	5.138	B	594
Montenegro (aftershock)		5/24/1979	6.2	thrust	17	1.708	B	229
	Kefallinia island	1/23/1992	5.6	thrust	14	2.223	B	6040
	Ano Liosia	9/7/1999	6	normal	14	2.159	B	1714

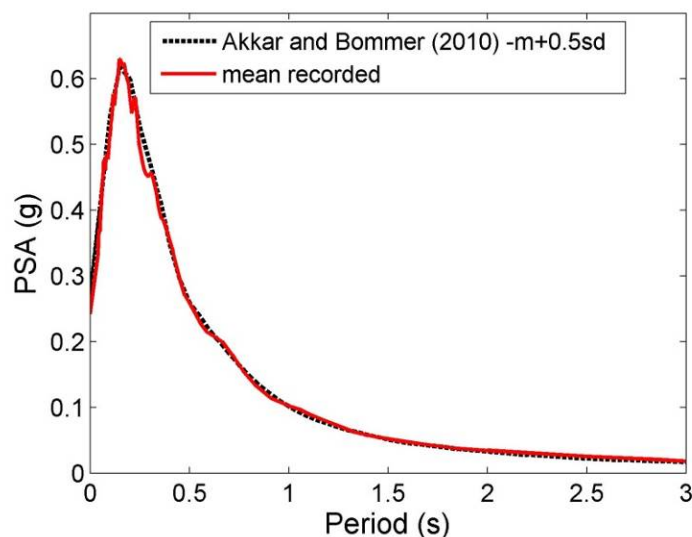


**Fig. 6.20 Average elastic response spectrum of the input motions in comparison with the corresponding median plus 0.5 standard deviations Akkar and Bommer (2010) spectrum for the 475 years scenario**

For the 4975 years scenario the selection of real records to fit the median plus one standard deviation Akkar and Bommer (2010) spectrum that corresponds to the extreme event was not possible as records were not available. Thus, synthetic accelerograms to fit the median plus one standard deviation Akkar and Bommer (2010) spectrum were computed with



SeismoMatch code starting from a set of recorded waveforms (4975 years scenario I). SeismoMatch is an application capable of adjusting earthquake accelerograms to match a specific target response spectrum, using the wavelets algorithm proposed by Abrahamson (1992) and Hancock et al. (2006). This procedure is supported recently by Grant and Diaferia (2012) who have shown that spectrum matching does not seem to lead to significant bias in structural analysis results. The matching period range was adjusted as  $0.05 < T < 2.00$  sec and the required tolerance was set equal to 0.3. Table 6.9 presents the characteristics of the 10 real records used to derive the synthetic motions obtained from SHARE database ([www.share-eu.org](http://www.share-eu.org)). These are referring to rock and stiff soils (ground types A and B according to EC8) with  $M_w > 6.5$ ,  $0 < R < 60$  km and  $PGA > 0.4g$ . Finally, Fig. 6.21 presents the target spectrum, i.e. median plus one standard deviation Akkar and Bommer (2010) spectrum for the 4975 years scenario, and the corresponding matched spectra for the considered records.

**Table 6.9 List of records used to derive the synthetic motions for the 4975 years scenario**

Earthquake Name	Date	Mw	Fault Mechanism	Epicentral Distance [km]	PGA [ $m/s^2$ ]	EC8 Site class	Waveform ID
Cape Mendocino	25/04/1992	7.01	Reverse	4.51	6.499	B	NGA_828
Northridge-01	17 /01/1994	6.69	Reverse	8.48	9.161	B	NGA_1004
Loma Prieta	18/10/1989	6.93	Reverse-Oblique	7.17	6.315	B	NGA_753
Tabas	16/09/1978	7.35	Oblique	57.00	10.174	B	ESMD_60
Chi-Chi, Taiwan	20/09/1999	7.62	Reverse-Oblique	32.67	8.059	B	NGA_1197
Duzce, Turkey	36505	7.10	Strike-Slip	27.17	8.715	B	T-NSMP_1596
South Iceland	17/06/2000	6.57	Strike-Slip	15.00	5.536	A	ESMD_381
Kobe, Japan	16/01/1995	6.90	Strike-Slip	8.70	4.997	B	NGA_1111
Manjil, Iran	20/06/1990	7.37	Strike-Slip	40.43	5.048	B	NGA_1633
Hyogo - Ken Nanbu	16/01/1995	6.90	Strike-Slip	16.60	8.206	-	C&F_956

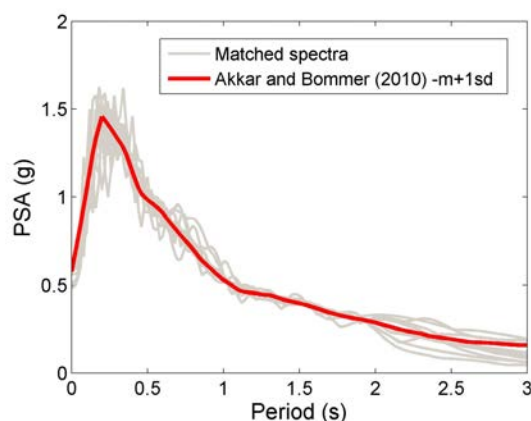


**Fig. 6.21 Target median plus one standard deviation Akkar and Bommer (2010) spectrum for the 4975 years scenario and matched spectra for the considered records**

In addition to the synthetic motions, broadband ground motions at each of the three selected sites (A, B and C) were generated to be used as input for non-linear site response analyses at the port sites using 3D physics-based “source-to-site” numerical simulations (4975 years scenario II). Numerical simulations of seismic wave propagation, including a full 3D model both of the seismic source and of the source-to-site propagation path, were carried out using a high-performance computer code called SPEED (Mazzieri et al., 2013), based on the Discontinuous Galerkin Spectral Elements Method (DGSEM). Further details regarding the numerical approach as well as the 3D model of the broader Thessaloniki area are provided in Smerzini et al. (submitted). For the aim of this work, earthquake ground motions at the port were simulated considering an extreme rupture scenario breaking the whole Anthemountas fault zone with  $M_w = 7$  and outcropping bedrock conditions, i.e.  $V_{S30} = 800$  m/s, under the hypothesis of linear visco-elastic behavior. The 3D spectral-element model is illustrated in Fig. 6.22. Note that it is a large-scale model which can propagate up to about 2 Hz and it extends over a volume of about  $82 \times 64 \times 31$  km<sup>3</sup>, leading to about  $60 \cdot 10^6$  degrees of freedom. The geometry and the main parameters of the kinematic fault rupture model assumed for the extreme scenario are summarized in Table 6.10.

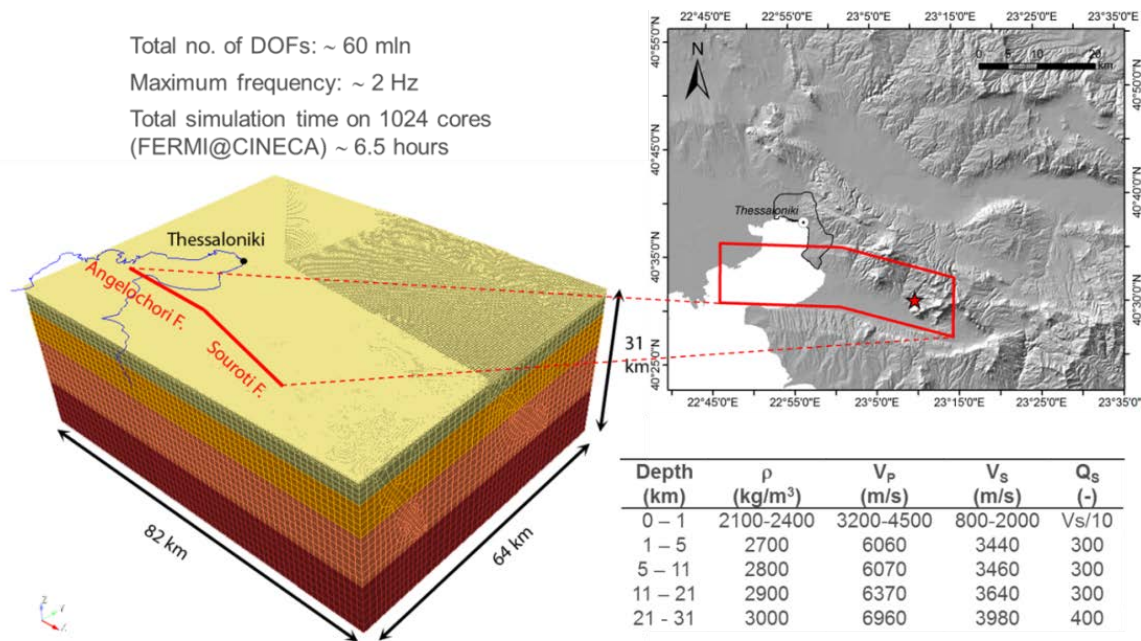


**Fig. 6.22 3D spectral element model to simulate deterministically the extreme scenario.**

Results provided by 3D numerical simulations are limited to relatively low frequency, up to about 2 Hz. To make 3D waveforms usable in engineering applications, broadband (BB) time histories at the selected Thessaloniki port sites were generated relying on a hybrid method (see e.g. Frankel, 2009; Graves and Pitarka, 2010; Mena et al., 2010; amongst others). Specifically, for each site, Low-frequency (LF) waveforms obtained by SPEED are combined with high-frequency (HF) synthetics obtained through the method by Sabetta and Pugliese (1996), using suitable matching filters in the frequency domain (frequency range = 1.4-1.8 Hz). Broadband ground motions are, then, post-processed with an acausal bandpass 3<sup>rd</sup> order Butterworth filter between 0.05-50 Hz and baseline correction according to the procedure proposed by Paolucci et al. (2011). Two-component horizontal (EW and NS)

acceleration time histories and the corresponding pseudo-acceleration response spectra (at 5% damping) are provided at each of the three selected sites: Pier 3 (Profile A), Pier 6 (Profile B) and Pier 1 (Profile C). Thus, for each site, the computed two horizontal (EW and NS) acceleration time histories are used as input on outcropping bedrock motion ( $V_{s,30} = 800$  m/s) for two separate 1D site response analyses.

**Table 6.10 Kinematic source parameters for the 3D extreme scenario.**

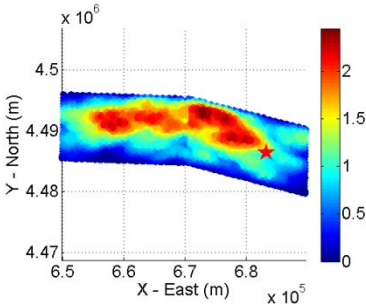
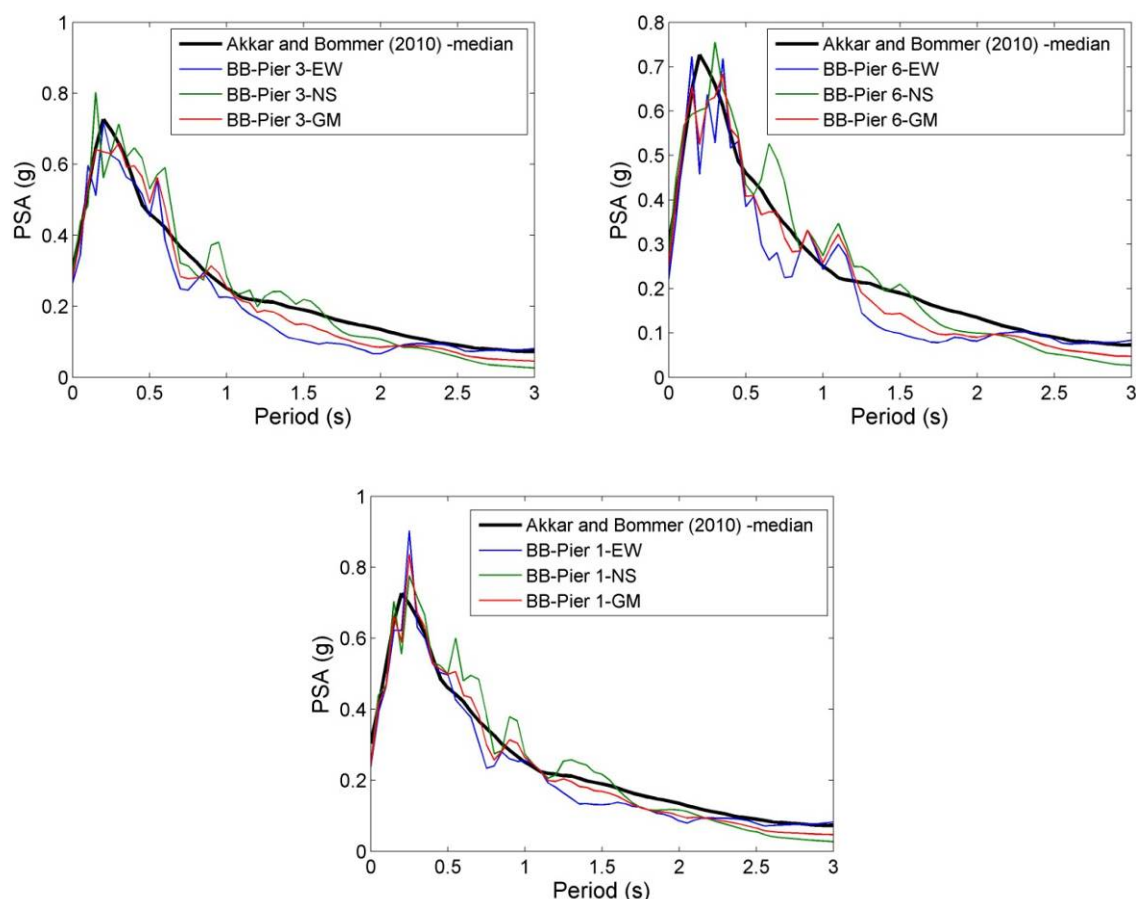
Parameter	Extreme scenario E00564
Seismic Fault	Anthemountas (Souroti + Angelochori)
$M_w$	7.0
L x W (km)	41 x 21
Top depth (km)	0
Hypocenter (°E, °N)	(23.163,40.508)
Focal Depth (km)	8.8
Strike (°)	272-285
Dip (°)	60
Rake (°)	-90 (pure normal)
Rise Time $\tau$ (s)	0.6
Rupture Velocity $V_R$	$0.85 \cdot V_s$
Slip time function	$s(t) = 1/2 \cdot \left[ 1 + \operatorname{erf} \left( 4 \cdot \frac{t - 2\tau}{\tau} \right) \right]$ (erf=error function)
$k^2$ slip distribution (Herrero and Bernard, 1994)	

Fig. 6.23 depicts the computed pseudo-acceleration response spectra (at 5% damping) of the two horizontal components and the geometric mean of horizontal components in comparison with the median Akkar and Bommer (2010) spectrum for the three port sites. A good agreement of the computed response with the corresponding median predicted spectrum of Akkar and Bommer (2010) is generally shown.



**Fig. 6.23** 5% damped pseudo-acceleration response spectra of the two horizontal components (EW and NS) and the geometric mean of horizontal components (GM) in comparison with the median Akkar and Bommer (2010) spectrum for the three Thessaloniki port sites (piers 3, 6 and 1).

#### Site response analyses for the selected seismic scenarios

Detailed one-dimensional (1D) equivalent linear analyses (EQL) and nonlinear (NL) seismic response analyses which take also into account the potential for liquefaction are performed for the selected seismic scenarios. Three representative soil profiles (denoted as A, B and C, see Fig. 6.3) are considered for the site response analyses defined based on previous studies and new measurements (see section 6.2.1.2). The numerical codes Strata (Rathje and Kottke (2010) and Cyclic1D (Elgamal et al., 2015) are used in the computations.

Strata performs 1D linear-elastic and equivalent-linear site response analyses using time series or random vibration theory ground motions. It allows for stochastic variation of the site properties, including the shear modulus reduction and material damping curves, shear-wave velocity, layering and depth to bedrock. In particular, time-domain 1D equivalent-linear site response analyses are carried out in Strata for the three representative soil profiles using as input motions at the seismic bedrock the ones estimated and selected for the 475 years and 4975 years seismic scenarios (I and II). Appropriate modulus reduction and damping curves that describe the variation of shear strain ( $\gamma$ ) with material shear modulus ( $G$ ) and hysteretic damping ratio ( $D$ ) derived for the Thessaloniki port soil types (Pitilakis and Anastasiadis, 1998) are used.

To investigate the impact of the uncertainty in the shear wave velocity ( $V_s$ ) profiles on the simulation results, the analyses are performed considering the base-case geotechnical models for the three sites, but with varying velocities to reflect the shear-wave velocity profiles considering a standard deviation of the natural logarithm of the  $V_s$  equal to 0.2. In particular, 100 realizations of the  $V_s$  profiles are considered in Strata using Monte Carlo simulations and the calculated response from each realization is then used to estimate statistical properties of the seismic response. In total 1500 simulations are performed for the 475 years scenario and 1200 simulations for the 4975 (I and II) scenarios. The randomization of the shear-wave velocity and the incorporation in Monte Carlo simulations is performed through the use of the model proposed by Toro (1995), which provides a framework for generating layering and then to vary the shear-wave velocity of these layers incorporating the correlation between the velocities in adjacent layers. First, the statistical distribution and properties of the soil need to be characterized. The shear-wave velocity at mid-depth of the layer is described by a log-normal distribution. The correlation model that is a function of both the depth and the thickness of the layer is adopted based on the  $V_{s,30} = 180$  to 360 m/s site class as defined in Toro (1995).

The results are presented in terms of median values and median  $\pm 1$  standard deviation for each of the three representative soil profiles and for the selected seismic scenarios with return periods 475 and 4975 years respectively. In particular, the following parameters were calculated for each of the 100 profiles of  $V_s$ :

- 5% damped elastic acceleration response spectra at the ground surface;
- spectral amplification ratios (the ratio of 5% damped acceleration response spectra at the ground surface to the 5% damped acceleration response spectra at the bedrock);
- Fourier amplitude ratios (Fourier amplitude spectra at the ground surface to the Fourier amplitude at the bedrock);
- variation of peak ground acceleration (PGA) with depth;
- variation of maximum shear strain with depth;
- variation of maximum shear stress with depth;
- comparison of the computed elastic acceleration response spectra with the corresponding spectra provided by EC8, SHARE and Pitilakis et al. (2012, 2013).

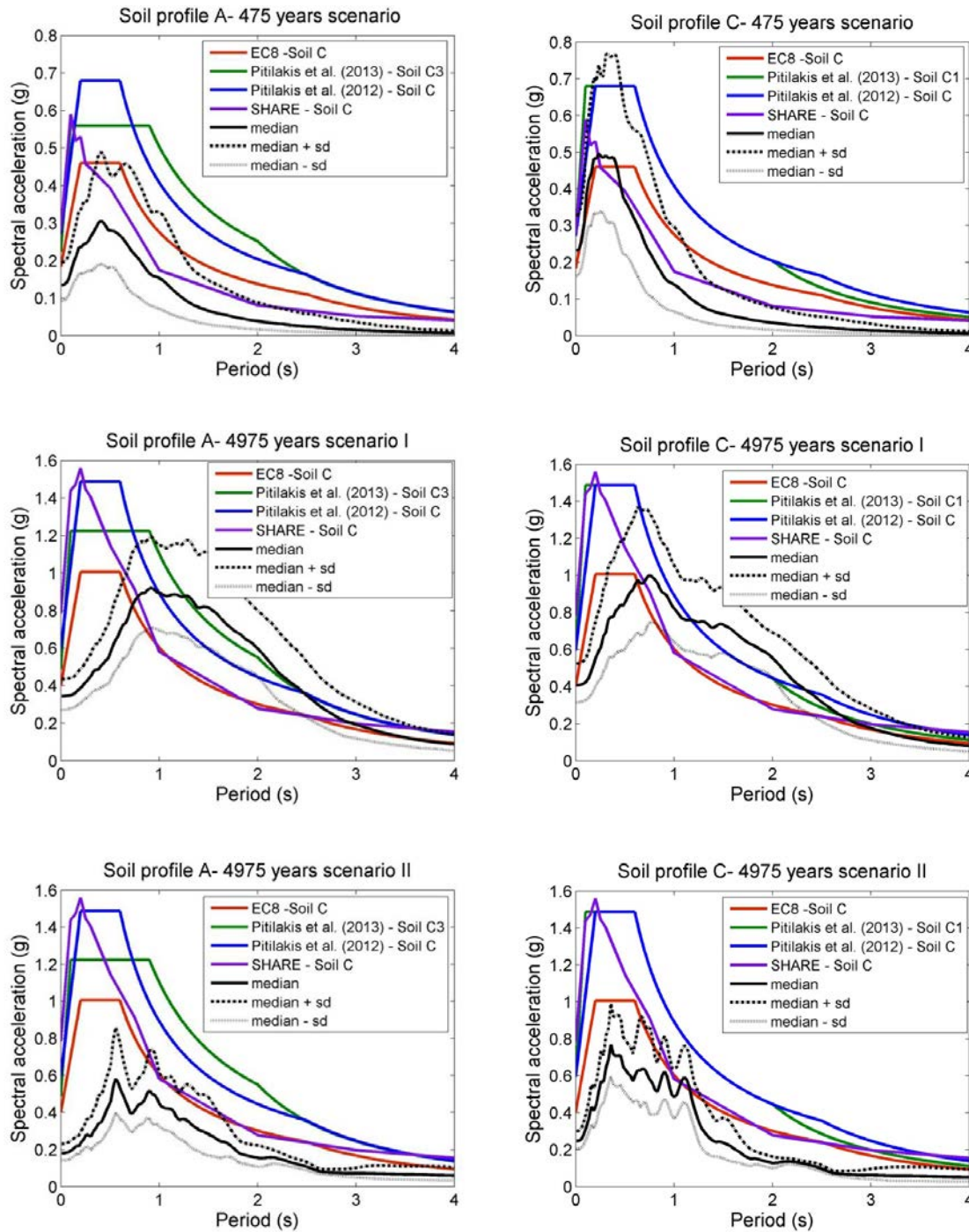
Due to space limitations only some indicative results in terms of PGA at the ground surface and acceleration response spectra are shown herein while representative results for all seismic scenarios and soil profiles in comparison with the NL approach are presented in Appendix B. Table 6.11 shows a comparison of the computed median PGA at the ground surface derived from the EQL approach for soil profiles A, B and C with the corresponding PGA values provided by EC8, Pitilakis et al. (2012, 2013) and SHARE for the selected seismic scenarios. It is observed that among the three soil profiles, soil profile C is associated with larger PGA values at the ground surface for all seismic scenarios. For the 475 years scenario, the computed PGA values for all soil profiles are generally in good agreement with the corresponding values provided by EC8, SHARE and Pitilakis et al. (2012, 2013) with EC8 and SHARE providing the lower and higher PGA values respectively. For the extreme scenario, SHARE largely overpredicts the computed PGA values for all soil profiles while Pitilakis et al. (2012, 2013) predicts also relatively higher PGA values. Finally, EC8 may underestimate or overestimate the computed PGA values depending on the soil profile and the considered scenario (4975 years I or II).

Fig. 6.24 illustrates the computed median and the median  $\pm 1$  standard deviation 5% damped elastic acceleration response spectra at the ground surface indicatively for soil profiles A and C in comparison with the corresponding elastic spectra given in EC8, Pitilakis et al. (2012, 2013) and SHARE spectra considering period dependent amplification factors to account for site effects (Pitilakis et al., 2015). Although not presented herein, it is noted that the derived response spectra shapes and amplification for soil profile B are quite similar with the ones shown for soil profile C. It is seen that for the 475 years scenario the computed median spectral values for soil profile A are lower compared with the relative values of literature spectra while SHARE and EC8 do not provide conservative results for all periods of the corresponding spectrum for soil profile C. The comparisons for the extreme scenario I show that, although SHARE and Pitilakis et al. (2012, 2013) predict larger PGA values for the extreme scenario (see Table 6.11), none of the literature spectra can predict the computed higher spectral values at higher periods. Among the considered normalized spectra, the one provided by Pitilakis et al. (2013) seems to capture more closely the computed seismic response for the 4975 years scenario I. Finally, the comparisons for the extreme scenario II indicate that the median computed spectra are generally overpredicted by all literature spectra.

**Table 6.11 Comparison of the computed median PGA at the ground surface derived from the EQL approach for soil profiles A, B and C with the corresponding PGA provided by EC8, Pitilakis et al. (2012, 2013) and SHARE for the selected seismic scenarios**

Method	Scenario	PGA (g)
EC8_Soil C	475	0.184
	4975	0.403
Pitilakis et al (2012)_Soil C	475	0.272
	4975	0.595
Pitilakis et al (2013)_Soil C1	475	0.272
	4975	0.595
Pitilakis et al (2013)_Soil C3	475	0.224
	4975	0.490
SHARE_Soil C	475	0.280
	4975	0.784
Soil profile A_EQL	475	0.149
	4975 I	0.362
	4975 II	0.208
Soil profile B_EQL	475	0.233
	4975 I	0.414
	4975 II	0.248
Soil profile C_EQL	475	0.244
	4975 I	0.467
	4975 II	0.269





**Fig. 6.24 Comparison of the computed elastic response spectra derived from the EQL approach for soil profiles A (left) and C (right) with the corresponding spectra provided by EC8, Pitilakis et al. (2012, 2013) and SHARE for the selected seismic scenarios**

For the evaluation of the liquefaction potential, a thorough understanding of the site conditions, soil stratigraphy, material properties and their variability as well as the spatial extent of potentially liquefiable layers need to be developed. Investigations required for this purpose should as a minimum include the execution of either in situ Standard Penetration Tests (SPT) or Cone Penetration Tests (CPT) to characterize the soil conditions. Thus,

before the onset of the detailed liquefaction assessment using Cyclic1D, a preliminary evaluation of the liquefaction potential to identify the layers susceptible to liquefy, was performed according to EC8, NCEER 97 and Seed et al. (2003).

By taking into account the guidelines of EC8 as well as the available geotechnical information of the port (see Fig. 6.3) we have quantitatively evaluated the liquefaction potential of the subsoil layers at soil profiles A and C where SPT and laboratory data were made available (Table 6.1). For soil profile A, the liquefiable soil formations were found at depths  $z=-9\div 11\text{m}$ ,  $z=-14\div 20\text{m}$  and  $z=-26.5\div 36\text{m}$ , while for soil profile C at depths  $z=-4\div 20\text{m}$ , which are basically silty/clayey sands and non-plastic silts with low values of  $N_{\text{SPT}}$ .

According to the guidelines of Robertson and Wride (1998) and NCEER 97, liquefaction potential was evaluated in the position of boreholes B-3, B-70 and B-71 where CPT data were available (see Table 6.1). All these boreholes are located close to the selected soil profile C. Liquefiable layers are found at several depths ( $z=-4.4\div 6.8\text{m}$ ,  $z=-7.6\div 7.8\text{m}$ ,  $z=-9.2\text{m}$ ,  $z=-16.6\text{m}$ ,  $z=-17.2\div 17.4\text{m}$  and  $z=-20\text{m}$ ) but not greater than twenty meters from the ground surface.

In order to evaluate the potential of liquefaction of the very loose fine-grained soil layers found in soil profile A, the liquefaction susceptibility criteria proposed by Seed et al. (2003) were applied for the fine-grained soil layers of profile A. Potentially liquefiable soil formations are found at depths  $z=-4\div 5\text{m}$  and  $z=-6\div 9\text{m}$ .

Based on the preliminary evaluation of the liquefaction potential and the available in situ and laboratory data, Cyclic1D is used to perform NL site-response analyses including liquefaction for the considered soil profiles and seismic scenarios. The finite element formulation implemented in Cyclic1D is based on a fully coupled solid-fluid approach (known as u-p formulation) (e.g. Chan, 1988). The liquefaction model employed (Parra, 1996; Yang, 2000) was developed within the framework of multi-yield-surface plasticity (e.g. Prevost, 1985). The liquefiable soil formations considered were found at depths  $z=-2\div 11\text{m}$ ,  $z=-15\div 20\text{m}$  and  $z=-27\div 36\text{m}$  for soil profile A, at depths  $z=-3\div 14\text{m}$  for soil profile B and at depths  $z=-5\div 20\text{m}$  for soil profile C. The granular soils (e.g. sands, gravels, non-plastic silts) that are not susceptible to significant pore pressure build-up are simulated using an elastic-plastic material in which a confinement-dependent shear response is considered. For the clay/rock materials an elastic-plastic material is considered where shear behavior is insensitive to the confinement change.

The corresponding variability in the  $V_s$  profile was assessed considering except for the base-case  $V_s$  model, upper-range and lower-range models utilizing appropriate logarithmic standard deviations for the  $V_s$  profile. In particular, three runs were performed for each soil profile and input motion considering the base-case model and the base-case  $\pm 1$  logarithmic standard deviation models. The natural logarithm of the  $V_s$  was taken equal to 0.2 consistently with the Strata simulations.

The results are presented again for the three representative soil profiles (considering for each soil profile the base-case and the base-case  $\pm 1$  logarithmic standard deviation  $V_s$  models) for the 475 years and the 4975 years (I and II) scenarios. In particular, the following parameters were calculated:

- 5% damped elastic acceleration response spectra at the ground surface;
- spectral amplification ratios (the ratio of 5% damped acceleration response spectra at the ground surface to the 5% damped acceleration response spectra at the bedrock);



- the variation of peak ground acceleration (PGA) with depth;
- the variation of maximum shear strain with depth;
- the variation of maximum shear stress with depth;
- the variation of residual horizontal and vertical displacements with depth;
- the variation of effective confinement with depth;
- the variation of excess pore water pressure with depth;
- shear stress-strain curves at various depths;
- effective stress path response at various depths.

Only some indicative plots are presented herein whereas representative results for all seismic scenarios and soil profiles are presented in Appendix B. Fig. 6.25 shows comparative graphs between the EQL and NL approaches for the 475 years and 4975 years I scenarios for profile A while Fig. 6.26 depicts typical results of the NL analysis.

Observed differences especially between the EQL and the NL modeling approaches are commented in the following. It is shown that the EQL approximation is generally associated with larger PGA values at the ground surface than the NL analysis. The differences between the two approaches in the estimated PGA values are more pronounced for soil profile C and for the extreme seismic scenario (4975 years scenario I). The spectral shapes and hence the fundamental soil frequencies are well compared between the two approaches for the 475 year scenario while the response is very different for the 4975 years scenarios (especially for the 4975 scenario I) that is associated with increasing shear strain accumulation (see Fig. 6.25). For both scenarios, the EQL spectral shapes are flatter and have less period-to-period fluctuations than the NL spectral shapes. The smaller spectral values predicted by the NL approach for the extreme seismic scenario are attributed to larger high-strain damping predicted by Cyclic1D model. Using nonlinear backbone curve models, it is relatively easy to match the modulus reduction curves, but the use of Masing or extended Masing rules with the backbone curves often provides poor fits to damping curves (overestimating damping at high levels of strain). Moreover, the liquefaction model employed in Cyclic1D is able to accommodate yielding and build-up of excess pore pressure which may result in loss of effective confining stress and shear strength, degradation of shear stiffness and permanent ground deformations due to lateral spreading at high strain levels. Near-surface yield and the subsequent liquefaction-induced permanent deformations will attenuate high-frequency surface motions, which cannot be simulated by the EQL analysis. EQL and NL analyses are also compared examining spectral amplification ratios. EQL spectral amplification ratios are smaller from NL ratios for the 475 years scenario at certain periods generally associated with the fundamental periods of the soil profiles while they are significantly larger for the extreme seismic scenario (4975 years scenario I). It is also worth noting that the results of the EQL approach are associated with relatively larger standard deviation values. The difference in the variability computed by the two approaches is generally more pronounced for the extreme scenario (e.g. see Fig. 6.25, bottom). This could be attributed to the larger number of EQL computations performed with varied  $V_s$  profiles (using Monte Carlo simulations) compared to the NL ones.

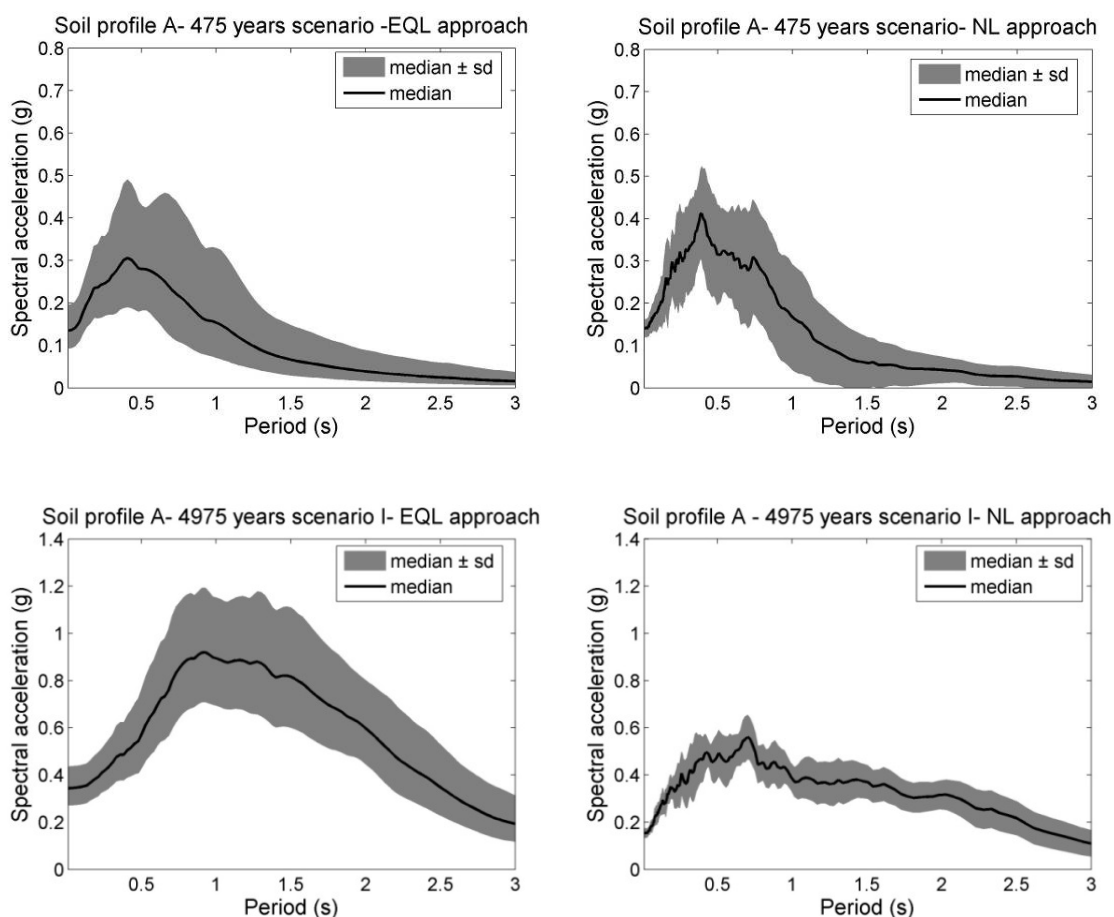


**Fig. 6.25 Median  $\pm$  standard deviation elastic 5% response spectra at the ground surface for soil profile A using the EQL (left) and NL (right) approaches for the 475 years scenario (top) and the 4975 years scenario I (bottom).**

The results of the NL approach indicate (although not fully presented herein) that liquefaction is evident for all soil profiles and scenarios. However, for the extreme scenario the liquefiable layers are larger and extended to greater depths (up to 35m, e.g. see Fig. 6.26-left). Among the three representative soil profiles, liquefaction effects are shown to be more pronounced in profile A. Large variability in the computed permanent displacements is shown for the different seismic input motions (e.g. see Fig. 6.26-right). Generally low-frequency input motions increase the accumulation of lateral deformations and settlements. The computed maximum horizontal displacement values (resulting from lateral spreading) when considering the basic geotechnical models are 4.5 cm and 18.6 cm for the 475 and 4975 years seismic scenarios respectively, while the corresponding values for the vertical displacements (that refer to settlements resulting from the reconsolidation of the liquefied or partially liquefied soil) are 4.8 cm and 11.0 cm.

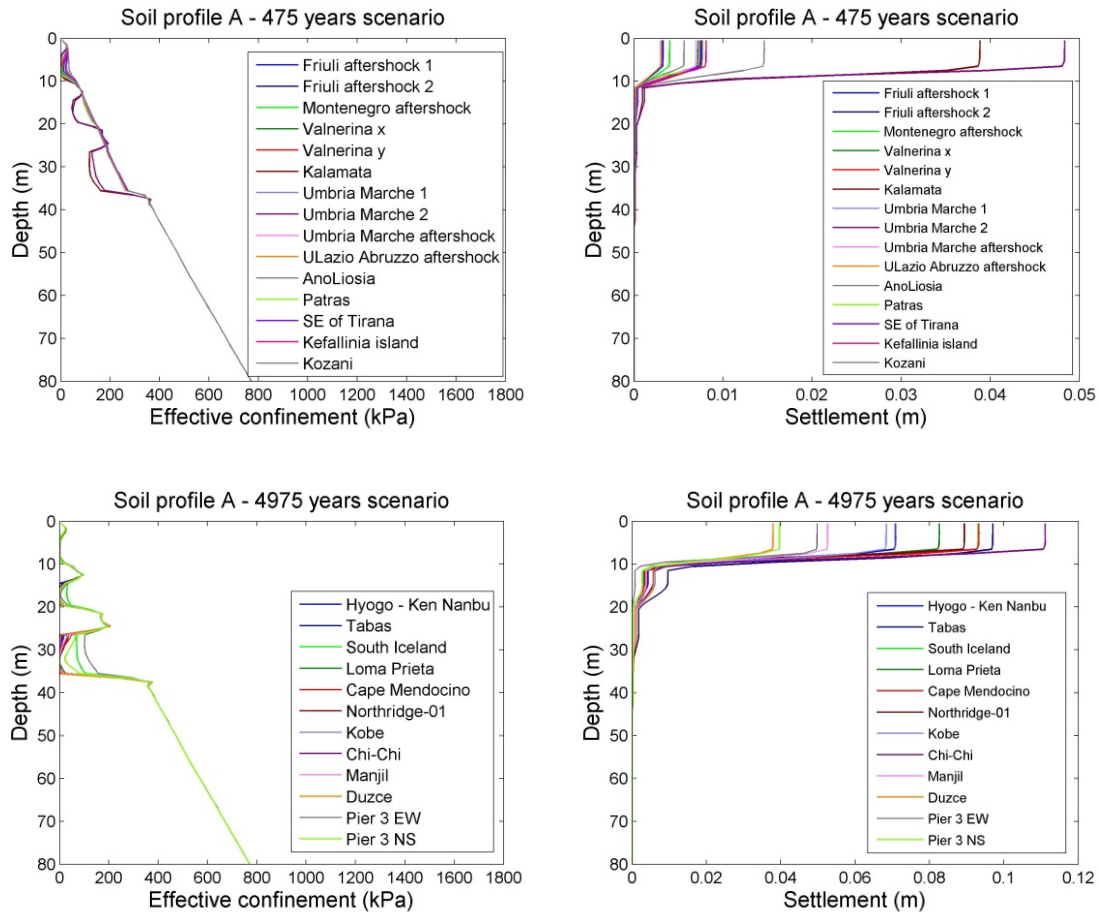


**Fig. 6.26** Variation of effective confinement (left) and settlement with depth (right) for soil profile A for the 475 years scenario (top) and the 4975 years scenario (bottom).

### Scenario based risk analysis

The scenario-based risk assessment of the port buildings and infrastructures is initially performed taking into account the potential physical damages and corresponding losses of the different components of the port. Buildings, waterfront structures, cargo handling equipment and the power supply system are examined using the fragility models for ground shaking and liquefaction (

Table 6.5). In particular, the vulnerability assessment is performed for the 475 and 4975 years scenarios (I and II) based on the EQL and NL site-response analyses. The results from soil profile A, B or C were considered in the fragility analysis, depending on the proximity of each component to the location of the three soil profiles. In particular, for the EQL approach, the calculated PGA values at the ground surface from the total analysis cases (i.e. 2200 analyses) for each soil profile were taken into account for the vulnerability assessment due to ground shaking. For the NL approach, in addition to the PGA values, the PGD (horizontal and vertical) values at the ground surface were also considered to evaluate the potential damages to buildings and infrastructures due to liquefaction effects. Finally, the combined damages are estimated by combining the damage state probabilities due to the liquefaction ( $P_L$ ) and ground shaking ( $P_{GS}$ ), based on the assumption that damage due to ground shaking is independent and not affect the damage due to liquefaction (NIBS, 2004). Once the probabilities of exceeding the specified DS are estimated, a median  $\pm 1$  standard deviation damage index  $d_m$  is evaluated, to quantify the structural losses as the ratio of cost of repair to cost of replacement taking values from 0: no damage (cost of repair equals 0) to 1: complete damage (cost of repair equals the cost of replacement). Due to the fact that the cost of the RC and steel (including the infills) structural systems as well as the masonry system totals less than the cost of a (new) building, which also includes non-structural members, the damage indices are multiplied with a reductive coefficient i.e. 0.33 for RC (or 0.38 for RC buildings with more than 5 storeys) and 0.5 for URM and steel buildings, to derive the final damage index. A weighted loss index (WLI) is finally calculated for the buildings to weight the damage index with respect to the built area.

The spatial distribution of the estimated losses for buildings (e.g. Fig. 6.27 to Fig. 6.30) indicates that a non-negligible percentage of the port buildings is expected to suffer significant losses (higher than moderate). The median values of this percentage range from 7% for the design scenario (NL approach) to 37% for the 4975 years scenario I (EQL approach). This is to be expected taking into account that all buildings were constructed with low or no seismic code provisions. Among the considered building typologies, the RC structures appear to be less vulnerable compared to the steel and URM systems.

The estimated losses are also significantly dependent on the analysis approach. In particular, the EQL approach is associated with higher damages and losses even for the design scenario, while for the NL approach the losses to the cranes, waterfronts and electric power substations are expected solely for the 4975 scenario I. The larger damages and losses computed by the EQL approach to port buildings and infrastructures could be attributed to the significantly higher PGA values calculated using the EQL approximation, which, considering that the selected fragility functions for ground shaking use PGA as IM (Table 6.5), lead to higher estimated probabilities of exceeding the specified DS. Thus, even though the vulnerability using the NL approach is assessed considering both ground shaking and liquefaction hazards, the estimated combined exceedance probabilities are still quite lower compared to the ones predicted by the EQL approach. It should be noted, however, that PGA may not be an appropriate IM to characterize the seismic motion especially for the extreme scenario associated with increased shear strain accumulation and deformation demands. Thus, further research is needed on the development of site-specific fragility functions with more efficient scalar or vector IMs that would be able to better characterize not only the seismic intensity (as PGA) but also the total energy content of the earthquake excitation. Finally, the fragility functions used for the liquefaction hazard are generic (NIBS, 2004) reducing the reliability of the finally computed damages and losses for the NL



approach. Hence, as for ground shaking, future work should be also oriented towards the generation of site-specific fragility models for the liquefaction hazard.

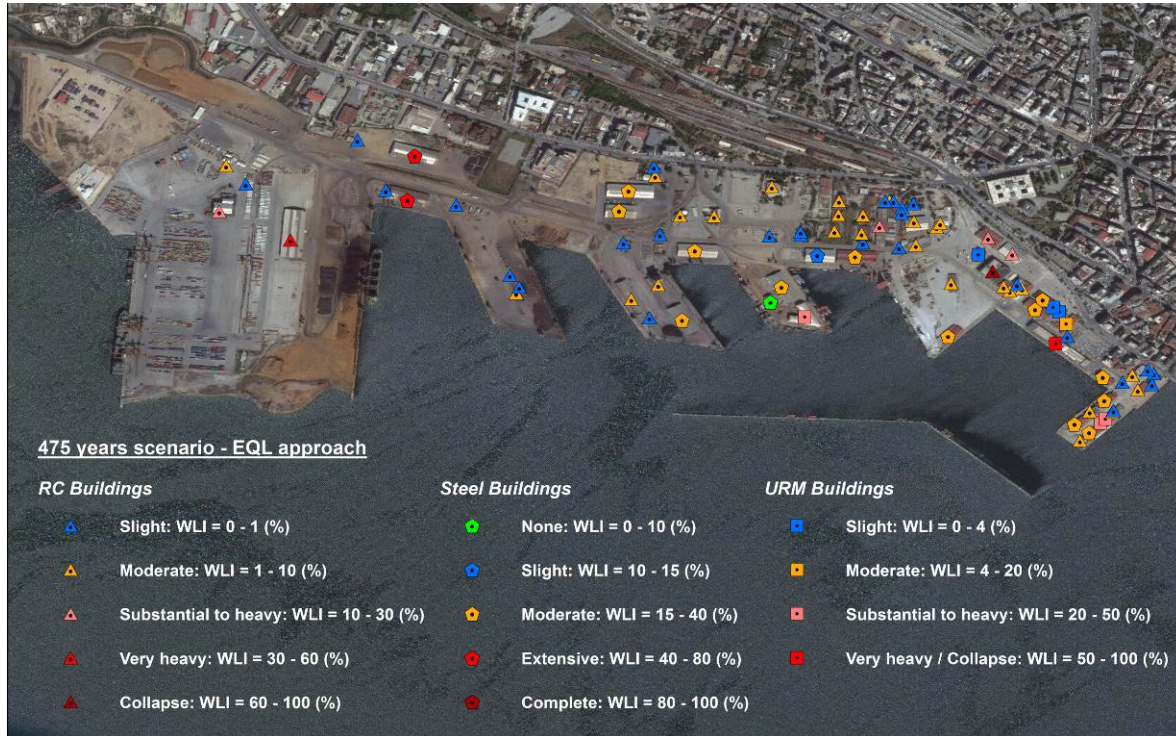


**Fig. 6.27 Spatial distribution of the losses of Thessaloniki's buildings for the 475 years scenario - EQL approach**

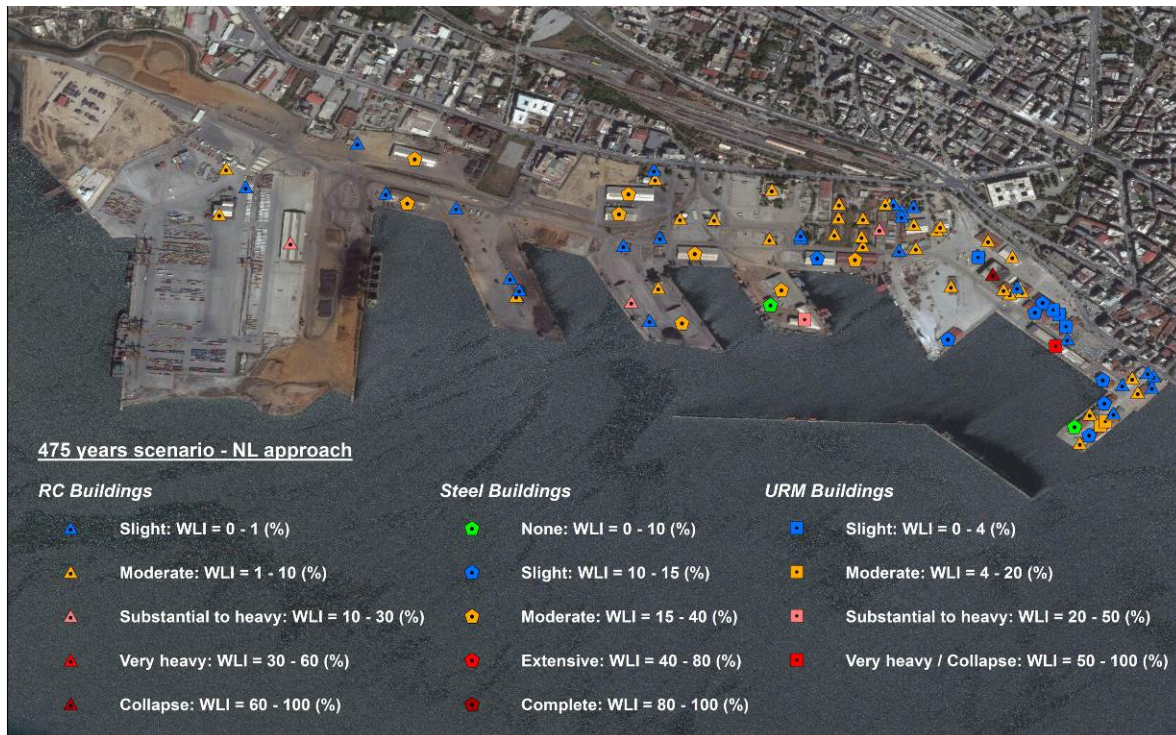


**Fig. 6.28 Spatial distribution of the losses of Thessaloniki's buildings for the 475 years scenario - NL approach**



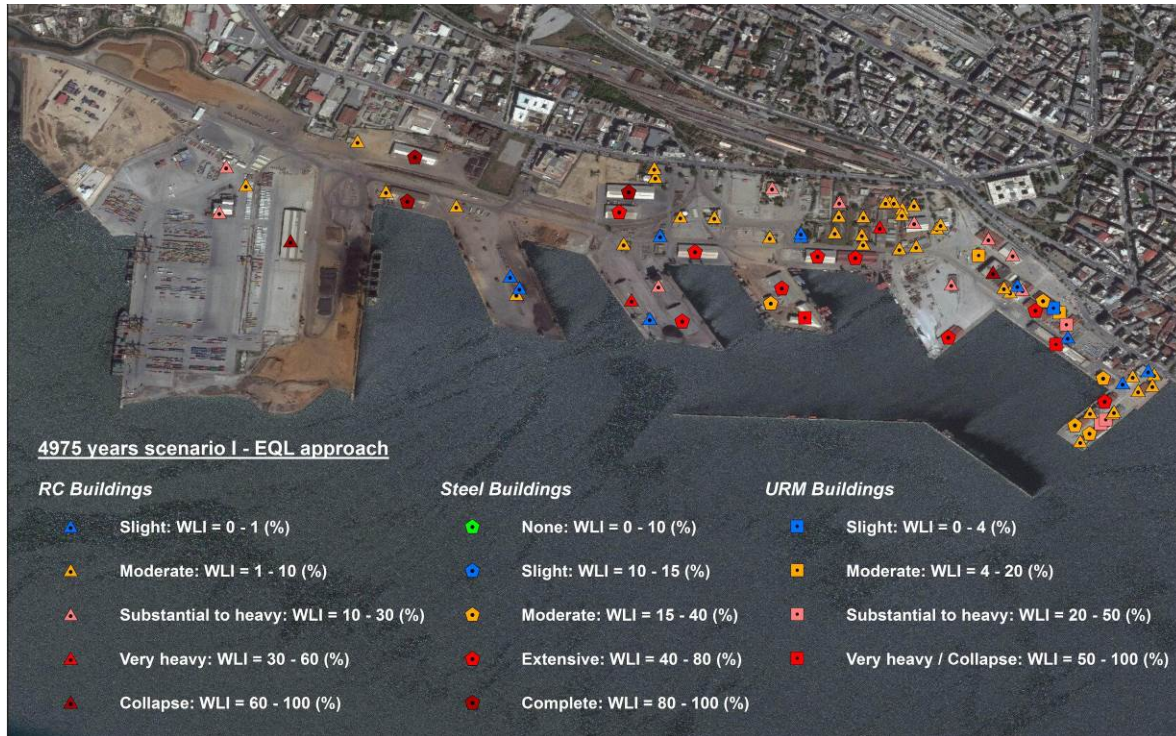


**Fig. 6.29 Spatial distribution of the losses of Thessaloniki's buildings for the 4975 years scenario I- EQL approach**

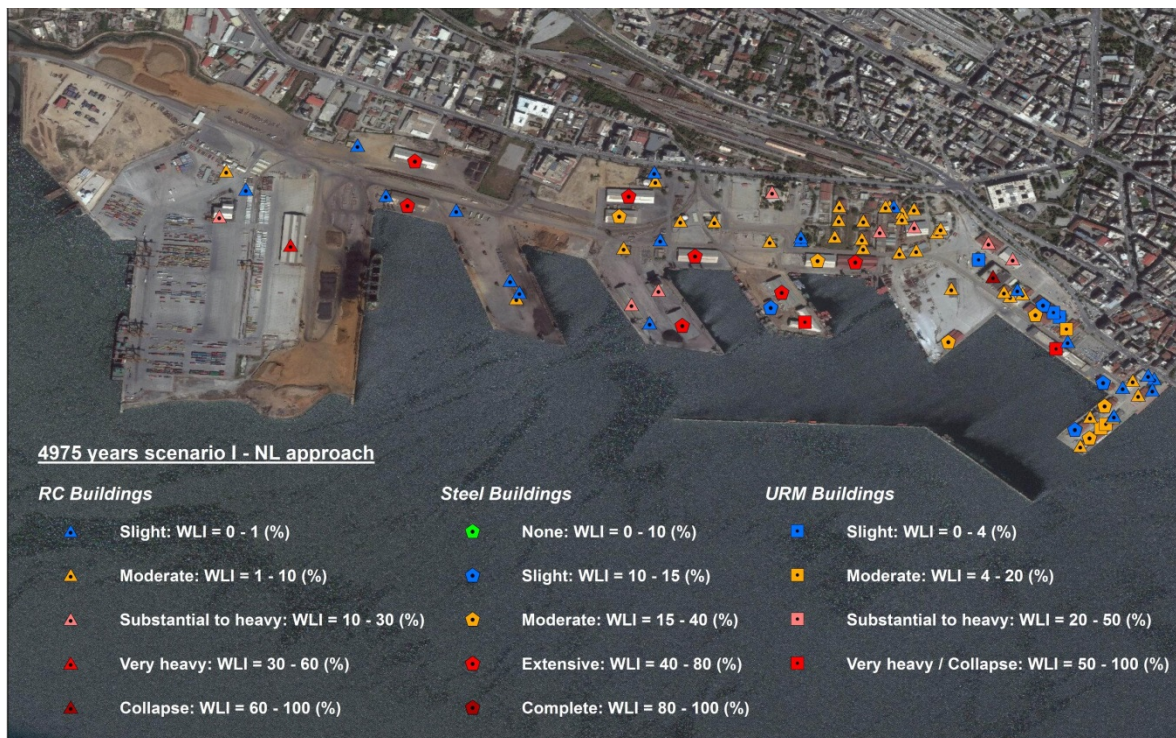


**Fig. 6.30 Spatial distribution of the losses of Thessaloniki's buildings for the 4975 years scenario I- NL approach**

The systemic risk is assessed following the methodology presented in the previous section (PRA approach) taking again into account the interdependencies of specific components. It

is observed that the EQL approach is associated with higher number of non-functional components for all considered seismic scenarios whereas for the NL approach non-functional components are present only for the 4975 years scenario I (see e.g. Fig. 6.31 to Fig. 6.34). The estimated PIs of the port are normalized to the respective value referring to non-seismic conditions. Table 6.12 presents the PIs of the port system in terms of the median normalized performance loss ( $1-PI/PI_{max}$ ) for the different analysis approaches and seismic scenarios. As also evidenced by the estimated functionality state of each component, the port system is non-functional both in terms of TCaH and TCoH for the 4975 years scenario I. A 100% and 67% performance loss is estimated for the TCoH and TCaH respectively when considering the EQL approach for the 475 years and 4975 years II scenarios, while the port is fully functional when considering the NL approach both in terms of TCaH and TCoH for the latter scenarios. Thus, it is observed that among the four different outcomes determined for the extreme scenario for both PIs, the CI passes the stress test in the 4975 years scenario II and NL method, which could be judged as the most reliable. It is noted that the estimated PIs do not change when considering the median+1standard deviation damage indices in the computation of the components' functionality. However, when the median-1standard deviation damage indices are taken into account in the calculations, a 100% performance loss is estimated only for the 4975 years scenario I while the port is fully functional for all the other analysis cases both in terms of TCaH and TCoH.

In the basic analysis, the waterfronts and the distribution electric power substations were considered fully functional if they sustained minor damages and non-functional for higher levels of damage. An alternative analysis is performed where waterfront structures and distribution electric power substations are considered as fully (100%) functional if they suffer minor damages, partially (50%) functional if they suffer moderate damages and non-functional for higher levels of damage. It is noted that the functionality definition for cranes is kept the same as for the basic analysis considering that occurred damages higher than slight in cranes usually necessitate the withdrawal or even their replacement. A minor reduction (1%) of the port performance loss is shown compared to the basic analysis only for the TCaH for two analysis cases (i.e. for the 475 years and 4975 years II scenarios- EQL approach) while all the other cases remained unchanged.

**Table 6.12 Estimated median normalized performance loss of the port system for TCaH and TCoH and comparison with risk objectives for the scenario based assessment.**

Scenario	Analysis type	Performance loss ( $1-PI/PI_{max}$ )		Risk objectives			Stress test outcome	
		TCaH	TCoH	AA-A	A-B	B-C	TCaH	TCoH
475 years	EQL	0.67	1.00	0.10	0.30	0.50	Fail	Fail
	NL	0.00	0.00				Pass	Pass
4975 years I	EQL	1.00	1.00	0.30	0.50	0.70	Fail	Fail
	NL	1.00	1.00				Fail	Fail
4975 years II	EQL	0.67	1.00	Partly pass	Fail			
	NL	0.00	0.00	Pass	Pass			



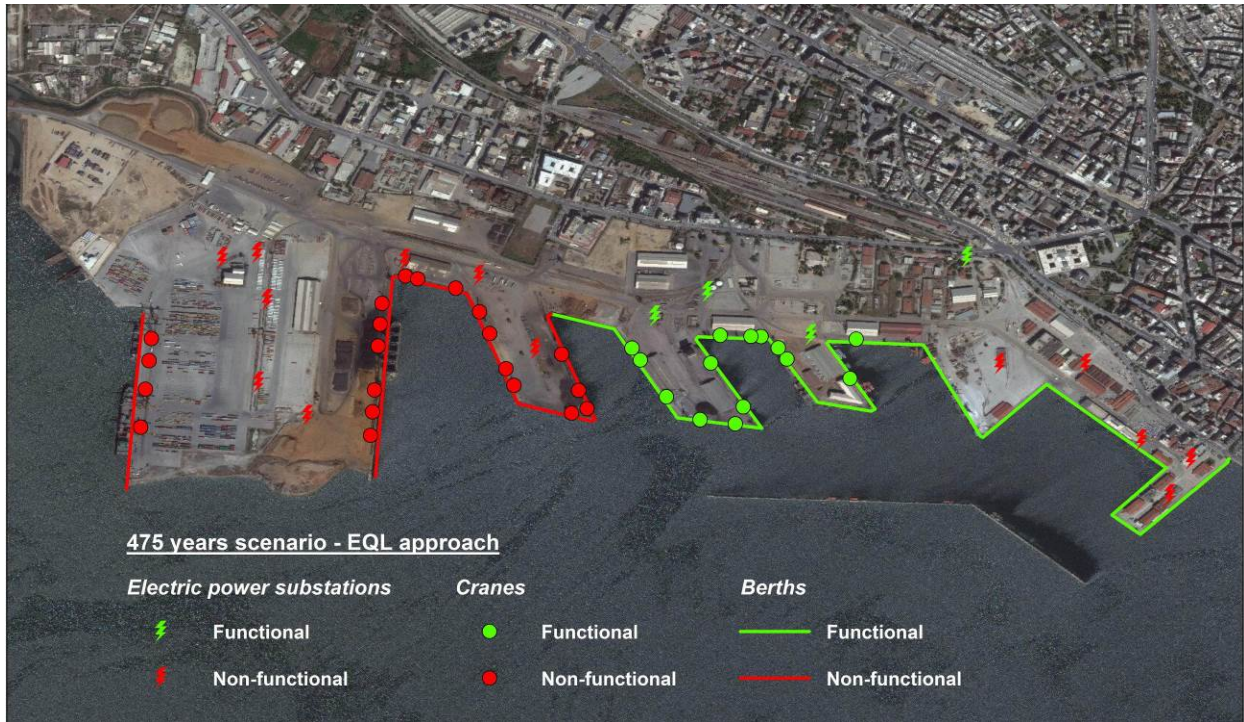


**Fig. 6.31 Spatial distribution of the components functionality for the 475 years scenario - EQL approach**



**Fig. 6.32 Spatial distribution of the components functionality for the 475 years scenario - NL approach**





**Fig. 6.33 Spatial distribution of the components functionality for the 4975 years scenario I- EQL approach**



**Fig. 6.34 Spatial distribution of the components functionality for the 4975 years scenario I- NL approach**

## 6.4 PHASE 3: DECISION PHASE

### 6.4.1 Risk objectives check

In the first step of the decision phase, the risk assessment results are compared with the defined risk objectives to check whether the port system passes, partially passes or fails the stress test and to define the grading system parameters for the next evaluation of the stress test since the performance of the CI or performance objectives can change over time (STREST D5.1 Esposito et al., 2016).

In Fig. 6.11 risk boundaries are plotted together with the MAF curves of the assessed performance loss. With reference to both bulk cargo and container terminals (TCaH, TCoH curves) the port obtains grade B, meaning that the risk is possibly unjustifiable and the CI partly passes this evaluation. The basis for redefinition of risk objectives in the next evaluation of stress test is the characteristic point of risk, which is defined as the point associated with the greatest risk above the ALARP region (blue and red dots for TCaH and TCoH curves respectively). These points are the farthest from the A-B boundary (blue line). The proposed grading system foresees the reduction of the boundary between grades B and C (red line) in the next stress test, which is equal to the amount of risk beyond the ALARP region assessed, represented in this application by the corresponding red dashed lines in case of the bulk cargo and cargo terminals. The plot in Fig. 6.15 (left panel) indicates that the CI receives grade AA (negligible risk), and as expected in this example application, passes the stress test for the tsunami hazard. Indicative scalar performance boundaries in terms of the normalized performance loss are shown in Table 6.12 together with the corresponding results of the scenario based assessment. It is seen that the CI may pass, partly pass or fail for the specific evaluation of the stress test (receiving grades AA, B and C respectively) depending on the selected seismic scenario, the analysis approach and the considered risk metric (TCaH, TCoH). Based on the proposed grading system, for the case which the port obtains grade B and partly passes the stress test, the BC boundary in the next stress test is reduced (i.e. BC: 53% performance loss) while the other boundaries remain unchanged. It is noted that different grades can be derived from the probabilistic and scenario-based assessments varying between AA (for the scenario based and the probabilistic tsunami risk assessments) and C (for the scenario-based and probabilistic seismic risk assessments). It is also worth noting that the risk objectives and the time between successive stress tests should be defined by the CI authority and regulator. Since regulatory requirements do not yet exist for the port infrastructures, the boundaries need to rely on judgments.

### 6.4.2 Disaggregation/Sensitivity Analysis

In order to evaluate the contribution of certain components on the overall performance of the network the correlation between damaged components and system's functionality is estimated. For Stress Test Levels 2 (System Level Assessment for Single Hazard ST-L2), the most critical elements for the functionality of the port system are defined through correlation factors to the system PIs based on all simulations. This type of analysis, as it is based on the results of each single event, preserves the information about system's topology, its behavior in case of spatial correlated damages (related to single events) and functional inter-dependencies. Thus, it allows identifying the most critical elements for the functionality of the port system (i.e., the damaged components that tend to control the

performance of the harbor). For the case of PRA for ground shaking Fig. 6.35 and Fig. 6.36 show the level of correlation (low, medium, high) between the TCaH and TCoH and the distribution of damages in cranes and the non-functionality of electric power distribution substations respectively. In this way the most critical components can be identified in relation with their contribution to the performance loss of the system.

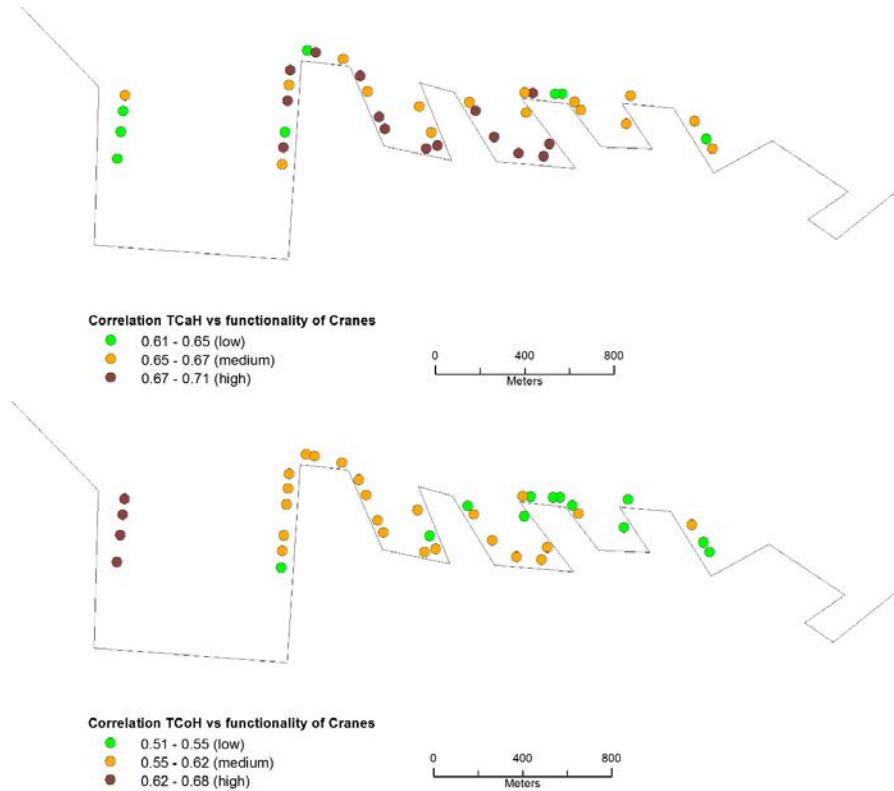


**Fig. 6.35 ST-L2b – Ground Shaking: Correlation of damaged cranes to port performance (TCaH and TCoH)**



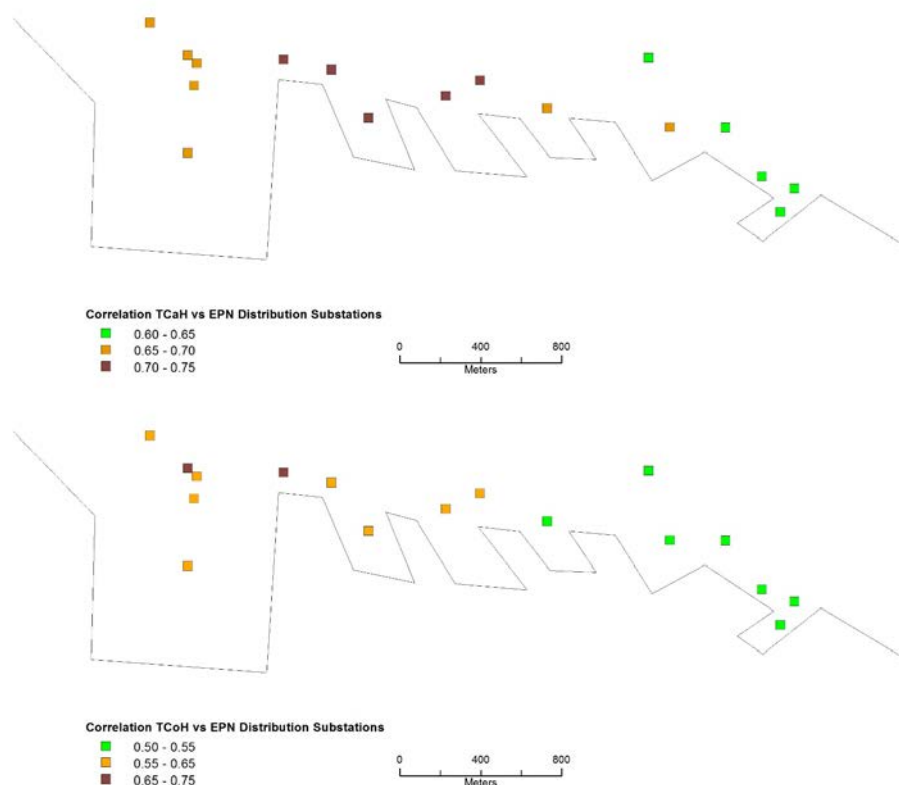


**Fig. 6.36 ST-L2b – Ground Shaking: Correlation of non-functional EPN distribution substations to port performance (TCaH and TCoH).**

### 6.4.3 Guidelines and critical events

For the selected target probabilities of collapse, all port components are deemed as unsafe towards seismic hazards at the component level assessment, while only few cranes are characterized as safe against exceedance of the collapse limit state for the tsunami hazard. These results cannot be judged unconditional to the fact that regulatory requirements for port infrastructures do not yet exist and the boundaries rely on judgments.

For ST-L2, and for the seismic case, several electric power distribution substations present high failure risk and contribute to the performance loss of the port due to loss of power supply to the cranes. It is recommended to investigate further the response of the substations under seismic shaking and consider potential upgrade or/and alternative power sources such as diesel generators. The systemic risk for the tsunami hazard is very low, however it is recommended to extend the model and investigate the effect of floating ships that may hit the different components of the harbor, which is now neglected.

For the scenario based assessment (ST-L2d/L3d) the estimated losses are significantly dependent on the analysis approach. In particular, the EQL approach is associated with higher losses even for the design scenario (475 years), while for the NL approach the losses to the cranes, waterfronts and electric power substations are expected solely for the 4975 scenario I. Among the four different outcomes determined for the extreme scenario for both PIs, the CI passes the stress test in the 4975 years scenario II and NL method, which could be judged as the most reliable.

## 6.5 PHASE 4: REPORT PHASE

The final stage of the test involves reporting the findings, which are summarized in Table 6.13.

**Table 6.13 Summary report of the Stress Test outcomes**

<b>Level 1</b>		<b>Component level – Seismic Hazard</b>			
		Buildings	Cranes	Quay walls	Electric power stations
Number of components		85	35	25	17
Target probability of collapse*		$4.7 \times 10^{-6}$ - $6.3 \times 10^{-6}$	$4.9 \times 10^{-6}$ - $6.3 \times 10^{-6}$	$4.7 \times 10^{-6}$ - $6.3 \times 10^{-6}$	$4.7 \times 10^{-6}$ - $6.3 \times 10^{-6}$
Outcome		0% pass 100% fail	0% pass 100% fail	0% pass 100% fail	0% pass 100% fail
<b>Level 1</b>		<b>Component level – Tsunami Hazard</b>			
		Buildings	Cranes	Electric power stations	
Number of components		85	35	17	
Target probability of collapse*		$5.8 \times 10^{-6}$ - $9.3 \times 10^{-6}$	$6.6 \times 10^{-6}$ - $8.8 \times 10^{-6}$	$5.8 \times 10^{-6}$ - $7.9 \times 10^{-6}$	
Outcome		0% pass 100% fail	83% pass 17% fail	0% pass 100% fail	
<b>Level 2b</b>		<b>System level – Seismic Hazard (PRA)</b>			
Risk measure		TCoH		TCaH	
Objectives boundaries (annual probability for 100% loss, logarithmic slope = 1)		B-C: $4.5 \times 10^{-3}$ A-B: $2.0 \times 10^{-3}$ , AA-A: $7.5 \times 10^{-4}$		B-C: $4.5 \times 10^{-3}$ A-B: $2.0 \times 10^{-3}$ , AA-A: $7.5 \times 10^{-4}$	
Grade		B		B	
Outcome		partially pass		partially pass	
Next stress test objectives		B-C: $2.5 \times 10^{-3}$ A-B: unchanged, AA-A: unchanged		B-C: $3.5 \times 10^{-3}$ A-B: unchanged, AA-A: unchanged	
<b>Level 2b</b>		<b>System level – Tsunami Hazard (PRA)</b>			
Risk measure		TCoH		TCaH	
Objectives boundaries (annual probability for 100% loss, logarithmic slope = 1)		B-C: $4.5 \times 10^{-3}$ A-B: $2.0 \times 10^{-3}$ , AA-A: $7.5 \times 10^{-4}$		B-C: $4.5 \times 10^{-3}$ A-B: $2.0 \times 10^{-3}$ , AA-A: $7.5 \times 10^{-4}$	

Grade	AA	AA
Outcome	pass	pass
Next stress test objectives	unchanged	unchanged
<b>Level 2d/3d</b>	<b>System level – Seismic Hazard (Scenario based)</b>	
Risk measure	TCoH	TCaH
Objectives-475 years scenario (% loss)	B-C: 50, A-B: 30, AA-A: 10	
Objectives-4975 years scenario (% loss)	B-C: 70, A-B: 50, AA-A: 30	
Grade		
475 EQL	C	C
475 NL	AA	AA
4975 years I EQL	C	C
4975 years I NL	C	C
4975 years II EQL	C	B
4975 years II NL	A	A
Outcome		
475 EQL	fail	fail
475 NL	pass	pass
4975 years I EQL	fail	fail
4975 years I NL	fail	fail
4975 years II EQL	fail	partially pass
4975 years II NL	pass	pass
Next stress test objectives		
Objectives-4975 years scenario (% loss)	B-C: 53, A-B: unchanged, AA-A: unchanged	



## **6.6 CLASSICAL EXPERT ELICITATION IN IMPLEMENTATION OF STRESS TEST**

### **6.6.1 Introduction**

Within STREST, an engineering risk-based multi-level stress test has been developed for the safety of non-nuclear critical infrastructure (STREST D5.1 Esposito et al., 2016). Initially, it consists of three categories: Level 1; Level 2; and Level 3. Level 1 is a qualitative risk assessment of an infrastructure against all types of natural hazards such as 'what if' and 'check list' analyses. The second level, Level 2, is based on probabilistic risk assessments for single hazards for which the assessment can be carried out without considering epistemic uncertainty (2a) or with quantifying the epistemic uncertainty (2b). If the exploration of epistemic uncertainty is somehow limited for technical reasons, also scenario-based assessment should be performed (3c) as complementary to the probabilistic assessment. The last level, Level 3, follows the same rules of Level 2, but it should consider multiple hazards within a multi-risk framework.

The involvement of multiple experts is critical in the implementation of stress test at levels 2b/c and 3b/c, in order to produce robust and stable results while considering the quantification of epistemic uncertainty. The experts can provide valuable judgments for the assessment in managing subjective choices and making critical decisions such as the selection of the significant hazards and/or combinations of hazards, the choices of suitable data set and models, and the ranking of the selected models. Therefore, a formalized process involving several key experts has also been developed within STREST called EU@STREST (Selva et al., 2015).

To show a practical implementation of this procedure, we developed an exemplificative experiment to simulate the procedure to be followed during a future stress test for non-nuclear critical infrastructures, following the protocol defined in STREST (Selva et al., 2015; Esposito et al., 2016; 2017). This exemplificative experiment has been carried out for the case study of the port of Thessaloniki (Greece). In order to make this exemplificative experiment as much informative and complete as possible, it has been decided to simulate a level 3b stress test, which represents the most complex level defined for stress tests (multiple-hazards with the quantification of epistemic uncertainty). It must be noted that, for this reason, this experiment has been carried out in parallel with the effective implementation of the risk analysis for the port of Thessaloniki (Greece), since this analysis started well before the final definition of the multiple-expert process. For example, this stress test has been planned during the preparation phase of STREST for seismic and tsunami single hazards only. Therefore, the results of this experiment are not implemented into the effective risk analysis for the port of Thessaloniki, but it has a purely exemplificative nature.

The formalized process (Selva et al., 2016a) has been integrated in developed stress test (Esposito et al., 2016; 2017). The key experts involved in the implementation of the stress test process are Project Manager (PM), the Technical Integrator (TI), the Evaluation Team (ET), the Pool of Experts (PoE), and the Internal Reviewers (IR). All these actors should interact along the stress test to assure transparency and accountability of the different actors, while PM, TI and IR should be independent to guarantee fairness of the results. In few words, the PM and TI have the political and technical coordination of the project. The ET assists the TI in the implementation of the assessments. The IR performs a participatory review of the project. The PoE represents the Larger Technical Community (SSHAC 1997),

and it provides input to the ET and PM in taking critical and subjective choices. More details on their definitions, roles, and participations in different levels of stress test are explicitly described in the project STREST D3.1 (Selva et al., 2015).

For assisting PM and TI in all the critical choices required during the implementation of the stress test, EU@STREST makes an extensive use of classical expert elicitations (e.g. Bedford and Cooke, 2001) of the PoE. Classical Expert Elicitation (cEE) refers to drawing out of knowledge from several experts, which act independently. It is regarded as being the process of translating experts' beliefs about some uncertain quantities of interest for which there is lack of clarity, evidence or information. The expert elicitation is an important research area of science and has played a large role in the application of scientific methods such as risk assessment and decision making (e.g. Morgan, 2014; Saaty, 1980). In the implementation of stress at level 3b for the Port of Thessaloniki (PoTh) following the suggested guidelines of formalized process, many expert elicitation tasks based on the classical Expert Elicitation (cEE) are needed. Among others the most important tasks include:

- i) selection of single and multiple natural hazards posing threat to PoTh, to be included as hazard initiators;
- ii) selection of single and interdependent port infrastructures of the PoTh, to be included into the system modeling; and
- iii) weighting the alternative acceptable models used in the performing the stress test for PoTh, to be used for quantifying the technical community distribution of the epistemic uncertainty (SSHAC, 1997; Marzocchi et al., 2015).

We employed these expert elicitation tasks in relation to the implementation of stress test for the PoTh. Any or all tasks may not be needed that if not required by the stress test level. In the following, we give an overview of the tasks, the selection of Pool of Experts (PoE) including the activities performed with experts, the employed methods, the results obtained. In the selected PoE, We note that all the experts in PoE are external to STREST, so they volunteered to participate to this experiment. They are not liable to any results and we warmly thank all of them for this effort.

### **6.6.2 Overview of the expert elicitation tasks**

The expert elicitation tasks were divided into two phases: Phase 1 (pre-assessment phase of EU@STREST); and Phase 2 (assessment phase of EU@STREST). In each phase, the experts were asked to provide their judgments through specific questionnaires on the topics of her/his specific competence. Below is the short detail what was performed in each phase.

Phase 1 (pre-assessment): In this phase, the PoE is defined and a kick-off meeting is organized. Then, natural hazards and port infrastructures concerning the PoTh were screened and prioritized. This was done on single and interactive bases of hazards and port infrastructures. The task was performed in two separate rounds: Round A, and Round B. The screening of single hazards and port infrastructures was done in Round A, whereas the prioritization of hazards and port infrastructures was done in Round B. Note that the outcome B was relying on the outcome of the round A.

Phase 2 (assessment): In this phase, the selected plausible alternative models were ranked to be used for tsunami hazard assessment at the site of PoTh. The ranking was made by estimating numerical scores ranging from 0 to 1 using a decision model on each alternative

model. The estimated numerical scores to the selected alternative models may then be considered either as weights of an ensemble model (e.g. Selva et al., 2016a), or as subjective probabilities of a logic tree (e.g. Kulkarni, 1984).

Pool of Experts (PoE): The choice of experts in the Pool of Experts (PoE) having the required expertise for the tasks in question is a crucial issue. The choice of experts means to select those experts who have relevant background knowledge to provide informed predictive judgments as required, which could be used with confidence. Having in mind the tasks of the expert elicitation, we sought experts who had the relevant knowledge and experience of natural hazards and/or the target system infrastructure of the PoTh and its location, both in general or/and specifically for the target location. The basic required expertise within the pool of experts was: i) on natural hazards in general; ii) on natural hazards in the target area of Thessaloniki; iii) on the system infrastructure of port in general; iv) on the system infrastructure of target port of Thessaloniki.

Experts merging one or more of the above-mentioned expertise were very welcome keeping the good balance of the chosen expertise that was required. Therefore, we prepared a series of “profiles” to help selecting experts for the PoE. The experts could come from port authority, government, and/or academia. Basically, two groups of experts were required.

Group 1. PoE-H: experts in hazard analysis (e.g. physicists, seismologists);

Group 2. PoE-V: experts in vulnerability/fragility analysis (e.g. engineers).

The grouping of experts was needed when assigning their roles in the judgmental process. For instance,

PoE-H and PoE-V were requested to provide their opinions to screen out the relevant natural hazards and port infrastructures.

PoE-H were requested to provide their opinions for ranking and prioritization of hazards, and their interactions, and

PoE-V were requested to provide their opinions for ranking and prioritization of port infrastructures, and their interactions.

The following activities were performed with experts before the actual elicitation was undertaken.

Selection of experts in PoE: In order to select the experts in the PoE, twenty one experts were identified by the Evaluation Team (ET), together with the assistance of Project Manager (PM) and the Technical Integrator (TI), having the required expertise; the experts having expertise in hazard/vulnerability/risk assessments. Most of them were connected to academia in Thessaloniki. A few of them were from other cities of Greece and other European countries.

Invitation letter: A formal invitation letter was sent out to all the identified experts on behalf of the Project Manager (PM) and the Technical Integrator (TI). In the letter, it was clearly explained supported by additional documents that what are the goals of the elicitation tasks, what would be their role, what we want from them, and how and when we want to conduct the elicitation tasks. Also, it was clearly highlighted that their participation is as volunteering and they are not liable to any outcome of the elicitation tasks.

Kick-off meeting: A half day kick-off meeting was organized on 25 February, 2016 in Thessaloniki and the experts were invited to attend it. The PM, TI, and ET presented the whole process of implementation and the role of experts in this process, enabling an

effective discussion with experts to clarify the scope of the tasks of expert elicitations and their role within the stress test. The participation of experts was very encouraging and fifteen experts attended the meeting.

Weights on Experts: At the end of the kick-off meeting, two activities were also performed in order to assign weights on experts.

The first activity was to quantify the weights of experts within a performance-based weighting scheme, in which weights are assigned based on their performance in answering to a set of questions (seed questions) whose answers exist (Bedford and Cooke, 2001). A set of sixteen questions related to hazard and risk assessment of natural hazards was presented to experts whose answers were already known to TI and ET. The questions were intentionally very precise and the experts were not expected to know the answers. The experts were asked to provide their best and uncertain estimates for each question. Following the Cook's approach (Cooke, 1991), the weights on individual experts were estimated, making use of the Cook's Classical Model Software – Excalibur, that is a software package for structured expert judgment elicitation using Cooke's Classical Model.

The other activity was to quantify the weights of experts within an acknowledgement-based weighting scheme, in which weights are quantified on the basis of the mutual recognition among experts expressed through a blind procedure (Selva et al., 2012). A list of all participated experts with names was given to each expert, asking the experts to vote to each other. Each expert was strictly requested to vote himself with weight 1 and to two other colleagues with weights 1 and 2 respectively.

### **6.6.3 Elicitation experiments**

Three different methods were employed in order to meet the objectives of expert elicitation tasks in both phases. Below are the descriptions of the employed methods.

#### **Phase 1, Round A: Screening of hazards and port infrastructures based on screening criteria**

For the round 1 of the Phase A, the experts were requested to screen the hazards and port infrastructures through questionnaires based on the defined sets of screening criteria defined below. The set of screening criteria are given in the section below.

1. single hazards from a provided list of twenty one natural hazards;
2. multiple hazards from a provided 21×21 matrix of all possible interaction of identified hazards;
3. single port infrastructures from a provided list of eleven port infrastructures; and
4. interdependent port infrastructures from a provided 11×11 matrix of identified interactive port infrastructures.

The identified potential single hazards taken from Gill & Malamud (2014) along with their hazard group and hazard code are listed in the

Table 6.14.

**Table 6.14 Identified potential hazards**

<b>Hazard group</b>	<b>Hazard</b>	<b>Code</b>
Geophysical	Earthquake	t <sub>1</sub>
	Tsunami	t <sub>2</sub>
	Volcanic eruption	t <sub>3</sub>
	Landslide	t <sub>4</sub>
	Snow avalanche	t <sub>5</sub>
Hydrological	Flood	t <sub>6</sub>
	Drought	t <sub>7</sub>
Shallow Earth processes	Regional subsidence	t <sub>8</sub>
	Ground collapse	t <sub>9</sub>
	Soil (local) subsidence	t <sub>10</sub>
	Ground heave	t <sub>11</sub>
Atmospheric	Storm	t <sub>12</sub>
	Tornado	t <sub>13</sub>
	Hailstorm	t <sub>14</sub>
	Snowstorm	t <sub>15</sub>
	Lightning	t <sub>16</sub>
	Extreme temperatures (heat)	t <sub>17</sub>
	Extreme temperatures (cold)	t <sub>18</sub>
Biophysical	Wildfires	t <sub>19</sub>
Space/Celestial	Geomagnetic storms	t <sub>20</sub>
	Impact events	t <sub>21</sub>

The taxonomy of Port of Thessaloniki (PoTh) along with their port infrastructures, components and infrastructure code is given in

Table 6.15. The asterisk (\*) in the table shows that port infrastructures are connected with the corresponding external networks.



**Table 6.15 Taxonomy of Port of Thessaloniki (PoTh)**

<b>Port Infrastructures</b>	<b>Components</b>	<b>Code</b>
Waterfronts	Waterfront structures	HBR01
Cargo Handling	Cranes	HBR02
Buildings	Sheds and Warehouses, Office Buildings, Maintenance Buildings, Passenger Terminals, Control and Clock Towers, Older Buildings	HBR03
Liquid Fuel	Fuel storage tanks	HBR04
	Pump equipment	
Electric Power *	Substations	HBR05
	Back-up power (generator)	
	Lines	
Water *	Storage Tanks	HBR06
	Pipelines	
Waste-Water *	Pumping (Lift) Station	HBR07
	Pipelines	
Communications *	Telecommunication center	HBR08
	Transmission lines	
Fire-Fighting	Fire-hydrant	HBR9
Roadway *	Road pavements	HBR10
	Bridges	
Railway *	Tracks	HBR11

Ten experts provided their judgments for (ir)relevancy of hazards and port infrastructures. Their judgments and decisions made on their judgments for screening of hazards and port infrastructures are given in the following.

It is important to note here that the criteria in Tables 6.16 and 6.18 for screening single hazards and single port infrastructures are defined a way that the irrelevant single hazards and port infrastructures are identified. The criteria in Tables 6.17 and 6.19 for screening multiple hazards and interdependent port infrastructures are defined in a way that relevant multiple hazards and interdependent port infrastructures are identified.

Specific questionnaires have been sent to the experts by email in March 22<sup>nd</sup>, asking for sending back the filled questionnaires by April 15<sup>th</sup>. To increase the awareness of experts, the following supporting material has been prepared and sent to the experts:

- Definition of terms used;
- Description of the area of the Port of Thessaloniki;
- Description of the Port of Thessaloniki, including a complete list of all present infrastructures;

### **Phase 1, Round B: Prioritization of hazard and infrastructures based on semi-quantitative risk assessment**

For the prioritization of natural hazards (Round B, Phase 1), only the screened single and natural hazards have been used. A semi-quantitative risk assessment approach was taken into account which based on the experts judgments (Iqbal et al., in prep). The experts were asked for their judgments for elements of risks on a numerical scale from 1 to 7 translated from a verbal scale. The judged numerical scale of elements was normalized by dividing 7. The experts were asked for the following elements:

- I. the relative likelihood of significant intensities of the screened hazards;
- II. the likelihood of significant damages to the screened port infrastructures given significant intensities of single or combined hazards;
- III. the non-functionality of the screened port infrastructures, given significant damages;
- IV. the impact on the performance of port; in terms of two performance indicators: 1) the total cargo/containers handled (loaded and unloaded) denoted by p1 and 2) the total cargo/containers handled and delivered (to the port's gate) denoted by p2.

Specific questionnaires have been sent to the experts by email in May 13<sup>th</sup>, asking for sending back the filled questionnaires by May 27<sup>th</sup>. To increase the awareness of experts, the following supporting material has been prepared and sent to the experts:

- I. A summary of the outcomes of phase 1, round A;
- II. Definitions required for the new questionnaires

### **Phase 2: Weighting of alternative models based on Analytic Hierarchy Process (AHP)**

The goal of the target assessment is to assign weights on a set of alternative models based on their relevancy to the area where the Port of Thessaloniki (PoTh) is located.

The target analysis here is Seismic Probabilistic Tsunami Hazard Analysis (SPTHA), as formulated for the area of the port of Thessaloniki within the STREST project (Selva et al., 2016a, European Geophysical Union Meeting). The site specific hazard is obtained by starting from regional analysis for the whole Mediterranean Sea and by applying a two-stage filtering procedure to select a subset of events to model local inundation (Lorito et al., 2015). The formulation is based on the general formulation proposed in Selva et al. (2016a). This formulation foresees the following STEPS:

STEP 1: Exploration of the aleatory variability of all potentially relevant sources through an Event Tree (Selva et. al., 2016); in this application, all potential sources of the Mediterranean sea are considered.

STEP 2: Propagation of all potential sources to the tsunami offshore (50m isobath), based on unit Gaussian sources (Molinari et al., 2016, submitted).

STEP 3: Cluster analysis to find cluster of sources causing similar tsunamis in the target area; to each cluster, an event is selected to represent the all cluster and its inundation in the target area is explicitly modeled (Lorito et al., 2015).

STEP 4: Alternative implementations of STEPS 1 to 3 are weighted, and an ensemble model is produced (Marzocchi et al., 2015), quantifying simultaneously both aleatory and epistemic uncertainty.

More details can be found in Selva et al. (2016a) and references therein.

In this application, we implement alternatives only in STEP 1, regarding the modeling approach adopted to quantify the aleatory uncertainty on seismic sources. The formulations of alternatives are structured in several levels (level of the Event Tree, see Selva et al., 2016a), which can be summarized in the following simplified version:

LEVEL 1: here, we quantify the frequency-size distribution of earthquakes in a number of seismic regions, to be assumed independent to each other. Here, we propose 48 alternative implementations, organized in two sublevels with 8 and 6 alternatives respectively.

LEVEL 2: Subduction interfaces are particularly important for tsunamis, since larger events are expected to occur in such interfaces. Given that a large amount of information is available for such interfaces (with respect to other sources, like offshore crustal sources), subduction interface seismicity (hereinafter IS) is treated separately from the rest of the seismicity (background seismicity, hereinafter BS). In the regions where subduction interfaces are present (in our case, the regions including the Hellenic and the Calabrian Arcs), IS and BS coexist. The goal of LEVEL 2 is to separate IS and BS, by quantifying the probability that a given random earthquake of a given magnitude occurring in the region occurs on the interface (that is, it is part of the IS class) or not. Here, we propose 12 alternative implementation of this assessment, organized in two sublevels with 3 and 4 alternatives respectively.

BS-branch: given a seismic source owing to BS, we quantify the probability of the location (x,y) in a regular grid and the depth z of the center of the potential fault, as well as, its potential focal mechanism (strike, dip, rake). Here, we propose 4 alternative implementations.

IS-branch: given a seismic source owing to IS, we know that the center of the fault is forced to be in the subduction interface; however, alternative interpretation of the interface are still possible, as for example allowing or not the propagation of the rapture into the shallowest part of the interface (not strictly seismogenic), consequently increasing the potential magnitude of the event. Here, we propose 2 alternative implementations.

A detailed description of all the alternative implementations, at all levels, can be found in Selva et al. (2016a).

In order to assign weights on the alternative models based on the opinion of PoE, we employed an Analytic Hierarchy Process (AHP). As case study, we consider here the alternative models considered in the tsunami hazard assessment for the PoTh, as well as, for the case study relative to the refinery of Milazzo (Italy). Analytical Hierarchy Process (AHP) is a multi-criterion decision model introduced by Thomas Saaty (1980). The AHP takes input as absolute numbers, translated from the verbal scales, ranging from one (equal important or preferred) to nine (extremely important or preferred). This numbers are actually the integer approximation of two weights assigned to each models when compared in pairs. The scale enables the expert to incorporate experience and knowledge intuitively and indicate how many times a model dominates another with respect to the goal of the assessment. Based on experts' judgments, the final scores (positive numerical values) are generated following steps of the AHP, which determine the weights on the alternative models.

#### 6.6.4 Elicitation results

##### Screening criteria

As mentioned above, in order to screen the single hazards, multiple hazards, single port infrastructures, and interdependent port infrastructures, we defined the four different sets of screening criteria given in Tables 6.16-6.19. The defined sets of criteria for single and multiple hazards are reported in Tables 6.16 and 6.17, and the defined sets of criteria for single and inter-dependent port infrastructures are reported in Tables 6.18 and 6.19. In all the cases, the experts were given liberty to define and make use of any other screening criteria. The idea of screening comes from the nuclear industry, similar criteria defined in the documents of nuclear industry (US NRC. NUREG, 1985; Knochenhauer and Louko, 2004) were used to screen natural hazards.

**Table 6.16 Screening criteria for Single Hazards (SHs)**

Relevancy	Criterion code	Definition
Site	SH-C1	<i>Not pertinent in the region</i> (prefecture of Thessaloniki): The hazard cannot occur in the region.
Site	SH-C2	<i>Negligible for the region</i> (prefecture of Thessaloniki): The hazard can occur in the region with mean frequency of occurrence significantly (including uncertainty) lower than the target limit mean annual frequency ( $10^{-6} \text{ yr}^{-1}$ )
Site	SH-C3	<i>Redundant</i> : The hazard is included in the definition of another hazard.
PoTh	SH-C4	<i>Not pertinent for PoTh</i> : The hazard can occur in the region, but has no potential to affect the PoTh
PoTh	SH-C5	<i>Negligible for PoTh</i> : The hazard can occur in the region, but its potential is significantly less than the intensity for which the infrastructure has been designed.
Other	SH-C6	Other criterion

**Table 6.17 Screening criteria for Multiple Hazards (MHs)**

Relevancy	Criterion code	Definition
Site	MH-C1	<i>Hazard triggering interaction:</i> the first hazard may trigger or significantly increase the probability of occurrence of the second hazard in the region
Site	MH-C2	<i>Hazard simultaneous interaction:</i> two hazards can occur simultaneously in the region.
Site	MH-C3	<i>Vulnerability interaction:</i> the occurrence of the first hazard may significantly increase the vulnerability of the PoTh components (probability of damage and/or non-functionality) to the second hazard.
PoTh	MH-C4	<i>Exposure interaction:</i> the occurrence of the first hazard may significantly increase the exposure (value at risk, considering the target performance indicators i.e., the total cargo/containers handled and/or delivered) to the second hazard.
Other	MH-C5	Other criterion

**Table 6.18 Screening criteria for Single Port Infrastructures (SPIs)**

Relevancy	Definition
SPI-C1	<i>Contribution to the target performance of PoTh:</i> the port infrastructure functionality does not influence the target performance indicators i.e., the total cargo/containers handled and/or delivered.
SPI-C2	<i>Port infrastructure vulnerability:</i> the functionality of the port infrastructure (and its components) is not vulnerable to all the relevant hazards for the PoTh.
SPI-C3	<i>Port infrastructure protection:</i> The port infrastructure (and its components) cannot be reached by any of the relevant hazards, since it is physically protected.
SPI-C4	Other criterion

**Table 6.19 Screening criteria for Interaction/Interdependent Port Infrastructures (IPIs)**

<b>Criterion code</b>	<b>Definition</b>
IPI-C1 (Phy)	Physical/functional interdependency (direct interaction): : the function of the first component (or of one of its subcomponents) physically depends on the supply provided by the other component, e.g. the material output of one infrastructure is used by another, one infrastructure system needs commodities or outputs from other systems to maintain its function.
IPI-C2 (Inf)	Informational interdependency: the state of an infrastructure system depends on information transmitted through the information infrastructure, e.g. infrastructures utilize electronic information and control systems.
IC-C3 (Geo)	Geographical interdependency (Collocation, geographic, space interdependency - physical damage propagation): the functionality of the first component (or of one of its subcomponents) may be compromised by damages on the second component (e.g. the second component collapses over the first component, a local environmental event can create state changes in all of them e.g. infrastructures are co-located in a common corridor)
IPI-C4 (Res)	Restoration interdependency (Restoration - recovery interdependency): interactions occur during the procedure of recovering and rescuing, e.g. interference for system recovery or reconstruction between buried lifelines.
IPI-C5 (Sub)	Substitute interdependency: back-up functions of substitute systems, influences on alternative systems, e.g. failure of one system will result in the excessive requirement for the other.
IPI-C6 (Seq)	Sequential interdependency (Sequential interdependency - scaling effects): increasing impacts on a lifeline due to initial inadequacies.
IPI-C7 (Log)	Logical interdependency (Logical interdependency, financial markets - policy/procedural interdependency), e.g. infrastructures are linked through financial markets
IPI-C8 (Soc)	Societal interdependency: an event on an infrastructure component may impact on societal factors such as public opinion, public confidence, fear and cultural issues.
IPI-C9 (Gen)	General interaction/interdependency: a dependency that exists between infrastructures that does not fall into one of the above categories.

**PHASE 1, Round A**

**Screening of single and multiple hazards**

The screening of all identified single and selective multiple hazards relevant to PoTh under three weighting schemes – Equal Weighting (EW) in blue; Acknowledgment-based Weighting (AW) in red; and Performance-based Weighting (PW) in yellow – is shown in Fig. 6.37. The PW based on hazard questions and risk questions, respectively, denoted by PW-H and PW-R. In both parts of the figure, Fig. 6.37a) and Fig. 6.37b), the horizontal axes represent the natural hazards to be screened and the vertical axes represent the assessment on experts' judgments in the term of a fraction value. The fractional form of expert judgments for each hazard was obtained by dividing number of experts in favor of hazards over the total number of experts who provided their judgments. For screening the hazards, ten experts provided their judgments.

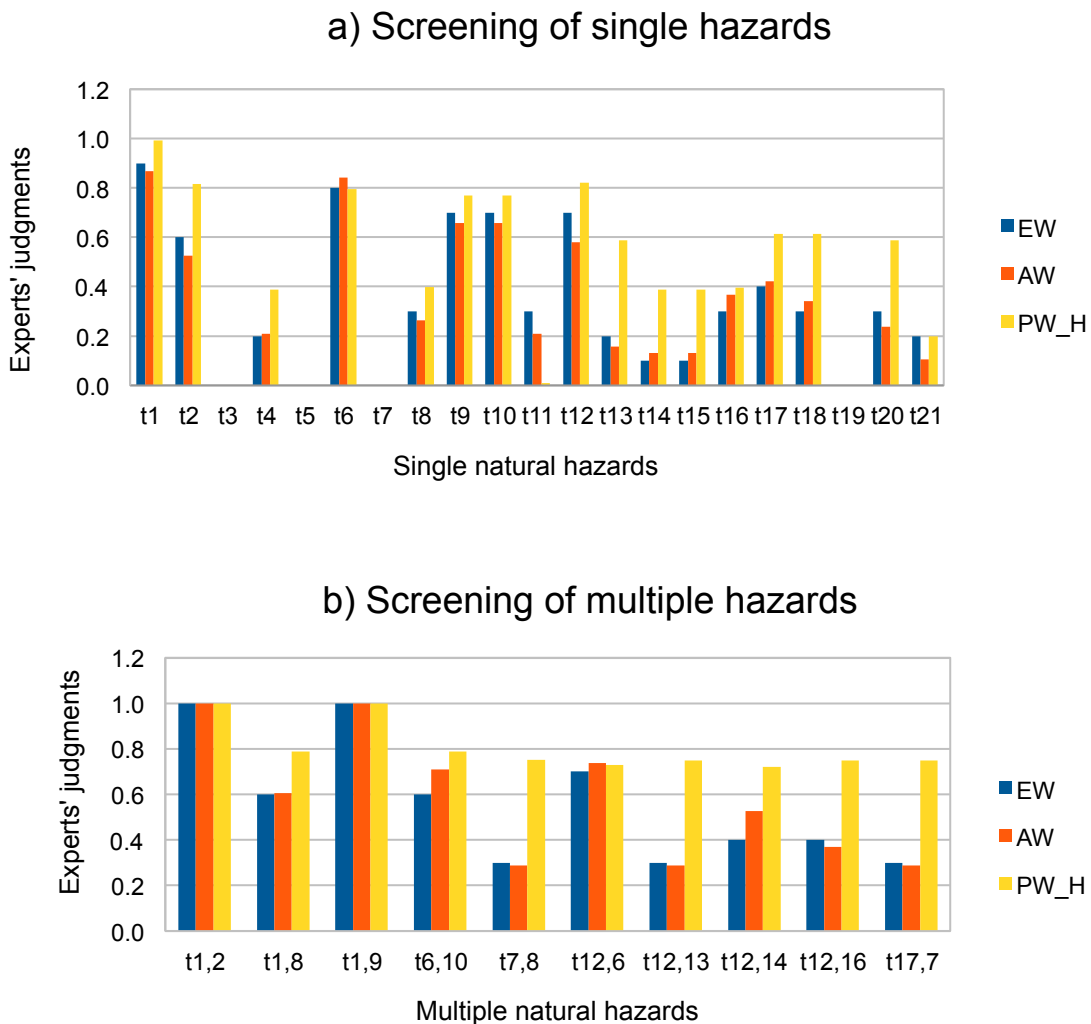


**Fig. 6.37 Assessment of experts' judgments for screening the all identified single and selective multiple natural hazards relevant to PoTh**

In Fig. 6.37a), the expert assessment of all considered single natural hazards is reported. Based on the empirical distribution of the scores, a distinct group of single hazards emerged



with high relevancy to PoTh. The relevancy of single hazards to PoTh based on EW and AW was similar. However, the relevancy of hazards under PW-H was relatively higher compared to other schemes except  $t_6$  and  $t_{11}$ . Setting the fractional value 0.5 for all the weighting schemes, six single hazards ( $t_1, t_2, t_6, t_9, t_{10}, t_{12}$ ) were recognized the relevant ones to PoTh. Amongst the relevant ones, the first and second most relevant ones are  $t_1$  and  $t_2$ , respectively, posing threat to PoTh. The hazards  $t_3, t_5, t_7,$  and  $t_{19}$  are unlikely to occur in the region.

In Fig. 6.37b), the expert assessment of selective multiple natural hazards is reported. Only those multiple hazards were selected which got minimum 0.7 score (fractional value) from at least one of the weighting schemes. Among the selective multiple hazards, likewise in single hazards, the relevancy of multiple hazards to PoTh based on EW and AW was similar and the relevancy of most of the multiple hazards under PW-H was relatively higher compared under other schemes. The consistent results under three weighting scheme was seen for  $t_{1,2}, t_{1,9},$  and  $t_{12,6}$ . These three multiple hazards selected the most relevant ones in which the equally most relevant ones are  $t_{1,2}$  and  $t_{1,9}$ , and then comes the  $t_{12,6}$ . The rest of multiple hazards are considered to be irrelevant to PoTh in the present study. To account for potential cascade effects with more than two hazards, we joined the pair chains with origin-hazard in common, to form longer chains. Doing this, we define one further multiple hazard chain ( $t_{1,2,9}$ ) that emerged as relevant for the PoTh, to be added to all the pairs already screened.

The screened hazards based on defined screening criteria along with their hazard type, code and name are presented in the following table, Table 6.20.

**Table 6.20 Screened hazards considered to be most relevant to PoTh**

Hazard type	Hazard code	Hazard name
Single	$t_1$	Earthquake
Single	$t_2$	Tsunami
Single	$t_6$	Flood
Single	$t_9$	Ground Collapse
Single	$t_{10}$	Local Soil subsidence
Single	$t_{12}$	Storm
Multiple	$t_{1,2}$	Earthquake and Tsunami
Multiple	$t_{1,9}$	Earthquake and Ground Collapse
Multiple	$t_{12,6}$	Storm and Flood
Multiple	$t_{1,2,9}$	Earthquake, Tsunami and Ground Collapse

### Screening of single and inter-dependent port infrastructures

The screening of all port infrastructures relevant to PoTh under three weighting schemes – Equal Weighting (EW) in blue; Acknowledgment-based Weighting (AW) in red; and Performance-based Weighting (PW-R) in yellow – is shown in Fig. 6.38. The PW was based on risk questions; therefore it is denoted by PW-R. In Fig. 6.38, the horizontal axis represents the port infrastructures to be screened and the vertical axis represents the assessment on experts' judgments in the term of a fraction value. The fractional form of

expert judgments for each port infrastructure was obtained by dividing number of experts in favor of port infrastructures over the total number of experts who provided their judgments. For screening the port infrastructures, ten experts provided their judgments.

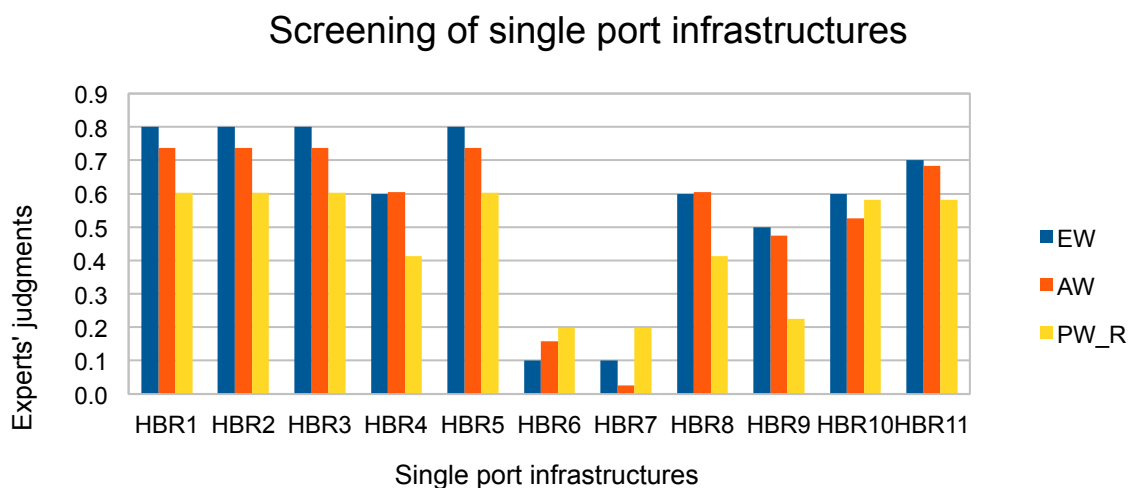


**Fig. 6.38 Assessment of experts' judgments for screening the all identified port infrastructure relevant to PoTh. The asterisk (\*) sign shows that those port infrastructures are connected to the external networks of the port**

Differently from the hazard screening, most of port infrastructures seem to be relevant to PoTh. The AW and EW have again similar results, identifying most of the infrastructures with the exception of waste-water (HBR6) and water systems (HBR7). The PW-R results tend to confirm the same trend, however it provides an intermediate score (still larger than the waste-water and water systems, but smaller than the others) for 3 infrastructures, namely, the fire-fighting (HBR09), the communication (HBR08) and liquid fuel systems (HBR04).

The experts' judgments for screening the interdependent port infrastructures are given in Table 6.21, which is based on only the equal weighting. In the table, the port infrastructures in rows have impact on the port infrastructures in columns. The number in fractional form in each entry of the table shows how many experts expressed their opinions experts in favor of port infrastructures over the total number of experts who provided their judgments for the possible interdependencies of port infrastructures which are relevant to PoTh.

**Table 6.21 Experts' judgments for the port infrastructures for the relevancy to PoTh**

Hazard	Code	HBR 01	HBR 02	HBR 03	HB R04	HBR 05	HBR 06	HBR 07	HBR 08	HB R09	HBR 10	HBR 11
Waterfronts	HBR01		0.7	0.3	0.1	0.3	0.1	0.3	0	0.2	0.6	0.6
Cargo Handling	HBR02	0.6		0.3	0.3	0.6	0	0	0.4	0.2	0.4	0.4
Buildings	HBR03	0.3	0.4		0	0.7	0.6	0.5	0.7	0.5	0.6	0.4
Liquid Fuel	HBR04	0.1	0.1	0.3		0.1	0	0	0	0.5	0.3	0.2
Electric Power	HBR05	0	0.5	0.8	0.3		0.1	0.1	0.4	0.2	0.2	0.1
Water	HBR06	0	0	0.4	0	0		0	0	0.2	0	0
Waste-Water	HBR07	0	0	0.3	0.2	0.2	0.2		0.2	0	0	0
Communications	HBR08	0	0.4	0.7	0.1	0.4	0	0		0.2	0.4	0.3
Fire-Fighting	HBR09	0.2	0.2	0.4	0	0.2	0.4	0	0.3		0.4	0
Roadway	HBR10	0.3	0.7	0.6	0	0.1	0.1	0.2	0.5	0.4		0.2
Railway	HBR11	0.3	0.7	0.4	0	0.1	0	0	0.3	0	0.1	

As for the single port infrastructures, also in this case the results are less clear than for the cases related to the hazards. In Fig. 6.39, the relevancy is categorized in three classes from non-relevant to relevant, based on the empirical distribution of the scores. The relevant port infrastructure interdependencies (with 0.7 fractional values, green boxes in the table) are given in Table 6.22. Note that HBR03 and HBR05, and HBR03 and HBR08 have been judged relevant in inter-dependency in both directions (from 1 to 2 and from 2 to 1), while all the other are uni-directional. This information is reported in the last column of the table.

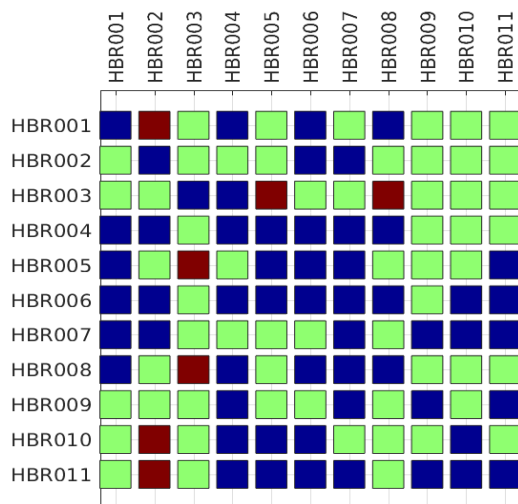


**Fig. 6.39** Three categories are identified: non relevant (blue), partially relevant (light green), and relevant (red). The category is assigned based on the equal weights only as votes smaller or equal to 1, between 2 and 6, and larger or equal to 7, respectively

**Table 6.22** Most relevant interdependencies for the Port of Thessaloniki (PoTh)

Port infrastructures	Infrastructure code	Directivity of the link
Waterfronts and Cargo Handling	HBR01 and HBR02	Unidirectional
Buildings and Electric Power	HBR03 and HBR05	Bidirectional
Buildings and Communications	HBR03 and HBR08	Bidirectional
Roadway and Cargo Handling	HBR10 and HBR02	Unidirectional
Railway and Cargo Handling	HBR11 and HBR02	Unidirectional

## PHASE 1, Round B

### Prioritization of hazards

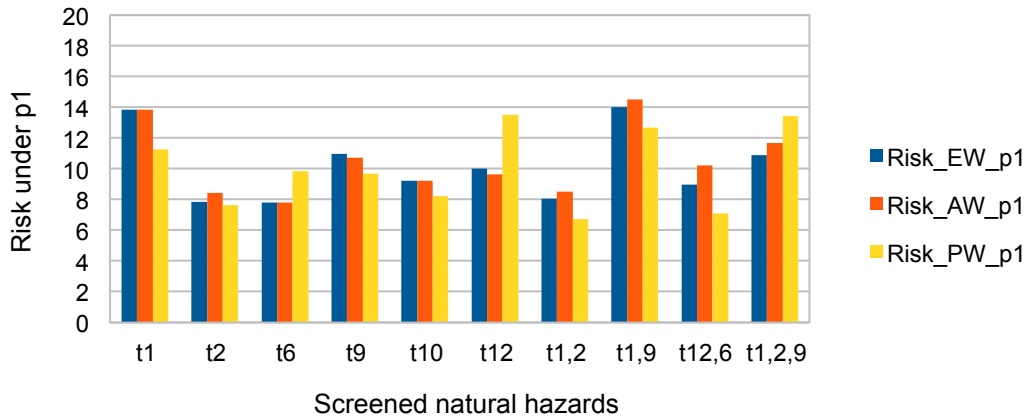
Based on the expert judgments, the comparisons of semi-quantitative *assessed risks*, in scores, of screened single and multiple hazards for two performance indicators – p1 and p2 defined above – is shown in Fig. 6.40. The risk for a hazard is assessed in terms of performance loss due to the occurrence of a given hazard that is measured by taking into account the relative likelihood of significant intensity of the hazard; the likelihood of significant damages to the screened port infrastructures given significant intensity of the

hazard; the non-functionality of the screened port infrastructures given significant damages; the impact on the performance of port on p1 and p2.

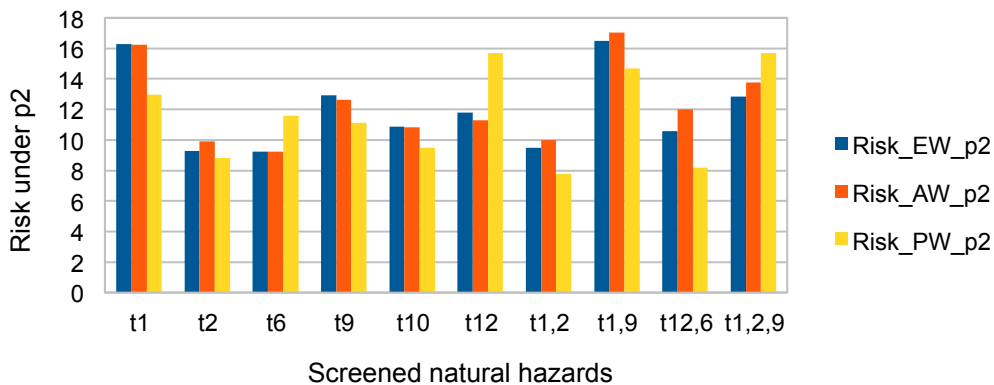
The comparisons are done for three considered weighting schemes: Equal Weighting (EW) in blue; Acknowledgment-based Weighting (AW) in red; and Performance-based Weighting (PW) in yellow. In both parts of the figure, Fig. 6.40a) and Fig. 6.40b), the horizontal axes represent the screened natural hazards and the vertical axes represent the assessed risks. Both the hazards and risk questions were used to estimate weights on the performance of experts; therefore the weighting is denoted by PW.

Fig. 6.40 shows that there were little differences between the assessed risks for screened hazards under EW and AW. However, the differences were relatively higher when compared assessed risks under EW or AW with PW. This is seen for both the performance indicators p1 (see Fig. 6.40a) and p2 (see Fig. 6.40b). Also, for each hazard, the risk for p2 was relatively higher compared to corresponding hazard risk for p1.

a) Comparisons of risks of hazards under EW, AW and PW for p1



b) Comparisons of risks of hazards under EW, AW and PW for p2



**Fig. 6.40 Comparisons of assessed risks of screened hazards under EW, AW and PW for p1 and p2**

The prioritization of ten screened hazards concerning the PoTh is reported in Tables 6.23 and 6.24 along with their estimated scores, emerging from Fig. 6.40. The priority of an individual or a multiple hazard can clearly be seen under three weighting schemes for two performance indicators. In most cases, the priorities of hazards alter under three weighting schemes in each table, but the priority list remains the same for both performance indicators. However, a rather univocal picture can be derived from these results. A few consistencies were found comparing the priority lists with different weighting schemes, but overall not a single hazard got the same priority under three weighting schemes. The multiple hazard  $t_{1,9}$  ( $t_6$ ) was the most (least) threatening hazard to PoTh under EW and AW,  $t_{12}$  ( $t_{1,2}$ ) was the most (least) threatening multiple hazard to PoTh under PW.

**Table 6.23 Prioritization of the screened hazards to PoTh under three weighting schemes for p1**

Prioritization	EW_p1		AW_p1		PW_p1	
	Hazard	Risk score	Hazard	Risk score	Hazard	Risk score
Priority 1	$t_{1,9}$	14.00	$t_{1,9}$	14.54	$t_{12}$	13.52
Priority 2	$t_1$	13.86	$t_1$	13.87	$t_{1,2,9}$	13.44
Priority 3	$t_9$	10.96	$t_{1,2,9}$	11.69	$t_{1,9}$	12.70
Priority 4	$t_{1,2,9}$	10.88	$t_9$	10.75	$t_1$	11.25
Priority 5	$t_{12}$	10.02	$t_{12,6}$	10.23	$t_6$	9.84
Priority 6	$t_{10}$	9.21	$t_{12}$	9.65	$t_9$	9.70
Priority 7	$t_{12,6}$	8.98	$t_{10}$	9.22	$t_{10}$	8.22
Priority 8	$t_{1,2}$	8.06	$t_{1,2}$	8.53	$t_2$	7.65
Priority 9	$t_2$	7.87	$t_2$	8.45	$t_{12,6}$	7.09
Priority 10	$t_6$	7.81	$t_6$	7.82	$t_{1,2}$	6.73

**Table 6.24 Prioritization of the screened hazards to PoTh under three weighting schemes for p2**

Prioritization	EW_p2		AW_p2		PW_p2	
	Hazard	Risk score	Hazard	Risk score	Hazard	Risk score
Priority 1	$t_{1,9}$	16.50	$t_{1,9}$	17.06	$t_{12}$	15.72
Priority 2	$t_1$	16.30	$t_1$	16.25	$t_{1,2,9}$	15.68
Priority 3	$t_9$	12.92	$t_{1,2,9}$	13.76	$t_{1,9}$	14.68
Priority 4	$t_{1,2,9}$	12.86	$t_9$	12.62	$t_1$	12.96
Priority 5	$t_{12}$	11.80	$t_{12,6}$	12.02	$t_6$	11.57
Priority 6	$t_{10}$	10.86	$t_{12}$	11.31	$t_9$	11.14
Priority 7	$t_{12,6}$	10.60	$t_{10}$	10.82	$t_{10}$	9.48
Priority 8	$t_{1,2}$	9.50	$t_{1,2}$	10.01	$t_2$	8.82
Priority 9	$t_2$	9.27	$t_2$	9.92	$t_{12,6}$	8.18
Priority 10	$t_6$	9.26	$t_6$	9.22	$t_{1,2}$	7.76

### Prioritization of port infrastructures

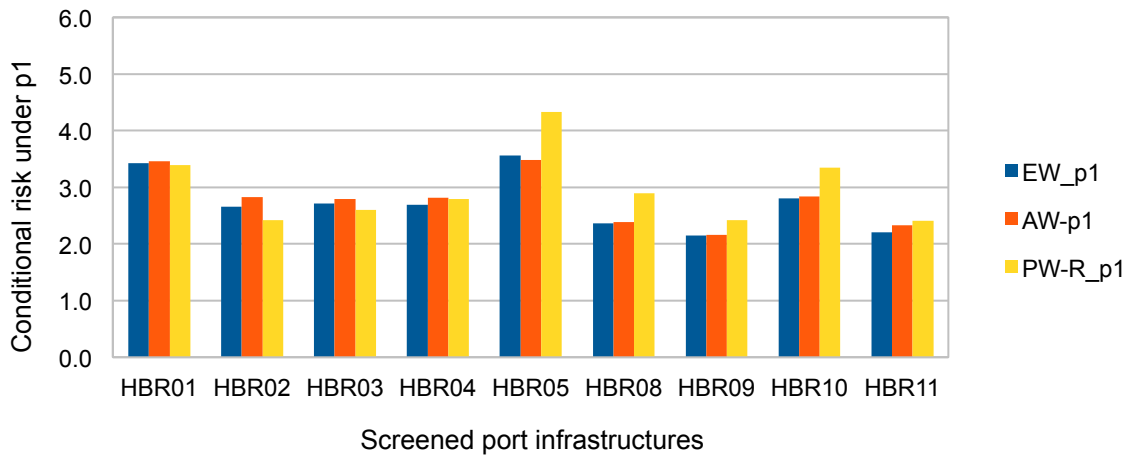
Based on the expert judgments, the comparisons of semi-quantitative assessed conditional risks, in scores, of screened port infrastructures for two performance indicators – p1 and p2 defined above – is shown in Fig. 6.41. The conditional risk of a port infrastructure is assessed in terms of a performance loss due to damages to a given port infrastructure occurrence of a given port infrastructure that is measured by taking into account the non-functionality of the screened port infrastructures given significant damages; and the impact on the performance of port on p1 and p2.

The comparisons are done for three considered weighting schemes: Equal Weighting (EW) in blue; Acknowledgment-based Weighting (AW) in red; and Performance-based Weighting (PW) in yellow. In both parts of the figure, Fig. 6.41a) and Fig. 6.41b), the horizontal axes represent the screened port infrastructures and the vertical axes represent the assessed conditional risk (performance loss, in this case) due to damages to the single structures. Only the risk questions were used to estimate weights on the performance of experts; therefore the weighting is denoted by PW-R. Note that we treated every port infrastructure individually to assess the likelihood of performance loss of PoTh given significant damages of a given port infrastructure.

Fig. 6.41 shows that there were little differences between the assessed non-functionalities for screened port infrastructures under EW and AW. However, the differences were relatively higher when compared assessed non-functionalities under EW or AW with PW. This is seen for both the performance indicators p1 (see Fig. 6.41a) and p2 (see Fig. 6.41b). Also, for each port infrastructure, the non-functionality for p2 was relatively higher compared to corresponding port infrastructure non-functionality for p1.

The prioritization of nine port infrastructures of PoTh is reported in Tables 6.25 and 6.26 along with their estimated scores, emerging from Fig. 6.41. The priority of an individual and interactive port infrastructure can clearly be seen under three weighting schemes for two performance indicators. In many cases, priorities of port infrastructures alter under three weighting schemes as well as for both performance indicators. However, a rather univocal picture can be derived from these results. The most vulnerable port infrastructure (HBR05) is same under three weighting schemes for p1 and p2. Further, the priority list under EW is more similar to priority list under AW for both performance indicators when comparing priority lists PW-R and EW, or PW-R and AW. The least vulnerable port infrastructure was HBR09 under EW and AW for both p1 and p2. And the least vulnerable port infrastructure under PW-R was: HBR11 for p1 and HBR02 for p2.

a) Comparisons of conditional risks of port infrastructures under EW, AW and PW-R for p1



b) Comparisons of conditional risks of port infrastructures under EW, AW and PW-R for p2

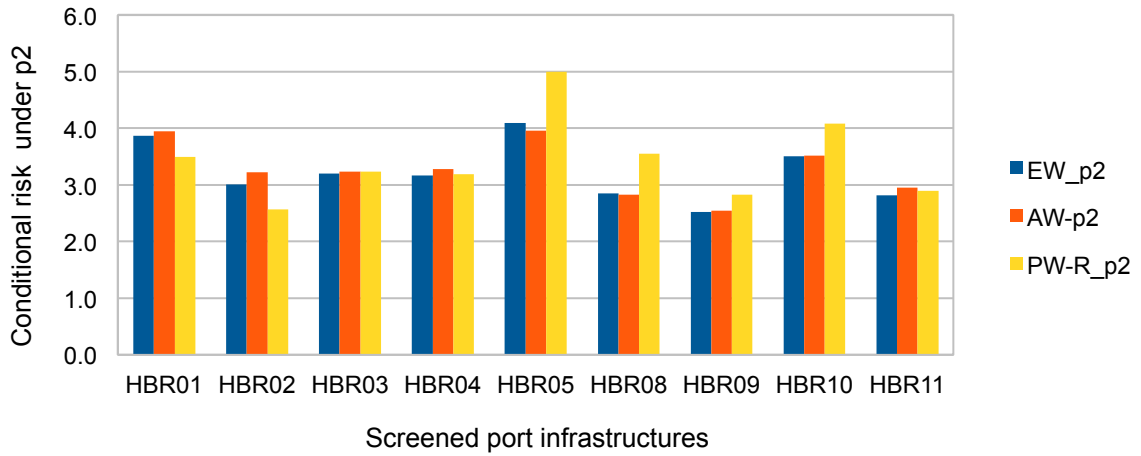


**Fig. 6.41 Comparisons of conditional assessed risks of screened port infrastructures under EW, AW and PW for p1 and p2**



**Table 6.25 Prioritization of the screened port infrastructures under three weighting schemes for p1**

Prioritization	EW_p1		AW_p1		PW-R_p1	
	Port Infrastructure	Conditional risk score	Port Infrastructure	Conditional risk score	Port Infrastructure	Conditional risk score
Priority 1	HBR05	3.57	HBR05	3.48	HBR05	4.33
Priority 2	HBR01	3.43	HBR01	3.47	HBR01	3.40
Priority 3	HBR10	2.80	HBR10	2.84	HBR10	3.34
Priority 4	HBR03	2.71	HBR02	2.83	HBR08	2.90
Priority 5	HBR04	2.70	HBR04	2.81	HBR04	2.79
Priority 6	HBR02	2.65	HBR03	2.80	HBR03	2.61
Priority 7	HBR08	2.37	HBR08	2.39	HBR09	2.42
Priority 8	HBR11	2.21	HBR11	2.33	HBR02	2.42
Priority 9	HBR09	2.15	HBR09	2.16	HBR11	2.40

**Table 6.26 Prioritization of the screened port infrastructures under three weighting schemes for p2**

Prioritization	EW_p2		AW_p2		PW-R_p2	
	Port Infrastructure	Conditional risk score	Port Infrastructure	Conditional risk score	Port Infrastructure	Conditional risk score
Priority 1	HBR05	4.09	HBR05	3.96	HBR05	5.00
Priority 2	HBR01	3.86	HBR01	3.95	HBR10	4.08
Priority 3	HBR10	3.51	HBR10	3.52	HBR08	3.55
Priority 4	HBR03	3.20	HBR04	3.28	HBR01	3.49
Priority 5	HBR04	3.16	HBR03	3.23	HBR03	3.24
Priority 6	HBR02	3.01	HBR02	3.23	HBR04	3.19
Priority 7	HBR08	2.85	HBR11	2.96	HBR11	2.90
Priority 8	HBR11	2.82	HBR08	2.83	HBR09	2.83
Priority 9	HBR09	2.52	HBR09	2.55	HBR02	2.56

## PHASE 2

### Weighting the alternative models

The weighting of alternative models in terms of scores are presented for four alternative branches – LEVEL 1, LEVEL 2, BS-branch, and IS-branch – of STEP 1 in an aggregated form based on the assessments of the four experts. The scores are reported under three weighting schemes: Equal Weights (EW); Acknowledge-based Weights (AW); and Performance-based Weights based on Hazard questions (PW-H).

LEVEL 1: The LEVEL 1 was about the estimation of mean annual rates of earthquakes at the different magnitudes in each seismic region (Selva et al., 2016a). As the models in LEVEL 1 was separated into two sub-levels that is LEVEL 1a and LEVEL 1b, therefore two different questions were designed for judgments for each sub-level. The sub-level, LEVEL 1a, concerned the shape of the frequency-size distribution and the sub-level, LEVEL 1b concerned the GR parameters: a and b-values. Therefore, we present the scores on set of alternative models in each sub-level – LEVEL 1a, and LEVEL 1b – of LEVEL 1 reported in Tables 6.27 and 6.28. The estimated scores on alternative models in this level are also presented in the form of pie charts for a clearer picture, see Fig. 6.42 and Fig. 6.43.

In most cases, the models got the similar scores under three weighting. In LEVEL 1a, the model M5\_L1a got the highest score. In the same level, two models M3\_L1a, M4\_L1a and obtained the same scores. In LEVEL 2b, the model M5\_L1b got the highest scores for all the weighting schemes.

**Table 6.27 Estimated scores on alternative models for LEVEL 1a**

No.	Model code	Description	Scores		
			EW	AW	PW-H
1	M1_L1a	Truncated Pareto with Mmax = 7.5 for crustal seismicity and Mmax = 8.8 for subduction interfaces	0.07	0.07	0.10
2	M2_L1a	Truncated Pareto with Mmax = 7.5 for crustal seismicity and Mmax = 9.1 for subduction interfaces	0.13	0.14	0.11
3	M3_L1a	Truncated Pareto with Mmax = 8.0 for crustal seismicity and Mmax = 8.8 for subduction interfaces	0.10	0.10	0.10
4	M4_L1a	Truncated Pareto with Mc = 8.0 for crustal seismicity and Mc = 9.1 for subduction interfaces	0.10	0.10	0.10
5	M5_L1a	Tapered Pareto with Mmax = 7.5 for crustal seismicity and Mmax = 8.8 for subduction interfaces	0.18	0.17	0.18
6	M6_L1a	Tapered Pareto with Mc = 7.5 for crustal seismicity and Mc = 9.1 for subduction interfaces	0.16	0.15	0.16
7	M7_L1a	Tapered Pareto with Mc = 8.0 for crustal seismicity and Mc = 8.8 for subduction interfaces	0.12	0.12	0.13
8	M8_L1a	Tapered Pareto with Mc = 8.0 for crustal seismicity and Mc = 9.1 for subduction interfaces	0.15	0.16	0.13

**Table 6.28 Estimated scores on alternative models for LEVEL 1b**

No.	Model code	Description	Scores		
			EW	AW	PW-H
1	M1_L1b	a-value as mean of the Likelihood distribution and b-value equal to 1	0.20	0.21	0.19
2	M2_L1b	a-value as mean of the Likelihood distribution and b-value estimated from data (MLE)	0.14	0.14	0.09
3	M3_L1b	a-value as 10th percentile of the Likelihood distribution and b-value equal to 1	0.14	0.15	0.20
4	M4_L1b	a-value as 10th percentile of the Likelihood distribution and b-value estimated from data (MLE)	0.11	0.11	0.10
5	M5_L1b	a-value as 90th percentile of the Likelihood distribution and b-value equal to 1	0.26	0.25	0.29
6	M6_L1b	a-value as 90th percentile of the Likelihood distribution and b-value estimated from data (MLE)	0.15	0.14	0.14

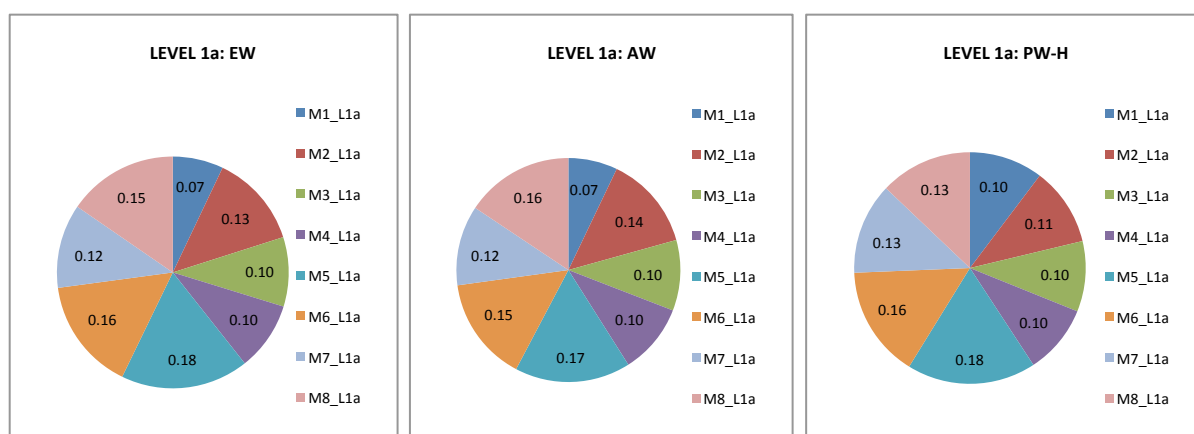


**Fig. 6.42 Pie chart representation of scores on models in LEVEL 1a under three weighting schemes**

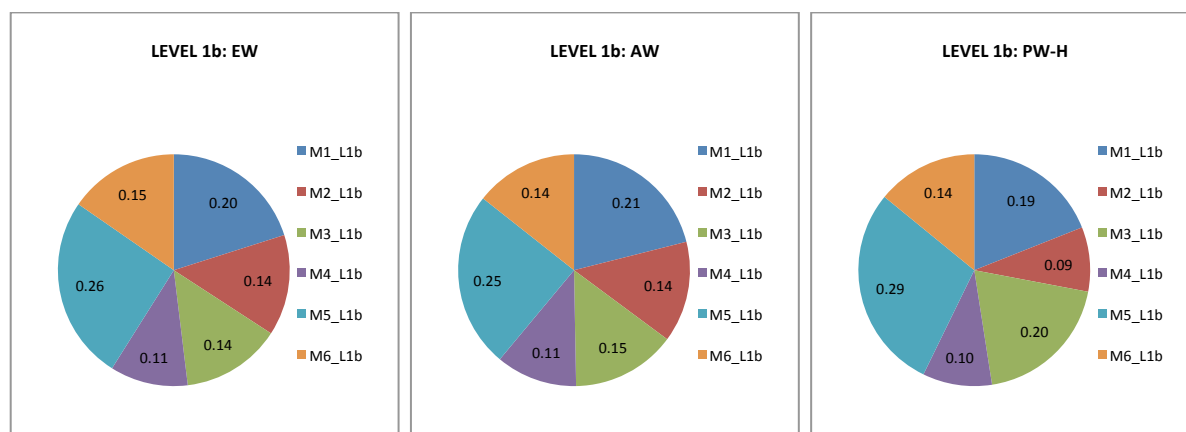


**Fig. 6.43 Pie chart representation of scores on models in LEVEL 1a under three weighting schemes**

LEVEL 2: The LEVEL 2 was about the separation of subduction interface seismicity and background seismicity (in subduction regions: Hellenic Arc and Calabrian Arc). As the models in LEVEL 2 was separated into two sub-levels that is LEVEL 2a and LEVEL 2b, therefore two different questions were designed for judgments for each sub-level. The sub-level, LEVEL 2a, concerned the events in seismicity catalogs can be assigned to the subduction interface based on their hypocentral depth and the sub-level, LEVEL 2b concerned the functional form of the separation, as a function of the magnitude  $M$ . Therefore, we present the scores on set of alternative models in each sub-level – LEVEL 2a, and LEVEL 2b – of LEVEL 2 reported in Tables 6.29 and 6.30. The estimated scores on alternative models in this level are also presented in the form of pie charts for a clearer picture, see Fig. 6.44 and Fig. 6.45.

Likewise in LEVEL 2, in most cases, the models got the similar scores under three weighting. In LEVEL 2a, the model M3\_L2a got the highest score and M1\_L2a got the minimum scores. In LEVEL 2b, the model M4\_L2b got the highest scores and M1\_L2b got the minimum scores under all the weighting schemes.

**Table 6.29 Estimated scores on alternative models for LEVEL 2a**

No.	Model code	Description	Scores		
			EW	AW	PW-H
1	M1_L2a	Buffer of 5 km around the position of the subduction interface (2.5 km over and 2.5 km under the subduction)	0.08	0.08	0.09
2	M2_L2a	Buffer of 10 km around the position of the subduction interface (2.5 km over and 2.5 km under the subduction)	0.43	0.41	0.37
3	M3_L2a	Buffer of 15 km around the position of the subduction interface (2.5 km over and 2.5 km under the subduction)	0.49	0.51	0.54

**Table 6.30 Estimated scores on alternative models for LEVEL 2b**

No.	Model code	Description	Scores		
			EW	AW	PW-H
1	M1_L2a	$M_f = 5.0$ and $f(M)$ linear with $f(M_f) = f_m$ and $f(8) = 1$	0.09	0.09	0.09
2	M2_L2a	$M_f = 5.0$ and $f(M)$ exponential with $f(M_f) = f_m$ and $f(8) = 1$	0.22	0.23	0.12
3	M3_L2a	$M_f = 6.0$ and $f(M)$ linear with $f(M_f) = f_m$ and $f(8) = 1$	0.22	0.21	0.26
4	M4_L2a	$M_f = 6.0$ and $f(M)$ exponential with $f(M_f) = f_m$ and $f(8) = 1$	0.48	0.47	0.53

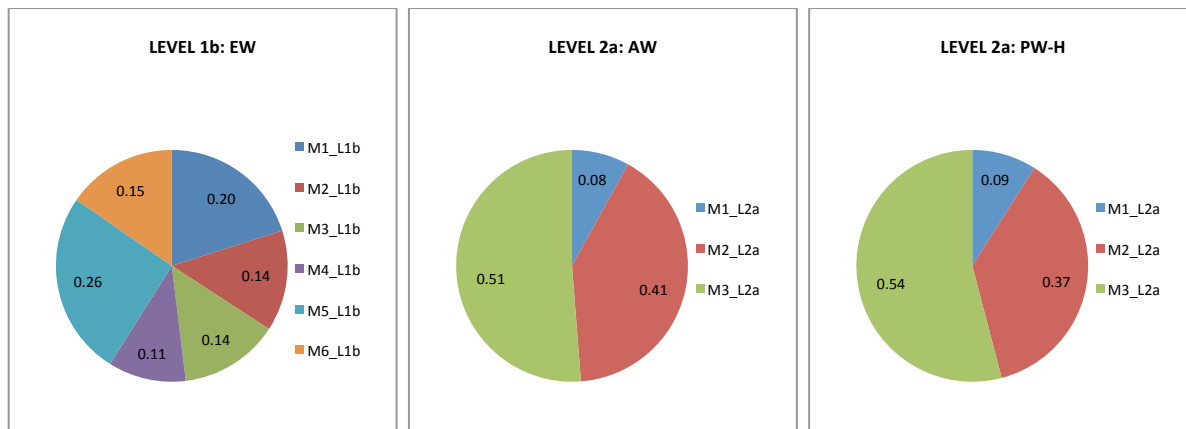


**Fig. 6.44** Pie chart representation of scores on models in LEVEL 2a under three weighting schemes

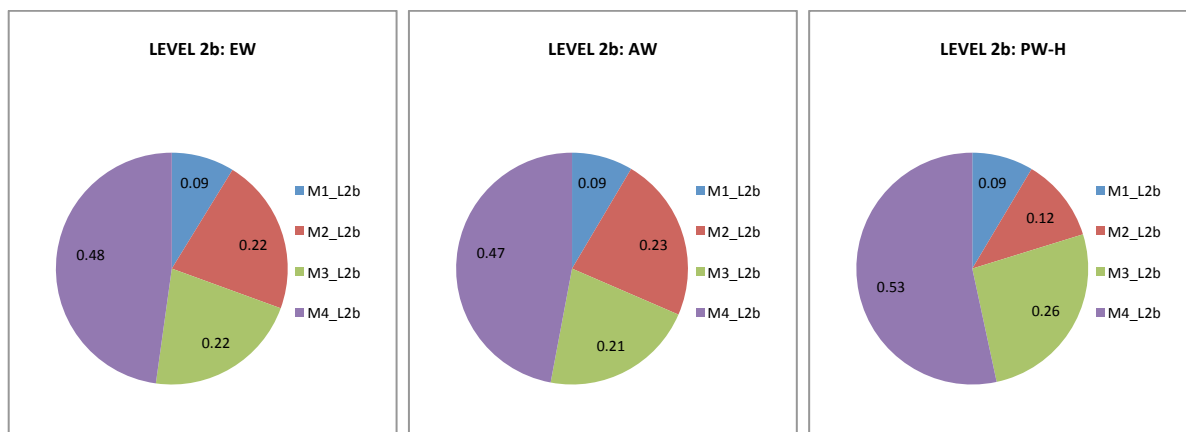


**Fig. 6.45** Pie chart representation of scores on models in LEVEL 2b under three weighting schemes

BS-Branch: This branch was about the distribution of epicenters and of focal mechanisms, based on observed seismicity. The scores on set of alternative models on the BS-Branch are reported in Table 6.31. The estimated scores on alternative models in this level are also presented in the form of pie charts for a clearer picture, see Fig. 6.46.

The model M3\_BS obtained the highest scores under three weighting schemes. The model M1\_BS secured the minimum equal score under EW, AW and PW-H. Also, the differences among the scores under three schemes were not very significant.

**Table 6.31 Estimated scores on alternative models for BS-Branch**

No.	Model code	Description	Scores		
			EW	AW	PW-H
1	M1_BS	Uniform distribution of events over individual seismic regions (LEVEL BS-1) and focal mechanisms based on all CMT (global + regional) catalog (LEVEL BS-3)	0.12	0.12	0.12
2	M2_BS	Uniform distribution of events over individual seismic regions (LEVEL BS-1) and focal mechanisms based on EMMA catalog (LEVEL BS-3)	0.11	0.10	0.08
3	M3_BS	Smoothed seismicity of background events over individual seismic regions (LEVEL BS-1) and focal mechanisms based on allCMT (global + regional) catalog (LEVEL BS-3)	0.43	0.43	0.50
4	M4_BS	Smoothed seismicity of background events over individual seismic regions regions (LEVEL BS-1) and focal mechanisms based on EMMA catalog (LEVEL BS-3)	0.35	0.34	0.30

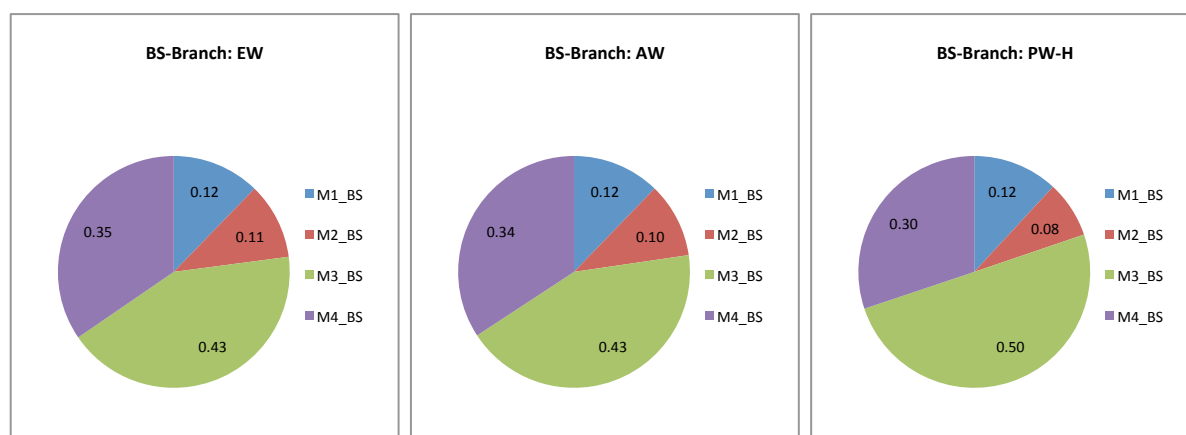


**Fig. 6.46 Pie chart representation of scores on models in BS-Branch under three weighting schemes**

IS-Branch: This branch was about the distribution of epicenters in subduction interfaces. The scores on set of alternative models on the IS-Branch are reported in

Table 6.32. The estimated scores on alternative models in this level are also presented in the form of pie charts for a clearer picture, see Fig. 6.47. In IS-Branch, the model M1-IS obtained relatively higher scores compared to model M2-IS under three weighting schemes.

**Table 6.32 Estimated scores on alternative models for IS-Branch**

No.	Model code	Description	Scores		
			EW	AW	PW-H
1	M1_IS	Rupture is allowed to propagate into the “propagation area”	0.52	0.52	0.71
2	M2_IS	Rupture is forced to be completely included into the “nucleation area”	0.48	0.48	0.29

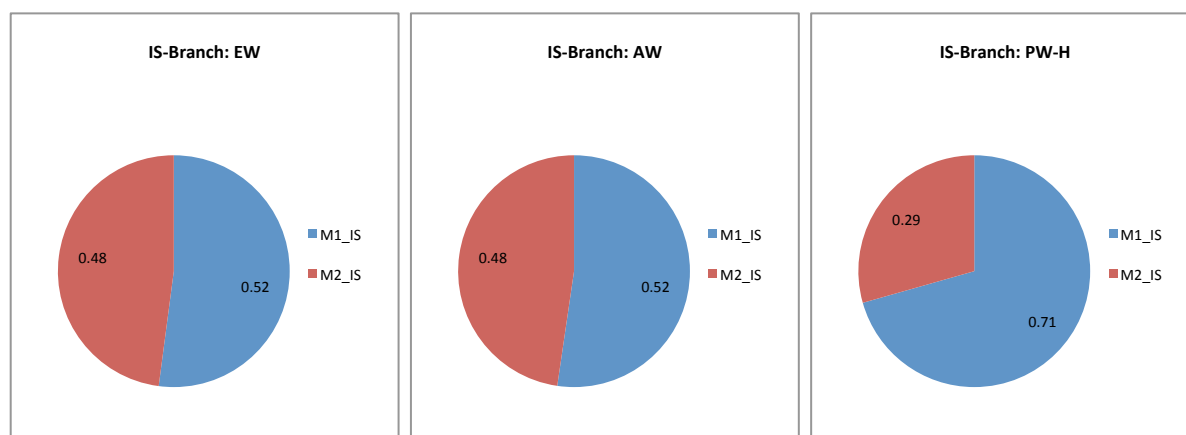


**Fig. 6.47 Pie chart representation of scores on models in IS-Branch under three weighting schemes**



## 7 CI-C1 Industrial district, Italy

### 7.1 INTRODUCTION

The industrial building stock in Northern Italy, and more specifically in the region of Tuscany, has been considered for the CI-C1 case study application of the STREST methodology. The document “Guidelines for performance and consequences assessment of multiple-site, low-risk, high-impact, non- nuclear critical infrastructures”, i.e. STREST D4.3 (Crowley et al., 2015), provides a detailed description of the hazard, vulnerability and exposure models and associated probabilistic risk methodology that has been applied in this case study Stress Test. The exposure data for this case study has been provided by the industrial partner in this case study: the Sezione Sismica, Regione Toscana. Only seismic hazard has been considered in this case study, as it is the predominant hazard to which the industrial building stock in Tuscany is exposed. The limited budget for a Stress Test of an industrial district (given that these facilities do not serve the same critical functions as other infrastructure considered herein) has conditioned the level of detail and complexity of the Stress Test. Nevertheless, the simplicity of the case study allows the full probabilistic risk assessment and disaggregation methodology of STREST to be fully demonstrated.

### 7.2 PHASE 1: PRE-ASSESSMENT PHASE

#### 7.2.1 Data collection

##### Data related to the industrial facilities

Most of the typical reinforced concrete precast industrial buildings in the Tuscany region can be categorized into three classes, according to the design code level, type of structure and type of cladding (see Fig. 7.1).

The code level of the buildings has been defined as pre-code or low-code, depending on whether the building was constructed before or after 1996, respectively. Pre-code buildings were designed to withstand lateral loads equal to 2% of the building self-weight, whilst for the low-code structures a value of 7% of the building self-weight was chosen as representative of the seismic design level in the seismic zones of Tuscany between 1996 and 2008.

These structures are formed of parallel portals, which consist of beams placed on corbel connections at the top of the columns. The columns are fixed at the bottom by socked foundations and the capacity of a beam-to-column connection can be either friction force or friction force and dowels, depending on the design code. It has been assumed that the beam-to-column connections of pre-code buildings rely on friction alone, whereas in the connections of low-code buildings dowels are also used.

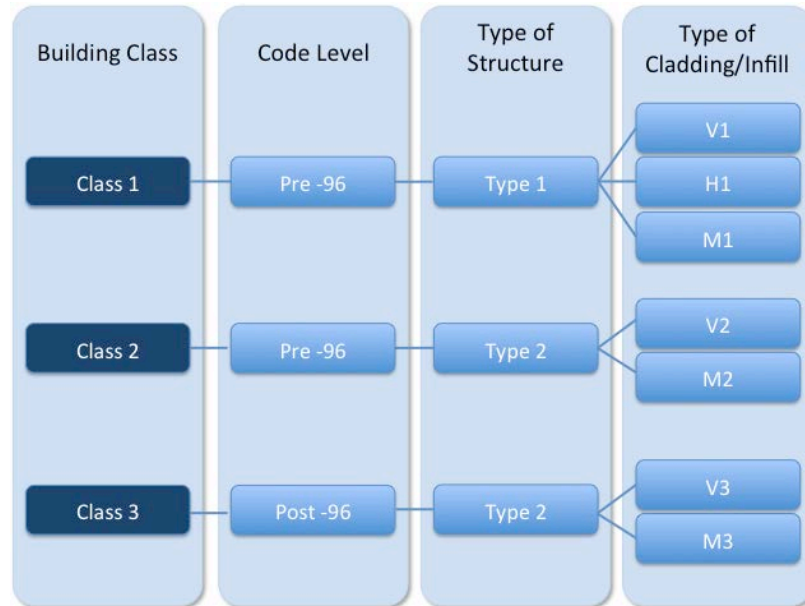


**Fig. 7.1 Definition of the industrial precast buildings considered for Tuscany**

The structural configuration is herein termed as type 1 for buildings with long saddle roof beams, and as type 2 for buildings with shorter rectangular beams and larger distance between the portals. These two configurations are depicted in Fig. 7.2.



**Fig. 7.2 Structural configuration and assumed position of openings in a) Type 1 and b) Type 2 industrial building (Casotto et al., 2015)**

According to information provided by *Regione Toscana*, the most common types of cladding in the region of Tuscany are vertical precast panels (V), horizontal panels (H) and concrete masonry infills (M). All three types of cladding were considered for type 1 buildings, which belong to class 1. Due to the large spans of the portals that characterize type 2 buildings, only the vertical and masonry infills were considered appropriate (classes 2 and 3), leading to seven subclasses, as depicted previously in Fig. 7.1 (see STREST D4.3 Crowley et al., 2015) for more information on the structural and non-structural characteristics of these different building classes).

*Regione Toscana* has also provided details on a large number of industrial buildings in the region, including coordinates, year of construction, floor area, structural type, non-structural elements, and other data useful for identifying value of contents, type of business, and

extent of customer base. The geographical distribution of these 425 industrial facilities in Tuscany is illustrated in Fig. 7.3, and these have been used to develop an exposure model for risk analysis. The number of buildings within each subclass in this exposure model is reported in

It can be observed from Table 7.1 that the majority of buildings have been designed following the pre-code guidelines, with the fewest buildings designed according to low-code.

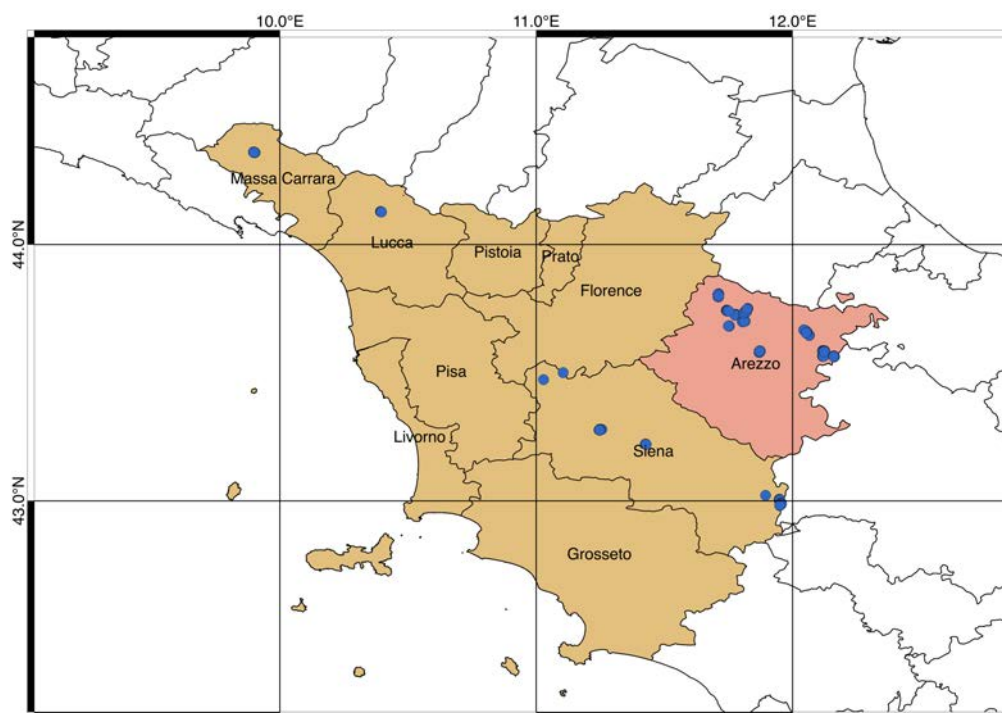


Fig. 7.3 Location of the 425 industrial facilities in the *Regione Toscana* database

Table 7.1 Number of buildings in *Regione Toscana* database according to subclass

Class	Subclass	Number of Buildings
1	V1	22
	H1	58
	M1	47
2	V2	178
	M2	72
3	V3	41
	M3	7

To each specific building in the exposure model, in addition to the building subclass, the value of the structural elements, non-structural elements, contents and business interruption (per day) needs to be assigned. The construction costs for an industrial facility are used to assign the value of the structural and non-structural elements, and this has been estimated

using the mean market prices of industrial/typical warehouses as a function of the so-called OMI zone<sup>2</sup> where the building is located. This price is given per floor area, and so the total construction cost has been estimated by multiplying the market price by the floor area of each building in the exposure database. This total cost has then been divided into a structural and a non-structural value by assuming (through engineering judgment) that 25% is related to the structural elements and 75% covers the cost of the non-structural elements. Only the cladding/infill is explicitly modeled as a non-structural element herein, hence it is assumed that the response of other non-structural components (such as the heating, ventilation and air conditioning equipment, electrical equipment and plumbing equipment) is fully correlated with the cladding/infill. The cost of the contents has been estimated according to FEMA (2012), wherein the value of the contents for the type of facilities considered herein is assumed to be 44% of the total value of the construction. Finally, the business interruption costs have been estimated using the HAZUS methodology (FEMA, 2003), which prices the daily business interruption value for these types of facilities as 0.95 dollars per square foot (and this has been converted to Euros assuming a conversion rate of 0.96).

### **Data related to seismic hazard**

In order to generate a large set of ground motion fields characterizing the seismicity of a given region, a probabilistic seismic hazard model comprised of the following three components is required: a seismological/source model that describes the location, geometry, and seismic activity of the sources; a ground-motion model that describes the probability of exceeding a given level of ground motion at a site, conditioned on a set of event and path characteristics; and a site condition model that describes the characteristics of the soil at each site.

The seismological/source model can generate catalogues of potential earthquake ruptures, termed stochastic event sets. The events from the source model can be used to produce a ground motion field based on: a list of ground motion prediction equations (GMPEs) for each tectonic region in the input model, and a random selection of the inter-event residual for the event and a random selection of the intra-event residual for each site in the model (see e.g. Crowley and Bommer, 2006). The spatial correlation of the intra-event residuals should be accounted for when sampling this variability at each site where an industrial facility is located, using models such as that proposed by Jayaram and Baker (2009). As all of the vulnerability models considered herein use the same intensity measure type (peak ground acceleration, PGA), it has not been necessary to consider cross-correlation of the intensity measures (see e.g. Weatherill et al., 2015).

The European project “Seismic Hazard Harmonization in Europe” (SHARE, 2009–2013) has produced a European seismic hazard model (Woessner et al., 2015) with three source models (one based on area sources, one that uses fault sources and a third based on distributed seismicity). The three aforementioned models can be used separately to produce a hazard model, although it was recommended by the SHARE consortium that these models should be combined in a logic tree, together with additional logic tree branches to describe

---

<sup>2</sup>

<http://www.agenziaentrate.gov.it/wps/content/nsilib/nsi/documentazione/omi/banche+dati/quotazioni+immobiliari>

the epistemic uncertainty in the GMPEs. The SHARE seismological models are available from the European Facility for Earthquake Hazard and Risk portal ([www.efehr.org](http://www.efehr.org)), and can be used to generate spatially correlated ground-motion fields using the Global Earthquake Model’s hazard and risk software, the OpenQuake-engine (Silva et al., 2014b).

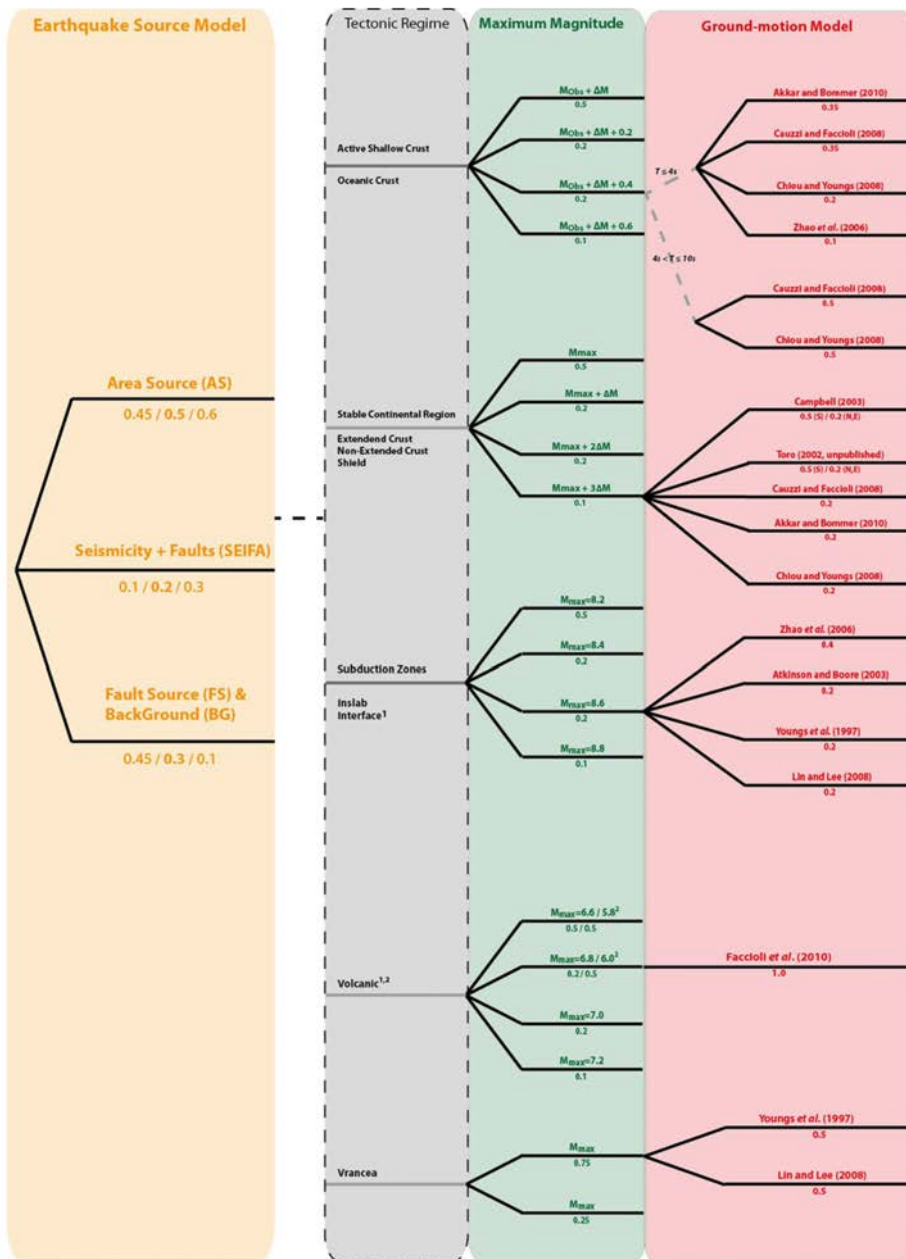
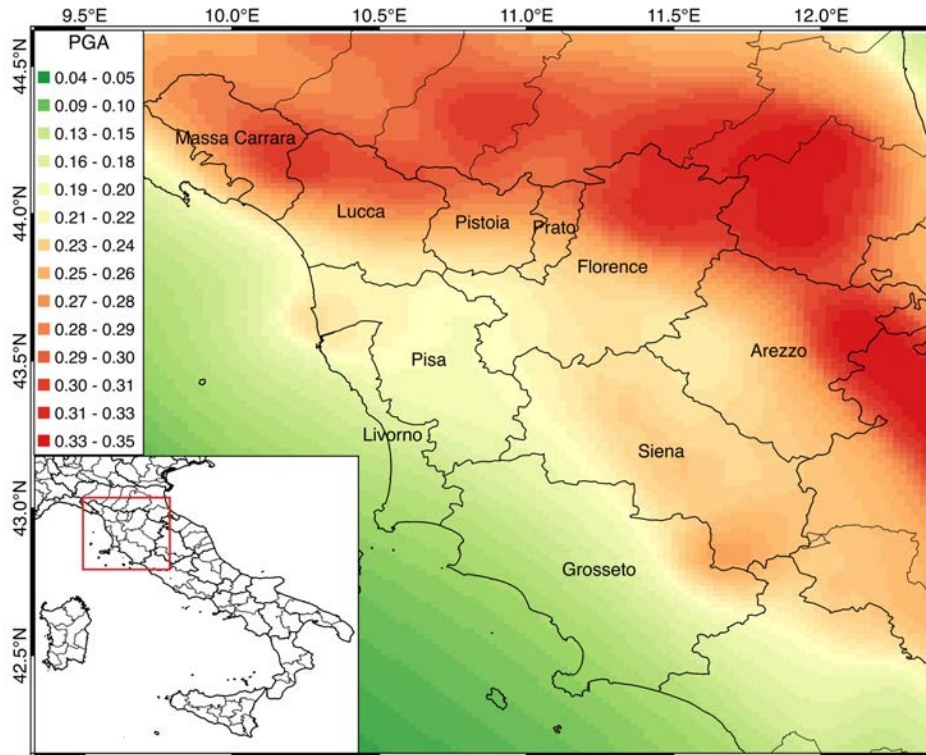


Fig. 7.4 SHARE logic tree (Woessner et al., 2015)

The information presented in the SHARE logic tree is illustrated in Fig. 7.4. The colors represent the branching levels for the earthquake source models (yellow), maximum magnitude models (green) and ground motion models (red). The corresponding weights are indicated below the black lines. Although tectonic regionalization is not a branching level (grey) of the model, it defines the GMPEs to be used.

Fig. 7.5 presents the mean hazard map that has been calculated for Tuscany, with the OpenQuake-engine and the SHARE hazard model, in terms of PGA with a 10% probability of exceedance in 50 years. In order to account for site amplification, the  $V_{s30}$  value of the soil at each location in the exposure model is needed. This is not currently available for the locations of the 425 industrial facilities in the exposure model, and so an estimation of the value of  $V_{s30}$  based on a proxy (topography) has been employed<sup>3</sup>, as shown in Fig. 7.6.



**Fig. 7.5 Mean hazard map for Tuscany based on SHARE logic tree with  $V_{s30} = 800$  m/s (in terms of PGA with 10% probability of exceedance in 50 years)**

<sup>3</sup> <http://earthquake.usgs.gov/hazards/apps/vs30/predefined.php>



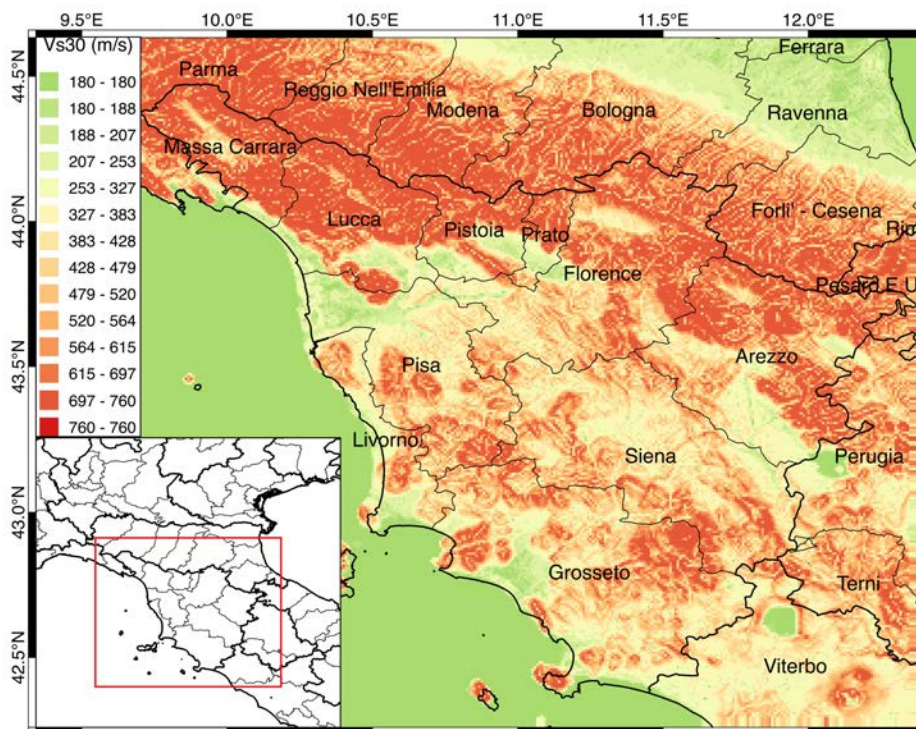


Fig. 7.6 Estimates of site conditions in Tuscany from topographic slope (<http://earthquake.usgs.gov/hazards/apps/vs30/predefined.php>)

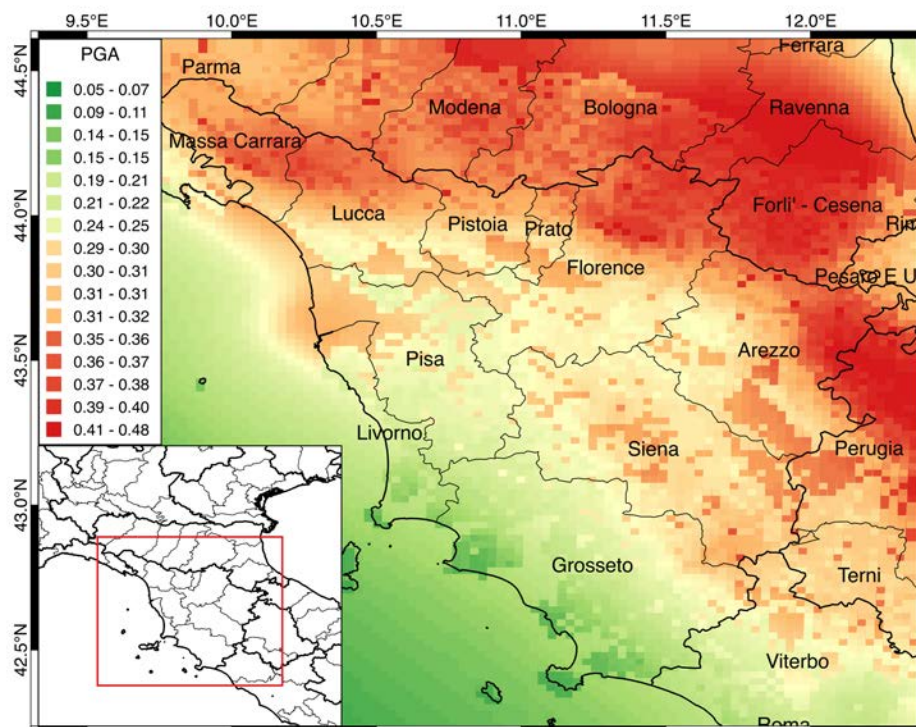
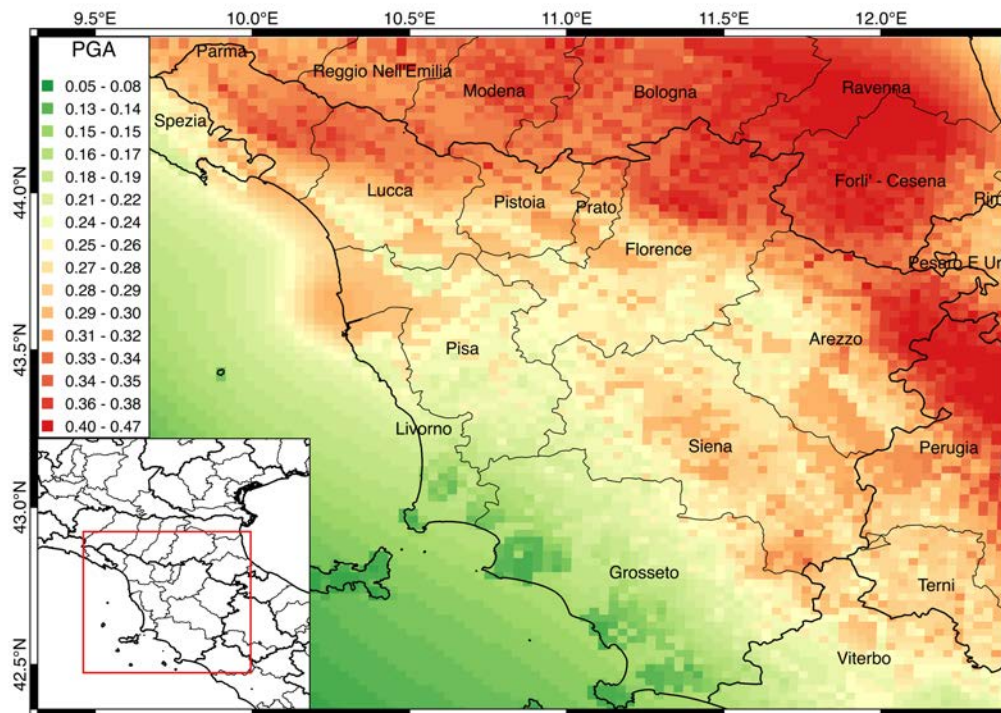


Fig. 7.7 Mean hazard map for Tuscany based on SHARE logic tree with local site conditions based on Vs30 proxy (in terms of PGA with 10% probability of exceedance in 50 years)



In order to model the spatial correlation of the intra-event residuals in the risk assessment, the model of Jayaram and Baker (2009) has been used. It has been necessary, however, to modify the SHARE logic tree as not all of the GMPEs have a separation of the aleatory variability into the intra- and inter-event variability components. The following GMPEs in the SHARE logic tree could not be used in the final probabilistic risk assessment and were thus removed, and the weights of the remaining branches were reassigned accordingly: Cauzzi and Faccioli (2008), Toro et al. (2002), Campbell (2003) and Faccioli et al. (2010). Fig. 7.8 shows the mean seismic hazard map with this updated, reduced logic tree, and it can be seen that the mean hazard is not significantly influenced by the aforementioned changes to the logic tree.



**Fig. 7.8 Mean hazard map for Tuscany based on *reduced* SHARE logic tree with local site conditions based on  $V_{s30}$  proxy (in terms of PGA with 10% probability of exceedance in 50 years)**

### 7.2.2 Risk Measures and Objectives

Definition As stated by Masden et al. (1986), various design codes such as the International Building Code (IBC, 2000) or the NEHRP Provisions (BSSC, 2004) agree that it is not possible to ensure complete safety in a structure, and that instead an acceptable level of risk should be established. The acceptable level of seismic risk can either be defined as the annual collapse probability or the total collapse probability for the life expectancy of the structure. Hence, for the component level Stress Test assessment carried out herein (wherein each industrial facility is considered as an individual component) the annual probability of structural collapse has been taken as the risk measure, and the required objective has been sought by reference to European design norms.

ASCE (2010) establishes an acceptable national risk of 1% in 50 years (about  $2.0 \times 10^{-4}$  annually) for the territory of the United States. On the other hand, Douglas et al. (2012)

considered several studies from the literature (e.g. Duckett (2004); Goulet et al. (2007); Fajfar and Dolsek (2012)), in which the annual probability of collapse of a number of structures designed according to modern regulations was determined. These researchers concluded that a value of  $1.0 \times 10^{-5}$  annually is instead a reasonable value. This value has also been proposed by the JCSS probabilistic model code (JCSS, 1999) for the most common design situation, and this has been used in the calibration of the Eurocodes, though these values were not necessarily proposed for seismic actions, but traditional loading cases. It is thus proposed to use a value of  $1.0 \times 10^{-5}$  for the boundary A-B and  $2.0 \times 10^{-4}$  for the boundary B-C of the grading system of the STREST methodology (see Fig. 7.9).

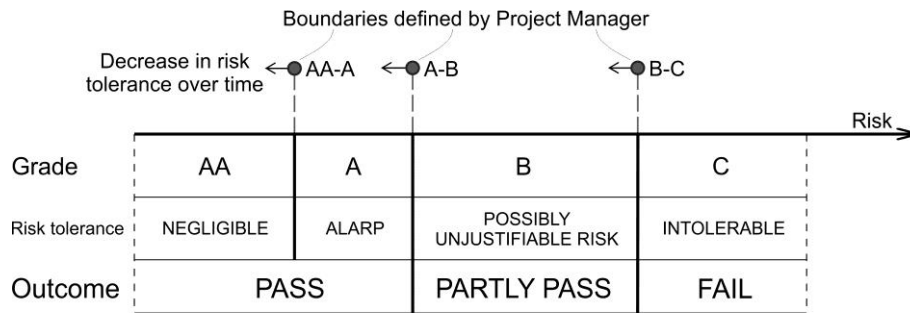


**Fig. 7.9 Grading system for global outcome of stress test**

For the system level assessment (where the combined influence of seismic damage to a whole industrial district is considered), economic loss-based measures and objectives have been used, given the large economic losses that were experienced in Italy following the Emilia-Romagna earthquakes in May 2012 (see STREST D2.3 Krausmann et al., 2014). The economic loss has been estimated considering the loss due to structural damage, non-structural damage, contents damage and associated direct business interruption. Indirect business interruption is inferred from the customer base of the facilities contributing most to the loss.

The risk objectives need to be defined by the main stakeholders, which in this case is considered to be the *Regione Toscana*. Through discussions with *Regione Toscana* it is become clear that their interest for this case study lies in reducing the economic impact on the region, and not just on a single industrial facility. The two types of risk metrics considered herein are:

- Average annual loss
- Mean annual rate of specific level of loss

Specific objectives for these risk metrics have not been defined by *Regione Toscana*, and so hypothetical values have been considered herein for illustrative purposes of the methodology. It has been decided to use the following objectives for the total average annual loss: the boundary A-B would be less 0.05% of the total exposure value and 0.1% would define boundary B-C. For the second objective, the mean annual rate of a loss due to business interruption equal to 7 times the daily business interruption exposure (i.e. 10 Million Euro) should not be higher than  $10^{-4}$  (i.e. 1 in 10,000 years) for boundary A-B and this would be 30 days for boundary B-C (42 Million Euro).

### 7.2.3 Set-up of the Stress Test

The limited budget for a Stress Test of an industrial district, given that these facilities do not serve the same critical functions as other infrastructure considered in the STREST project, has conditioned the choice of Stress Test Level and Technical Accuracy Level. However, the availability of existing data and methods to assess the probabilistic risk of these facilities means that the test goes beyond the minimum requirements.

The component-based assessment will focus on the structural components of industrial facilities (as these are the only components that need to be legally considered in design) and this will be undertaken with a risk-based approach (L1a Risk-Based) given the availability of structural fragility functions. A single hazard, single expert level 2 analysis with epistemic uncertainty (L2b) will be undertaken at the system level, given that the main threat to these structures is seismic risk and the available budget and relative importance of these facilities (with respect to other critical infrastructure) does not warrant the use of multiple experts.

Following discussions with the *Regione Toscana*, it was decided that the stress test would just be applied to the province of Arezzo, where the majority of the industrial facilities within the database are located (Fig. 7.10). Table 7.2 and Table 7.3 present the number of buildings in Arezzo in each sub-class and customer base, respectively.

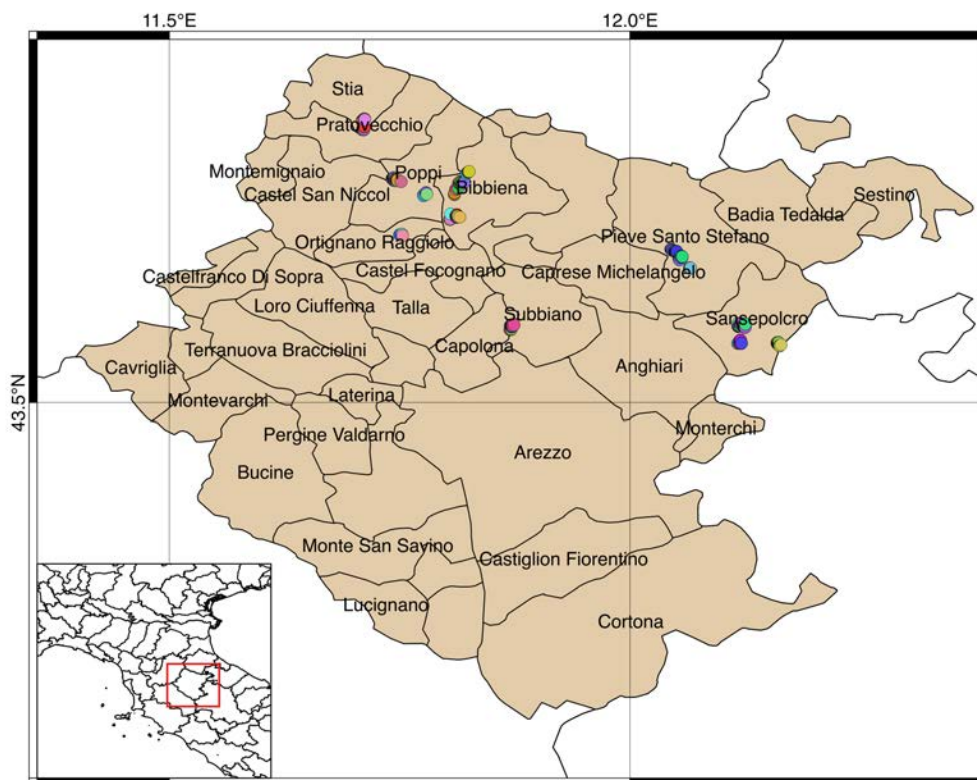


Fig. 7.10 Location of the 300 industrial facilities in the province of Arezzo

**Table 7.2 Number of buildings in Arezzo according to subclass**

Class	Subclass	Number of Buildings
1	V1	17
	H1	40
	M1	26
2	V2	140
	M2	45
3	V3	30
	M3	2

**Table 7.3 Number of buildings in Arezzo according to customer base**

Customer base	Number of Buildings
Not Determined (ND)	37
Comune (municipality)	26
Province	97
Regional	90
National	45
International	5

## 7.3 PHASE 2: ASSESSMENT PHASE

### 7.3.1 Component Level Assessment (ST-L1a)

A risk-based component level assessment has been undertaken for all 425 industrial facilities in the Regione Toscana database (Fig. 7.3) using hazard curves (i.e. PGA versus annual probability of exceedance) estimated with the OpenQuake-engine using the SHARE hazard model (Woessner et al., 2015), and amplified considering topography-based Vs30 estimates (Fig. 7.6), together with the complete damage structural fragility functions for each sub-class of structure (see Table 7.4), that were derived in STREST D4.3 (Crowley et al., 2015).

**Table 7.4 Parameters (median  $\theta$  and logarithmic standard deviation  $\beta$ ) of lognormal fragility functions for structural components (STREST D4.3)**

Subclass	Moderate		Extensive		Near Complete		Complete	
	$\theta$ [g]	$\beta$	$\theta$ [g]	$\beta$	$\theta$ [g]	$\beta$	$\theta$ [g]	$\beta$
V1	0.1	0.61	-	-	0.66	0.43	0.81	0.56
H1	0.09	0.43	-	-	0.5	0.81	0.6	0.92
M1	0.08	0.3	-	-	0.6	0.36	0.7	0.46
V2	0.1	0.61	-	-	0.61	0.37	0.74	0.47
M2	0.08	0.23	-	-	0.57	0.36	0.66	0.43
V3	0.16	0.72	0.21	0.87	0.52	0.53	0.6	0.53
M3	0.08	0.43	0.08	0.43	0.39	0.49	0.39	0.48

The process to estimate the annual probability of collapse for each individual building in the database is as follows:

1. For each location of an industrial facility, an amplified seismic hazard curve is obtained;
2. The seismic hazard curves are converted from probability of exceedance ( $PoE_{PGA}$ ) of PGA in 50 years ( $T$ ), into annual rate of exceedance ( $\lambda_{PGA}$ ) of PGA:

$$\lambda_{PGA} = -\frac{\ln(1-PoE_{PGA})}{T} \quad (7.1)$$

3. These curves are divided into a large number ( $m$ ) of segments, and the rate of occurrence of the associated central PGA value of each segment is derived.
4. The probability of collapse conditioned on the central PGA value of each segment ( $P(C|pga_i)$ ) is obtained from the complete fragility functions for the building subclass under consideration;
5. The conditioned probability of collapse of each segment is multiplied by the associated rate of occurrence for PGA values belonging to that segment, thus leading to a distribution of rate of collapse for a set of ground motion intensities. By numerically integrating this distribution, the annual collapse rate ( $\lambda_c$ ) is obtained:

$$\lambda_c = \sum_{i=1}^m P(C|pga_i) \cdot \left| \frac{d\lambda_{PGA}(pga_i)}{d(pga_i)} \right| \Delta pga_i \quad (7.2)$$

6. The annual collapse rate is converted into annual probability of collapse (PC) assuming a Poissonian process.

Histograms of the annual probability of collapse (PC) for the industrial facilities in Tuscany within each sub-class of building are presented in Fig. 7.11, Fig. 7.12 and Fig. 7.13, and for all facilities in Fig. 7.14. The values of annual probability of collapse presented in these figures are compared with acceptable levels in Section 7.4.1.

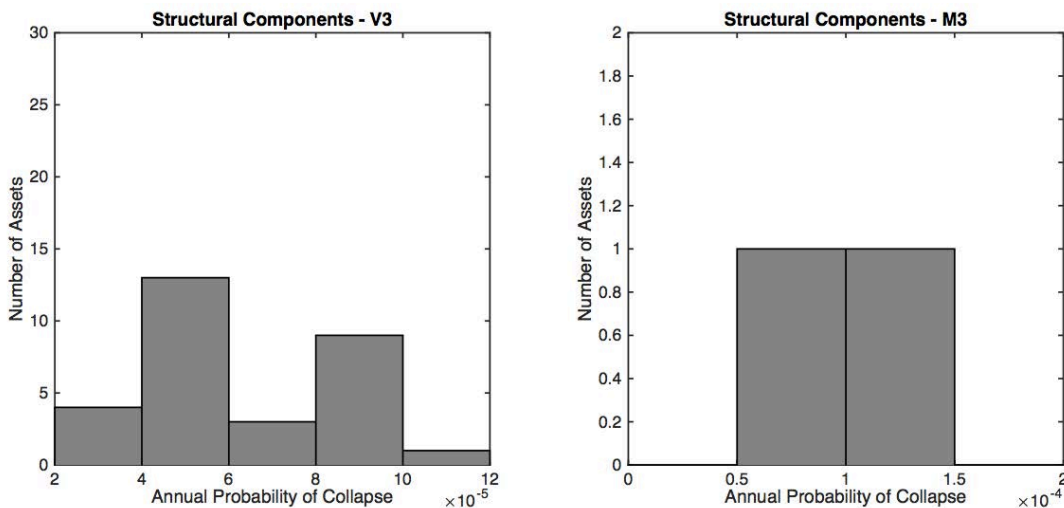


**Fig. 7.11 Annual probability of collapse of the low-code Type 2 buildings in Arezzo**

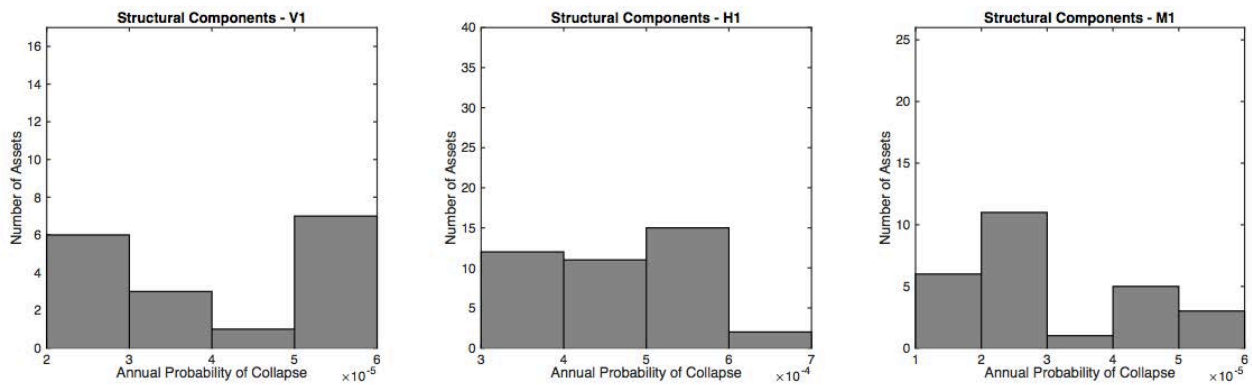


Fig. 7.12 Annual probability of collapse of the pre-code Type 1 buildings in Arezzo

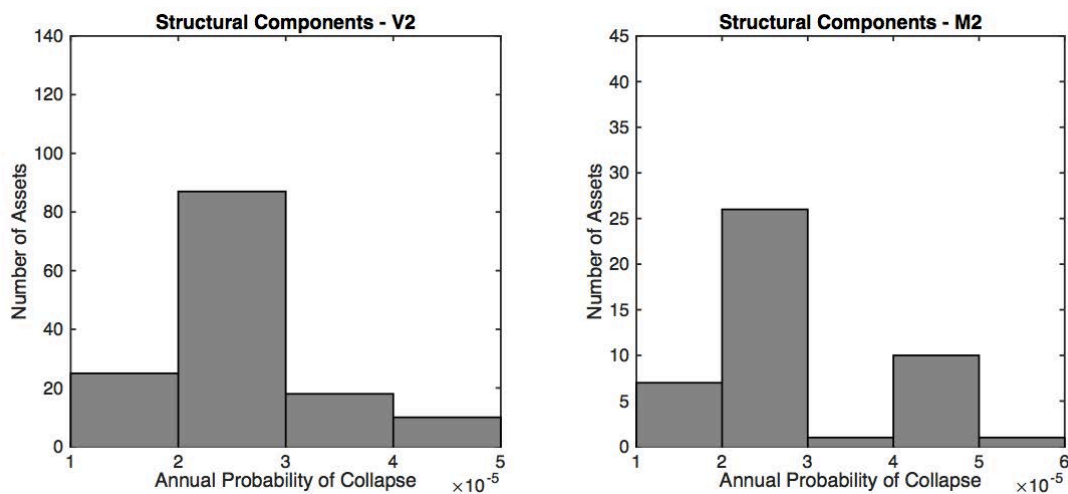


Fig. 7.13 Annual probability of collapse of the pre-code Type 2 buildings in Arezzo

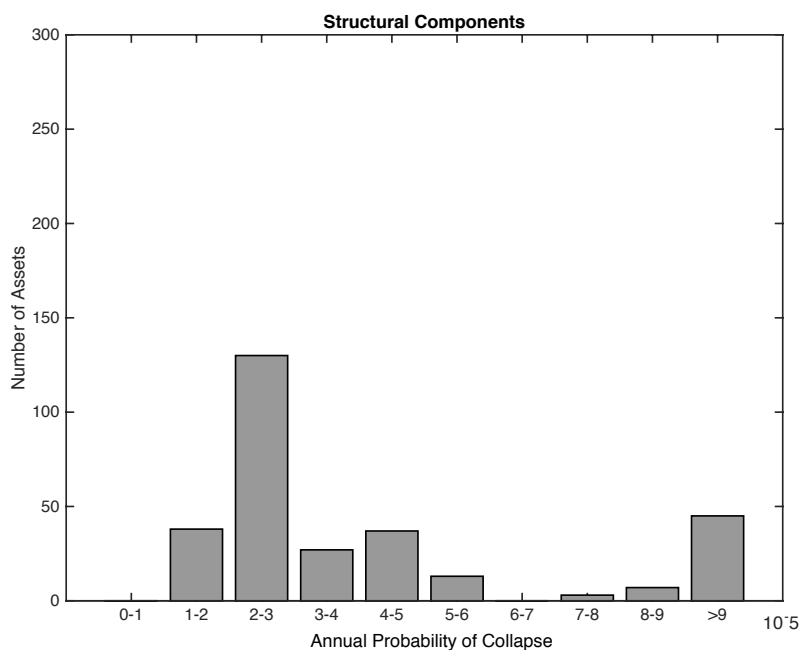


Fig. 7.14 Annual probability of collapse of all industrial buildings in Arezzo



### 7.3.2 System Level Assessment for Single Hazard (ST-L2b)

#### 7.3.2.1 Probabilistic Risk Assessment

The structural, non-structural, contents and business interruption fragility and vulnerability functions for each sub-class of structural type have been developed following the methodology and assumptions outlined in STREST D4.3 (Crowley et al., 2015) and are presented in the following plots. The uncertainty in these models is not presented in the plots, but has been accounted for as described in STREST D4.3 (Crowley et al., 2015). Furthermore, in the risk calculations, this uncertainty has been assumed to be fully correlated for all facilities of the same sub-class.

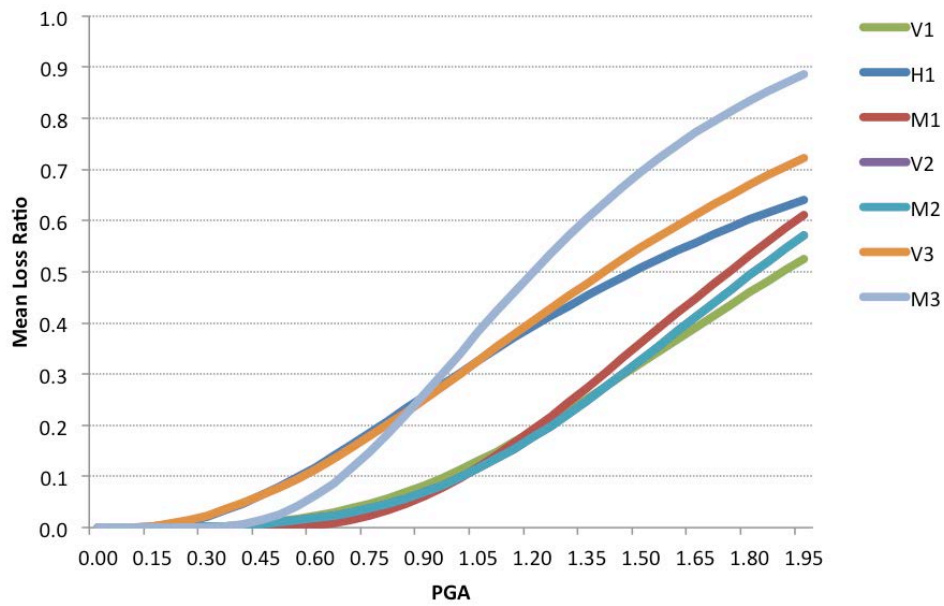


Fig. 7.15 Mean vulnerability model for structural components

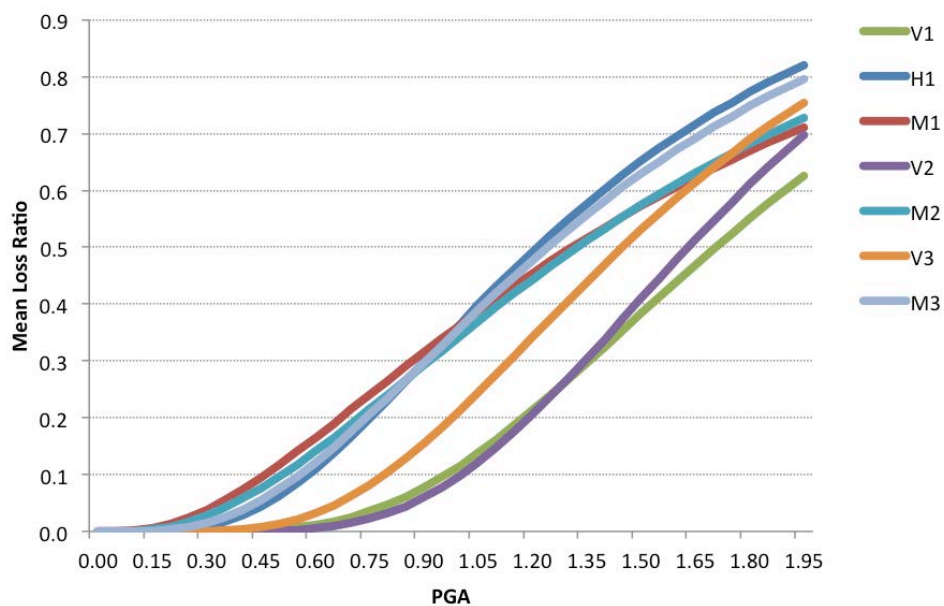
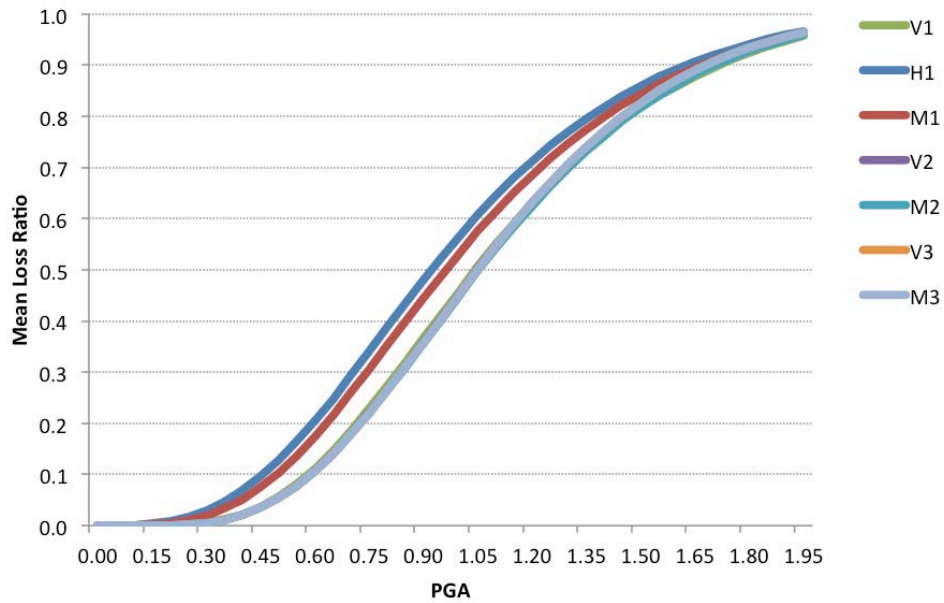
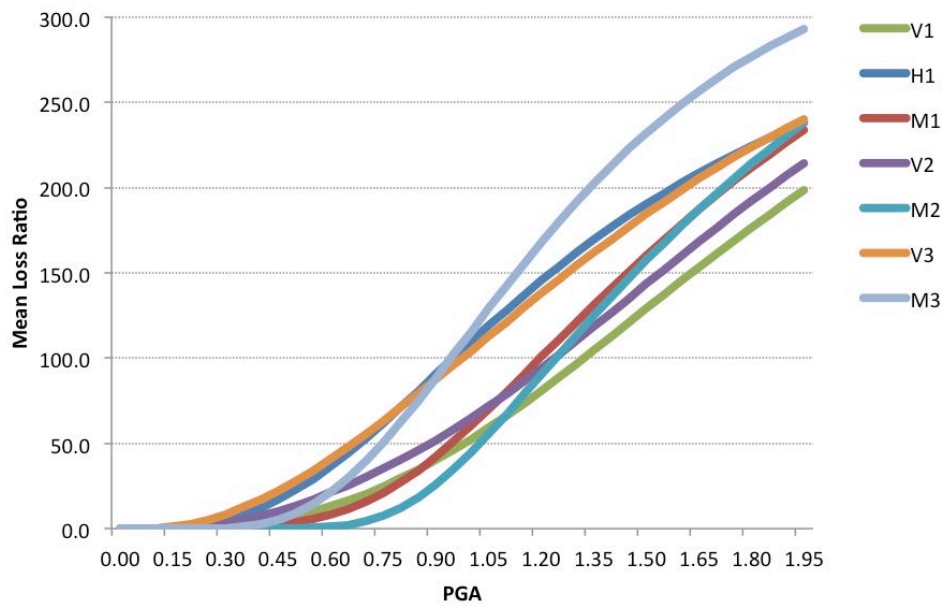


Fig. 7.16 Mean vulnerability model for non-structural components





**Fig. 7.17 Mean vulnerability model for contents**



**Fig. 7.18 Mean vulnerability model for business interruption (the y axis in this case also represents the mean number of days of disruption)**

As discussed previously, the reduced SHARE logic tree and the topography-based site conditions have been used to model the seismic hazard. In order to calculate probabilistic seismic risk for a spatially distributed portfolio of assets in Tuscany, the Probabilistic Event-Based Risk calculator from the OpenQuake-engine (Silva et al., 2014b) has been employed. This calculator is capable of generating loss exceedance curves and risk maps for various return periods based on probabilistic seismic hazard, with an event-based Monte Carlo approach. Loss curves and loss maps can be computed for five different loss types such as: structural components, non-structural components, contents, downtime losses and fatalities. The loss exceedance curves describe the probability of exceedance of different loss levels and the risk maps describe the loss values for a given probability of exceedance, over the

specified time period. Additionally, aggregated loss exceedance curves can also be produced using this calculator, which describe the probability of exceedance of different loss levels for all assets in the exposure model.

The probabilistic event-based risk calculator requires the definition of an exposure model, a vulnerability model for each loss type, and a set of ground motion fields representative of the seismicity of the region over the specific time period. In this calculator, losses for a certain industrial facility are calculated using a stochastic event set (SES). The associated ground motion fields for each event (within the SES) are combined with the vulnerability model, where structural/non-structural/contents loss ratio and downtime are defined. The loss ratios and downtime of each asset contained in the exposure model are multiplied by their corresponding value. The workflow of the Probabilistic event-based risk calculator is depicted in Fig. 7.19.

The results of the probabilistic risk assessment for the portfolio of industrial facilities in Arezzo are shown in the following figures in terms of loss exceedance curves. The results for each loss component are shown separately, as well as the total loss due to all components. The loss exceedance curve for each of the branches of the logic tree is shown with a thin line and the mean across all branches is shown with a thick line.

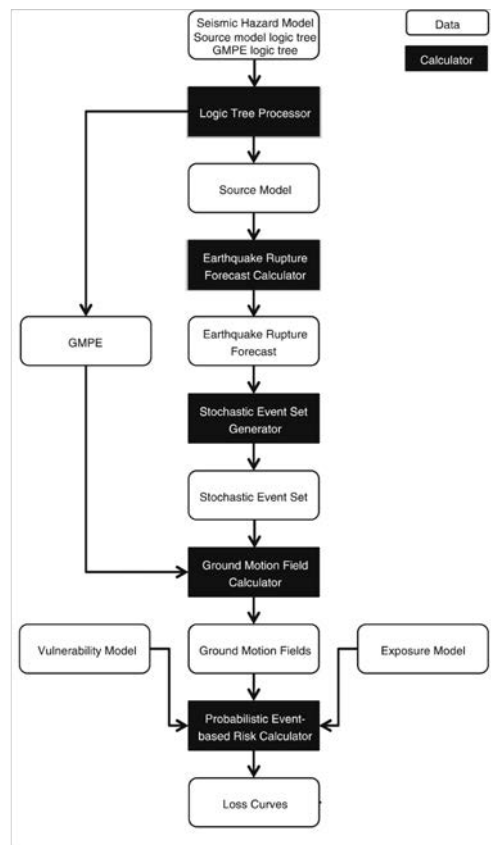
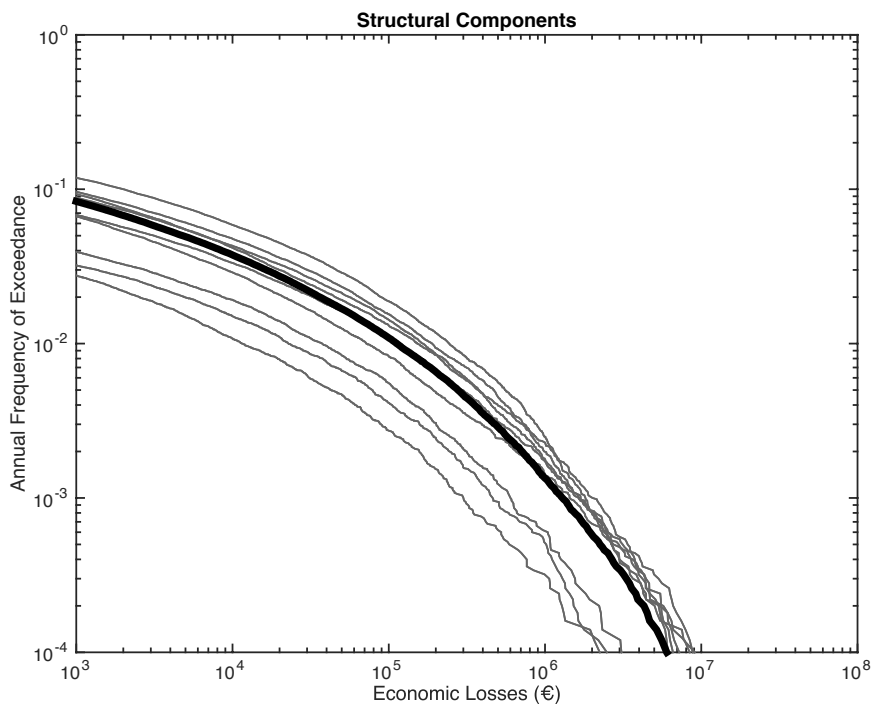
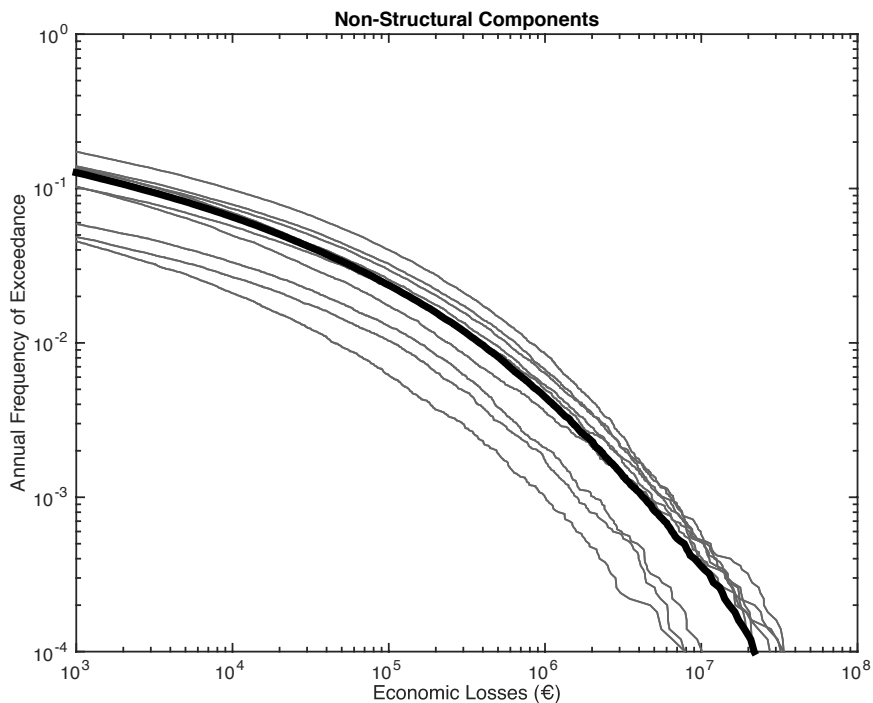


Fig. 7.19 Workflow for developing loss exceedance curves (Silva et al., 2014b)



**Fig. 7.20** Loss exceedance curves for all structural components in Arezzo (the loss exceedance curve for each of the branches of the logic tree is shown with a thin line and the mean across all branches is shown with a thick line)



**Fig. 7.21** Loss exceedance curves for all non-structural components in Arezzo (the loss exceedance curve for each of the branches of the logic tree is shown with a thin line and the mean across all branches is shown with a thick line)

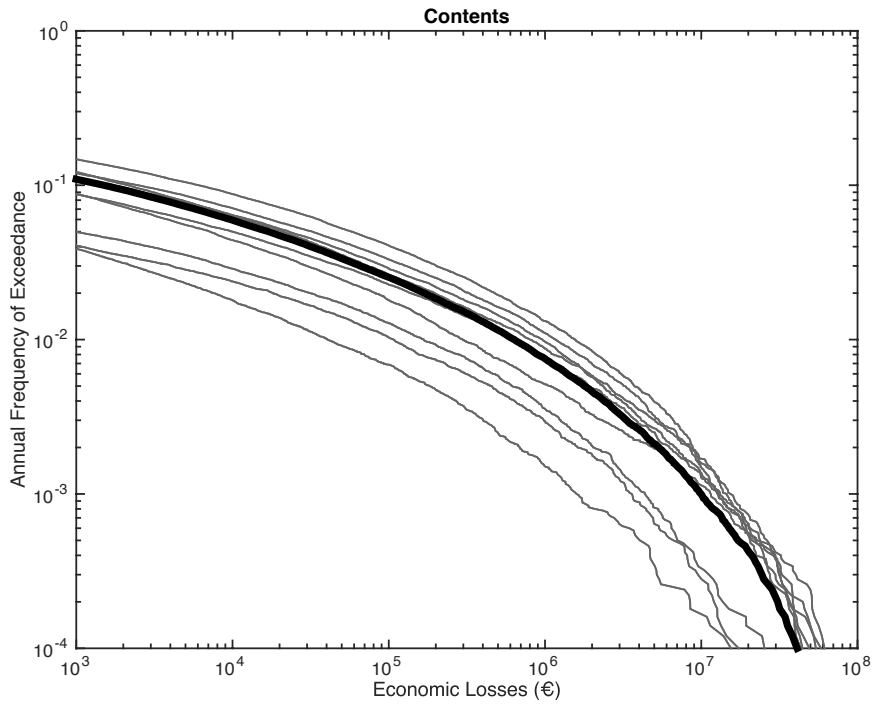


**Fig. 7.22 Loss exceedance curves for all contents of industrial facilities in Arezzo (the loss exceedance curve for each of the branches of the logic tree is shown with a thin line and the mean across all branches is shown with a thick line)**

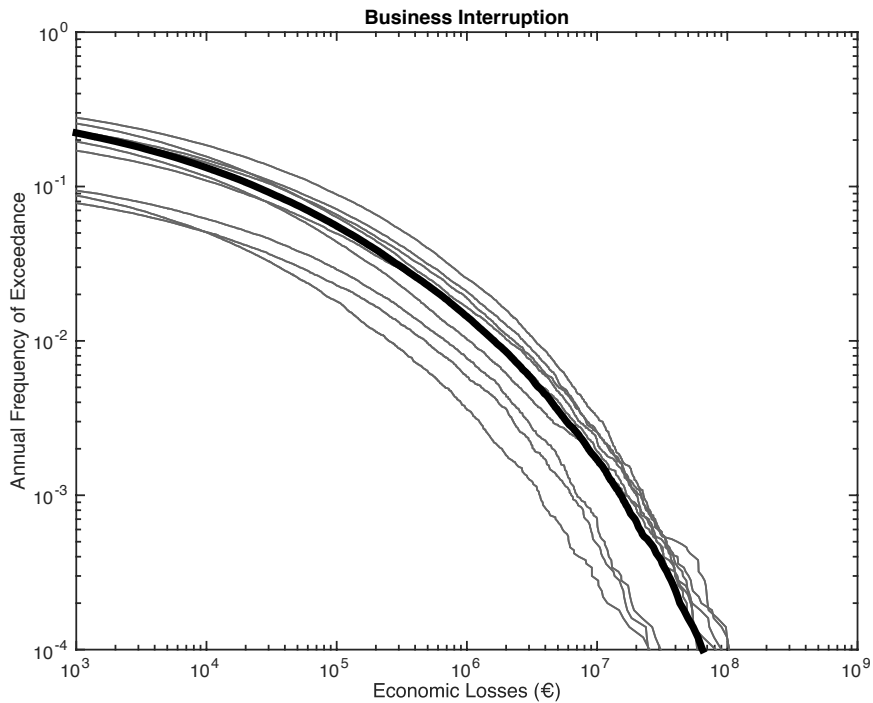


**Fig. 7.23 Loss exceedance curves for all business interruption in Arezzo (the loss exceedance curve for each of the branches of the logic tree is shown with a thin line and the mean across all branches is shown with a thick line)**

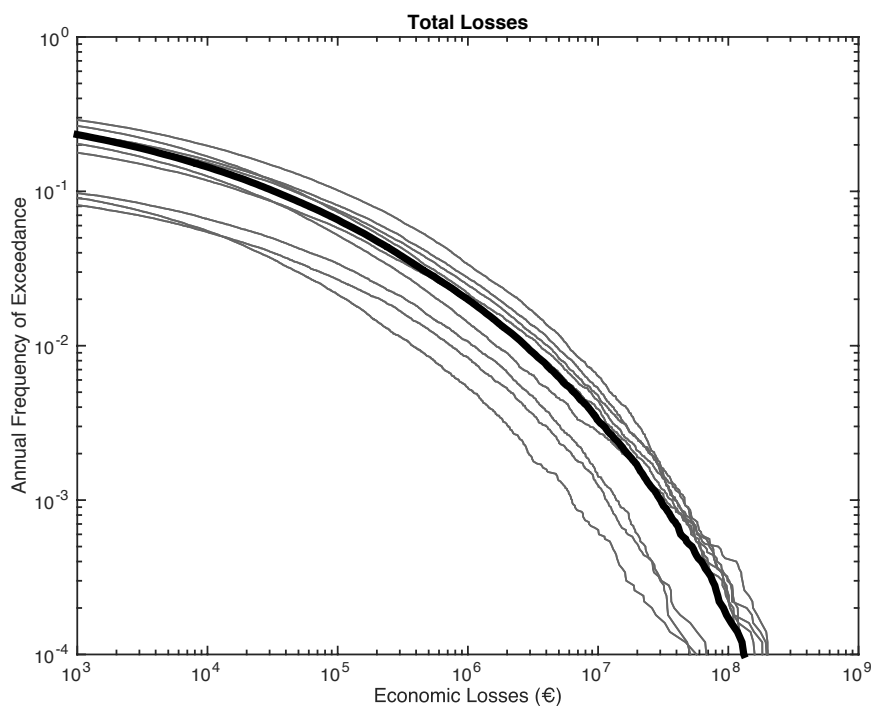


**Fig. 7.24 Total loss exceedance curves for all industrial facilities in Arezzo (the loss exceedance curve for each of the branches of the logic tree is shown with a thin line and the mean across all branches is shown with a thick line)**

The average annual losses (AAL) have been calculated from the loss exceedance curves and the results are presented in Table 7.5. This table shows that the largest component of loss is given by business interruption. The values of AAL as well as the mean annual rates of specific loss values will be checked against the risk objectives in Section 7.4.1.

**Table 7.5 Average annual losses for Arezzo portfolio**

	<b>Average Annual Losses</b>	<b>Average Annual Loss Ratio (%)<sup>1</sup></b>
<b>Structural</b>	€ 7,330	0.016
<b>Non-Structural</b>	€ 25,047	0.018
<b>Contents</b>	€ 49,022	0.033
<b>Business Interruption</b>	€ 93,932	0.067
<b>Total Losses</b>	€ 175,330	0.052

<sup>1</sup> Calculated as AAL / exposure value for each component

### 7.3.2.2 Scenario based Assessment

It was not necessary to perform additional scenario-based assessments as part of the Stress Test, as all expected seismic events were already included in the probabilistic risk assessment presented in the previous section.

### 7.3.3 System Level Assessment for Multiple Hazards

As discussed previously, based on the setup of the stress test (see Phase 1, step 3) it was decided not to perform this stress test level (L3).

## 7.4 PHASE 3: DECISION PHASE

### 7.4.1 Risk objectives check

This step of the Stress Test requires a comparison of the results of the risk assessment with the risk objectives, to check whether the industrial facilities pass each level of the Stress Test. According to the grading system, 260 facilities are assigned grade B (partly pass) and 40 facilities are assigned grade C (and thus fail the stress test).

The results also show that the A-B system level assessment objective is not met as the total AAL percentage is 0.052%, but the B-C level is met. Hence the grading would be B (partly pass) for this objective. The business interruption loss at a mean annual rate of exceedance of  $10^{-4}$  is 64 Million Euro (which can be translated as an average of 45 days of business interruption), and so the grading would be C (fail) for this objective.

### 7.4.2 Disaggregation/Sensitivity Analysis

The critical components for each loss, according to the disaggregation of the average annual loss are given in Fig. 7.25 and tabulated in Table 7.6. It can be noted that the most critical typologies might depend on the type of loss that is of most concern.

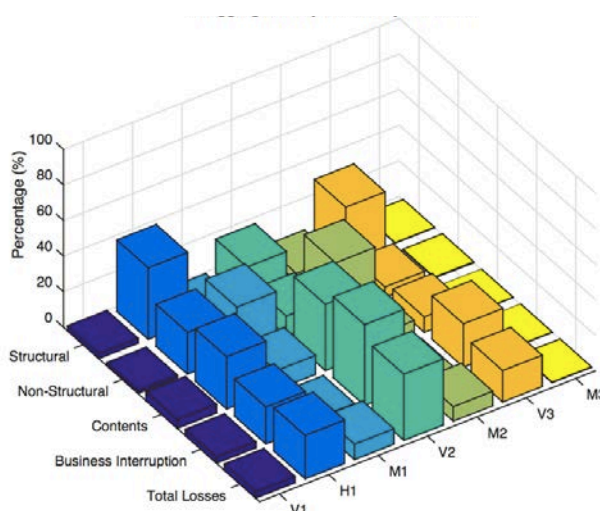


**Fig. 7.25 Disaggregation of average annual loss according to building sub-class for each component of loss**

**Table 7.6 Contribution of each building subclass to each component and total average annual loss**

	V1	H1	M1	V2	M2	V3	M3
<b>Structural</b>	2.8	40.3	1.9	19.1	4.7	31.0	0.3
<b>Non-structural</b>	1.7	23.6	26.9	11.1	30.2	5.9	0.6
<b>Contents</b>	4.9	29.5	10.8	37.3	8.8	8.6	0.2
<b>Business Interruption</b>	3.5	20.8	3.4	45.5	2.3	24.3	0.2
<b>Total Losses</b>	3.6	24.4	8.7	37.2	8.2	17.6	0.3

Fig. 7.26 shows how disaggregation at different levels of loss (which in this case is for a single component, business interruption loss, but could also be for the total loss according to all components) can be used to identify the hazard events that contribute most to that level of loss. The contribution of typologies to these loss values can also be obtained (similar to Fig. 7.25). Two different return periods are shown in Fig. 7.26, both the return period used in the stress test (10,000 years), and a lower return period of 1000 years.

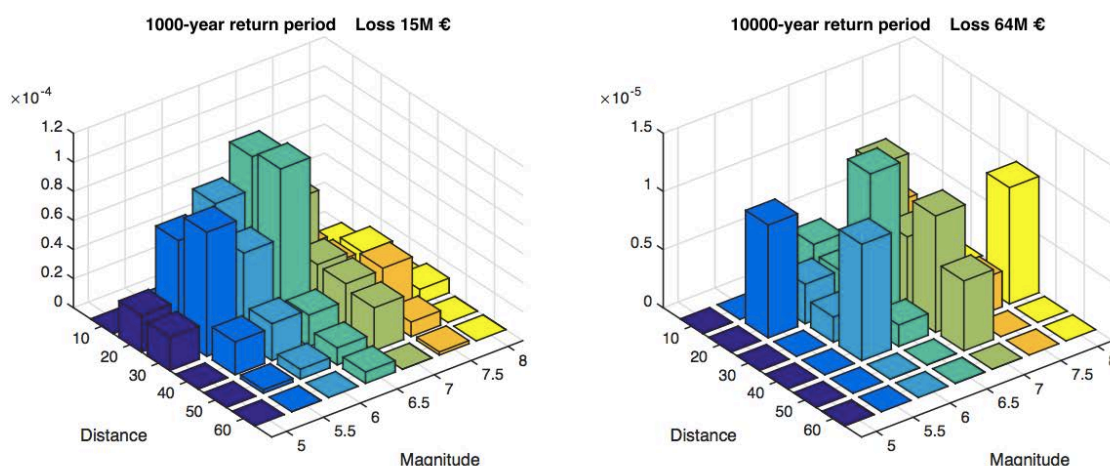


**Fig. 7.26 Disaggregation of hazard events contributing to business interruption loss with mean annual rate of  $10^{-3}$  and  $10^{-4}$**

In order to understand the indirect impact of the business interruption losses on the region and/or whole country, the customer base of the facilities that are contributing to the average annual business interruption loss can also be presented (a similar calculation could be done also for any value of loss calculated herein). The percentage of each customer base AAL, as a portion of the total AAL, is given in



Table 7.7, where it can be seen that 45% of the business interruption AAL is caused by facilities that have a customer base that goes beyond the province of Arezzo, and could thus cause additional indirect losses at a regional, national and international scale (in a decreasing order of importance).

**Table 7.7. Percentage of each customer base AAL to the total business interruption AAL**

<b>Customer base</b>	<b>Percentage of AAL (for BI) %</b>
Not Determined (ND)	21
Comune (municipality)	8
Province	27
Regional	23
National	18
International	3

### 7.4.3 Guidelines and critical events

There are 40 facilities that fail the component level assessment and should be targeted for structural investigation and potential upgrade. They all belong to the H1 subclass (i.e. pre-code type 1 portal frame with horizontal cladding).

As shown previously in Fig. 7.25, the sub-typologies that contribute most to the total average annual losses are V2 (i.e. pre-code type 2 portal frame with vertical cladding), H1 (i.e. pre-code type 1 portal frame with horizontal cladding) and V3 (i.e. low-code type 2 portal frame with vertical cladding). Hence, in addition to investigating further the H1 sub-class buildings, the V2 and V3 typologies should also be addressed, and the customer base of the facility should also be used as a prioritization tool to identify the facilities to investigate and potentially retrofit first, in order to also reduce the impact of indirect losses from these facilities.

The event disaggregation, shown here for business interruption loss (which is also the largest contribution to total loss), shows that a wide range of events contribute to the loss from lower magnitude close events to higher magnitude distance events. This implies that these losses are not just driven by the rare events, and thus mitigation efforts to protect against business interruption should be given high priority. Given that business interruption is directly related to structural and non-structural damage, this can be addressed through the retrofitting activities mentioned above.

## 7.5 PHASE 4: REPORT PHASE

The final stage of the test involves reporting the findings, which are summarized in

Table 7.8. The final overall outcome of the stress test is deemed to be C (intolerable/fail), and thus this should stimulate stakeholders to upgrade the existing industrial districts such that they will improve their grading in the following stress test cycle.

**Table 7.8. Summary report of the Stress Test outcomes**

<b>Level 1</b>	<b>Component level – Seismic Hazard</b>	
	Structural elements of buildings	
Number of components	300	
Target probability of collapse	$1 \times 10^{-5}$ - $2 \times 10^{-4}$	
Outcome	260 partly pass (grade B) and 40 fail (grade C)	
<b>Level 2b</b>	<b>System level – Seismic Hazard (PRA)</b>	
Risk measure	Average Annual Loss (as percentage of total exposure)	1 in 10,000 year business interruption loss
Objectives boundaries	A-B: 0.05%	A-B: 7 days
	B-C: 0.1%	B-C: 30 days
Grade	B	C
Outcome	partly pass	fail
Next stress test objectives	A-B (as above)	B-C (as above)



## 8 Conclusions-Discussion

In the context of STREST project, an engineering risk-based methodology for stress test critical non-nuclear infrastructures, named ST@STREST, has been developed. In particular, a multi-level framework has been proposed where each level is characterized by a different scope and by different levels of risk analysis complexity. This allows flexibility and application to a broad range of infrastructures, while producing comparable results. The selection of the appropriate stress test level depends on regulatory requirements, different importance of the CI, and the available human/financial resources to perform the stress test. The framework is composed of four main phases and nine steps to be conducted sequentially. First the goals, the method, the time frame and the total costs of the stress test are defined. Then, the stress test is performed at component and system levels and the outcomes are checked and compared to the acceptance criteria. A stress test grade is assigned and the global outcome is determined by employing a grading system. According to the outcome, the parameters of the following evaluation of stress test are adjusted. Finally, the results are reported and communicated to stakeholders and authorities.

ST@STREST has been applied and tested in six critical infrastructures in Europe. The objective was to demonstrate how the proposed framework is implemented in different classes of CIs exposed to variant hazards. Different Stress Test Levels were selected according to the characteristics and available resources in each case study. In this context, reasonable assumptions or simplifications were made in some steps of the applications. For example, the risk objectives were defined based on assumptions due to lack of regulatory boundaries in most of CIs. The results of the applications are summarized below. It is noted that the STREST consortium takes no responsibility in the research results provided in this report, as these results should not be considered formal stress tests.

The stress test to the ENI/Kuwait oil refinery and petrochemical plant in Milazzo in Italy (CI-A1) includes System Level (ST-L2b) and Scenario based Assessment (ST-L2d) under the impact of earthquakes and tsunamis. It has been shown that tsunami damages a limited number of the atmospheric storage vessels along the shore line. Hence the increase on the total risk is limited. Nonetheless, the overloading of emergency response should be considered, at least for the tanks along the coastline. Of more importance is the effect of an earthquake, which significantly increases the failure frequency of atmospheric storage tanks. Neither an earthquake nor a tsunami significantly increases the failure frequency of, and hence the risk imposed by, pressurized vessels (like LPG spheres). As for the considered site the risk is largely dominated by the LPG tanks (which fail due to industrial-related causes), while the impact of the natural hazards is limited.

The large dams in the Valais region of Switzerland (CI-A2) have been studied under multi-hazard effects, considering earthquakes, floods, internal erosion, bottom outlet malfunctions, and hydropower system malfunction. In particular, the stress test assessment included Component Level (ST-L1a), System Level for Single Hazard (ST-L2b / L2d) and for Multiple Hazards (ST-L3c / L3d). Even considering for a wide range of uncertainties and hazards, with a return period of 25 000 years for failures, the dam meets the desired objective of having, on average, one breach per 10 000 years. In what concerns damages in the downstream area, the goal was to limit expected damages to the loss of one habitation per

100 years. After integrating expected losses in the downstream area, however, a substantially higher value of 200 m<sup>3</sup> of built volume lost per year was estimated. As a consequence, the second risk objective was not met. The F-N curve for the studied conceptual case has been presented along with the predefined risk thresholds (AA-A, A-B, and B-C). A-B boundary is never crossed, as thus the risk associated with the conceptual dam following the characteristic point of risk approach is acceptable.

The major hydrocarbon pipelines in Turkey (CI-B1) have been tested following the ST-L1a and ST-L2a focusing to seismic threats at pipe-fault crossing locations. It has been shown that the probability of BTC pipeline failure due to fault offsets within 2475 years are still very high ranging from around 40% to 50%. Therefore, according to the grading system proposed in STREST, the pipeline risk is falling in the Grade B: possibly unjustifiable risk. Thus, retrofit is potentially needed for the pipes at pipe-fault intersection locations.

The Gasunie national gas storage and distribution network in Holland (CI-B2), were exposed to earthquake and liquefaction effects. ST-L1a considers individual components and a risk based approach is applied for individual stations and pipe segments making use of the ST-L2b results. For ST-L2b a full Probabilistic Risk Analysis using Monte Carlo simulations is performed for the network analysis. With respect to components, both types (pipe sections and stations) are found to contribute evenly to the network performance indicators. Specific pipe sections, which were identified to be the weakest links in the network, should be checked on their current actual state assessing the need for upgrading, while retrofitting of specific stations might be also necessary. Soil liquefaction is proved to be the dominant failure mechanism. As much uncertainty still exists in the liquefaction fragilities, further studies into these fragilities and their geographical distribution is recommended.

ST@STREST has been also applied to the port infrastructures of Thessaloniki in Greece (CI-B3) subjected to earthquake, tsunami and liquefaction hazards. The application included component level risk based assessment (ST-L1a), probabilistic single hazard analysis with epistemic uncertainty (ST-L2b) and scenario based single-risk (ST-L2d) (i.e. due to ground shaking) and multi-risk (ST-L3d) (i.e. due to ground shaking and liquefaction) assessments at the system level. It has been shown that the port obtains grades B (the risk is possibly unjustifiable) and AA (negligible risk) for the PRA of earthquake and tsunami hazards respectively, meaning that the CI partly passes or passes this evaluation of the stress test. In particular, for the seismic case, several electric power distribution substations present high failure risk and contribute to the performance loss of the port due to loss of power supply to the cranes. Thus, potential upgrade or/and alternative power sources such as diesel generators should be considered. The systemic risk for the tsunami hazard is very low, however it is recommended to extend the model and investigate the effect of floating ships that may hit the different components of the harbor, which is now neglected. For the scenario based assessment the estimated losses are significantly dependent on the analysis approach. Among the four different outcomes determined for the extreme scenario for both PIs, the CI passes the stress test in the 4975 years scenario II and NL method, which could be judged as the most reliable. Based on the different outcomes of the stress test from the probabilistic and scenario-based assessments, it is up to the port Authority to decide to take specific measures to improve and upgrade or not the performance of the port.

Finally, ST@STREST was applied to the industrial district in the region of Tuscany in Italy (CI-C1) exposed to seismic hazard. ST-L1a (component level) and ST-L2b (system level) were applied. According to the grading system, 260 facilities are assigned grade B (partly pass) and 40 facilities are assigned grade C and thus fail the stress test. The latter facilities



that belong to the H1 subclass (i.e. pre-code type 1 portal frame with horizontal cladding) should be targeted for structural investigation and potential upgrade. The results also show that the A-B system level assessment objective is not met but the B-C level is met. Hence the grading would be B (partly pass) for this objective. The business interruption loss at a mean annual rate of exceedance of  $10^{-4}$  is 64 Million Euro (which can be translated as an average of 45 days of business interruption), and so the grading would be C (fail) for this objective. Thus mitigation efforts to protect against business interruption should be given high priority. The sub-typologies that contribute most to the total average annual losses are V2 (i.e. pre-code type 2 portal frame with vertical cladding), H1 (i.e. pre-code type 1 portal frame with horizontal cladding) and V3 (i.e. low-code type 2 portal frame with vertical cladding). Hence, in addition to investigating further the H1 sub-class buildings, the V2 and V3 typologies should also be addressed.

Table 8.1 summarizes the results of the six applications in terms of the grading range that is defined in each level and hazard considered. In the framework of the case studies the objectives boundaries have been set mainly based on judgments, however, formulation of risk acceptance criteria is not a straightforward task. In practice, setting objectives and establishing risk measures is very difficult and strongly dependent on legal, socio-economic and political contexts and they should be defined by the corresponding stakeholders. Nevertheless, the results of the stress test will stimulate stakeholders to take specific measures to upgrade or not the existing infrastructure such that they will improve their grading in the following stress test cycle.

**Table 8.1. Grading range for the six case studies of STREST**

Case study	Hazard	Grading range								
		ST-L1a	ST-L2a	ST-L2b	ST-L2c	ST-L2d	ST-L3a	ST-L3b	ST-L3c	ST-L3d
CI-A1	Earthquake	AA-C	-	AA-C	-	AA-C	-	-	-	-
	Tsunami	AA-C	-	AA-C	-	AA-C	-	-	-	-
CI-A2	Earthquake/ Flood/ Internal erosion/ Outlet malfunction/ Hydropower system malfunction	AA-A	-	AA-A	-	AA-A	-	-	AA-A	AA-A
CI-B1	Earthquake	B	B	-	-	-	-	-	-	-
CI-B2	Earthquake/ Liquefaction	AA-A	AA-A	-	-	-	-	-	-	-
CI-B3	Earthquake	C	-	-	-	-	-	-	-	-
	Tsunami	AA-C	-	AA	-	-	-	-	-	-
	Earthquake/ Liquefaction	-	-	B	-	AA-C	-	-	-	AA-C
CI-C1	Earthquake	B-C	-	B-C	-	-	-	-	-	-

---

## References

- Abrahamson, N. A. 1992. Non-stationary spectral matching, *Seismological Research Letters*, 63(1), p. 30.
- Acton, M. R., T. R. Baldwin, and E.E.R. Jager 2002. *Recent Developments in the Design and Application of the PIPESAFE Risk Assessment Package for Gas Transmission Pipelines*, ASME International. Proceedings of the International Pipeline Conference (IPC), 29 September – 3 October, Calgary, Canada.
- Altarejos-Garcia, L., F. Silva-Tulla, I. Escuder-Bueno, and A. Morales-Torres. 2014. Practical risk assessment for embankments, dams, and slopes, in: Phoon, K.-K., Ching, J. (Eds.), *Risk and Reliability in Geotechnical Engineering*. CRC Press.
- Aki, K. 1957. Space and Time Spectra of Stationary Stochastic Waves, with Special Reference to Microtremors. *Bull. Earthquake Res. Inst. Tokyo Univ.* 25, pp. 415-457.
- Aki, K., and P. G. Richards. 1980. *Quantitative Seismology*. Second Edition, University Science Books.
- Akkar, S., and J. J. Bommer. 2010. Empirical equations for the prediction of PGA, PGV and spectral accelerations in Europe, the Mediterranean and the Middle East. *Seismol Res Lett* 81:195–206.
- Akkar, S., M. A. Sandikkaya, and J. J. Bommer. 2014a. Empirical ground-motion models for point- and extended source crustal earthquake scenarios in Europe and the Middle East. *Bulletin of Earthquake Engineering* 12(1):359–387. doi:10. 1007/s10518-013-9461-4.
- Akkar, S., M. A. Sandikkaya, and J. J. Bommer. 2014b. Erratum to: Empirical ground-motion models for point- and extended-source crustal earthquake scenarios in Europe and the Middle East. *Bulletin of Earthquake Engineering* 12(1):389–390.
- Akkar, S., and Y. Cheng. 2015. Application of a Monte-Carlo simulation approach for the probabilistic assessment of seismic hazard for geographically distributed portfolio. *Earthquake Engineering and Structural Dynamics*. 45(4): 525–541.
- American Lifeline Alliance (ALA). 2005. *Design Guidelines for Seismic Resistant Water Pipeline Installations*. Report FEMA, NIBS and ALA 2005/03. G&E Engineering Systems Inc.
- American Lifelines Alliance (ALA). 2001. *Seismic Fragility Formulations for Water Systems*, Part 1–Guideline. <http://www.americanlifelinesalliance.org>
- Anastasiadis, A., D. Raptakis, and K. Pitilakis. 2001. Thessaloniki’s detailed microzoning: subsurface structure as basis for site response analysis, *Pure and Applied Geophysics*, 158: 2597-2633.
- Apostolidis, P., D. Raptakis, Z. Roumelioti, and K. Pitilakis. 2004. Determination of S-wave velocity structure using microtremors and spac method applied in Thessaloniki (Greece), *Soil Dynamics and Earthquake Engineering* 24: 49-67.
- ASCE. 2010. *Minimum Design Loads for Buildings and Other Structures* (ASCE 7-10), American Society of Civil Engineers, Reston, VA.
- Baker, J.W., and C.A. Cornell. 2005. A vector valued ground motion intensity measure consisting of spectral acceleration and epsilon. *Earthquake Engineering and Structural Dynamics* 34:1193-1217.
- Baker, J. W. 2015. Efficient Analytical Fragility Function Fitting Using Dynamic Structural Analysis. *Earthquake Spectra* 31(1):579-99.

- Basili, R., M. M. Tiberti, V. Kastelic, A. Piatanesi, J. Selva, and S. Lorito. 2013. Integrating geologic fault data into tsunami hazard studies. *Natural Hazards and Earth System Sciences* 13,1025-1050, DOI: 10.5194/nhess-13-1025-2013.
- Bedford, T., and R. Cooke. 2001. Probabilistic risk analysis: foundations and methods, *Cambridge University Press*, Oxford, UK.
- Bommer, J. J. 2013. Proposals for New GMPEs for the Prediction of PGA and PGV in the Groningen Gas Field. *NAM internal note*, 37pp.
- Bommer, J.J., and A. B. Acevedo. 2004. The use of real accelerograms as input to dynamic analysis, *Journal of Earthquake Engineering* 8(1):43-91, DOI: 10.1080/13632460409350521.
- Boore, D. M., and G.M. Atkinson. 2008. Ground-motion prediction equations for the average horizontal component of PGA, PGV, and 5%-Damped PSA at spectral periods between 0.01s and 10.0s, *Earthquake Spectra*, 24(1), 99-138.
- Bourne, S. J., S. J. Oates, J. van Elk, and D. Doornhof 2014. A seismological model for earthquakes induced by fluid extraction from a subsurface reservoir, *J. Geophys. Res. Solid Earth*, 119, 8991–9015, doi:10.1002/2014JB011663.
- Building Seismic Safety Council (BSSC). 2004. *NEHRP Recommended provisions for seismic regulations for new buildings and other structures*, 2003 edition (FEMA 450), Building Seismic Safety Council, National Institute of Building Sciences, Washington D.C., USA.
- Campedel, M., V. Cozzani, A. Garcia-Agreda, and E. Salzano. 2008. Extending the Quantitative Assessment of Industrial Risks to Earthquake Effects. *Risk Analysis* 5, 1231-1246.
- Caputo, R., A. Chatzipetros, S. Pavlides, and S. Sboras. 2012. The Greek Database of Seismogenic Sources (GreDaSS): state-of-the-art for norther Greece. *AnnGeophys-Italy* 55(5):859-894.
- CAROLA. 2010. Program version 1.0.0.51. Associated Technology Pipeline Ltd and Rijksinstituut voor Volksgezondheid en Milieu ([www.rivm.nl/milieuportaal/bibliotheek/modellen/carola.jsp](http://www.rivm.nl/milieuportaal/bibliotheek/modellen/carola.jsp))
- Casotto, C., V. Silva, H. Crowley, R. Nascimbene, and R. Pinho. 2015. Seismic Fragility of Italian RC Precast Industrial Structures, *Engineering Structures*, 94, 122-136.
- Cauzzi, C., E. Faccioli, M. Vanini, and A. Bianchini. 2015. Updated predictive equations for broadband (0.01–10 s) horizontal response spectra and peak ground motions, based on a global dataset of digital acceleration records. *Bulletin of Earthquake Engineering* 13/6: 1587–612. DOI: 10.1007/s10518-014-9685-y.
- Chan, A. H. C. 1988. A Unified Finite Element Solution to Static and Dynamic Problems in Geomechanics, *Ph.D. dissertation*, University College of Swansea, U. K.
- Cheng, Y., and S. Akkar. 2016. Probabilistic permanent fault displacement hazard via Monte Carlo simulation and its consideration for the probabilistic risk assessment of buried continuous steel pipelines. *Earthquake Engineering and Structural Dynamics* (accepted).
- Chioccarelli, E., and I. Iervolino. 2013. Near-source seismic hazard and design scenarios. *Earthquake Engineering and Structural Dynamics*, 42, 603–622.
- Cooke, R. M. 1991. Experts in Uncertainty: Opinion and Subjective Probability in Science. *Oxford University Press*, Oxford.
- Cornell, C., and H. Krawinkler. 2000. Progress and challenges in seismic performance assessment. *PEER News*, 3 (2).
- CPR 18E. 1999. Guidelines for quantitative risk assessment. Committee for the Prevention of Disasters (CPR).

- Crowley, H. and J. J. Bommer. 2006. Modeling seismic hazard in earthquake loss models with spatially distributed exposure. *Bulletin of Earthquake Engineering* 4(3), 249-273.
- Crowley, H., C. Casotto, M. Dolšek, and A. Babič. 2015. *Deliverable D4.3: Guidelines for performance and consequences assessment of multiple-site, low-risk, high-impact, nonnuclear critical infrastructures (exposed to multiple natural hazards, etc.)*. STREST project: Harmonized approach to stress tests for critical infrastructures against natural hazards.
- Crowley, H., C. Casotto, K. Pitilakis, K. Kakderi, S. Argyroudis, S. Fotopoulou, G. Lanzano, E. Salzano, I. Iervolino, A. Basco, J. P. Matos, A. Schleiss, E. Uckan, S. Miraglia, and W. Courage. 2016. *Deliverable D4.4: Report on the taxonomy of CIs based on their vulnerability characteristics and exposure to natural hazard initiating events*. STREST project: Harmonized approach to stress tests for critical infrastructures against natural hazards.
- Danciu, L., and G. A. Tselentis. 2007. Engineering ground-motion parameters attenuation relationships for Greece. *Bull Seismol Soc Am* 97:162–183.
- Datta, T. K. 1999. Seismic response of buried pipelines: a state-of-the-art review. *Nuclear Engineering and Design* 192(2-3): 271-284.
- Dorwick, D. J., and D. A. Rhoades. 2004. Relations between earthquake magnitude and fault rupture dimensions: How regionally variable are they? *Bulletin of the Seismological Society of America*, 94, 776-788.
- Dost, B., M. Caccavale, T. Van Eck, and D. Kraaijpoel. 2013. *Report on the expected PGV and PGA values for induced earthquakes in the Groningen area*. KNMI report, 26pp. ([http://bibliotheek.knmi.nl/knmipubDIV/Report\\_on\\_the\\_expected\\_PGV\\_and\\_PGA\\_values\\_for\\_induced\\_earthquakes.pdf](http://bibliotheek.knmi.nl/knmipubDIV/Report_on_the_expected_PGV_and_PGA_values_for_induced_earthquakes.pdf))
- Douglas, J., T. Ulrich and C. Negulescu. 2013. Risk-targeted seismic design maps for mainland France. *Natural Hazards* 65, 1999–2013, DOI: 10.1007/s11069-012-0460-6.
- Drucker, H., C. J. C. Burges, L. Kaufman, A. Smola, and V. Vapnik. 1996. Support vector regression machines, in: *Advances in Neural Information Processing Systems*. MIT Press, Denver, Colorado, USA, pp. 155–161.
- Duckett, W. 2004. *Risk analysis and the acceptable probability of failure*. In: Henderson Colloquium (British Group of the International Association for Bridge and Structural Engineering).
- Eidinger, J. M., and E. A. Avila. 1999. *Guidelines for the seismic evaluation and upgrade of water transmission facilities* (Vol. 15). ASCE Publications.
- Elgamal, A., Z. Yang, and J. Lu. 2015. *Cyclic1D Seismic Ground Response Version 1.4, User's Manual*, University of California, San Diego, Department of Structural Engineering.
- EN 1998-5, 2004. Eurocode 8: Design of structures for earthquake resistance - Part 5: Foundations, retaining structures and geotechnical aspects.
- Esposito, S. 2011. Systemic seismic analysis of gas distribution networks. *Ph.D. thesis*, University of Naples Federico II, Italy, Advisor: I. Iervolino. Available at: <http://wpage.unina.it/iuniervo/>
- Esposito, S., A. d'Onofrio, A. Santo, F. Cavalieri, and P. Franchin. 2015. Simulation-Based Seismic Risk Assessment of Gas Distribution Networks. *Computer-Aided Civil and Infrastructure Engineering* 30(7): 508-523.
- Esposito, S., B. Stojadinovic, A. Mignan, M. Dolšek, A. Babič, J. Selva, S. Iqbal, F. Cotton, and I. Iervolino. 2016. *Deliverable D5.1: Report on the proposed engineering risk assessment methodology for stress tests of non-nuclear CIs*. STREST project: Harmonized approach to stress tests for critical infrastructures against natural hazards.

- Esposito, S., and B. Stojadinović. 2016. *Deliverable D5.3: Tools and strategies to incorporate stress tests into the long-term planning and life cycle management of non-nuclear Cis*. STREST project: Harmonized approach to stress tests for critical infrastructures against natural hazards.
- Esposito, S., B. Stojadinovic, A. Babič, M. Dolšek, S. Iqbal, and J. Selva. 2017. *Engineering Risk-Based Methodology for Stress Testing of Critical Non-Nuclear Infrastructures (STREST project)*. In 16<sup>th</sup> World Conference on Earthquake (16WCEE) Santiago Chile, January 9-13.
- Fabbrocino, G., I. Iervolino, F. Orlando, and E. Salzano. 2005. Quantitative risk analysis of oil storage facilities in seismic areas. *Journal of Hazardous Materials*, 12, 361-69.
- Fajfar, P., and M. Dolšek. 2012. A practice-oriented estimation of the failure probability of building structures. *Earthquake Engng Struct. Dyn* 41 (3): 531–547.
- Favre, A.-C., S. El Adlouni, L. Perreault, N. Thiémonge, and B. Bobée. 2004. Multivariate hydrological frequency analysis using copulas. *Water Resources Research* 40, W01101, doi:10.1029/2003WR002456.
- Federal Office for Water and Geology. 2002. *Sécurité des ouvrages d'accumulation ver. 1.1 - Ordonnance sur la sécurité des ouvrages d'accumulation (OSOA)*. Directives. FOWG, Biel, Switzerland.
- FEMA. 2003. *Multi-hazard Loss Estimation Methodology, Earthquake Model, HAZUS*. Federal Emergency Management Agency and National Institute of Buildings Sciences, Washington DC.
- FEMA 2012. FEMA E-74: Reducing the risks of nonstructural earthquake damage – a practical guide, Report by Federal Emergency Management Agency.
- FEMA. 2004. *Multi-hazard loss estimation methodology-earthquake model: HAZUS MR4 technical manual*. Report by Federal Emergency Management Agency. Washington DC.
- FEMA. 2008. Guidelines for Design of Structures for Vertical Evacuation from Tsunamis. FEMA P646 prepared by Applied Technology Council for Federal Emergency Management Agency, June, Washington, D.C.
- Franchin, P., F. Cavalieri, P.E. Pinto, A. Lupoi, I. Vanzi, P. Gehl, B. Kazai, G. Weatherill, S. Esposito, and K. Kakderi. 2011. *Deliverable 2.1: General methodology for systemic seismic vulnerability assessment*. Syner-G Project, <http://www.vce.at/SYNER-G/>
- Frankel, A. 2009. A constant stress-drop model for producing broadband synthetic seismograms: Comparison with the Next Generation Attenuation relations. *Bulletin of the Seismological Society of America* 99 (2A): 664–680.
- Froehlich, D. C. 2008. Embankment Dam Breach Parameters and Their Uncertainties. *Journal of Hydraulic Engineering* doi:10.1061/(ASCE)0733-9429(2008)134:12(1708).
- Gielisse, M., M. T. Dröge, and G.R. Kuik. 2008. Risicoanalyse aardgastransportleidingen. Gasunie report DEI 2008.R.0939. 2008 (in Dutch)
- Giardini, D. et al. 2013. Seismic Hazard Harmonization in Europe (SHARE). Online Data Resource, <http://portal.share-eu.org:8080/jetspeed/portal/>, doi:10.12686/SED-00000001-SHARE.
- Gill, J. C., and B. D. Malamud. 2014. Reviewing and visualizing the interactions of natural hazards. *Reviews of Geophysics*, 52(4), 680-722.
- González, F. I., E. L. Geist, B. Jaffe, U. Kânoglu, H. Mofjeld, C. E. Synolakis, V. V. Titov, D. Arcas, D. Bellomo, D. Carlton, T. Horning, J. Johnson, J. Newman, T. Parsons, R. Peters, C. Peterson, G. Priest, A. Venturato, J. Weber, F. Wong, and A. Yalciner. 2009. Probabilistic tsunami hazard assessment at Seaside, Oregon, for near- and far-field seismic sources, *J. Geophys. Res.* 114, C11023, 10.1029/2008JC005132.

- González, Vida, J. M., J. Macias, M. Castro, M. de la Asuncion, D. Melini, F. Romano, R. Tonini, S. Lorito, A. Piatanesi, and I. Molinari. 2015. Tsunami-HySEA: a GPU based model for the Italian candidate tsunami service provider, in *EGU General Assembly*, Vienna, EGU2015-13797.
- Goulet, C., C. Haselton, J. Mitrani-Reiser, J. Beck, G. Deierlein, K. Porter, and J. Stewart. 2007. Evaluation of the seismic performance of a code-conforming reinforced-concrete frame building - from seismic hazard to collapse safety and economic losses. *Earthquake Engineering & Structural Dynamics* 36:1973–1997.
- Grant, D.N., and R. Diaferia. 2012. Assessing adequacy of spectrum-matched ground motions for response history analysis. *Earthquake Engineering and Structural Dynamics* 42(9): 1265-1280.
- Graves, R. W., and A. Pitarka. 2010. Broadband ground motion simulation using a hybrid approach. *Bulletin of the Seismological Society of America* 100(5): 2095-2123.
- Grimaldi, S., and F. Serinaldi. 2006. Asymmetric copula in multivariate flood frequency analysis. *Advances in Water Resources*, 29, 1155–1167, doi:http://dx.doi.org/10.1016/j.advwatres.2005.09.005.
- Gunn, R., M. Balissat, P. Manso, L. Mouvet, and A. J. Schleiss. (Eds.) 2016. Proceedings of the 13<sup>th</sup> *International Benchmark Workshop on Numerical Analysis of Dams*, in: ICOLD Proceedings. Swiss Committee on Dams, Lausanne, Switzerland.
- Hancock, J., J. Watson-Lamprey, N. A. Abrahamson, J. J. Bommer, A. Markatis, E. McCoy, and R. Mendis. 2006. An improved method of matching response spectra of recorded earthquake ground motion using wavelets. *Journal of Earthquake Engineering* (10): 67–89.
- Hartford, D. N. D., and G. B. Baecher. 2004. Risk and uncertainty in dam safety. Thomas Telford Publishing, London, U.K.
- Herrero, A., and P. Bernard. 1994. A kinematic self-similar rupture process for earthquakes, *Bulletin of the Seismological Society of America* 84(4): 1216–1228.
- Honegger, D. G., and D. Wijewickreme. 2013. Seismic risk assessment for oil and gas pipelines. In *Handbook of Seismic Risk Analysis and Management of Civil Infrastructure Systems*, pp.682-715. Elsevier.
- ICOLD. 2014. *Selecting seismic parameters for large dams: guidelines*, Bulletin 148. International Commission on Large Dams (ICOLD), Paris, France.
- ICOLD. 2012. *Bulletin on safe passage of extreme floods*, Bulletin 142. International Commission on Large Dams (ICOLD Bulletin 142), Paris, France.
- ICOLD. 2003. *Dams and floods: guidelines and case histories*, Bulletin 125. International Commission on Large Dams (ICOLD), Paris, France.
- ICOLD. 2001. *Design features of dams to resist seismic ground motion: guidelines and case studies*, Bulletin 120. International Commission on Large Dams (ICOLD), Paris, France.
- ICOLD. 2000. *Risk assessment in dam safety management. A reconnaissance of benefits, methods and current applications*, Bulletin 130. International Commission on Large Dams (ICOLD), Paris, France.
- ICOLD. 1992. *Selection of design flood*, Bulletin 82. International Commission on Large Dams (ICOLD), Paris, France.
- Idriss, I. M., and R. W. Boulanger. 2008. Soil Liquefaction during earthquake, EERI monograph MNO-12 on earthquake engineering. *Earthquake Engineering Research Institute*, Oakland (CA), USA.
- Iervolino, I., C. Galasso, E. Cosenza. 2010. REXEL: Computer aided record selection for code-based seismic structural analysis. *Bulletin of Earthquake Engineering* 8:339-362.
- International Building Code (IBC). 2015. *International Code Council*, Washington, DC.

- ITSAK's Equipment and Instrumentation Upgrade project, funded by Region of Central Macedonia, 3rd CSF, Operational Development Programme of Central Macedonia 2000-2006.
- Jayaram, N., and J. W. Baker. 2009. Correlation model of spatially distributed ground motion intensities. *Earthquake Engineering and Structural Dynamics* 38 (15): 1687–1708.
- Joint Committee on Structural Safety (JCSS). 1999. *Probabilistic Assessment of Existing Structures*. RILEM Publications S.A.R.L., France, edited by D. Diamantidis.
- Jonkman, S. N., P. H. A. J. M. Van Gelder, and J. K. Vrijling. 2003. An overview of quantitative risk measures for loss of life and economic damage. *Journal of Hazardous Materials*, 99(1):1-30.
- Kajiura, K. 1963. The leading wave of a tsunami, *Bull. Earthq. Res. Inst. Univ. Tokyo*, 41:535–571.
- Kakderi, K., S. Fotopoulou, S. Argyroudis, S. Karafagka, K. Pitilakis, A. Anastasiadis, C. Smerzini, J. Selva, G. Giannopoulos, L. Galbusera, W. Courage, J. Reinders, Y. Cheng, S. Akkar, M. Erdik, and E. Uckan. 2015. *Deliverable D4.2: Guidelines for performance and consequences assessment of geographically distributed, non-nuclear critical infrastructures exposed to multiple natural hazards*. STREST project: Harmonized approach to stress tests for critical infrastructures against natural hazards.
- Kappos, A. J., C. Panagiotopoulos, G. Panagopoulos, and E. I. Panagopoulos. 2003. WP4-Reinforced concrete buildings (Level I and II analysis), RISK-UE: An advanced approach to earthquake risk scenarios with applications to different European towns.
- Kappos, A. J., G. Panagopoulos, C. Panagiotopoulos, and G. Penelis. 2006. A hybrid method for the vulnerability assessment of R/C and URM buildings. *Bulletin of Earthquake Engineering* 4:391-419.
- Karafagka, S., S. Fotopoulou, and K. Pitilakis. 2016. Tsunami fragility curves for seaport structures. In 1<sup>st</sup> International Conference on Natural Hazards & Infrastructure, 28-30 June, Chania, Greece.
- Karamitros, D. K., G. D. Bouckovalas, and G. P. Kouretzis. 2007. Stress analysis of buried steel pipelines at strike-slip fault crossings. *Soil Dynamics and Earthquake Engineering* 27(3): 200-211.
- Karamitros, D. K., G. D. Bouckovalas, G. P. Kouretzis, and V. Gkesouli. 2011. An analytical method for strength verification of buried steel pipelines at normal fault crossings. *Soil Dynamics and Earthquake Engineering* 31(11): 1452-1464.
- Katayama, T., K. Kubo, and N. Sato. 1975. Earthquake Damage to Water and Gas Distribution Systems, Proceedings of the *U.S. National Conference on Earthquake Engineering*, Oakland.
- Knochenhauer, M., and P. Louko. 2004. Guidance for External Events Analysis. In Probabilistic Safety Assessment and Management (pp. 1498-1503). Springer London.
- Konstantinou, K. I. 2014. Moment magnitude-rupture area scaling and stress-drop variations for earthquakes in the Mediterranean region. *Bulletin of the Seismological Society of America*, 104, 2378-2386.
- Kottke, Albert R., and Ellen M. Rathje. 2008. *Technical Manual for Strata*. PEER Report 2008/10. University of California, Berkeley, California.
- Kourkoulis, R., F. Gelagoti, M. Loli, and G. Gazetas. 2014. Interplay of container port cranes and Quay-Walls during earthquake shaking, Second European Conference on Earthquake Engineering and Seismology, Istanbul, Aug. 25-29.
- Krausmann, E., V. Cozzani, E. Salzano, and E. Renni. 2011. Industrial accidents triggered by natural hazards: an emerging risk issue. *Natural Hazards and Earth System Sciences*, 11, 921–929.



- Krausmann, E., R. Piccinelli, B. Ö. Ay, H. Crowley, E. Uckan, M. Erdik, G. Lanzano, E. Salzano, I. Iervolino, S. Esposito, A. Pistolas, K. Kakderi, D. Pitilakis, K. Pitilakis, and R. Steenbergen. 2014. Deliverable D2.3: *Report on lessons learned from recent catastrophic events*. STREST project: Harmonized approach to stress tests for critical infrastructures against natural hazards.
- Kulkarni, R. B., R. R. Youngs, and K. J. Coppersmith. 1984. Assessment of confidence intervals for results of seismic hazard analysis, In Proc. *Eighth World Conference on Earthquake Engineering*, San Francisco, California, Vol. 1, pp. 263-270.
- Laheij, G. M. H., and C. J. Theune. 2010. *Consequences of a risk based approach for natural gas pipelines*. 5<sup>th</sup> Pipeline Technology Conference, Hannover.
- Lanzano, G., E. Salzano, F. Santucci de Magistris, and G. Fabbrocino, 2013. Seismic vulnerability of gas and liquid buried pipelines, *Journal of Loss Prevention in the Process Industries*. <http://dx.doi.org/10.1016/j.jlp.2013.03.010>
- Lazar, N., and M. Dolšek. 2013. Application of the risk-based seismic design procedure to a reinforced concrete frame building. In 4<sup>th</sup> ECCOMAS Thematic Conference on Computational Methods in Structural Dynamics and Earthquake Engineering, M. Papadrakakis, V. Papadopoulos, V. Plevris (eds.) Kos Island, Greece, 12–14 June.
- Lorito, S., J. Selva, R. Basili, F. Romano, M. M. Tiberti, and A. Piatanesi. 2015. Probabilistic Hazard for Seismically-Induced Tsunamis: Accuracy and Feasibility of Inundation Maps. *Geophys. J. Int.* 200(1), 574-588.
- Madsen, H. O., S. Krenk, and N. C. Lind. 1986. *Methods of structural safety*. Prentice Hall, Inc., Englewood Cliffs, N.J.
- Mai, P. M., P. Spudich, and J. Boatwright. 2005. Hypocenter locations in finite-source rupture models. *Bulletin of the Seismological Society of America*, 95, 965-980.
- Marzocchi, W., M. Taroni M, and J. Selva. 2015. Accounting for Epistemic Uncertainty in PSHA: Logic Tree and Ensemble Modeling. *Bulletin of the Seismological Society of America* 105 (4), doi: 10.1785/0120140131.
- Mashaly, E-SA, and T. K. Datta. 1989. Seismic risk analysis of buried pipelines. *Journal of transportation engineering* 115(3): 232-52.
- Matos, J. P., A. Mignan, and A. J. Schleiss. 2015. Vulnerability of large dams considering hazard interactions: conceptual application of the Generic Multi-Risk framework, in: *13<sup>th</sup> ICOLD International Benchmark Workshop on Numerical Analysis of Dams*. Lausanne, Switzerland.
- Mazzieri, I., M. Stupazzini, R. Guidotti, and C. Smerzini. 2013. SPEED: Spectral elements in elastodynamics with Discontinuous Galerkin: a non-conforming approach for 3D multi-scale problems, *International Journal for Numerical Methods in Engineering* 95(12): 991–1010.
- McGuire, R. K. 1988. Seismic risk to lifeline systems: critical variables and sensitivities. Proceedings of *9<sup>th</sup> World Conference on Earthquake Engineering*, Tokyo-kyoto, Japan.
- McGuire, R. K. 2004. *Seismic Hazard and Risk Analysis*, Earthquake Engineering Research Institute, Oakland, CA.
- Mena, B., P. M. Mai, K. B. Olsen, M. D. Purvance, and J. N. Brune. 2010. Hybrid broadband ground-motion simulation using scattering Green's functions: Application to large magnitude events. *Bulletin of the Seismological Society of America* 100(5A): 2143–2162.
- Mignan, A., L. Danciu, J. P. Matos, and A. J. Schleiss. 2015. *Report on cascading events and multi-hazard probabilistic scenarios*, STREST. Harmonized approach to stress tests for critical infrastructures against natural hazards. Zurich, Switzerland.

- Mignan, A., S. Wiemer, D., and Giardini. 2014. The quantification of low-probability–high-consequences events: part I. A generic multi-risk approach. *Natural Hazards* 1–24. doi:10.1007/s11069-014-1178-4.
- Min, I & E. 2010. *Besluit Externe Veiligheid Buisleidingen (Decree External Safety Pipelines)*, Ministry of Infrastructure and Environment.
- Miraglia, S., W. Courage, and P. Meijers, 2015. *Fragility functions for pipeline in liquefiable sand: a case study on the Groningen gas-network*. In Haukaas, T. (Ed.) Proceedings of the 12<sup>th</sup> International Conference on Applications of Statistics and Probability in Civil Engineering (ICASP12), Vancouver, Canada, July 12-15.
- Molinari, I., R. Tonini, A. Piatanesi, S. Lorito, F. Romano, D. Melini, Vida J. M. Gonzalez, J. Macias, M. Castro, and M. de la Asuncion. 2016. Fast evaluation of tsunami scenarios: uncertainty assessment for a Mediterranean Sea database, submitted to NHESS (Under review).
- Morgan, M. G. 2014. Use (and abuse) of expert elicitation in support of decision making for public policy, *Proc. Nat. Acad. Sci.* 111(20); 7176-7184, DOI:10.1073/pnas.1319946111.
- Mousavi, M., M. Hesari, and A. Azarbakht. 2014. Seismic risk assessment of the 3<sup>rd</sup> Azerbaijan gas pipeline in Iran. *Natural Hazards* 74(3):1327-48.
- Nakamura, Y. 1989. A method for dynamic characteristics estimation of subsurface using microtremors on the ground surface, *QR Railway Tech. Res. Inst.* 30, 1.
- National Institute of Building Sciences, NIBS. 2004. Direct physical damage—general building stock. HAZUS-MH Technical manual, Chapter 5. Federal Emergency Management Agency, Washington, D.C.
- Okada, Y. 1985. Surface deformation due to shear and tensile faults in a half-space. *Bull. seism. Soc. Am.* 75, 1135–1154.
- Omidvar, B., M. Eskandari, and E. Peyghaleh. 2013. Seismic damage to urban areas due to failed buried fuel pipelines case study: fire following earthquake in the city of Kermanshah, Iran. *Natural Hazards* 67(2):169-92.
- O'Rourke, M. 2009. Analytical Fragility Relations for Buried Segmented Pipe,” *Proc. of TCLEE Lifeline Earthquake Engineering in a Multihazard Environment*, Oakland.
- O'Rourke, T., and S. Jeon. 1999. Factors Affecting the Earthquake Damage of Water Distribution Systems, *Proceedings 5<sup>th</sup> U.S. Conference on Lifeline Earthquake Engineering*, Seattle.
- O'Rourke, M., E. Filipov, and E. Uçkan. 2014. Towards Robust Fragility Relations for Buried Segmented Pipe in Ground Strain Areas. *Earthquake Spectra* doi: <http://dx.doi.org/10.1193/032311EQS076M>,
- Paolucci, R., F. Pacor, R. Puglia, G. Ameri, C. Cauzzi, and M. Massa. 2011. Record processing in ITACA, the new Italian strong-motion database, in *Earthquake Data in Engineering Seismology, Geotechnical, Geological, and Earthquake Engineering* (S. Akkar, P. Gülkan, and T. van Eck, Eds.), 14, 99–113
- Papaioannou, 2004. Seismic hazard scenarios- Probabilistic seismic hazard analysis, SRM-Life Project: Development of a global methodology for the vulnerability assessment and risk management of lifelines, infrastructures and critical facilities. Application to the metropolitan area of Thessaloniki (in greek).
- Parra, E. 1996. Numerical Modeling of Liquefaction and lateral Ground Deformation including Cyclic Mobility and Dilative Behavior in Soil Systems. *PhD Dissertation*, Department of Civil Engineering, Rensselaer polytechnic Institute, Troy, NY.
- Parsons, T., and E. L. Geist. 2009. Tsunami probability in the Caribbean region, *Pure appl. Geophys.* 165: 2089–2116.

- 
- Petersen, M. D., T. E. Dawson, R. Chen, T. Cao, C. J. Wills, D. P. Schwartz, and A. D. Frankel. 2011. Fault displacement hazard for strike-slip faults. *Bulletin of the Seismological Society of America* 101(2): 805-825.
- PIANC. 2001. *Seismic Design Guidelines for Port Structures*. International Navigation Association, Balkema, 474 p.
- Pineda-Porras, O.A., and M. Ordaz. 2012. Seismic Damage Estimation in Buried Pipelines Due to Future Earthquakes-The Case of the Mexico City Water System. *Earthquake-Resistant Structures-Design, Assessment and Rehabilitation-Chapter 5*. INTECH Open Access Publisher.
- Pitilakis, K., and A. Anastasiadis. 1998. Soil and site characterization for seismic response analysis, Proceeding of the XI ECEE, Paris 6-11 Sept. 1998, Inv.Lectures, pp.65-90.
- Pitilakis, K., E. Riga, and A. Anastasiadis. 2012. Design spectra and amplification factors for Eurocode 8. *Bulletin of Earthquake Engineering* 10:1377-1400. doi: 10.1007/s10518-012-9367-6.
- Pitilakis, K., E. Riga, and A. Anastasiadis. 2013. New code site classification, amplification factors and normalized response spectra based on a worldwide ground-motion database. *Bulletin of Earthquake Engineering* doi: 10.1007/s10518-013-9429-4.
- Pitilakis, K., P. Franchin, B. Khazai, and H. Wenzel (Eds) 2014. *SYNER-G: Systemic seismic vulnerability and risk assessment of complex urban, utility, lifeline systems and critical facilities. Methodology and applications*. Series: Geotechnical, Geological and Earthquake Engineering, 31, Springer, Netherlands.
- Pitilakis, K., E. Riga, and A. Anastasiadis. 2015. New design spectra in Eurocode 8 and preliminary application to the seismic risk of Thessaloniki, Greece, In: Ansal A., Sakr M. (eds.), *Perspectives on Earthquake Geotechnical Engineering*. Series: Geotechnical, Geological and Earthquake Engineering, Vol. 37, Springer Netherlands, pp 45-91.
- Pohl, R. 2000. Failure frequency of gates and valves at dams and weirs. *International Journal on Hydropower & Dams* 77-81.
- Prevost, J. H. 1985. A Simple Plasticity Theory for Frictional Cohesionless Soils. *Soil Dynamics and Earthquake Engineering* 4(1): 9-17.
- Raptakis, D., and K. Makra, 2010. Shear wave velocity structure in western Thessaloniki (Greece) using mainly alternative SPAC method, *Soil Dynamics and Earthquake Engineering* 30 (4), pp. 202-214.
- Rathje, E. M., and A. Kottke. 2010. "Strata," <https://nees.org/resources/strata>.
- Robertson, P. K., and C. E. Wride. 1998. Evaluating cyclic liquefaction potential using the cone penetration test, *Canadian Geotechnical Journal* 35(3): 442-459 CrossRef, ISI.
- Saaty, T. L. 1980. *The Analytic Hierarchy Process, Planning, Priority Setting, Resource Allocation*. McGraw-Hill, New York.
- Sabetta, F., and A. Pugliese. 1996. Estimation of Response Spectra and Simulation of Nonstationary Earthquake Ground Motions, *Bulletin of the Seismological Society of America* 86: 337-352.
- Salzano, E., I. Iervolino, and G. Fabbrocino. 2003. Seismic risk of atmospheric storage tanks in the framework of Quantitative Risk Analysis. *Journal of Loss Prevention in the Process Industry*, 16, 403-409.
- Salzano, E., A. Garcia-Agreda, A. Di Carluccio, and G. Fabbrocino. 2009. Risk assessment and early warning systems for industrial facilities in seismic zones. *Reliab. Eng. Syst. Saf.* 94, 1577-1584.
- Salzano, E., A. Basco, V. Busini, V. Cozzani, E. Renni, and R. Rota. 2013. Public Awareness Promoting New or Emerging Risk: Industrial Accidents Triggered by Natural Hazards. *Journal of Risk Research*, 16, 469-485.

- Salzano, E., A. Basco, S. Karafagka, S. Fotopoulou, K. Pitilakis, A. Anastasiadis, J. P. Matos, and A. J. Schleiss. 2015. *Deliverable D4.1 Guidelines for performance and consequences assessment of single-site, high-risk, non-nuclear critical infrastructures exposed to multiple natural hazards*. STREST project: Harmonized approach to stress tests for critical infrastructures against natural hazards. Zurich, Switzerland.
- Sarrasin, O. 2015. Numerical simulation and evaluation of the risk posed by impulse waves on the Mattmark reservoir (*M.Sc. Thesis*). École Polytechnique Fédérale de Lausanne (EPFL).
- Seed, R. B., K. O. Cetin, R. E. S Moss, A. Kammerer, J. Wu, J. Pestana, M. Riemer, R. B. Sancio, J. D. Bray, R. E. Kayen, and A. Faris. 2003. Recent advances in soil liquefaction engineering: A unified and consistent framework. Keynote presentation, in 26<sup>th</sup> *Annual ASCE Los Angeles Geotechnical Spring Seminar* Long Beach, CA.
- Selva, J. 2013. Long-term multi-risk assessment: statistical treatment of interaction among risks. *Natural Hazards* 67 (2): 701-722.
- Selva, J., S. M. Iqbal, M. Taroni, W. Marzocchi, F. Cotton, W. Courage, L. Abspoel-Bukman, S. Miraglia, A. Mignan, K. Pitilakis, S. Argyroudis, K. Kakderi, D. Pitilakis, G. Tsinidis, and C. Smerzini. 2015. *Deliverable D3.1: Report on the effects of epistemic uncertainties on the definition of LP-HC events*. STREST project: Harmonized approach to stress tests for critical infrastructures against natural hazards.
- Selva, J., Tonini, R., Molinari, I., Tiberti, M. M., Romano, F., Grezio, A., Melini, D., Piatanesi, A., Basili, R. and Lorito, S., 2016a. Quantification of source uncertainties in Seismic Probabilistic Tsunami Hazard Analysis (SPTHA), *Geophys. J. Int.*, doi:10.1093/gji/ggw107.
- Selva, J., Tonini, R., Romano, F., Volpe M., Brizuela B., Piatanesi A., Basili R., and Lorito S., 2016b, From regional to site specific SPTHA through inundation simulations: a case study for three test sites in Central Mediterranean, EGU General Assembly 2016, Abstract #EGU2016-16988, 17-22 April 2016, Vienna, Austria.
- Silva, V., H. Crowley, and P. Bazzurro. 2014a. Risk-targeted hazard maps for Europe. In *Second European Conference on Earthquake Engineering and Seismology*, Istanbul, 24-29 August, Turkey.
- Silva, V., H. Crowley, M. Pagani, and R. Pinho. 2014b. Development of the OpenQuake engine, the Global Earthquake Model's open-source software for seismic risk assessment, *Natural Hazards* Volume 72, Issue 3, pp 1409-1427.
- Smerzini, C., K. Pitilakis, and K. Hasmemi, submitted. 2016. Evaluation of earthquake ground motion and site effects in the Thessaloniki urban area by 3D finite-fault numerical simulations, *Bulletin of Earthquake Engineering*.
- Sørensen, M. B., M. Spada, A. Babeyko, S. Wiemer, and G. Grünthal. 2012. Probabilistic tsunami hazard in the Mediterranean Sea, *J. Geophys. Res.* 117, B01305, 10.1029/2010JB008169.
- SRM-LIFE Research project, *Deliverable D5, 2005. Technical report presenting 1D and 2D seismic response analyses*. (in Greek). Collaboration of the Laboratory of Soil Mechanics, Foundation and Geotechnical Earthquake Engineering of AUTH and the Institute of Engineering Seismology and Earthquake Engineering.
- SSHAC (Senior Seismic Hazard Analysis Committee). 1997. *Recommendations for probabilistic seismic hazard analysis: Guidance on uncertainty and use of experts*. U.S. Nuclear Regulatory Commission Report NUREG/CR-6372.
- Stapp, J. C., I. Wong, J. Whitney, R. Quittmeyer, N. Abrahamson, G. Toro, R. Youngs, K. Coppersmith, J. Savy, and T. Sullivan. 2001. Yucca Mountain PSHA Project Members.

- Probabilistic seismic hazard analyses for ground motions and fault displacement at Yucca Mountain, Nevada. *Earthquake Spectra* 17:113–150.
- Suppasri, A., E. Mas, I. Charvet, R. Gunasekera, K. Imai, Y. Fukutani, Y. Abe, and F. Imamura. 2013. Building damage characteristics based on surveyed data and fragility curves of the 2011 Great East Japan tsunami. *Natural Hazards* 66, 319–341. doi:10.1007/s11069-012-0487-8.
- Uckan, E., B. Akbas, J. Shen, W. Rou, F. Paolacci, and M. O'Rourke. 2015. A simplified analysis model for determining the seismic response of buried steel pipes at strike-slip fault crossings. *Soil Dynamics and Earthquake Engineering* 75:55-65.
- UPGRADE Research project, 2015. *Deliverable D8.2 Technical reports with the calculation results of the vulnerability of specific Greek port facilities*. (in Greek). Contemporary Evaluation Methodology of Seismic Vulnerability and Upgrade of Port Facilities, Collaboration of the Laboratory of Soil Mechanics, Foundation and Geotechnical Earthquake Engineering of AUTH and the National Technical University of Athens (NTUA).
- US NRC. NUREG. 1985. Methods for External Event Screening Quantification: Risk Methods Integration and Evaluation Program (RMIEP) Methods Development.
- TNO. 2015. RISKCURVES, risk assessment software, version 10.0.3, TNO.
- Toro, G. R. 1995. Probabilistic models of site velocity profiles for generic and site-specific ground-motion amplification studies. Upton, New York: Brookhaven National Laboratory.
- Vazouras, P., S. A. Karamanos, and P. Dakoulas. 2010. Finite element analysis of buried steel pipelines under strike-slip fault displacements. *Soil Dynamics and Earthquake Engineering* 30(11):1361–76.
- Vazouras, P., S. A. Karamanos, and P. Dakoulas. 2012. Mechanical behavior of buried steel pipes crossing active strike-slip faults. *Soil Dynamics and Earthquake Engineering* 41:164-80.
- Vetsch, D., R. Fäh, D. Farshi, and R. Müller. 2005. BASEMENT - an object-oriented software system for the simulation of natural hazards, in: Festtagskolloquium 75 Jahre VAW. Mitteilung VAW 190, Swiss Federal Institute of Technology Zurich (ETHZ), Zurich, Switzerland.
- Volpe M., J. Selva, R. Tonini, F. Romano, B. Brizuela, Argyroudis S, Pitilakis K, A. Piatanesi, R. Basili, and S. Lorito, in prep: From regional to site specific SPTHA through inundation simulations: a case study for Milazzo (Italy) and Thessaloniki (Greece).
- VROM. 2005a. *Methods for the calculation of physical effects*. (Yellow Book), PGS 2, Ministry of Housing Spatial Planning and the Environment (VROM), The Hague.
- VROM. 2005b. *Methods for the determination of possible damage to people and objects resulting from releases of hazardous materials*. CPR16E, first edition 1992.
- VROM. 2005c. *Guidelines for quantitative risk assessment*. (Purple Book), PGS 3, Ministry of Housing Spatial Planning and the Environment (VROM), The Hague, 2005.
- VROM. 2005d. *Methods for determining and processing probabilities*. (Red Book), PGS 4, Ministry of Housing Spatial Planning and the Environment (VROM), The Hague, 2005.
- Weatherill, G., S. Esposito, I. Iervolino, P. Franchin, and F. Cavalieri. 2014. Framework for seismic hazard analysis of spatially distributed systems, in: K. Pitilakis et al. (eds). Systemic seismic vulnerability and risk assessment of complex urban, utility, lifeline systems and critical facilities. Methodology and applications. *Springer Netherlands*, 57-88.
- Weatherill, G., V. Silva, H. Crowley, P. Bazzurro. 2015. Exploring the impact of spatial correlations and uncertainties for portfolio analysis in probabilistic seismic loss estimation. *Bulletin of Earthquake Engineering* DOI: 10.1007/s10518-015-9730-5.

- Wells, D. L., and K. J. Coppersmith. 1994. New empirical relationships among magnitude, rupture length, rupture width, rupture area and surface displacement. *Bulletin of the Seismological Society of America*, 84, 974-1002.
- Wijewickreme, D., D. Honegger, A. Mitchell, and T. Fitzell. 2005. Seismic vulnerability assessment and retrofit of a major natural gas pipeline system: A case history. *Earthquake Spectra* 21(2):539-67.
- WINN\_TA-NAM. 2016. *Technical Addendum to the Winningsplan 2016*, (in Dutch), NAM, April 1<sup>st</sup>.
- Woessner J., L. Danciu, D. Giardini, H. Crowley, F. Cotton, G. Grunthal, G. Valensise, R. Arvidsson, R. Basili, M. Demircioglu, S. Hiemar, C. Meletti, R. Musson, A. Rovida, K. Sesetyan, and M. Stucchi. 2015. The 2013 European Seismic Hazard Model - Key Components and Results *Bulletin of Earthquake Engineering* DOI 10.1007/s10518-015-9795-1.
- Yang, Z. 2000. Numerical Modeling of Earthquake Site Response Including Dilation and Liquefaction. *Ph.D. Dissertation*, Dept. of Civil Engineering and Engineering Mechanics, Columbia University, New York, NY.
- Youd, T. L., and I. M. Idriss. eds. 1997. Proc., *NCEER Workshop on Evaluation of Liquefaction Resistance of Soils*, Nat. Ctr. for Earthquake Engrg. Res., State Univ. of New York at Buffalo.
- Youngs, R. R., W. J. Arabasz, R. E. Anderson, A. R. Ramelli, J. P. Ake, D. B. Slemmons, J. P. McCalpin, D. I. Doser, C. J. Fridrich, F. H. Swan, A. M. Rogers, J. C. Yount, L. W. Anderson, K. D. Smith, R. L. Bruhn, P. L. K. Knuepfer, R. B. Smith, C. M. dePolo, D. W. O'Leary, K. J. Coppersmith, S. K. Pezzopane, D. P. Schwartz, J. W. Whitney, S. S. Olig, and G. R. Toro. 2003. A methodology for probabilistic fault displacement hazard analysis (PFDHA). *Earthquake Spectra* 19(1):191-219. doi: <http://dx.doi.org/10.1193/1.1542891>
- Zenz, G., and M. Goldgruber. (Eds.) 2013. Proceedings of the 12<sup>th</sup> *International Benchmark Workshop on Numerical Analysis of Dams*. ICOLD, Graz, Austria.





## A Appendix

Table A.1 Geotechnical characteristics of soil profile A

Depth (m)	USCS	G- $\gamma$ -D curves for soil type	$V_s$ (m/sec)	c (kN/m <sup>2</sup> )	$\phi$ (°)	$Y_m$ (kN/m <sup>3</sup> )
1.0	SM	DB-3-->A	300	5	37	18.00
1.5	SM	DB-3-->A	270	5	37	18.00
2.0	SM	DB-3-->A	240	5	32	19.75
4.0	CH/CL	C	224	10	26	16.34
5.0	CH/CL	C	211	10	26	16.34
6.0	CH/CL	C	198	10	26	16.34
9.0	CH/CL	C	121	10	26	16.34
11.0	SM	C	115	1	32	19.75
12.0	CL	B*	118	20	23	20.55
14.0	CL	B*	154	20	23	20.55
20.0	SC	B*	274	5	31	20.80
24.0	CL	B*	274	15	30	20.27
26.5	CL	B*	299	15	30	20.09
31.0	SC	B1	375	15	33	20.80
32.0	SC	B1	404	15	30	20.80
36.0	SC	B1	479	15	30	20.80
42.0	CL	RCL-H--> E	558	30	25	19.82
44.0	SC	RCL-H--> E	339	15	36	20.80
45.0	CL	RCL-H--> E	300	26	25	20.81
46.0	CL	RCL-H--> E	260	30	25	20.81
48.0	CL	RCL-H--> E	244	30	25	20.68
50.0	CL	RCL-H--> E	281	30	25	20.68
53.0	CL	RCL-H--> E	453	60	27	19.97
55.5	CL	RCL-H--> E	400	60	27	19.97
56.0	SC	RCL-H--> E	396	-	-	21.21
60.0	SC	RCL-H--> E	447	-	-	21.21
62.0	SW-SM	RCL-H--> E	546	-	-	21.21
64.0	-	RCL-H--> E	682	-	-	21.21
66.0	ML	RCL-H--> E	577	-	-	21.21
68.0	CL	RCL-H--> E	602	-	-	20.67
70.0	CL	RCL-H--> E	562	-	-	20.67

72.0	CL	RCL-H--> E	600	-	-	20.67
73.0	CL	RCL-H--> E	655	-	-	21.16
74.0	CL	RCL-H--> E	710	-	-	21.16
76.0	CL	RCL-H--> E	744	-	-	21.16
78.0	CL	RCL-H--> E	633	-	-	20.98
80.0	CL	RCL-H--> E	627	-	-	20.98
170.0	CL	RCL-H--> E	627			21.00

Table A.2 Geotechnical characteristics of soil profile B

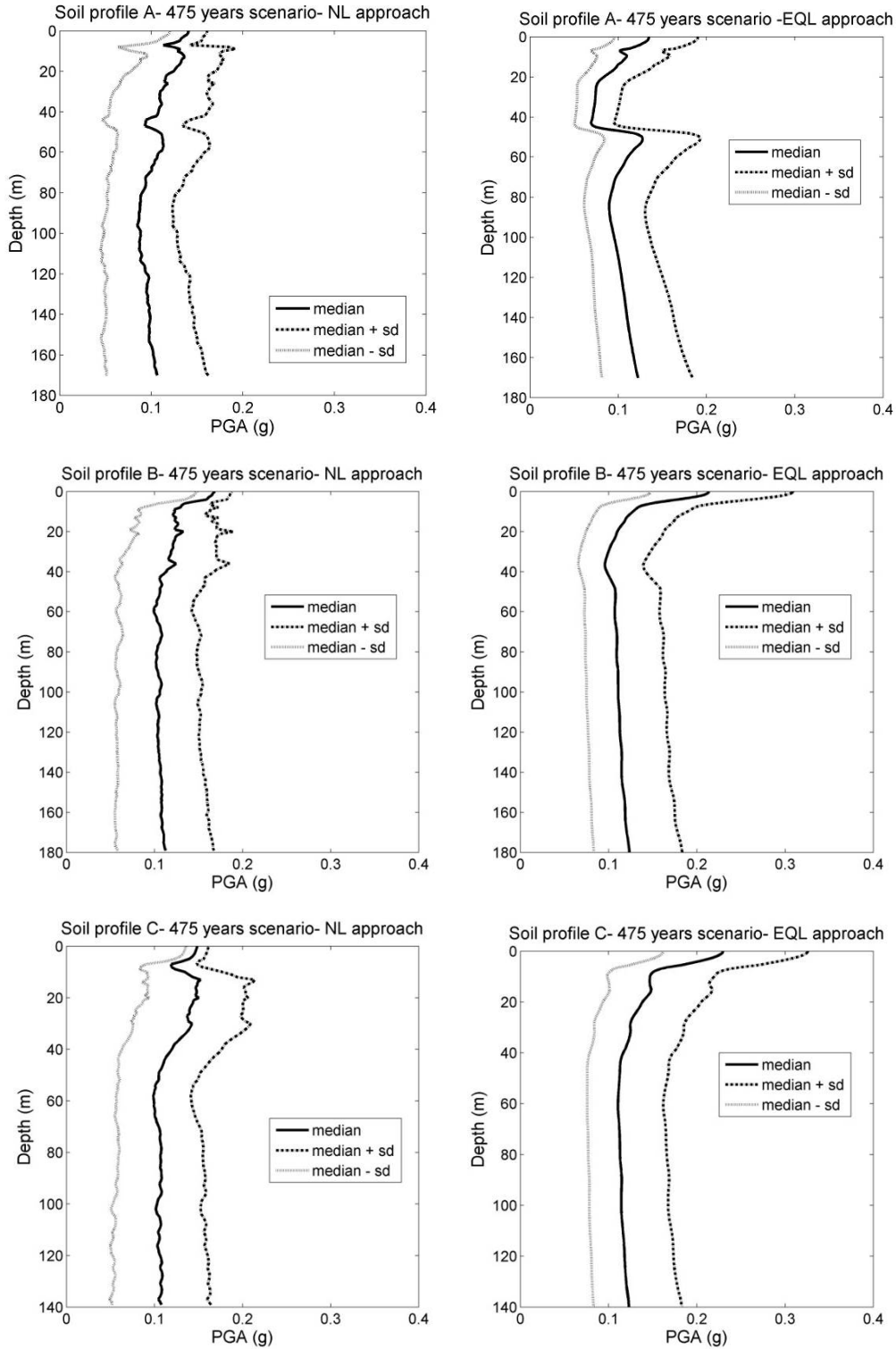
	Depth (m)	USCS	G- $\gamma$ -D curves for soil type	$V_s$ (m/sec)	$c$ (kN/m <sup>2</sup> )	$\phi$ (°)	$Y_m$ (kN/m <sup>3</sup> )
H <sub>2</sub> O↓	2.0	SC-CL 60% & SM,GM, GP	DB-3-->A	225	5	37	18.00
	8.0	ML,SM,ML-OL, SM-ML, SC-SM	C	180	10	26	18.50
	14.0	CL,SC, SC(SM), CL-ML,CH(MH)	B*	200	20	23	20.00
	20.5	CL,SC, SC(SM), CL-ML,CH(MH)	B*	250	20	23	20.00
	28.0	CL,SC, SC(SM), CL-ML,CH(MH)	B*	350	20	30	20.00
	36.0	CL,SC: 80% SC(SM)	B1	400	30	25	21.00
	48.0	CL: 90% SC(GC)	RCL-H--> E	400	30	25	21.00
	68.0	CL: 90% SC(GC)	RCL-L--> E	450	60	27	21.00
	88.0	CL: 90% SC(GC)	RCL-L--> E	500	60	27	21.00
	108.0	CL: 90% SC(GC)	RCL-L--> E	550	60	27	21.00
	128.0	CL: 90% SC(GC)	RCL-L--> E	600	60	27	21.00
	152.0	CL: 90% SC(GC)	RCL-L--> E	650	60	27	21.00
	176.0	CL: 90% SC(GC)	RCL-L--> E	700	60	27	21.00
	180.0	CL: 90% SC(GC)	RCL-L--> E	750	60	27	21.00

Table A.3 Geotechnical characteristics of soil profile C

	Depth (m)	USCS	G- $\gamma$ -D curves for soil type	$V_s$ (m/sec)	c (kN/m <sup>2</sup> )	$\phi$ (°)	$\gamma_m$ (kN/m <sup>3</sup> )
H <sub>2</sub> O↓	1.5	SC-CL 60% & SM,GM, GP	DB-1--> A	225	5	37	18.00
	5.5	SC-CL 60% & SM,GM, GP	DB-1--> A	225	5	33	20.00
	14.5	ML,SM,ML-OL, SM-ML, SC-SM	C	200	10	26	18.50
	20.5	CL,SC: 80% SC(SM)	B1	250	20	23	21.00
	30.5	CL,SC: 80% SC(SM)	B1	300	20	30	21.00
	38.5	CL: 90% SC(GC)	B1	500	30	25	21.00
	46.5	CL: 90% SC(GC)	B1	500	30	25	21.00
	66.5	CL: 90% SC(GC)	RCL-L--> E	550	60	27	21.00
	86.5	CL: 90% SC(GC)	RCL-L--> E	600	60	27	21.00
	110.5	CL: 90% SC(GC)	RCL-L--> E	650	60	27	21.00
	138.5	CL: 90% SC(GC)	RCL-L--> E	700	60	27	21.00
	142.5	CL: 90% SC(GC)	RCL-L--> E	750	60	27	21.00



## B Appendix



**Fig. B.1** Variation of median PGA and median PGA  $\pm 1$  standard deviation with depth for the 475 years scenario

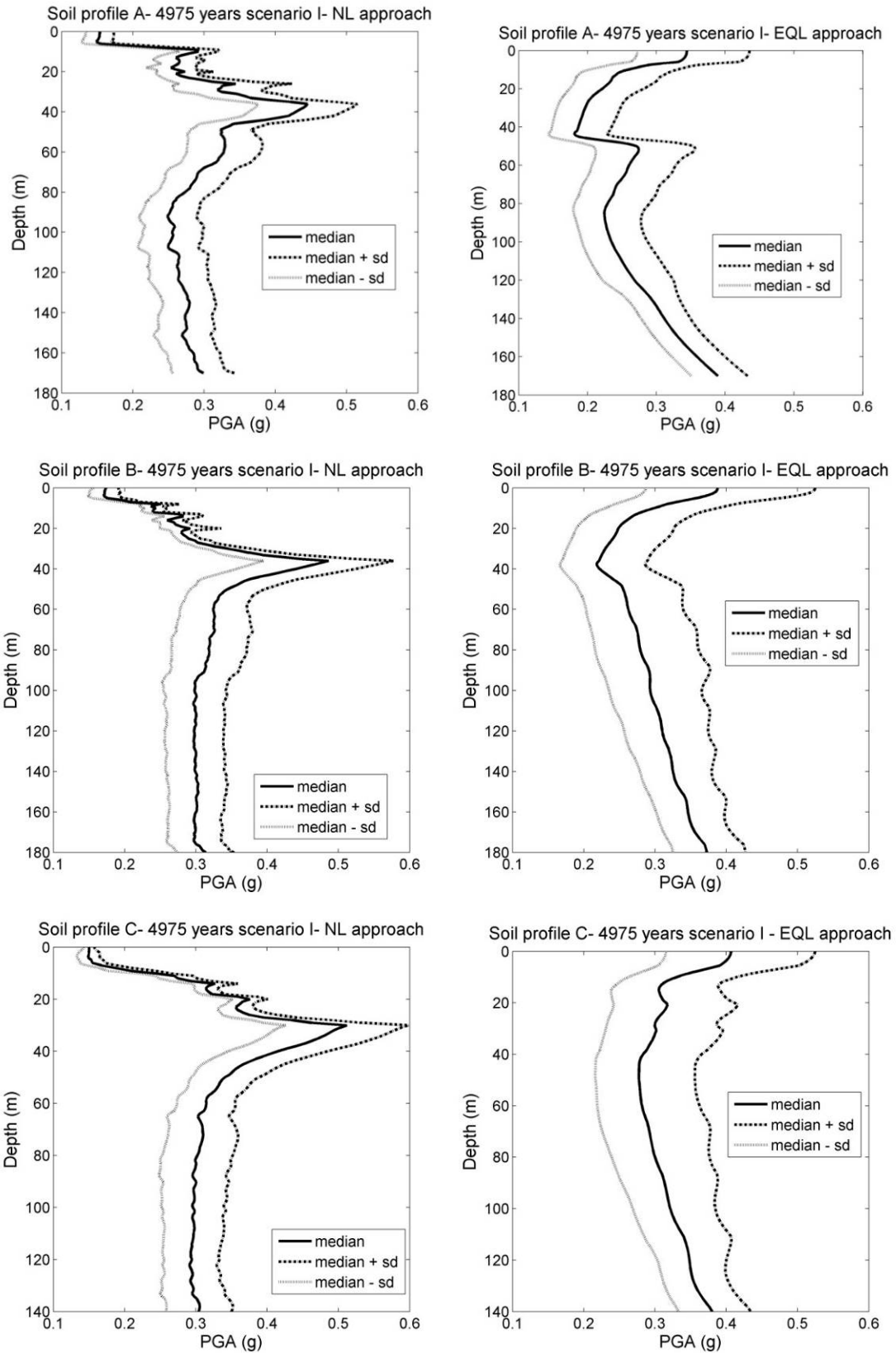


**Fig. B.2** Variation of median PGA and median PGA  $\pm 1$  standard deviation with depth for the 4975 years scenario I

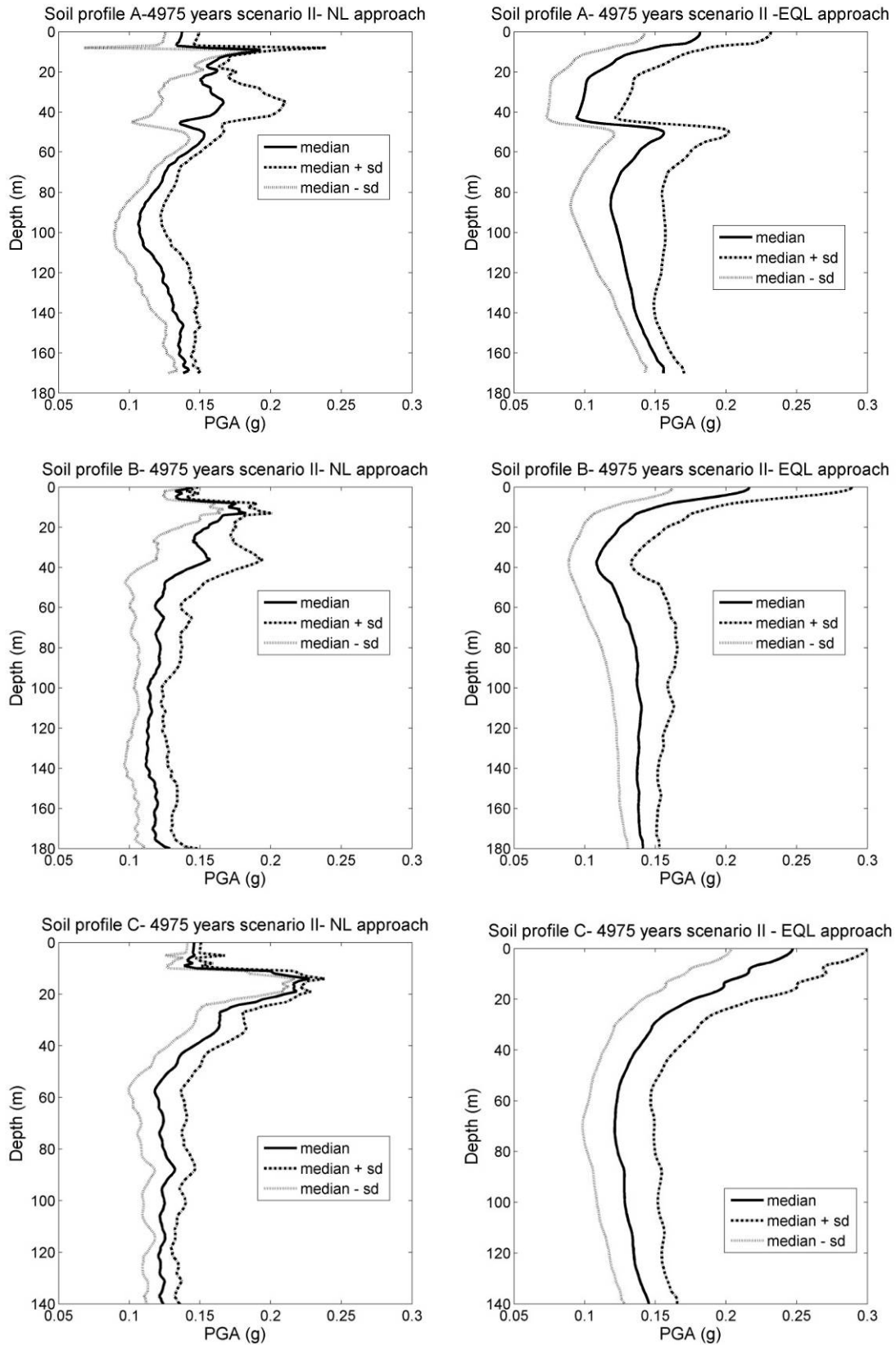


**Fig. B.3** Variation of median PGA and median PGA  $\pm 1$  standard deviation with depth for the 4975 years scenario II



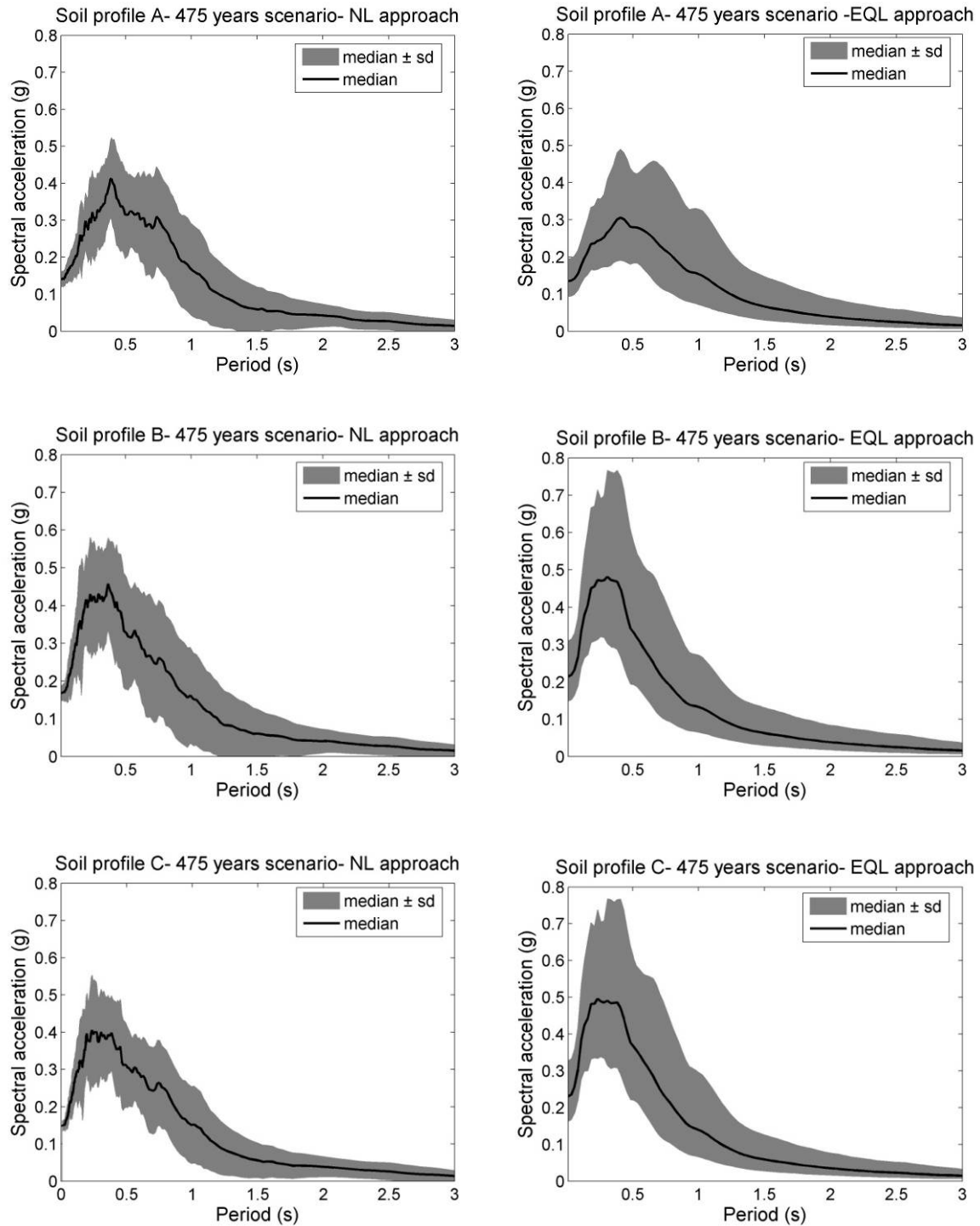


**Fig. B.4 Elastic 5% damped median and median±1standard deviation acceleration response spectra at the ground surface for the three soil profiles derived from the EQL and NL approach for the 475 years seismic scenario**

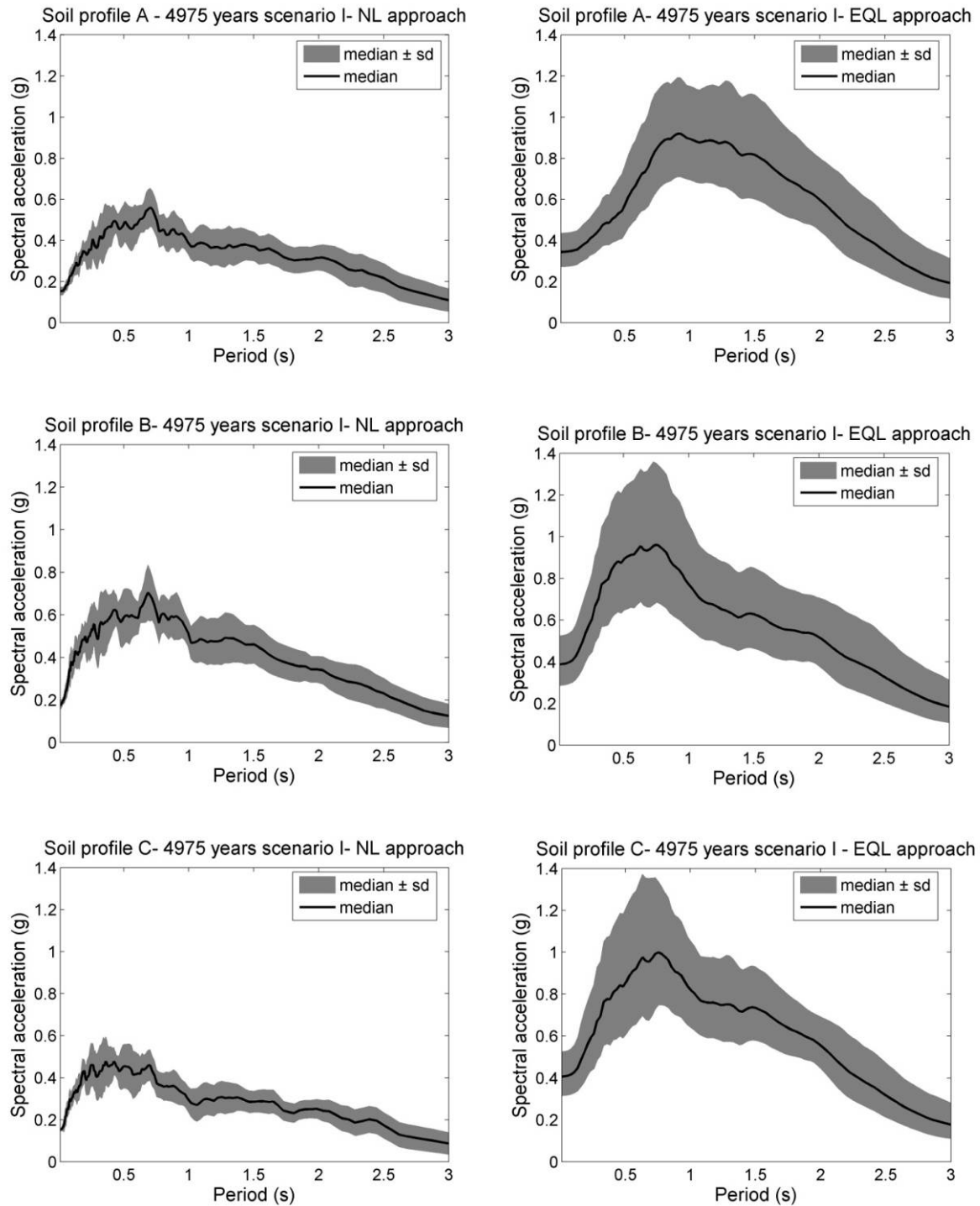


**Fig. B.5 Elastic 5% damped median and median±1standard deviation acceleration response spectra at the ground surface for the three soil profiles derived from the EQL and NL approach for the 4975 years seismic scenario I**

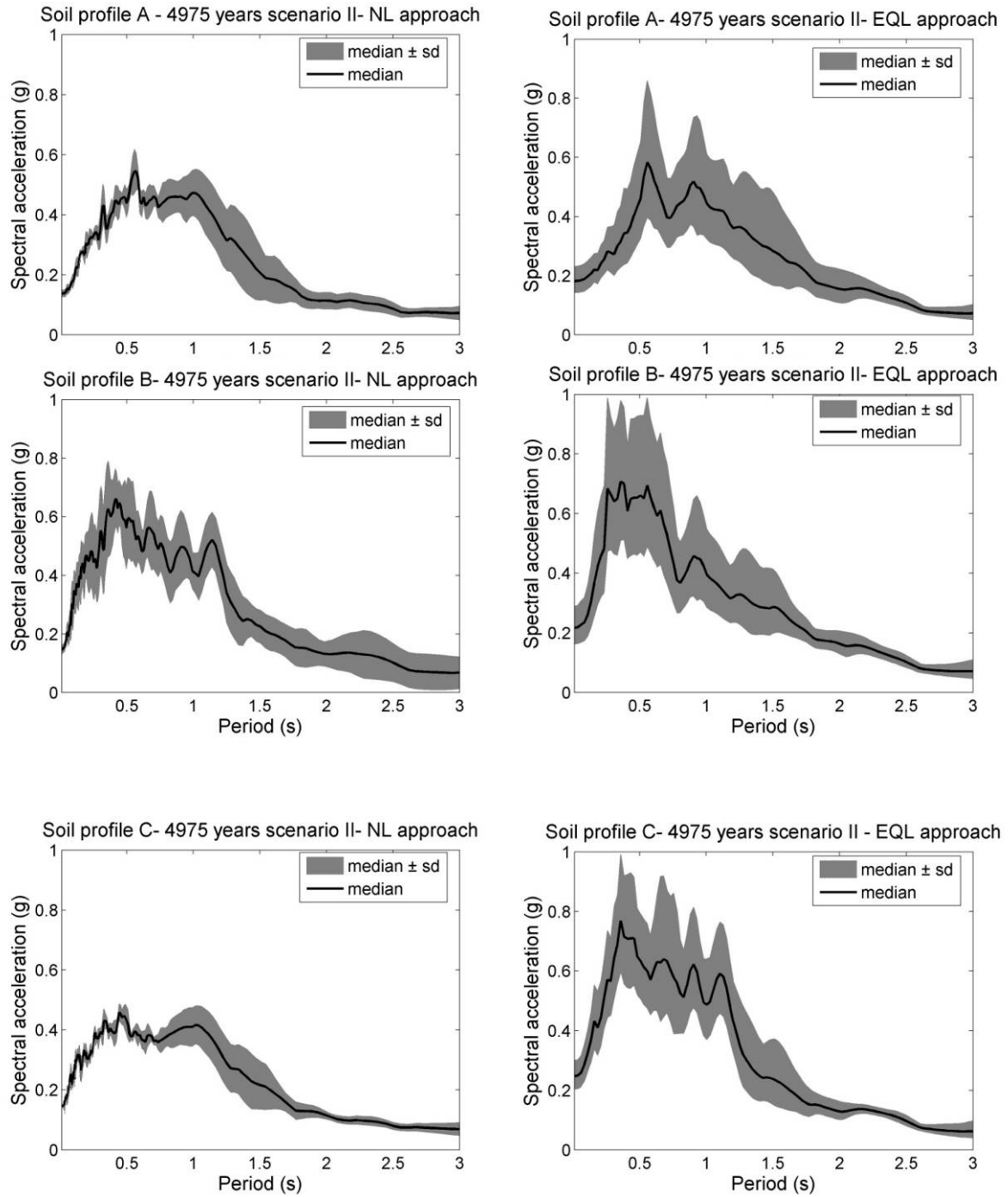


**Fig. B.6 Elastic 5% damped median and median±1standard deviation acceleration response spectra at the ground surface for the three soil profiles derived from the EQL and NL approach for the 4975 years seismic scenario II**

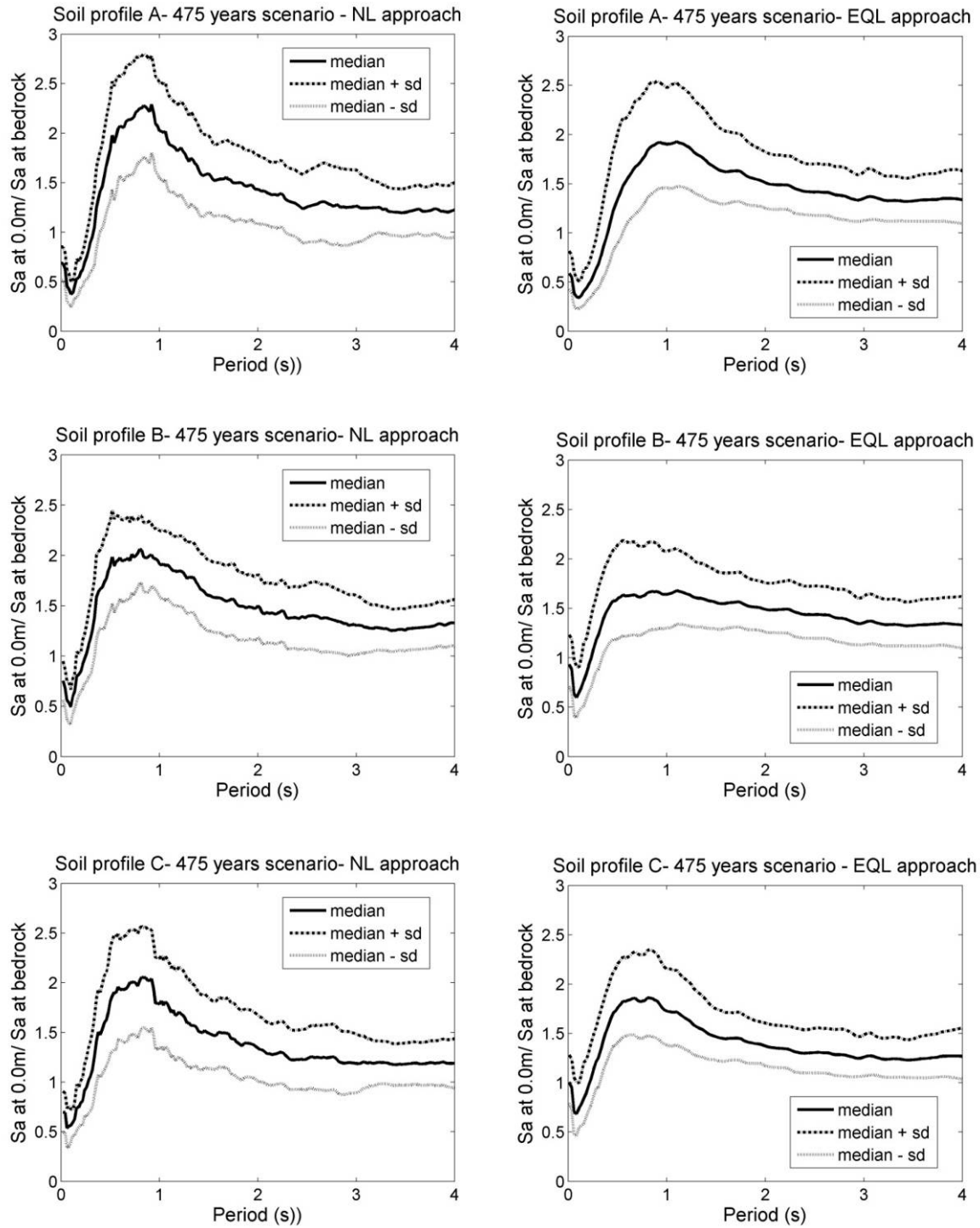


**Fig. B.7 Median and median±1standard deviation spectral ratios for the three soil profiles derived from the EQL and NL approach for the 475 years seismic scenario**

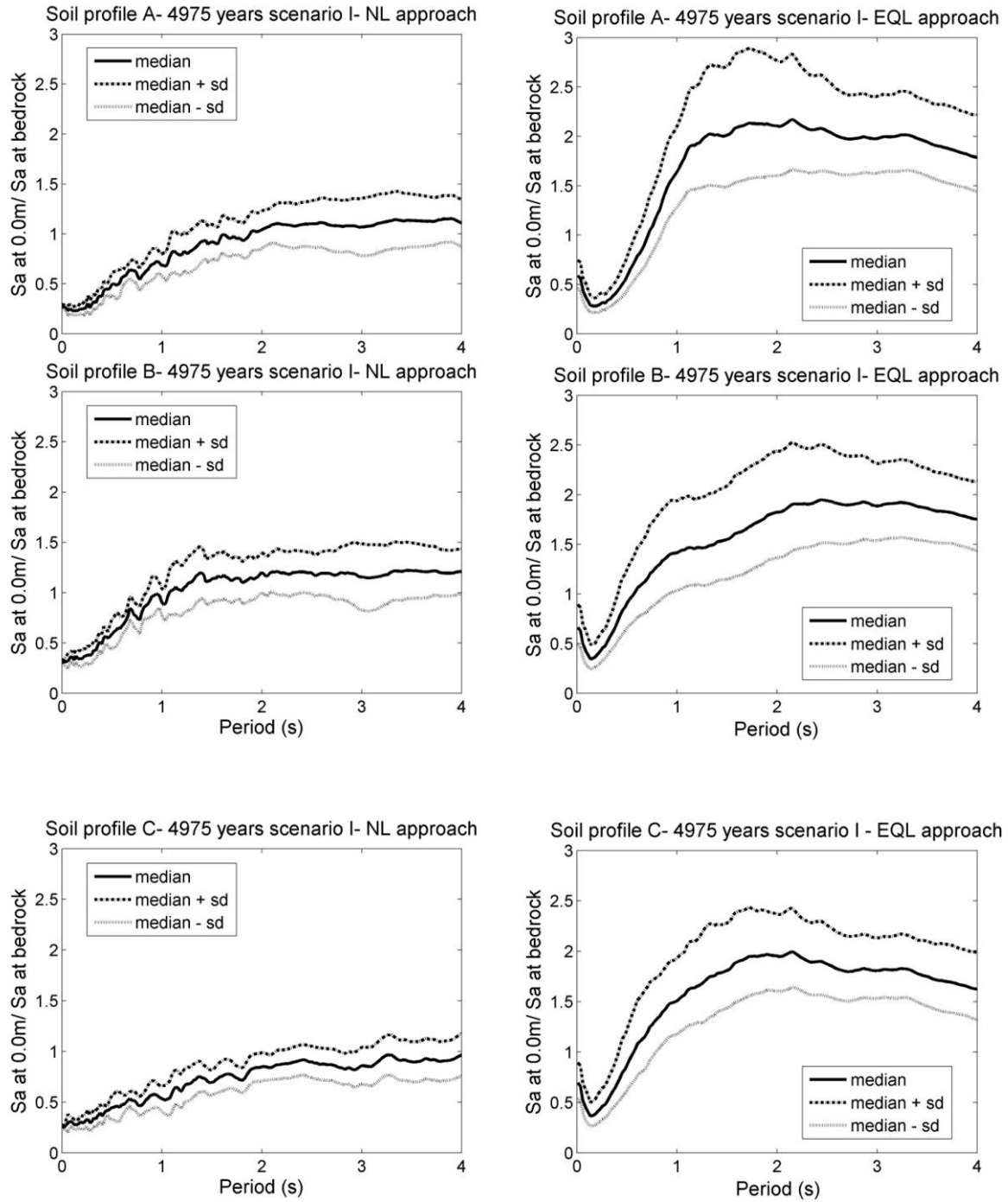


**Fig. B.8 Median and median±1 standard deviation spectral ratios for the three soil profiles derived from the EQL and NL approach for the 4975 years seismic scenario I**

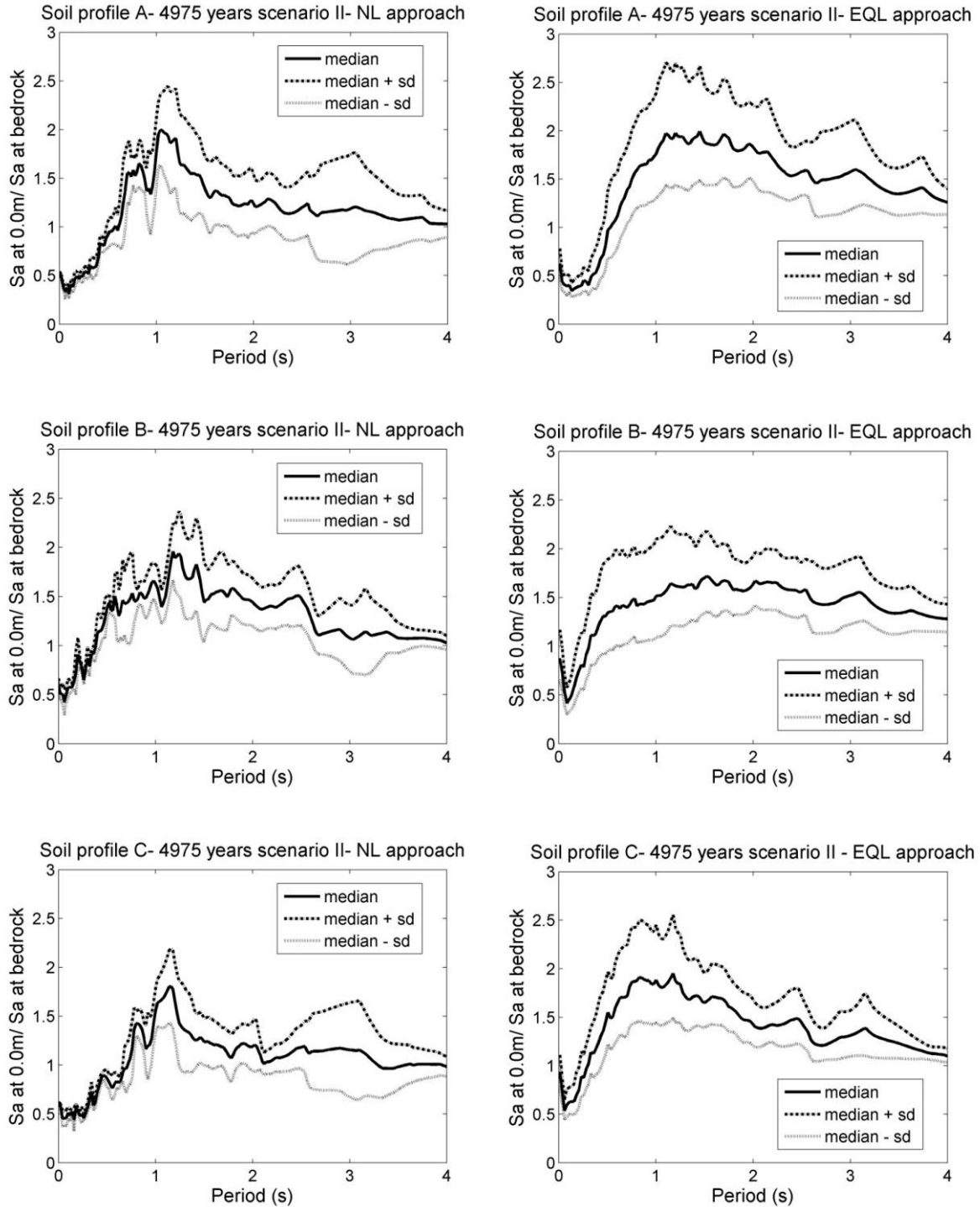


**Fig. B.9 Median and median±1standard deviation spectral ratios for the three soil profiles derived from the EQL and NL approach for the 4975 years seismic scenario II**

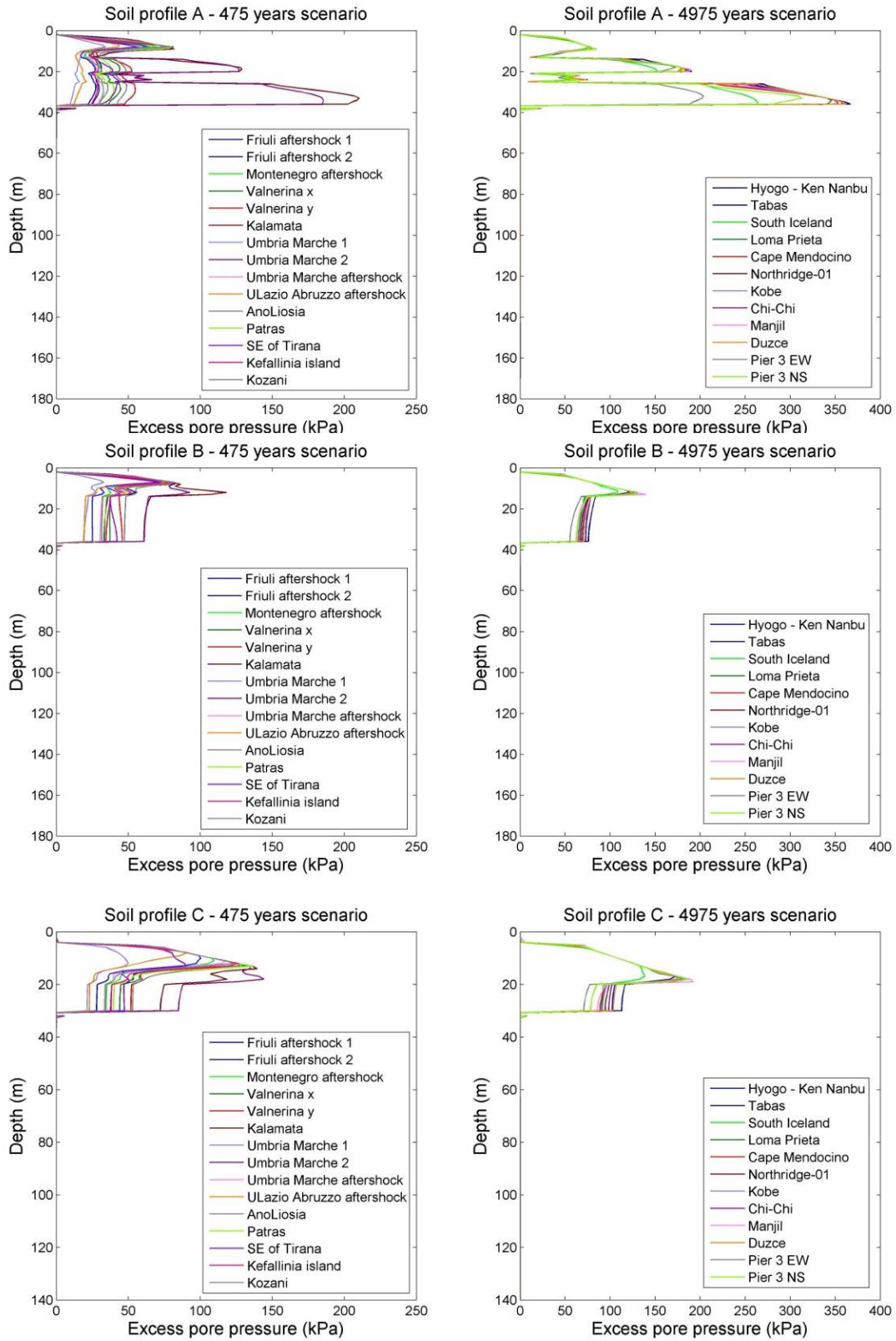


**Fig. B.10** Variation of excess pore pressure profiles with depth for the three soil profiles for the 475 years (left) and 4975 years (right) scenarios

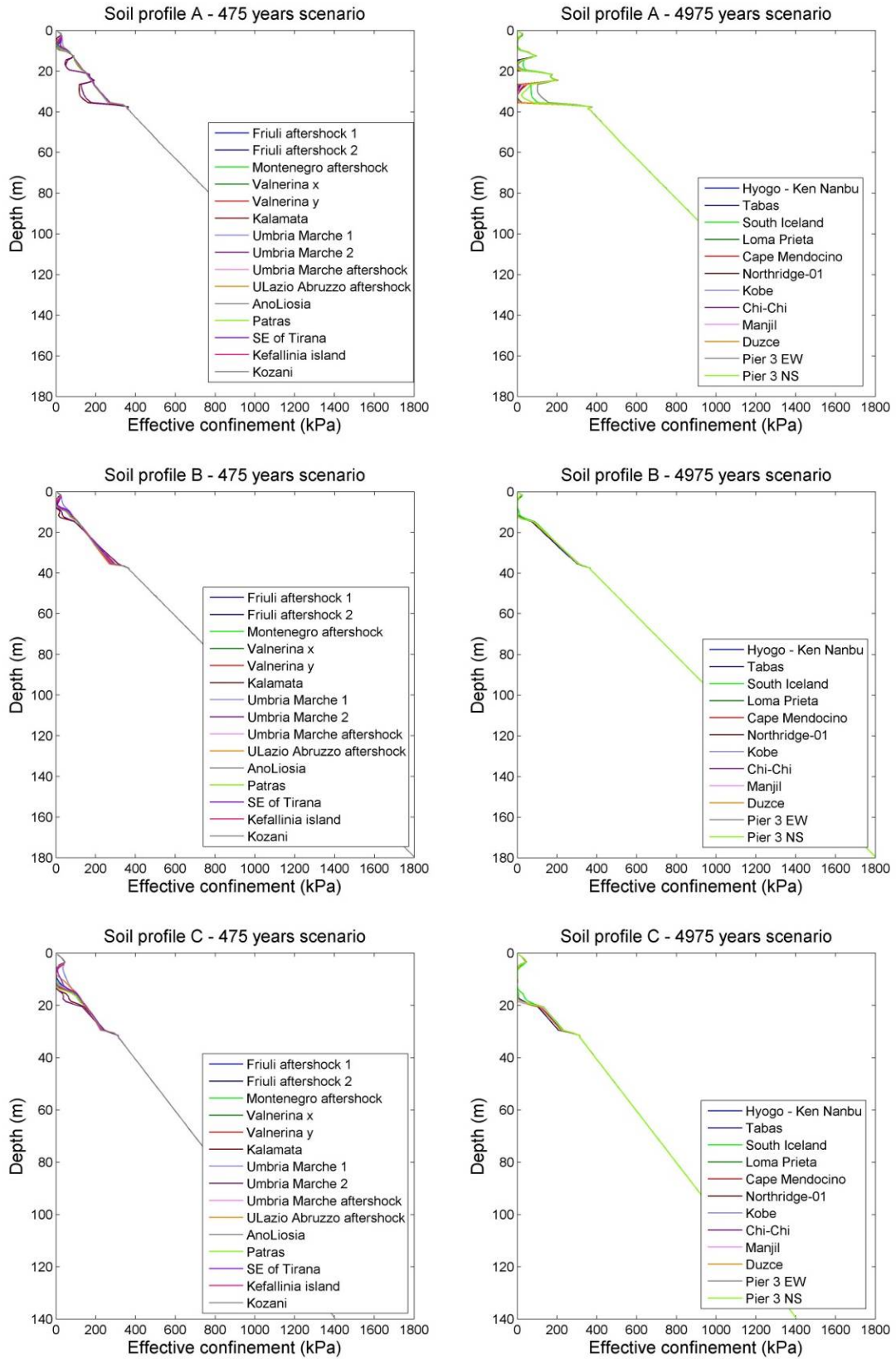


**Fig. B.11** Variation of effective confinement with depth for the three soil profiles for the 475 years (left) and 4975 years (right) scenarios



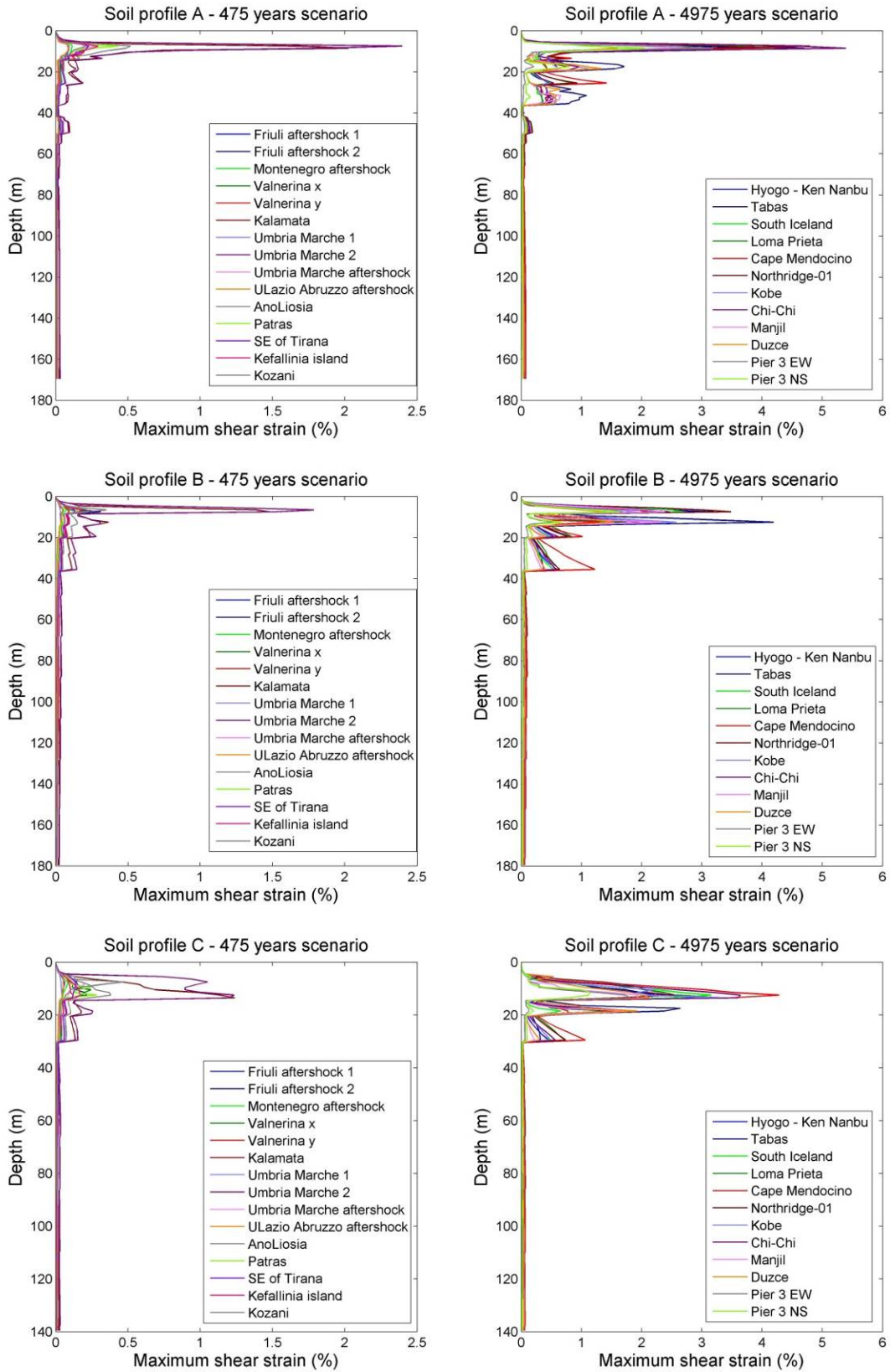


**Fig. B.12** Variation of maximum shear strain profiles with depth for the three soil profiles for the 475 years (left) and 4975 years (right) scenarios

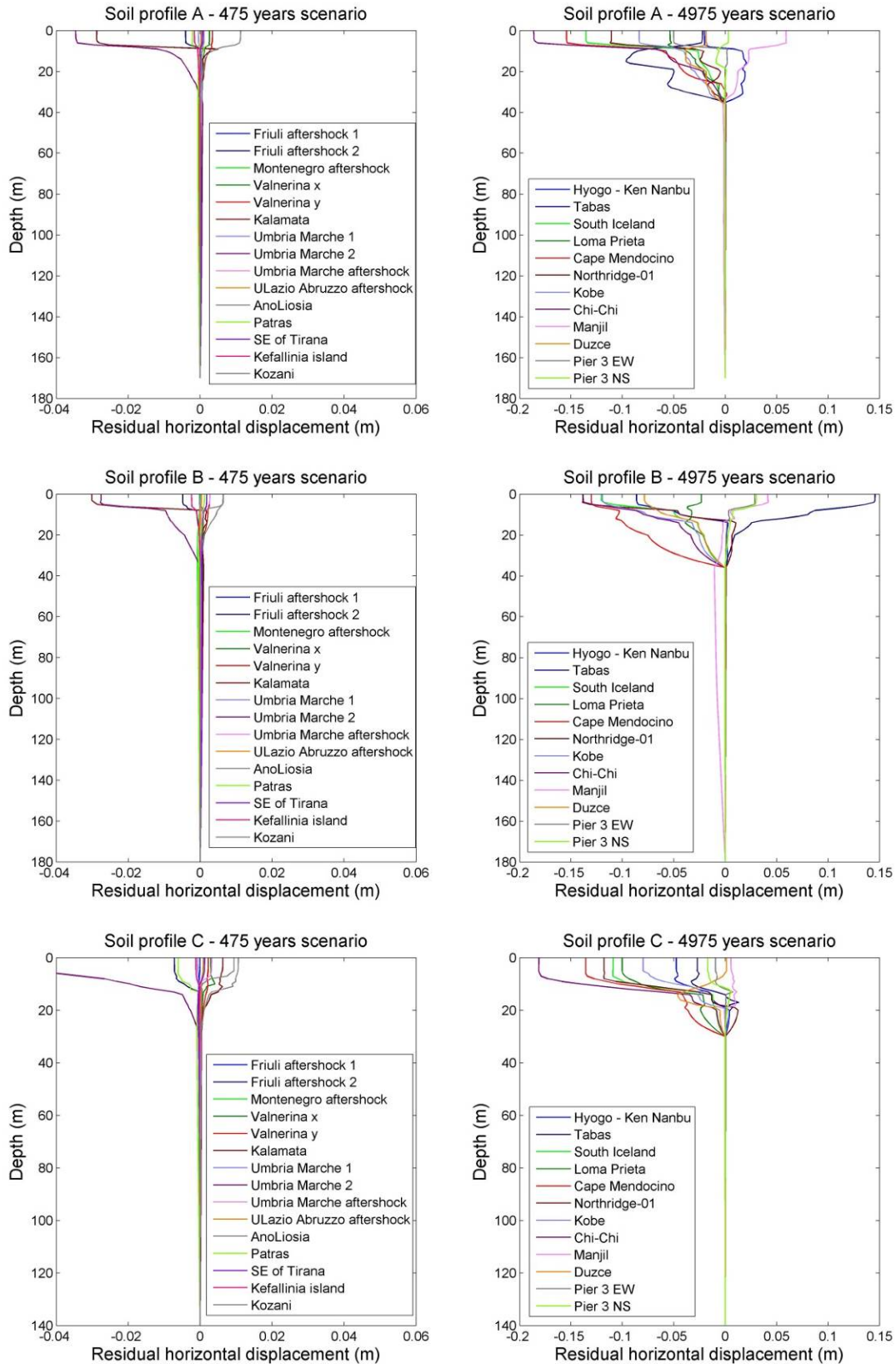


**Fig. B.13** Variation of maximum residual horizontal ground displacement profiles with depth for the three soil profiles for the 475 years (left) and 4975 years (right) scenarios

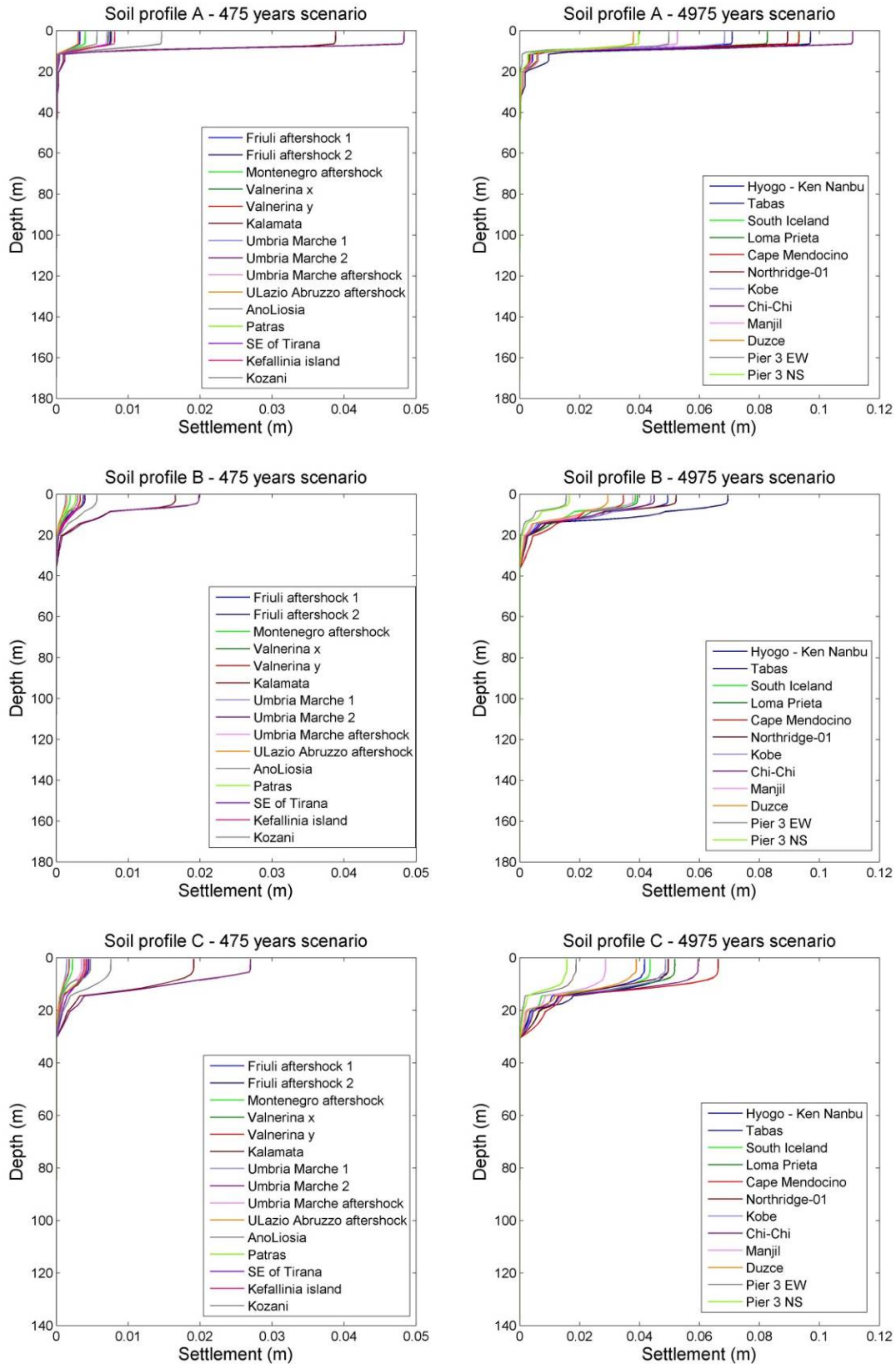


**Fig. B.14** Variation of maximum vertical ground displacement profiles with depth for the three soil profiles for the 475 years (left) and 4975 years (right) scenarios